From micro to nanostructure: an investigation into the connective tissue of the ageing human optic nerve head

A thesis submitted to Cardiff University for the degree of

Doctor of Philosophy

Laura Paletto

School of Optometry and Vision Sciences,

Cardiff University

July 2019

Abstract

The purpose of this thesis was to investigate the micro- and nanostructural changes of the optic nerve head (ONH) regions, namely lamina cribrosa (LC), peripapillary sclera (ppsclera) and region of insertion (RoIns) as a function of age and glaucoma.

The microstructure of ageing and glaucomatous ONHs have been explored following nonlinear microscopy [two-photon excited fluorescence (TPEF) and second harmonic generation (SHG)]. Small-angle (SAXS) and wide-angle (WAXS) X-ray diffraction have been used to explore into the nanoarchitecture of collagen and elastic fibre in the ageing ONH. X-ray microtomography (XMT) was used to assess microstructural changes of the ONH in age and glaucoma. Micro- and nanomechanics have been explored following Brillouin microscopy and the combination of SAXS/WAXS, respectively.

In the ageing ppsclera, collagen crimp period increased from 19.64 ± 6.41 μm at the age 2 to 22.04 ± 10 μm at the age of 88 years ($p=0.004$). Elastic fibre content significantly increased from 0% in the 2 years old up to 29% in the 88 years old ($p=0.003$) in the LC and from 0% up to 49% ($p=0.019$) in the region of insertion. Significant increase in collagen fibril diameter [from 98.98 nm ± 0.9 at 22 years old to 113.01 nm ± 1.5 at the age of 85 ($p=0.026$)] and intermolecular Bragg spacing [from 1.44 nm ± 0.12 to 1.53 nm ± 0.32 ($p=0.022$)] were found along with a decreased interfibrillar spacing [from 37.63 nm ± 7.22 to 12.6 nm ± 4.54 ($p=0.003$)]. Collagen crimp significantly increased in the LC and region of insertion in moderate ($p=0.013$, $p=0.013$) and advanced ($p=0.021$, $p=0.033$) glaucoma. XMT enabled the discrimination of the connective tissue from the surrounding neuronal pores and 3D reconstruction of XMT dataset showed altered LC and pore shape in glaucomatous ONH.

In conclusion, changes in the connective tissue of the ageing and glaucomatous ONH at both micro- and nanostructure aided in a better understanding on how the ONH responds to intraocular pressure elevation.

Acknowledgment

First and foremost, I would like to thank my supervisors Dr. Julie Albon, Prof. Vic Duance and Dr. Craig Boote, without their guidance, encouragement and dedication this PhD thesis would have not been possible. Thank you for your endless patience and support throughout these years. Thank you, Vic, for having cheered me up when I thought my English was not good enough for this PhD. Thank you, Craig, for all your immense knowledge about x ray diffraction and for having answered thousands of silly questions about SAXS and WAXS. Finally, I cannot thank you enough Julie, for all your friendly words which have made my bad days at least little bit better. Thank you for having supported me anyway and anyhow and for having answered silly questions. Thank you for helping me to grow as a person and as a researcher, thank you for having made me see things with other eyes and perspective and thank you for all the times you made me think with my own brain.

I would like to thank the Filton Eye Bank and the Mayo Clinic (Rochester, USA) for providing healthy and glaucomatous donor eyes, without which this project would have not been possible. Especially, thank you to Dr. Paul Rooney and Prof. Mike Fautsch for agreeing in sending us globes for our research and for being there to sort out transfer agreements and payments.

I would like to thank Diamond Light Source facilities in Didcot, Oxford, especially people on beamline I22 and I13-2. My special thanks go to Dr. Olga Shebanova, Prof. Nick Terril and Dr. Tim Snow as part of the scientific team on beamline I22. Without this team all my SAXS and WAXS experiments would not have been possible. A special thank goes to Olga who helped and supported me during long days on station I22. Thank you to Tim, the guru of DAWN software for x ray analysis, thank you for having taught me how to analyses SAXS and WAXS data properly, thank you for all the endless email exchange trying to sort out problems.

I would also like to thank all the team on I13-2 x ray microtomography beam line. Thank you to Dr. Andrew Bodey and Prof Chris Rau for the endless support that they gave us throughout the 48 hours beamtime. Also, my big thank goes to Dr. Kas Walik for all the support and data reconstruction advices. Thank you for staying outside your working hours and for all the Savu coding. Without Kas, chapter 4 would have not been possible.

I am also grateful to the people of the Department of Geology and biophysics of the University of Perugia, Italy for hosting me and teaching me the basics of Brillouin and Raman spectroscopy. I would like to express my sincere thank you to Prof. Daniele Fioretto and Martina Alunni Cardinali for all the help on spectra analysis and interpretation. I specifically express my gratitude

to Martina for having done the double Brillouin fitting and having shared all the results. I would also like to thank Dr. Francesca Palombo and Dr. Ellen Green from Exeter University for providing the contacts of researchers in Perugia and samples of purified nuchal ligament and porcine ear used, respectively, in chapter 3 and 5.

I would also express my sincere gratitude to all the people that kept me sane and calm during these years. In particular, people in office 2.11 (and upstairs) who supported me throughout the years with endless conversations about each other's project. Also, I thank Ryan, the "other half" of the optic nerve head group for all the morning coffees and breaks that kept me awake, sane and provided distractions during my writing up desperation.

My sincere gratitude also goes to Nick, for being there all the time answering my silly questions about microscopy. Nick has been there for the whole PhD journey, supporting and encouraging me even during desperation time due to my little knowledge about physics and math. Thank you for having taught me 90% of the techniques presented in this thesis and for always being available no matter what the issue was.

Last but not the least, my family and my *husband to be*. Thank you, guys, for being there. Thank you to my parents for the endless conversation we had, trying to explain simply what I do. They probably never really understood it, but they always said they did. Thank you for all the encouragement you gave me, thank you for being there, no matter what, thank you for always believing in me.

Thank you lovely "hubby-to-be" for being my friend, my soul and my professor all at once. Thank you for teaching me MATLAB (although I am still not sure I really learnt it), thank you for spending hours trying to make me understand basics of physics and math, thank you for being there no matter what. Thank you for having shown me the good of being a researcher, a scientist. Thank you for being there, always!

Finally, thank you to School of OPTOM and BIOSI to fund my PhD and allowed me to travel throughout the UK and Italy to carry out experiments. Thank you for allowing me to attend several conferences that made my CV better.

Thank you to DSTL people and colleagues (Ben, Sian, Julie and Keith) for allowing me to get on the project meantime I was still writing up. This has been great, and it has allowed me to do different experiments and focus my mind on something new.

Dedication

I dedicate this thesis to the people that witnessed the beginning of this journey but that unfortunately could not see the end.

To my grandparents, who witnessed my departure from Turin four years ago looking for a treasure somewhere else. I strongly believe they see me, and they are with me at all time. They always thought I could have made it, they were sure I was made for this job and even though sadly, they encouraged me to leave Italy and to be extraordinary.

To Nick White, our microscopy guru, the person that taught me how to ask myself questions, even though there is not an answer. Nick trained me and taught me most of the techniques presented in this thesis and he has always been there to answer my silly physics-related questions. He was always willing to repeat concepts and stories until he was sure I understood it. He was the person you go to when any problem related to math, physics or microscopy of any kind arise.

Thank you, grandparents, to have always believed in me.
Thank you, Nick, for all the discussion and for always been willing to answer any question I had.

Table of contents

List of Figures

List of tables

List of Abbreviations

AGE	Advanced glycation end products
ANOVA	Analysis of variance
ASCO	Anterior scleral canal opening
AUC	Area under the curve
BROPA	Brain-wide Reduced Osmium Pyragallol-mediated Amplification
CaF	Calcium fluoride slide
CNS	Central nervous system
CoR	Centre of Rotation
CRA	Central retinal artery
CSF	Cerebrospinal fluid
CTGF	Connective tissue growth factor
DAWN	Data Analysis Work bench
DHO	Damped harmonic oscillator
DLS	Diamond light source
ECM	Extracellular matrix
EF	Elastic fibre
EM	Electron microscopy
FACIT	Fibril-associated collagens with interrupted triple helices
FAD	Flavin adenine dinucleotide
FT	Fibril transform
FWHM	Full width at half maximum
GAG	Glycosaminoglycan
GFAP	Glial Fibrillar acid protein
GHOST	Group of High-resolution Optical Spectroscopy and related Techniques
HA	Hyaluronan
HP	Hydroxyproline
HTA	Human tissue act
ICP	Intracranial pressure
IF	Interference function
IOP	Intraocular pressure
IQR	Interquartile range
LC	Lamina cribrosa
LED	Light emitting diode
LOX	Lysis oxidase

LP	Lysyl pyridinoline
LS	Longitudina
MD	Mean deviation
MIP	Maximum intensity projection
MMP	Metalloproteases
mRNA	Messenger RNA
MULTIPLEXIN	Multiple triple-helix domains and interruptions
MYOC	Myocilin
NaCl	Sodium chloride
NADH	Nicotinamide adenine dinucleotide
NaOH	Sodium hydroxide
NCAM	Neural cell adhesion molecule
NDD	Non-descanned detector
NHSBT	NHS Blood and Transplant
NIH	National institute of health
NIR	Near infrared
NLO	Nonlinear optics
NOS	Nitric oxide synthase
NT	Neurotrophin
ON	Optic nerve
ONH	Optic nerve head
PBS	Phosphate buffer saline
PFA	Paraformaldehyde
PG	Proteoglycan
PNS	Peripheral nervous system
POAG	Primary open angle glaucoma
PostL	Postlaminar region
ppsclera	Peripapillary sclera
PreL	Prelamina
PTA	Phosphotungstic acid
RGC	Retinal ganglion cell
RNA	Ribonucleic acid
RNFL	Retinal nerve fibre layer
ROI	Region of interest
RoIns	Region of insertion
RPE	Retinal pigment epithelium
RTA	Rat aorta

RTT	Rat tail tendon
SALS	Small angle light scattering
SAXS	Small angle X-ray scattering
sd	Standard deviation
SEM	Scanning electron microscopy
SHG	Second harmonic generation
TA	Tannic acid
TE	Tropoelastin
TEM	Transmission electron microscopy
TGF-β	Transform growth factor β
TPEF	Two-photon excited fluorescence
TS	Transverse
WAXS	Wide angle X-ray scattering
XMT	X-ray microtomography
α-SMA	alpha-smooth muscle actin

Chapter 1 – General introduction

1.1 Introduction

The optic nerve (ON) is the second cranial nerve and consists of axons that transmit visual information from the retina to the brain. In humans, the ON consists of over 1 million retinal ganglion cell (RGC) axons and glial cells (Anderson, 1973). The ON extends from the optic disc to the optic chiasm and continues as the optic tract to the lateral geniculate nucleus (Selhorst and Chen, 2009). These axons converge at the optic disc and enter the ON at the optic nerve head (ONH).

Glaucoma is the most common cause of irreversible blindness affecting 80 million people worldwide by 2020 (Quigley and Broman, 2006). Glaucoma is associated with progressive vision loss due to RGC death. The lamina cribrosa (LC) of the ONH has been proposed to be the main site of axons damage (Howell et al., 2007, Quigley and Addicks, 1981, Quigley et al., 1981, Vrabec, 1976).

1.2 The optic nerve head

The ONH presents an oval shape, in which the mean diameter in the Caucasian population is 1.88 mm vertically and 1.70 mm horizontally (Quigley et al., 1990). When viewed in longitudinal sections, central retinal vessels, neural retina and dural sheaths can be recognised (figure 1.1). The ONH is mechanically interesting as it is considered a "weak" spot within the surrounding stiff sclera and it can suffer from changes in the structure such as those that happen in glaucoma (Quigley and Addicks, 1981, Jonas et al., 1991, Tezel et al., 2004).

1.2.1 Anatomy of the optic nerve head

Histologically, the ONH can be divided into three zones. These include the prelamina (preL) (anterior part terminating at the vitreous), lamina cribrosa (LC) and postlaminar (postL) ON.

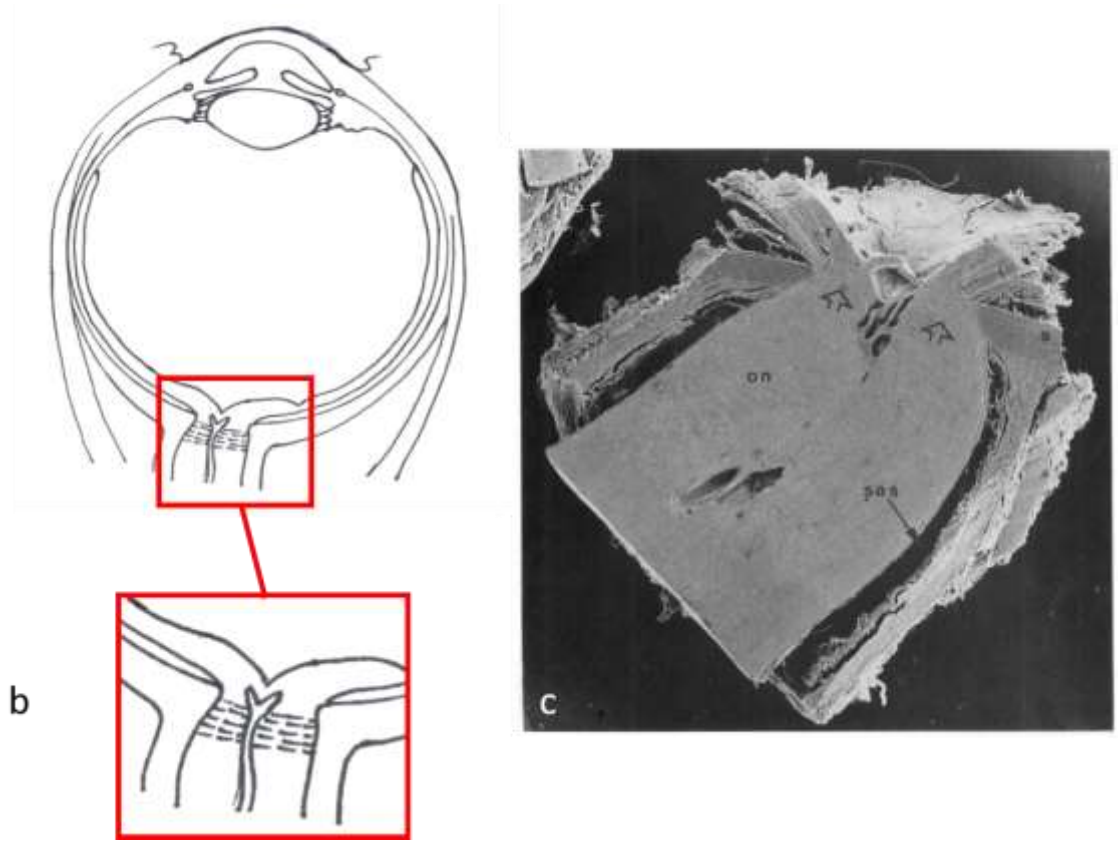

Figure 1.1.The human optic nerve head. Schematic diagram (a) showing the human globe and the position of the optic nerve head. Scanning electron microscopy (b) image of a longitudinal section of the ONH revealing anatomical boundaries with the LC (open arrow). Note the diameter of the optic nerve (on) increases when the distance from the LC increases. The subarachnoidal space (sas), the sclera (s) and the retina (r) are also shown and the central retinal vessels were cut obliquely to show their path through the ON. Copied from (Elkington et al., 1990) and reprinted with permission from Elsevier Limited (see appendix IV.1).

1.2.1.1 Prelamina

The preL consists of RGC axons that converge at the optic disc where they aggregate and enter the ON. The inner surface is covered by a lining of astrocytes; the layer of Elschnig, and at the centre of the disc, this layer of astrocytes become thicker into a central meniscus, known as the meniscus of Kuhnt. The preL mostly consists of ON fibres grouped into bundles, called fascicles, which are surrounded by astrocytes, which provide support to the fascicles (Anderson, 1969).

1.2.1.2 Lamina cribrosa

The lamina cribrosa (LC) is a sieve-like structure consisting of successive connective tissue plates which surround pores through which RGC axons pass on their way to the brain (figure 1.2a). The LC forms a support for the nerve fibre fascicles, and it strengthens the posterior eye, protecting it from injuries at the site where the ON exits (Hogan et al., 1971). In this role, the lamina cribrosa of primates (e.g. human) has developed an intricate and robust network of three-dimensional (3D) connective tissue.

The LC has approximately 10 plates called cribriform plates (figure 1.2a) composed by connective tissue fibres (collagen and elastin) that extend to the sclera (Hogan et al., 1971). The LC cribriform plates contain pores, that range between 20-200μm in diameter, which forms a sieve-like structure (figure 1.2b) (Elkington et al., 1990, Oyama et al., 2006).

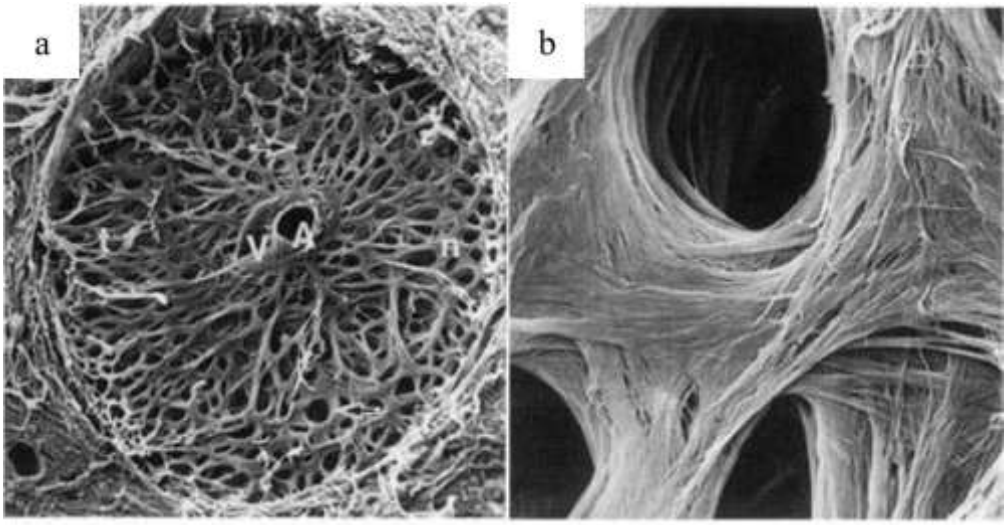

Figure 1.2. Scanning electron microscope image of the LC. The LC is a sieve-like structure composed by connective tissue surrounding pores (a) through which RGC axons pass. n=nasal, t=temporal. Note the central retinal artery (A) and vein (V) in the centre. A magnified pore (b) showing the collagenous network in which fibrils appear circularly oriented around the pores. Adapted and reprinted from (Thale et al., 1996) with permission from the International journal of ophthalmology (see Appendix IV.2).

The LC is not a homogeneus tissue as demonstrated by Quigley and Addicks (1981). The inferior and superior regions have larger pores and less connective tissue supporting axons when compared to the nasal and temporal regions (Quigley and Addicks, 1981, Radius and Gonzales, 1981, Oyama et al., 2006). Additionally, the size of the pores

increases as the distance from the central region towards the periphery increases (Jonas et al., 1991). It has been reported in an *in vivo* study, that the mean pore area in the healthy human LC was 1713 ± 1413 μm^2, with a range from 154 μm^2 to 6637 μm^2 (Ivers et al., 2011). More pores have been observed at the posterior LC surface, with anterior pores being larger than those in the posterior LC (Ogden et al., 1988). Pores are not continuous through the LC depth, (Quigley and Addicks (1981), as they appear to subdivide as they travel through the LC.

1.2.1.2.1 Cells of the lamina cribrosa

In the LC, astrocytes provide support to the axons within the neuronal pores, (Anderson, 1969). Overall, there are regional and functionally different astrocytes that provide cellular support and they synthesise extracellular matrix (ECM). Two different sub-population of astrocytes have been observed in the human LC. Type 1A astrocytes are interspersed within the glial columns at the edges of the cribriform plates and they express glial fibrillar acid protein (GFAP), a marker for astrocytes, but do not express neural cell adhesion molecule (NCAM). Type 1B astrocytes express both GFAP and NCAM and they are the major glial cell population and the major source of ECM (Hernandez, 1992, Hernandez et al., 1991, Ye and Hernandez, 1995). GFAP and NCAM positive astrocytes type 1B surround the nerve fascicles, separating them from the connective tissue beams (Oyama et al., 2006).

In addition to astrocytes, LC cells were found located within cribriform plates which can be distinguished from astrocytes as they do not express GFAP (Hernandez et al., 1988). These, in association with astrocytes, play an important role in maintaining and synthesising the ECM (Hernandez et al., 1988).

Studies have characterised human LC cells from explants, reporting the expression of α-smooth muscle actin (α-SMA) by LC cells, but not ONH astrocytes (Tovar-Vidales et al., 2016, Rogers et al., 2012). Recently, messenger RNA (mRNA) expression of neurotrophins 3 and 4 (NTs) has been identified in both LC cells and ONH astrocytes, suggesting that these contribute to RGC rescue after injury (Lambert et al., 2004a, Lambert et al., 2004b, Lambert et al., 2001). Additionally, quiescent microglia cells have been found in the LC, located within the wall of blood vessels and surrounding capillaries within the cribrifom plates (Neufeld, 1999a). Microglia protect neural tissue and can play an important role in defending and repairing damaged tissue (Kreutzberg, 1996).

1.2.1.3 Postlaminar optic nerve

In the postL ON, axons become myelinated and the connective tissue septae penetrate the ON from the pia mater, dividing it into 300–400 fascicles (Goldbaum et al., 1989). The pia mater is the inner layer of meninges, the membranes surrounding the brain and the spinal cord as well as the ON. Its main function is to cover and protect the central nervous system (Millen and Woollam, 1961). Connective tissue septae are thicker than the LC beams (Oyama et al., 2006), and are proposed to be responsible for giving tensile strength to the ON bundles.

1.2.2 The extracellular matrix of the lamina cribrosa

The ECM of the LC is composed of connective tissue components such as collagen, elastin and proteoglycans and provides support for the axons that are passing through the LC pores.

1.2.2.1 Collagen

Collagen is the most abundant structural protein in animals and it is important in giving structure, support and tensile strength to tissues (Vogel, 1980). In humans, collagen comprises one third of the total protein and it is the most prevalent component of the ECM. There are 29 different types of collagen, composed of 46 distinct polypeptide chains (Shoulders and Raines, 2009, Söderhäll et al., 2007). Collagen consists of three polypeptide chains, known as α chains, numbered with Arabic numerals. These three α-chains are then twisted around to produce the triple-helix that forms the collagen molecule (Ramachandran and Kartha, 1954). The fibrillar collagens are asymmetric and have three distinct domains, the NH_2-terminal domain, the COOH- terminal domain and the central helical domain (figure 1.3).

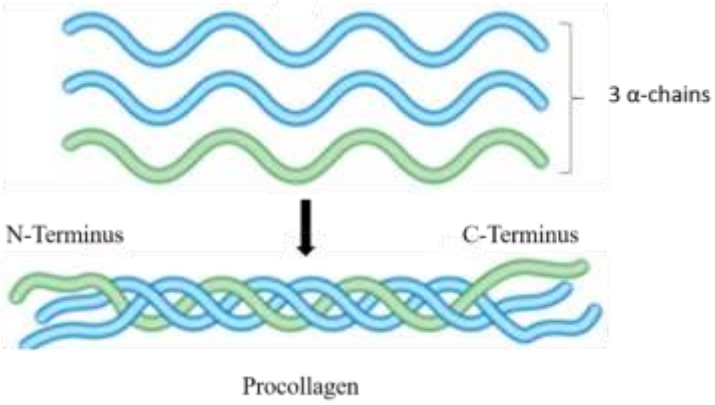

Figure 1.3. Collagen molecule. Three α-chains are wrapped around and assembled to produce the triple helix that forms the molecule. The asymmetric molecule has a NH_2-terminal domain and the COOH- terminal domain. Adapted and reprinted from (Tang et al., 2017) with permission from Elsevier Limited (see appendix IV.3).

The triple-helical structure of collagen is dependent on an unusual abundance of three amino acids: glycine, proline, and hydroxyproline. These amino acids make the characteristic repeating motif Glycine-X-Y, where X and Y can be any on these two amino acids but often, the amino acid at X is proline, and at Y is 4-hydroxyproline (Fallas et al., 2009).

1.2.2.1.1 Collagen types

Beyond the existence of 29 different collagen types, more variety exists in the collagen family due to several molecular isoforms of the same collagen type (e.g. collagen types IV and VI) or a hybrid isoform composed of chains of two different collagen types (e.g. type V/XI molecule) (Ricard-Blum and Ruggiero, 2005, Ricard-Blum, 2011).
Each α-chain of the fibrillar collagens contains approximately 1050 amino acid residues (Miller and Wray, 1971) on which collagen types are classified. Overall, collagen can be classified into fibrillar, network-forming, MULTIPLEXIN (multiple triple-helix domains and interruptions) (Shoulders and Raines, 2009) and FACIT (fibril-associated collagens with interrupted triple helices). The predominant collagen types within the ONH are fibril forming collagens, namely collagen types I, III and V (Albon et al. 1995).

Collagen type I is the most abundant collagen type in skin, tendons, ligaments and cornea (Fleischmajer et al., 1990). Collagen type III is a homotrimer of three α chains and it is

usually found in tissues where collagen type I is the major component (von der Mark, 1981). Types V and XI are formed as heterotrimers of three different α chains and types III and V collagen can form heterotypic fibrils with type I collagen, contributing to the control of fibril diameter (Birk, 2001). Type VI is a heterotrimeric molecule of three different α chains, whereas type X and VIII are related to short chain collagens. Type IV is the most abundant collagen in the basement membranes, integrating with laminin (Hudson et al., 1993). Collagen types IX, XII, XIV, XVI and XIX belong to the fibril associated collagen with interrupted triple helix (FACIT). The structure of these collagens is characterised by domains interrupted by short non-helical domains.

The classical fibril forming collagens include collagen types I, II, III, V and XI, which are characterised by an ability to self-assemble into highly orientated supramolecular aggregates with the typical superstructure, the quarter-staggered fibril array (figure 1.4), with diameters between 25-400nm.

Collagen fibrils consist of tropocollagen molecules with a length of 300 nm and a diameter of 1.5 nm, arranged in a staggered configuration. This structure creates the periodicity known as D-band/period, where D = 67 nm. However, the length of each collagen molecule is not a multiple of D, but instead measures 4.46D Within fibrils, molecules are deposited side by side and parallel, but staggered with respect to each other. There is a gap between two consecutive molecules that measures 0.54D (Petruska and Hodge, 1964). Collagen fibrils in tendon have a diameter of 100-500 nm and they are formed by several microfibrils which each contains a cluster of 5 molecules (Moeller et al., 1995) (figure 1.4). It is this structure that enables small angle and wide-angle x ray diffraction experiments to quantify collagen nanostructure.

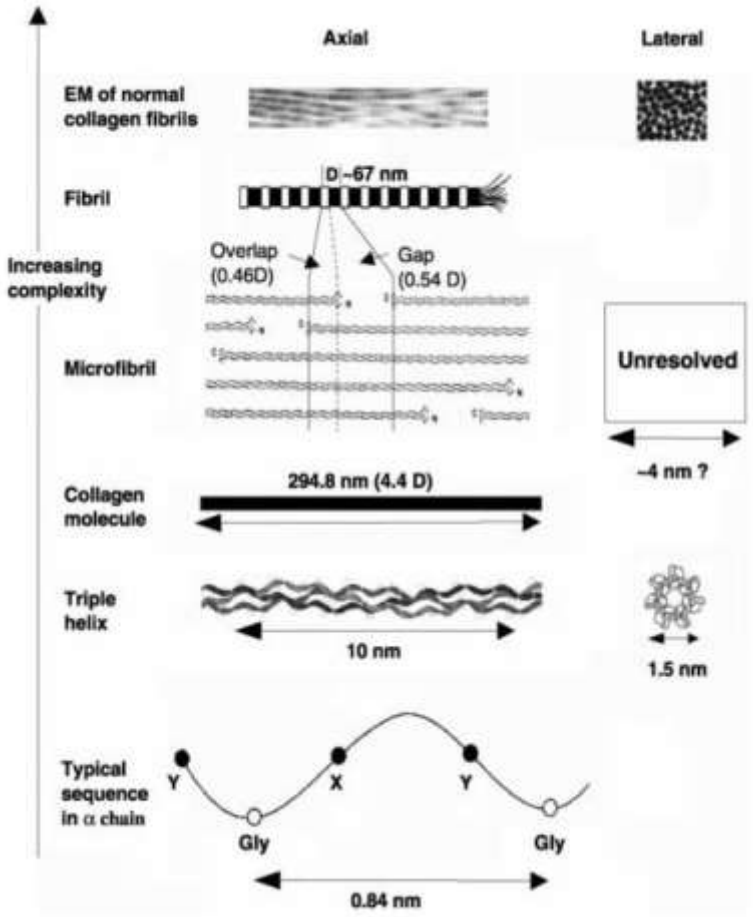

Figure 1.4. Hierarchical structure of collagen fibrils. Triple helices are axially staggered by D (~67nm) and regularly organised in the lateral direction. The hierarchical structure of polypeptide to fibril is shown from bottom to top of the figure, where collagen complexity increases. Copied and reprinted from (Orgel et al., 2001) with permission from Elsevier Limited (see appendix IV.4).

1.2.2.1.2 X ray diffraction

X ray diffraction is not considered an imaging technique as the substructure of the tissue is not visualised in real space. However, x ray diffraction allows investigation at nanoscale level, due to the diffraction pattern created when the x ray is shone onto the tissue and scattered, producing the diffraction pattern of collagen. The scatter produced by the x ray can be subdivided into equatorial, perpendicular to the collagen fibril axis and meridional, parallel to the fibril axis (Quantock et al., 2015). The equatorial scatter of a single collagen fibril is the product of the fibril (i.e. a cylinder) transform (FT; summed scatter from a series of individual cylindrical fibrils), the interference function (IF; lattice point describing the fibril packing) and the background derived from non-

collagenous components (B(K)) (Oster and Riley, 1952, Meek and Quantock, 2001). This can be expressed as following:

$$\mathrm{I(K)} = \mathrm{FT} \times \mathrm{IF} \times \mathrm{B(K)}$$

Where K = scattering vector (light) defined as:

$$K = \frac{2\pi}{\lambda}$$

The mechanical strain on collagen is distributed over different hierarchical level (molecules and fibrils) (Gupta et al., 2004, Gupta et al., 2005, Gupta et al., 2006), therefore to determine how collagen confers mechanical properties to the tissues such as skin and tendon, it is necessary to understand the mechanics at different hierarchical levels, from a biochemical and molecular level upward.

1.2.2.1.3 Collagen synthesis

Collagen is synthesised as procollagen which is subsequently secreted into the ECM as collagen. After the removal of the C- and N- terminal propeptides by peptidase cleavage, procollagen undergoes post-translational modification in the extracellular space. The newly formed collagen molecules are packaged within the Golgi compartment into vesicles and released into the extracellular space. Following secretion, the procollagen trimers are processed. Collagen fibril assembly (fibrillogenesis) is a complex process in which the fibril-forming collagen type (e.g. I, II, III, V or XI) spontaneously aggregate into an ordered fibrillar structure. The molecular arrangement into fibrils is additionally stabilised by cross-links which contribute to the mechanical resilience of collagen fibrils. There are three types of collagen cross-links: disulphide bonding, lysyl oxidase-mediated cross-links and non-enzymatic glycation (Kadler et al., 2008, Kadler et al., 1996, Silver et al., 1992).

Intra- and intermolecular disulphide bridges are in collagen types containing cysteine; representative types are collagen III, IV and VI in the LC. They form between adjacent SH group on the cysteine amino acid (figure 1.5). The role of disulphide bonds is to align the three α-chains to initiate the helix formation (Rajpal and Arvan, 2013).

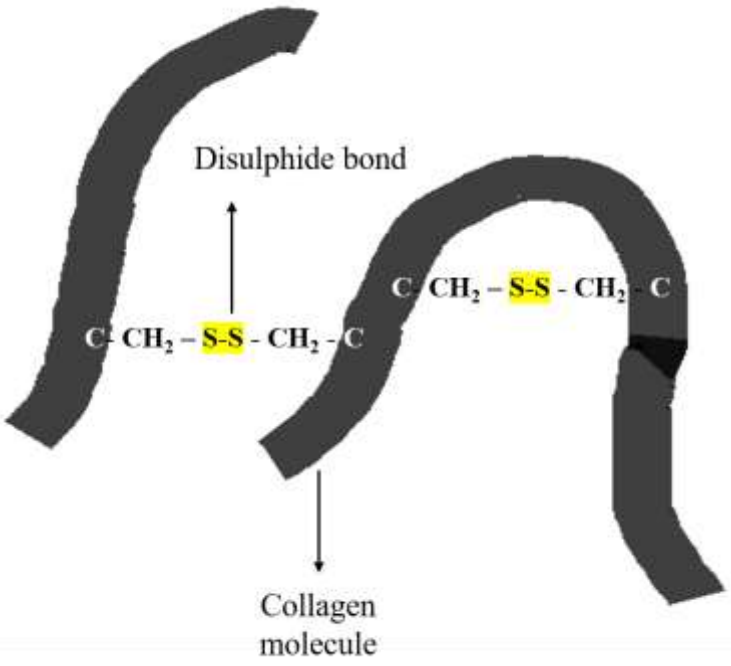

Figure 1.5. Schematic representation of collagen intra- and intermolecular disulphide bonds.

Stabilisation of newly formed collagen fibrils occur through the formation of lysyl oxidase (LOX)-mediated cross-links whereby lysine or hydroxylysine residues in the non-helical portions of the molecule are converted into aldehydes, which then condense with hydroxylysine and other residues in neighbouring molecules to form intermolecular bonds. Although all cross-linking reactions subsequent to aldehyde formation occur spontaneously, these are facilitated by the highly ordered, three-dimensional array of collagen molecules within the assembling fibril. Lysyl pyridinoline (LP) and hydroxylysyl- pyridinoline (HP) are the predominant mature forms of LOX-mediated cross-links in most tissues (Robins, 2007).

Non-enzymatic glycation or Maillard reaction occurs between reducing sugars and amino group of collagens. The Maillard reaction involves the amino group of lysine or hydroxylysine to react with aldehyde group of reducing sugar, forming Schiff base which undergoes Amadori reaction to form Amadori products. The latter can be degraded into products containing carbonyl groups. These can undergo further transformation including

cross linking which lead to the production of Advanced Maillard products, also known as Advanced glycation end (AGE) products (Monnier, 1990).

1.2.2.1.4 Collagen content in the human lamina cribrosa

Several studies have examined the collagenous ECM of the LC in humans by immunolocalisation of collagen types I, III, IV, V and VI (Albon et al., 1995, Albon et al., 2000a, Goldbaum et al., 1989, Hernandez et al., 1986, Hernandez et al., 1987, Morrison et al., 1989b, Rehnberg et al., 1987).

Type I and III are the major fibrillar components of the ECM of the LC (Hernandez et al., 1986, Hernandez et al., 1987, Morrison et al., 1988, Goldbaum et al., 1989, Morrison et al., 1989a, Quigley et al., 1991a, Albon et al., 1995), whereas type IV is a component of basement membrane of the astrocytes surrounding the axonal fascicles (Morrison et al., 1989b). Fibrillar collagen types I and III have been found to co-distribute within the cores of the cribriform plates and blood vessel walls (Albon et al., 1995, Goldbaum et al., 1989, Hernandez et al., 1986, Hernandez et al., 1987, Morrison et al., 1988, Quigley et al., 1991b). Hernandez et al., (1987) and Albon et al., (1995) showed immunolocalisation of type IV collagen in the LC, where it was distributed between elastic fibres.

Type I and III are the major fibrillar components of the ECM of the LC, whereas type IV is a component of basement membrane and type V and VI connect the fibrillar collagen to the rest of the connective tissue (Keene et al., 1988, Modesti et al., 1984). Collagen type VIII has also been localised to the cribriform plates in the human ONHs (Tamura et al., 1991).

1.2.2.2 Elastic fibre

Ultrastructural studies have shown the structural complexity of mature elastic fibre (EFs) (Kielty et al., 2007), which are composed of two distinct components; i) fibrillin-rich microfibrils and ii) a central amorphous elastin core (Greenlee et al., 1966, Ross and Bornstein, 1969). The composition of EFs does not vary, but their organisation changes according to the tissue they are found in and their functional role. For instance, in the aorta, EFs are organised into a sheet forming circular rings of elastic lamellae surrounding the lumen of the aorta (Tsamis et al., 2013).

1.2.2.2.1 Elastin

Elastin, the inner core of EFs, is primarily found in all elastic tissues in the human body, such as lungs and vasculature where it provides elasticity. For instance, in the aorta, EFs experience 42 million pressure pulses every year (Vrhovski and Weiss, 1998). With an average life of 70 years, elastin is the longest lasting protein in the human body. Elastin can withstand billions of stretch-relaxation cycles over a lifetime without damage or deformation.

Elastin represents 90% of the amorphous core of the mature EF, surrounded by 10-12 nm microfibrils (Rosenbloom et al., 1993). The elastin gene is localised on chromosome 7 in humans and it is expressed by various cell types during the early stages of development. The product is tropoelastin (TE), a protein with 786 amino acids, which consists of hydrophobic and cross-linking domains, consisting predominantly of glycine (Gly), valine (Val), proline (Pro), leucine (Leu) and alanine (Ala) residues. Like collagen, elastin is rich in glycine and proline, determining around 33% and 11% of amino acids residues, respectively (Rosenbloom et al., 1993). Unlike tropocollagen, the secondary structure of elastin is highly disordered and not well defined, even though x ray studies (Baldock et al., 2011) and ultrastructural studies (Pasquali-Ronchetti and Baccarani-Contri, 1997) have proposed that the monomer has some sort of organisation and it appears to be laterally packed.

1.2.2.2.2 Microfibrils

Microfibrils are complex structures which are found in arteries (Krauhs, 1983) as well as in non-elastic tissues such as the ciliary zonules of the eye (Streeten and Licari, 1983). In the mature EF, microfibrils represent nearly 10% of the total mass (Kielty et al., 2002, Kielty et al., 2005). It has been proposed that microfibrils facilitate cross link formation by interacting with the enzyme lysyl oxidase (LOX) (Wagenseil and Mecham, 2007).

1.2.2.2.3 Elastic fibre synthesis

Elastogenesis is a complex process which leads to mature elastin within EFs and begins with the deposition of microfibrils as a scaffold for TE (Kielty et al., 2002). The latter is secreted into the ECM where it aggregates spontaneously into globules. In this first stage of TE alignment, hydrophobic residues of serial monomers self-aggregate under optimal

conditions of pH and temperature (Mithieux and Weiss, 2005). Finally, the lysine-rich domains are cross-linked through the action of the enzyme LOX, facilitating the formation of the mature fibre (figure 1.6).

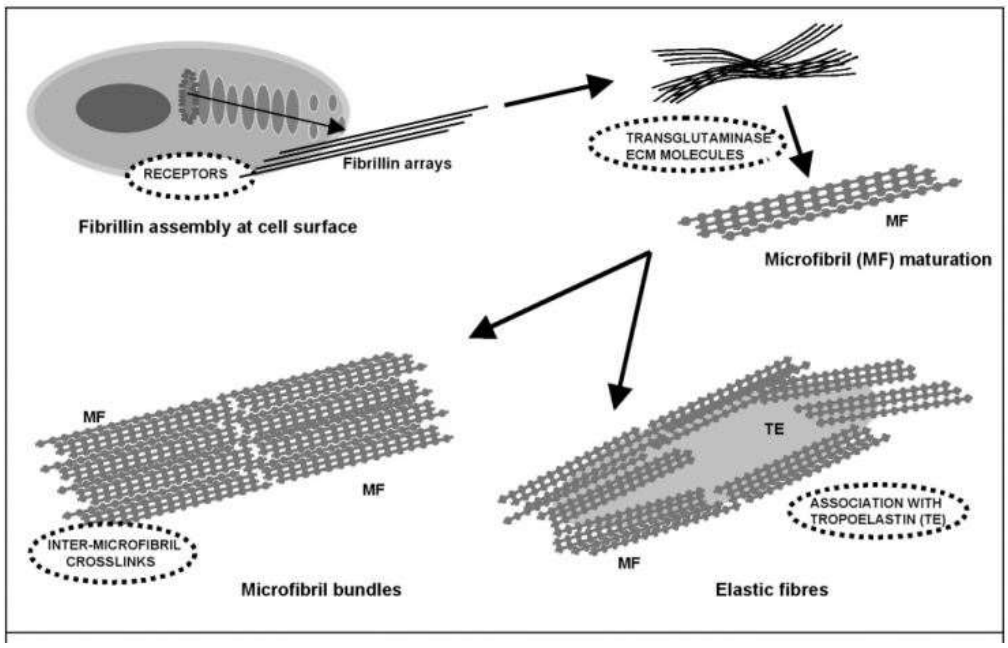

Figure 1.6. EF formation. At the cell surface, fibrillins are assembled into microfibrils, which undergo maturation into transglutaminase-crosslinked microfibrils. Mature microfibrils (MF) form bundles and are stabilised by inter-microfibril cross-links. TE is then deposited onto microfibrils and stabilised by lysyl oxidase-derived crosslinks. Adapted with permission from Journal of Cell Science (http://www.biologists.com/journal-of-cell-science) from (Kielty et al., 2002) (see Appendix IV.5).

1.2.2.2.4 Distribution of elastin in the lamina cribrosa

The EF within the human LC has been investigated with different techniques such as electron microscopy (Quigley et al., 1991b), immunofluorescence (Hernandez et al., 1987, Hernandez et al., 1989, Hernandez, 1992) and histological stains (Oyama et al., 2006). Within the ONH, EFs run parallel with collagen in the LC plates (Hernandez et al., 1987, Quigley et al., 1991a, Oyama et al., 2006). EFs ring around the LC and enter the LC plates as fibres orientated perpendicularly from the circumference (Hernandez et al., 1987, Quigley et al., 1991a). Additionally, immunolabelling studies have shown that the peripapillary sclera (ppsclera), a circular collagenous network within 1 mm from the optic canal (Jones et al., 2015), contains more elastin and microfibrils than the sclera beyond this region (Morrison et al., 1989b, Quigley et al., 1991b).

1.2.2.3 Proteoglycans

Proteoglycans (PGs) represent a major component of the extracellular matrix and they are proteins with a covalently attached glycosaminoglycans (GAG). One of the role of PG relates to the GAG component of the molecule, which provides hydration and support to the tissue to withstand compressional forces (Yanagishita, 1993). GAGs are highly sulphated carbohydrate chains that are bound to a protein core. Each of the GAGs keratan sulphate, chondroitin sulphate, dermatan sulphate, heparin and heparan sulphate is comprised of a unique combination of monosaccharides that forms a characteristic repeating disaccharide unit.

PGs in the LC have been identified using immunohistochemistry (Caparas et al., 1991, Morrison et al., 1988) and electron microscopy (Fukuchi et al., 1992, Sawaguchi et al., 1992). The latter found three types of cuprolinic blue positive staining associated with collagen in the core of the cribriform plates. Cuprolinic blue is a cationic dye that binds to the sulphated GAG residues of PG (Scott, 1980). These were identified as chondroitin sulphate and dermatan sulphate GAGs co-localising in the LC plates. Chondroitin 4 sulphate has been reported to be limited to the ppsclera and LC (Caparas et al., 1991, Morrison et al., 1988), whereas chondroitin 6 sulphate was found within the LC plates (Caparas et al., 1991) and ON septae (Morrison et al., 1994). Heparan sulphate PGs were also present along the margins of the LC plates (Fukuchi et al., 1992, Sawaguchi et al., 1992) extending into the region of insertion (RoIns).

Decorin, a small dermatan/chondroitin sulphate PG, localised to the LC plates (Morrison and Johnson, 1992), has a role in the regulation of collagen fibril diameter and assembly of ECM components (Vogel et al., 1984). Biglycan, another small dermatan/chondroitin sulphate PG may have a key role in the development of the tissue

1.2.3 Age related changes in the extracellular matrix of the LC

Age is an important risk factor in glaucoma (Anderson, 1989) and, the LC has been implicated as one of the main sites of damage to the retinal ganglion cell axons (Quigley and Anderson, 1976). Collagen, EFs and PG form the ECM of the LC, which has been shown to alter as a function of age.

1.2.3.1 Collagen

Total collagen, as a percentage of dry tissue, has been shown to increase from 20% in young LC to 50% in the elderly (Albon et al., 1995), suggesting that the cribriform plates become thicker (Hernandez et al, 1989; Morrison et al, 1989b). Type III collagen is usually found in extensible tissues such as skin and foetal tissue (Montes et al., 1984) while type I collagen is less flexible than type III, and absent in neonatal LC (Morrison et al., 1989a). In the LC, type III collagen as a percentage of total fibrous collagen decreased from 23% to 3% as a function of age (Albon et al., 1995). The altered type III to I collagen ratio agreed with Morrison et al (1989a) findings, which suggested that type III collagen is predominant in immature LC and is replaced by type I collagen in the adult LC (Morrison et al., 1989a). Collagen type IV has also been observed to increase in density with age (Hernandez et al., 1986).

All these results are supported by molecular studies that demonstrated that collagen types I and IV mRNA expression is not seen in foetal ONH but instead is highly expressed in adult ONH suggesting age related accumulation of these types of collagen due to continuous synthesis (Hernandez et al., 1991). Furthermore, it has been proposed that in the ageing LC, the stiffening of the LC (Albon et al., 2000b) might be partly due to an increase in non-enzymatic cross-links (Albon et al., 1995).

1.2.3.2 Elastin

Elastin, within the human ONH, is known to alter with age (Albon et al., 1995, Albon et al., 2000a, Hernandez, 1992, Hernandez et al., 1989). Like collagen, elastin has been found to increase as a function of age, from 7% to 28% as a percentage of dry tissue weight (Albon et al., 2000a). However, there is no evidence of EF degradation within the cribriform plates (Hernandez, 1992). Elastin accumulates in the LC (Hernandez et al., 1989) and as a result, it may bind to other proteins.

Within the LC beams, elastin has been shown to run parallel with the collagen bundles (Hernandez et al., 1987, Quigley et al., 1991a, Hernandez, 1992, Oyama et al., 2006). Immunohistochemical analysis revealed that longitudinal elastin containing fibres formed part of the core of the cribriform plates with collagen type III (Hernandez et al., 1987, Hernandez and Neufeld, 1989, Hernandez, 1992).

Electron microscopy (Quigley et al., 1991a) and immunolabelling of α-elastin (Hernandez, 1992) showed no labelling in the foetal lamina cribrosa and in the newborn eye, elastin appeared irregular. In the young adult (19 years old), α-elastin labelling was localised to thin long EFs running longitudinally within the cribriform plates, whereas in normal elderly LC (81 years old), elastin appeared localised within long, tubular and thicker fibres, when compared to that in the young (Hernandez et al., 1990, Hernandez, 1992).

1.2.3.3 Proteoglycans

The shorter cuprolinic blue positive filaments of dermatan and chondroitin sulphate PG and heparan sulphate PG in older eyes were suggested to indicate a decrease in GAG chain length or a reduction in sulphation (Sawaguchi et al., 1992, Sawaguchi et al., 1993). Immunolabelling studies demonstrated no change in dermatan sulphate PG, and an age-related decrease in the ratio of chondroitin 6 sulphate to chondroitin 4 sulphate (Caparas et al., 1991, Morrison et al., 1994). Additionally, sulphated GAGs showed a significant decrease in age (Albon et al., 2000a).

1.3 The optic nerve head in glaucoma

Glaucoma is a generic term used to describe a group of ON diseases that can lead to axon degeneration and loss of RGCs. It is the most common cause of irreversible blindness, attributing to approximately 10% of blindness (NICE 2009) worldwide and occurring in about 2% of people over 40 years of age in the UK (NICE 2009). In 2020, 80 million people are predicted to be affected by primary open angle glaucoma (Quigley and Broman, 2006). This optic neuropathy usually presents with optic disc cupping, retinal nerve fibre layer (RNFL) thinning and vision loss (Quigley and Broman, 2006).

The primary division is open-angle and closed angle (or angle-closure) glaucoma. The angle refers to the angle where the iris meets the cornea, it is normally wide and open enabling outflow of the fluid from the inside of the eye. The angle contains the trabecular meshwork, which acts as a filtration system for the aqueous fluid draining from the eye. When this angle is narrowed or closed, pressure can increase, and it may damage the ON leading to loss of vision (Foster et al., 2002). In closed-angle glaucoma the iris is pushed or pulled up against the trabecular meshwork within the angle of the anterior chamber of

the eye. This results in the aqueous humour drainage blockage, thereby increasing the intraocular pressure (IOP). Primary open angle glaucoma (POAG) refers to slow closure of the drainage canals (trabecular meshwork) due to deficiencies in the ability of the trabecular meshwork to manage aqueous humour outflow, partly attributed to accumulation of ECM molecules blocking the outflow (Grant, 1955, Weinreb and Khaw, 2004). This results in increased eye pressure which causes progressive ON damage.

The most common form of glaucoma is POAG, where a gradual loss of the visual field occurs, starting with peripheral vision (Grant, 1955, Weinreb and Khaw, 2004). POAG progresses slowly and usually it occurs bilaterally (Broman et al., 2008). The mean age of onset is 60 years and the incidence of glaucoma increases with age (Quigley, 2011). Many studies suggest that the damage to RGC axons occurs within the LC and that therefore this structure is the most important aspect of the pathophysiology of glaucoma, (Anderson and Hendrickson, 1974, Minckler et al., 1977, Quigley and Anderson, 1976) (figure 1.7a,b).

Elevated IOP [(above 21 mmHg (NICE 2017)] is considered one of the most important risk factors for the development of POAG (Alward et al., 1998). IOP is determined by the rate of aqueous humour secretion and outflow. In POAG there is higher resistance to aqueous outflow via the trabecular meshwork (Johnson et al., 2002), which leads to an increase in IOP and subsequent damage to RGCs.

IOP acts as a source of stress, resulting in a possible chain of cellular events which culminate in RGC axonal damage. It has been proposed that the individual's response to IOP depends on the anatomy and the composition of the eye, which can contribute to build an individual's susceptibility to high IOP (Burgoyne et al., 2005a). The LC has been shown to compress and deform backwards in human glaucoma (Quigley et al., 1983, Quigley et al., 1981) as also demonstrated by *in vivo* studies (Furlanetto et al., 2013, Jung et al., 2014) and experimental models of monkey ocular-hypertension (Bellezza et al., 2003b, Roberts et al., 2009, Yang et al., 2007) (figure 1.7c-f).

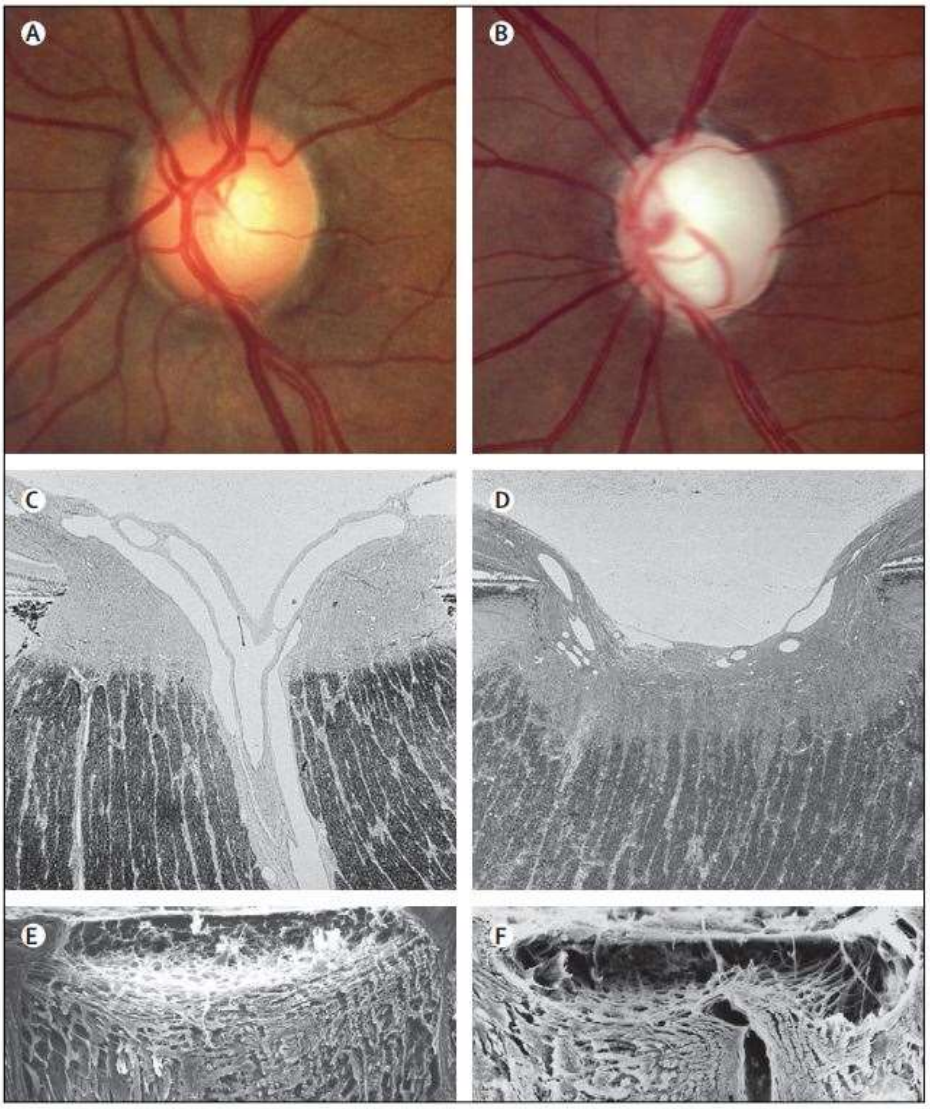

Figure 1.7. Clinical and microstructural features of healthy and glaucomatous eye. Healthy people without glaucoma present pale central area (cup), surrounded by the neuroretinal rim (A). People affected by glaucomatous optic neuropathy present a larger cup that occupies most of the optic disc and the neuroretinal rim disappears (B). Microscopically, normal ONH (C) changes with glaucoma (D) where loss of tissue is visible at the neuroretinal rim and the cup is excavated. The connective tissue network in healthy people presents collagenous beams surrounding pores (E). This structure changes in glaucomatous ONHs where the LC is excavated and has a "W" shape (F). Copied and reprinted from (Quigley, 2011) with permission from Elsevier Limited (see appendix IV.6).

Changes in the structure of the LC along with axonal damage (Vrabec, 1976) have led to the hypothesis that this structure within the ONH is a major pathological site in POAG. There are several theories describing the onset of glaucomatous damage (figure 1.8), some are summarised below. The mechanical hypothesis suggested that the LC is deformed and strained by the increased IOP. Changes include altered compliance and

alteration in the ECM, which can in turn lead to compression of RGC axons passing through the pores (Bellezza et al., 2000, Bellezza et al., 2003b, Burgoyne et al., 2005b, Downs et al., 2008, Roberts et al., 2009, Sigal and Ethier, 2009).

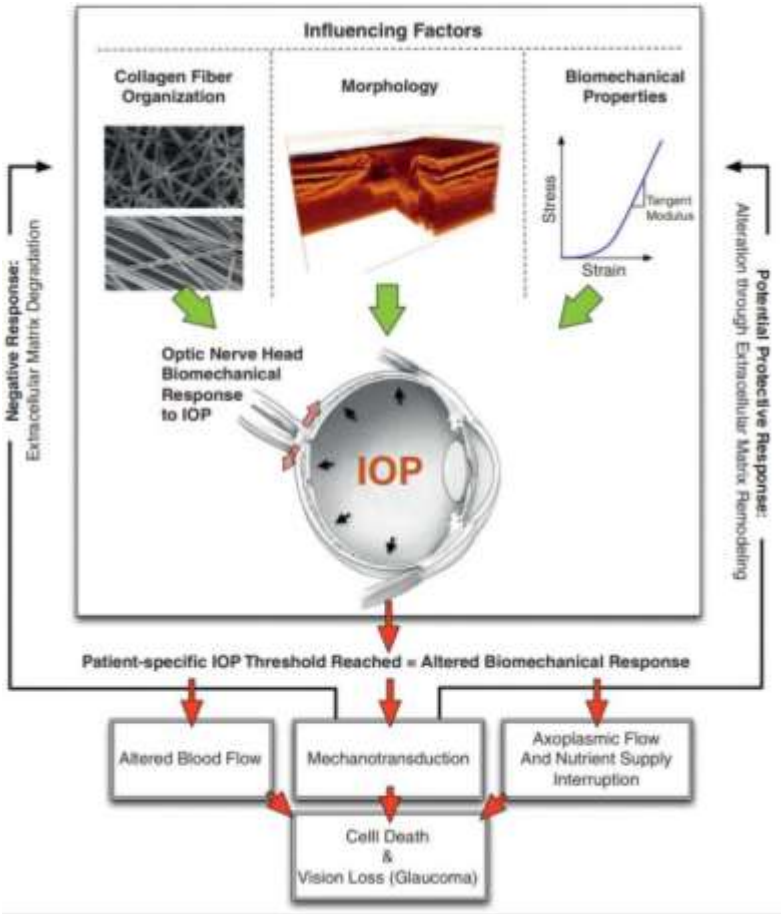

Figure 1.8. Schematic representation of ONH biomechanics and influential factors in the development of POAG. Multiple biomechanical factors influence the individual's susceptibility to glaucoma. Collagen fibre organisation, ONH morphology and LC/peripapillary sclera stiffness and geometry play an important role in determining ONH biomechanics. Increased IOP can influence non-IOP factor such as inflammation, astrocytes activation and axoplasmic flow which will in turn influence the diffusion of nutrients to astrocytes. These can in turn determine RCG axons death via apoptosis. Copied and reprinted from (Strouthidis and Girard, 2013) with permission from Elsevier Limited (see appendix IV.7).

The vascular theory suggests that there is a change in the translaminar pressure gradient due to an increase in IOP and alteration in cerebrospinal fluid (CSF) pressure, which in turn leads to a perfusion instability within the ONH. This alteration can cause problems in ocular blood flow and a reduced blood supply to the ONH leading to RGC axonal damage and ultimately their death (Fechtner and Weinreb, 1994, Grieshaber et al., 2007).

The glial hypothesis suggested that the activation of glial cells and astrocytes due to increased IOP initially protects the neuronal tissue. However, this response can reduce neurotrophic support to axons and therefore create a harmful toxic environment (Hernandez, 2000, Neufeld et al., 1997, Tezel, 2006). For instance, in rat models reactive astrocytes and glial cells synthesise nitric oxide synthase (NOS-2), an enzyme that may be neurotoxic to RGC axons (Neufeld, 1999a, Neufeld, 1999b, Neufeld et al., 1997). However, POAG is a multifactorial disease and it is possible that a combination of mechanisms contributes to the onset and progression of glaucoma and none of them are exclusive.

1.3.1 Genetic predisposition

Up to 50% of patients with POAG have a positive family history, suggesting that genetic defects may contribute to cause the disease (Tielsch et al., 1994). First degree relatives of an affected person have 22% risk of developing glaucoma (Wolfs et al., 1998). Early onset of POAG has been associated to the myocilin gene (MYOC). More than 180 variants have been detected in the MYOC gene and almost 40% of these have been associated with glaucoma (Hewitt et al., 2008). Mutations of myocilin are generally associated with an early adult form of POAG, and a high intraocular pressure (Aldred et al., 2004). Myocilin associated disease is transmitted as an autosomal dominant Mendelian trait and people carrying MYOC mutation develop glaucoma in 90% of cases (Alward et al., 1998).

MYOC was the first gene identified as genetic cause of juvenile POAG in the GLC1A locus located on chromosome 1 (Morissette et al., 1995). MYOC gene encodes for the myocilin protein, found in the trabecular meshwork and ciliary body, regulating the intraocular pressure. Its function is not well understood but it is thought to help to control the intraocular pressure (Tamm, 2002). Within normal eyes, myocilin protein is secreted into the aqueous humour for unknown purposes. However, studies have shown that the altered protein that is produced by myocilin mutations, is retained within the trabecular meshwork (Gobeil et al., 2004, Jacobson et al., 2001, Joe et al., 2003, Liu and Vollrath, 2004). Up to 33% of patients with juvenile open-angle glaucoma have mutations in the MYOC gene and it has also been detected in some people with primary congenital glaucoma (Svidnicki et al., 2018). Myocilin protein has been found in the trabecular meshwork (Sakai et al., 2007), optic nerve head (Karali et al., 2000), ciliary body (Karali

et al., 2000), vitreous and aqueous humour (Fautsch and Johnson, 2001, Rao et al., 2000, Russell et al., 2001).

Myocilin might influence mitochondrial function, in fact, the overexpression of the protein in the trabecular meshwork cells reduced mitochondrial respiration (Sakai et al., 2007). This might lead to altered function of the cells, which in turn can lead to an altered IOP maintenance. Interestingly, the loss of trabecular meshwork cells has been proposed before (Alvarado et al., 1984) and the level of myocilin has been found to accumulate in the trabecular meshwork interfering with the normal flow pattern, leading to an increased IOP (Nguyen et al., 1998). This was supported by immunohistochemical studies indicating that some POAG eyes had elevated levels of myocilin (Lutjen-Drecoll et al., 1998).

1.3.2 Clinical features

One of the most common clinical features in glaucoma is optic disc cupping (see figures 1.7a,b). The optic cup is the white, cup-like area in the centre of the optic disc (Armaly and Sayegh, 1969). Normally, the cup is round and horizontally oval and the cup-to-disc ratio may vary based on the disc size (Kirsch and Anderson, 1973).The cup-to-disc ratio compares the diameter of the "cup" portion of the optic disc with the total diameter of the optic disc (Hitchings and Spaeth, 1976). "Cupping" refers to the increased cup-to-disc ratio. Normally, glaucomatous eyes have larger cup-to disc ratio and lower amount of RGC than a healthy eye (Tatham et al., 2013).

1.3.3 Ageing and glaucoma

A major risk to develop glaucoma is age, associated with visual field loss (Medeiros et al., 2005). Johnson et al (1987), have reported a variation in total axon population, axon diameter, ON area and axon density with age. They found that the total axon population ranged from about 1,685,000 axons per optic nerve in a 42 years old eye, to 759,000 axons per optic nerve in a 74 years old ON, suggesting that the elderly ON had fewer axons (Johnson et al., 1987).

The quality of life of people with glaucoma is reduced, as they may have problems with routine actions, like eating and driving to work. Therefore, preventing vision loss could

be the first step towards maintaining independence and a good quality of life (Bramley et al., 2008).

1.3.3.1 Glaucomatous changes in the ONH

A thinning of the LC in glaucoma has previously been reported in both histological (Jonas et al., 2012, Ren et al., 2009) and *in vivo* (Lee et al., 2012, Park et al., 2012) studies.
The ECM of the LC is extensively remodeled in POAG leading to a tissue morphologically different from the healthy LC (Burgoyne et al., 2005, Hernandez et al., 1990, Hernandez and Pena, 1997, Jonas et al., 2003, Quigley, 2011, Yang et al., 2011a, Yang et al., 2011b).

1.3.3.1.1 Basement membrane

An increase in basement membrane components, including heparan sulphate PG and thickness has been shown in glaucomatous eyes (Hernandez et al., 1990). Activated astrocytes are responsible for the newly synthesised basement membrane. Additionally, basement membrane like materials were also found disorganised, with deposition identified within the pore regions (Hernandez et al., 1990, Morrison et al., 1990).

1.3.3.1.2 Collagen

mRNA expression of collagen type IV from astrocytes has been shown to increase in glaucomatous ONH when compared to normal ONHs (Hernandez et al., 1994b). Within the LC, collagen type I, III and IV were observed between beams and occupying space normally occupied by axons (Morrison et al., 1990). Collagen type I appeared compact, whereas collagen type III showed no significant changes when compared to normal ONHs (Hernandez et al., 1990).

1.3.3.1.3 Elastin

Within the core of the cribriform plates in glaucomatous ONHs, there is a marked disorganisation in the composition of elastin and loss of EFs, as well as elastotic degeneration (Pena et al., 1998) and curling of EFs (Quigley et al., 1991a, Quigley et al., 1994). The EFs appeared also disconnected from the surrounding collagen matrix (Hernandez, 1992, Hernandez et al., 1990, Quigley et al., 1991a). Hernandez has reported

significant changes in elastin within the ONH, suggesting a loss of EFs within the core of the cribriform plates and the tubular appearance was no longer visible (Hernandez et al., 1990, Hernandez, 1992).

Other studies, however, showed controversial results. In fact, a few studies proposed no changes in the number of EFs in experimental glaucoma (Quigley et al., 1991b), as well as in the morphology (Quigley et al., 1996), when compared to normal eyes. However, these reports do not agree with immunolabelling studies (Hernandez et al., 1990, Hernandez, 1992), electron microscopy and immunogold labelling of elastin showing elastosis (Pena et al., 1998, Netland et al., 1995). Additionally, *in situ* hybridisation studies have shown more elastin mRNA expression in glaucomatous LC when compared to non-pathological eyes (Hernandez et al., 1994a), suggesting there are newly synthesised EFs in glaucoma.

As a function of disease progression, electron microscopy studies have shown a correlation between changes in EFs and severity of glaucoma. In mild glaucoma elastin became curvilinear in some LC beams, and the longitudinal appearance was no longer visible (Quigley et al., 1991a). It appeared that the 'curling' occurred in 61% of eyes with a history of glaucoma indicating that it is caused by the disease (Quigley et al., 1994). The normally long, tubular distribution of elastic fibres within the LC also changed, with small fragments of microfibrils interspersed throughout the LC beams (Hernandez, 1992). This change was more pronounced in moderate glaucoma with the curvilinear appearance observed in most of the LC plates (Quigley et al., 1991a) and at the insertion region (Hernandez, 1992). In advanced glaucoma, the curling of EFs was accompanied by neural loss (Quigley et al., 1991a); at this stage the organisation of EFs was completely disrupted. In fact, the EFs seemed dissociated from the collagenous components and an abundance of non-fibrillar elastin aggregates (Hernandez, 1992) was observed.

1.4 Biomechanics of the ONH

The ONH is considered a biomechanical structure where IOP related stress and strain act as a crucial determinant of the physiological and pathophysiological behaviour of the ONH tissues (Bellezza et al., 2000, Downs et al., 2008).

The connective tissue network of the LC and ppsclera are proposed to strengthen the eyeball, resisting tensile, compressive and shear (Grytz et al., 2014, Sigal et al., 2011b)

stresses. In fact, the porous LC, a ‘weak spot’ in the eye globe, is only a third of the thickness of the sclera (Downs and Girkin, 2017). Thus, the LC is asked to provide structural support to the ONH by withstanding IOP-related strain and at the same time provide an opening for the axons to leave the eye. This makes the LC more susceptible to damage from the increased IOP (Beotra et al., 2018) as the mechanical stress could be thus concentrated at the region of insertion (RoIns) due to a difference in biomechanical properties between ppsclera and the weaker LC.

1.4.1 Mechanical environment of the ONH and peripapillary sclera

The sclera is the main load bearing tissue within the eye and therefore plays an important role in maintaining the mechanical properties of the ocular tissue (Girard et al., 2009, Sigal et al., 2004, Norman et al., 2011). In this context, the ppsclera surrounding the ONH is a anisotropic circumferentially orientated collagen ring (Jones et al., 2015, Morrison et al., 1989b, Pijanka et al., 2013, Pijanka et al., 2012, Winkler et al., 2010) with a contribution of elastin (Albon et al., 2000a, Hernandez et al., 1986, Quigley et al., 1991b, Quigley et al., 1991a).
Computational modelling has proposed that this circumferential organisation of collagen fibres around the ONH is optimal to protect the human LC from stress and to reduce the strain at the LC insertion region (Zhang et al., 2015, Grytz et al., 2011). Therefore, the ppsclera has been suggested to function as a protective structure to limit the scleral canal expansion due to IOP fluctuation (Coudrillier et al., 2012, Girard et al., 2009, Grytz et al., 2014).

In the response of the ONH to elevated IOP, the expansion of the scleral canal pulls the LC within the scleral plane making it more resistant to the posterior displacement (Sigal et al., 2011a, Sigal et al., 2011b). On the other hand, a stiffer and more rigid sclera may allow less expansion of the scleral canal. As a result the LC becomes stiffer and less deformable to IOP increase (Downs, 2015) (figure 1.9). However, it seems that as a response to an increased IOP, the LC would *in vivo* be posteriorly displaced (Furlanetto et al., 2013, Park et al., 2013, Fazio et al., 2016). Thus, the characterisation and the understanding of both the LC and peripapillary sclera biomechanics is crucial in knowing the effects and the response of the ONH to stress.

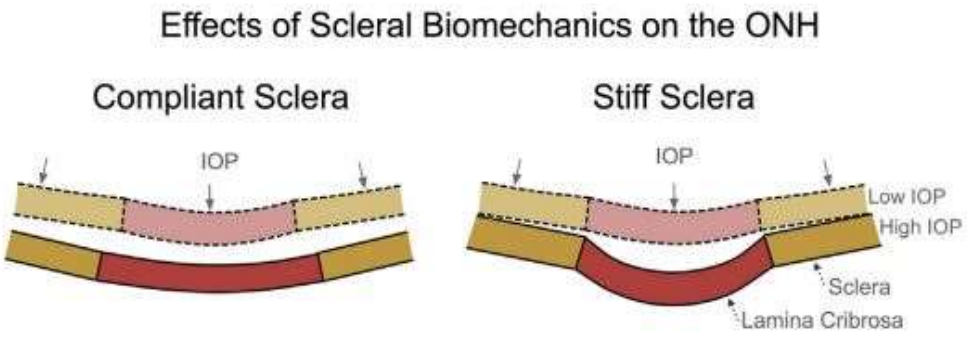

Figure 1.9. Optic nerve head biomechanics. The surrounding ppsclera has an important influence on the ONH biomechanics and it has been suggested that it functions as a protective structure to limit scleral canal expansion. Within a compliant sclera, IOP causes great scleral canal expansion that pull the LC taut. A stiff sclera, on the other hand, allows a little scleral canal expansion with elevated IOP and less stretching of the LC, which consequently, is posteriorly displaced. Copied and reprinted from (Downs, 2015) with permission from Elsevier Limited (see appendix IV.8).

1.4.2 Influence of an IOP-driven mechanism

Over a lifetime, the physiological fluctuation of IOP and the strain applied to the ppsclera, alter the connective tissue within the ONH, which lead to the normal ageing process. IOP perturbation, however, not only has effects on the ECM of the LC, but also influences the ppsclera and activate cells and damages axons (Burgoyne, 2011). Although lowering the IOP is the only effective treatment to prevent the progression of the disease (Heijl et al., 2002), the actual role of IOP in progressing glaucoma is not well understood. This is confirmed by clinical observation of glaucomatous ONHs in subjects with a normal IOP range, while other individuals, with high IOP, presented no signs of glaucoma (Klein et al., 1992).

Interestingly recent data showed that the sclera (Coudrillier et al., 2012, Fazio et al., 2014), lamina cribrosa (Albon et al., 2000), and cornea (Knox Cartwright et al., 2011) stiffen significantly with age. It might be assumed that a stiffer tissue resists deformation better than a compliant tissue, however, it has been suggested that a stiffer sclera leads to an increase in IOP spikes (Clayson et al., 2017) within an eye that lacks elasticity to support the strain. Similarly, the stiffening of the sclera and LC in glaucoma can be related to a more protective environment against mechanical strain, since a stiffer connective tissue resists more strain than a compliant tissue. However, the stiffening also may induce

a remodelling of the eye, which might be more susceptible to IOP fluctuation (Fazio et al., 2014).

Researchers have shown that ONH collagen and elastin are altered as a function of age (Albon et al., 1995, Albon et al., 2000a, Hernandez et al., 1989, Morrison et al., 1989a) and glaucoma (Quigley and Addicks, 1981, Quigley et al., 1982, Quigley et al., 1981, Hernandez et al., 1990) and are therefore likely to affect an ONH's response to IOP changes.

1.4.3 Cerebrospinal fluid pressure on the ONH biomechanics

Recently, researchers have focused on the role of cerebrospinal fluid on the biomechanics of the LC (Feola et al., 2017, Hua et al., 2017, Ren et al., 2010). The ONH normally experiences a complex and dynamic biomechanical environment and it is exposed to two pressurised, independent regions: i) the intraocular space anteriorly and ii) the subarachnoid space posteriorly. Normal IOP ranges between 10 to 21 mmHg whereas the pressure within the subarachnoid space, namely the cerebrospinal fluid pressure, is between 5 to 15 mmHg (Quigley et al., 1996). In this environment the LC is the primary structure that divides the two regions (Goetz, 2007). The difference in pressure between them is called translaminar pressure gradient and can cause changes in the optic disc if the pressure is altered (figure 1.10).

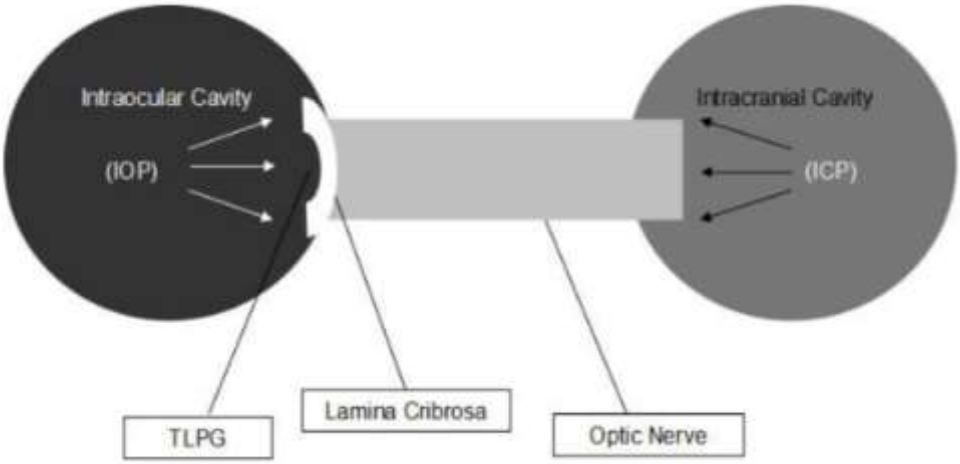

Figure 1.10. Schematic diagram showing the relationship between intraocular pressure (IOP), intracranial pressure (ICP) and translaminar pressure gradient (TLGP). Anteriorly, the ONH is exposed to the IOO, whereas posteriorly to the ICP. Therefore, there is a pressure inclination across the ON which is the trans-lamina cribrosa pressure gradient (TLPG) that can be formulated as IOP minus ICP. Despite the raised IOP contributes towards glaucoma development, individuals with normal IOP could also develop the disease. In those patients, large TLPG, as a result of abnormal decreases ICP, is thought to be the cause that contributes towards glaucoma, despite IOP being in the normal range. Adapted from (Hou et al., 2016) and reprinted with permission from Springer Link (Appendix IV.9).

The circumferential stress (hoop stress) generated by the IOP can result in scleral expansion which contributes to LC deformation (Bellezza et al., 2003a, Downs et al., 2008, Ethier et al., 2004, Roberts et al., 2010). In this context, the role of the cerebrospinal fluid pressure has begun to receive more attention as an important factor in ONH biomechanics. For instance, even though IOP is a major risk factor, reduced cerebrospinal fluid pressure has also been proposed as a risk factor for the development of glaucoma (Berdahl et al., 2008, Morgan et al., 2008, Ren et al., 2010). These studies suggested that the cerebrospinal fluid pressure had an extensive impact on the strain distribution within the LC and an elevated cerebrospinal fluid pressure is positively correlated with increased deformation of the LC (Feola et al., 2017, Morgan et al., 2002).

In fact, Ren et al., (2010), suggested that in POAG with normal IOP, the cerebrospinal fluid pressure was low, leading to an abnormally high translaminar pressure difference which might lead to abnormal function and ON damage due to changes in axonal

transportation, deformation of the lamina cribrosa, altered blood flow, or a combination leading to glaucomatous damage (Ren et al., 2010).

1.5 Hypothesis and aims

Microstructural changes in the ECM of the ONH occur as a function of age, leading to an overall increase in connective tissue content (Albon et al., 1995, Albon et al., 2000a, Hernandez et al., 1989, Morrison et al., 1989a) and reduced compliance (Albon et al., 2000b). Glaucoma is the most common cause of irreversible blindness worldwide (Quigley and Broman, 2006) in which age is a major risk factor (Coleman and Miglior, 2008). Previous work has proposed the lamina cribrosa of the ONH is the main site of RGC axonal damage in POAG (Quigley et al., 1983, Quigley et al., 1981).
The hypothesis of this study was that micro- and nanostructure of the ONH is altered as a function of age and glaucomatous optic neuropathy.

To test this, the study aimed to further investigate the major connective tissue components of the ONH, namely collagen and elastin, in order to better understand the role of these as a function of ageing and disease and in tissue biomechanics. To achieve this, the aims of this PhD were to:

1. To evaluate and quantify ONH and collagen microstructural parameters (namely LC, cribriform plates and ppsclera thickness; and collagen crimp and fibre orientation parameters) as a function of age and glaucoma.
2. To visualise EF organisation and quantify ONH elastin as a function of age and glaucoma
3. To investigate collagen and elastin nanostructure in the ONH, as a function of age.
4. To determine if changes in micro-/nanostructural parameters underpinned changes in ONH micro- and/or nanomechanics

Chapter 2. An investigation into the connective tissue microstructure of the ageing and glaucomatous human optic nerve head

2.1 Introduction

The lamina cribrosa (LC) of the optic nerve head (ONH) is a sieve-like structure of successive connective tissue plates, which comprise elastic fibres (EFs), collagen and proteoglycans. In the human LC, immunolocalisation studies identified collagen types I, III, IV, V and VI (Albon et al., 1995, Albon et al., 2000a, Goldbaum et al., 1989, Hernandez et al., 1986, Hernandez et al., 1987, Morrison et al., 1989b, Rehnberg et al., 1987). Electron microscopy (Quigley et al., 1991b), immunofluorescence (Hernandez et al., 1987, Hernandez et al., 1989, Hernandez, 1992) and histological stains (Oyama et al., 2006) have found EFs to run parallel with collagen in the LC plates (Hernandez et al., 1987, Quigley et al., 1991a, Oyama et al., 2006) and they form a ring at the site of the RoIns into the LC (Quigley et al., 1991a).

EFs and collagen are the major load bearing components within the human ONH and are known to alter with age (Albon et al., 1995, Albon et al., 2000a, Hernandez et al., 1989, Hernandez et al., 1987, Hernandez et al., 1991, Morrison et al., 1989a). It is likely that these changes, at least in part, contribute to the decreased resilience and stiffening of the ageing human LC (Albon et al., 2000b). Since age is a major risk factor in glaucoma (Coleman and Miglior, 2008), and ONH biomechanics are relevant to the disease process (Sigal et al., 2005a), it is important to analyse both collagen and EF in the ONH. Changes in the organisation or content of these components, as a function of age and glaucoma, would inevitably alter the biomechanical response of the ONH to IOP. Thus, characterisation of the load-bearing connective tissue microarchitecture of the ONH as a function of age is essential in understanding its biomechanical behaviour.

Multiphoton microscopy, based on two-photon excited fluorescence (TPEF) and second harmonic generation (SHG), is a recent and important advancement in biological imaging (Zipfel et al., 2003). Second harmonic generation is a nonlinear optical process, in which photons with the same frequency interacting with a nonlinear material are combined to generate new photons with twice the energy, and therefore twice the frequency and half

the wavelength of the initial photons (Mohler et al., 2003) (figure 2.1b). SHG light is emitted coherently and it occurs at non-centrosymmetric loci (i.e. lacks a centre of symmetry) (Millard et al., 2005), such as collagen (Williams et al., 2005) and cellulose (Brown Jr et al., 2003).

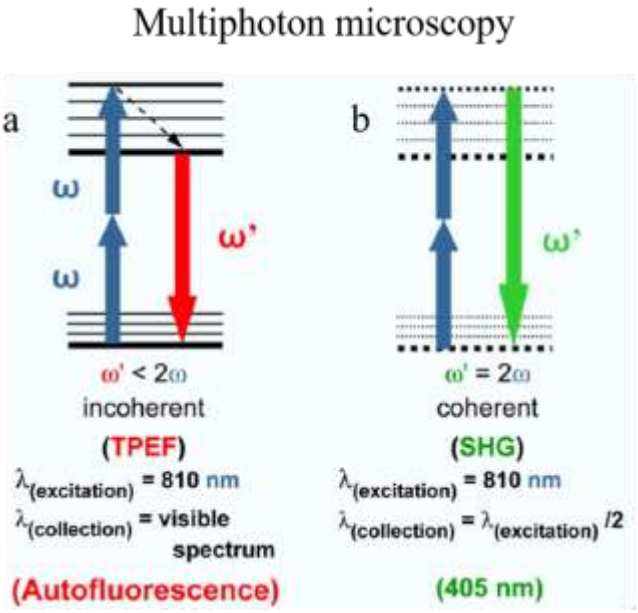

Figure 2.1. Schematic representation of TPEF and SHG. In TPEF, two photons excite a molecule which emits energy as fluorescence normally in the visible spectrum. The emitted wavelength is shorter than the excitation wavelength (incoherent) (a). In SHG, the emitted signal is always exactly half of the excitation wavelength (coherent) (b). Copied and reprinted from (Gailhouste et al., 2010) with permission of Elsevier (see appendix IV.10).

SHG was first demonstrated decades ago (Freund et al., 1986), and since then it has been widely used to study collagen within different tissues such as ovary (Kirkpatrick et al., 2007), skin (Lin et al., 2006), ONH (Jones et al., 2015), mouse cornea (Lo et al., 2006), chick cornea (Koudouna et al., 2018a, Koudouna et al., 2018b, Young et al., 2019), and in diseases such as osteogenesis imperfecta (LaComb et al., 2008) and liver fibrosis (Sun et al., 2008).

SHG has been used to characterise the microstructure and reconstruct the network of collagen fibrils within the ONH (Brown et al., 2007, Winkler et al., 2010) and more recently to characterise collagen fibril orientation (Pijanka et al., 2019). Another important application of SHG has been the characterisation of collagen crimp in a number of tissues, for example, porcine tendon (Lee et al., 2017a), porcine cruciate ligament (Lee

et al., 2017b), rat tail tendon (RTT) (Goulam Houssen et al., 2012) and rat collateral ligament (Franchi et al., 2010).

TPEF is a fluorescence imaging technique that allows imaging of living tissue (Zipfel et al., 2003), in which two excitation photons from a pulsed laser combine to excite a fluorescent molecule. The molecule releases its excitation energy as a fluorescence photon (typically a visible wavelength) (figure 2.1a). TPEF has been used to image EF in different tissues such as heart valves (Schenke-Layland et al., 2004), porcine heart and ovine arteries (Konig et al., 2005) and skin (Chen et al., 2009).

Because TPEF and SHG involve different contrast mechanisms, they can be used simultaneously to provide complementary information regarding tissue structure and function. Specifically, SHG signals depend on the orientation, polarisation, and local symmetry properties of chiral molecules, whereas TPEF results from the nonlinear excitation of molecular fluorescence.
The combination of SHG and TPEF has been used previously to investigate into collagen and EF properties, respectively, of human adipose tissue (Alkhouli et al., 2013), equine cartilage (Mansfield et al., 2009, Mansfield et al., 2013, Moger et al., 2009), bovine and human cartilage (Mansfield et al., 2019) and human cornea (Lewis et al., 2016).

Changes in the connective tissue fibre orientation has been demonstrated before in both healthy ageing and in the glaucomatous ONH (Jones et al., 2015). This study used small angle light scattering (SALS) to further investigate the microarchitecture of the connective tissue within the LC. A key finding of this study was the identification of higher collagen alignment in the infero-temporal LC quadrant in most aged ONHs, with increased alignment in glaucomatous ONHs. However, the authors could not conclude that the fibre alignment and preferred alignment altered as a function of glaucoma stage due to the low sample number. Therefore, more investigations were needed to clarify and confirm the importance of fibre alignment in the glaucomatous ONH.

Regional ONH analysis is important because the superior and inferior regions of the LC have been proposed to be the first damaged in early glaucoma (Quigley et al., 1981, Quigley and Addicks, 1981) and secondly, the infero-temporal region of the LC has been proposed to be the site of focal defects, such as disruption of cribriform plates, (Kiumehr

et al., 2012) and disc haemorrhages (Siegner and Netland, 1996). Additionally, it has been shown previously that this region presented a more pronounced neuroretinal rim loss (Caprioli et al., 1987, Garway-Heath and Hitchings, 1998, Jonas et al., 1993).

This chapter aimed to determine if ONH anatomical, collagen and EF microstructural features are altered in the ageing and/or glaucomatous ONH. Additionally, this study aimed to determine if collagen alignment, found to be higher in the infero-temporal LC in glaucoma, could be detected within SHG image datasets of glaucomatous ONH. Therefore, the combination of SGH and TPEF was used.

In order to achieve this, the objectives of this chapter were to determine:

1. if ONH anatomical features namely, LC, cribriform plate and ppsclera thickness
2. if fibrillar collagen crimp
3. if LC collagen content and fibre orientation

   altered regionally, or as a function of age or glaucoma
4. how LC pore parameters (i.e. pore count, area and circularity, collagen content) alter within glaucomatous LCs

2.2 Materials and methods

2.2.1 Source of tissue

Human eye globes from donors with no history of eye disease (n=28, aged 2 to 88 years) were received from the NHS Blood and Transplant Eye bank (Filton, Bristol, UK) in moist tissue chamber. Globes were immersion fixed on arrival in 4% paraformaldehyde (volume/volume in phosphate buffer solution (PBS), pH 7.4; PFA, see appendix I.1 for preparation). Eight eye globes with glaucomatous optic neuropathy (diagnosed prior to death by a glaucoma ophthalmologist, with mean deviations of the visual field from -1.45 to -23.63 dB), were received from the Mayo Clinic (Rochester, USA) in 4% PFA.
All globes in this thesis, were received, stored and used for research in accordance with Human Tissue Act regulations, under the Cardiff University Cathays Park HTA licence.

2.2.2 Sample preparation

Globes were washed in three changes of PBS (for preparation of lab stock, see appendix I.2) over 72 hours. All eyes were orientated by observing the position of the macula and superior rectus muscles (figure 2.2).

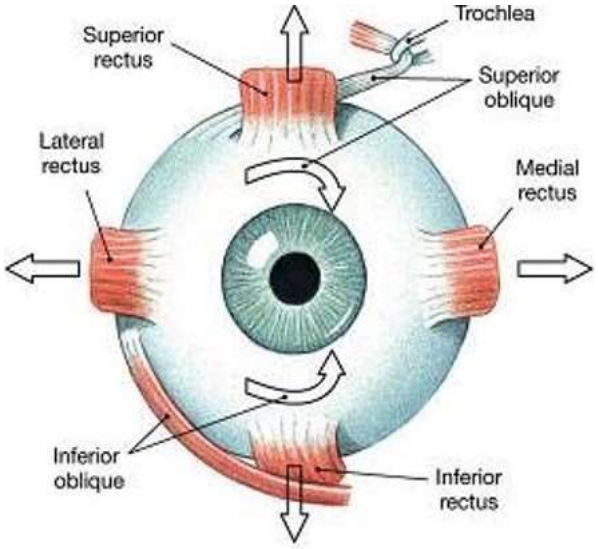

Figure 2.2. Schematic representation of the eyeball's muscles, with the focus on superior rectus muscle which allowed to determine the orientation of the human globes. Taken from https://www.improveeyesighthq.com/eye-muscles.html.

Extraocular muscles and fat, the iris and vitreous humour were gently removed. ONHs with surrounding ppsclera were mounted onto a sledge microtome (Microm HM 440E, Thermo Fisher, UK) and frozen to -35°C.

The right ONHs of 9 pairs (aged 22 to 85 years) were sectioned longitudinally at 250 µm thickness through the Superior-Inferior axis; the left ONHs of the same 9 pairs were cut through Nasal-Temporal axis. The left eye of each pair from 10 healthy (aged 2 to 88 years) and 8 glaucomatous ONHs (see Table 2.1) was cut transversally at 100 µm thickness. All sections were mounted in 1:1 PBS:glycerol on Superfrost Plus slides.

2.2.3 Nonlinear microscopy: Second Harmonic Generation (SHG) and Two Photon Excited Fluorescence (TPEF)

All ONH sections were subjected to TPEF and SHG imaging. A wavelength tuneable ultra-fast pulsed laser system (mode-locked, Ti:Sapphire laser, Chameleon^{TM}, Coherent Lasers, UK) with 140 fs pulses coupled to a Laser Scanning Microscope (LSM880 NLO

with AxioExaminer^{TM} stand, Carl Zeiss Ltd, UK), a Plan-Apochromat 20x/0.8 NA objective lens and ZEN software v2.2 was used to acquire 3D TPEF and SHG images. Total TPEF signal was collected with an epi- (backscattered), non-descanned (external) detector (NDD) using a near-infrared (NIR) blocking band pass filter (505nm ± 60nm bandwidth Brightline^{TM}, Semrock/Laser2000 UK) (figure 2.3). Forward scattered SHG was collected following transmission through the sample at half (400 nm) of the excitation wavelength (800 ± 6 nm).

High resolution SHG and TPEF 3D tiled stacks were simultaneously acquired from longitudinal (n=18, aged 22 to 85 years) and transverse glaucomatous ONHs (n=8, aged 72 to 91 years) plus three age-matched controls (n=3, aged 85, 87 and 88 years) as sequences of optical slices (1024x1024 pixels) at 2μm increments of focus using a fully automated motorised stage. Additionally, high resolution single tiles of the nasal region from transverse (n=10, aged 2 to 88 years) ONHs sections were also acquired for crimp measurements.

Images presented in this chapter have been adjusted in brightness to best represent those observed on the microscope.

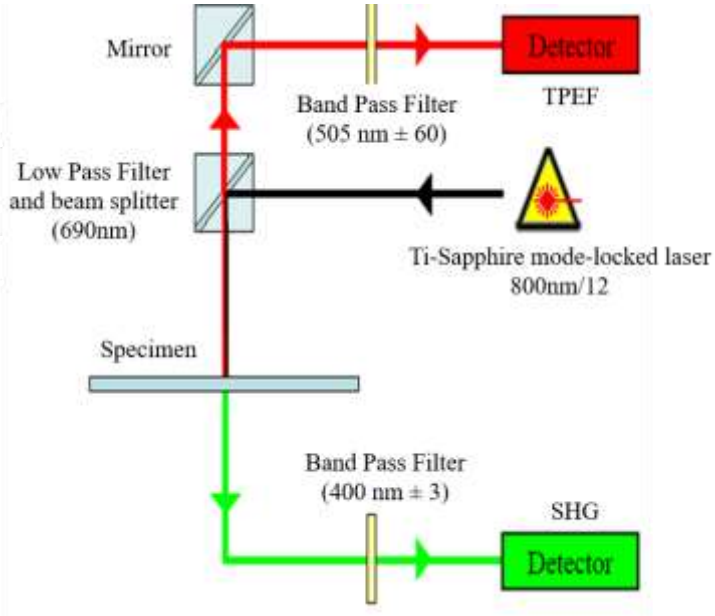

Figure 2.3. Schematic optical set up of the LSM880 laser scanning microscope used in the current study to acquire SHG and TPEF. SHG signal (Excitation 800nm/Emission 400nm) was collected as forward light. TPEF signal (Excitation 800nm/Emission 505nm) was collected in an epi-detector. The low pass filter ensured that wavelength above 690nm were reflected onto the sample and below 690nm were transmitted to the TPEF detector.

Glaucomatous eyes			
Age (years)	**Sex**	**Mean Deviation (dB)**	**Glaucoma Severity**
GL1 (91)	F	+ 1.42	Early
GL2 (72)	F	- 1.54	Early
GL3 (91)	F	- 1. 05	Early
GL4 (87)	F	- 4.35	Early
GL5 (77)	M	- 8.77	Moderate
GL6 (87)	F	- 11.35	Moderate
GL7 (77)	F	- 12.81	Advanced
GL8 (87)	F	- 23.63	Advanced

Table 2.1. Donor demographics of human glaucomatous globes. Visual field sensitivity is measured as vision loss in units of mean deviation (MD), compared to a control population. Glaucoma severity is divided into early: MD < -6 dB; moderate; MD < -12 dB and advanced; MD > -12 dB, based on Hoddap – Parrish – Anderson (Chakravarti 2017) criteria.

2.2.4 Anatomical features of the human ONH as a function of age and region

Anatomical features of the human ONH, namely LC thickness, LC cribriform plates thickness and ppsclera thickness were measured within 18 longitudinal ONH sections, from 9 paired ONHs aged 22 to 85 years old. Nonlinear images were acquired as described in section 2.2.3. Briefly, 3D tiled stacks of longitudinal ONH sections were acquired at 2 μm increments of focus into 250 μm tissue depth. Microscope settings described in section 2.2.3 were applied to all samples to ensure all ONH sections were treated in the same way. Images from the young ages of 22 and 34 years old varied in clarity, therefore visualisation judgment were made to ensure consistency throughout the experiment. Images that did not show a clear discrimination of the collagenous cribriform plates and the LC throughout the depth of the ONH section, were excluded and image acquisition was repeated. The latter was performed by uploading the same setting parameters used for the first run of acquisition.

2.2.4.1 Lamina cribrosa thickness

The lamina cribrosa was defined as the region from the first observed horizontally oriented collagenous plate to last where the postL ON connective tissue septae appeared i.e. where the collagen became vertically oriented (see delineated anterior and posterior surfaces in figures 2.4b and c). ONH datasets were saved as .tiff files and imported into Image J version 1.52s (http://rsb.info.nih.gov/ij). LC thickness measurements (perpendicular distance between the anterior and posterior LC limits) were computed, equidistant between LC periphery and central retinal vessel sheath edge, in 5 optical slices for each LC region (superior, inferior, nasal and temporal) (figure 2.4b).

2.2.4.2 Lamina cribrosa plates thickness

LC plate thickness was measured perpendicular to the upper and lower edges of the plate, within 10 cribriform plates in each of the anterior, mid and posterior e LC (figure 2.4c,e). Three optical slices within each region (superior, inferior, nasal and temporal) were analysed

2.2.4.3 Peripapillary sclera thickness

The ppsclera was defined as the annular ring within 1 mm from the scleral canal (Jones et al 2015). Regional ppsclera thickness was measured perpendicular to its anterior and

posterior surface (figure 2.4d) at 100 µm intervals, starting at 300 µm outside the optic canal, within five optical slices.

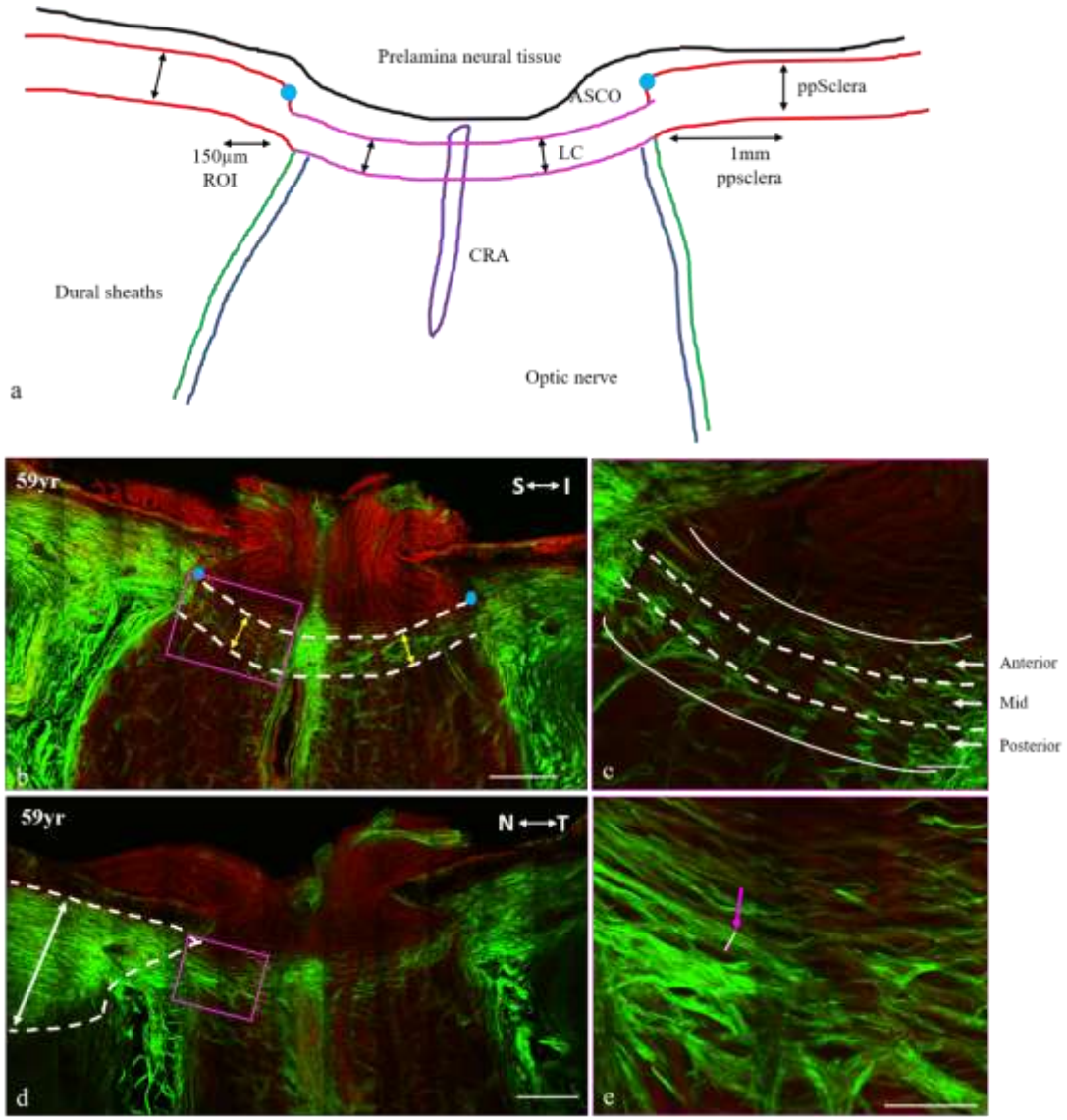

Figure 2.4. Anatomical features measured within longitudinal sections of ONH. Measurements are shown in a schematic view of the ONH (a). Longitudinal section of a 59yr ONH through superior-inferior (b) and nasal-temporal (d) axis. LC thickness (b) was measured perpendicular (b, yellow arrows) to the anterior and posterior surfaces (b, dashed lines). Blue dots represent the anterior scleral canal opening (ASCO). LC plate thickness measurements were performed in the anterior, mid and posterior (c) LC. A perpendicular line between upper and lower plate surfaces (e, white line) defined the thickness of the cribriform plates (e, pink arrows). Ppsclera thickness was measured between and perpendicular (d, white arrow) to its anterior and posterior boundaries (d, dashed line). Scale bars represent 500 µm in b,d and 100 µm in c,e.

2.2.5 Quantification of collagen crimp parameters in the ageing human ONH

High resolution single tile SHG image stacks (100 µm thick) of the nasal region of the ageing and glaucomatous ONHs were converted to sequential 25 µm substacks. Maximum intensity projections (MIPs) of each sub stack from the regions LC, RoIns and ppsclera were created. To visualise the collagen bundles, each MIP was zoomed to 200%. Only collagen bundles that were not overlapping, blurred and/or incomplete (i.e. disappeared into another plane of view) were used in this analysis. A total of 20 measures of each parameter (as previously determined by Jan et al., 2018 to be sufficient for this purpose) were performed in each region.

Collagen crimp period, amplitude, angle and degree of crimping (n=20 measures for each, within triplicate images for each donor ONH) were quantified in the LC, ppsclera and RoIns, in a masked fashion (i.e. all images were assigned anonymised codes by a person not performing measurements. Following analysis, the sample identifier number was reassigned to unmask the data for analysis)

A schematic representation of collagen crimp and measurements performed using Image J software is shown in figure 2.5.

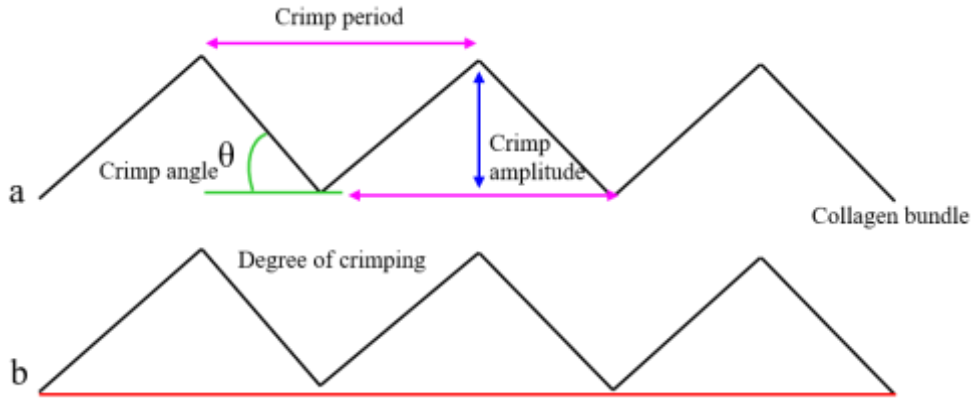

Figure 2.5. Schematic representation of crimp measures performed on high resolution SHG images within the ppsclera, LC and RoIns. a) Crimp period (pink double-head arrow), amplitude (blue double-head arrow) and angle (green line) are shown. b) Degree of crimp was measured as the ratio between the waviness of 3 waves and the end-to-end (straight) line using Neuron J, an image J plugin developed to trace neurites within images of cells in culture.

Measurements were performed only within a clearly visible collagen bundle within a single plane. A straight line measured between two peaks represented the crimp period (figure 2.6a). A perpendicular line measured from the highest point of the peak to the crimp period line (figure 2.6b) represented crimp amplitude. Using the angle tool function, the angle between each period and amplitude combination was drawn and measured in degrees (figure 2.6c). The Image J plugin, Neuron J, (first developed by the Biomedical Imaging Group, Laboratory of Cellular Neurobiology, Swiss Federal Institute of Technology, Lausanne, Switzerland) to trace neurites within neurons for instance in the hippocampus (Meijering et al., 2004)) was used to track the collagen bundles for three consecutive waves. Then an end-to-end line was added and the ratio between the two was calculated (figure 2.6d).

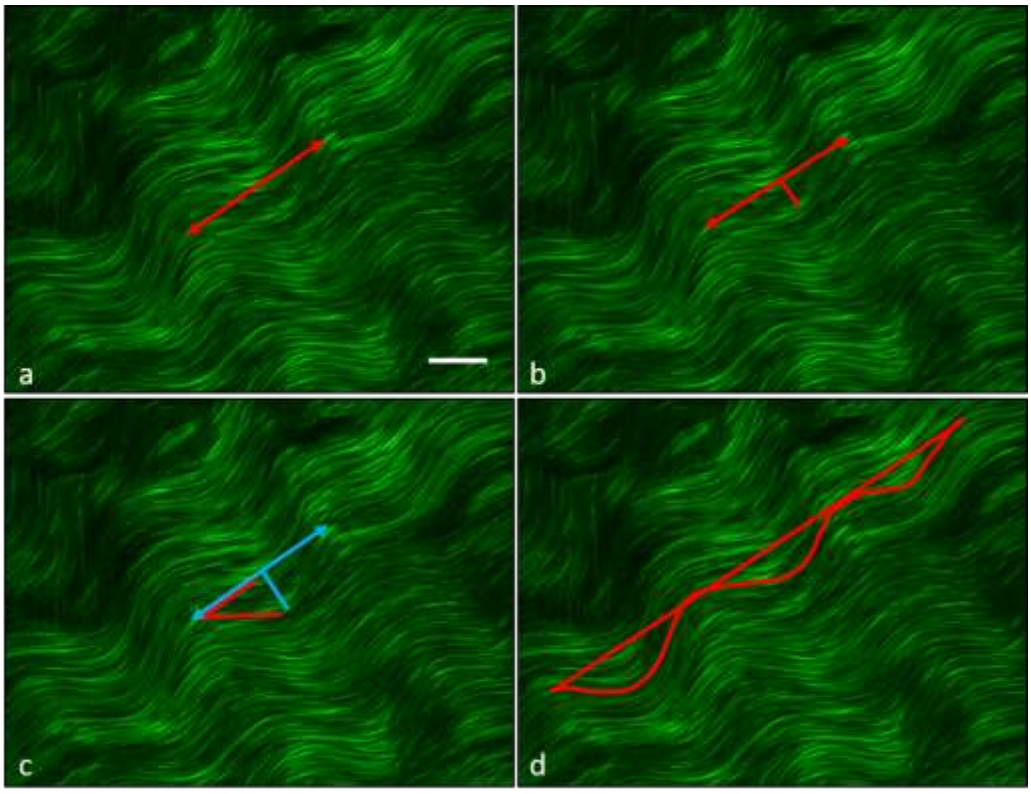

Figure 2.6. Crimp parameters measurements within high resolution SHG images. Crimp period (a) was measured as the distance between two consecutive peaks, amplitude (b) was measured as the perpendicular line from the highest point to the line of the period, the angle (c) between each amplitude and period was measured with the angle tool of Image J and degree of crimp (d) was measured as the ratio between the line of three consecutive waves and the end-to-end line using Neuron J of Image J. Scale bar represent 10µm.

2.2.6 Anatomical features of the human glaucomatous ONH

2.2.6.1 3D Reconstruction of ONH SHG image datasets

Due to the high amount of autofluorescence from ONH components making EFs segmentation impossible, 3D reconstruction of glaucomatous ONHs and age-matched controls was limited to SHG image datasets. 3D SHG datasets of serial transverse sections of ONH, from first section containing preL to postL ON were imported into Amira software (version 6.5, Visualization Sciences Group, Germany) and a noise reduction median filter was applied. The individual 3D ONH datasets from each section were aligned to each other using the "transform editor" module in Amira and assembled together with an overlap of 10% (to remove optical slices without signal) using the "merge" module to reconstruct the 3D ONH.

Next the 3D reconstructed ONH (figure 2.7a) was "thresholded" using the segmentation tool to separate the SHG voxels from the non-SHG voxels. The central retinal artery (CRA) and surrounding vascular sheaths were manually segmented using the brush tool to exclude associated pixels. The segmented ONH dataset was imported into Image J and saved as an 8-bit binary image stack (figure 2.7b).

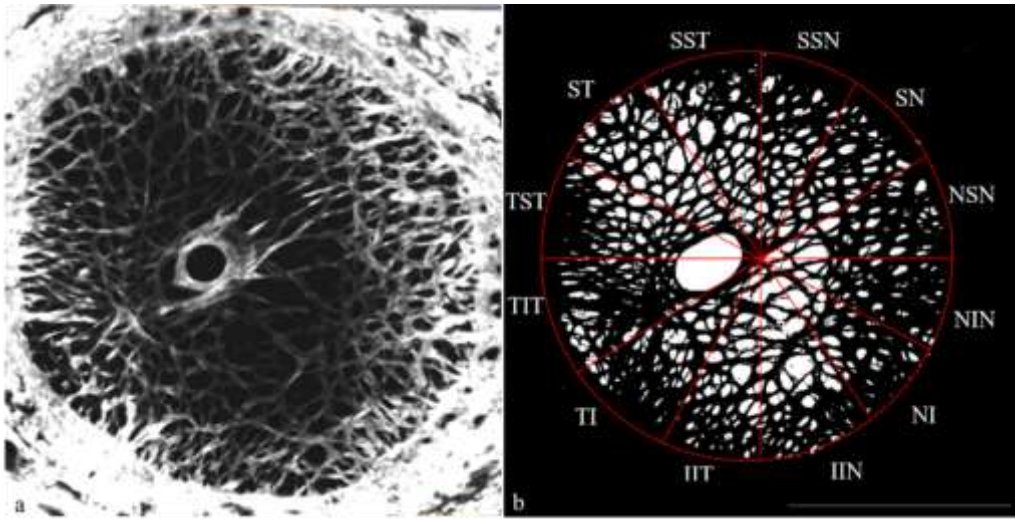

Figure 2.7. ONH SHG data processing and segmentation. Each SHG dataset (a) was segmented in Amira using the "Segmentation tool" and converted into binary (b) in Image J. Sectors in b represent supero-superior/temporal (SST), supero-superior/nasal (SSN), superior-temporal (ST), superior-nasal (SN), temporo-superior/temporal (TST), nasal-superior/nasal (NSN), temporo-inferior/temporal (TIT), nasal-inferior/nasal (NIN), temporal-inferior (TI), nasal-inferior (NI), infero-inferior/temporal (IIT), infero-inferior/nasal (IIN). Scale bar represent 1000 µm.

2.2.6.2 Analysis of pore parameters within control and glaucomatous ONHs

The 3D reconstructed ONH (figure 2.7a) were imported into Amira, and a threshold applied which allowed automatic masking of the pores. This threshold could be adjusted accordingly, resulting in the connective tissue to be highlighted, separating it from the pores (figure 2.7b). The optical section is then manually masked using the brush tool in the Amira segmentation editor, ensuring that only the pores were segmented. The central retinal artery (CRA) and surrounding vascular sheaths were manually segmented using the brush tool to exclude associated pixels.

Pore analysis starts at the segments in which the pores start to form, progressing in depth through the segments until the posterior boundary of the lamina cribrosa is reached.
The segmented ONH dataset was imported into Image J and saved as an 8-bit binary image stack (figure 2.7b).

Each binary 3D ONH dataset (figure 2.8a) was imported into Image J and pore parameters (i.e. pore count, area and circularity) were calculated using the "Analyse particle" function. The minimum and the maximum pixel area size and roundness (circularity) were manually adjusted to exclude anything that was not an object of interest in the image. Pixel area size was set between 0 and infinity to ensure that all pores were included. Roundness was set between 0 and 1 to ensure that all pore shapes were included in the analysis. Pore area size and roundness outside the specified ranges imported in image J were ignored from the analysis. Particles (pores) touching the sector borders and interior holes (i.e pores within larger pores) were excluded from the analysis.

Pore count (total number of pores per mm^2), pore area (area occupied by pores in each mm^2 expressed as a percentage) and circularity (pore roundness; 1.0: perfect circle, 0.0: elongated polygon) were calculated. For regional analysis, a grid defining 12 sectors was overlaid using a custom-made macro named "*ONH-seg.mac*" that divided the optic nerve opening into 12 clock hour sectors (figure 2.8b). Regional analysis was performed by adding together SST-SSN for superior, IIT-IIN for inferior, NSN-NIN for nasal and TST-TIT for temporal.

Sectors SN, NI, TI, ST of the LC were excluded from the analysis to ensure no overlapping of superior, inferior, nasal and temporal regions. Each sector was analysed separately using the ROI manager function of image J. Each ROI (e.g. the inner circle for the iner LC or the SSN sector) was separately selected and results recorded in Excel.

To compare pore parameters between inner and outer LC regions, a circle was manually drawn onto the image, equidistant from the LC insertion and the central retinal vessels, to create inner and outer circle LC regions.

For overall analysis, data within LC regions [superior (SST-SSN), inferior (IIT-IIN), nasal (NSN-NIN) and temporal (TST-TIT)] were added together.

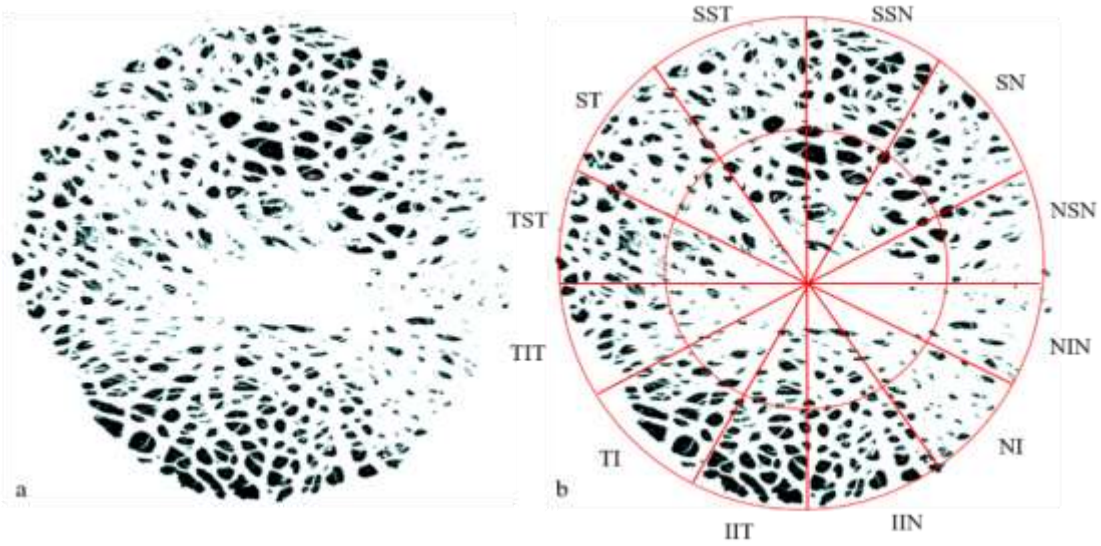

Figure 2.8. Pores segmentation from SHG datasets. Binary image of segmented pores (a) with overlay grid to create regions for analysis. Data in between sectors (i.e. SN, NI, TI, ST) (b) was excluded from the analysis to ensure no overlapping. Note that the central retinal vessel area was excluded from the analysis.

2.2.6.3 LC surface reconstruction to quantify LC thickness and volume

Segmented 3D ONH datasets as binary image stacks were imported into Amira and visualised as 2D ortho-slices to reconstruct the anterior and posterior surfaces of each LC. On the first optical slice corresponding to the anterior surface of the LC ONH stack, multiple landmarks were placed around the optic canal, at the RoIns (figure 2.9a). Then the ortho-slice visualisation of the LC was moved to the last optical slice corresponding

to the posterior LC surface. Multiple landmarks were placed around the optic canal as described above (figure 2.9b). Ortho-slices were then removed to allow the visualisation of the landmarks (figure 2.9c) of the anterior and posterior LC surface. Once all landmarks were placed upon the anterior and posterior surfaces, the “point wrap triangulation” tool module was applied to link the landmarks together to recreate the volume of the LC (figure 2.9d). The ortho slices were included to allow the visualisation of the reconstructed surface enclosing the LC volume along with 2D images (figure 2.9e).

The reconstructed LC enclosed within the ’surface’ was imported into Amira and the “Surface Thickness” module applied to calculate the distance between landmarks of the anterior and posterior LC surfaces. The output text file with measurements of LC thickness was opened in Microsoft Excel and a mean of LC thickness calculated for each reconstructed LC surface within three age-matched controls and eight glaucomatous ONHs. Thickness maps were computed and generated within the Amira Surface View module for each glaucomatous and control ONH. (figure 2.9f).

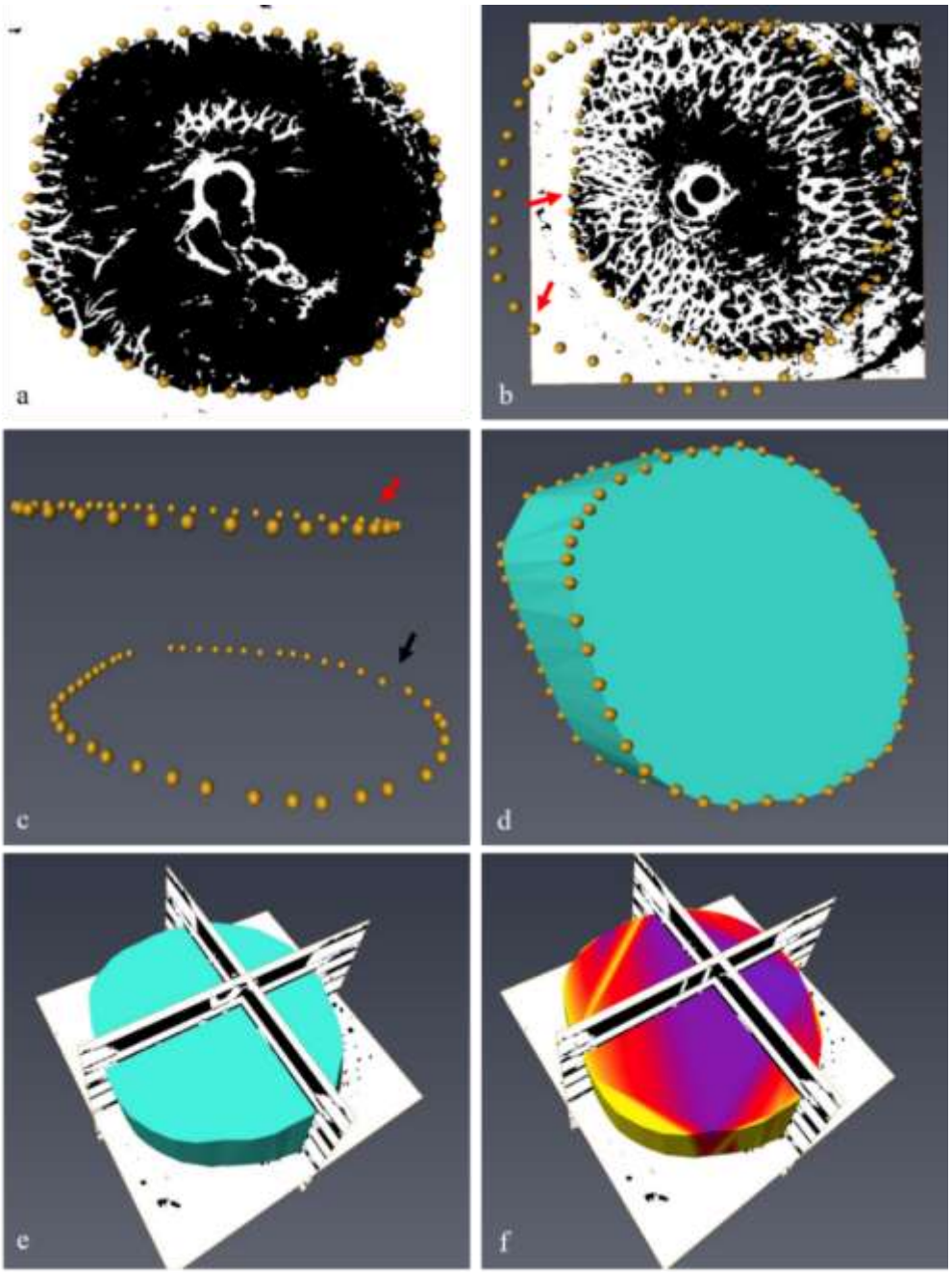

Figure 2.9. LC surface reconstruction using the Amira landmark module. Multiple landmarks were placed at the region of insertion, onto the anterior (a) and posterior (b) surface of the LC, visualised as 2D with the ortho slice module (red arrows in b showed the landmarks positioned onto the surfaces). Landmarks were separately visualised as radial (c) and *enface* (d) to ensure correct positioning around the edges of the LC (red and black arrows in c showed the landmarks onto the anterior and posterior surfaces, respectively). The Amira point wrap tool was usedto join landmarks together (d) and reconstruct the whole surface to enclose the LC volume (e). LC volume area and thickness were calculated for each ONHs and thickness maps recreated with pseudo-colour coded legends (f).

2.2.7 Analysis of fibrillar collagen within glaucomatous ONH

2.2.7.1 Quantification of relative fibrillar collagen content

Each 3D ONH binary stack was imported into Image J and a grid defining 12 sectors (see figure 2.7b) was overlaid as described in 2.2.6.2.
For regional analysis, the total number of SHG pixels in each LC sector [superior (SST-SSN), inferior (IIT-IIN), nasal (NSN-NIN) and temporal (TST-TIT)] was calculated using Image J "Analyse particle" by importing each sector separately into image J and calculated within each optical slice. Regional analysis was performed by adding together SST-SSN for superior, IIT-IIN for inferior, NSN-NIN for nasal and TST-TIT for temporal. The total number of SHG pixel within each region was divided by the total number of pixels and expressed as a percentage.

For overall fibrillar collagen content, the number of SHG pixel within the LC regions (SST-SSN, NSN-NIN, TST-TIT and IIT-IIN) were added together and divided by the total area and expressed as a percentage. To investigate the infero-temporal region of the LC, sectors named IT, IIT and TIT were added together and divided by the sum of respective area and expressed as a percentage.

2.2.7.2 Analysis of fibrillar collagen alignment within the glaucomatous ONH

Image J Orientation J Analysis (Puspoki et al., 2016, Rezakhaniha et al., 2012, Fonck et al., 2009) was used to compute colour coded maps of local orientation and coherency values within the LC, from maximum intensity projections of eight glaucomatous and three controls ONHs SHG datasets. Orientation J was used to create colour-coded orientation coherence maps to allow visualisation of the areas of the ONH with preferred orientation and higher connective tissue alignment. Angle of collagen fibril orientation was assigned to a pixel hue (colour), indicating an angle range between +90° to -90°, whilst pixel saturation (intensity of hue) represented the coherency (i.e. related to the numbers of fibrils oriented in a particular direction). Pixel brightness referred to the original image. As an example of a tissue with highly ordered collagen fibres, SHG images were acquired of rat tail tendon (RTT), as described in 2.2.3 (see figure 2.10a), and orientation maps were computed (figure 2.10b)

For regional analysis, the 12 LC sector grid (see 2.2.6.2) was overlaid onto the SHG image dataset and coherency values calculated as described in 2.2.7.1. To investigate the infero-temporal region of the LC, sectors we added together as described in 2.2.7.1.

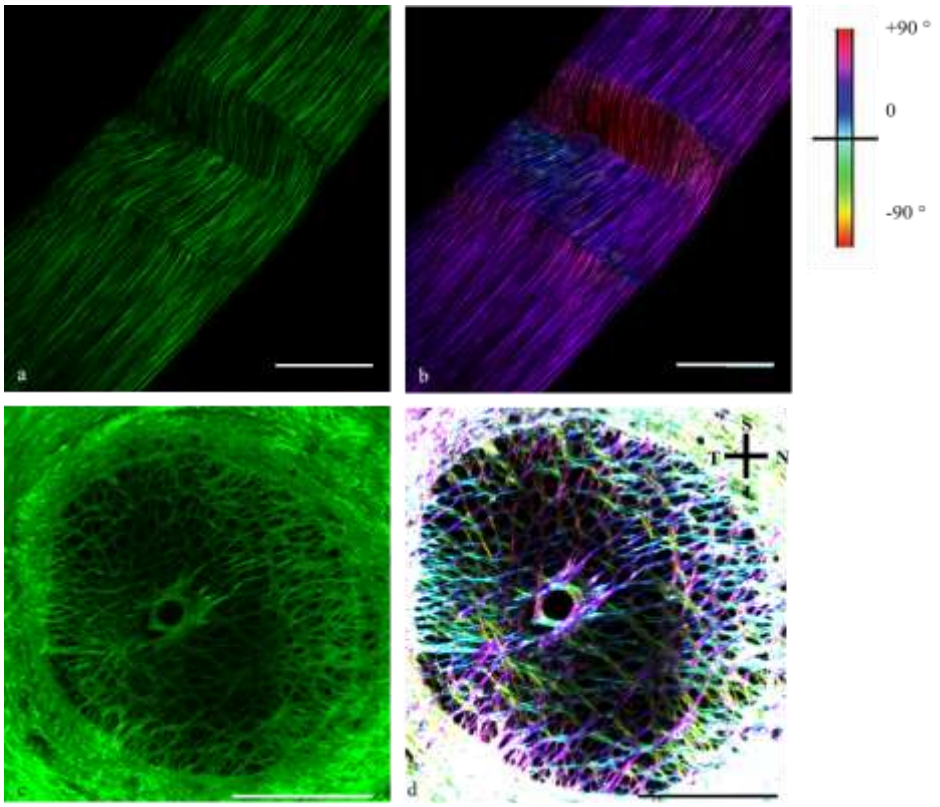

Figure 2.10. Orientation J output from high resolution SHG images of RTT (a,b) and ONH (c,d). The colour-coded survey maps (b,d) were computed to show collagen orientation (colour). This plugin defined orientation as the dominant direction of the features within a region of interest, with the outcome a value between ± 90°. A result of 0° represented the horizontal x-axis, +90° was the vertical y-axis in the superior direction and -90° represented the inferior vertical superior direction. The orientation represented in the colour coded maps allows to identify regions in the ONH of highly aligned collagen. Scale bars in a,b and c,d represent 100 µm and 500 µm, respectively.

2.2.7.3 Quantification of collagen crimp parameters in the human glaucomatous ONH

Collagen crimp parameters were quantified in the nasal region of high-resolution SHG images acquired from transverse sections of 3 glaucomatous ONHs (aged 72, 77 and 77 years) as described in 2.2.5.

2.2.8 Statistical analysis

All statistical analyses, except for crimp angle, were performed in SPSS v.23 (SPSS Inc., USA). Normality of data was determined using the Shapiro-Wilk test with a significance level of $p>0.05$. LC, cribriform plates and ppsclera thickness data were analysed using Pearson's correlation and One-Way ANOVA to determine correlation as a function of age and differences between regions. Crimp period, amplitude and degree of crimping were analysed using Spearman's rank correlation and Mann Whitney test to test for correlation as a function of age and differences between glaucoma and age-matched controls, respectively. Pores, LC thickness, LC volume, collagen content as the percentage of SHG pixels and coherency measurements deemed to be normally distributed, therefore One-Way ANOVA and Independent T-test were used.

To account for potential nonlinearities in the relationships between crimp parameters and age, three transforms for each parameter were considered: no transform (linear), logarithmic, and square root.

To test for differences in the crimp angle measurements, circular statistics were performed using Oriana software (Kovach Computing Services, UK). The measures were checked for a preferred direction with Rayleigh test at $p<0.05$ (null hypothesis is that the data is distributed in uniform manner) so at $p<0.05$ the null hypothesis is rejected. To test for normality, circular data were was tested for a von Mises distribution (corresponds to testing for normal distribution) with the Watson U test with $p<0.05$. (i.e. if $p<0.05$, data is not normally distributed). Mean angles were automatically computed by Oriana software.

LC and ppsclera angle measurements as a function of age did not fall into a von Mises distribution. The circular linear correlation coefficient test was used to determine if a circular variable (angle) correlated with a linear one (age). In the LC, glaucoma angle measurements were found to be normally distributed so then the Watson Williams F test was used to compare age-matched controls and glaucoma. Ppsclera data was normally distributed, so a non-parametric Mardia-Watson-Wheeler Test was used to compare age-matched controls and glaucoma. To test for differences in the angle measures between LC and ppsclera at each age and glaucoma, the Hotelling's Paired Test was used. This test checked whether the paired observations differ between the two samples.

2.3 Results

2.3.1 Anatomical features of the human ONH as a function of age and region

High resolution 3D tiled ONH datasets were obtained from longitudinal sections at different ages (figure 2.11). Fibrillar collagen was evident within the cribriform plates at LC (figure 2.11d-f) and ppsclera (figure 2.11a-c) as intense SHG signal within the latter. Horizontally oriented cribriform plates were visible throughout the LC thickness (figure 2.11d-f). The SHG signal was also seen in the vascular sheaths surrounding the central retinal vessels, which passed through the LC (figure 2.11a-c). In the postL ON, collagen became longitudinally oriented within connective tissue septae (figure 2.11a-c).
The TPEF signal associated with EFs appeared visible at all ages (figure 2.11a-c), although minimal in the young 34 years old ONH (figure 2.11a).

2.3.1.1 Lamina cribrosa thickness

LC thickness ranged from 334.13 ± 5.8 μm at the age of 22 years to 353.11 ± 7.6 μm at the age of 85 year (Table 2.2), although no significant correlation was found with age ($p=0.367$, $r=0.342$, figure 2.12a) or LC regions ($p=0.449$, figure 2.12b). No regional differences ($p=0.416$) or correlation with age were observed [superior ($p=0.272$, $r=0.411$), inferior ($p=0.276$, $r=0.408$), nasal ($p=0.229$, $r=0.446$) and temporal ($p=0.270$, $r=0.412$)].

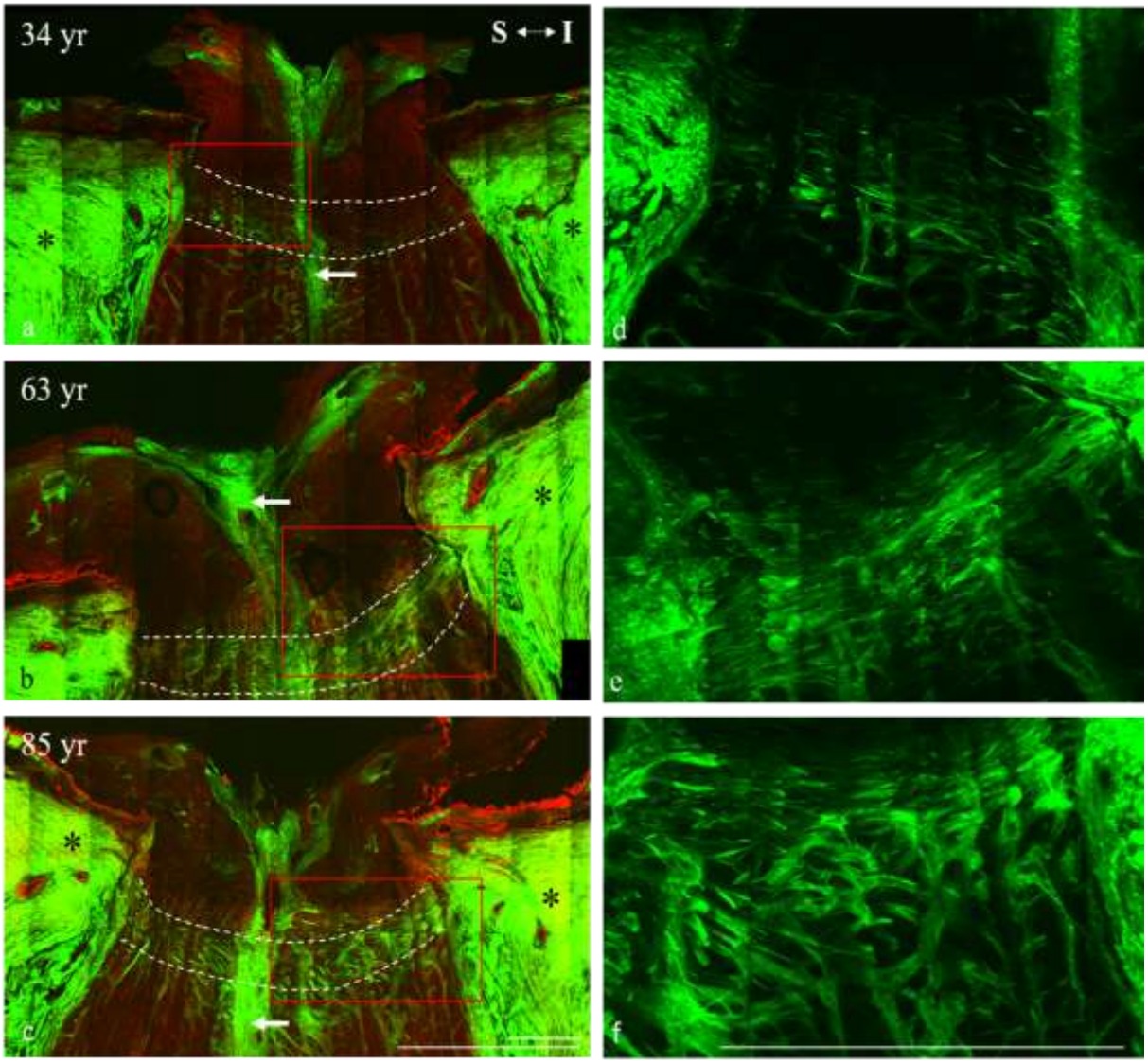

Figure 2.11. High resolution tiled images showing pseudo-colour coded nonlinear signals [SHG: green (collagen); TPEF: red (EF)] in young 34-year-old (a,d), middle age 63-year-old (b,e) and elderly 85 year old (c,f) ONHs sections. TPEF signal depicting EF appeared less intense in the young 34yr (g) then in the 63yr (b) and 85yr (c). SHG signal depicting fibrillar collagen appeared stronger in the ppsclera than in the LC at all ages (a-c, black asterisks). The LC enclosed in the dashed lines (a-c) appeared as a thick layer of connective tissue. The lamina cribrosa was defined as the region from the first observed horizontally oriented collagenous plate to last where the postL ON connective tissue septae appeared. The upper markers to define the upper surface of the LC were placed where the first collagenous visible cribriform plate appeared inserted in the surrounding sclera. The lower markers to define the lower surface of the LC were placed where the last collagenous cribriform plate was inserted into the sclera and just before collagenous bundles appeared vertically orientated, which defined the postlaminar ON. Strong SHG signal also appeared from the CRA (a-c, white arrows). At higher magnification (d,e,f), strong SHG signal appeared within the LC plates. Scale bars are 500µm.

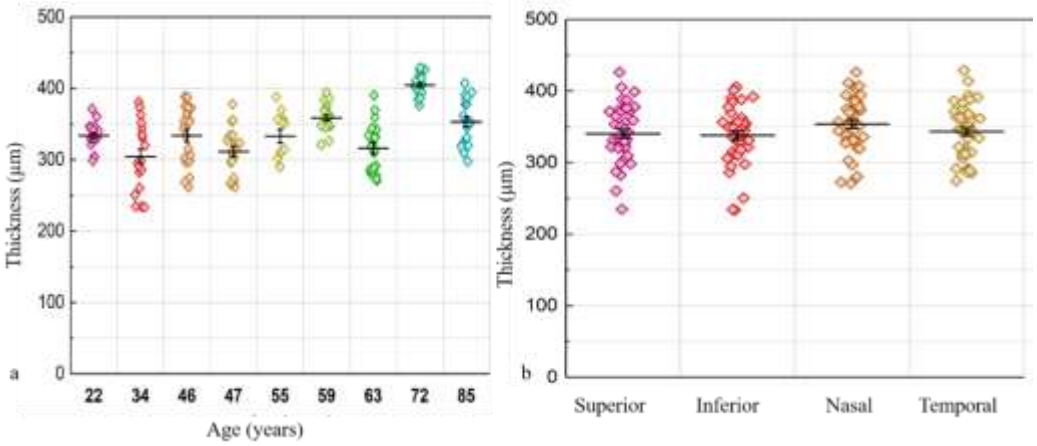

Figure 2.12. LC thickness as a function of age and region (mean +/-sd). LC thickness ranged from 334.13 ± 5.8 µm at the age of 22 year to 353.11 ± 7.6 µm at the age of 85 year (a), although no significant changes were found within age or regions (b).

2.3.1.2 Lamina cribrosa plates thickness

LC cribriform plates thicknesses (Table 2.2), ranged from 14.85 ± 0.3 µm at the age of 22 years to 16.39 ± 0.3 µm at the age of 85 years but no significant correlation with age was observed (p=0.120, r=0.556), (figure 2.13a) or region (p=0.826), (figure 2.13b). No differences (p=0.657) or correlation between regions and age [superior (p=0.243, r=0.434), inferior (p=0.407, r=0.316), nasal (p=0.144, r=0.528) and temporal (p=0.09, r=0.803)], [anterior (p=0.118, r=0.558), mid (0.085, r=0.605) and posterior (p=0.112, r=0.567) was observed (figure 2.13c).

Age (years)	LC thickness (µm) ± sd	LC Plates thickness (µm) ± sd	Ppsclera thickness (µm) ± sd
22	334.13 ± 5.8	14.85 ± 0.3	806.09 ± 32.8
34	310.24 ± 7.8	14.53 ± 0.1	774.40 ± 25.7
46	371.57 ± 5.9	14.54 ± 0.07	910.48 ± 18.1
47	308.26 ± 9.5	16.39 ± 0.1	795.79 ± 27.7
55	332.94 ± 9.3	15.37 ± 0.2	809.71 ± 24.2
59	365.12 ± 10.4	15.93 ± 0.6	925.64 ± 14.6
63	315.90 ± 9.7	14.71 ± 0.1	987.71 ± 29.6
72	403.17 ± 5.7	19.51 ± 0.3	896.96 ± 22.8
85	353.11 ± 7.6	16.39 ± 0.3	958.05 ± 24.6

Table 2.2. LC, cribriform plates and ppsclera thicknesses as a function of age (mean +/-sd).

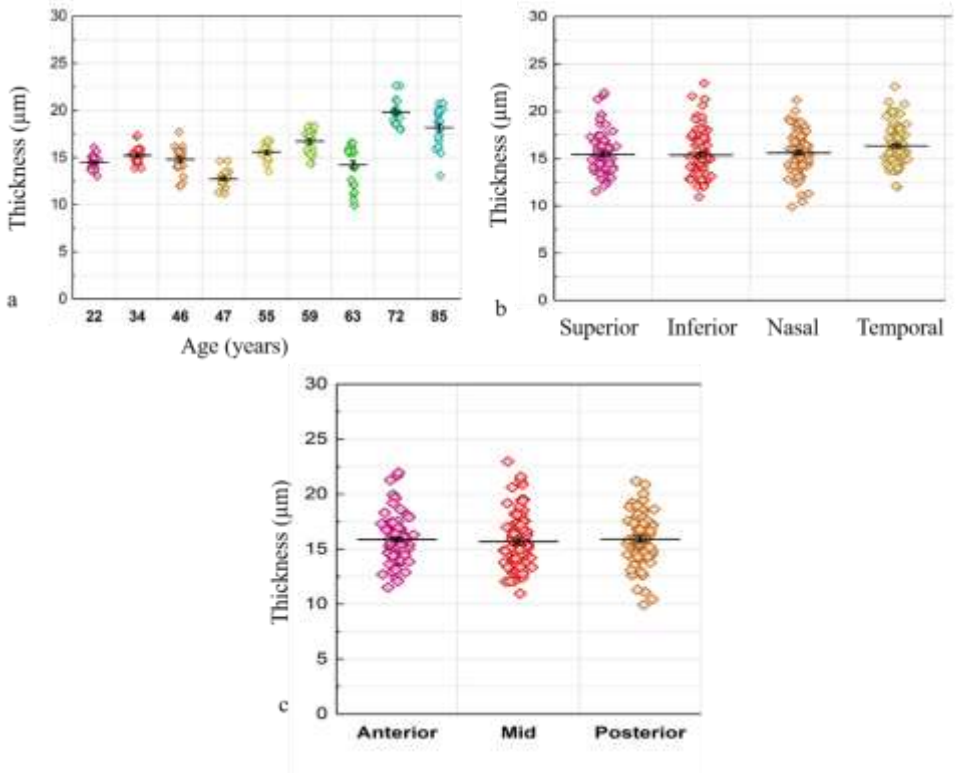

Figure 2.13. LC cribriform plate thickness as a function of age and regions (mean +/-sd). No significant changes were observed with age (a) or regions (b) and between anterior, mid and posterior LC (c).

2.3.1.3 Ppsclera thickness

Ppsclera thickness ranged from 806.09 ± 32.8 µm at the age of 22 year to 958.05 ± 24.6 µm at the age of 85 year (Table 2.2), however it did not show significant increase in age (p=0.571, r=0.219) (figure 2.14a). When data was pulled together for regional analysis, no significant differences were found between regions (p=0.578) or in age [superior (p=0.658, r=-0.172), inferior (p=0.478, r=0.273), nasal (p=0.602, r=0.251) and temporal (p=0.516, r=0.202)] (figure 2.14b).

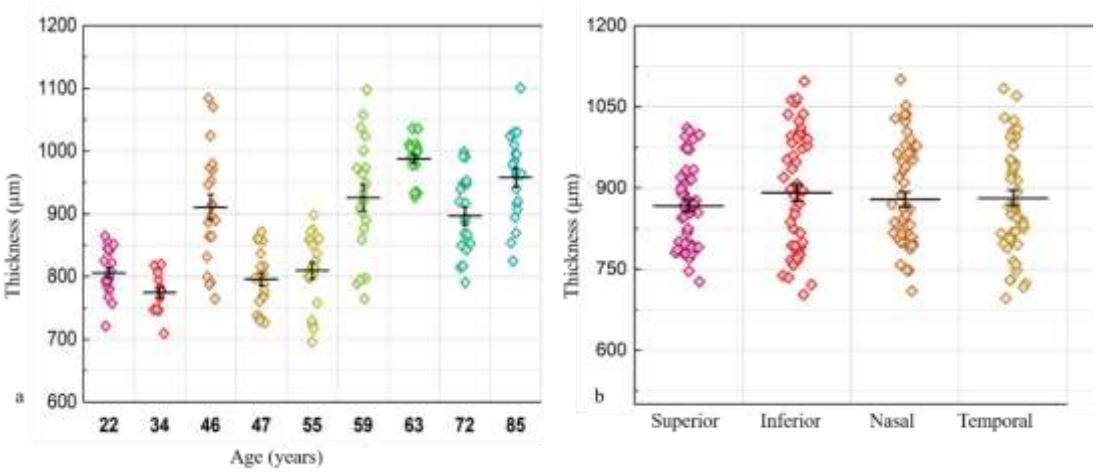

Figure 2.14. Ppsclera thickness as a function of age and regions (mean +/-sd). Ppsclera thickness ranged from 806.09 ± 32.8 µm at the age of 22 year to 958.05 ± 24.6 µm at the age of 85 year (a), however, it did not significantly change in age or regions (b).

2.3.2 Quantification of collagen crimp parameters

Single images of healthy elderly human ONH at level of LC show distribution of collagen within the cribriform plates and RoIns. Collagen crimp within the cribriform plates was visible at the age of 6 years (figure 2.15a) and 46 years (figure 2.15b), but not at 63 (figure 2.15c) and 85 years old (figure 2.15d). TPEF signal showed an intense fluorescence due to EFs within the LC and other endogenous fluorescence (figure 2.15e-h). Combined SHG and TPEF signals (figure 2.15i-n) demonstrated the absence of EFs within the 6-year-old (figure 2.15i). However, EFs were co-distributed with collagen within the cribriform plates LC greater than 46 years (figure 2.15l-n).

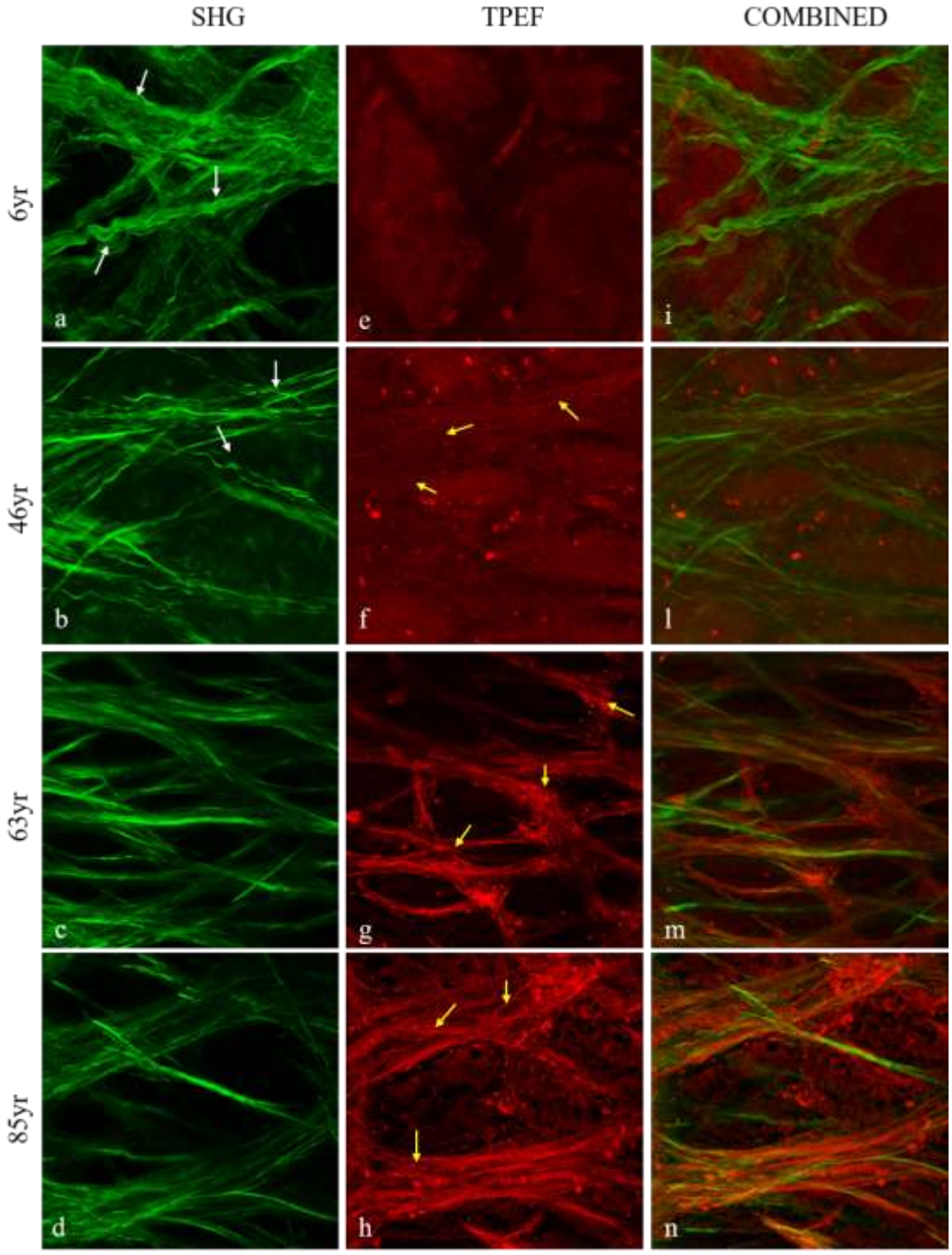

Figure 2.15. High resolution single images from nasal region of healthy ageing LC showing pseudo-colour coded nonlinear signals [SHG: green (collagen); TPEF: red (elastin)]. SHG signal appeared intense at all ages (a-d) and the collagen crimp was observed at the young ages of 6 years (a, white arrows) and 46 years old (b, white arrows) but not at older ages (c,d). TPEF signal appeared less intense at the ages of 6 years (e) compared to older ages (f-h). EFs were not observed at the age of 6 years old (e) compared to older ages (f-h) where they appeared visible within the cribriform plates (f-h, yellow arrows). Combined images (i-n) showing EFs running parallel with collagen within the cribriform plates. Scale bar represents 50 μm.

2.3.2.1 Fibrillar collagen crimp parameters in the ageing LC

In the young LC (figure 2.16a-c) collagen crimp was observed in all cribriform plates, whereas at the age of 46 and 57 years old (figure 2.16d,e), some wavy-like bundles were seen in between straight fibre bundles. Above the age of 60 years, no wavy-like appearance was evident (figure 2.16f-l). No significant increase as a function of age was observed in the collagen crimp period ($p=0.668$, $rs=0.167$) (figure 2.16m), crimp amplitude ($p=0.444$, $rs=0.293$) (figure 2.16n), degree of crimping ($p=0.546$, $rs=0.233$) (figure 2.16p) or crimp angle ($p=0.999$, $r=0.012$) (figure 2.16o). Data transformation did not show differences in the ageing LC period [square, square root and log data ($p=0.726$)], amplitude [square, square root and log data ($p=0.424$)] and degree of crimping [square, square root and log data ($p=0.376$)].

2.3.2.2 Fibrillar collagen crimp parameters in the ageing region of insertion

Similarly, fibrillar collagen was visible in the RoIns at the young ages of 2 and 6-year-old (figure 2.17a,b). Some wavy like collagen bundles were also evident at the ages of 21 and 46-year-old (figure 2.17c,d). However, at the age of 57 and above, collagen waviness was no longer visible (figure 2.17e-l). In the RoIns, no significant changes were observed in the collagen crimp period ($p=0.265$, $rs=0.417$) (figure 2.17m), crimp amplitude ($p=0.244$, $rs=-0.433$) (figure 2.17n), degree of crimping ($p=0.406$, $rs=-0.317$) (figure 2.17p) or crimp angle ($p=0.322$, $r=0.432$) (figure 2.17o). Data transformation did not show differences in the ageing period [square, square root and log data ($p=0.310$)], amplitude [square, square root and log data ($p=0.172$)] and degree of crimping [square, square root and log data ($p=0.710$)].

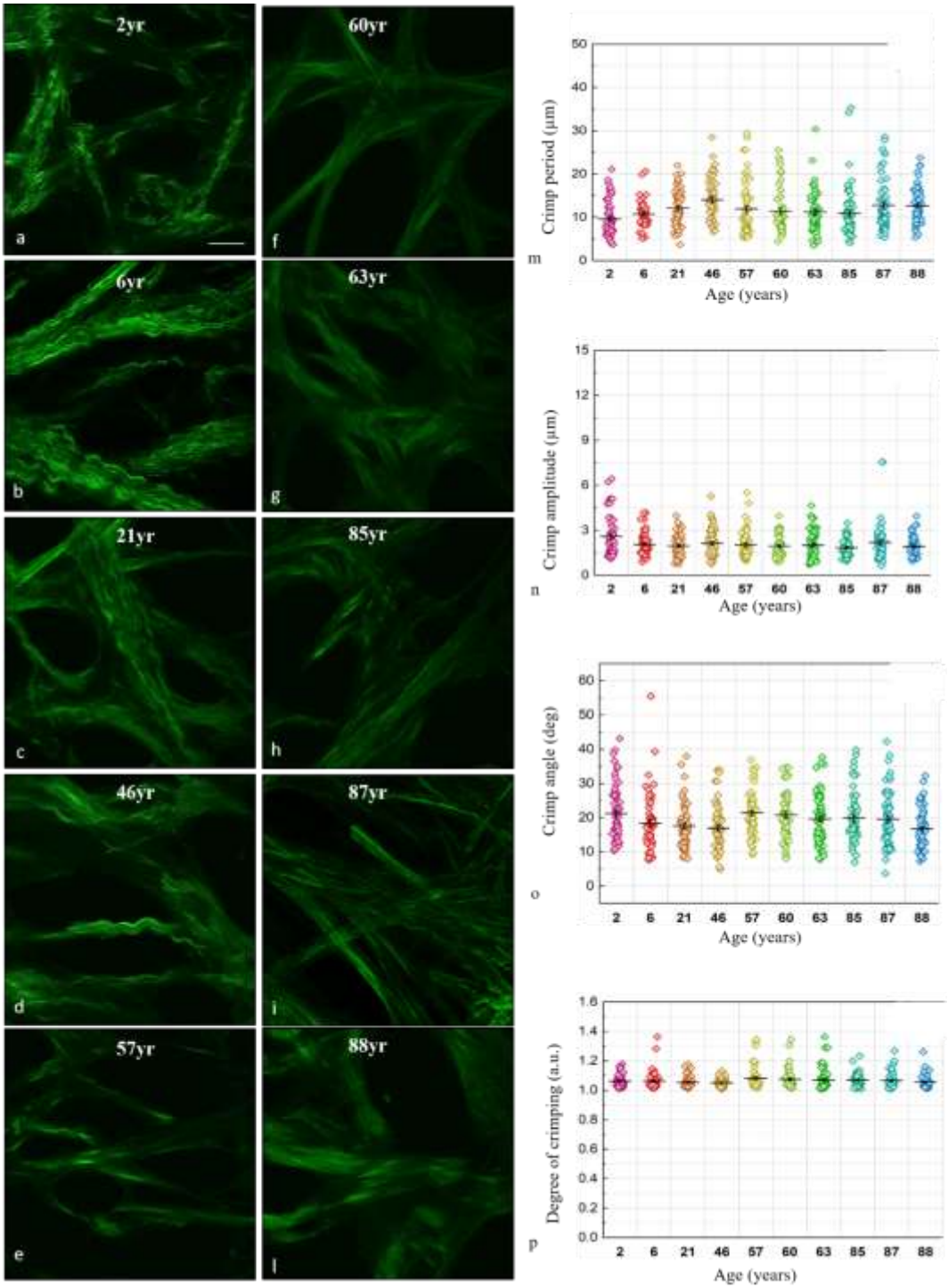

Figure 2.16. High resolution nonlinear imaging showing fibrillar collagen appearance in the LC at different ages. Fibrillar collagen crimp had a wavy-like appearance at young age of 2 (a), 6 (b) and 21 (c) year old. Waviness was still visible at the age of 46 (d) and 57-year-old (e), although only within a few regions of interests. Above the age of 60 year, wavy-like appearance was no longer visible (f-l). Crimp period (m), amplitude (n), angle (o) and waviness (p), did not show any significant changes as a function of age. Scale bar represents 30μm.

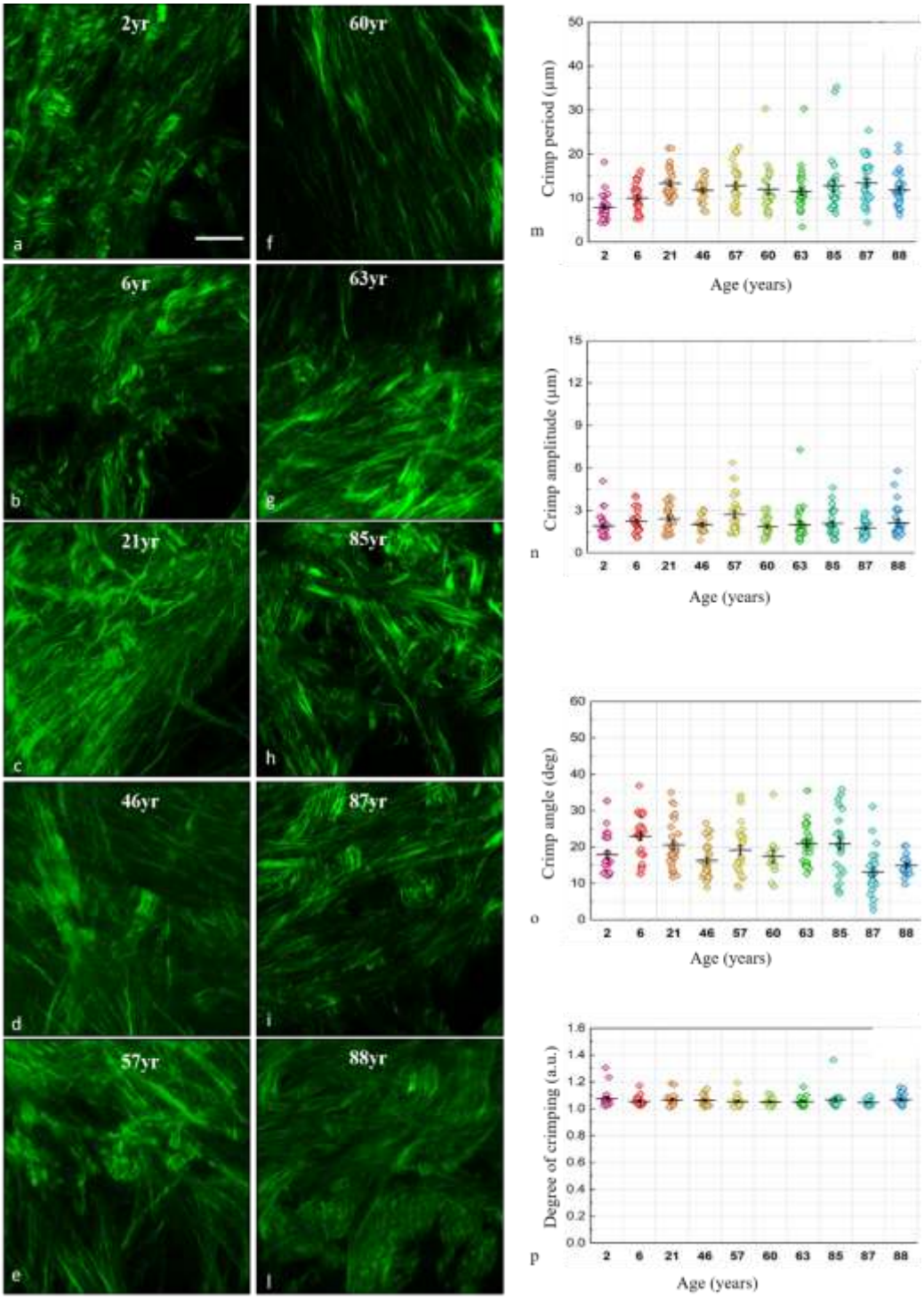

Figure 2.17. High resolution nonlinear imaging showing fibrillar collagen appearance in the RoIns at different ages. Fibrillar collagen crimp had a wavy-like appearance at young age of 2 (a), 6 (b) and 21 (c) year old. Waviness was still visible at the age of 46 (d), although only within few regions of interests. Above the age of 57 year, wavy-like appearance was no longer visible (e-l). Crimp period (m), amplitude (n), angle (o) and waviness (p), did not show any significant changes as a function of age. Scale bar represents 30 µm.

2.3.2.3 Fibrillar collagen crimp parameters in the ageing ppsclera

In the ppsclera, crimped collagen bundles were clear at young ages of 2, 6 and 21 years old (figure 2.18a-c).

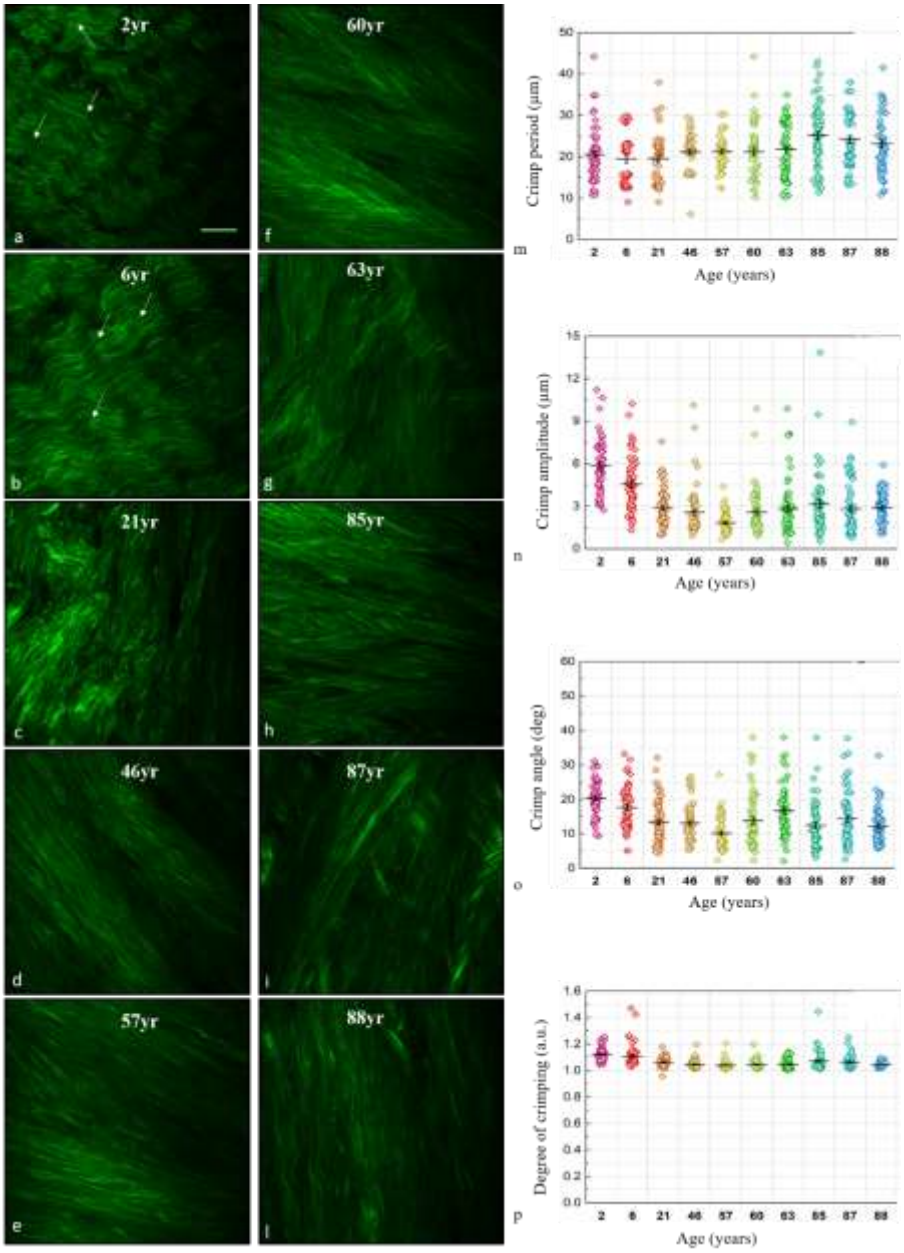

Figure 2.18. High resolution nonlinear imaging showing fibrillar collagen appearance in the ppsclera at different ages. Fibrillar collagen crimp had a wavy-like appearance at young age of 2 (a, white arrows), 6 (b, white arrows) and 21 (c) year old. Waviness was still visible at the age of 46 (d), although only within few regions of interests. Above the age of 57 year, wavy-like appearance was no longer visible (e-l). Collagen crimp period (m) significantly increased as a function of age from 19.64μm ± 6.41 at the age 2 to 22.04μm ± 10 at the age of 88 years (p=0.004), however, crimp amplitude (n), angle (o) and waviness (p) did not show any significant changes in age. Scale bar represents 30 μm.

From the age of 46 to older ages (figure 2.18d-l), no wavy like collagen bundles were observed and fibrillar collagen bundles were mostly straight in appearance. Within the ppsclera, the collagen crimp period significantly increased as a function of age from 19.64 ± 6.41 µm at the age 2 to 22.04 ± 10 µm at the age of 88 years (p=0.004, rs=0.850) (figure 2.18m). However, no significant differences were found in any other parameters [crimp amplitude (p=0.112, rs=0.567), degree of crimping (p=0.170, rs=0.500) and crimp angle (p=0.062, rs=0.659)] (figure 2.18n-p). Interestingly, the ppsclera crimp period (p=0.008) and crimp amplitude (p=0.008) were significantly larger than those in the LC. Data transformation showed a significant increase in ppsclera crimp period [square, square root and log data (p=0.001)] but not in the amplitude [square, square root and log data (p=0.553)] and degree of crimping [square, square root and log data (p=0.235)].

2.3.3 Anatomical features of the human glaucomatous ONH

2.3.3.1 3D Reconstruction of ONH SHG image datasets

Visualisation of transverse 3D reconstructed datasets (figure 2.19a,c,e,g) showed areas of interrupted connective tissue in the superior region within early, moderate and advanced glaucomatous ONHs (figure 2.19d,f,h). In early glaucoma, some disruption of the collagenous beams was seen in the superior region (figure 2.19d) in the *enface* view. In moderate (figure 2.19f) and advanced glaucoma (figure 2.19h), disruption of collagenous beams was visible from the *enface* view and appeared more pronounced than in early glaucoma.

2.3.3.2 Analysis of pore parameters within the glaucomatous ONH

Overall, pores appeared larger and more defined towards the edges of the LC and in the superior/inferior regions compared to nasal and temporal, giving the LC the characteristic hour-glass shape, previously described (Quigley and Addicks, 1981, Radius, 1981, Jonas et al., 1991).

In advanced glaucoma, pores appeared more elongated and oval (figure 2.19g,h) compared to those observed in healthy eyes, which appeared relatively circular (figure 2.19a,b). In both moderate (figure 2.19e,f) and advanced (figure 2.19g,h) glaucoma, pores also appeared bigger with less connective tissue surrounding them.

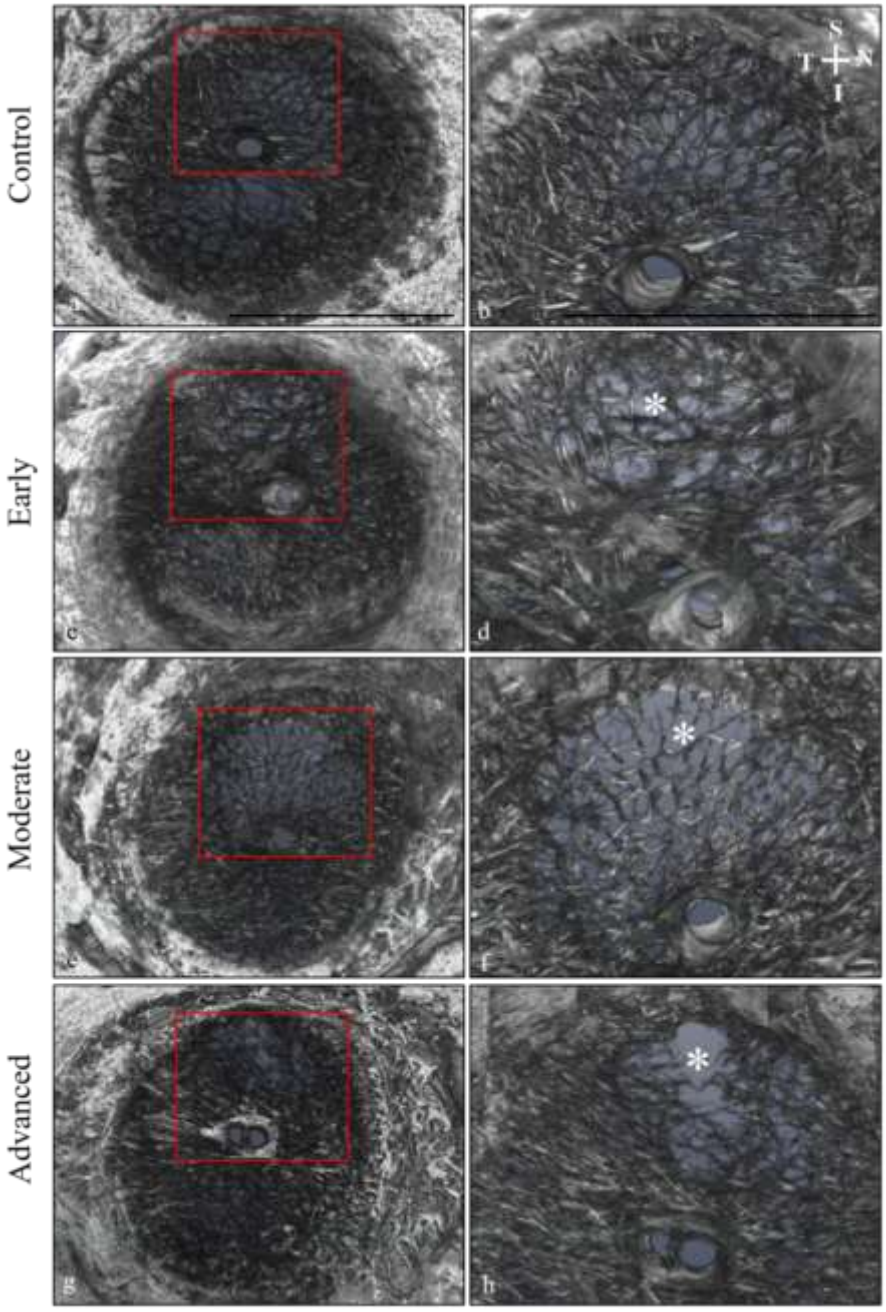

Figure 2.19. 3D volume rendering of reconstructed SHG datasets of human ONH from age-matched controls and glaucoma. In the control, less collagenous beams appear in the superior-inferior regions (a) compared to the nasal-temporal. A magnification of a (b) showed an intact collagenous network. In early (c), moderate (e) and advanced (g) glaucoma, disruption and misalignment of the collagenous beams were identified in the superior region. A magnification on the superior region of early (d), moderate (f) and advanced glaucoma (h) showed some fragmented collagenous beams (white asterisks). Scale bars represent 1mm.

Pore count (see Table 2.3) showed an overall decrease in all glaucomatous LC (p=0.006) compared to controls (figure 2.20a). Circularity was significantly lower in advanced glaucoma (p=0.006) compared to controls (figure 2.20c). No differences were found in pore area (p=0.056) (figure 2.20b). Regional analysis showed a significant lower pore count (figure 2.20d) in all regions [superior (p=0.019), inferior (p=0.015), nasal (p=0.033) and temporal (p=0.002)] whereas no differences were observed in pore area [superior (p=0.055), inferior (p=0.908), nasal (p=0.198) and temporal (p=0.125)] (figure 2.20e) compared to controls. Circularity appeared significantly lower in the temporal region only in advanced glaucoma (p=0.045) (figure 2.20f). When pores parameters were quantified between inner and outer LC, pore count was significant lower in moderate and advanced glaucoma in the inner LC compared to controls and early glaucoma (p=0.029) (figure 2.20g). No differences in the outer LC were observed in count (p=0.065), area (p=0.125) and circularity (p=0.104).

Pore count (number of pores) ± sd				
	Superior	Inferior	Nasal	Temporal
Age-matched controls	414.48 ± 135.7	356.06 ± 242.48	468.29 ± 144.20	592.61 ± 99.86
Early GL	171.33 ± 156.93	268.12 ± 126.18	277.79 ± 128.39	254.55 ± 151.80
Moderate GL	203.68 ± 139.11	206.72 ± 96.99	295.70 ± 96.14	226.5 ± 107.38
Advanced GL	137.39 ± 86.53	140.87 ± 167.42	188.31 ± 72.23	218.77 ± 81.73
Pore area (%) ± sd				
	Superior	Inferior	Nasal	Temporal
Age-matched controls	20.86 ± 4.77	21.68 ± 4.22	21.95 ± 3.77	21.89 ± 3.95
Early GL	21.78 ± 4.22	22.34 ± 9.80	19.53 ± 13.14	19.36 ± 9.35
Moderate GL	22.38 ± 3.77	22.60 ± 16.83	18.93 ± 12.22	20.58 ± 13.83
Advanced GL	22.15 ± 3.95	18.14 ± 10.59	20.36 ± 9.52	19.78 ± 6.32
Pore circularity (a.u.) ± sd				
	Superior	Inferior	Nasal	Temporal
Age-matched controls	0.70 ± 0.02	0.70 ± 0.02	0.70 ± 0.02	0.71 ± 0.01
Early GL	0.69 ± 0.02	0.69 ± 0.07	0.68 ± 0.07	0.69 ± 0.03
Moderate GL	0.68 ± 0.02	0.68 ± 0.03	0.68 ± 0.04	0.69 ± 0.03
Advanced GL	0.68 ± 0.01	0.68 ± 0.03	0.69 ± 0.03	0.67 ± 0.03

Table 2.3. Pore parameters (mean +/-sd) within glaucomatous ONHs.

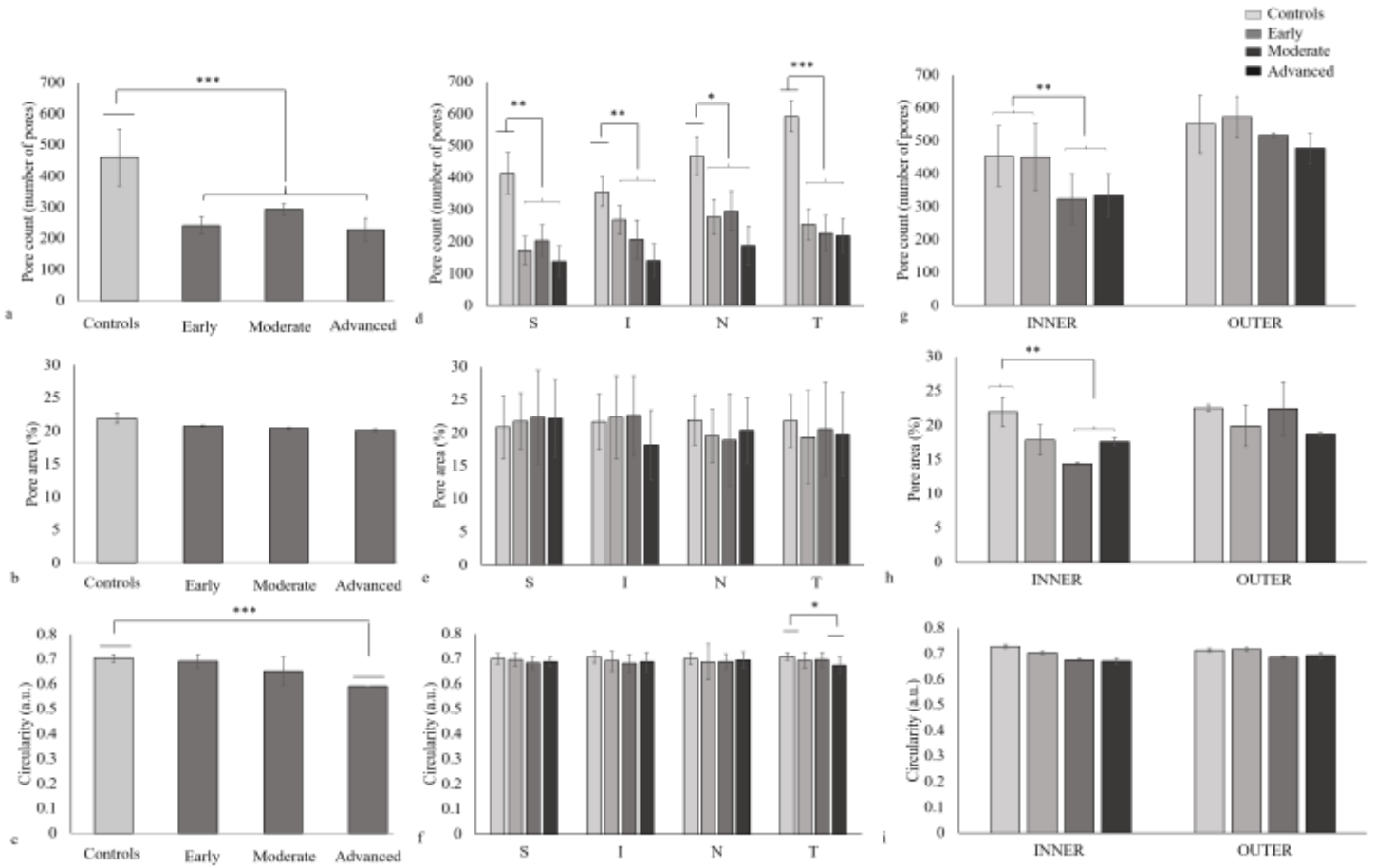

Figure 2.20. Lamina cribrosa pore count, circularity and area (mean ± sd) within glaucomatous ONHs. (a) Pore count decreased significantly within the LC at all glaucoma stages compared to control LC (p=0.006), consistent with a significantly lower pore count in all regions (d)Data comparison between glaucoma groups, identified a pore count significantly lower (p=0.029) in moderate and advanced glaucoma, compared to early and controls (g) in the inner LC, but no differences within the outer LC (b) No differences in the overall pore area (c) or between regions (e) were observed. However, pore area was significantly lower in moderate and advanced glaucoma (p=0.031) compared to controls in the inner LC (h), with no differences identified within the outer LC. LC pore roundness i.e. circularity was significantly lower in advanced glaucoma (p=0.006), suggesting pore elongation compared to controls. Regional analysis revealed lower circularity in the temporal region (p=0.045) (f) of advanced glaucoma. No differences were observed in circularity (i).

2.3.3.3 LC surface reconstruction to quantify LC thickness and volume

LC thickness maps were produced from the reconstructed and segmented SHG signal from each ONH section and therefore represented the anatomy of the LC as the fibrillar collagen only. Regional variation was observed in the thickness of the LC in age matched controls and glaucoma (figure 2.21). Thickness maps indicated that the superior and inferior regions were thinner compared to the nasal and temporal in all glaucoma (figure 2.21b-d) and control (figure 2.21a).

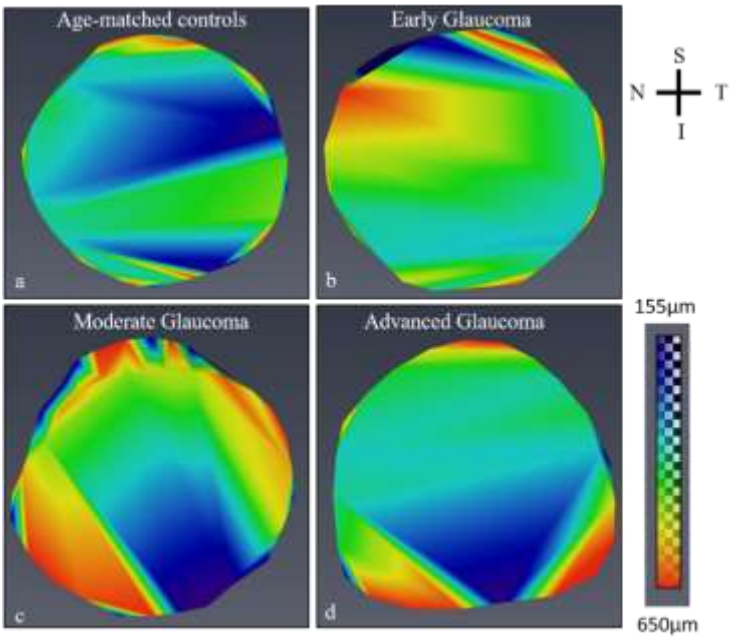

Figure 2.21. Regional LC thicknesses represented as 3D thickness maps from age-matched controls (a) and glaucomatous (b-d) ONHs. Regional variation in LC thickness was observed in all samples. The superior and inferior regions appeared to be the thinnest.

The average LC thickness (Table 2.3) between glaucoma and controls (n=3) did not show differences between early (p=0.056), moderate (p=0.054) and advanced (p=0.055) glaucoma (figure 2.22).

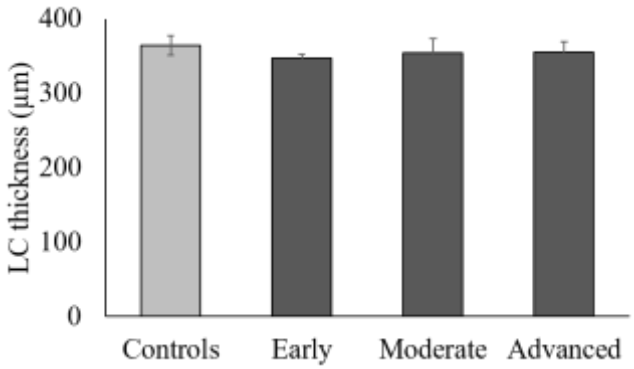

Figure 2.22. LC thickness (mean +/-sd) in glaucomatous ONH. LC thickness did not show differences between early, moderate and advanced glaucoma.

LC volume was significantly greater in moderate (p=0.017) and advanced (p=0.005) glaucoma compared to controls (figure 2.23) (Table 2.4). No differences were found in early glaucoma (p=0.065).

	LC Volume (mm^3)	LC Thickness (µm) ± sd
Age-matched controls	1.07	364.53 ± 13.33
Early GL	1.20	347.36 ± 5.34
Moderate GL	1.50	354.64 ± 18.7
Advanced GL	1.38	355.46 ± 13.82

Table 2.4. LC thickness (mean +/-sd) and volume within glaucomatous ONHs.

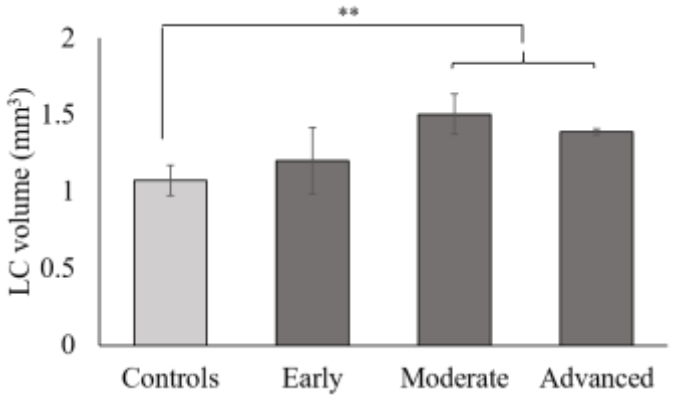

Figure 2.23. LC volume (mean +/-sd) within glaucomatous LC. LC volume was significantly greater in moderate (p=0.017) and advanced (p=0.005) glaucoma compared to controls.

2.3.4 Analysis of fibrillar collagen within glaucomatous ONH

SHG datasets allowed the visualisation of the fibrillar collagen network within age-matched controls and glaucomatous ONHs (figure 2.24).

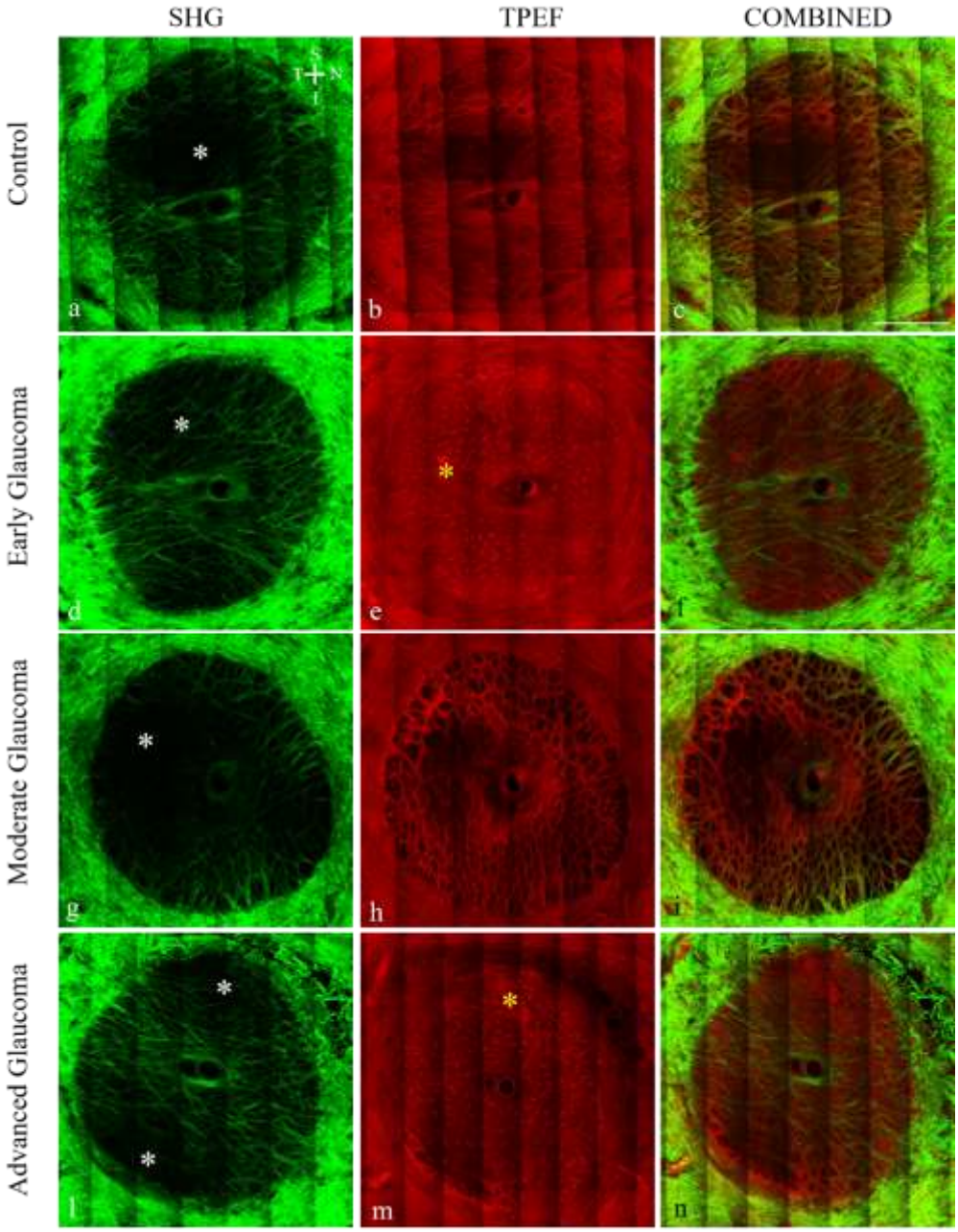

Figure 2.24. High resolution nonlinear images showing connective tissue organisation within glaucomatous ONHs. Disruption of the connective tissue was observed in the superior-inferior regions in early (d), moderate (g) and advanced (l) glaucomatous ONH sections. TPEF signal showed accumulation of TPEF fluorescent material within pores in the superior region of advanced glaucoma (m) and within LC plates of moderate (h) glaucoma. White asterisks in a,d,g,l show the lack of SHG signal and yellow asterisks in e,m the accumulation of fluorescent material within the pores. No differences were observed in early glaucoma (e) and control (b). Scale bar represents 300 µm.

SHG images showed a disorder of the collagenous beams from the superior-inferior regions in early, moderate and advanced glaucomatous ONHs (figure 2.24d,g,l). Early glaucoma showed a similar discontinuity in the superior-inferior regions (figure 2.24d), although it did not appear as severe as in the advanced glaucomatous ONH where collagenous beams were totally disrupted (figure 2.24l). In the superior region of the 87yr (figure 2.24a) a small break with missing connective tissue was observed. The elastin-associated TPEF signal did not show any differences between age-matched controls and early glaucoma (figure 2.24b,e). However, moderate (figure 2.24h) and advanced glaucoma (figure 2.24m) showed an accumulation of fluorescent TPEF material within plates and pores, respectively.

2.3.4.1 Quantification of relative fibrillar collagen content

Fibrillar collagen content, quantified as percentage SHG pixels, was significantly greater in early ($p=0.006$) and moderate ($p=0.002$) glaucoma compared to controls. Additionally, percentage collagen content in advanced glaucoma was significantly lower than that in LC of early ($p=0.010$) and moderate ($p=0.002$) glaucoma ONHs (figure 2.25a). Regional analysis showed lower LC collagen content in moderate glaucoma in the inferior ($p=0.001$) region, compared to nasal and temporal. In advanced glaucoma, collagen content was significantly lower in the superior LC region ($p=0.006$), compared to inferior, nasal and temporal (figure 2.25b). Interestingly, when the infero-temporal region was analysed (figure 2.25c) collagen content in the early glaucomatous LC was greater ($p=0.017$) compared to controls.

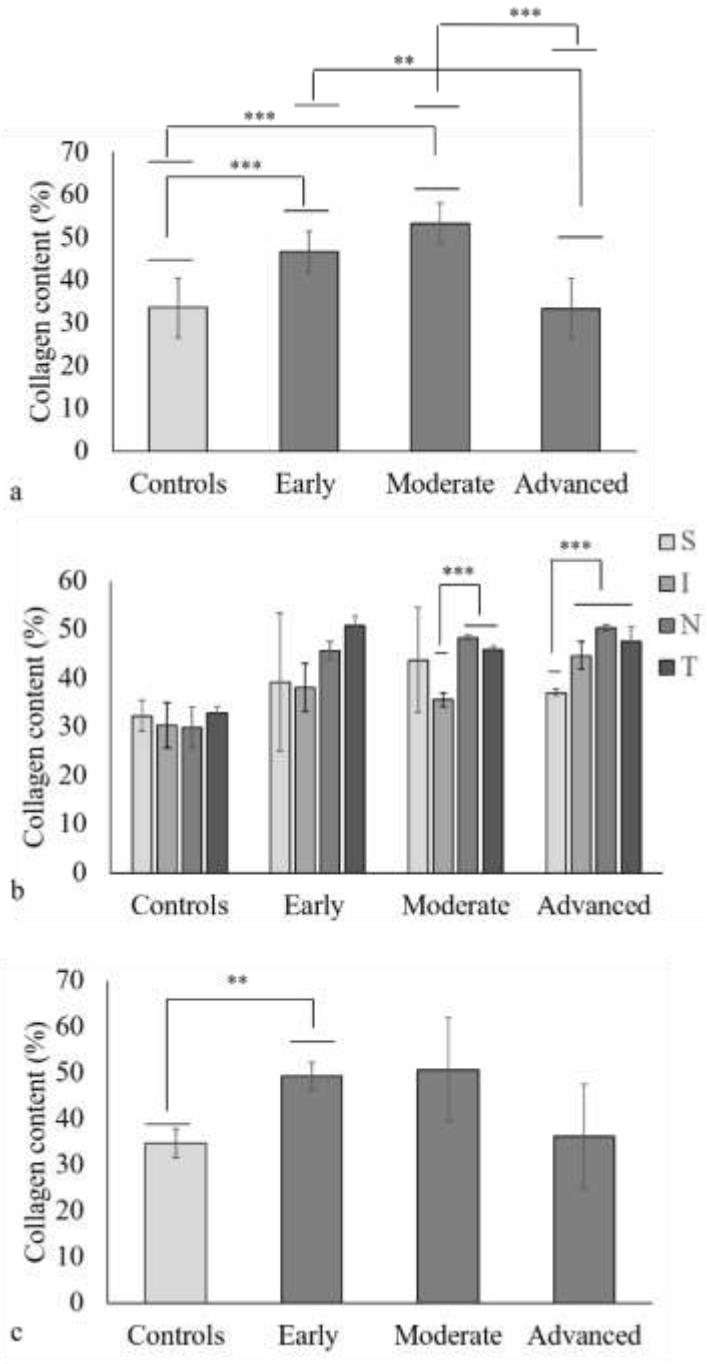

Figure 2.25. Relative collagen content as a percentage of SHG related pixel to the total LC pixel count (mean ± sd). Fibrillar collagen content (a) appeared significantly greater in early (p=0.006) and moderate (p=0.002) glaucoma and significantly lower in advanced glaucoma compared to early (p=0.010) and moderate (p=0.002). Regional analysis (b) showed lower collagen content in moderate glaucoma in the inferior (p=0.001) region compared to nasal and temporal. In advanced glaucoma, collagen content was significantly lower in the superior region (p=0.006) compared to inferior, nasal and temporal. Within the infero-temporal region (c), collagen content significantly greater in early glaucoma (p=0.017) compared to controls.

2.3.4.2 Analysis of fibrillar collagen alignment within the glaucomatous ONH

Colour-coded images computed from SHG (figure 2.26a-d) showing fibrillar collagen alignment showed region of higher alignment (yellow) in the infero-temporal region in glaucoma (figure 2.26f-h) and control (figure 2.26e).

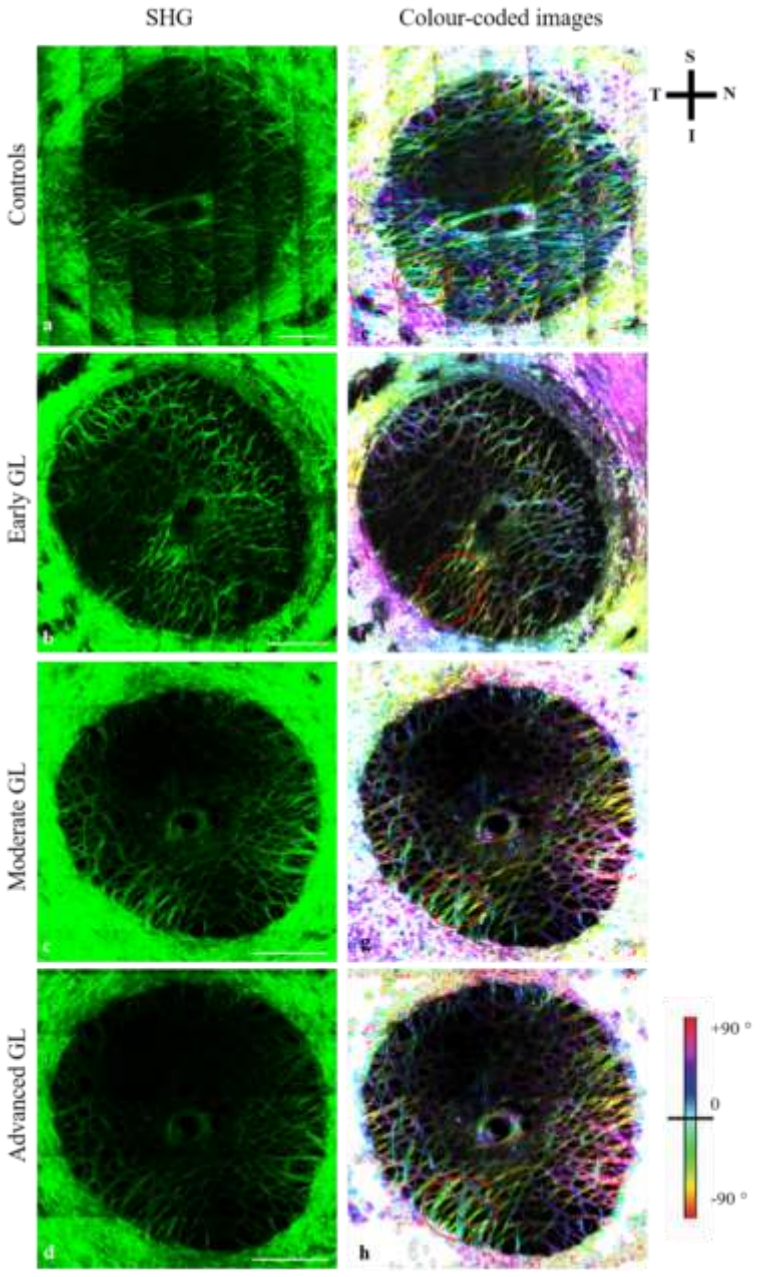

Figure 2.26. High resolution non-linear imaging and correspondent colour-coded collagen orientation within glaucomatous ONH. SHG images depicting fibrillar collagen (a-d) are showing collagenous structure. Some spots of highly aligned collagen (yellow in colour) (e-h, red circles) were observed in the LC within the infero-temporal region. Scale bars represent 500 µm.

Coherency values as a measure of anisotropy were computed for each region within glaucoma and controls (Table 2.5). Regional analysis revealed greater coherency in the nasal region of advanced glaucoma compared to early (p=0.017) and controls (p=0.045). Coherency in the temporal region appeared greater in moderate glaucoma compared to controls (p=0.024) and early glaucoma (p=0.005) (figure 2.27a).

Comparison within groups revealed greater coherency in the nasal (p=0.036) and temporal (p=0.019) regions compared to superior in advanced glaucoma. Additionally, greater coherency was also found in the nasal (p=0.017) and temporal (p=0.029) regions compared to inferior in moderate glaucoma. No differences were observed in controls (p=0.110) and early glaucoma (p=0.133) (figure 2.27a).

When coherency was investigated within the infero-temporal region, early glaucoma presented lower values compared to moderate (p=0.006) and advanced (p=0.003) glaucoma but not compared to controls (p=0.051) (figure 2.27b).

	S	I	N	T	Infero-temporal
Age-matched controls	0.28	0.24	0.34	0.367	0.31
Early GL	0.23	0.24	0.30	0.26	0.26
Moderate GL	0.36	0.26	0.43	0.43	0.37
Advanced GL	0.36	0.33	0.46	0.39	0.39

Table 2.5. Mean coherency values computed for each glaucomatous LC region.

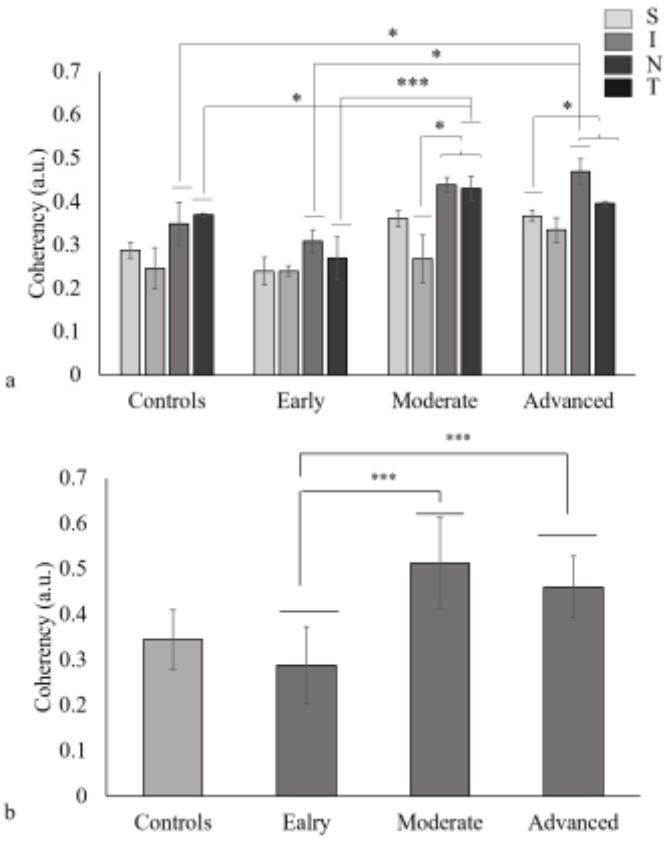

Figure 2.27. Coherency values (mean +/-sd) within glaucomatous LC and regions. Regional analysis (a) revealed greater coherency in the nasal region of advanced glaucoma compared to early (p=0.017) and controls (p=0.045). Coherency in the temporal region appeared greater in moderate glaucoma compared to controls (p=0.024) and early glaucoma (p=0.005). Within the infero-temporal region (b), early glaucoma presented lower values compared to moderate (p=0.006) and advanced (p=0.003) glaucoma. Comparison within groups showed greater coherency in the nasal (p=0.036) and temporal (p=0.019) regions compared to superior in advanced glaucoma and greater coherency in the nasal (p=0.017) and temporal (p=0.029) regions compared to inferior in moderate glaucoma.

2.3.4.3 Quantification of collagen crimp parameters in the human glaucomatous ONH

In glaucoma, some wavy-like appearance was spotted at all stages of the disease, in the LC (figure 2.28a-c), RoIns (figure 2.28d-f) and ppsclera (figure 2.28g-i), although collagen fibres appeared mostly straight. The ppsclera appeared more wavy-like at all stages of disease compared to the LC and RoIns, where only a few collagenous crimped bundles were seen.

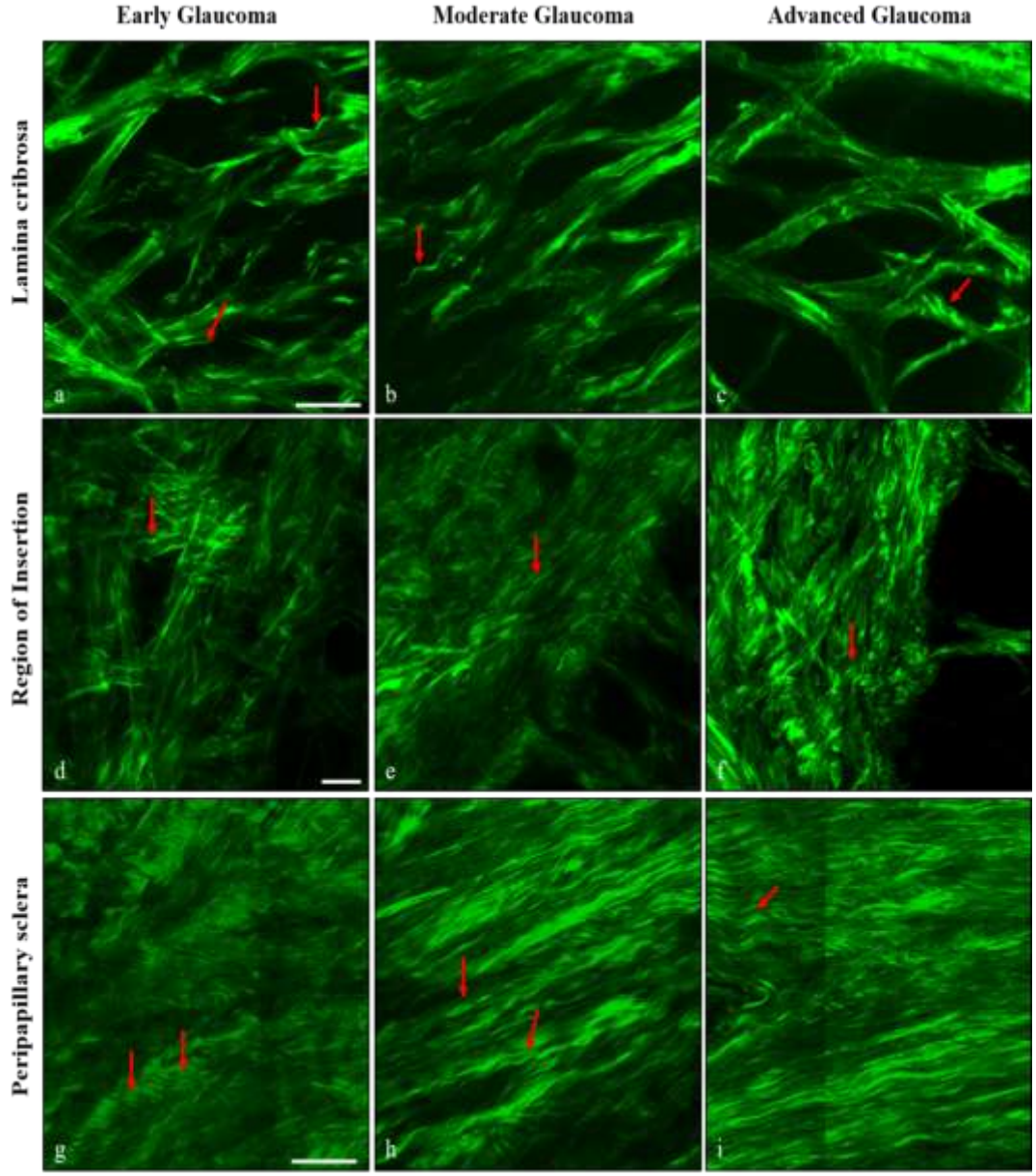

Figure 2.28. High resolution nonlinear images showing fibrillar collagen appearance in the LC, RoIns and ppsclera at different stage of glaucomatous neuropathy. Some wavy-like appearance was visible (red arrows) in early (a,d,g), moderate (b,e,h) and advanced glaucoma (c,f,i) in all regions. However, in the LC (a-c) and RoIns (d-e) only few collagenous bundles showed waviness in contrast to those in the ppsclera (g-i) where almost all collagen bundles appeared wavy. Scale bars represent 30 μm and 50 μm in a-c/g-h and d-f, respectively.

Within glaucomatous ONH, crimp period was significantly greater in moderate (p=0.013) and advanced (p=0.021) glaucomatous LC (figure 2.29a). No differences were found in

LC amplitude (p=0.728) (figure 2.28b), angle (p=0.223) (figure 2.29c) and degree of crimping (p=0.332) (figure 2.29d).

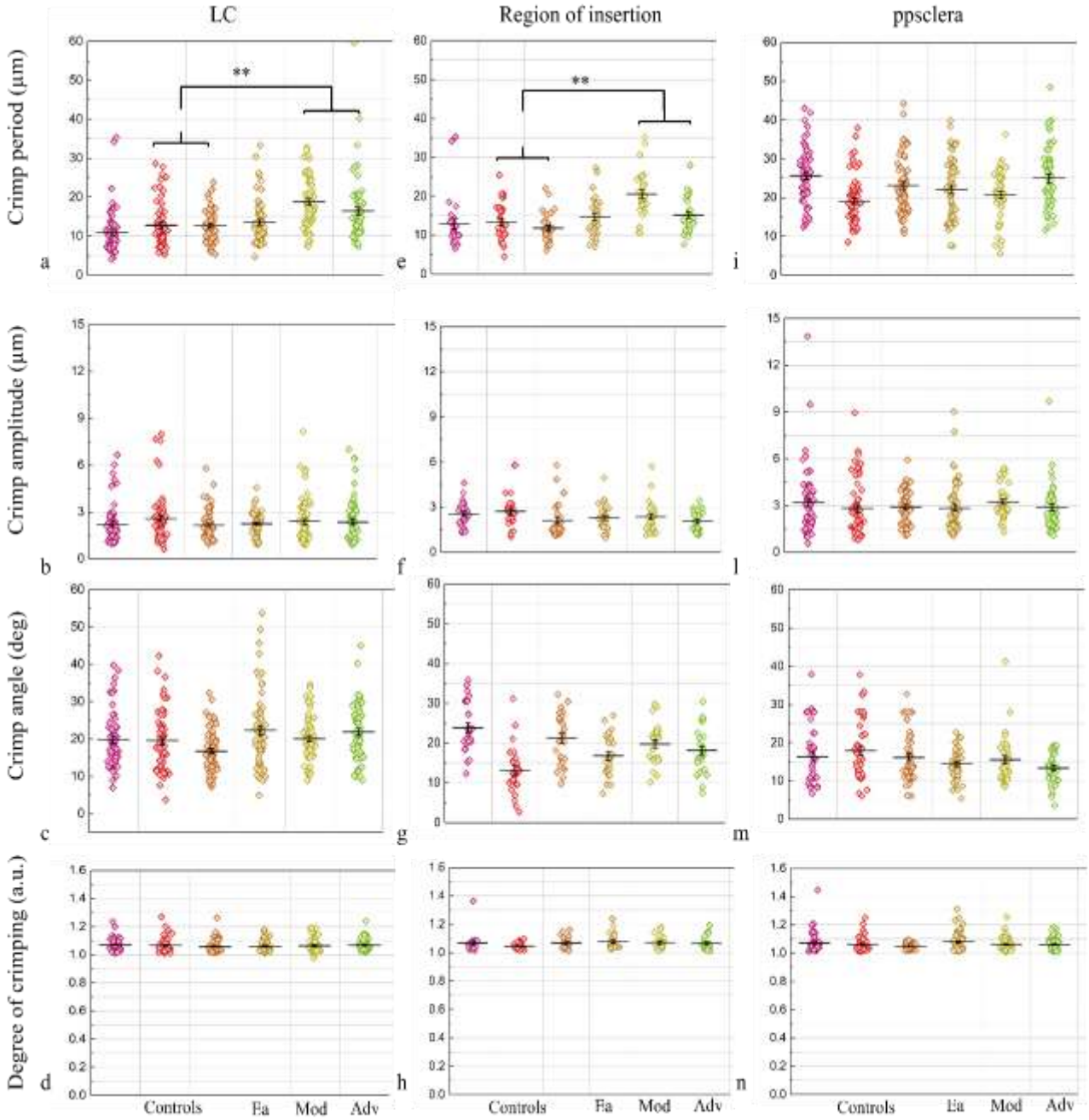

Figure 2.29. Collagen crimp parameters within three glaucomatous (Ea = early, Mod = Moderate, Adv = Advanced) ONHs. Crimp period in the LC (a) and RoIns (e) was significantly greater in moderate and advanced glaucomatous ONH. No differences were observed in the other parameters in the LC [amplitude (p=0.728) (b), angle (p=0.223) (c) and waviness (p=0.332) (d)] and RoIns [angle (p=0.143) (f), amplitude (p=0.518) (g) and waviness (p=0.079) (h)]. No significant differences were found in any of the parameters within the ppsclera. [period (p=0.728) (i), amplitude (p=0.308) (l), waviness (p=0.411) (m) or angle (p=0.180) (n)].

Similarly, within the RoIns, the crimp period was significantly greater in moderate (p=0.013) and advanced (p=0.033) glaucomatous ONHs (figure 2.29e). However, no differences between age-matched controls and glaucoma were found in the angle (p=0.143) (figure 2.29g), amplitude (p=0.518) (figure 2.29f) and degree of crimping (p=0.079) (figure 2.29h). Interestingly, within the ppsclera no significant differences were found in any of the parameters: period (p=0.728), amplitude (p=0.308), degree of crimping (p=0.411) or angle (p=0.180) (figure 2.29i-n).

2.4 Discussion

Nonlinear microscopy technique enabled the investigation of the distribution of fibrillar collagen and EFs within the LC and surrounding tissues and the subsequent ONH 3D reconstruction. Unfortunately, due to the number of endogenous fluorescent contributing factors other than elastin, the latter could not be easily segmented and quantified from the nonlinear ONH datasets. Therefore, the 3D reconstruction and segmentation was limited to the SHG datasets.

The 3D reconstructed ONH facilitated the visualisation of the whole connective tissue network within the LC as well as the porous structure. The stacked 3D structure showed that the LC is less than a stacked series of cribriform plates on the top of each other but rather a complex structure through which apertures/pores, are running through the anterior to posterior surfaces. A similar structure has been demonstrated before (Ogden et al., 1988).

2.4.1 Lamina cribrosa, cribriform plates and ppsclera thickness

Fibrillar collagen was found as bundles within the LC beams, the central retinal vessel and ppsclera within longitudinal ONH sections. LC thickness ranged from 334.13 ± 5.8 µm at the age of 22 year to 353.11 ± 7.6 µm at the age of 85 year, although not significant, but similarly to those observed in previous studies (Jonas et al., 2003, Jonas and Holbach, 2005, Kotecha et al., 2006). Cribriform plate thickness ranged from 14.85 ± 0.3 µm at the age of 22 year to 16.39 ± 0.3 µm at the age of 85 year.

Previous studies have investigated the morphometry of the LC and found that the LC thickness is not associated with age (Jonas and Holbach, 2005, Ren et al., 2010, Ren et al., 2009), which support the result presented in this chapter. However, Kotecha et al.,

(2006) found a significant correlation between LC/LC beam thickness and age. Discrepancy between Kotecha's results and the current study might be due to the imaging technique used. For instance, measures on 2D longitudinal ONH after SHG/TPEF imaging did not consider GAG contribution, which even though in small amount, will contribute to LC thickness and it has been shown to be involved in the age-related thickening of basement membranes (Timpl, 1989). Additionally, non-fibrillar collagen components, such as type IV, which has been shown to increase with age (Hernandez et al., 1986, Hernandez et al., 1989) and hence contribute to LC thickness but it is not imaged by SHG. Since collagen content increases as a function of age (Albon et al., 1995, Hernandez et al., 1989), it is possible that LC collagen fibril become more compact with age, affecting the flexibility of the structure. A more compact and more rigid (Albon et al., 2000b) elderly LC may lead to a greater susceptibility of the RGC axons to be damaged as a function of IOP changes.

Ppsclera thickness ranged from 806.09 ± 32.8 µm at the age of 22 year to 958.05 ± 24.6 µm at the age of 85 year, however not significant. Previous studies have measured the thickness of the ppsclera outside the meningeal sheaths in human (Norman et al., 2010, Ren et al., 2010) and monkey (Downs et al., 2007). Ren et al., (2010) showed that the ppsclera thickness decreases with increasing axial length, independently from glaucoma.

2.4.2 Fibrillar collagen crimp in the ageing ONH

Age-related differences in SHG related fibrillar collagen were also observed in the current study. High resolution SHG images of the LC, RoIns and ppsclera revealed fibrillar collagen to be wave-like in the young ONH, specifically at the ages of 2, 6, 21 and 47-year-old. This wavy-like appearance of fibrillar collagen was not evident in the elderly LC, RoIns and ppsclera. This appearance of fibrillar collagen is named *collagen crimp* and it is thought to be related to the biomechanical behaviour of the fibre and represents the relaxed state of collagen when fibres are not under mechanical stress (Weiss and Gardiner, 2001). The change of appearance in the elderly ONHs might suggest an uncoiling process of the crimp which might represent the first step to the nonlinear response of the fibres to load (Freed and Doehring, 2005). The relaxed (crimped) state of fibrillar collagen in the young ONH tissue and the disappearance of crimping in the elderly is consistent with the age-related decrease in LC reversibility/compliance and increase in stiffness (Albon et al., 2000b).

Age-related decrease in collagen crimp and the stiffening of collagen fibres with age has been previously studied in other tissues such as rat tendon (Diamant et al., 1972), horse tendon (Patterson-Kane et al., 1997a, Patterson-Kane et al., 1997b) and mice tendon (Legerlotz et al., 2014). A study conducted on the craniofacial tendons in zebrafish suggested that age-related changes in the mechanical function of the tendon is related to the loss of nonlinearity, which has been proposed to be due to a decrease in collagen crimp (Shah et al., 2015).

Interestingly, when crimp parameters were measured in the ppsclera, a significant increase in crimp period was found as a function of age. Burgoyne et al (Bellezza et al., 2000, Burgoyne et al., 2005) described a model of the ONH as a biomechanical structure and suggested that stress and strain generated by IOP are concentrated around the ppsclera and the scleral canal. The material properties of the ppsclera are likely to determine the mechanical response to IOP fluctuations. An increase in crimp period in age might suggest that it is the ppsclera that responds to IOP fluctuation, protecting and preventing the expansion of the LC, which correlates with previous studies proposing the ppsclera as a protective structure to limit scleral canal expansion (Coudrillier et al., 2012, Girard et al., 2009, Grytz et al., 2014). A recent study showed that collagen crimp parameters have a distinct pattern over the globe (figure 2.30), suggesting an existent mechanism that controls collagen fibres properties within regions of the globe (Jan et al., 2018).

An interesting finding presented in this chapter indicates that the collagen crimp period in the LC was significantly smaller than that observed in the ppsclera. Jan et al., 2018 found that regions with a small crimp period are likely to have large conformity, which is defined as the amount of connected similarly orientated collagen bundles. This suggests that collagen bundles in the LC tend to stack together to form large groups with similar orientation.

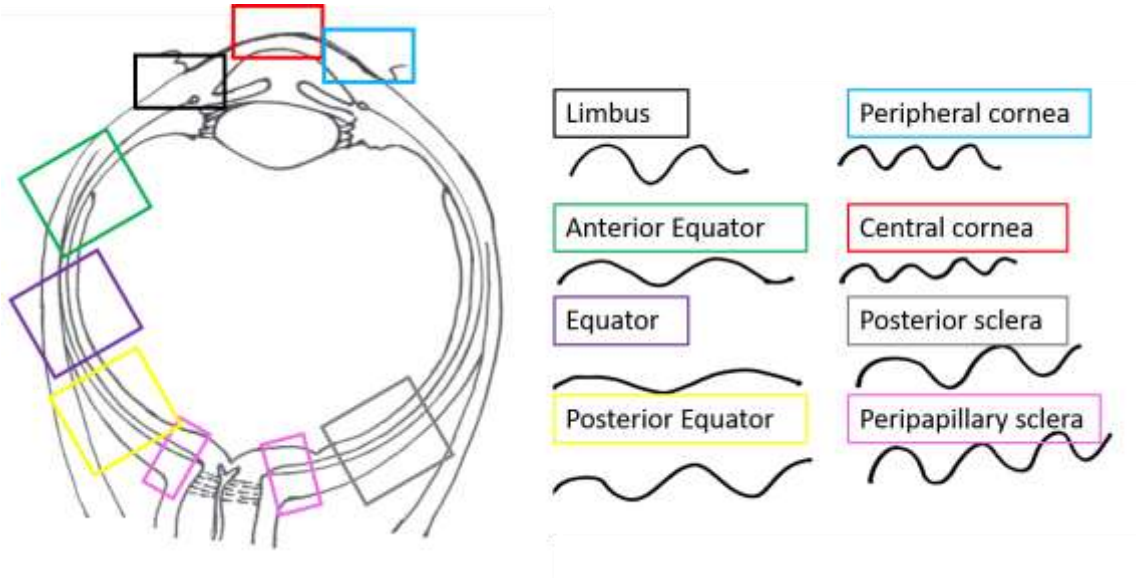

Figure 2.30. Schematic diagram of crimp pattern around the globe. Different crimp patters have been visualised in different regions of the human eye.

This might imply that crimp period in the LC was more uniform than that observed in the ppsclera (Jan et al., 2018), which has been hypothesised to have less gradual stiffening response to strain compared to regions with more variable crimp (Diamant et al., 1972). This behaviour might indicate that the LC can stretch and stiffen simultaneously which results in a more even response to changes in IOP across the LC to avoid the strain being concentrated in one specific region which could damage the axons. These results also correlate with the more radially oriented aligned collagen found in the LC (Jones et al., 2015) which might relate with the smaller fibril diameter found in the LC and the larger in the equator compared to the ppsclera (Quigley et al., 1991b), supporting a similar pattern of crimp period found in the current study.

Similarly to other tissues (Fata et al., 2014, Hansen et al., 2002, Hill et al., 2012), collagen crimp within the ONH represents a key factor on the eye's nonlinear biomechanical response explaining the increase in stiffness as the IOP increases (Ethier et al., 2004). Age-related stiffening is thought to contribute to the increased susceptibility of the elderly eye to develop glaucoma (Liu et al., 2018). Therefore, knowing and understanding the collagen crimp and how it changes with age might be a step forward to a better understanding of glaucoma mechanism.

2.4.3 Anatomy of the glaucomatous lamina cribrosa

The current study found that the LC volume was significantly greater in moderate and advanced glaucoma compared to controls.

There was no significant change in the volume of the LC in early glaucoma and there were non-significant trends between stages of glaucoma, i.e. there was an increase in early and moderate glaucoma in LC volume compared to controls, however, slightly decreased in advanced glaucoma. This latter increase in volume is consistent with LC thickening and remodelling, as previously shown in monkey models (Yang et al. 2011) and is worthy of further investigations.

Thinning of the LC in glaucomatous ONH might be due to the continuous stress and strain the LC is subjected, caused by elevated IOP. The IOP produces an expansion of the scleral shell which generates tensile forces on the scleral wall. As a result, the scleral canal opening expands, which stretches the LC, causing it to thin. A compliant ppsclera supports the IOP where the thickness of the LC and scleral canal opening are not altered. When the IOP is elevated, the pressure creates an expansion of the scleral canal which in turn generates tensile forces at the sclera. These act on the scleral wall causing an expansion of the sclera canal which in turn stretches the LC. Thus, the LC is more anteriorly displaced and thinned (Bellezza et al., 2003). It is known that the LC becomes stiffer with age (Albon et al., 2000b) and it might be that glaucomatous ONH presents stiffer LC. The ppsclera might therefore responds to the IOP elevation pulling the LC taut, causing it to elongate and therefore thinning.

2.4.3.1 Pores parameters within glaucomatous ONHs

The superior and inferior regions of the LC contain larger pores compared to nasal and temporal (Quigley and Addicks 1981). In glaucoma, these regions seem to be preferentially affected since they contain less connective tissue, therefore less protection and increased axon susceptibility to damage (Gaasterland et al., 1978). Pores vary in size and more pores are reported at the posterior LC surface than the anterior surface, with anterior pores larger than posterior (Ogden et al. 1988). Additionally, pores divide as they travel down through the LC (Quigley and Addicks 1981, Ogden et al. 1988, Albon et al. 2007) and they appear larger in the peripheral (outer) LC compared to the central (inner) LC (Jonas et al., 1991). LC pores, through which axons pass on their way to the brain, are

proposed to alter in shape and size in glaucoma. Therefore, studying alteration in pores parameters (namely shape, area and count) is essential to the understanding of the basics of ONH degeneration in glaucoma and their potential use as a biomarker for disease.

Pore parameters namely pore count, area and circularity showed differences between glaucoma and controls. Specifically, pore count was significantly lower in all glaucomatous ONHs. Regional analysis revealed a significant lower pore count within all regions of glaucomatous ONH compared to controls and lower circularity within the temporal region of advanced glaucoma. Analysis of the inner and outer LC showed a lower pore count and circularity in moderate and advanced glaucoma only in within the inner LC.

Pore shape is a potential factor in relation to glaucoma, where a more elongated shape is thought to be associated with the late stage of disease (Miller and Quigley, 1988, Tezel, 2006). Several investigations have focused on LC and pore shape *in vivo* (Akagi et al., 2012, Fontana et al., 1998, Ivers et al., 2015, Miller and Quigley, 1988, Nadler et al., 2014, Omodaka et al., 2018, Shoji et al., 2017, Sredar et al., 2013, Tezel et al., 2004, Wang et al., 2013, Zwillinger et al., 2016) and *ex vivo* (Reynaud et al., 2016, Voorhees et al., 2017, Winkler et al., 2010).

Measurement of pore circularity can be an excellent structural parameter for glaucoma diagnosis, as pore shape can drastically change if subjected to high IOP, causing even more damage to the axons that are passing through. When an increased IOP pushes the LC to move backwards, the LC could stretch on the sides as the pressure has also effects on the ppsclera which pull the LC taut, causing a stretching in the LC, which might become more elongated and therefore a change in pores shape occurs. In fact, it has been previously reported that pore elongation is significantly correlated with glaucoma progression, implying that pores become oval shaped and elongated as a function of disease progression (Miller and Quigley, 1988). Pores parameters (e.g. shape, count) might be a key factor to explain the risk that axons experience when passing through pores, implying that axons passing through more elongated pores might be under inhomogeneous stress, which might be associated with nerve fibre bundle impairment associated with glaucoma (Shoji et al., 2017).

The smaller pore count found in glaucomatous LC agrees with a previous study (Allingham et al., 1992) that showed a decreased pore count in the glaucomatous ONH compared to controls. Smaller area and lower pore count in glaucoma compared to controls might suggest that the connective tissue is expanded and increased. In fact, it is known that collagen and EFs are damaged and increased in glaucoma (Hernandez et al., 1990, Hernandez, 1992) when compared to healthy controls. This also correlated well with the basement-membrane material which is deposited within the pores, causing the area occupied by pores and the pores number to decrease.

Any deformation of the pores might imply that axons passing through will be damaged eventually, which might correlate with the vulnerability of the axons to mechanical damage that results in glaucoma.

2.4.4 Fibrillar collagen content within glaucomatous ONH

3D reconstructed ONH showed differences in the connective tissue content between glaucoma and corresponding age-matched controls. Specifically, disruption of collagenous beams in the superior-inferior axes was observed at all stages of the disease, consistent with the concept previously suggested that the superior and inferior regions of the LC are the first damaged in glaucoma (Quigley et al., 1981).

Fibrillar collagen content as a percentage of SHG pixels did not show any significant changes at any stage of glaucomatous optic neuropathy as well as within regions. Interestingly, when collagen content was quantified within the infero-temporal region it was significantly greater in early glaucoma compared to controls but not in moderate and advanced. This could be a result of early LC modification such as LC cribriform plates compression, deformation and disorganisation (Hernandez et al., 1994a, Hernandez et al., 1994b, Quigley and Addicks, 1981, Quigley and Green, 1979) and LC remodelling such as synthesis and/or degradation of connective tissue components that has been shown in human (Hernandez, 2000, Kirwan et al., 2004, Quigley et al., 1981, Quigley and Broman, 2006, Quigley et al., 1983), rats (Johnson et al., 2007) and monkey (Agapova et al., 2003) glaucoma.

The increase collagen content in the infero-temporal region in early but not in moderate and advanced glaucoma could be due to an early modification of the ECM as a function of IOP increase. As shown by Hernandez et al., (1994b) mRNA expression of collagen type IV from astrocytes has been shown to increase in glaucomatous ONH when compared to normal ONHs (Hernandez et al., 1994b). Additionally, within the LC, collagen type I, III and IV were observed between beams and occupying space normally occupied by axons (Morrison et al., 1990). The latter could explain the augmented collagen content which spread over the pores therefore increasing the percentage of total collagen. In late stage of glaucomatous neuropathy, the collagen content might decrease due to the intervention of metalloproteases (MMP), enzymes known to degrade the ECM in age and disease (Agapova et al., 2003, Yan et al., 2000) that can remodel the microenvironment on the ONH, leading to a decreased collagen content.

SHG imaging gives minimal background signal due to no requirement of staining. However, SHG intensity could be dependent on collagen substructure, such as cross links (Robinson et al., 2016).

Fibrillar collagen diameter increase might be a consequence of the reduction in cross links, as shown before in type II collagen in chondrocytes (Wong et al., 2002). With an increase in collagen diameter might suggest that the space between collagen molecules is increased. During SHG imaging, the SHG signal intensity might depend on the space between molecules, therefore SHG signal might vary when the collagen diameter is increased. The parallel orientation of collagen fibrils is described as the same orientation of the C- and N- termini of adjacent collagen fibrils. It might be possible that reduced cross links could promote parallel orientation and therefore increase the SHG intensity (Lutz et al., 2012).

Within the LC, collagen type I, III and IV were observed between beams and occupying space normally occupied by axons (Morrison et al., 1990). Collagen type I appeared compact, whereas collagen type III showed no significant changes when compared to normal ONHs (Hernandez et al., 1990).

An increased collagen content has been also found within other tissues, such as human skin affected by scleroderma (Rodnan et al., 1979), intestinal tissues of people affected by Crohn's disease (Stallmach et al., 1992), cerebral vessels of people with Alzheimer's disease (Kalaria and Pax, 1995) and degenerated mitral valve (Purushothaman et al., 2017). Purushothaman et al., (2017) suggested that the increased collagen content contributed to a derangement of the ECM composition, which led to an increase in the thickness of the valve layers which as a result influenced the function of the valve. Similarly, Kalaria and Pax (1995) showed an augmented collagen content in the cerebral micro-vessels as measured by the hydroxyproline content and suggested the greater content of collagen lead to an altered function of vessels observed in Alzheimer's disease. Interestingly, Stallmach et al., (1992) suggested that in Crohn's disease the increased collagen type III synthesis could be involved in the pathogenesis of fibrosis and lead to a chronic inflammation of the intestine. Changes observed in other tissues might correlate well with increased collagen content that occur in glaucoma, leading to a fibrotic tissue which in turn alters the biomechanical function of the LC to support RGCs axons.

In disease, such as cystic medial degeneration, atherosclerosis and inflammation, the collagen content within the aorta increased, specifically within abdominal-thoracic aorta (Cattell et al., 1993, Gao et al., 2012). The human aorta normally possesses a high degree of elasticity which aids in pumping blood in the downstream circulation (Westerhof et al., 2018). The microstructure of collagen and elastin supports the aorta in its function (Halloran et al., 1995, Holzapfel et al., 2007), therefore alterations in the quantity and/or architecture of the collagenous fibres leads to mechanical and functional changes associated to aortic disease (Tsamis et al., 2013, Tsamis et al., 2011, Tsamis et al., 2009, Zulliger et al., 2004).

2.4.4.1 Fibrillar collagen alignment

The infero-temporal region has been previously demonstrated to present some areas of highly aligned collagen (Jones et al., 2015) in both ageing and glaucomatous ONHs, which became more pronounced at late stage of disease. The infero-temporal region has been proposed to have a greater susceptibility to nerve damage in early glaucoma (Quigley and Addicks, 1981). Winkler et al., (2010) have shown that the this region has a low collagen alignment when compared to the other regions (Winkler et al., 2010),

which supports findings in the current study of lower coherency in early glaucoma as described in 2.3.4.2.

Orientation and alignment of connective tissue strongly depends on the amount and nature of stress they experience (Culav et al., 1999). In fact, the orientation of collagen fibres within the ECM allows extension of the tissue and it is responsible of the nonlinear behavior. The long-range extensibility of skin is due to a significant reorientation of collagen fibre networks (Gabella, 1987, Purslow, 1989). These connective tissues become stiffer as they are extended, and collagen fibres become more aligned in the direction of the stretch. This nonlinear behavior has been related to the effects of the strain on the reorientation of stiff collagen in blood vessels (Bigi et al., 1981, Roveri et al., 1980). For instance, in tendon collagen fibres are highly aligned allowing them to bear the rotational forces during movements (Kannus, 2000).

In early glaucoma, coherency values were found lower compared to moderate and advanced, suggesting that at the late stages of disease collagen fibril were more aligned. This result is supported by Winkler et al. (2010) who showed a low degree of collagen alignment in the infero-temporal region compared to other regions and this result is also supported by Jones et al. (2015) who found a high degree of collagen alignment in the infero-temporal region within advanced glaucoma and they appeared as spots of highly aligned collagen following SALS imaging. This is important as focal defects (Kiumehr et al., 2012) and disc hemorrhages (Siegner and Netland, 1996) predominate in the infero-temporal region. Additionally, it has been shown previously that this region presented a more pronounced neuroretinal rim loss (Caprioli et al., 1987, Garway-Heath and Hitchings, 1998, Jonas et al., 1993) and has a greater susceptibility to damage in early glaucoma (Quigley and Addicks, 1981). This region might be therefore an indication of disease progression and/or spots of higher susceptibility. However, more investigations in this respect are needed.

Overall, coherency analysis revealed the highest alignment in the nasal and temporal regions. Nasal and temporal LC regions have been shown to contain higher connective tissue than the superior and inferior regions (Jonas et al., 1991, Ogden et al., 1988, Quigley and Addicks, 1981). It is believed that the reduced support in the superior and inferior regions predispose the RGC axons to IOP related damage (Quigley and Addicks,

1981, Quigley et al., 1981). The greater connective tissue density and the higher fibre alignment within the nasal and temporal regions reinforce the hypothesis that these two regions better support RGC axons.

2.4.4.2 Fibrillar collagen crimp in the glaucomatous ONH

Crimp parameters were also quantified and compared between three age-matched controls and three different stages of glaucoma. Interestingly, in the LC and RoIns, but not ppsclera, the crimp period showed a significant increase in moderate and advanced glaucoma compared to the respective age-matched controls. No changes were found in any parameter at early stages of disease. This result might imply that fibrillar collagen is not affected until later in the diseases and not at the level of the ppsclera, which correlates with the fact that the LC has been proposed to be the main and first site of axonal damage in glaucoma (Quigley et al., 1981, Quigley and Addicks, 1981).

The alteration of collagen crimp and morphology has been studied before in mouse tendons as a function of type II diabetes progression. Tendons have a complex biomechanical behaviour that exhibits nonlinearity and anisotropy based on the grade of the collagen crimp (Connizzo et al., 2013b, Duenwald et al., 2010). Alteration in collagen structure and composition could lead to an altered mechanical behaviour and functional response. Studies have shown structural changes in tendon affecting the way they respond to load, in particular re-alignment and collagen fibril uncrimping (Connizzo et al., 2013a, Dourte et al., 2012). It has been shown that type II diabetes alters collagen structure and subsequently mechanical function (Gonzalez et al., 2014, Grant et al., 1997).

At the LC and ppsclera fibrillar collagen showed some crimped bundles, in contrast to the correspondent age-matched controls where collagen bundles appeared straight. This result might imply that excessive pressure-induced deformation/degradation of the LC triggers biochemical events that eventually lead to a reestablishment of the collagen crimping. The ONH ECM is very much disturbed in glaucoma, resulting in extensive remodelling, including the loss of fibrillar collagen, reduction in elastin content, and an accumulation of glycosaminoglycans (Hernandez et al., 1990, Hernandez and Pena, 1997, Hernandez et al., 1994a, Hernandez and Ye, 1993, Quigley et al., 1994, Quigley et al., 1991a, Quigley et al., 1991b). Additionally, it has been proposed that collagen and elastin of a glaucomatous ONH appear detached from the surrounding ECM (Quigley et al.,

1991a). This implies there is a loss or partial degradation of the straight fibres and suggesting they are no longer under tension which keeps them in the stretched state such that the collagen fibres appear wavy-like.

In the recent years studies have focused on the potential effects that glaucoma has on the microarchitecture of collagen using diffraction methods such as WAXS (Pijanka et al., 2012) and SALS (Danford et al., 2013, Jones et al., 2015). However, these studies focused on the changes in fibrillar collagen orientation in glaucoma and none of them investigated the collagen crimping. Other studies provided information regarding collagen microstructural changes in glaucoma, although only with mathematical models (Bellezza et al., 2000, Grytz et al., 2011, Norman et al., 2011, Sigal et al., 2005b). It is likely that microstructural changes occurring in glaucoma increase the matrix stiffness which could occur during non-enzymatic glycation cross-linking of collagen fibres. Advanced glycation end products (AGEs) naturally occur with age (Schmidt et al., 2000, Thornalley, 1998) and they have been found in the cribriform plates of the LC during ageing (Albon et al., 1995, Amano et al., 2001).

Oxygen and reactive oxygen species (ROS) accelerate AGE formation (Gkogkolou and Böhm, 2012). Based on the role of oxidative stress in glaucomatous degeneration (Alvarado et al., 1984, Ko et al., 2000, Sacca et al., 2005, Zhou et al., 1999), Tezel et al., (2007) aimed to find a correlation between glaucoma and AGE. With immunohistochemical labelling, the authors compared AGE deposition between glaucomatous and controls ONHs and they found an increase in AGE in glaucoma. Since it is well known that AGE deposition is related to ageing (Schmidt et al., 2000, Thornalley, 1998), the findings presented by Tezel et al suggested that glaucomatous degeneration is associated with the accelerated ageing process (Tezel et al., 2007). Since glaucoma is a disease of the elderly, the AGE deposition could be enhanced in glaucoma, influencing the ability of the ONH to withstand elevation of IOP. Current studies in fact support that the accelerated deposition and accumulation of AGE in the ageing LC accompanies other ECM alteration in the glaucomatous ONH, which can increase the axonal damage by compromising the ability of the LC to bear strain caused by elevated IOP (Burgoyne et al., 2005, Quigley et al., 1983).

2.5 Conclusion

In conclusion, although a considerably amount of work has been done to characterise the microstructure of the ppsclera and LC, this study reports a first investigation of different microstructural features (i.e. collagen crimp) of the LC, RoIns and ppsclera in normal healthy and glaucomatous eyes. The results suggest that the increase in crimp period in the ppsclera as a function of age but not in the LC or RoIns, lead to a first response of the ppsclera to the IOP alteration, where collagen stretches first preventing the LC and the optic canal to expand.

The results presented provide evidence in support of the hypothesis that microstructural alteration of the ppsclera and LC with age influence the ONH biomechanics leading to increased susceptibility to develop glaucoma. This study also showed alteration in the superior – inferior axes of the glaucomatous LC as well as alteration in the connective tissue contents when compared to the age-matched controls. This is consistent with and supports previous research showing disruption of the collagenous beams and damage of the LC in glaucoma within the superior and inferior regions. Therefore, in certain susceptible eyes, the age-related changes in the microstructural features of the LC, RoIns and ppsclera may result in an exaggerated response to IOP, leading to a deformation of the ONH and eventually in axonal loss.

2.6 Limitation

This study presented with couple of limitations. Four of the eight glaucomatous eyes used in the study were diagnosed with early stage of disease and among the remaining four, two were moderate and two advanced. This might have affected the statistical significance of findings and comparisons between age-matched controls and glaucoma, although changes have been found in collagen crimp and orientation. No samples younger than 22yr were available for this characterisation or from the mid-age range. This would have limited the statistical significance of the measurements. Computational alignment of thick tissue sections for 3D reconstruction might be subjected to imprecision and therefore limiting the accuracy of the reconstructed volume stacks. This might have had effect on the collagen content and preventing the statistical significance.

2.7 Future work

An increase in sample size, especially young and mid-age range, would allow a better understanding and confirm or disprove the absence of a relationship between age and LC, RoIns and ppsclera thicknesses. More glaucomatous ONHs are required especially at moderate and advanced stage of disease, which will increase the understanding of microstructural changes as a function of glaucoma and improve statistical confidence. An additional goal of this research to consider crimp parameters will involve the development of mathematical models similar to that presented by Grytz and Meschke (2009) to predict stiffness of collagen fibrils within ppsclera, RoIns and LC (Grytz and Meschke, 2009). This model will also consider collagen fibril diameter measured with small angle x ray diffraction (see chapter 5) to investigate and determine potential differences in stiffness between the soft LC tissue and harder tissue of the ppsclera to confirm the role of the ppsclera to support and prevent expansion of the scleral canal and therefore limit axonal damage due to deformation of the LC.

Chapter 3 - Determination of an elastic fibre spectral signature using spectral imaging to quantify optic nerve head elastic fibre content

3.1 Introduction

Elastin is one major component of the ECM within the human ONH (Elkington et al., 1990, Hernandez et al., 1986, Hernandez et al., 1987, Morrison et al., 1989a). Electron microscopy (Quigley et al., 1991b), immunofluorescence (Hernandez et al., 1987, Hernandez et al., 1989, Hernandez, 1992) and histological stains (Oyama et al., 2006) have found elastic fibres (EFs) running parallel with collagen within the LC plates (Hernandez et al., 1987, Quigley et al., 1991a, Oyama et al., 2006). Additionally, EFs form a ring at the site of the region of insertion (RoIns) into the LC (Quigley et al., 1991a). Elastin, within the human optic nerve head (ONH) (Hernandez et al., 1987, Hernandez et al., 1986), is known to increase with age (Albon et al., 1995, Albon et al., 2000a, Hernandez, 1992, Hernandez et al., 1989) and EFs are altered in glaucoma (Hernandez, 1992, Hernandez et al., 1990, Quigley et al., 1991b).

With an average half-life of 70 years, elastin is the longest-lasting protein of the human body (Shapiro et al., 1991). Elastin, a major component of EFs, has been explored in the ECM as a major endogenous fluorophore (Blomfield and Farrar, 1969), present in ovine and porcine arteries (Konig et al., 2005, Schenke-Layland, 2008, Schenke-Layland et al., 2004a). EFs are normally associated with tissues, such as blood vessels, that can withstand pressure changes (Shadwick, 1999) and tissues that require elasticity and recoil. EFs have been detected in arteries, lungs, skin, intervertebral discs and elastic cartilage (Jacob, 2006, Kelleher et al., 2004, Kielty, 2006, Wagenseil and Mecham, 2009). Elastin is capable of deforming to large extension under small forces and it is thought that it behaves like a biological rubber and provides connective tissue with elasticity (Hoeve and Flory, 1974).

The morphology of EFs are highly tissue specific (Kielty et al., 2002, Mithieux and Weiss, 2005). For instance, within arteries, such as the aorta, EFs form concentric fenestrated lamellae within the medial wall surrounded by smooth muscle cells. In

arteries, EFs play a vital role in maintaining the mechanics of the vessel, which is essential for blood circulation (Davis, 1993a, Davis, 1993b).

Elastin has been explored in the ECM as a major endogenous fluorescent component of the EF in ovine and porcine arteries (Konig et al., 2005, Schenke-Layland, 2008, Schenke-Layland et al., 2004). Early studies suggested that the enhanced emission fluorescence as a function of age in human aortas (John and Thomas, 1972, Konova et al., 2004, Lansing et al., 1951, Labella and Lindsay, 1963), skin (Na et al., 2001) and rat arteries (Bruel and Oxlund, 1996) was due to a rise in polar hydrophilic amino acids (Labella et al., 1966, Spina and Garbin, 1976, John and Thomas, 1972) known to exhibit internal fluorescence (Molnár-Perl, 2005). These studies purified elastin from different tissues using the hot alkali method (John and Thomas, 1972, Labella and Lindsay, 1963) or sequential enzymic digestion (Nejjar et al., 1990, Ross and Bornstein, 1969), proposing that the increase in hydrophilic amino acids observed was a consequence of the contamination of other proteins (Spina et al., 1983, Labella and Lindsay, 1963, Gotte and Serafini-Fracassini, 1963, Partridge and Keeley, 1974) which are deposited during the ageing process and they are resistant to hot alkali digestions (Lansing, 1955). However, Labella et al in 1966 suggested that the increased fluorescence is associated to the oxidation of tyrosine, a polar amino acid, which generates fluorescence derivatives (Labella et al., 1966).

Spectral imaging, a combination of imaging and spectroscopy, is an analytical technique that collects spectroscopic and imaging information at the same time. Spectral imaging collects spectral information across a wide range of wavelengths at the same time as recording the spatial information in an image. The data collected is called a “hypercube”, which contains spatial data in the x and y and spectral data along a third dimension (z) for each pixel in the image. Spectral imaging has been previously used to determine an EF spectral signature in human skin (Chen et al., 2009), aorta (Zoumi et al., 2004) and cells (Tsurui et al., 2000, Zimmermann et al., 2002, Zimmermann et al., 2003) using spectral imaging.

The hypothesis of this study was that the i) determination of an elastin-specific spectral signature will enable characterisation and quantification of EFs within the human ONH and ii) EF content is altered in ageing and glaucomatous ONHs. Therefore, the overall

aim of this chapter was to develop an EF (elastin) associated TPEF signature which could be used to quantify and analyse changes in elastin and/or EFs within the ageing and glaucomatous ONH.

To achieve this aim, the objectives were to:

1. Characterise the spectral signature of elastin within the EFs of the rat aorta
2. Confirm that the elastin derived signature from 1 is similar in human tissue, namely human CRA
3. Characterise the elastin signature within the human ONH connective tissue, using optimised parameters identified in 1 and 2
4. Spectrally unmix elastin fluorescence from other endogenous fluorescence
5. Quantify elastin content within the LC, RoIns and ppsclera
6. Determine if ONH EFs alter with age or glaucoma.

3.2 Methods

3.2.1 Source of tissues

Thirteen eye globes from donors with no history of ocular disease (aged 2 to 88 years) were received from the NHS Blood and Transplant Eye bank (Filton, Bristol, UK) in moist tissue chamber, with consent for research purposes. Ten globes were immersion fixed on arrival in 4% PFA (weight/volume in PBS, pH 7.4), whereas three (aged 63, 72 and 80 years) remained in the moist chamber. Additionally, eight glaucoma globes (diagnosed prior to death by a glaucoma specialist) in 4% PFA, were received from the Mayo Clinic (Rochester, USA) as described in 2.2.1. Glaucomatous ONHs have been divided in GL1- GL4: early glaucoma with a visual field mean deviation (MD) of +1.42 to -4.35 dB; GL5 and GL6: moderate glaucoma, MD -8.77 and -11.63 dB, and GL7 (MD: -12.81 db) and GL8 (MD: -23.60 dB) had advanced glaucoma. All globes were stored at +4°C as described in 2.2.1.

Rat aorta (RTA), known to contain EFs in the tunica media (Keech, 1960, O'Connell et al., 2008) and RTT, rich in collagen type I (Rowe, 1985) were harvested from Wistar rats within one hour of death and immersion fixed in 4% PFA. Purified EFs preparations (i.e. digested preparations of bovine nuchal ligament and porcine ear) were provided by Exeter University (a gift from Dr. Ellen Green). Bovine nuchal ligament and porcine ear had

been subjected to the Lansing procedure (Soskel et al., 1987) to digest away all non-EFs components (Green, 2012). In brief, strips of nuchal ligament and ear were delipidated in chloroform: methanol (3:1 v:v) for 1 hour, then immersed in acetone for 1 hour and washed in 0.15M NaCl. Both tissues were then immersed in 0.1M NaOH within a water bath at 95˚C for 45 minutes, left to cool at room temperature, and washed in distilled water to lower the pH to 7.0. Tissues were stored at 4˚C in 0.15M NaCl with 0.1% sodium azide in distilled water to prevent bacterial growth.

3.2.2 Sample preparation

All globes were washed in three changes of PBS over 72 hours and transverse 100 μm sections were prepared as described in 2.2.2. 100 μm thick sections of RTA, RTT, bovine nuchal ligament and porcine ear were cut using a sledge microtome (Microm HM 440E, Thermo Fisher, UK) and mounted in PBS:glycerol (1:1 v:v) on Superfrost Plus slides.

3.2.3 Development of an elastic fibre signature using spectral imaging.

3.2.3.1 Spectral imaging

TPEF was performed using a wavelength tuneable ultra-fast pulsed laser system as described in 2.2.3. Spectrally resolved detection of TPEF was conducted using the programmable slit (10 nm) of the Laser Scanning Microscope instrument's epi-detection emission spectrometer. Excitation and emission lambda stacks of 1024x1024x20x8 bit pixel resolution were acquired using ZEN software version 2.2 with a scan speed of 9 (0.42 μsec/pixel dwell time) and spatial sampling steps (pixel distance) of 0.28 μm. Excitation lambda stacks were collected with an epi (backscatter), non-descanned (external) detector (NDD) using a near-infrared (NIR) blocking bandpass filter of 505 nm ± 60 nm bandwidth (Brightline^{TM}, Semrock/Laser2000 UK). Emission lambda stacks were collected using a laser power of 1.8% with a fully open confocal spectrometer pinhole (601.3 Airy Unit) over an emission range of 432-642 nm using the Gallium Arsenide Phosphide (GaAsP) internal detector. The latter was selected to avoid acquisition of collagen-derived second harmonic generation (SHG) signals between 370nm to 400nm (Freund et al., 1986, Zipfel et al., 2003b).

All excitation and emission lambda stack maximum intensity projections (MIPs) presented in this chapter were adjusted in brightness to best resemble those observed on the microscope.

3.2.3.2 Determination of elastic fibre signature from the elastic lamellae of rat aorta

RTA sections in triplicate were excited from 700 nm to 900 nm in 10 nm steps. To ensure a constant laser power at different excitation wavelengths, the mean laser power output was normalised during acquisition of excitation spectra using the calibration file *ExcitationFingerprint_12_12_2016* (Table 3.1). Once the optimal excitation wavelength range had been determined, the next step was to determine the optimal emission wavelength for EFs associated TPEF. Emission lambda stacks were collected following excitation of the RTA at 740 nm, 760 nm, 780 nm and 800 nm with laser power of 1.8%.

Excitation λ (nm)	700	710	720	730	740 - 800	810	820	830	840	850	860	870	880	890	900
Laser power (%)	3.6	3.0	2.6	2.0	1.8	2.2	2.4	2.6	2.8	3.2	3.6	4.0	4.4	4.8	5.8

Table 3.1. Laser power expressed as a percentage at different excitation wavelengths. The calibration file *ExcitationFingerprint_12_12_2016* was uploaded during acquisition of excitation spectra to ensure a constant laser power at different wavelengths.

3.2.3.2.1 Analysis of relative intensities values within excitation and emission lambda stacks.

Excitation and emission lambda stacks data collected from the aortic elastic lamellae were subsequently opened with ZEN software version 2.2. Each lambda stack was visualised as MIP. The contrast was adjusted, and the image was zoomed to 200% to enable the observation of the elastic lamellae within the aorta wall (figure 3.1). A region of interest (ROI) was manually drawn within three regions of the aortic elastic lamellae known to contain EFs (figure 3.1a,b). Relative intensities within these ROIs were output using the ZEN software and saved as .xls files.

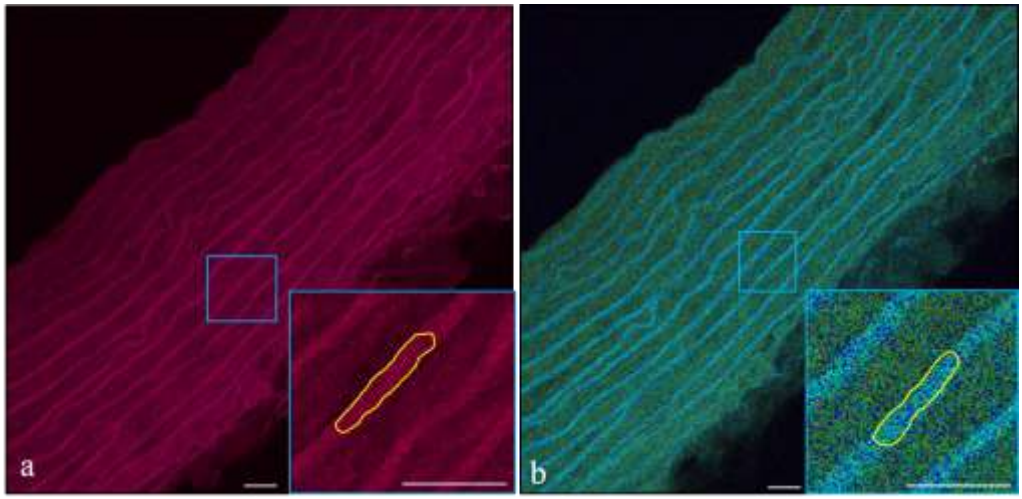

Figure 3.1. Maximum intensity projections (MIPs) of excitation and emission lambda stack within RTA. In MIPs, for each X and Y coordinates, the pixel with the highest fluorescence intensity along the λ axes is represented by the colour of the corresponding wavelength. Excitation (Ex: 700-900 nm) (a) and emission (Em: 432-642 nm at Ex: 800 nm) (b) MIPs of the elastic lamellae of RTA with ROIs containing EFs (insets in a and b). Scale bar represents 50μm and 20μm in insets.

Relative intensities of emission spectra, following excitation at 740 nm, 760 nm, 780 nm and 800 nm, were manually normalised to the square of the laser power, by dividing each intensity value by a calibration coefficient. At these excitation wavelengths, a percentage of laser power of 1.8% was used. The latter was firstly converted to an integer number by removing the percentage then normalised to the square to obtain a *calibration coefficient* of 0.000324 as shown below.

$$Calibration\ Coefficient = \left(\frac{1.8\%}{100}\right)^2$$

Relative intensities of emission spectra were divided by the calibration coefficient to obtain normalised intensities. Normalised data was imported into MATLAB where the mean intensity of the three ROIs was computed and plotted against excitation and/or emission wavelength using a custom-written MATLAB script (see appendix II.1 "EF_Intensity_Profile_v1").

3.2.3.3 Determination of the elastic fibre signature of the elastic lamina of the human central retinal artery

Human CRA in triplicate sections, were imaged as described in section 3.2.3.2. Excitation and emission lambda stacks were visualised as described in section 3.2.3.2.1 to enable the visualisation of the elastic laminae within the CRA (figure 3.2). ROIs were manually drawn within the elastic lamina (figure 3.2a,b). Relative intensities of these ROIs were output, normalised and plotted versus wavelength as described in section 3.2.3.2.1.

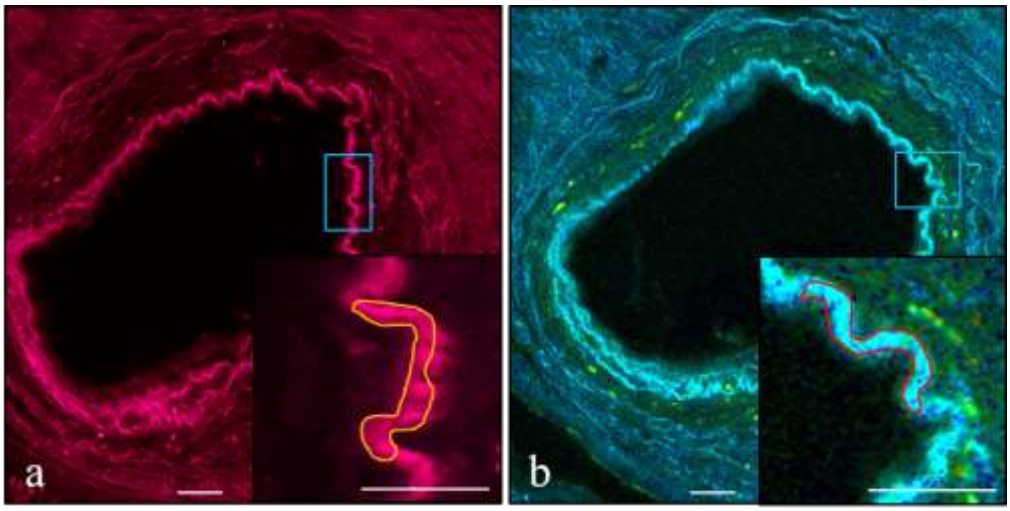

Figure 3.2. Maximum intensity projections (MIPs) of excitation and emission lambda stacks of the human CRA. Excitation (Ex: 700-900 nm) (a) and emission (Em: 432-642 nm at Ex: 800 nm) (b) MIPs of the elastic laminae of the artery with ROIs containing elastic lamina (insets in a and b). Scale bar represents 50µm and 20µm in insets.

3.2.4 Validation of the TPEF elastic fibre signature

To confirm that the selected excitation and emission wavelengths did not overlap with fibrillar collagen signals, RTT sections, rich in type I collagen (Rowe, 1985), were subjected to spectral imaging as described for the RTA in section 3.2.3.2. Relative intensities of ROIs were output, normalised and plotted versus wavelength as described in section 3.2.3.2.1.

To validate the elastic signature obtained from RTA and CRA, purified (to remove none EFs) elastin preparations of porcine ear skin and bovine nuchal ligament were subjected to spectral imaging as described in section 3.2.3.2. Relative intensities of ROIs within

emission lambda stacks were output, normalised and plotted versus wavelength as described in section 3.2.3.2.1.

3.2.5 Characterisation of elastic fibre spectral signature in the human aged ONH and regions

To determine if EF signature could be generated from human ONH connective tissue, three elderly human ONHs (aged 85, 87 and 88 years old) were excited at 800 nm ± 6 and emission spectra were acquired within 10 nm slit widths from 432 to 642 nm. The EF signature was examined within the superior, inferior, nasal and temporal LC, the RoIns and ppsclera.

Emission lambda stacks of each ONH area were visualised as MIPs as described in section 3.2.3.2.1. ROIs in triplicate, were manually drawn to include EFs present within the LC cribriform plates (figure 3.3a), RoIns and ppsclera of each ONH. Additionally, ROIs were also drawn within the neuronal pores (figure 3.3b) as an example of an area not containing EFs. The relative intensities of the ROIs analysed here were subtracted from the corresponding ONH EFs intensity value output from the LC, RoIns and ppsclera ROIs to determine if this ROI could be used as a measure of background intensity. Since excitation was at a single wavelength (800 nm), normalisation of relative intensities to the square of the laser power was not performed.

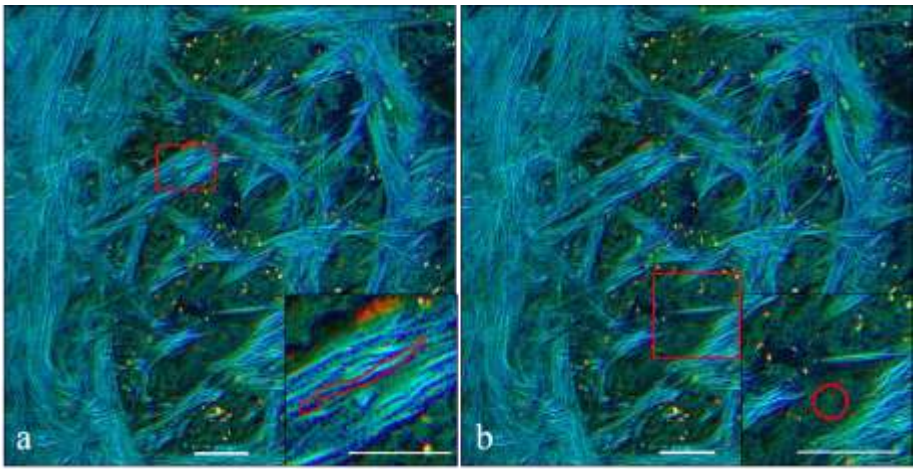

Figure 3.3. Maximum intensity projections (MIPs) of excitation and emission lambda stack within human ONH. Insets in a and b showed the ROIs drawn at the edges of the EFs within the cribriform plates (a). Regions were also drawn within neuronal pores (b). White arrows in a,b point to small particles observed at the ONH. Scale bar represents 50µm and 20µm in insets.

However, within the LC and postL ON sections, small, irregular, yellowish particles (figure 3.3a,b) were observed. Previously lipofuscin has been identified in the ONH (Cubeddu et al., 1999, Delori et al., 2001, Feldman et al., 2010). To determine if those particles had a similar spectrum to lipofuscin, an aliquot of purified human retinal pigment epithelial (RPE) lipofuscin (a gift from Professor Mike Boulton) (Boulton and Marshall, 1985) was excited at 800 nm ± 6 as described in 3.2.5.

Relative intensities from emission lambda stacks of both lipofuscin granules and the ONH granular component were output and plotted versus wavelength as described in section 3.2.3.2.1. Due to the excitation with single wavelength (800 nm), the normalisation to the square of the laser power was not performed.

3.2.6 Elastic fibre spectral signature in unfixed ONHs

To investigate whether fixation had any effect on TPEF fluorescence, the EF signature within three unfixed ONHs (aged 63, 72 and 80 years old) was compared to that of fixed ONHs. ONHs were subjected to spectral imaging as described in 3.2.5 and relative intensities of emission lambda stacks were output and plotted versus wavelength as described in 3.2.3.2.1. As a single excitation wavelength of 800 nm was used, normalisation to the square of the laser power was not performed.

Areas under the curve (AUC) were calculated using the *Trapezoidal* rule to determine if the EFs relative intensity altered between fixed and unfixed.

$$AUC = \frac{1}{2}\sum_{k=1}^{N-1}(y_{k+1} + y_k)(\lambda_{k+1} - \lambda_k)$$

where

N = 14 is the range of wavelengths

y_k = relative intensity at a given wavelength λ (i.e. λ_k)

3.2.7 Elastic fibre spectral signature in the human ageing ONH

EFs spectral signature was analysed within the nasal regions of the LC, RoIns and ppsclera of ten ONHs, without pathology, aged 2 years to 88 years old. Sections from LC, RoIns and ppsclera were subjected to spectral imaging as described in 3.2.5. Relative intensities of emission lambda stack from LC, RoIns and ppsclera were output using the ZEN software, saved as .xls files and plotted as intensity versus wavelength.
To determine changes in shape of the spectral curves, relative intensities of emission lambda stacks within LC, RoIns and ppsclera were normalised to the maximum intensity value and plotted versus wavelength.

3.2.8 Spectral unmixing of the ONH elastic fibre spectral signature

The spectral unmixing (Zimmermann et al., 2002, Zimmermann et al., 2014, Zimmermann, 2005) was performed using the "Unmixing" tool of ZEN software. Proof of concept was first performed within the RTA, CRA and the elderly human ONHs. The aim of the spectral unmixing was to separate (unmix) the EF TPEF from other fluorophores. Emission lambda stacks from RTA (figure 3.4a), CRA (figure 3.4b) and elderly human LC (figure 3.4c) were imported into the ZEN software as .tiff. Three distinct ROIs corresponding to three different components namely i) component 1: EFs (figure 3.4d-f), ii) component 2: matrix adjacent to elastic laminae (figure 3.4g-i) and iii) component 3: an area without EFs (figure 3.4l-n) were drawn onto the emission lambda stacks. The "Unmixing" tool of ZEN software was applied.

Distinct region of interests, corresponding to three different fluorophores, were unmixed from the original image. From the equation above, the Cn corresponded to the concentration of the elastic fibre (component 1), matrix adjacent to elastic fibre (component 2) and an area without elastic fibre (component 3). The spectrum intensity of the fluorophore (i.e. elastic fibre, matrix and area non-containing elastic fibre) was measured within each pixel of the lambda stack at different emission wavelength. The linear unmixing algorithm measures the spectrum intensity $I(\lambda)$ of a given fluorophore in each pixel at different wavelengths. By measuring the spectrum at different lambda, it is possible to estimate the concentration of several components within the same pixel by using a least square fitting.

Thus, each pixel within each region of interest selected within the lambda stack is characterised by the sum of the intensities, which depends on the concentration of fluorophores in that pixel. The higher the concentration, the higher the intensity. Each pixel in the spectral image is categorised as representing a mixture of fluorophore signals (intensities) whiting the measured spectrum I(λ)**.** The latter can be deconvolved into the concentration (Cn) of each individual fluorophore's spectrum (Rn), when all values as summed. This can be expressed as:

$$I(\lambda) = \sum_{n=1}^{N} C_n R_n\,(\lambda)$$

Where

Cn = concentration of the fluorophore

Rn (λ) = spectrum intensity of the fluorophore

N = total number of fluorophores = 3

3.2.8.1 Quantification of elastic fibre TPEF contribution to the ONH

The unmixed images, representing the three components (figure 3.5a-c) were imported in Image J and segmented using the threshold method to determine an intensity boundary that separated the object and the background. Then the image was segmented by converting it to a binary image (figure 3.5d-f) based on the threshold. EFs associated TPEF (component 1) pixels in the LC, RoIns and ppsclera was expressed as percentage of the total pixels within the three components (i.e. total TPEF) in each ONH.

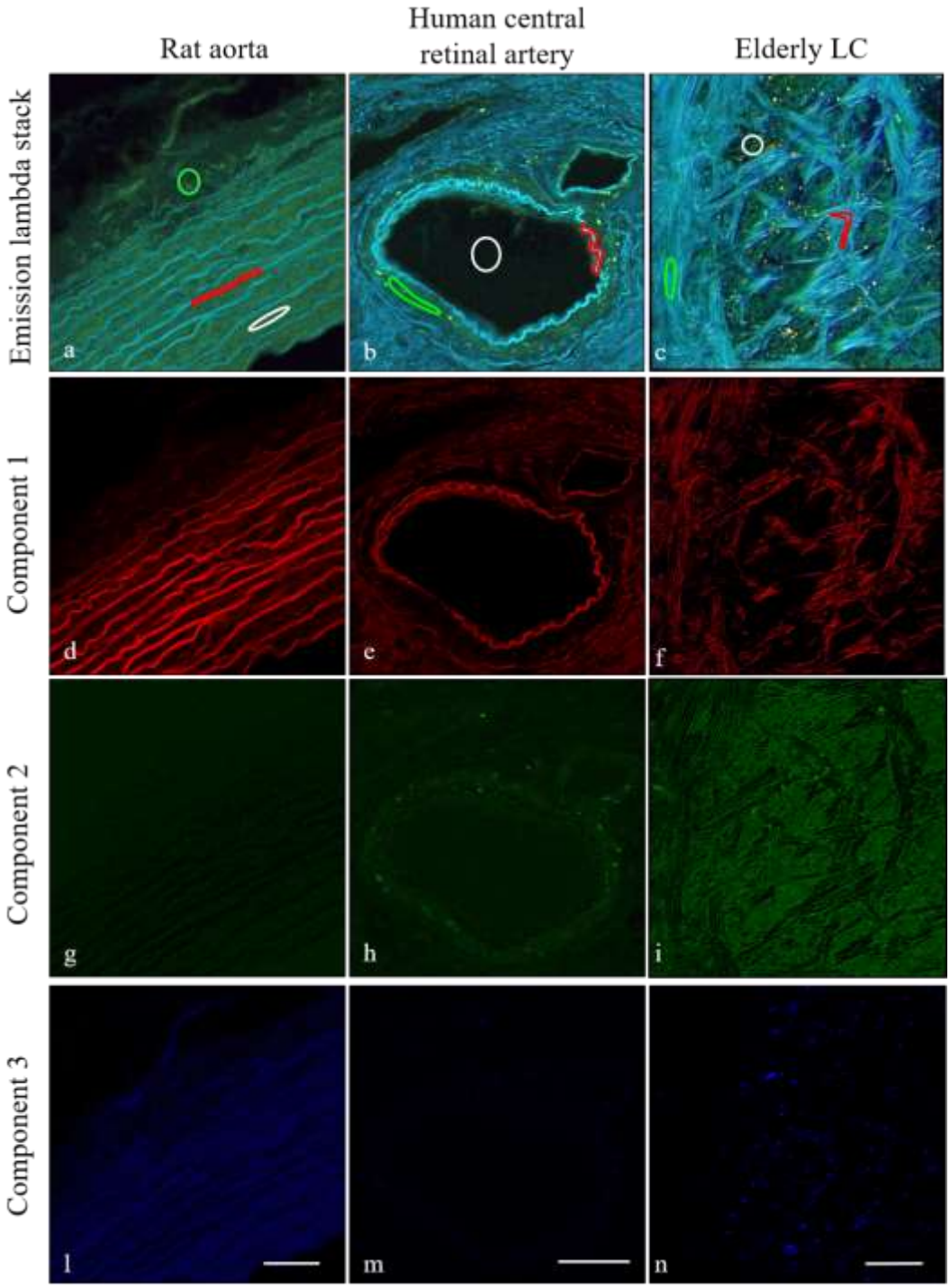

Figure 3.4. Linear unmixing output from lambda stacks. Three regions of interests corresponding to EFs (red polygons in a-c), matrix surrounding EFs (green polygons in a-c) and non-containing EFs areas (white polygons in a-c) were drawn on the lambda stacks of RTA (a), human CRA (b) and elderly human LC (c). Lambda stacks were then uploaded into Zen software and the linear unmixing algorithm applied. The latter separated the three components based on their spectral properties and output three pseudo-colour coded images of EFs (component 1, d-f), matrix (component 2, g-i) and non-containing EFs areas (component 3, l-n). Scale bars represent 50µm.

3.2.8.2 Quantification of elastic fibre content in the unmixed TPEF

To quantify EFs in the human ONH, EFs associated TPEF (component 1) pixels were segmented by thresholding as described in 3.2.8.1 and saved as a binary image. The number of EFs associated pixels were expressed as a percentage over the total number of pixels within the ROI. EFs content was quantified in an age range of ONHs (2-88 years old) within LC, RoIns and ppsclera

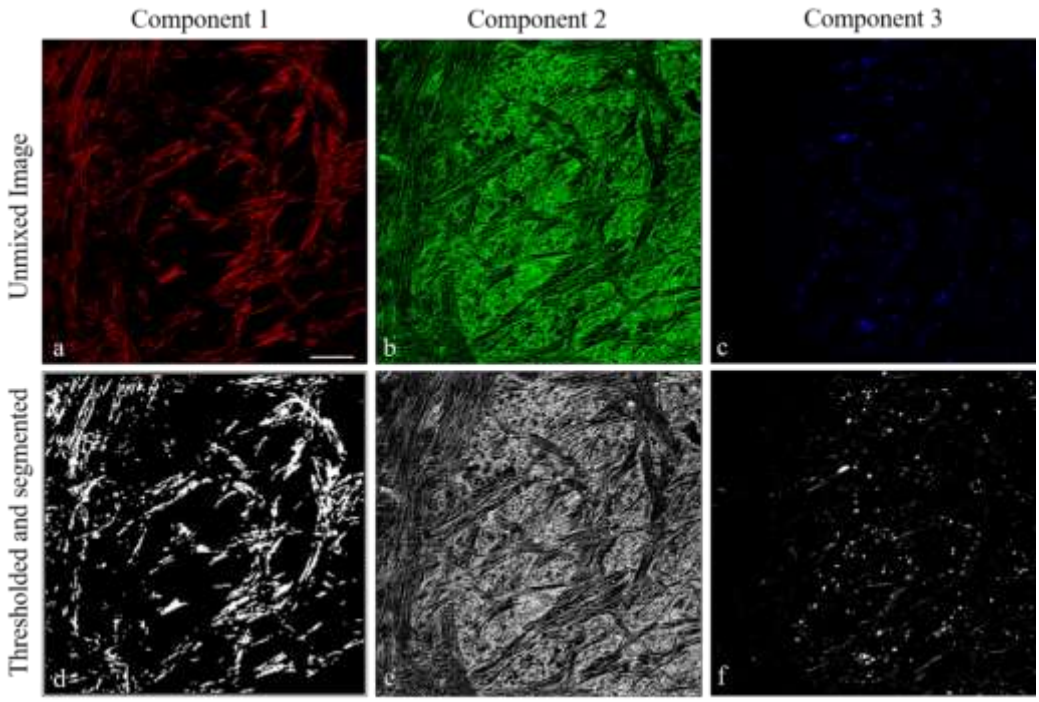

Figure 3.5. Spectral unmixing and segmentation of EFs within the ONH TPEF. Unmixed images representing component 1 (a), component 2 (b) and component 3 (c) and corresponding thresholded pixels of images representing component 1 (d), component 2 (e) and component 3 (f). Elastic fibre 'content' was represented by the number of thresholded pixels in component 1 as a percentage of r the total number of pixels in component 1 image. Elastic fibre 'contribution' to the TPEF signal was represented by the component 1 thresholded pixels as a percentage of the total number of all TPEF pixels (i.e. the pixel sum of all three components). Scale bar represents 50 µm.

3.2.9 Elastic fibre spectral signature in the human glaucomatous ONH

Glaucomatous ONHs (n=8) and three age-matched controls were subjected to spectral imaging as described in 3.2.5 to determine the EFs spectral signature. Relative intensities from emission lambda stacks were output and plotted as intensity versus wavelength as described in 3.2.3.2.1. Due to the excitation with single wavelength (800 nm), the

normalisation to the square of the laser power was not performed. EFs TPEF content was determined as described in section 3.2.8.

3.2.10 Statistical analysis

All statistical tests were performed with SPSS v.25. Normality of data was tested using Shapiro Wilk at a significance of $p>0.05$. To determine differences in EFs TPEF spectra shape, in normal, ageing and glaucomatous ONHs, Dunn's test multiple comparison was performed with significance of $p<0.05$. Linear correlation tests between intensities and ONH age were performed with Pearson's correlation using a level of significance $p<0.05$.

As data was deemed to be normally distributed, comparisons between AUCs of unfixed and fixed ONHs were analysed using one-way ANOVA and independent t-tests. EF content correlation with age was tested with Spearman's rank correlation as deemed to be not normally distributed. EF content was compared in glaucomatous ONHs with One-way ANOVA and independent t-test as deemed to be normally distributed.

3.3 Results

3.3.1 Determination of elastic fibre signature from the elastic lamellae of rat aorta

An example of excitation lambda stack generated from RTA sections at 700-900 nm is shown in figure 3.6a. Distinct elastic lamellae were evident within the MIP running horizontal to the RTA axes (figure 3.6b). Excitation spectra demonstrated an excitation range of 740-800 nm (figure 3.6e) consistent with the lambda stack montage (figure 3.6a). Intensity maxima were observed at 760 nm and 780 nm indicative of the highest intensity signals associated with elastic lamellae. The signal was weaker or not observed at wavelengths lower than 740 nm or greater than 810 nm (figure 3.6e).

A representative emission lambda stack collected following excitation at 740, 760, 780 and 800 nm, is shown in figure 3.6c. Distinct elastic lamellae (figure 3.6d) were evident in the corresponding MIP. Overall, EFs associated TPEF was observed over a broad emission range of 432-562 nm (figure 3.6c and 3.6f) with maximum signal values between ~470 nm to ~500 nm (figure 3.6f). Emission signals were less intense at wavelengths greater than 562 nm and highest following excitation at 760 nm (figure 3.6f).

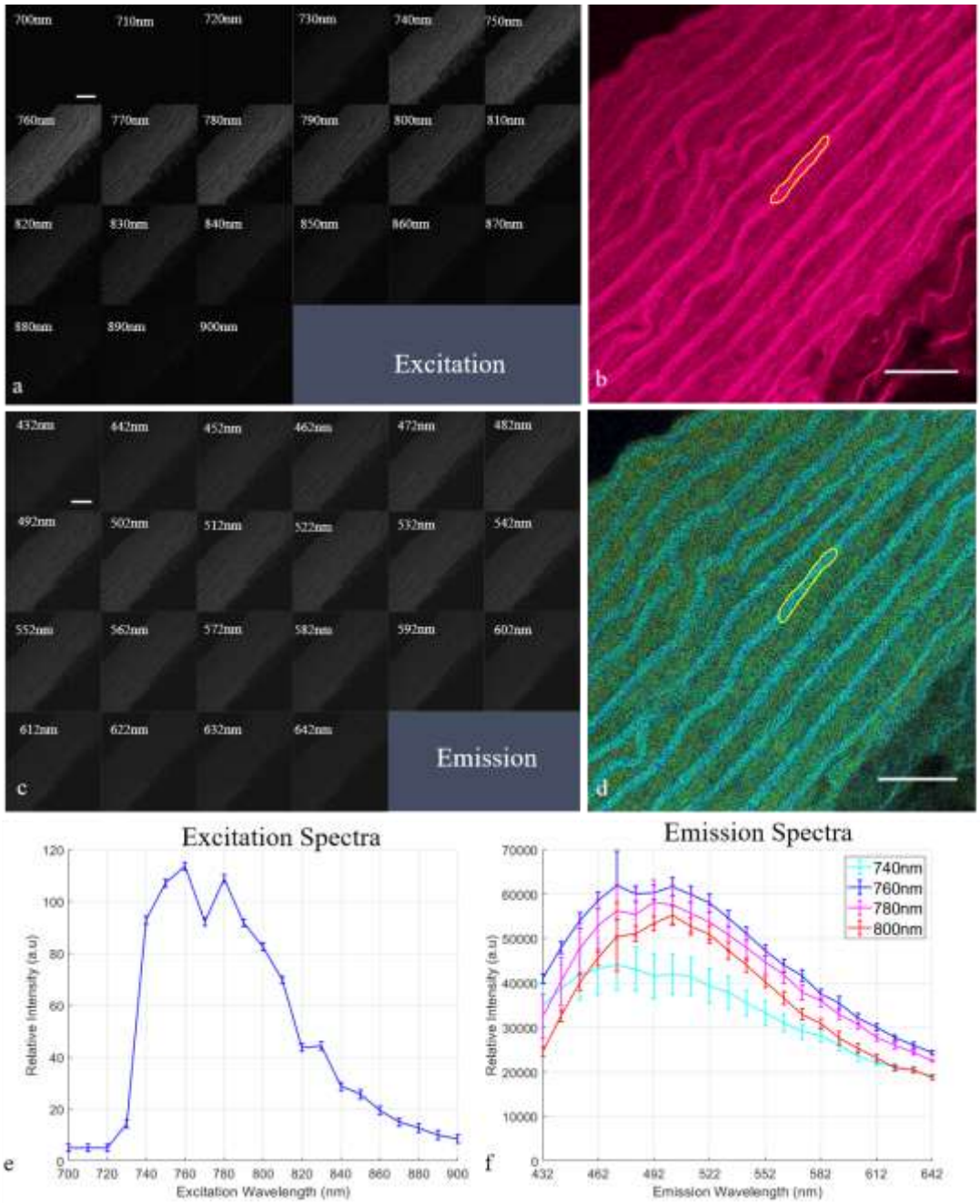

Figure 3.6. Excitation (a,b) and emission (c,d) lambda stacks of RTA elastic lamellae. a) Excitation lambda stack, Ex:700-900 nm at 10nm steps, Em:445-565 nm. c) Emission lambda stack, Ex:800 nm, Em: 432-642 nm at 10nm slit width. Distinct elastic lamellae were evident within the excitation (b) and emission (d) MIPs within the aorta tunica media. Relative intensities of elastic lamellae were highest when excited in the range 740-800 nm (e). The intensities of the elastic lamellae in the emission spectra were highest in the range 432-562 nm when excited with 760nm compared to excitation wavelengths of 740, 780 and 800 nm (f). Scale bars represent 50µm.

3.3.2 Determination of the elastic fibre signature of the elastic lamina of the human central retinal artery

An excitation lambda stack generated from human CRA (excitation: 700-900 nm) is shown in figure 3.7a. The distinct elastic lamina was evident within the MIP of the excitation lambda stack circularly orientated around the lumen (figure 3.7b). Excitation spectra had a maximum at 760 nm and 800 nm (figure 3.7e). The signal intensity was lower at wavelengths less than 740 nm and greater than 810 nm (figure 3.7e).

An emission lambda stack representative of those collected following excitation at 740, 760, 780 and 800 nm is shown in figure 3.7c. The elastic lamina (figure 3.7d) can be seen clearly in the excitation MIP. Overall, EFs associated TPEF was observed over a broad emission range of 432-562 nm (figure 3.7c and 3.7f) with maximum signal intensity values at ~470 nm and ~500 nm. Emission signals were decreased or negligible at wavelengths greater than 562nm. Emission intensity was greatest following excitation at 800 nm (figure 3.7f).

3.3.3 Validation of the TPEF elastic signature

Representative emission lambda stacks following 800 nm excitation derived from positive controls tissues, porcine ear and bovine nuchal ligament are shown in figure 3.8a and 3.8c respectively. MIPs of porcine ear (figure 3.8b) and nuchal ligament (figure 3.8d) showed the EFs distribution within these tissues. Porcine ear and nuchal ligament EFs associated TPEF emission spectra were similar to those observed for the CRA; higher intensity signal was observed in the range of 432-532 nm (figure 3.8e).

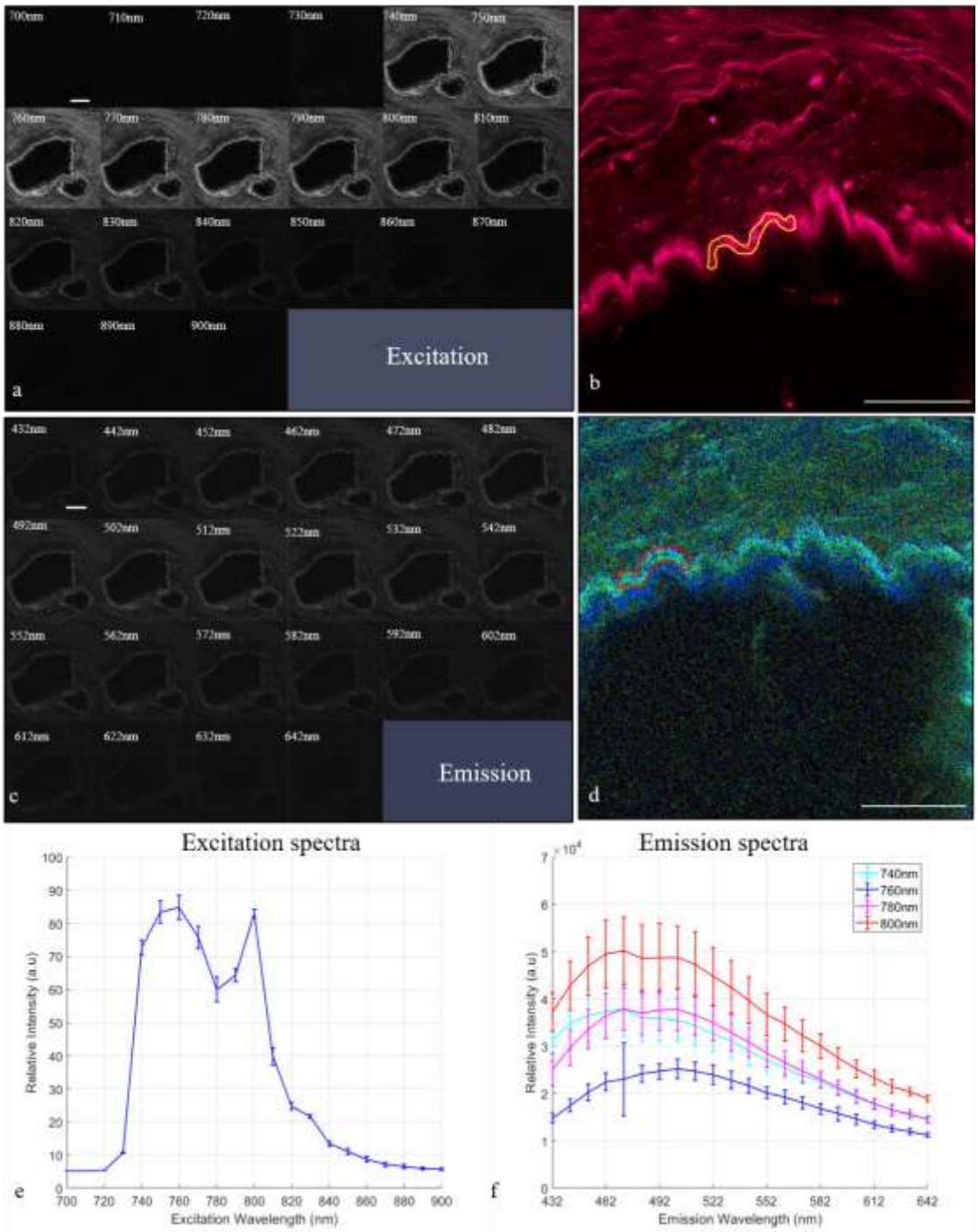

Figure 3.7. Excitation (a,b) and emission (c,d) lambda stacks of human CRA elastic lamina. a) Excitation lambda stack, Ex:700-900 nm at 10nm steps, Em:445-565 nm. c) Emission lambda stack, Ex:800 nm, Em: 432-642 nm at 10nm slit width. Distinct elastic laminae were evident within the excitation (b) and emission (d) MIPs within the tunica intima. Relative intensities of elastic laminae were highest when excited in the range 740-800 nm (e). The intensities of the elastic laminae in the emission spectra were highest in the range 432-562 nm when excited at 800 nm compared to excitation wavelengths of 740, 760 and 780 nm (f). Scale bars represent 50µm.

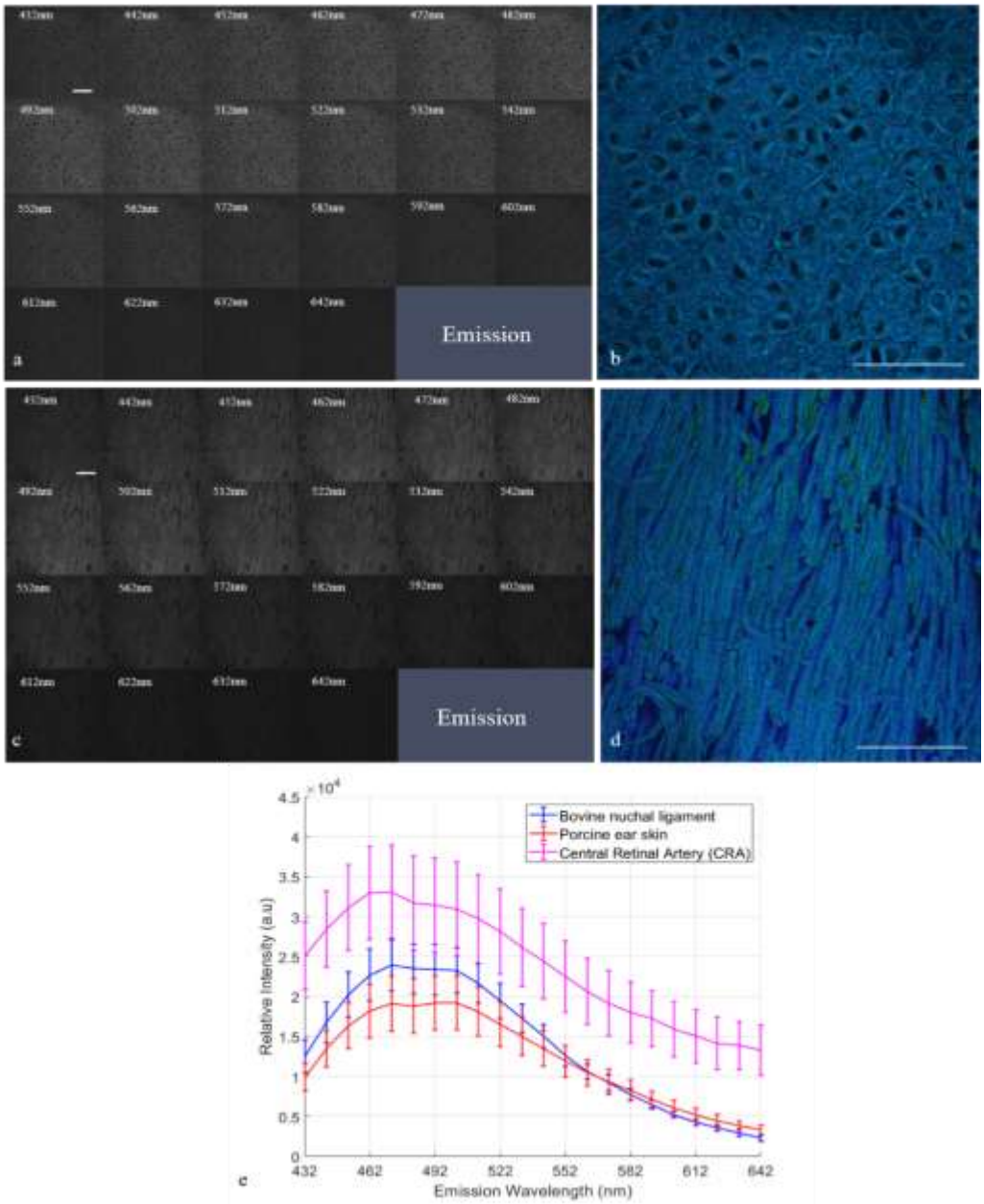

Figure 3.8. Emission lambda stacks of porcine ear skin [a, MIP (b)] and bovine nuchal ligament [c, MIP (d)]. Ex:800nm, Em: 432-642nm at 10nm slit width. The intensities of elastin in the emission spectra were highest in the range 432-562 nm (e). Scale bars represent 50µm.

An excitation lambda stack generated from RTT at 700-900 nm is shown in figure 3.9a. No signals from the tendon were retrieved in the excitation lambda stacks at 700-870 nm. However, at wavelength of 880 nm, 890 nm and 900 nm (figure 3.9e), signals derived from fibrillar collagen were recorded at half of the excitation wavelengths (figure 3.9b). Emission lambda stacks of RTT, representative of those acquired following excitation at

740, 760, 780 and 800 nm, is demonstrated in figure 3.9c. TPEF was not emitted from RTT in the range 432-642 mn (figure 3.9d,f).

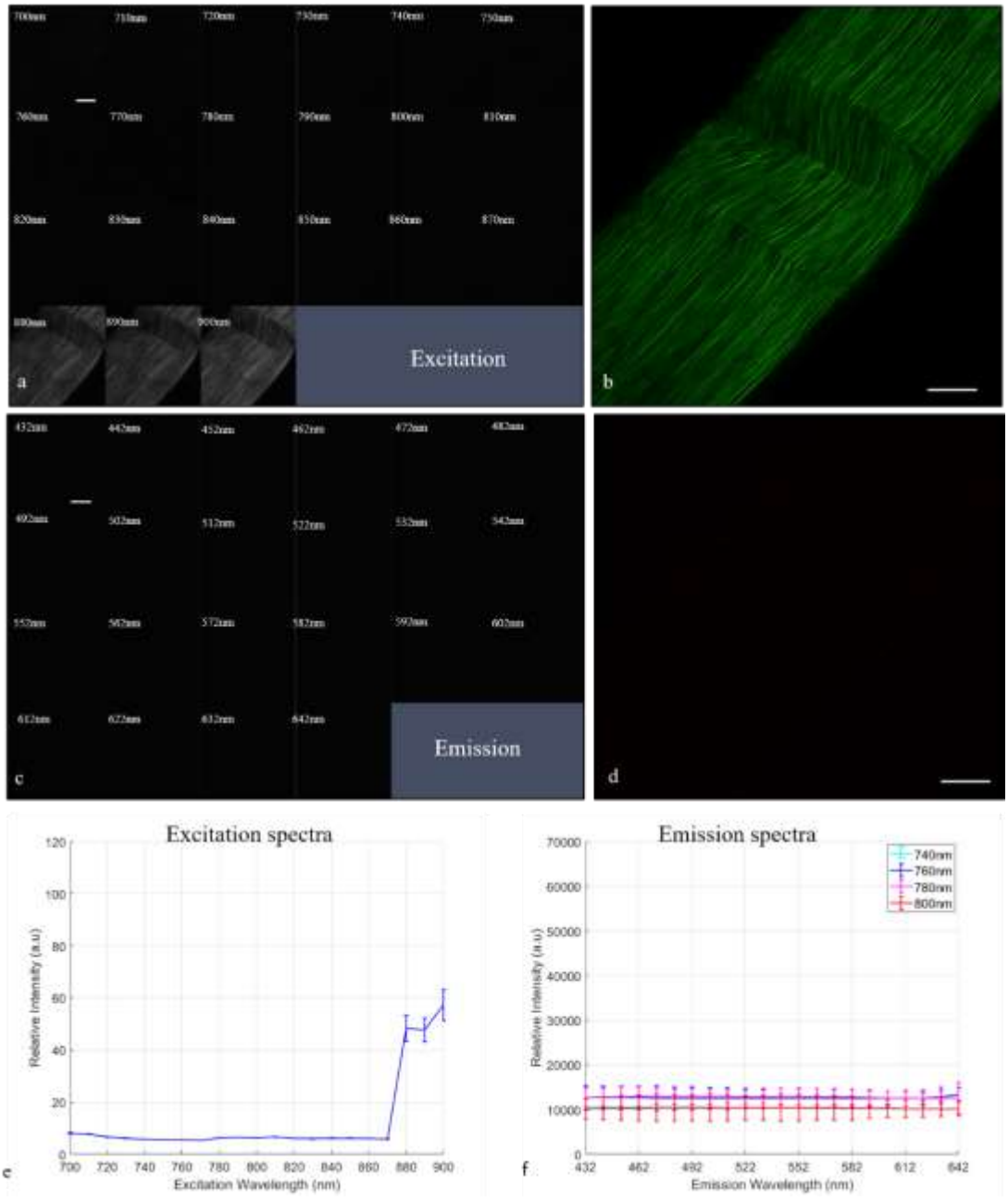

Figure 3.9. Excitation (a) and emission (c) lambda stack of RTT. Ex: 700-900nm at 10nm steps, Em:445-565nm. No signals from the tendon were retrieved in the excitation lambda stack (a) except for 880 nm, 890 nm and 900 nm wavelengths (e). TPEF was not emitted from RTT in the range 432-642 mn (d,f). Forward SHG signal (b) derived from fibrillar collagen were recorded at half of the excitation wavelengths (b). Scale bars represent 50μm.

3.3.4 Characterisation of elastic fibre spectral signature in the human aged ONH and regions

Representative emission lambda stacks and MIPs derived from human LC (figure 3.10a) and ppsclera (figure 3.10c) are shown in figure 3.10. EFs spectral signature in the ONH LC (figure 3.10e), RoIns (figure 3.10f) and ppsclera (figure 3.10g) showed similar maximum intensities of those observed in the RTA, CRA and purified tissues, from 450nm to 550 nm (see figures 3.7 and 3.8).

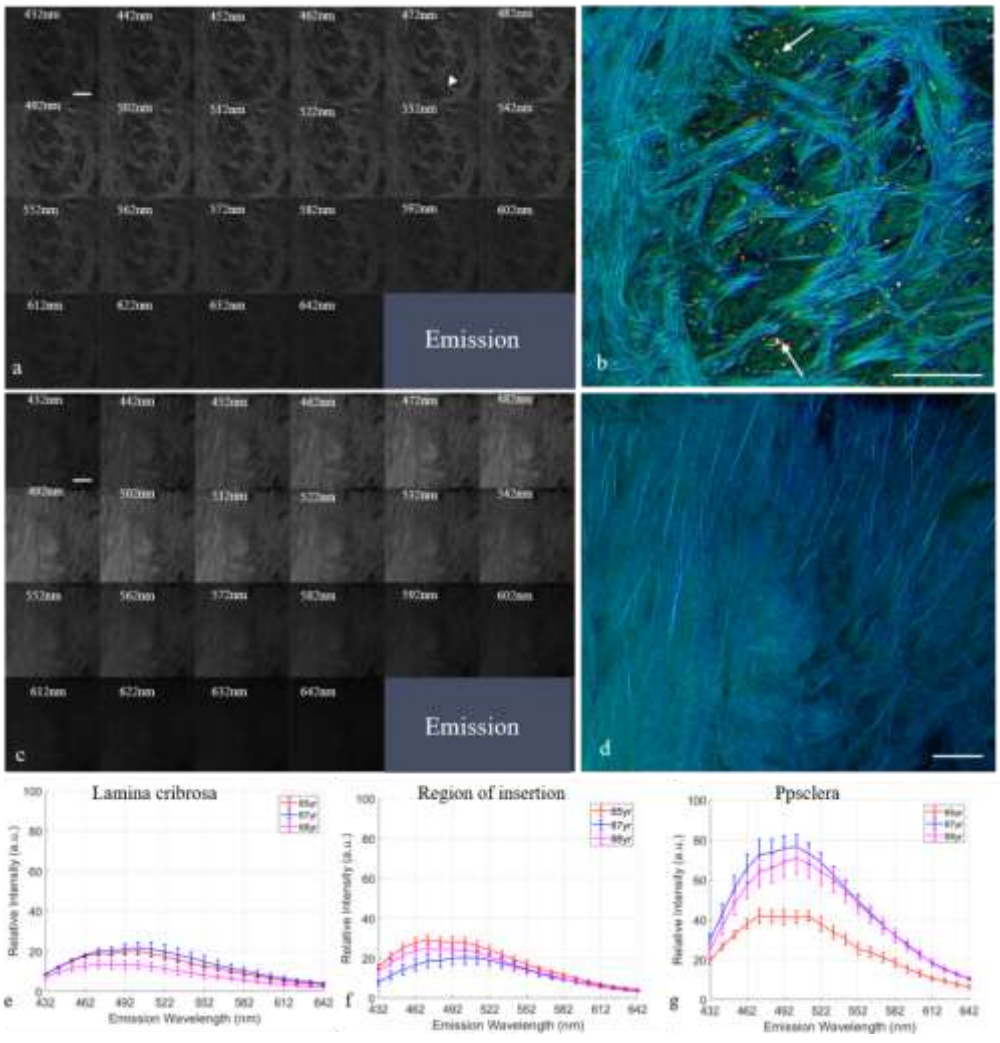

Figure 3.10. Emission lambda stacks from human ONH. Emission lambda stack from LC (a) and ppsclera (c) and MIPs (b,d, respectively) are shown. Relative intensities of EFs in the emission spectra were highest in the range 432-562nm when excited with 800nm in both LC (a), and ppsclera (c). EFs spectral signature in the ONH LC (e), RoIns (f) and ppsclera (g) showed similar maximum intensity to those acquired from controls and purified tissues. Fluorescent particles were observed in the LC pores (b, white arrows) but not in the ppsclera (d). Scale bars represent 50µm.

Fluorescent particles were observed within the LC pores (figure 3.10b). These particles appeared limited to the LC and were not observed within the ppsclera (figure 3.10d). Spectral imaging of lipofuscin from RPE (figure 3.11a) revealed a similar maximum intensity of those acquired from the granules within the ONH from 552 nm to 620 nm (figure 3.11b). However, the signature of lipofuscin granules was shifted towards higher wavelengths (in the red spectrum), therefore the spectrum had a different shape to that of EFs. Normalisation to the maximum showed significant changes in the spectrum shape (Dunn's test p=0.001).

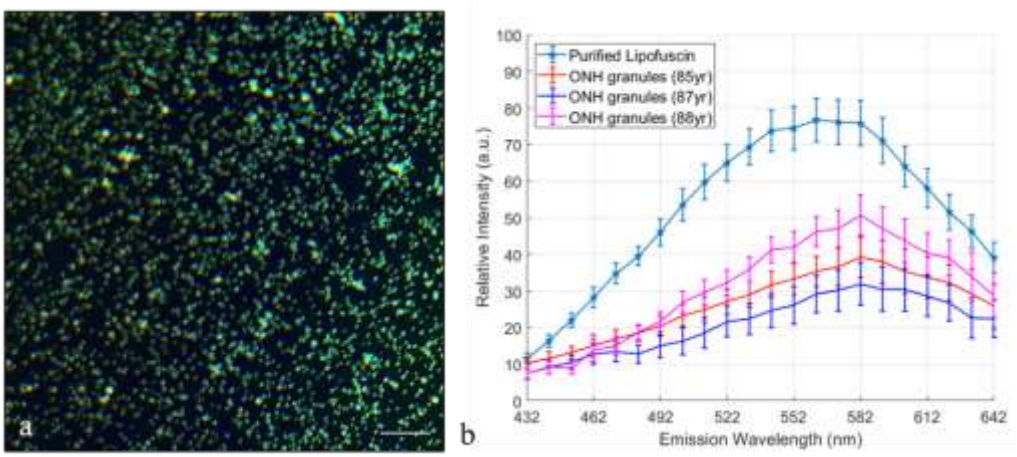

Figure 3.11. RPE-associated lipofuscin emission MIP (a) and spectral signature (b). MIP of emission lambda stack (a) showing RPE-associated lipofuscin granules. Relative intensities of these RPE particles were similar to those of granules observed in the LC. Spectral signature of RPE lipofuscin and LC granules shifted to higher wavelengths (b). Scale bar represents 50µm.

EFs spectral signature and AUCs comparison between fixed and unfixed elderly ONH is shown in figure 3.12. In all ONH regions, the EFs intensity was significantly greater in the fixed ONHs compared to unfixed ONHs [LC (p=0.021) (figure 3.12a,e), RoIns (p=0.011) (figure 3.12c,g), pores (p=0.020) (figure 3.12b,f) and ppsclera (p=0.016) (figure 3.12d,h)]. Normalisation to the maximum did not show changes in spectrum shape [LC (Dunn's test p=0.056), RoIns (Dunn's test p=0.086) and ppsclera (Dunn's test p=0.245)] between fixed and unfixed ONHs, except for pores (p=0.002).

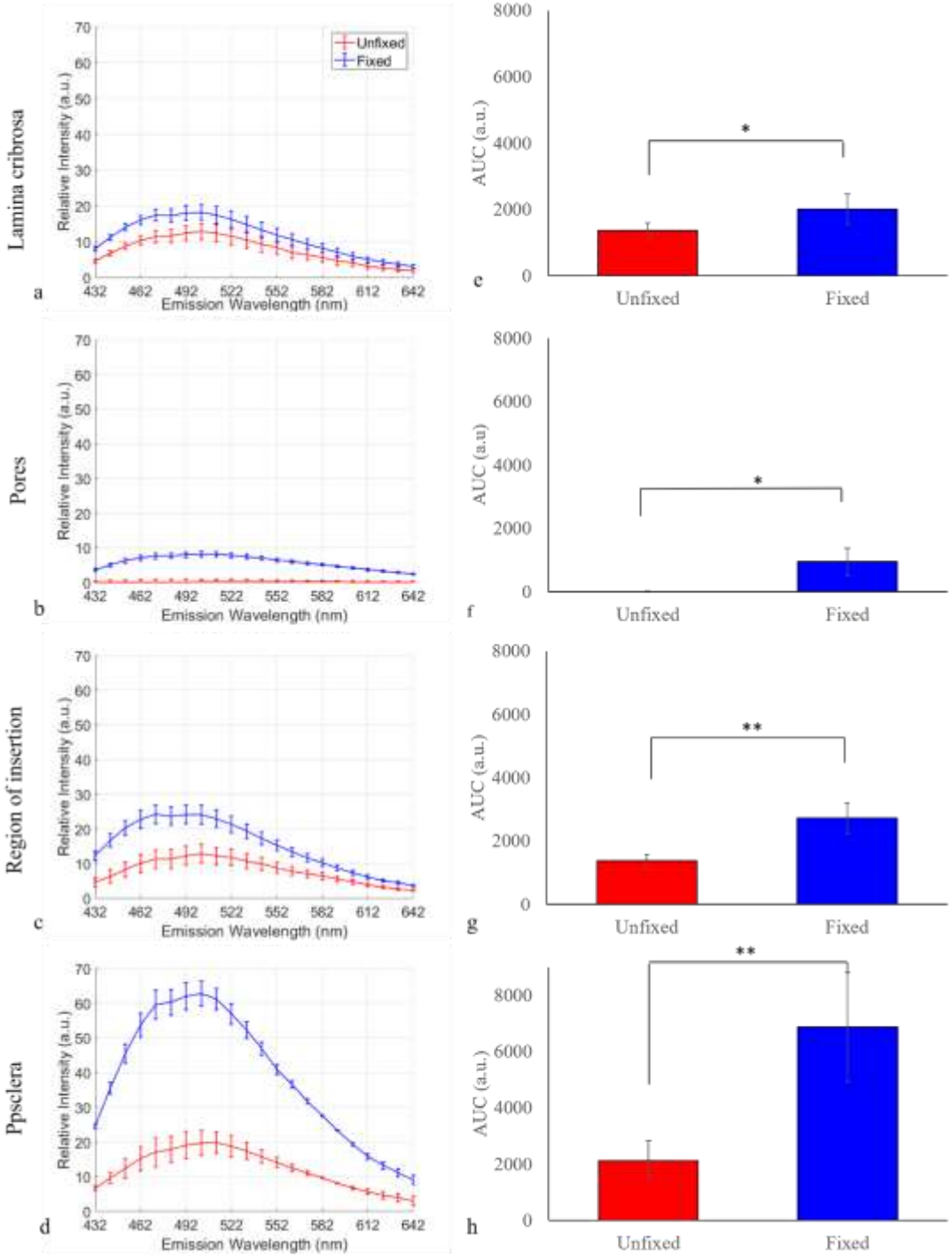

Figure 3.12. EFs spectral signature between fixed and unfixed ONHs. In all ONH regions, mean ± sd AUCs were greater in the fixed ONHs compared to unfixed ONHs [LC (p=0.021) (a,e), RoIns (p=0.011) (c,g), pores (p=0.020) (b,f) and ppsclera (p=0.016) (d,h).

EFs were not observed within the neuronal pores, through which the bundles of nerve axons pass (figure 3.10b). EFs spectral signature was thus explored before and after subtracting pores intensity values from the LC (figure 3.13a,d), RoIns (figure 3.13b,e) and ppsclera (figure 3.13c,f). EFs spectral signature did not change after pore subtraction [LC (Dunn's test p=0.161), RoIns (Dunn's test p=0.057) and ppsclera (Dunn's test p=0.271)]. Normalisation to the maximum did not show differences in the spectrum shape before and after pore intensity subtraction [LC (Dunn's test p=0.483), RoIns (Dunn's test p=0.617) and ppsclera (Dunn's test p=0.849)].

EFs spectral signature was explored in the superior, inferior, nasal and temporal regions of the aged ONHs (figure 3.14). No differences were found in the aged LC (figure 3.14a-c) within superior (Dunn's test p=0.152), inferior (Dunn's test p=0.123), nasal (Dunn's test p=0.051) and temporal (Dunn's test p=0.138) and RoIns [superior (Dunn's test p=0.064), inferior (Dunn's test p=0.147), nasal (Dunn's test p=0.164) and temporal (Dunn's test p=0.061) (figure 3.14d-f)]. Within the ppsclera, the EFs spectral signature within the nasal (Dunn's test p=0.004) (figure 3.14h,i) and temporal (Dunn's test p=0.002) (figure 3.14h,i) regions were significantly greater than superior and inferior.
Normalisation to the maximum did not show differences in any region within the LC superior (Dunn's test p=0.389), inferior (Dunn's test p=0.535), nasal (Dunn's test p=0.589) and temporal (Dunn's test p=0.659) regions, RoIns superior (Dunn's test p=0.764), inferior (Dunn's test p=0.810), nasal (Dunn's test p=0.810) and temporal (Dunn's test p=0.833) regions and ppsclera superior (Dunn's test p=0.880), inferior (Dunn's test p=0.865), nasal (Dunn's test p=0.976) and temporal (Dunn's test p=0.880).

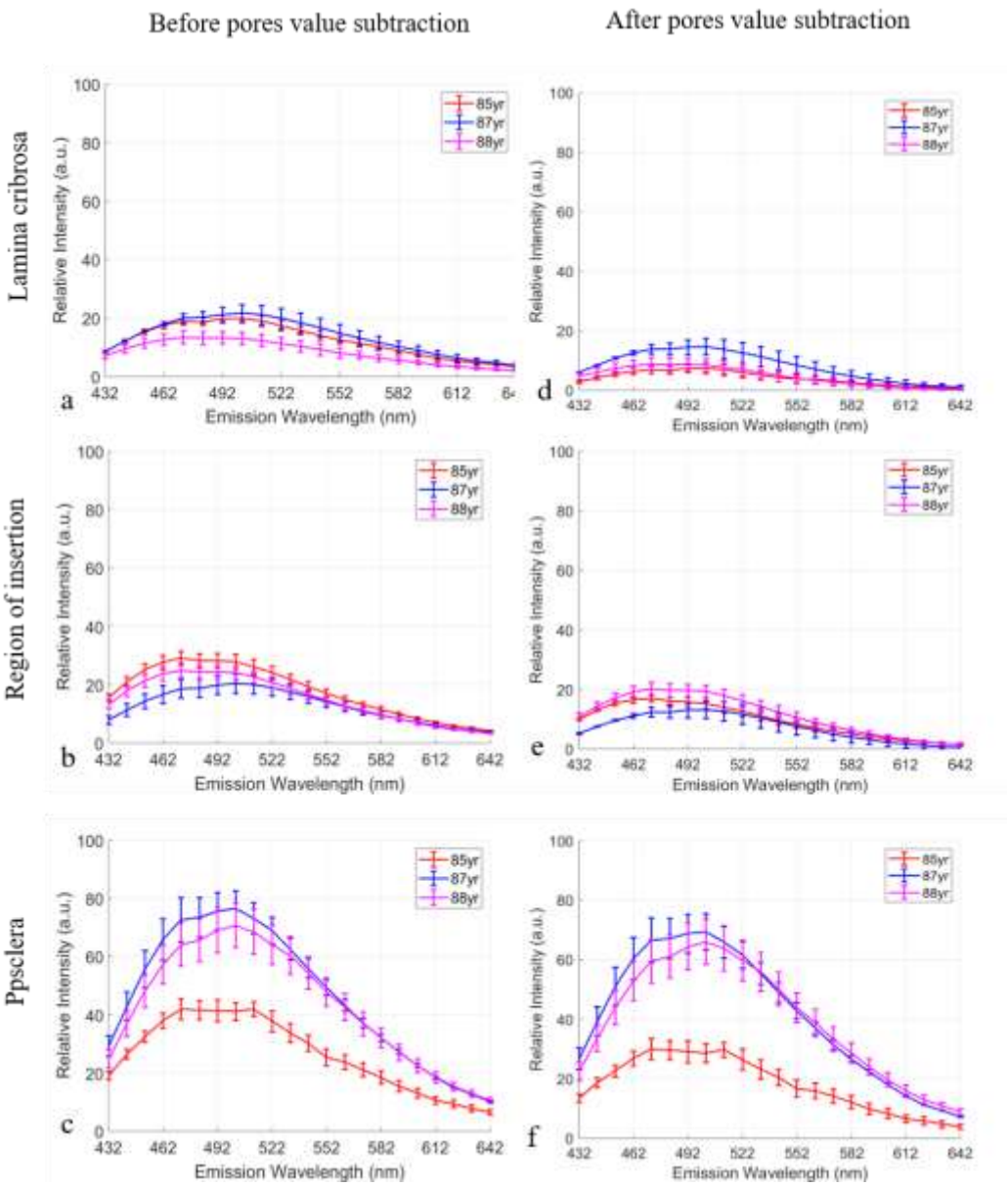

Figure 3.13. EFs spectral signature before and after intensity values of pores were subtracted. LC (b), RoIns (c) and ppsclera (d) before and LC (e), RoIns (f) and ppsclera (g) after values from pores were subtracted. EFs spectral signature did not change after pore subtraction.

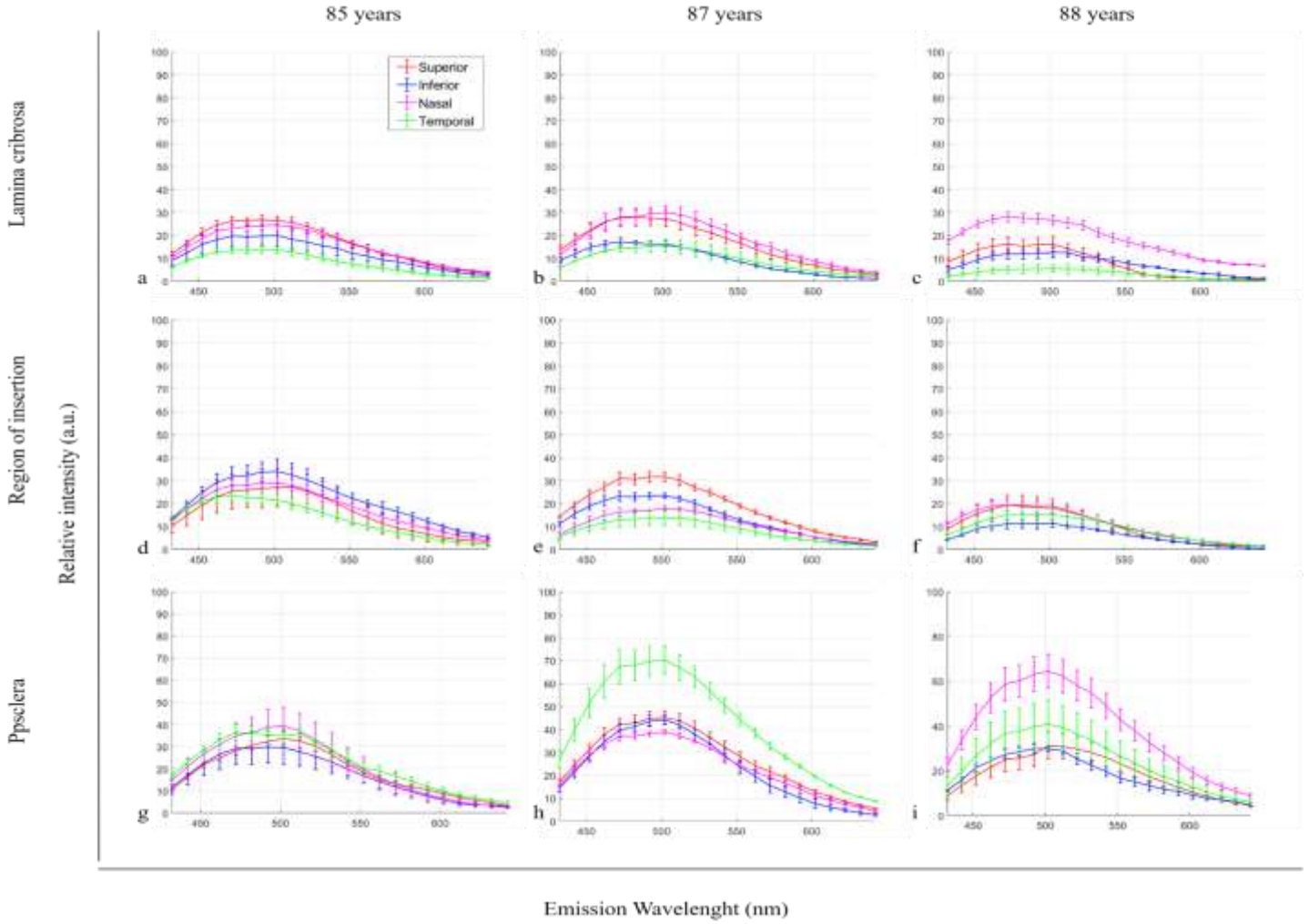

Figure 3.14. EFs spectral signature in the aged ONH regions. LC (a-c), RoIns (d-f) and ppsclera (g-i) showed similar spectral curves. Regional analysis and normalisation to the maximum did not show any differences between regions within the LC and RoIns. Within the ppsclera, the EFs spectral signature within the nasal (p=0.004) and temporal (p=0.002) regions were significantly greater than superior and inferior.

3.3.5 Elastic fibre spectral signature in the human ageing ONH

In the 2- and 6-years old ONH, visible EFs was not detected within the LC cribriform plates or RoIns, but were clearly demonstrated in those of elderly LC, RoIns and ppsclera. EFs spectral signature within each ONH region [i.e. LC (figure 3.15a), RoIns (figure 3.15b) and ppsclera (figure 3.15c)] showed similar emission range 432-552nm, to those previously identified in the CRA. Normalisation to the maximum showed no differences in the spectrum shape amongst ages within the LC (Dunn's test p=0.154), RoIns (Dunn's test p=0.251) and ppsclera (Dunn's test p=0.459).

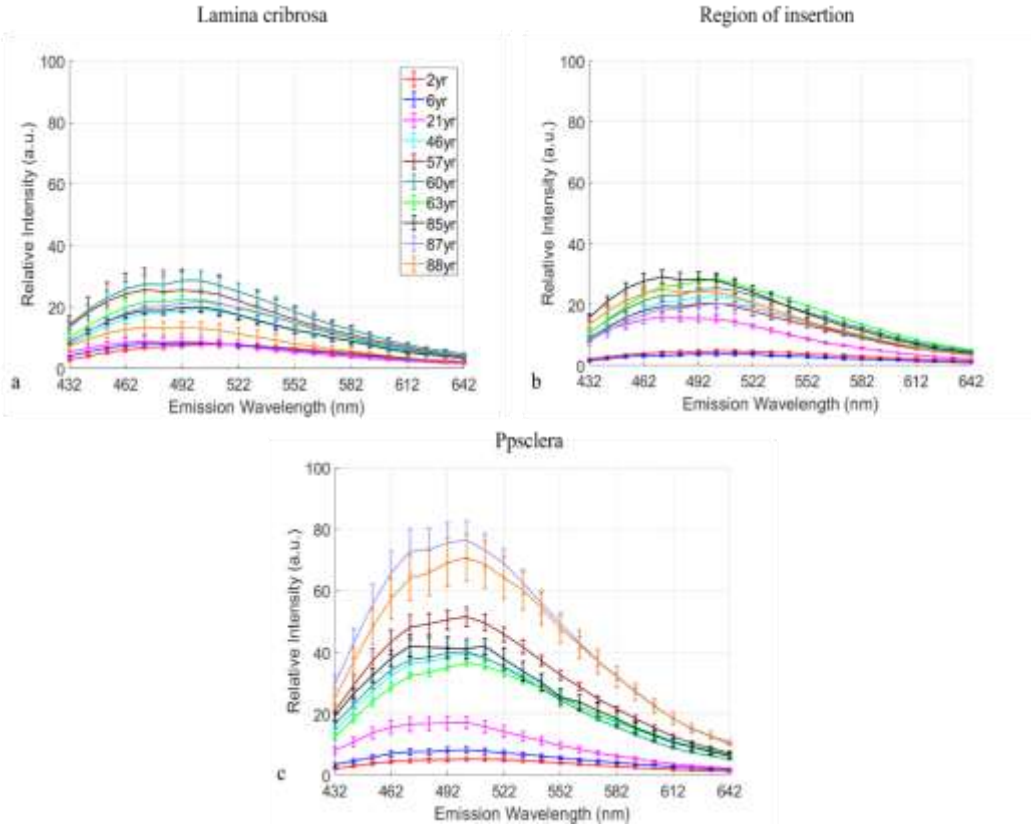

Figure 3.15. EFs spectral signature in the LC (a), RoIns (b) and ppsclera (c). At the ages of 2 and 6 years old, EFs relative intensity were lower when compared to elderly in the LC (a) and RoIns (b).

3.3.6 Spectral unmixing of the ONH elastic fibre spectral signature

Lambda stacks of young (figure 3.16a), middle age (figure 3.16b) and elderly ONHs (figure 3.16c) showed ROIs corresponding to EFs (figure 3.16a-c red polygon), matrix surrounding EFs (figure 3.16a-c, green polygon) and non-containing EFs areas (figure 3.16a-c, white ellipse). The linear unmixing separated the EFs derived TPEF signature (figure 3.16d-f) from component 2 (matrix) (figure 3.16g-i) and component 3 (non-containing EFs areas) (figure 3.16l-n).

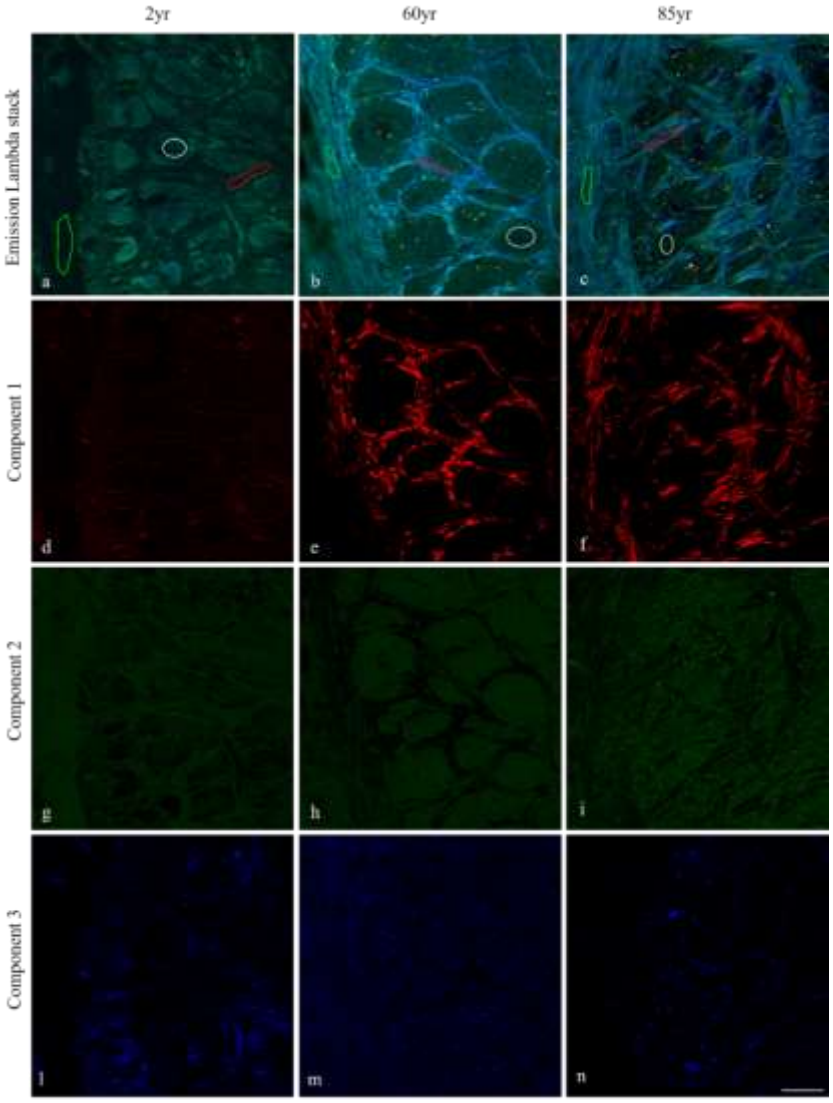

Figure 3.16. Linear unmixing from ageing ONH. Three regions of interests corresponding to EFs (red polygons in a-c), matrix surrounding EFs (green polygons in a-c) and non-containing EFs areas (white polygons in a-c) were drawn on the lambda stacks of young (a), middle age (b) and elderly human LC (c). Lambda stacks were then uploaded into Zen software and the linear unmixing algorithm applied. The latter separates the three components based on their spectral properties and output three pseudo-colour coded images of EFs (component 1, d-f), matrix (component 2, g-i) and non-containing EFs areas (component 3, l-n). Scale bars represent 50µm.

Unmixed TPEF images did not show visible EFs within the 2 years old ONH (figure 3.16a). Visible EFs within the cribriform plates and RoIns were seen in the 60 (figure 3.16d) and 85 years old (figure 3.16g). Unmixed images of component 2 showed the matrix surrounding EFs at all ages (figure 3.16b,e,h), where gaps appearing black corresponded to regions where the EFs were visible. Unmixed images of component 3 showed non-containing EFs regions at all ages (figure 3.16c,f,i).

3.3.6.1 Quantification of elastic fibre TPEF contribution to the ONH

EFs contribution in the human ONH significantly increased as a function of age in the LC from 0% at the age 2 years to 47.8% (pixel percentage) at the age of 88 years (rs=0.842, p=0.002) (figure 3.17a), RoIns from 0% to 39.0% (rs=0.952, p=0.000) (figure 3.17b) and ppsclera from 6.3% to 49.7% (r=0.988, p=0.000) (figure 3.17c).

3.3.6.2 Quantification of elastic fibre content in the unmixed TPEF

EFs content increased as a function of age in the LC from 0% at the age 2 years to 29.6% (pixel percentage) at the age of 88 years (rs =0.830, p=0.003) (figure 3.17d), RoIns from 0% to 44.2% (rs=0.721, p=0.019) (figure 3.17e) and ppsclera from 8.1% to 49.3% (rs = 0.903, p=0.000) (figure 3.17f).

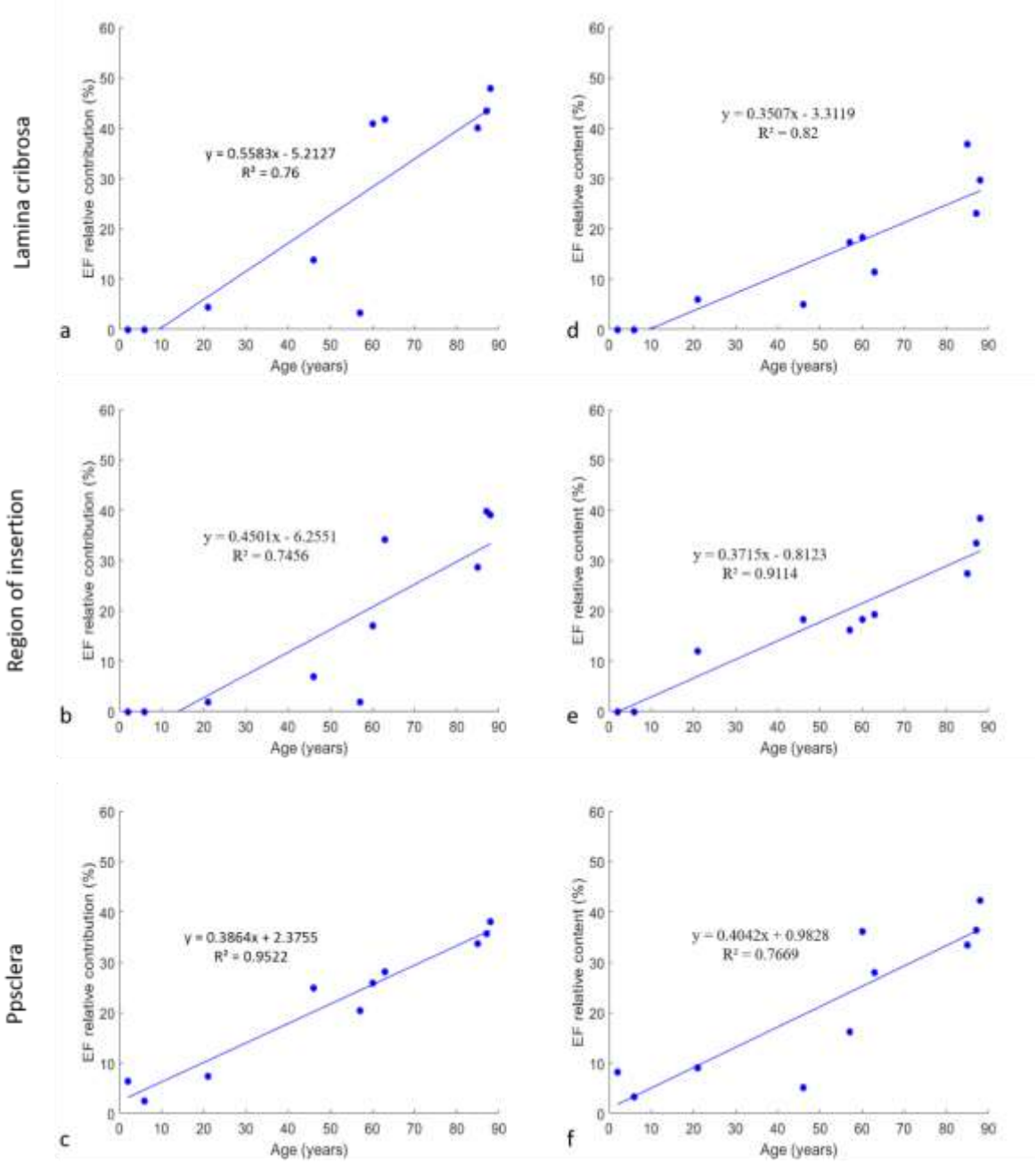

Figure 3.17. EFs content within he human ONH. EFs TPEF content significantly increased in the LC (p=0.003) (d), RoIns (p=0.019) (e) and ppsclera (p=0.000) (f). EFs contribution to the ONH significantly increased in the LC (p=0.002) (a), RoIns (p=0.000) (b) and ppsclera (p=0.000) (c).

3.3.7 Elastic fibre spectral signature in the glaucomatous ONH

Normalisation to the maximum did not show differences in the spectrum shape of glaucomatous ONH in any region of the LC [superior (Dunn's test p=0.687) (figure

3.18a), inferior (Dunn's test p=0.854) (figure 3.18b), nasal (Dunn's test p=0.702) (figure 3.18c) and temporal (Dunn's test p=0.693) (figure 3.18d)]; RoIns [superior (Dunn's test p=0.786) (figure 3.18e), inferior (Dunn's test p=0.884) (figure 3.18f), nasal (Dunn's test p=0.891) (figure 3.18g) and temporal (Dunn's test p=0.852) (figure 3.18h)] and ppsclera [superior (Dunn's test p=0.785) (figure 3.18i), inferior (Dunn's test p=0.701) (figure 3.18l), nasal (Dunn's test p=0.733) (figure 3.18m) and temporal (Dunn's test p=0.765) (figure 3.18n)].

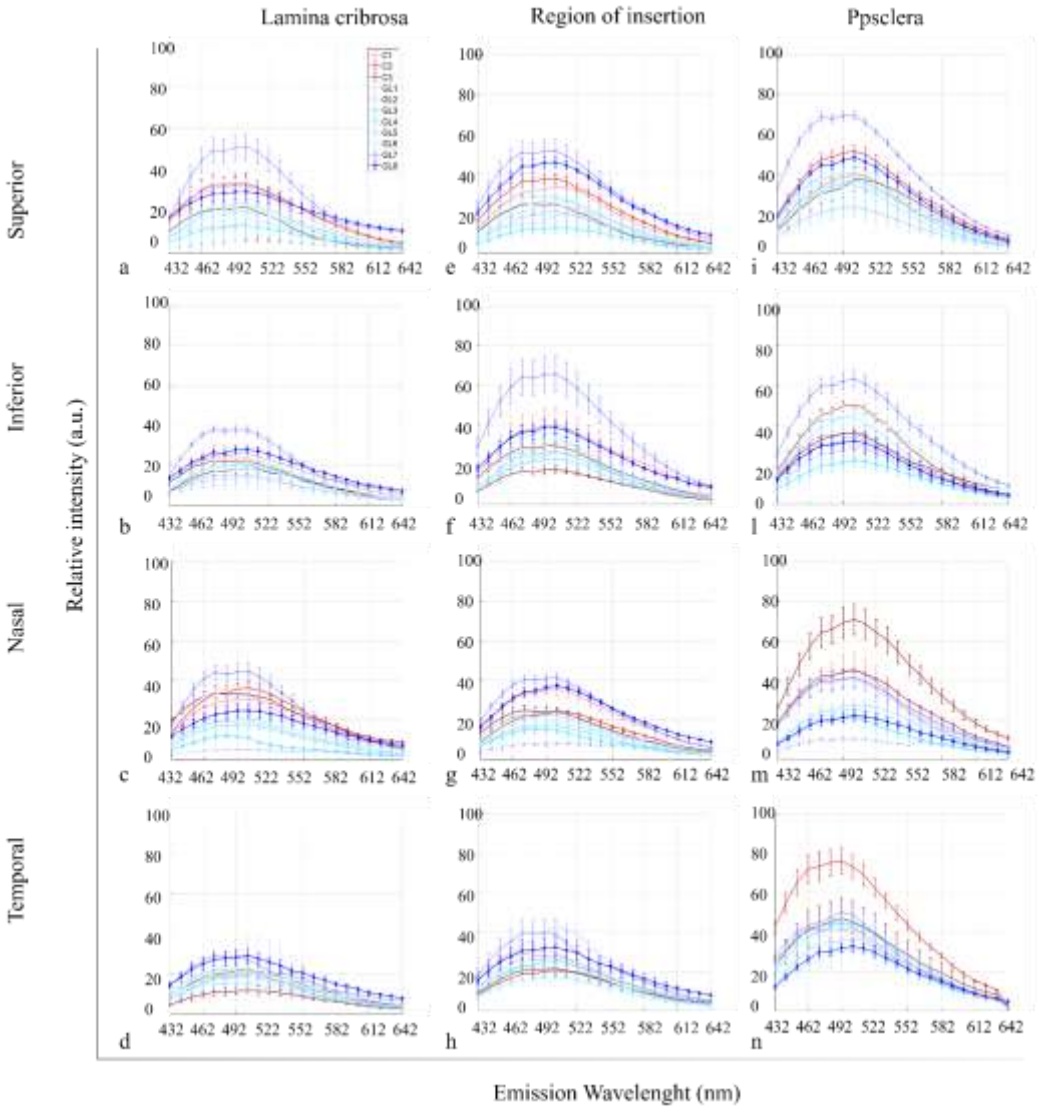

Figure 3.18. EFs spectral signature within glaucomatous LC (a-d), RoIns (e-h) and ppsclera (i-n). EFs spectra normalised to the maximum did not show any differences amongst regions in the LC [superior (a) (p=0.687), inferior (b) (p=0.854), nasal (c) (p=0.702) and temporal (d) (p=0.693)]; RoIns [superior (e (p=0.786), inferior (f) (p=0.884), nasal (g) (p=0.891) and temporal (h) (p=0.852)] and ppsclera [superior (i) (p=0.785), inferior (l) (p=0.701), nasal (m) (p=0.733) and temporal (n) (p=0.765)].

3.3.8 Spectral unmixing of the glaucomatous ONH elastic fibre signature

Representative unmixed images of early, moderate and advanced glaucomatous showed the separation of the EFs derived TPEF signature (figure 3.19a,d,g) from component 2 (figure 3.19b,e,h) and component 3 (figure 3.19c,f,i).

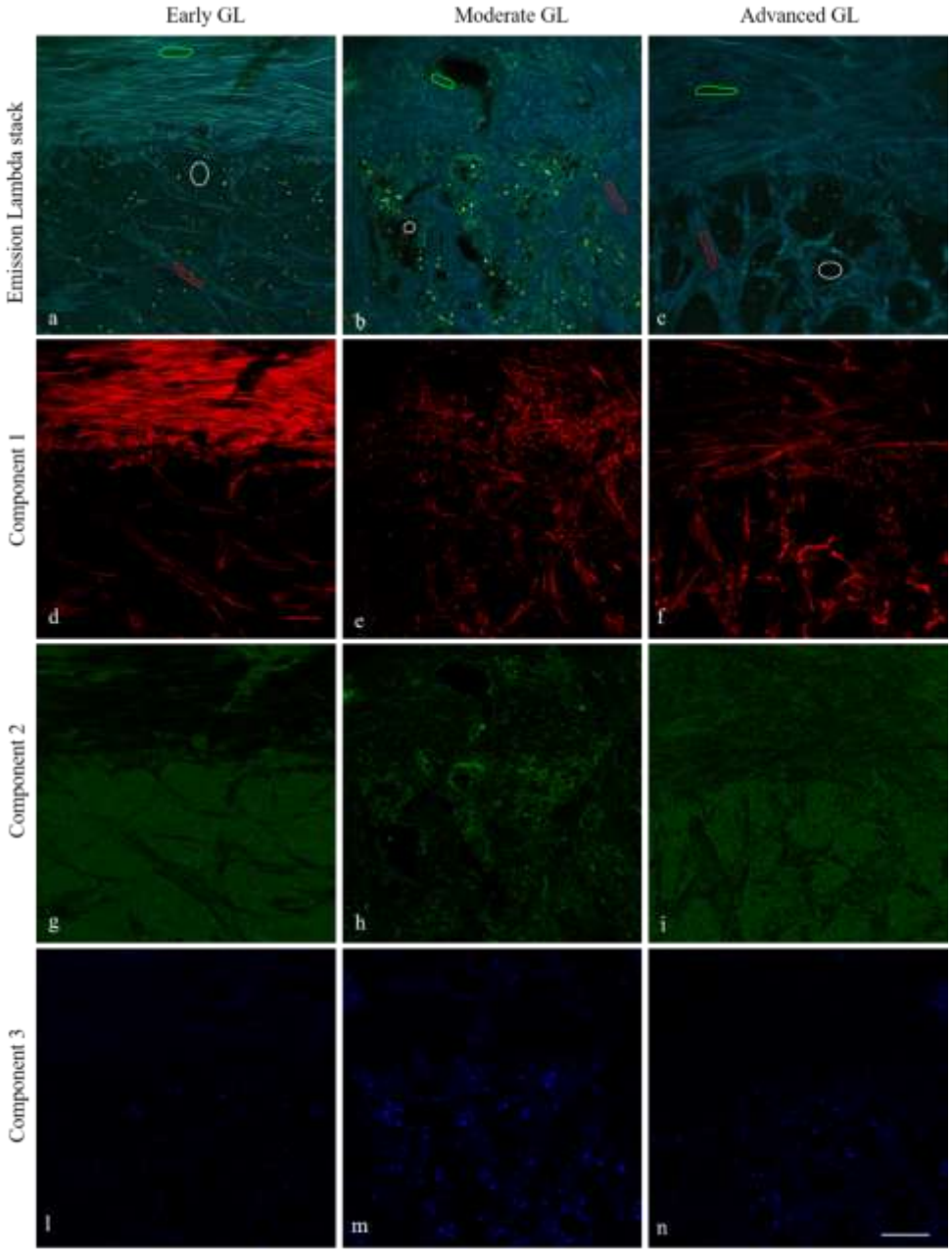

Figure 3.19. Linear unmixing from glaucomatous ONH. Three regions of interests corresponding to EFs (red polygons in a-c), matrix surrounding EFs (green polygons in a-c) and non-containing EFs areas (white polygons in a-c) were drawn on the lambda stacks of young (a), middle age (b) and elderly human LC (c). Lambda stacks were then uploaded into Zen software and the linear unmixing algorithm applied. The latter separates the three components based on their spectral properties and output three pseudo-colour coded images of EFs (component 1, d-f), matrix (component 2, g-i) and non-containing EFs areas (component 3, l-n). Scale bars represent 50µm.

Unmixed images of EF-associated TPEF showed EF within the LC plates and RoIns at all stages of glaucoma (figure 3.19a,d,g). In early glaucoma (figure 3.19a), EFs appeared mostly straight and relatively organised within LC plates and RoIns, similarly to those observed in controls (see figure 3.16g). In moderate glaucoma (figure 3.19d), EFs looked disorganised in the LC plates and RoIns. Similarly, in advanced glaucoma (figure 3.19g) EFs seemed more disconnected and disorganised to those observed in early glaucoma (figure 3.19a).

Unmixed images of component 2 showed the matrix surrounding EFs (figure 3.19b,e,h), where gaps appearing black corresponded to regions where the EFs were visible. Unmixed images of component 3 showed non-containing EFs regions, which could correspond to lipofuscin granules and fluorescent material (figure 3.19c,f,i)

3.3.8.1 Quantification of elastic fibre contribution in the human glaucomatous ONH

EFs contribution in the human glaucomatous ONH was significantly greater in the LC in advanced glaucoma ($p=0.001$) (figure 3.20a) but lower in early ($p=0.021$) and moderate ($p=0.041$) compared to controls. No differences were found in the ppsclera ($p=0.052$) (figure 3.20c) and in the RoIns ($p=0.149$) (figure 3.20b). Regional analysis showed the nasal ($p=0.010$) and temporal ($p=0.010$) EFs contribution was greater in advanced glaucomatous LC (figure 3.20d) compared to controls. No regional differences were found in the RoIns [superior ($p=0.829$), inferior ($p=0.964$), nasal ($p=0.087$) and temporal ($p=0.248$)] (figure 3.20e) and ppsclera [superior ($p=0.436$), inferior ($p=0.740$), nasal ($p=0.055$) and temporal ($p=0.853$)] (figure 3.20f).

Regional analysis within groups showed a significantly higher EFs contribution in the superior/inferior ($p=0.007$) and temporal ($p=0.022$) region compared to nasal (figure 3.20d) of early glaucoma. No differences were found within controls [plates ($p=0.586$), RoIns ($p=0.536$), ppsclera ($p=0.850$)], moderate [plates ($p=0.981$), RoIns ($p=0.332$), ppsclera ($p=0.922$)] and advanced glaucoma [plates ($p=0.143$), RoIns ($p=0.574$), ppsclera ($p=0.242$)]. In the RoIns, within controls, EF contribution was significantly greater in the nasal region compared to temporal ($p=0.021$) and superior/inferior regions. Additionally, the EF contribution in the inferior region of early glaucomatous was significantly greater than in the nasal ($p=0.010$) (figure 3.20e). In the ppsclera, EF contribution was

significantly greater in the inferior region of moderate glaucoma (p=0.031) compared to nasal and in the nasal region of advanced glaucoma compared to inferior and temporal (p=0.021) (figure 3.20f).

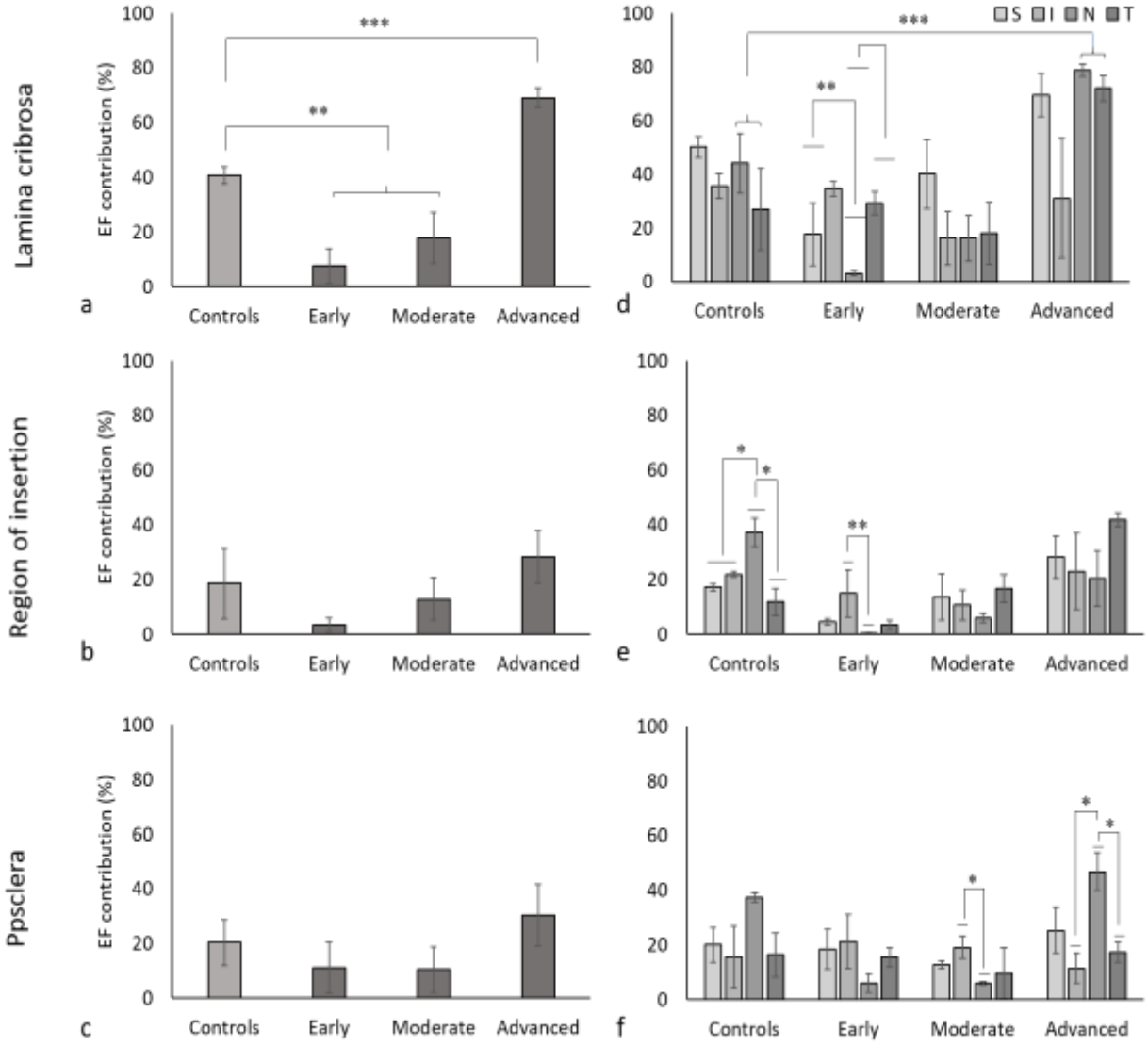

Figure 3.20. EF TPEF (mean +/-sd) contribution of the human glaucomatous ONH. EFs contribution was significantly greater in the LC in advanced glaucoma (p=0.001) (a) but lower in early (p=0.021) and moderate (p=0.041) compared to controls. No differences were found in the ppsclera (p=0.052) (c) and in the RoIns (p=0.149) (b). Regional analysis showed the nasal (p=0.010) and temporal (p=0.010) EFs contribution was greater in advanced glaucomatous LC (d) compared to controls. Regional analysis within groups showed a significantly higher EFs contribution in the superior/inferior (p=0.007) and temporal (p=0.022) region compared to nasal (d) of early glaucoma. In the RoIns, within controls, EF contribution was significantly greater in the nasal region compared to temporal (p=0.021) and superior/inferior regions. Additionally, the EF contribution in the inferior region of early glaucomatous was significantly greater than in the nasal (p=0.010) (e). In the ppsclera, EF contribution was significantly greater in the inferior region of moderate glaucoma (p=0.031) compared to nasal and in the nasal region of advanced glaucoma compared to inferior and temporal (p=0.021) (f).

3.3.8.2 Quantification of elastic fibre content in the human glaucomatous ONH

EFs TPEF content in advanced glaucomatous LC (p=0.001) (figure 3.21a) was significantly greater than the controls. In the RoIns (figure 3.21b), EF content was greater in moderate (p=0.043) compared to controls. No differences were observed in the RoIns (p=0.053) (figure 3.21b) and ppsclera (p=0.130) (figure 3.21c).

Regional analysis showed all LC regions in advanced glaucoma had greater EFs content (p=0.011) than controls (figure 3.21d). No differences in the RoIns [superior (p=0.820), inferior (p=0.964), nasal (p=0.087) and temporal (p=0.248)] (figure 3.21e) and ppsclera [superior (p=0.436), inferior (p=0.640), nasal (p=0.053) and temporal (p=0.857)] (figure 3.21f).

Regional analysis within groups showed a greater EFs content in the LC in the superior (p=0.001) and temporal (p=0.029) regions compared to inferior in early glaucoma (figure 3.21e). EF content was also greater in the inferior region (p=0.042) in moderate glaucoma compared to the superior (figure 3.21d). Additionally, in the RoIns the EFs content was greater in the inferior region (p=0.016) compared to temporal in early glaucoma and in the inferior region compared to nasal (p=0.023) in advanced glaucoma (figure 3.21e). In the ppsclera, EF content in the superior region of early glaucoma was significantly greater (p=0.003) then inferior (figure 3.21f).

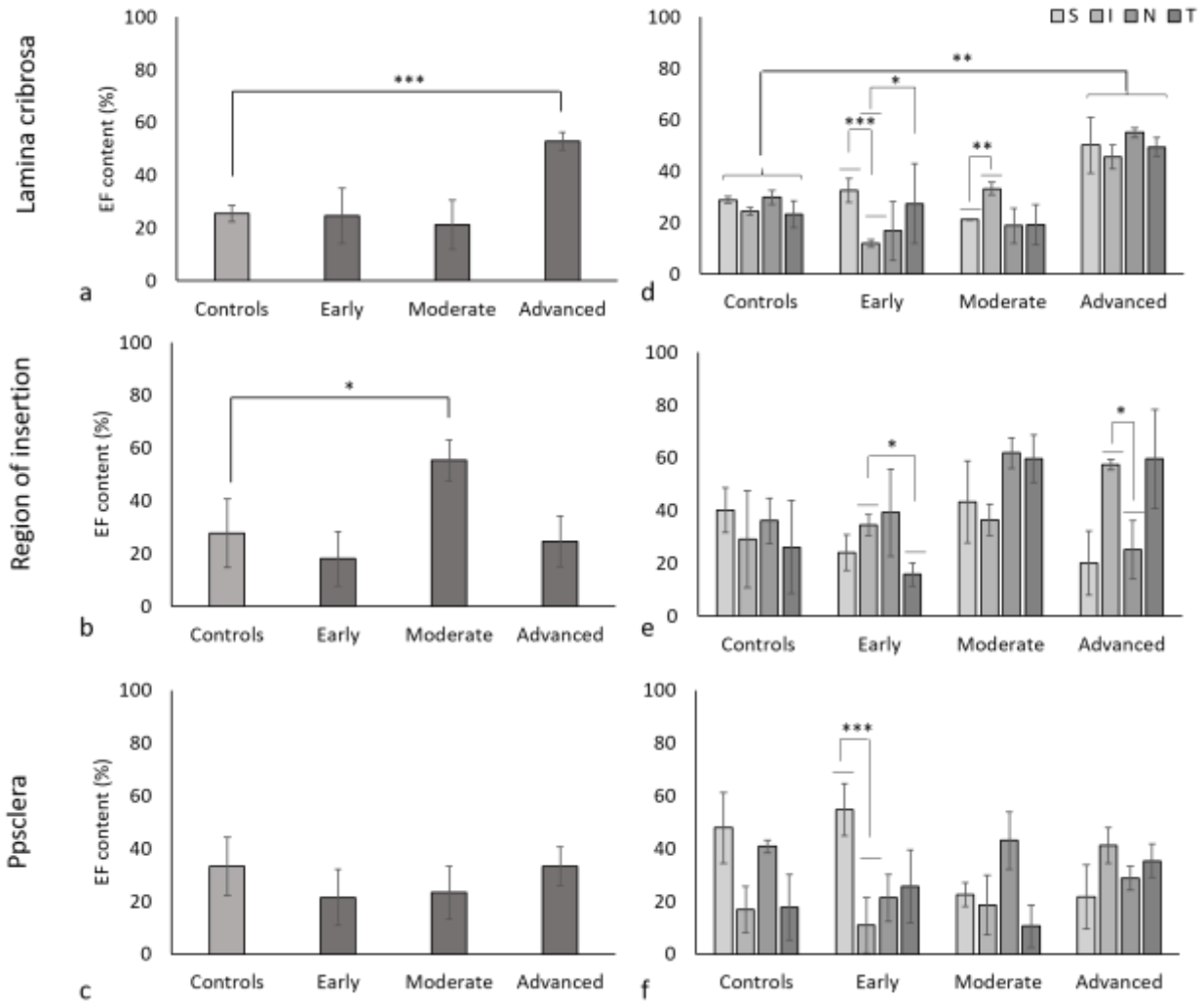

Figure 3.21. EF content (mean +/-sd) within human glaucomatous ONH. EFs content was greater in advanced glaucomatous LC (a) (p=0.001) and moderate RoIns (b) (p=0.043) compared to controls. No differences were observed in the ppsclera (p=0.130) (c). All LC regions in advanced glaucoma showed greater EFs content (p=0.011) than controls (d). Regional analysis within groups showed a greater EFs content in the LC in the superior (p=0.001) and temporal (p=0.029) regions compared to inferior in early glaucoma (e). EF content was also greater in the inferior region (p=0.042) in moderate glaucoma compared to the superior (d). Additionally, in the RoIns the EFs content was greater in the inferior region (p=0.016) compared to temporal in early glaucoma and in the inferior region compared to nasal (p=0.023) in advanced glaucoma (e). In the ppsclera, EF content in the superior region of early glaucoma was significantly greater (p=0.003) then inferior (f).

3.4 Discussion

In the current study, a TPEF spectral imaging protocol was developed and optimised to characterise the EFs associated TPEF within the ONH. The TPEF spectral parameters for RTA and human CRA of the optic nerve were optimised at 760 nm and 800 nm excitation, respectively, with optimal emission in the range 432-552 nm. TPEF signal was not emitted from RTT using these parameters, confirming that the EFs spectral signature did not contain any contribution from collagen.

The EFs TPEF signature in the aged ONH generated similar shaped curves to those observed in the CRA, RTA and controls such as nuchal ligament and porcine ear. This result provided supporting evidence that the spectral signature derived from the ONH was from EFs.

There has been an attempt previously to segment and quantify EFs (Jones, 2014), however, due to endogenous fluorescence contributing factors other than EFs, the latter could not be easily segmented and quantified. One of these factors are small, irregular, yellowish particles, similar in size and shape to those of purified retinal pigmented epithelium (RPE) lipofuscin. Lipofuscin has been found in healthy aged ONH (Dolman et al., 1980) and glaucomatous eyes (de Castro JP et al., 2013) and it has been found significantly increased within LC cells of glaucomatous ONHs (McElnea et al., 2014).

Fernandez de Castro et al. (2013) investigated and quantified lipofuscin in the ageing ON and found lipofuscin accumulation in the ON as a function of age. Lipofuscin is considered the best marker of age (Porta, 2002) and neuronal lipofuscin is thought to result from incomplete mitochondrial digestion (Sulzer et al., 2008). The lipofuscin spectrum presented in this chapter showed maxima in the range between 550-620 nm. Due to the orange-red spectrum of the lipofuscin spectrum compared to the blue-green (432-552 nm) of EFs, lipofuscin granules were easily separated spectrally from EFs TPEF.

3.4.1 Elastic fibre spectral signature in the ageing ONH

The EFs TPEF spectral signature showed, as a function of age, similar spectral characteristics of the three aged ONHs and the controls. In the LC, RoIns and ppsclera EFs TPEF spectral signature showed a broad emission spectrum of 432-562 nm with a maximum at ~502 nm. The normalisation of the EF's spectra to the maximum did not

show differences in spectrum shape, which imply the reliability of the EF's signature determined within the human ONH.

When the EFs signature was explored as a function of age, the 2 and 6 years old ONHs had a low EFs intensities, consistent with the lack of visible EFs within ONH tissues previously proposed (Albon et al., 2000a, Hernandez et al., 1989). Electron microscopy (Quigley et al., 1991a, Hernandez, 1992, Oyama et al., 2006) and immunolabelling of human elastin (Hernandez, 1992, Morrison et al., 1989a, Albon et al., 2000a) showed no labelling in foetal and young LC (Hernandez, 1992, Morrison et al., 1989a). This result implies lack of EFs within younger ONHs and that the low relative intensities in the 2 and 6 years old could be derived from other substances such as the microfibrils observed in the young LC (Hernandez, 1992).

TPEF has been used previously as a label-free technique to investigate into age-related changes of endogenous fluorophores. Watson et al., (2013) have assessed age-related changes of mouse ovarian tissue by imaging nicotinamide adenine dinucleotide (NADH), flavin adenine dinucleotide (FAD) and lipofuscin autofluorescence (Watson et al., 2013). The authors found an ageing increase in TPEF fluorescence, suggesting that TPEF is a reliable technique to investigate into age-related changes by imaging endogenous fluorescence.

Many intrinsic fluorophores within tissues are derived from the aromatic amino acids, such as Tryptophan (Trp), Tyrosine (Tyr) and Phenylamine (Phe), which emission ranges between 400-600 nm (Deyl et al., 1980). Examples of these are NAD(P)H (Zipfel et al., 2003a), flavoproteins, flavins (Benson et al., 1979, Aubin, 1979), and retinol (Zipfel et al., 2003a). Much of the intrinsic fluorescence observable with TPEF is in the range of 440-550 nm, therefore it is often difficult to discriminate between different sources.
However, the combination of TPEF and linear unmixing allowed to separate the EFs TPEF from other fluorophores and therefore assess the contribution of only EFs to the TPEF signal. Thus, the EFs contribution to the TPEF could be used as a label-free indicator of age in the human ONH. TPEF has therefore the potential to translate *ex vivo* assessment into *in vivo* investigation of the age-related changes of the EFs.

3.4.2 Elastic fibre spectral signature in the glaucomatous ONH

The EFs TPEF spectral signature was also explored within glaucomatous ONH. After normalisation to the maximum, EFs signature did not show differences in spectrum shape in glaucoma when compared to controls.

Changes in EFs have been previously reported in glaucoma (Hernandez et al., 1990, Hernandez, 1992, Quigley et al., 1991a). Quigley (1994) showed a curled appearance of the EFs, which was more pronounced with the progression of the disease (Quigley et al., 1994). Ultrastructural observation by immuno-electron microscopy showed different labelling of elastin as a function of glaucoma progression (Hernandez, 1992). In mild glaucoma EFs were no longer organised into tubules; they appeared fragmented with aggregates of microfibrils. The remaining intact EFs contained little α–elastin immunopositivity. In moderate glaucoma, these alterations appeared more pronounced and the normal EF was no longer visible. In advanced glaucoma, an abnormal elastin staining was observed within the cribriform plates and aggregates of nonfibrillar EFs-staining material were abundant throughout the plates (Hernandez, 1992). Disorganisation of the EFs was also observed in glaucoma, in which they appeared disconnected from the surrounding matrix (Hernandez et al., 1990, Hernandez, 1992). Previous studies also suggested that in glaucoma the ECM is remodelled by the reactive astrocytes. The latter synthesise ECM proteins such as tenascin and laminin that are not expressed in adult life. The synthesis of new ECM molecules and the degradation of ECM by metalloproteinases (MMPs) (Agapova et al., 2003, Yan et al., 2000) can remodel the microenvironment of the ONH, leading axons to be more susceptible damaged.

In human skin, the ageing process of the EFs has a profound effect on the function of the EFs system. Human skin accumulates damage due to both the normal ageing process and environmental factors, such as exposure to ultraviolet light (El-Domyati et al., 2002). The acute exposure to ultraviolet radiations might alter the smooth appearance of EF becoming gradually fragmented (Braverman and Fonferko, 1982, Suwabe et al., 1999, Tsuji and Hamada, 1981), which in turn might change the ability of EFs to recoil (Escoffier et al., 1989, Smalls et al., 2006, Takema et al., 1994).

In human skin elastosis is a hallmark of age and it is characterised by de novo synthesis of elastotic material, which includes deposition of new EFs, fibrillin (Chen et al., 1986)

and basophilic fibres (Mitchell, 1967, Muto et al., 2007). Multiphoton microscopy has been used previously to investigate changes in EFs in human skin (Koehler et al., 2006, Lentsch et al., 2019, Shirshin et al., 2017) and skin elastosis (Koehler et al., 2012), suggesting that the elastotic materials deposited during ageing skin retrieve fluorescence which could be investigate with TPEF.

EFs appear to be elastotic in glaucoma (Hernandez, 1992, Hernandez et al., 1990, Netland et al., 1995, Pena et al., 1998) which is defined as the aberrant proliferation and degeneration of EFs and has been described in ageing skin (Braverman, 1989, Werth et al., 1996) and blood vessels (Jakobiec et al., 2015).
Overall, alteration in the microstructure and content of EFs in tissues can lead to the mechanical and functional changing associated with diseases such as atherosclerosis and aneurism, with a reduced strength and elasticity of affected arteries.

3.4.3 Elastic fibre content in the ageing ONH

To aid in understanding the EF changes as a function of age and glaucoma, EF content following linear unmixing was investigated. The content of EFs increased significantly with age. This result is thus consistent with the increased EFs in ageing ONH previously described (Albon et al., 2000a, Hernandez et al., 1989) and the increase in EFs as a measure of the cross-links desmosine and isodesmosine (Albon et al., 2000a). A number of previous studies quantified elastin and EFs within the ONH using immune-labelling which is associated with the appearance and distribution of EFs in elderly (Hernandez et al., 1989, Hernandez, 1992, Morrison et al., 1989b, Morrison et al., 1989a) and glaucomatous ONH (Hernandez, 1992, Hernandez et al., 1990, Quigley et al., 1991b).

The novel approach presented in this study is a quantitative and valuable tool to detect and characterise EFs without stain and histological process the specimens. Therefore, it presents potentials for future investigation of the EFs spectral features that could be detected *in vivo* as a measure of glaucoma progression.

EFs content has been also investigated in other ageing tissue. Within arteries, EFs are concentrated in the internal and external elastic laminae (Kielty et al., 2007). The compliance and elasticity of main arteries play an important role in cardiac function,

hence age-related reduction of compliance (i.e. arteriosclerosis) leads to increased blood pressure, major risk factor for heart failure (Mitchell, 2008, O'Rourke and Hashimoto, 2007). It has also been reported that remodelling of human aorta, associated with age, is caused by EFs fragmentation (Toda et al., 1980), possibly a consequence of the force applied on the artery wall over life-time period (Greenwald, 2007, Hunter et al., 1996, Sans and Moragas, 1993). The stiffness of central arteries determined by in vitro mechanical testing (Bruel and Oxlund, 1996, Learoyd and Taylor, 1966) increases with age. Generally, EFs-rich tissues, such as skin, blood vessels, and lungs, lose their compliance in elderly individuals.

The increased in EFs observed in the ageing ONH, as previously reported (Albon et al., 2000a), could lead to similar effects observed within other tissues, such as decreased compliance, elasticity and increased stiffness. In fact, a decreased in LC compliance as a function of age has been demonstrated before (Albon et al., 2000b). The accumulation of EFs over age, with no evidence of degradation within the cribriform plates (Hernandez, 1992), leads to a stiffer LC, which in turns alter the its ability to support axons from IOP fluctuation. This in turn might predispose the elderly eye to glaucomatous optic neuropathy.

3.4.4 Elastic fibre content in the glaucomatous ONH

EFs ONH content significantly increased in advanced glaucoma in the LC compared to controls. Within the LC, EFs content was significantly greater in advanced glaucoma compared to controls. However, no differences were observed in the ppsclera and RoIns. Regional analysis in the LC, showed a significantly greater EFs content in all regions of advanced glaucoma compared to controls as well as greater EFs content in the superior and temporal regions compared to inferior within early glaucoma. Similarly, within the RoIns, greater EFs content was observed in the superior regions of early glaucoma compared to the nasal.

In glaucoma there appear to be an increased area of EFs-labelled material (Pena et al., 1998) suggesting that the presence of the elastotic fibre might consist of new synthesised EFs, as also demonstrated by the increased elastin (Hernandez et al., 1994) and TE mRNA expression (Pena et al., 1996). The increase in EFs-labelled material that occur in

glaucoma could explain the augmented EFs relative intensity observed in advanced glaucoma. The EFs-labelled materials observed might exhibit endogenous fluorescence and therefore determine an increase in relative intensities of the TPEF EFs.

The LC has been proposed to be the main site of axons damage (Howell et al., 2007, Quigley and Addicks, 1981, Quigley et al., 1981, Vrabec, 1976) and it is well known that the inferior and superior regions of the LC have larger pores and less connective tissue supporting axons when compared to the nasal and temporal region (Quigley and Addicks, 1981, Radius and Gonzales, 1981, Oyama et al., 2006). The superior and inferior poles (Quigley and Addicks, 1981), which are associated with areas conducting fibres of the arcuate bundles (Hoyt, 1962, Quigley and Addicks, 1981), are the first to be damaged in glaucoma (Quigley et al., 1981). The increased EFs content found in the superior region of the LC and RoIns does not agree with previous studies suggesting that these regions contain less connective tissue (Quigley and Addicks, 1981, Radius and Gonzales, 1981, Oyama et al., 2006). However, the increased level of TE mRNA found in glaucomatous ONH (Hernandez et al., 1994) could explain this result, which also appear more pronounced in advanced glaucoma in both the LC and the reigon of insertion. Since the superior and inferior regions are the first to be damaged as a function of glaucoma progression, the EFs might be subjected to damage in these regions first and consequently all the changes in EFs oberved in glaucoma along with the increased TE mRNA expression could have led to an increased in EFs content.

The increased in EFs content in the LC, is also consistent with molecular biology studies which found an activation of EFs (Hernandez et al., 1994) and TE (Pena et al., 1996) mRNA within the human ONH as a function of glaucoma progression. The observed increase in EFs content only in advanced glaucoma within the LC, might imply that the EFs are subjected to damage in the LC only at late stage of disease, which suggest that EFs could only be damaged after chronic exposure to elevated IOP. No changes were observed in the early and moderate stage of glaucoma, indicating that EFs is not significantly damaged at this stage or the newly synthesised EFs could replace the damaged ones, which in turn maintain some sort of ONH microenvironment. At later stage of the disease, the action of the MMP to degrade the ECM and the continues effects of the IOP onto the LC, could determine a significant damage to the EFs which are no longer capable of provide elasticity to the LC.

Hernandez (1992) suggested that as the disease progresses, the alterations in EFs are more pronounced. Newly synthesised EFs might begin at the early stage of the disease along with the proliferation of basement membranes. These mechanisms are similar to those observed in the atherosclerotic arteries where proliferating smooth muscle cells in the tunica intima synthesise basement membranes and EFs materials (Hedin et al., 1999).

An elderly eye, which already experienced IOP fluctuation over time, with an accumulation of EFs, might be more susceptible to develop the disease. Therefore all these changes in EFs likely influence the changes in compliance and resilience observed in the glaucomatous LC (Burgoyne et al., 1995, Zeimer and Ogura, 1989).
It can be concluded that the quantification of TPEF content could be a valuable tool to quantify *ex vivo* EFs associated fluorescence without the contribution of other sources of fluorescence within the tissue. The first experiments on *in vivo* TPEF imaging of human skin were performed in the late 1990s (Masters et al., 1997, Masters et al., 1998a, Masters et al., 1998b) and since then TPEF has been employed to translate the *ex vivo* investigation into clinical diagnosis, such as detection of melanoma (Dimitrow et al., 2009) and basal cell carcinoma (Balu et al., 2015). These studies suggest the potential of TPEF as non-invasive approach for *in vivo* diagnosis. The approach presented in this chapter enhances the ability of TPEF as a label-free technique to investigate into EFs changes by imaging its endogenous fluorescence.

3.5 Conclusion

This chapter introduced a novel approach that indirectly detects structural/compositional changes in EFs and has potential as an indicator of ageing and advanced glaucomatous optic neuropathy. The goal of this chapter was to identify a new method to potentially translate the *ex vivo* investigation into a non-invasive *in vivo* detection of EFs damage. The new approach described in this chapter offers novel means to qualitatively and quantitatively investigate EFs changes by studying its spectral signature. Several techniques have been used to detect changes in EFs in age (Hernandez et al., 1989, Hernandez, 1992, Morrison et al., 1989b, Morrison et al., 1989a) and glaucomatous ONH (Hernandez, 1992, Hernandez et al., 1990, Quigley et al., 1991b), however, findings presented in this chapter take the EFs studies a little further by proposing TPEF as a

reliable tool to reveal changes in EFs based on its spectral properties and without destroying specimens with antibody staining procedures.

3.6 Limitation

This study showed limitations. The preparation of ONH sections and the acquisition of lambda stack at different times and on different days introduced possible variation in sample preparation and instrument characteristics. A wide-open confocal spectrometer pinhole and the 10nm slit width allowed the maximum signal acquisition but also could smooth the acquired spectrum making peaks less distinct. The use of a narrower slit width (e.g. 5nm or 3nm) in future studies may make peaks sharper and more distinct. This chapter showed that fixation significantly increases the relative fluorescence within the tissue, therefore AUC calculation and comparison was not possible within ageing and glaucomatous ONHs. Future work will require unfixed sample to reduce to minimum the unspecific fluorescence.

3.7 Future work

Further experimental work is needed to better understand which residue(s) of EFs gives rise to the TPEF associated fluorescence. Further investigations are also needed to determine the origin of the alteration of EFs fluorescence in glaucoma and at different stage of disease. More glaucomatous specimens, especially at late stage of disease are required to complete the investigation and increase the statistical confidence. To better understand the changes in EFs in glaucoma based on the spectral signature, investigations are needed as a function of ONH depth, which requires spectral imaging to be performed on different sections of the same ONH. Additional work would be required to investigate the EFs TPEF signature within unfixed specimens, to enable the measures of relative intensities only associated with EFs and remove all fixation derived autofluorescence.

Chapter 4 – Investigation into the potential of X ray microtomography to investigate the optic nerve head 3D microarchitecture

4.1 Introduction

X-ray microtomography (XMT) is a non-destructive imaging technique used to study a broad variety of samples. The first system was created and built by Jim Elliott in the early 1980s to study small, biological hard tissues (Elliott and Dover, 1982). XMT uses x-rays to create multiple 2D images of a small object which are then reconstructed into a 3D image without destroying the sample. The internal structure of the sample is investigated by acquiring many projections images, known as radiographs, while rotating the sample through 180 degrees with a motorised stage. These projections can be reconstructed into a 3D volume to study the internal and external structure of the object (Vlassenbroeck et al., 2007).

The use of histological sections for 2D analysis, is frequently subjected to inaccuracies such as tissue distortion. In the current chapter, the potential of XMT was assessed as a non-invasive, section-free alternative tool to investigate the 3D microstructure of the ONH. However, it is important to note that XMT does not detect fibrillar collagen and does not provide the high level of resolution associated with SHG, therefore XMT should be treated as a complementary technique to further analyse the 3D ONH connective tissue microstructure and is not a replacement of SHG imaging.

Since the connective tissue structure of the ONH is made up by collagen and EFs (Albon et al., 1995, Albon et al., 2000a, Hernandez et al., 1986, Hernandez et al., 1987, Morrison et al., 1989a, Morrison et al., 1988, Morrison et al., 1989b), to analyse the 3D microarchitecture, contrast agents that enhance collagen and EF signals are needed. Contrast agents, previously used to enhance soft tissue contrast in XMT studies include phosphotungstic acid (PTA) for collagen (Descamps et al., 2014, Disney et al., 2017, Metscher, 2009a), tannic acid for EFs (Murakami, 1973, Roholl et al., 1981), Lugol's iodine for collagen (Disney et al., 2017, Gignac and Kley, 2014, Metscher, 2009b) and brain-wide reduced osmium pyragallol-mediated amplification (BROPA) staining for axons (Mikula and Denk, 2015).

The hypothesis of this study was that XMT can be used as a section-free, non-destructive imaging technique to investigate the i) overall 3D connective tissue microstructure of the ONH and ii) axons within the LC pores. In order to achieve this, the aims of this chapter were to:

1. Develop staining protocols to differentiate between the connective tissue components and the neuronal pores to analyse the 3D connective tissue microstructure of the ONH
2. Develop staining protocols to visualise axons within the LC pores

4.2 Materials and methods

4.2.1 Source of tissue

Eighteen fresh porcine globes were received from the local abattoir (W.T. Maddock, Wales, UK) within 12 hours of sacrifice. All globes were cleaned immediately with PBS to remove residues of blood, and extraorbital muscles and fat, retina, choroid and vitreous humour were gently excised from the ONH. ONHs were dissected from the globes and immersed in a solution of 4% PFA and stored at +4°C. Additionally, three right eye globes from human donors with no history of eye disease (aged 72, 81 and 85 years) were received from the NHS Blood and Transplant Eye bank (Filton, Bristol, UK) in moist tissue chamber. Two right eye and one left eye globes from donors with glaucomatous optic neuropathy (diagnosed prior to death by glaucoma ophthalmologists, aged 77, 84 years and unknown) were received from the Mayo Clinic (Rochester, USA). Human ONHs were dissected from all globes as described in 2.2.1.

4.2.2 Sample preparation

Porcine ONHs (n=15) were removed from 4% PFA, washed in three changes of PBS for 24 hours and immersed in various contrast agents, including tannic acid (TA) (n=3), phoshotungstic acid (PTA) (n=3), BROPA (n=3), and Lugol's iodine (n=3). The protocols used are described below for each contrast agent. Additionally, porcine ONHs (n=3) in 4% PFA and the human globes (n=6) were stored in 4% PFA.

4.2.3 Nonlinear microscopy of porcine ONHs

High resolution SHG and TPEF image stacks of porcine LC and ppsclera were acquired as described in 2.2.3 to confirm the connective tissue composition of the porcine ONH.

4.2.4 The use of contrast agents to enhance signals within the ONHs

4.2.4.1 PTA

PTA is a common negative stain for biological tissue known to enhance the collagen signal in electron microscopy. Tungsten specifically binds to collagen fibres (Malatesta, 2016) by selectively binding to the basic groups (lysine and arginine residues) of proteins (Jones, 1993, Höög et al., 2010). Porcine ONHs (n=3) were immersed in a solution of 2% (weight/volume) PTA (for preparation of lab stock, see appendix I.3) (Sigma-Aldrich, UK) in distilled water for 5 days, then washed in PBS for 2 hour and stored in 4% PFA at 4°C. Porcine ONHs (n=3) were then immersed in a solution of 2% PTA in 70% (volume/volume) ethanol. Prior to immersion in PTA 70% ethanol, samples were subjected to 2-hour incubations in 30% (volume/volume) ethanol (Sigma-Aldrich, UK), 50% ethanol and 70% ethanol. Following a 5-day immersion in 2% PTA 70% ethanol, samples were washed in 70% ethanol for 1 hour, then stored in 4% PFA at 4°C.

4.2.4.2 Lugol's Iodine solution

Lugol's iodine has been used to enhance contrast in soft tissues (Metscher, 2009a). Porcine ONHs (n=3) were immersed in 10% (volume/volume) Lugol's iodine (lab stock, see appendix I.4) (Sigma-Aldrich, UK) in distilled water for two weeks. Thereafter, ONHs were removed from the solution, washed in PBS for 2 hour and stored in 4% PFA at 4°C.

4.2.4.3 Tannic acid

Tannic acid (TA) has been suggested to enhance the signal of EF (Kageyama et al., 1985, Simmons and Avery, 1980), specifically the amorphous core (Damiano et al., 1979, Kageyama et al., 1985, Kajikawa et al., 1975, Ushiki and Murakumo, 1991). Porcine ONHs (n=3) were immersed in 2% (weight/volume) tannic acid (lab stock, see appendix

I.5) (Sigma-Aldrich, UK) in distilled water for two weeks. Thereafter, ONHs were removed from the solution, washed in PBS for 2 hour and stored in 4% PFA at 4°C.

4.2.4.4 Brain-wide reduced osmium pyragallol-mediated amplification (BROPA)

Three porcine ONHs were stained with BROPA to enhance visualisation of axons (Mikula and Denk, 2015), as the osmium tetroxide binds preferentially to lipids, including nerve-related lipids (Kiernan, 2001). During this procedure, ONHs were constantly rotated slowly at room temperature in the dark. First, ONHs were incubated for 96 hours in 30ml glass pots containing 40mM osmium tetroxide (OsO_4) (for preparation see Appendix I.6) (Electron microscopy Science, Ltd), 35mM of potassium hexaferrocyanate, (see Appendix I.7) 100mM sodium cacodylate buffer at 7.4 pH (see Appendix I.8) and 2.5M formamide (see Appendix I.9). The samples were then transferred into clear glass pots containing an aqueous solution of 40mM osmium tetroxide in 100mM sodium cacodylate buffer pH 7.4, for 48 hours, before being immersed into clear glass of 100mM sodium cacodylate buffer pH 7.4 for 4 hours to wash the residual of osmium tetroxide. Next, samples were transferred to 320 mM pyrogallol at pH 4.1 (see appendix I.10) for 72 hours. Following a final wash in 100mM sodium cacodylate buffer pH 7.4 for 4 hours, samples were transferred to 40mM aqueous osmium tetroxide for 72 hours. Then, immersed in PBS for storage at +4°C.

4.2.5 X ray microtomography (XMT)

Twenty-four hours prior to imaging, all ONHs were washed in PBS to remove any fixative residues, and finally transferred to PBS. XMT was carried out at station I13-2 at Diamond Light Source (DLS) (Didcot, Oxford) (figure 4.1a) within the Diamond-Manchester Imaging Branchline. (Rau et al., 2011, Rau et al., 2017).

4.2.5.1 Data collection and optimisation of scanning parameters

At Diamond Light Source, each hydrated ONH was removed from the PBS wash and mounted onto a CryoCap (Molecular Dimension, Ltd., Newmarket, Suffolk, UK) by gluing the back of the ON to the pin (figure 4.1c). Initially, moist tissue paper was placed onto the top of the sample to prevent dehydration during scanning (figure 4.1c). In some cases, samples were stabilised further using Blue Tac placed at the base of the CryoCap.

The sample was positioned onto the CryoPin (Molecular Dimension, Ltd., Newmarket, Suffolk, UK) (figure 4.1b) and placed in the beam path (figure 4.1a).

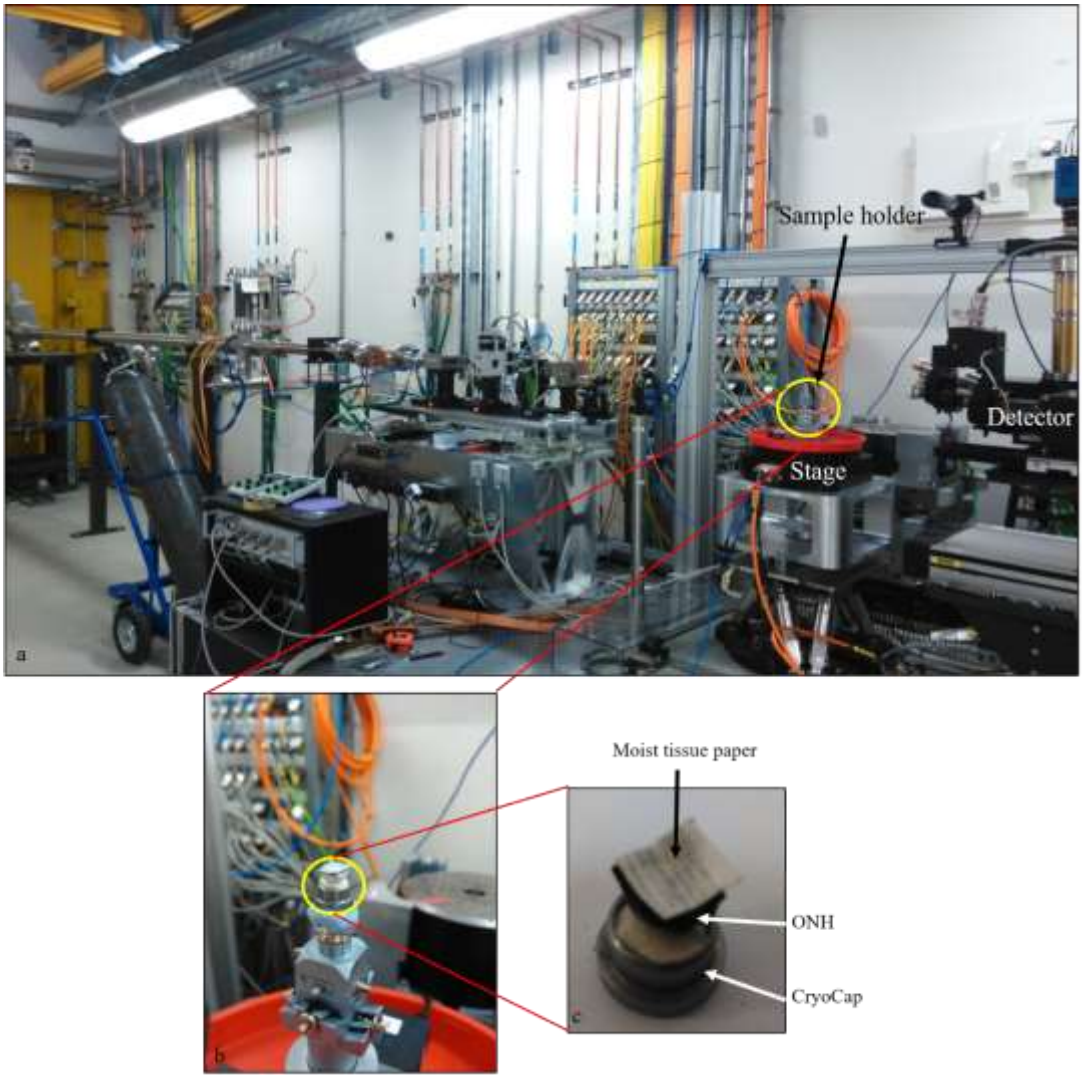

Figure 4.1.Experimental set up at station I13-2 at Diamond Light Source. Experimental hutch (a), sample holder on stage (b) and sample holder pin (c). The ONH was glued onto the CryoCap, which was placed onto the sample holder (b) and finally in the beam path (yellow circle in a).

All samples were scanned using a pink beam (3 GeV, 300mA) and scans were acquired through a 180° rotation with a step size 0.045-0.06° using a motorised stage onto which a pco.edge 5.5 scintillator-coupled detector (2560 x 2160 pixels and a pixel size of 6.5 μm^2) was mounted. Objective lens 1.25x, 4x and 10x were used to achieve the total magnification, effective pixel size and field of views as demonstrated in Table 4.1. After

parameters were optimised, image data acquisition on individual samples required between 2 and 5 hours.

Detector	Objective Lens	Total magnification	Effective pixel size (µm)	Field of view (mm)
pco.edge 5.5	1.25x	2.50x	2.6	6.7 x 5.6
	4x	8x	0.81	2.1 x 1.8
	10x	20x	0.33	0.83 x 0.70

Table 4.1. Images recorded using a pco.edge 5.5 detector at different magnifications. Note that the system provided a 2x magnification in addition to that provided by the objective lens.

4.2.5.2 Optimisation of exposure time and number of projections

Scans were acquired at different exposure times between 100-500 milliseconds with projections number between 2001-4001. A first scan included 3001 projections at 0.06° steps with 300 milliseconds exposure time and sample-detector distance of 245 mm.
Further optimising scans involved similar setting but with projections of 2001 and 4001 and step sizes of 0.045° with a detector-sample distance at 250 mm and 200 mm. Subsequent scan involved the same number of projections (4001) a step size of 0.045°, exposure time of 100 milliseconds and detector-sample distance at 250 mm. Additionally, the moist tissue paper was removed to prevent bubble formation and tissue deformation.

4.2.5.3 Optimisation of sample to detector distance

For all scans, 4001 projections were collected at 0.045° steps. The sample to detector distance and exposure times were varied between 50 to 200 mm and between 100-200 milliseconds, respectively. Additionally, ONH tissues were stabilised with Blue Tac placed at the bottom of the CryoCap.

4.2.6 Data processing in DAWN

All datasets were initially reconstructed using the DLS software DAWN (Basham et al., 2015) using the *tomo-centre* and *tomo-recon* functions (Table 4.2).

Script Name	Description
Tomo-centre	To find an optimal centre of rotation (CoR)
Tomo-recon	To perform the tomography reconstruction

Table 4.2. Tomo-centre and tomo-recon commands to define the CoR and reconstructing the datasets.

4.2.6.1 Tomo-centre

It was essential, for the quality of the reconstructions, to determine the location of the projected rotation axis, or the centre of rotation (CoR). Datasets as .nxs files were separately imported into DAWN and the CoR was determined as the number of the optical slice representing the middle of the whole dataset. The *tomo-centre* commands (see appendix III.1) were applied, to reconstruct the dataset with a series of different values of CoR which are smaller and/or larger than the input value. Datasets were then imported into DAWN and the CoR manually selected amongst those automatically found by the command.

4.2.6.2 Tomo-recon

Datasets with optimised CoRs were separately imported into DAWN and the *tomo-recon* command was applied (see appendix III.2). This reconstructed the whole dataset based on the optimal CoR previously found.

4.2.7 Data processing in Savu

After DAWN reconstruction, all datasets were refined using the cluster-based codes written in Savu (Atwood et al., 2015). All scripts used in Savu processing can be found in Appendices III.3-III.9. Savu data processing consisted of six refining steps, which are summarised in Table 4.3.

Process	Step	Command in Savu	Process Description
Initial	1	**NxtomoLoader**	To open and import raw data into Savu
	2	**DistortionCorrection**	To correct data for lens distortion and refine the CoR
Intermediary	1	**DarkFlatField Correction**	To apply the dark-and-flat-field normalisation to sample projections
	2	**CcpiRingArtefactFilter**	To suppress ring artefacts before applying Paganin filter
Final	1	**AstraReconGpu**	Reconstruct the dataset based on the CoR
	2	**TiffSaver**	Save the corrected and filtered dataset as tiff files

Table 4.3. List of processes to correct tomo-reconstructed datasets into Savu software. The whole process included six different steps to improve image quality by suppressing artefacts, removing artefact rings and refining the CoR.

The initial steps involved the loading of the tomo-reconstructed datasets into Savu and the refining of the CoR defined with *tomo-centre*. In a Savu processing window, the Savu *NxtomoLoader* was input to upload raw tomography data saved in. nxs format (see appendix III.3).

Next, the Savu command *DistortionCorrection* was used to (see appendix III.4) to refine the CoR previously determined with the *tomo-centre* by correcting raw data from lens distortion induced by image acquisition process.

The next two intermediary steps involved the Dark and Flat field correction and ring artefact suppression Savu *DarkFlatFieldCorrection* enabled the former (see appendix III.5). Flat-field correction is a technique used to improve quality in digital imaging and it is applied after projection images of the sample are acquired with and without the X-

ray beam turned on. Projections acquired with and without beam are referred to as flat fields (F) and dark fields (D), respectively. The purpose of flat fields correction is to remove artefacts from 2D images which are caused by variation in the sensitivity of the detector.

Then Savu *RingArtefactFilter* was applied to remove ring artefacts due to the rotation of the sample on a vertical axis (see appendix III.6).
Two final steps involved the reconstruction of the processed datasets using Savu *AstraReconGpu* (see appendix III.7) and Savu *TiffSaver* used to save the reconstructed datasets as .tiff formats (see appendix III.8).

4.2.7.1 Application of a Paganin Filter

Reconstructed datasets were imported into Savu to apply the Paganin filter *(PaganinFilter)*, a low pass filter which smoothed the image, removing residual artefacts. (see appendix III.9). Each dataset was processed with and without Paganin filter, to compare the effect of the filter in smoothing the images.

4.2.8 3D reconstruction of XMT datasets

Each Savu output ONH dataset in .tiff format was approximately 4 Gb, therefore prior to 3D reconstruction in Amira, the datasets were reduced in size by cropping (in Image J) optical slices that did not contain any information from the top and bottom of the image stacks. Each cropped human and porcine ONH dataset are visualised as a 3D reconstruction of the dataset volume using Amira "Volren" module. *Enface* visualisation was possible through a transverse cut into the depth using the "ROI cropping tool" of Amira. PreL (figure 4.2a), LC (figure 4.2b) and postL (figure 4.2c) were visualised for the porcine and human ONHs.

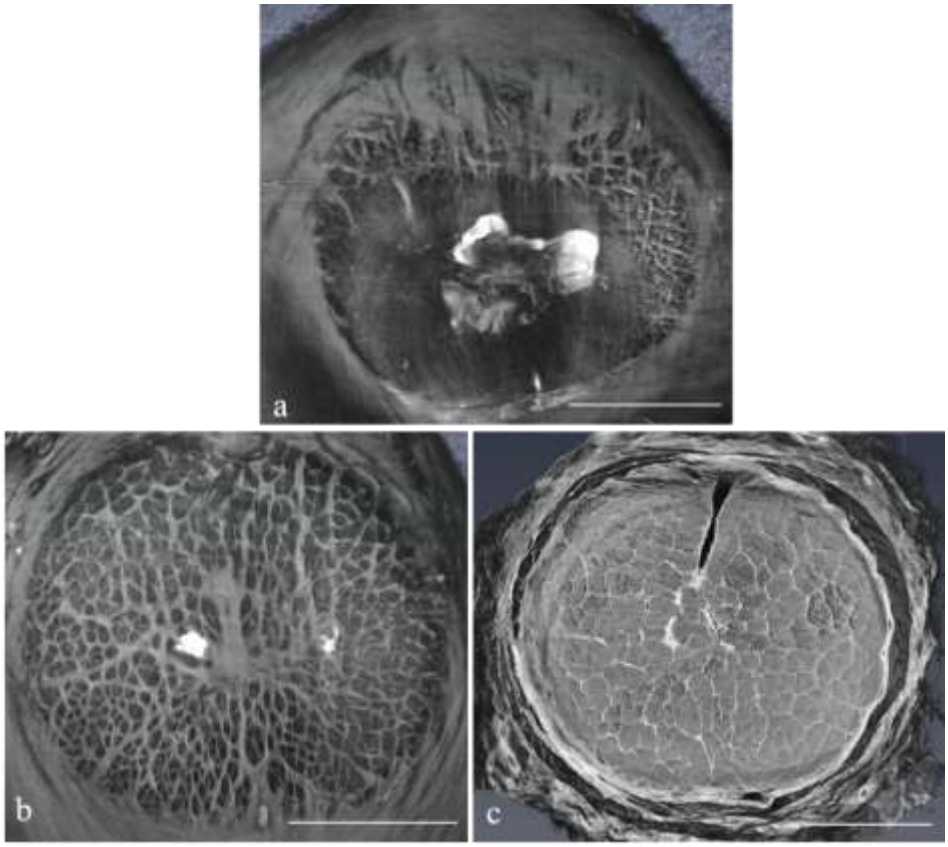

Figure 4.2. 3D reconstructed images of porcine ONH stained with PTA in ethanol. *Enface* images from the rendered ONH showed the preL (a), LC (b) and postL (c). Scale bars represent 1 mm.

4.2.9 Analysis of human lamina cribrosa structural parameters

Each human ONH dataset with the correct scale (2.6 μm^2 = 1 pixel for 1.25x objective lens) was imported into Amira and visualised as a 3D using the "Volren" module. Due to low contrast between the cribriform plates and the neuronal pores, automatic segmentation of the whole dataset was not possible, therefore the LC surface to calculate LC thickness and volume was not reconstructed.

The LC thickness measurements (perpendicular distance between the anterior and posterior LC limits) were computed within representative longitudinal optical slices (n=3) containing the central retinal vessels from each control (n=3) and glaucomatous (n=3) ONH using the "ruler" tool of Amira. Three measures were computed for each region (i.e. superior, inferior, nasal and temporal) within each optical slice. Mean ± standard deviation of overall and regional LC thickness was plotted as a bar chart.

4.2.9.1 Analysis of lamina cribrosa pore parameters

As mentioned above, due to low contrast between the cribriform plates and the neuronal pores, automatic segmentation of the connective tissue and subsequently the pores, using thresholding was not possible. Therefore, representative optical slices of the anterior (n=3 slices), mid (n=3 slices) and posterior (n=3 slices) LC of each glaucomatous (n=3) and controls (n=3) ONHs, were manually segmented using the "brush" tool to select pores (figure 4.3a). Each segmented optical slice was imported into image J and converted into a binary image (figure 4.3b). The central retinal vessels and surrounding sheaths were excluded from the LC area by manual removal using the "brush" tool. Pore parameters were calculated using "Analyse particle" as described in 2.2.6.2. Pore count (total number of pores per mm^2), pore area (area occupied by pores in each mm^2 expressed as a percentage) and circularity (pore roundness; 1.0: perfect circle, 0.0: elongated polygon) were calculated. Mean ± standard deviation of overall and regions LC pore parameters were plotted as a bar chart to show changes in pores as a function of glaucoma.

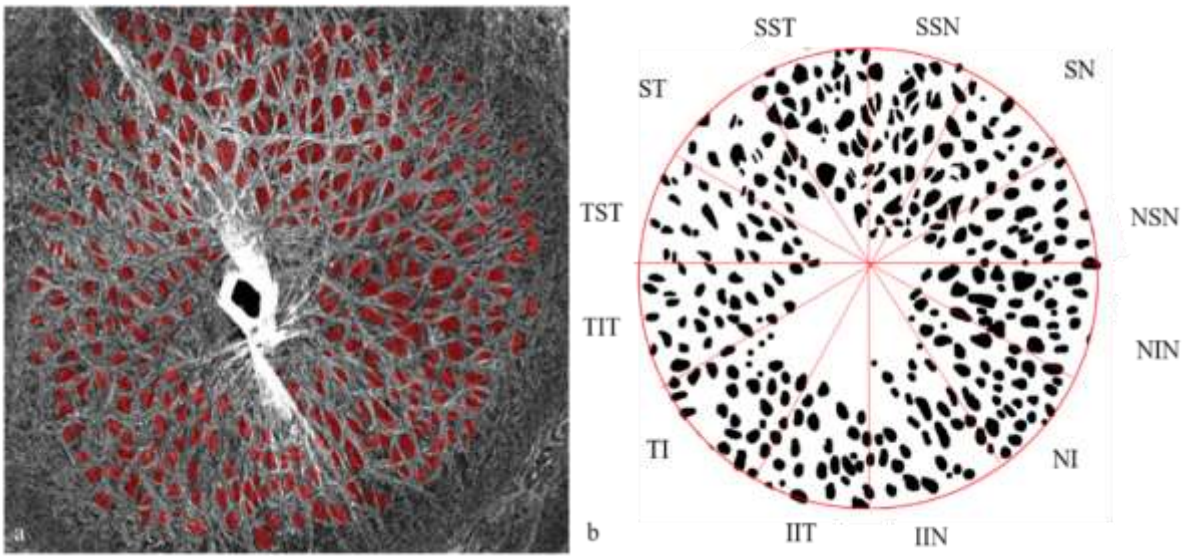

Figure 4.3. Manual pores segmentation from XMT optical slices. Three optical slices from each dataset were manually segmented in Amira v6.5. With the brush tool, pores were manually segmented (a), the image was then converted into binary (b) and a grid sector overlapped for regional analysis. Data in between sectors (i.e. SN, NI, TI, ST) was excluded from the analysis to ensure no overlapping. The central retinal artery was also excluded from the analysis.

4.2.9.2 Quantification of lamina cribrosa connective tissue

The LC connective tissue was also manually segmented in the three representative optical slices of the anterior, mid and posterior LC as described in 4.2.9.1, and converted into binary images in Image J. The number of connective tissue segmented pixels was calculated using the "Analyse particle" function and divided by the total number of pixels and expressed as a percentage as described in 2.2.7.1.

4.2.10 Statistical analysis

All statistical analysis was performed with SPSS version 25 (SPSS Inc., USA). The Shapiro-Wilk test was used to test for normally distributed data with a significance of $p>0.05$. Data were deemed to be normally distributed therefore one-way ANOVA and the independent sample T-test was used to test for differences between glaucoma and age-matched controls.

4.3 Results

4.3.1 Nonlinear microscopy of porcine ONH

SHG signal derived from fibrillar collagen appeared strong in the porcine LC (figure 4.4a), but no TPEF was observed (figure 4.4b).

4.3.2 Optimisation of scanning parameters

Exposure time, number of projections and signal to noise ratio were optimised using unstained porcine ONH. Table 4.4 summarises parameters and problems that occurred. These early scans generated some issues, such as i) cracks in the tissue and shrinking, possible due to dehydration (figure 4.5d) and ii) tissue deformation (figure 4.5a,b,c) and bubbles potentially due to the condensation of the moist tissue paper placed at the top of the sample.

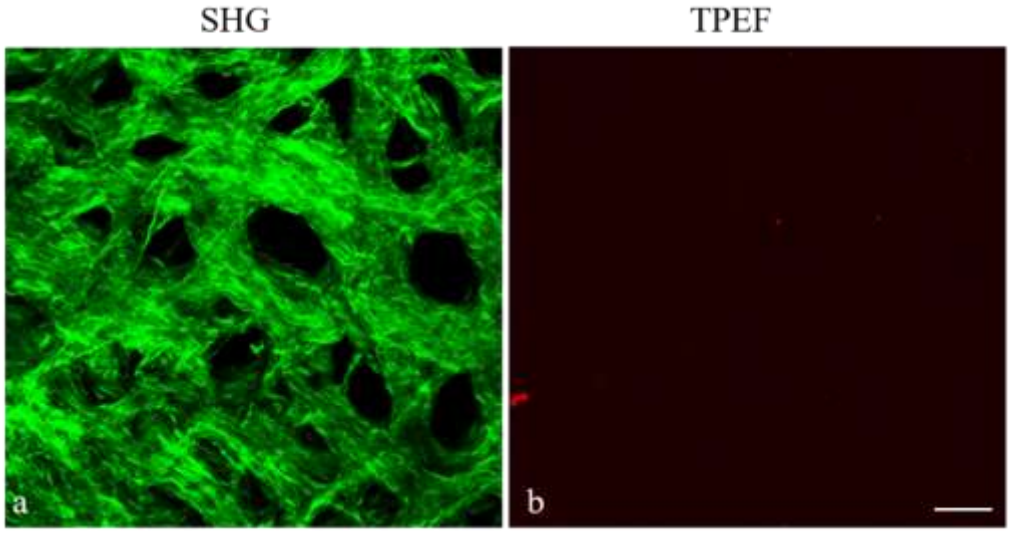

Figure 4.4. High resolution nonlinear images (SHG: green, TPEF: red) of porcine ONH. SHG signal derived from collagen appeared strong in the LC (a). TPEF signal was not observed in the LC (b). Scale bars represent 50 µm.

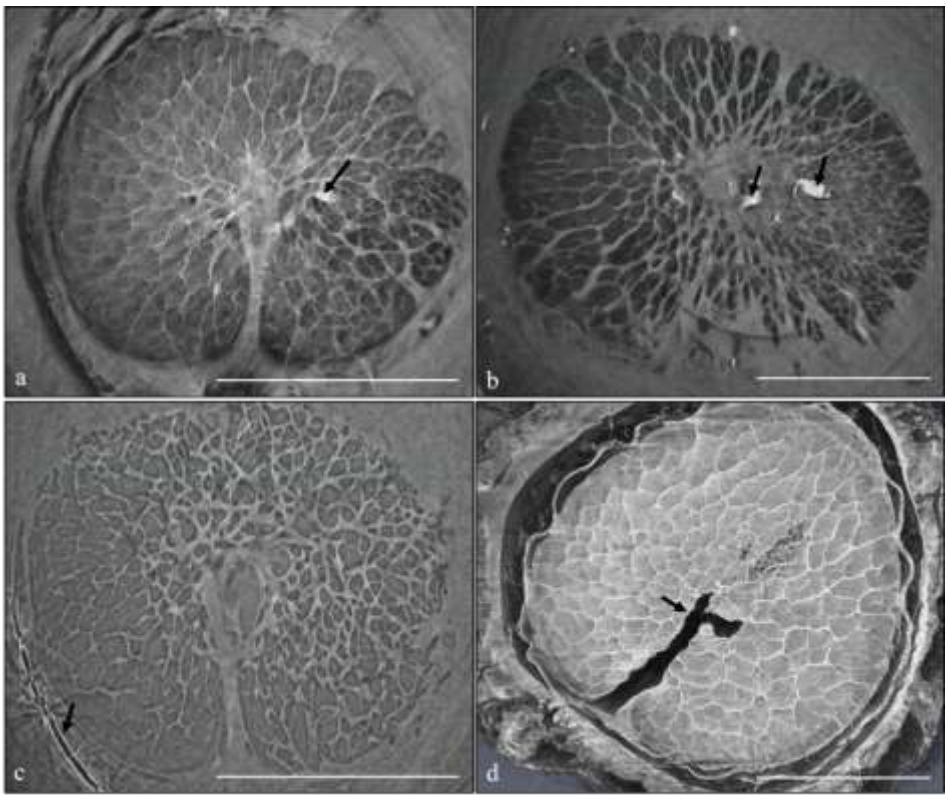

Figure 4.5. *Enface* sections of 3D reconstructed phase ONH. Tissue deformation (a,b black arrow), bubbles and cracks (c,d, black arrows) occurred during the first set of optimisation scans. Scale bars represent 1 mm.

Specimen	Magnification	Projections	Step size (°)	Exposure time (ms)	Sample-detector distance (mm)	Additional requirements	Outcome
Unstained porcine ONH (Phase)	2.50x	3001	0.06	300	245	Moist tissue paper to prevent from dehydration	• Crack in the tissue • Bubbles • Shrinking
	2.50x	2001	0.045	100	250	Moist tissue paper to prevent from dehydration	• Not enough contrast • Some tissue deformation
	2.50x	4001	0.045	100	200	Moist tissue paper to prevent from dehydration	• Not enough contrast • Deformation
	2.50x	4001	0.045	100	100	Tissue paper removed	• Not enough contrast • Deformation
	2.50x	**4001**	**0.045**	**100**	**250**	**Tissue paper removed**	• **Good contrast** • **Some tissue deformation** • **No bubbles**

Table 4.4. Details of the optimisation of exposure time and projections on unstained porcine ONHs. The optimal scan included 4001 projections at 100 msec exposure time with 250 mm propagation (highlighted in bold). This scan achieved a good contrast without bubbles and very little tissue deformation.

The next scan did not allow to achieve enough contrast for the naked eye to discriminate between pores and connective tissue (figure 4.6a,b). The final scan was chosen to be the optimal at 4001 projections, 100 millisecond exposure time and sample detector distance of 250 mm although some tissue deformation (figure 4.6c) was still visible, no bubbles and good contrast were achieved in both the longitudinal (figure 4.6c) and *enface* (figure 4.6d) views.

Next, optimisation of the sample detector distance was performed using PTA-stained porcine ONH. Table 4.5 summarises parameters and problems that occurred.

Specimen	Magnification	Projections	Step size (°)	Exposure time (ms)	Sample-detector distance (mm)	Additional requirements	Outcome
Porcine ONH in PTA (ethanol)	2.50x	4001	0.045	200	100	Blue tack to keep the tissue still	• Tissue deformation • Sample movement
	2.50x	4001	0.045	100	200	Blue tack to keep the tissue still	• Sample movement
	2.50x	4001	0.045	200	50	Blue tack to keep the tissue still	• Sample movement • Blue tack melting
	2.50x	4001	0.045	100	100	Blue tack removed	• Sample movement
	2.50x	**4001**	**0.045**	**100**	**200**	**Blue tack removed**	**• Little sample movement**

Table 4.5. Details of the optimisation parameters for detector-sample distance. The optimal scan included 200 mm propagation at 100 millisecond exposure (highlighted in bold). This scan achieved a good contrast without bubbles and very little sample movement.

Due to the high temperature inside the experimental hutch, the main issue that arose was the melting of the Blue Tack (figure 4.6e) which led to sample movement and therefore tissue deformation. Therefore, subsequent scans were performed without Blue Tack and the sample was glued onto the CryoCap (figure 4.6f). In PTA-ethanol stained ONHs, tissue deformation was also observed (figure 4.6e), likely due to the dehydration effects of ethanol.

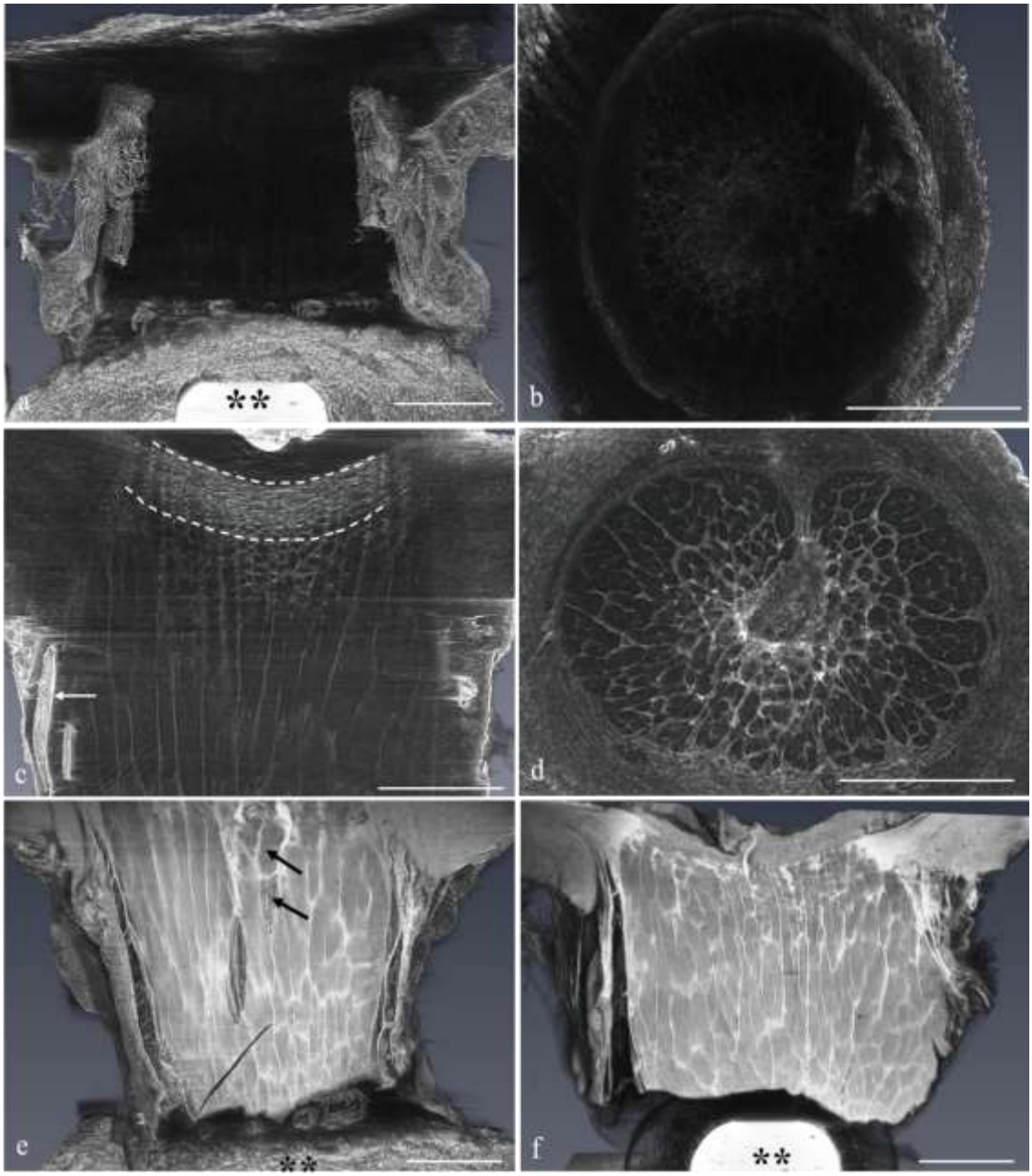

Figure 4.6. Longitudinal and *enface* sections of a phase contrast (unstained) (a-d) and PTA-stained (e,f) porcine ONH. The second scan did not generate enough contrast to discriminate neuronal pores from the surrounding connective tissue (a,b). Asterisks (a) indicated the metal pin, with overlapping blue tack added to stabilise the sample. Next scan on phase ONH, using 4001 projections, an exposure time of 100 ms and 250 mm sample detector distance, allowed good contrast (c,d) and little tissue deformation (c, white arrow). Next scan on PTA-stained ONH (e,f) showed the sample stabilised with Blue Tack (e, black asterisks). However, the Blue Tack melted causing sample movement and therefore tissue deformation (e, black arrows). Thus, final scan involved the removal of the blue tack and the sample was directly glued onto the CryoCap (f, black asterisks). Scale bars represent 1 mm.

4.3.3 3D reconstruction of porcine ONH

Representative images of the LC from 3D reconstruction of porcine ONHs with and without Paganin filter are shown in figure 4.7. Paganin filter smoothed the image and removed noise within phase (figure 4.7d), PTA in water (figure 4.7e) and ethanol (figure 4.7f), lugol's iodine (figure 4.7l), tannic acid (figure 4.7m) and BROPA (figure 4.7n). However, images appeared too smooth compared to those without filter. The connective tissue was more defined and visible when the filter was not applied within all ONHs [phase (figure 4.7a), PTA in water (figure 4.7b) and ethanol (figure 4.7c), lugol's iodine (figure 4.7g), tannic acid (figure 4.7h) and BROPA (figure 4.7i)]. Therefore, datasets were analysed without the Paganin filter.

Representative images of the LC from 3D reconstruction of porcine ONHs are shown in figure 4.8. All ONHs stained with different contrast agents showed a good differentiation of the connective tissue from the neuronal pores. Phase-contrast images (i.e. without contrast agents) showed a good discrimination of the connective tissue and pores, enabling observation of LC beam organisation surrounding the pores (figure 4.8a).

PTA staining provided the best differentiation between LC connective tissue and pores, in both water (figure 4.8b) and ethanol (figure 4.8c); the collagenous network within the cribriform plates was clearly visible. Lugol's iodine (figure 4.8d) penetrated the tissue, allowing a clear differentiation of the connective tissue from the neuronal pores. Tannic acid (figure 4.8e) stained ONHs showed good differentiation of connective tissue within the cribriform plates from the neuronal pores, which appeared grey/black surrounded by bright cribriform plates. The BROPA staining of ONHs showed a diffuse network within the pores (figure 4.8f) which appeared clearer at higher magnification (figure 4.8g,h). The connective tissue of the LC plates appeared black surrounding the brighter pores.

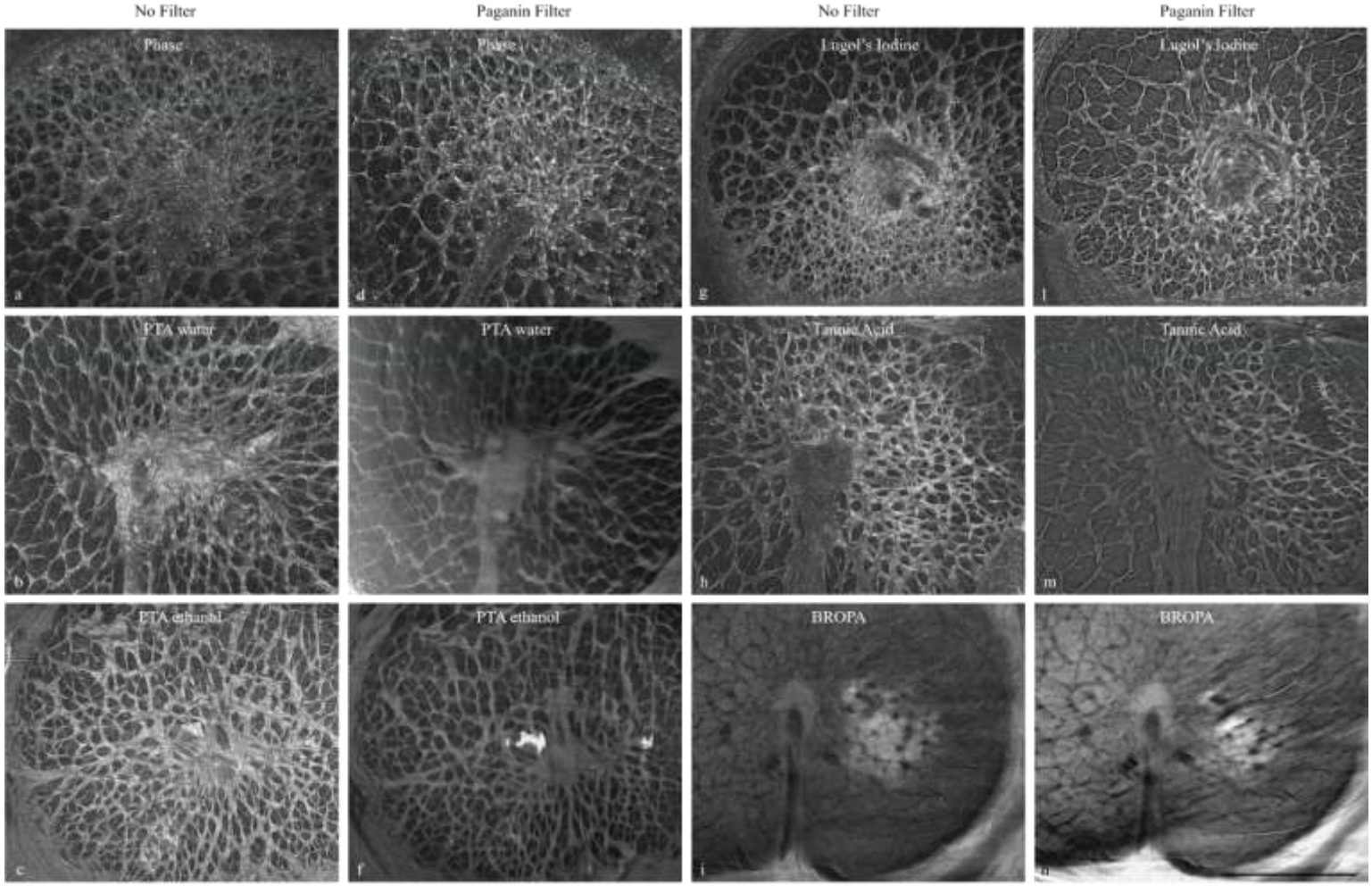

Figure 4.7. Representative porcine ONH optical slice before and after Paganin filter. Phase (a), PTA in water (b), PTA in ethanol (c), lugol's iodine (g), tannic acid (h) and BROPA (i), showed a better discrimination of the LC connective tissue from the pores before Paganin filter was applied. The filter caused too much smoothing within all images [phase (d), PTA in water (e), PTA in ethanol (f), lugol's iodine (l), tannic acid (m) and BROPA (n)]. Scale bar represents 1 mm.

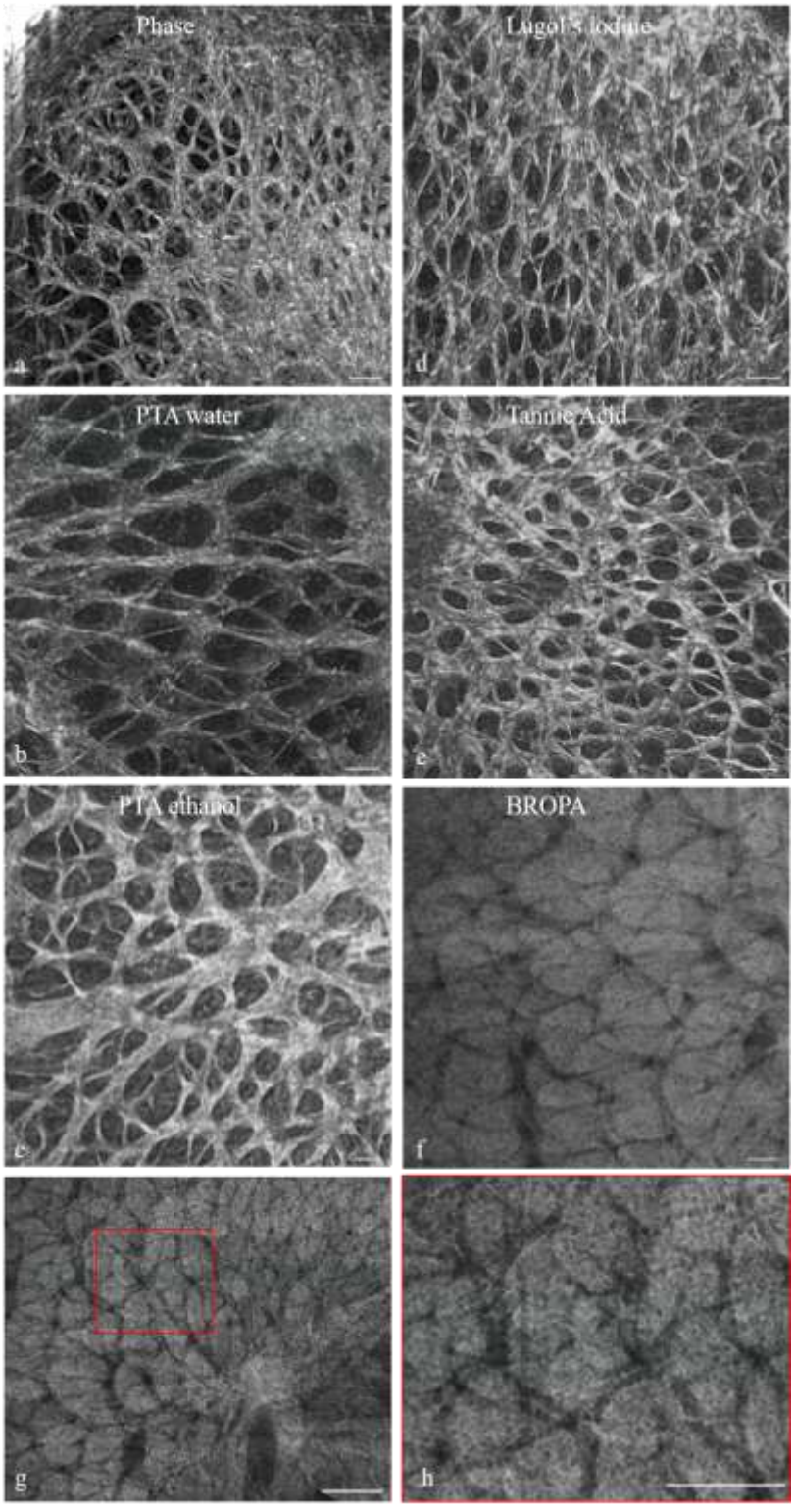

Figure 4.8. 3D reconstruction of the ONHs at 2.50x magnification. Phase-contrast (a), PTA in water (b), PTA in ethanol (c), tannic acid (e) and lugol's iodine (d) all showed a clear discrimination of the connective tissue from the neuronal pores. BROPA (f) stained ONHs showed contrast within the LC pores compared to the unstained black cribriform plates (g,h). However, magnification and resolution were not enough to discriminate the axons. Scale bars represent 100 µm.

When acquired at higher magnification, similar results were observed. Unfortunately, due to sample misalignment during scanning, no suitable images were available of BROPA stained ONHs and of any stained ONH at magnification of 20x.

The connective tissue within the LC cribriform plates was clearly visible within ONHs stained with Lugol's iodine (figure 4.9d), PTA in water (figure 4.9b) and PTA in ethanol (figure 4.9c). Phase-contrast (figure 4.9a) and tannic acid (figure 4.9e) did not show a good discrimination between pores and LC connective tissue.

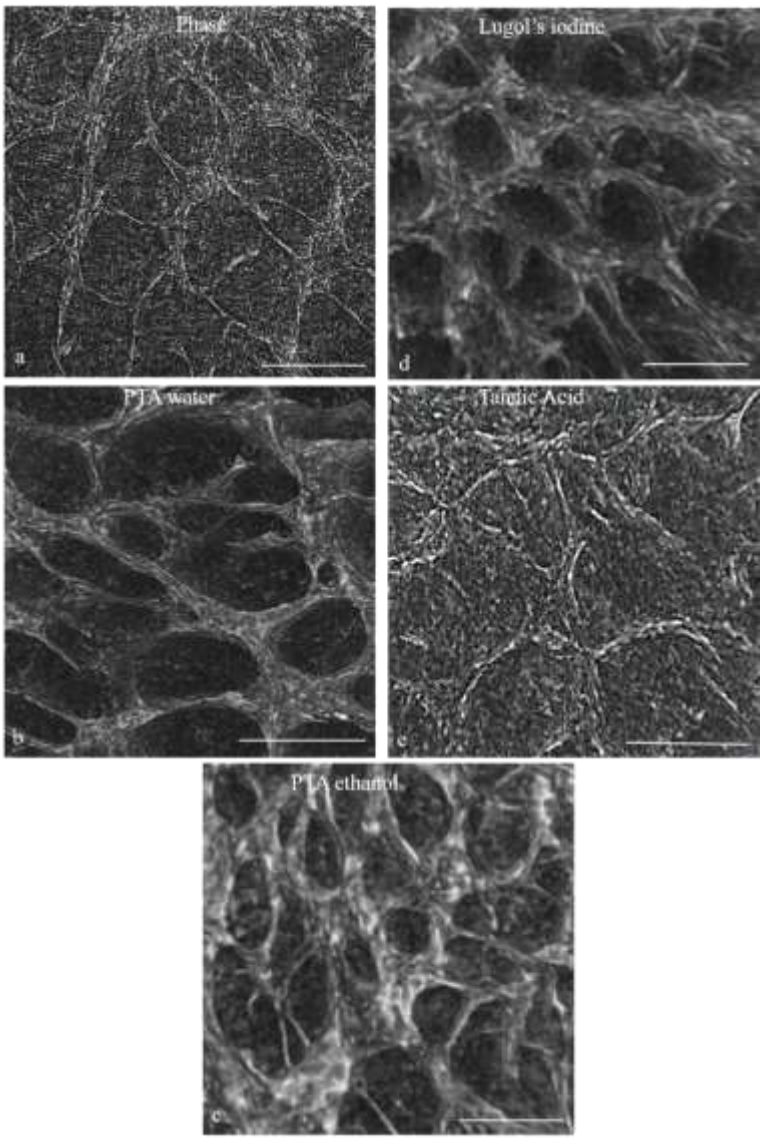

Figure 4.9. 3D reconstruction of the ONHs at 8x magnification. PTA in water (b), PTA in ethanol (c), and Lugol's iodine (d) all showed a clear separation of the connective tissue from neuronal pores. Phase-contrast (a) and tannic acid (e) did not show good discrimination and contrast between neuronal pores and LC cribriform plates. Scale bars represent 100 µm.

4.3.4 Reconstructions of human ONH datasets

No contrast agents were applied to the human samples and phase contrast imaging allowed an overall good visualisation of the LC connective tissue (figure 4.10b) in the healthy ONH. PreL (figure 4.10a) and postL ON (figure 4.10c) also showed good discrimination between pores and connective tissue. Phase contrast imaging of glaucomatous ONHs, showed a good contrasting differentiation of the LC (figure 4.10e) but not in the preL (figure 4.10d) and postL ON (figure 4.10f), where the optic canal border was difficult to identify. Within glaucomatous ONHs, the preL (figure 4.10d), LC (figure 4.10e) and postL ON (figure 4.10f) appeared more oval shaped compared to normal preL (figure 4.10a), LC (figure 4.10b) and postL ON (figure 4.10c).

4.3.5 Analysis of human lamina cribrosa structural parameters

4.3.5.1 Analysis of lamina cribrosa pore parameters

Differences in the LC pore shape were observed in the LC of glaucomatous ONHs compared to controls, where pores appeared relatively circular (figure 4.11a-c). A more elongated shape of the LC and the pores was observed in the glaucomatous ONHs. The LC shape appeared more oval in both the mid (figure 4.11e) and posterior LC (figure 4.11f), compared to anterior (figure 4.11d) LC. The elongated shape appeared more pronounced in the anterior (figure 4.11d) and mid (figure 4.11e) LC compared to the posterior (figure 4.11f). Note the altered shape of the posterior glaucomatous LC (figure 4.11f) in the inferior region. The image is not rotated by 90 degrees, but it showed an abnormal shape of the posterior LC compared to mid (figure 4.11e) and anterior (figure 4.11d).

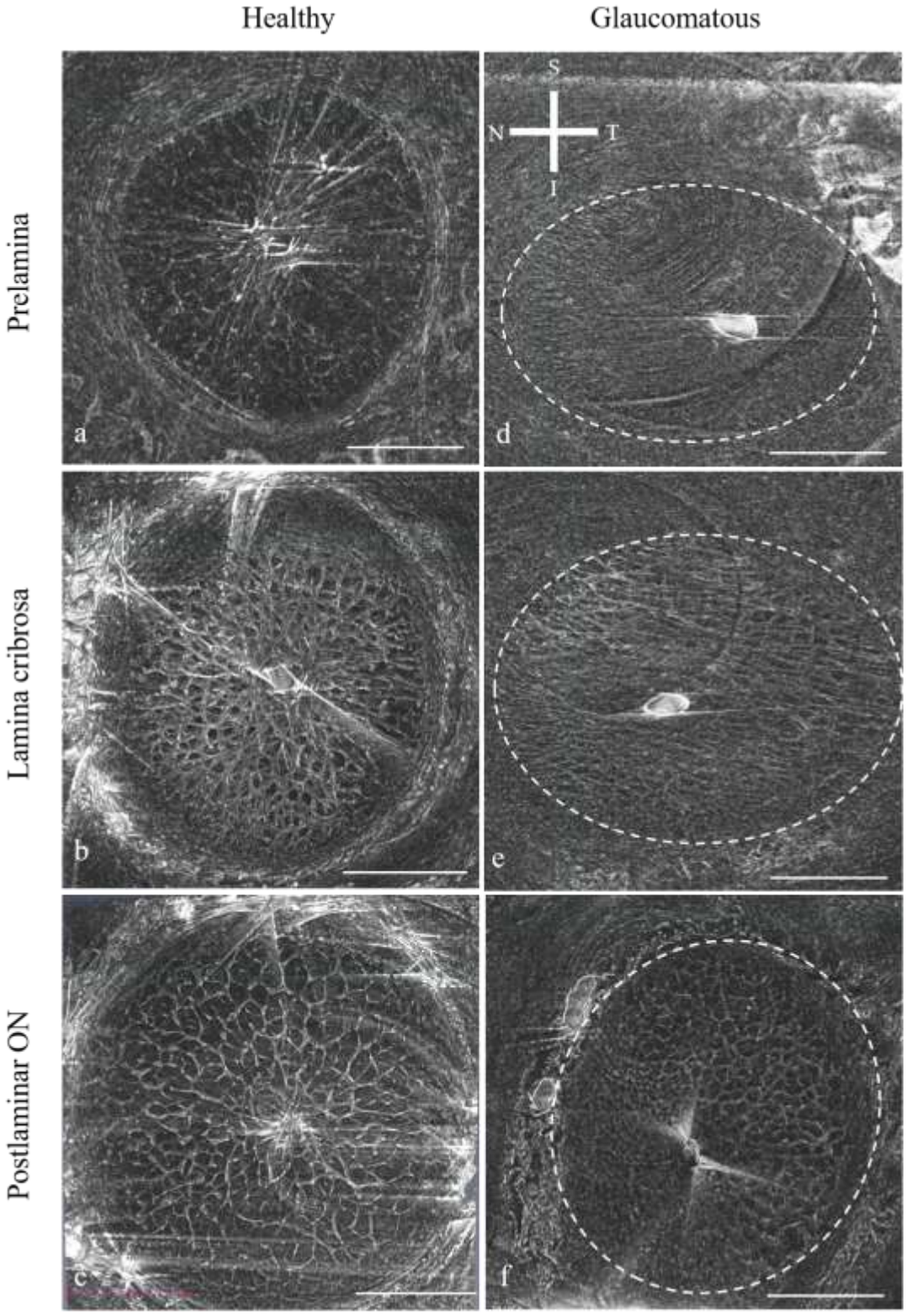

Figure 4.10. *Enface* images of preL, LC and postL of healthy normal and glaucomatous ONHs. Lower phase contrast was observed within glaucomatous ONHs. The borders of the preL (d), LC (e) and postL ON (f) were difficult to identify and are denoted by dashed white ellipses. Phase contrast of controls showed clear representation of preL (a), LC (b) and postL ON (d). Scale bars represent 1mm.

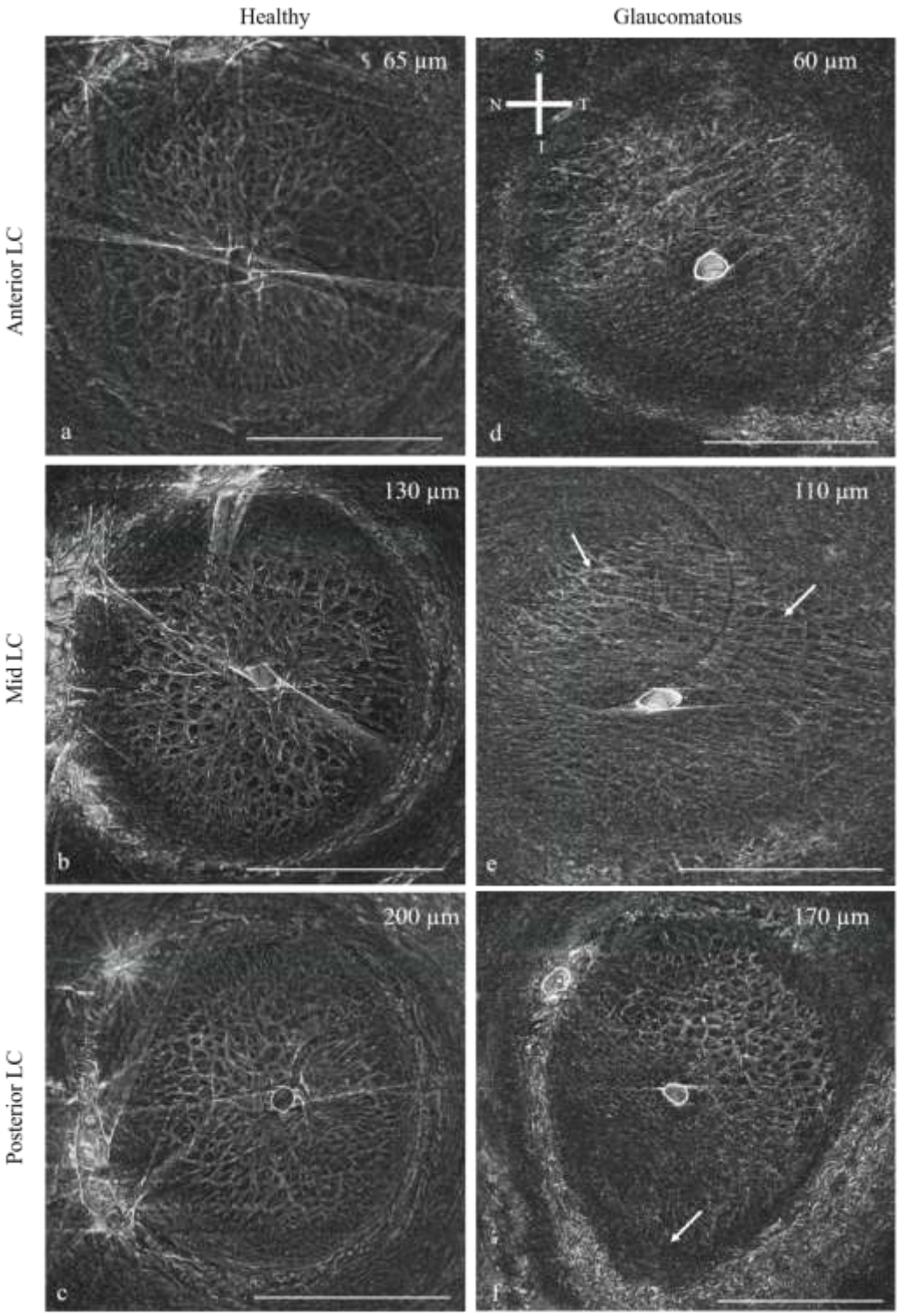

Figure 4.11. Anterior, mid and posterior LC images from healthy and glaucomatous ONH. Differences were observed in the LC and pore shape between glaucoma and control ONHs. In the controls, pores and LC appeared relatively circular and well defined in anterior (a), mid (b) and posterior (c). In contrast, glaucomatous LC showed more elongated pores in both anterior (d) and mid (e) LC. LC shape appeared more elongated in the nasal-temporal axes in the anterior (d) and mid (e, white arrows) regions. Note the altered shape in the inferior region of the posterior LC (f, white arrow). Image is not rotated 90 degrees. Scale bars represent 1 mm.

Pore parameters namely pore area (%), pore count and circularity showed a significant decrease in glaucomatous ONH when compared to controls [area (p=0.002) (figure 4.12a), count (figure 4.12b) (p=0.003), circularity (p=0.002) (figure 4.12c)].
Regional analysis showed that circularity was significantly lower in all regions in glaucoma compared to controls [superior (p=0.022), inferior (p=0.013), nasal (p=0.037), temporal (p=0.005) (figure 4.12f)]. Average pore count appeared significantly lower in the superior region only (p=0.037) (figure 4.12e). No differences were observed in pore area [superior (p=0.139), inferior (p=0.178), nasal (p=0.168), temporal (p=0.108) (figure 4.12d)].

When compared between inner and outer LC, pore count (p=0.039) (figure 4.12h) and circularity (p=0.026) (figure 4.12i) were significantly lower in glaucoma in the outer LC compared to controls. No differences were found in pore area [inner LC (p=0.082), outer LC (p=0.089)] (figure 4.12g), count (p=0.053) and circularity (p=0.073) in the inner LC.

LC was significantly thinner in glaucoma (p=0.007) (figure 4.13a) and in the inferior region (p=0.030) (figure 4.13b) when compared to controls.

4.3.5.2 Quantification of lamina cribrosa connective tissue

Table 4.6 summarises connective tissue content within regions in glaucoma and controls. Overall, no differences were found in connective tissue content between glaucoma and controls (p=0.568) (figure 4.14a). Regional analysis revealed no differences between glaucoma and controls in any region [superior (p=0.529), inferior (p=0.127), nasal (p=0.515), temporal (p=0.761)] (figure 4.14b).

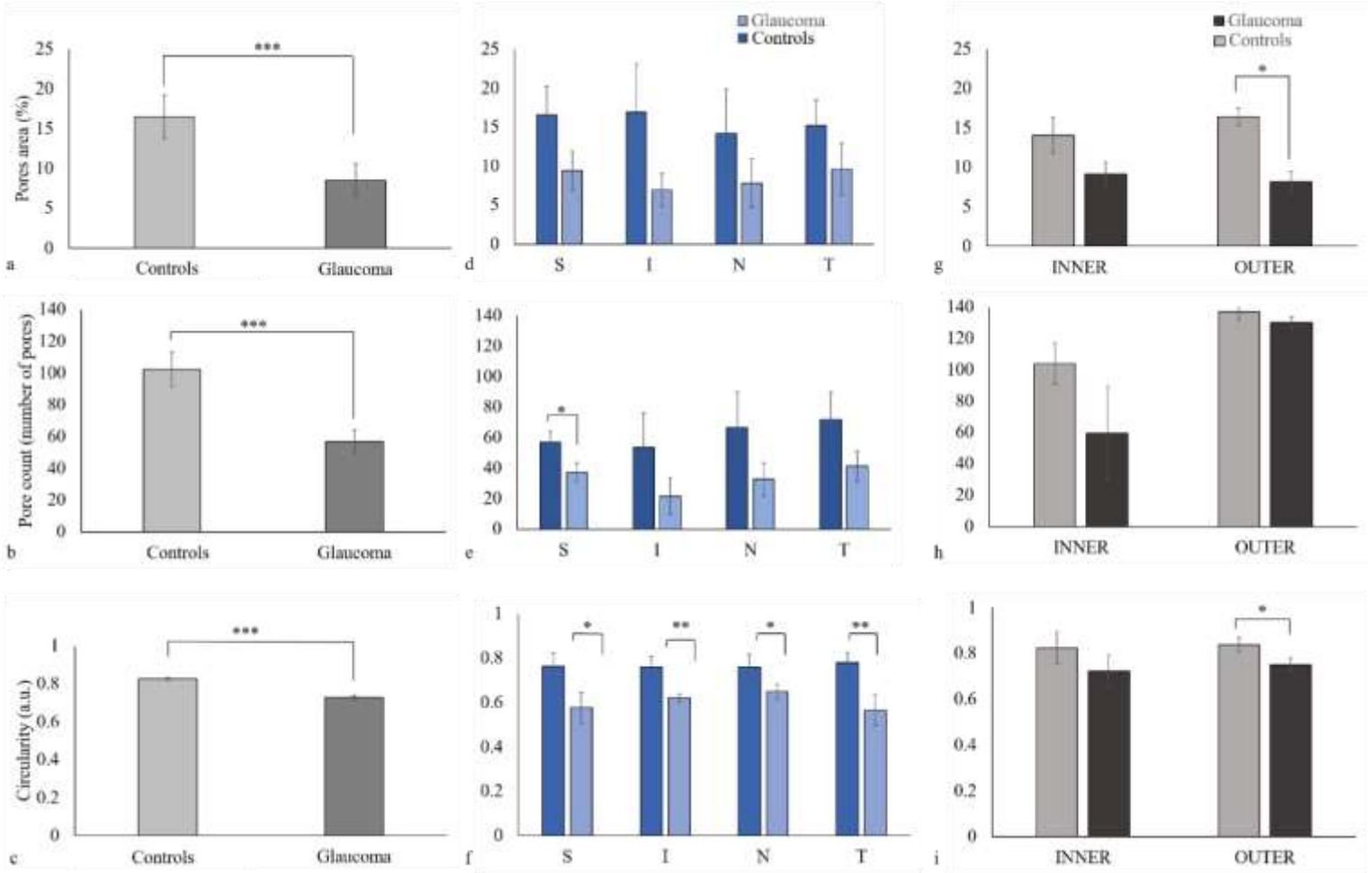

Figure 4.12. Pore parameters (mean +/-sd) in healthy and glaucomatous ONH. Pore area (%) (a) (p=0.002), count (b) (p=0.003) and circularity (c) (p=0.002) showed a significant decrease in glaucoma compared to controls. Regional analyses revealed that circularity (f) was significantly lower in all glaucoma regions compared to controls. Whereas count (p=0.037) was significantly lower only in the superior region (e), when compared to controls. When compared between inner and outer LC, pore count (p=0.039) (h) and circularity (p=0.026) (i) were significantly lower in glaucoma in the outer LC compared to controls. No differences were found in pore area [inner LC (p=0.082), outer LC (p=0.089)] (g), count (p=0.053) and circularity (p=0.073) in the inner LC.

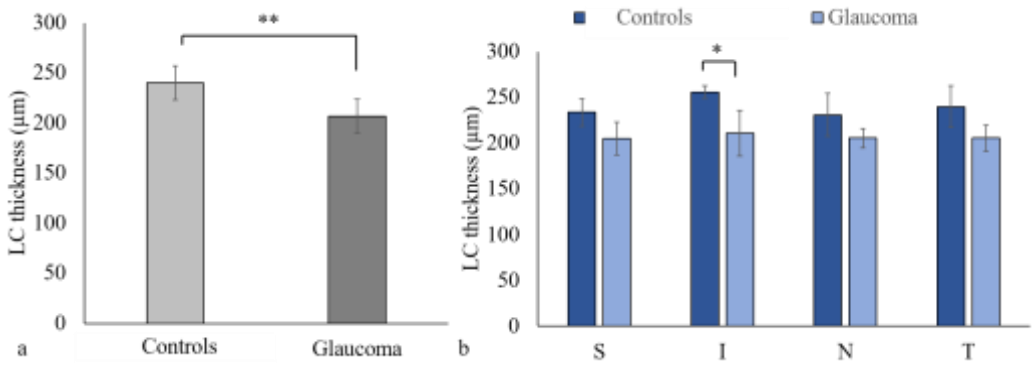

Figure 4.13. LC thickness (mean +/-sd) in glaucomatous ONH. LC was significantly thinner in glaucoma (p=0.007) (a) and in the inferior region (p=0.030) (b) compared to controls.

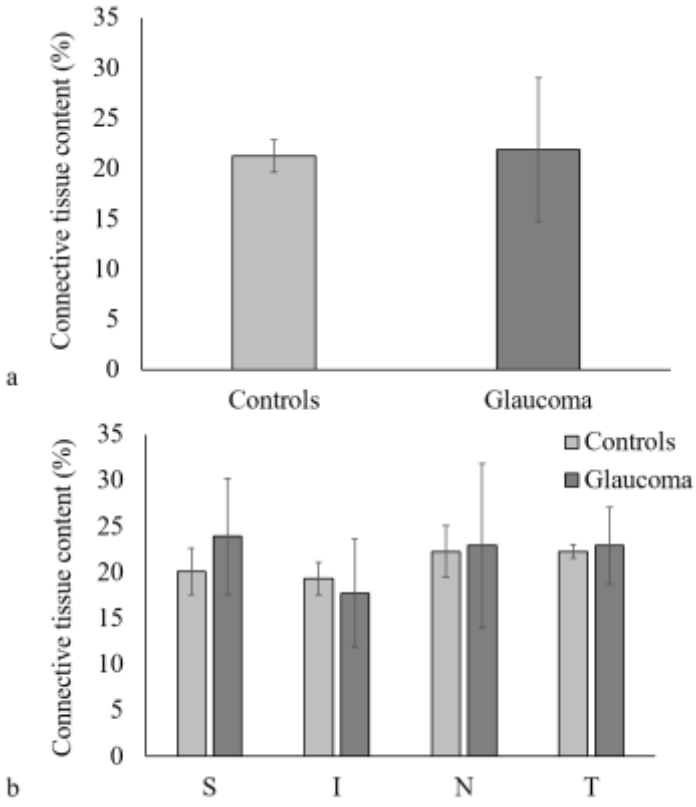

Figure 4.14. Connective tissue content (mean +/-sd) within glaucomatous ONHs. No differences were found in the overall connective tissue content between glaucoma and controls (a) (p=0.568) nor in regions (b) [superior (p=0.529), inferior (p=0.127), nasal (p=0.515), temporal (p=0.761)].

Age (years)	Collagen content (%) ± sd	Superior	Inferior	Nasal	Temporal
Age-Matched controls (81yr)	20.71 ± 3.90	21.35 ± 3.85	17.41 ± 1.78	20.71 ± 0.14	24.33 ± 4.26
Age-Matched controls (85yr)	20.027 ± 7.40	17.22 ± 0.62	19.90 ± 3.62	20.63 ± 0.26	23.51 ± 0.83
Age-Matched controls (72yr)	23.07 ± 8.10	21.85 ± 0.34	20.81 ± 0.24	25.54 ± 1.60	25.01 ± 0.59
Glaucoma (84yr)	13.90 ± 0.61	13.89 ± 6.45	11.23 ± 4.42	13.06 ± 3.36	18.56 ± 7.32
Glaucoma (77yr)	27.67 ± 1.33	35.18 ± 11.59	19.44 ± 12.2	30.36 ± 4.19	24.96 ± 3.67
Glaucoma (Unknown)	24.09 ± 2.74	22.74 ± 5.15	22.66 ± 2.01	25.34 ± 5.58	26.49 ± 0.60

Table 4.6. Connective tissue content within regions of three glaucomatous and three healthy controls ONHs.

4.4 Discussion

The purpose of this experiments was to test the potential of XMT as cutting-free technique to investigate the i) overall 3D connective tissue microstructure of the ONH and the ii) axons within the LC pores. Since its first application in 1980s, XMT has been widely and increasingly used, due to its capability as a non-invasive technique. In the last decade XMT has been introduced in arthritis research (Disney et al., 2017), cancer research (Paulus et al., 2000), soft tissue analysis (Descamps et al., 2014, Gignac and Kley, 2014) and assessment of the collagen network within porcine vessels (Nierenberger et al., 2015). XMT resolves many limitations of imaging techniques previously employed to study the ONH microstructure. Most importantly, XMT does not require tissue processing as in conventional histological techniques which alter tissue structure (Yan et al., 1994, Yang et al., 2009). In the current chapter the ability of XMT to be employed as an imaging technique for visualisation of the 3D microstructure of the ONH was investigated.

4.4.1 Optimisation of XMT scan parameters

Optimised parameters employed in this study for ideal XMT imaging of the 3D ONH connective tissue microstructure included overall optimisation at 2.50x magnification, with 4001 projections, exposure time of 100 millisecond and sample detector distance of 200 mm. However, it was not possible, likely due to tissue deformation and/or movement, to acquire scans at 8x total magnification or higher.

To prevent tissue distortion and movement, which were seen in acquired scans, short scan exposures of 100 millisecond were chosen as optimal. Artefacts due to sample movement would be an important issue which might lead to a misinterpretation and a misalignment of the 3D reconstructed dataset. Porcine ONHs reconstructions stained with PTA, Lugol's iodine and tannic acid enabled the connective tissue network of the ONH to be visualised, except for BROPA, where the low magnification and resolution limited the axon visualisation.

Overall, human healthy and glaucomatous phase contrast ONHs showed a similar result where the cribriform plates of the LC were differentiated from the neuronal pores. These results confirmed the potential of XMT as a reliable cutting-free technique to investigate the microarchitecture of the ONH.

Contrast agents are often needed for visualisation of connective tissue (Campbell et al., 2015). However, XMT does not always require the application of contrast agents for conventional imaging that relies on x-ray absorption. In fact, in the current study, porcine ONHs datasets acquired with phase contrast (unstained) showed an adequate contrast to discriminate the connective from the neuronal pores. This result might be a key factor in future investigation of ONH biomechanics where contrast agents are not suitable as they might alter sclera and LC tissue mechanical properties (Campbell et al., 2015). Therefore, XMT poses a powerful tool to investigate the biomechanical properties of the ONH (Coudrillier et al., 2016).

The best differentiation of porcine ONH connective tissue was observed in ONHs stained with PTA in ethanol, confirming the suitability of PTA to enhance collagen using this technique. PTA is a common negative stain for biological tissues used in transmission electron microscopy. Tungsten binds to fibres of connective tissues such as collagen

(Malatesta, 2016) and it selectively binds to the basic group (lysine and arginine residues) of proteins (Jones, 1993, Höög et al., 2010), hence it is a good candidate to enhance the resolution of the collagen network. ONHs stained both with PTA in water and ethanol showed some tissue alteration and deformation, potentially due to the effects of ethanol in dehydrating the tissue.

Porcine ONHs stained with Lugol's iodine and tannic acid showed a suitable contrast to discriminate between neuronal pores and surrounding connective tissue, though not as effectively as with PTA-stained ONHs. Lugol's iodine is a small molecule compared to PTA and it is known to diffuse rapidly and deeply into fixed (Metscher, 2009a) and soft tissues (Degenhardt et al., 2010). Lugol's iodine has been used to enhance contrast in soft tissues (Metscher, 2009a) and specifically it has been shown to stain muscle and connective tissue fibres (Cox and Jeffery, 2011, Jeffery et al., 2011). Lugol's iodine solution, a form of inorganic iodine, binds to glycogen (Hur and Yachimski, 2019), which has been found in astrocytes of the rat ON, to sustain axons after glucose deprivation (Wender et al., 2000). No differences in PTA and Lugol's iodine penetration within the tissue were observed, indicating that in the ONH, different stains penetration was not a problem. No alterations were observed in Lugol's iodine stained ONHs, suggesting that the majority of shrinking and alteration are due to PTA and ethanol.

Tannic acid has been widely used as a mordant for electron microscopy experiments (Afzelius, 1992, Roholl et al., 1981, Tzaphlidou et al., 1992) to enhance the electron-density of EF, specifically the amorphous core (Damiano et al., 1979, Kageyama et al., 1985, Kajikawa et al., 1975, Ushiki and Murakumo, 1991). The exact mechanism of interaction between tannic acid and EF is unknown but Hayat (1981) has proposed two theories (Hayat, 1981). One possibility is the ionic interaction between carboxylate anions of tannic acid and cationic sites on the protein. The second possibility is a hydrogen bond occurring at alkaline pH which involves binding of anionic oxygen to cationic groups. In fact, Kageyama showed that the maximum tannic acid staining was achieved at pH range of 7-9 (Kageyama et al., 1985). ONHs stained with tannic showed a good discrimination of the LC connective tissue from the pores. However, EFs were not identified in the porcine LC, as shown in this chapter by TPEF imaging. Therefore, tannic acid might have not bonded to EFs and hence the good differentiation of the connective tissue observed in tannic acid stained ONHs is due to phase contrast imaging. No alteration

and/or tissue deformation were observed in phase contrast images suggesting that the tissue deformation observed in ONHs with contrast agents applied, is likely due to the staining. This is an important result as for biomechanical studies phase contrast images are required. Phase imaging can be the suitable tool to differentiate the connective tissue from neuronal pores in investigation into the biomechanics of the ONH.

In an attempt to visualise axons, a modified version of BROPA published by Mikula and Denk (2015) was performed. BROPA has previously enabled both myelinated and unmyelinated axons to be tracked preserving enough ultrastructure of the specimen for the chemical synapses and spines to be identified by SEM (Mikula and Denk, 2015). The protocol described by Mikula and Denk (2015) was modified to extend immersion times into different chemicals due to the larger size of the ONH sample. In the scans of BROPA stained ONHs, axons could not be identified within the LC pores due to the low magnification. The main contrast agent included into BROPA staining is osmium tetroxide, commonly used in electron microscopy (EM) (Palay et al., 1962, Porter and Kallman, 1953). Osmium tetroxide is a highly toxic contrast agent interacting with unsaturated lipids, sometimes also interacting with proteins (Hayat, 1981, Wigglesworth, 1975).

Additional chemicals in BROPA staining included pyrogallol and potassium hexaferrocyanate. The first has been shown to act as a bridging agent to bind additional osmium tetroxide in subsequent steps (Mikula and Denk, 2015). The second is a mild oxidising agent for functional groups and both chemicals have been proposed to improve the penetration of the osmium tetroxide into the sample (Mikula and Denk, 2015). BROPA stained ONHs showed interesting features, where both the connective tissue and pores appeared differently stained compared to the other stained ONHs. The connective tissue appeared black surrounding white/grey neuronal pores. The content of the pores appeared more defined in the BROPA stained ONHs compared to other contrasted ONHs, which could indicate that axons might have been, at least in part, stained. Due to sample movement during acquisition scans, dataset collection was not possible at 8x magnification and higher. Total magnification of 2.50x was not appropriate to discriminate axons or bundles of axons. Therefore, the approach presented requires further optimisation.

Phase contrast images acquired from control and glaucomatous human ONH showed adequate contrast to discriminate pores from the surrounding connective tissue. Low contrast was observed in the preL, where connective tissue was not present, compared to the LC and postL ON where the cribriform plates and the connective tissue septae, respectively, appeared clearly distinguishable from the neuronal pores.

4.4.2 Pores parameters within the glaucomatous ONH

Differences were observed in the LC in glaucomatous ONHs, where pores appeared elongated, oval-shape and less circular compared to controls.
In the healthy ONH, the LC appeared circular and no specific differences were observed between the anterior, mid and posterior LC. On the other hand, in glaucomatous ONHs, pores were more elongated in the anterior and mid LC, compared to the posterior, where pores seemed smaller but more circular.

Several studies has focused on the pore parameters (namely, shape, area and elongation) *in vivo* (Akagi et al., 2012, Fontana et al., 1998, Ivers et al., 2015, Miller and Quigley, 1988, Nadler et al., 2014, Omodaka et al., 2018, Shoji et al., 2017, Sredar et al., 2013, Tezel et al., 2004, Wang et al., 2013, Zwillinger et al., 2016) and *ex vivo* (Reynaud et al., 2016, Voorhees et al., 2017, Winkler et al., 2010). Previous studies (Akagi et al., 2012, Fontana et al., 1998, Ivers et al., 2015) measured pore area in μm^2, ranging from 1456 μm^2 to 3103 μm^2. Circularity, as a measure of pore elongation, correlated well with that presented in previous studies, which showed in both healthy and glaucomatous ONH, pore circularity of 0.83 (Fontana et al., 1998) and 2.38, respectively (Akagi et al., 2012). Pore count presented in the current chapter also correlated well, with values ranging from 168 to 292 average pore count (Jonas et al., 1991). As described in 2.4.3.1, pore count, area and circularity appeared to be an indicators of glaucomatous progression as previously proposed that pore elongation, for example, is significantly correlated with glaucoma progression, implying that pores become oval shaped and elongated at moderate stage of disease progression (Miller and Quigley, 1988).

Results of the analysis of pores in healthy and glaucoma correlated well with data presented in chapter 2, in SHG image datasets. Both techniques showed a significant decrease in pore count in glaucoma compared to controls [from 414.48 in healthy ONH

to 137.39 in advanced glaucoma (SHG) and from 102.28 in controls to 57.02 in glaucoma (XMT)]. Similarly, circularity, showed comparable values and a significant decrease [from 0.70 in healthy ONH to 0.68 in advanced glaucoma (SHG) and from 0.82 in controls to 0.72 in glaucoma (XMT)] in glaucoma compared to controls. Although, pore area significantly decreased in glaucomatous ONHs, compared to controls in XMT image datasets, but not with SHG, values of pore area were comparable between the two techniques.

4.4.3 Connective tissue content within glaucomatous ONH

Connective tissue content as a percentage of the segmented connective tissue pixel did not show any significant difference between glaucoma and controls. The variability and the changes observed between the results presented in the current chapter and the ones in chapter 2 could be due to the sample reconstruction. Chapter 2 presented a quantification of collagen content as a percentage of SHG pixels, which signal is known to raise from non-centrosymmetric molecules (Millard et al., 2005), such as collagen (Williams et al., 2005). On the contrary, XMT allowed a full 3D reconstruction without sample alignment. The latter can cause inaccuracy in the reconstruction, leading to a limited statistical confidence. Even though, results presented in the current chapters confirm the suitability of XMT to allow quantification of collagen content as a function of glaucoma progression.

Fibrillar collagen imaged with SHG and presented in chapter 2, showed strong signal in both the LC and ppsclera. Data presented in the current chapter, following XMT imaging, showed that PTA could represent a reliable substance to enhance collagen signal, although data presented herein has been collected on porcine ONH. Elastic fibres imaged with TPEF and presented in chapter 3 showed strong TPEF fluorescent signal in the elderly and glaucomatous ONH. Tannic acid, as known to enhance elastic fibre signal (Kageyama et al., 1985, Simmons and Avery, 1980), has been used to stain porcine ONHs, as presented in the current chapter. Additionally, TPEF images have also been collected from porcine ONH as shown herein and, interestingly, no TPEF-associated elastic fibres were observed. Therefore, it is not possible to discriminate if tannic acid can bind to elastic fibres and therefore increase its signal. Pores structure imaged with SHG, as shown in chapter 2, showed a good representation of the sieve-like structure of the LC

and SHG allowed the automatic segmentation of the pores throughout the ONH depth. In the current chapter, the porous structure of the LC was clearly visible only after staining within porcine ONH. Phase images did not show a clear enough discrimination of pores and connective tissue to allow automatic threshold segmentation. However, XMT imaging enabled the characterisation of the 3D structure of the human ONH without sectioning and therefore allowing the whole reconstruction of the ONH structure without the need of combining tissue sections.

4.5 Conclusion

The study has demonstrated the ability of XMT as a valuable technique to investigate the microarchitecture of the ONH. Different staining procedures were tested and successfully enabled the connective tissue to be clearly differentiated from axonal pores. This was also achievable by phase, which is a key result for future investigation of the biomechanics of the ONH where contrast agents could alter the mechanical behaviour of the tissue.

As collagen is the major connective tissue component within the ONH, PTA has been proposed as the optimal contrast agent to achieve decent differentiation between connective tissue and neuronal pores. This method has the potential to characterise age-related structural changes in the collagenous network of the ONH. BROPA stained ONHs presented interesting feature, however, more optimisation is required (i.e. higher resolution and magnification) to discriminate and count axons.

As a proof of concept, results from the analysis of the LC geometry and composition presented following SHG imaging (chapter 2) and those in the current chapter, correlated well suggesting that XMT could have the potential as a cutting-free technique which does not require full sample preparation, therefore no tissue sectioning and/or staining would be required.

4.6 Limitations

This work presented several limitations. Long scans may have initiated a dehydration process, especially after the removal of moist tissue paper. Tissue deformation and sample movements could be due to the dehydration which might alter the subsequent 3D reconstruction.

Although BROPA seemed to have stained parts of the ONH, it did not allow the count of the axons within neuronal pores, likely due to the lack of resolution required for axonal count. Due to the small size of each axon (~1 μm), a high magnification is also required to enable counts. Staining is essential for the observation of nerve axons and from previous studies, phase contrast microtomography did not allow the visualisation of axons (Coudrillier et al., 2016), which implies the necessity of some contrasting agent to enhance the axon signal. even though phase contrast imaging showed enough differentiation of the LC connective tissue from the pores, the contrast achieved was not good enough for thresholding segmentation of pores and connective tissue, therefore, the result presented for pores parameters cannot be considered as representation of the whole ONH. Further optimisations are required to increase the contrast of phase imaging without the use of contrasting agents.

The low contrast within phase imaging of human ONHs limited the segmentation of the full ONH volume, which did not allow the reconstruction of LC surface to determine LC thickness and volume. This limited the LC thickness measurements within representative optical slices and requires further improvements.

Sample movement appeared to be an issue throughout the experiment since did not allow to acquire scans at greater magnification. This limited the visualisation of the axons and further connective tissue investigation within the cribriform plates.

4.7 Future work

Optimised connective tissue parameters and phase will be used to investigate the LC microstructure in human glaucomatous versus age-matched control ONHs. As mentioned in the conclusion, a good contrast was also achieved by phase imaging which will be important to investigate the ONH biomechanics. Additionally, sample movement requires further optimisation to enable acquisition of scans at higher magnification.
However, as mentioned above, the contrast was not good enough for full segmentation, therefore further optimisations are required to increase phase contrast imaging to enable the segmentation of the full ONH volume.

Future work will include the development of inflation testing to mimic the increased IOP that occurs in glaucoma, similar to that described in Albon et al. 2000b, Midgett et al. 2017. In this experiment, the IOP will be increased and samples will be scanned before and after elevation to aid in understanding the behaviour and structure of the LC as a function of mechanical stress. As part of this experiment, LC parameters (e.g. thickness and backward displacement), connective tissue content (e.g. collagen and elastin) and pore parameters (count, area and circularity) will be investigated as a function of mechanical stress.

Future work will also include more optimisation of BROPA staining to achieve axon count within neuronal pores. This will include the establishment of an embedding protocol to stabilise the ONHs at higher magnification to minimise sample movement. Axon count will aid in understanding the relationship between pores and connective tissue as a function of glaucoma progression. Additionally, axonal count will aid in grading the stage of glaucoma based on the number of retinal ganglion cell axons.

Chapter 5 –An investigation into the optic nerve head connective tissue nanostructure using X-ray diffraction

5.1 Introduction

Studies have suggested that the mechanical influence of the surrounding ppsclera is particularly crucial (Eilaghi et al., 2010, Norman et al., 2010, Sigal, 2009, Sigal et al., 2009) and that ppsclera stiffness is a key factor in determining IOP-derived lamina cribrosa strain (Sigal et al., 2009). Mathematical modelling has suggested that thickness, shape and material properties of the sclera are all influential factors (Eilaghi et al., 2010, Norman et al., 2010, Sigal, 2009, Sigal et al., 2009). Therefore, investigation into ppsclera, as well as LC, connective tissue micro- and nanostructure and architecture is required for understanding their physiological behaviour and potential implications in glaucoma. As previous mentioned, the mechanical compliance of the LC appears to decrease with age (Albon et al., 2000b) and in glaucoma (Zeimer and Ogura, 1989).

It has been suggested that biomechanical properties of collagenous tissues, such as the cornea, are significantly influenced by the fibrils that form the bulk of the corneal stroma (Meek, 2009). In fact, fibril diameter (Cintron et al., 1973, Kamma-Lorger et al., 2010, Rawe et al., 1994) and interfibrillar spacing (Cintron et al., 1973, Rawe et al., 1994) of stromal fibrils are altered after injury and changes persist in the long-term at the wound margin (Dawson et al., 2005, Hayes et al., 2010, Melles and Binder, 1990). It has been therefore proposed that some of these changes might be related to the observation that the mechanical strength of the corneal scar tissue does not ever fully recover (Steele, 2009). Additionally, changes in collagen fibril orientation have been proposed to influence corneal biomechanics and compromise its function (Boote et al., 2013).

X ray diffraction has been used to investigate collagen structure at the nanoscale level in ocular tissues, such as cornea collagen (Sayers et al., 1982, Meek and Quantock, 2001, Meek and Leonard, 1993, Meek and Boote, 2009, Meek et al., 1987, Boote et al., 2003, Pijanka et al., 2013, Pijanka et al., 2012, Coudrillier et al., 2015, Bell et al., 2018), human sclera (Quantock and Meek, 1988), ppsclera (Pijanka et al. 2012, Pijanka et al., 2013) and lens crystallins (Regini et al., 2004). Additionally, optic nerve myelin (Chandross et al., 1978, Schmitt et al., 1935, Schmitt et al., 1941), elastin (Ali et al., 2004, Serafini-

Fracassini and Field, 1977) and lipids (Winlove et al., 2004) have been studied. In this chapter, collagen and elastin nanostructure will be investigated in the LC and ppsclera using this technique.

When a focused beam of X-ray is passed through a collagenous structure such as the cornea or the sclera, some of it is scattered. The interference effects of the scattered waves produce a fibre diffraction pattern, or X-ray scatter pattern (figure 5.1) (Meek and Boote, 2009). The wide-angle and small angle patterns are recorded when X-rays are scattered at large and small angles respectively (Meek and Quantock, 2001). Small-angle scattering (SAXS) arises from interference of scattered light from collagen at the fibrillar level (figure 5.2a), while wide-angle scattering (WAXS) occurs from the collagen molecules making up the fibrils (figure 5.2b). The meridional X-ray scatter pattern arises when the beam is scattered parallel to the fibre axis, originating from the D period of the axial packaging of collagen (see section 1.2.2.1.1). X-ray scattering at different angles gives rise to the equatorial reflections, which originate from the lateral packing of collagen (Meek and Boote, 2009, Meek and Quantock, 2001).

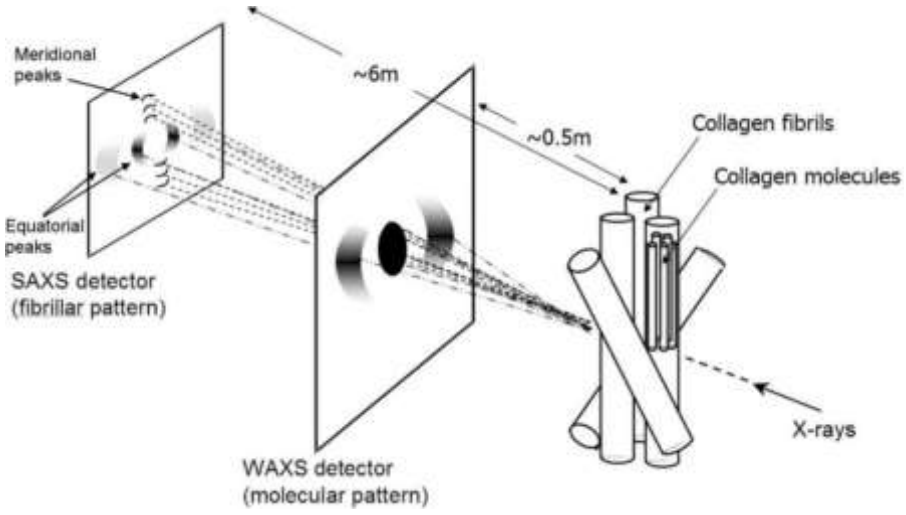

Figure 5.1. Schematic representation of X ray scattering. Small angle (SAXS) and wide angle (WAXS) x ray scattering is produced simultaneously. The collection of SAXS or WAXS data is dependent on the detector-sample distance, which is in the order of metres and millimetres for SAXS and WAXS, respectively. Equatorial SAXS reflections, arising from the lateral spacing of collagen fibrils, provides information on the interfibrillar spacing and fibril diameters. Meridional reflections, arising from the axial staggering of collagen fibrils, provide information on the D period (67 nm). Equatorial and meridional reflections of WAXS patterns are derived from the lateral packing of collagen molecules within the fibril and give rise to intermolecular Bragg spacing and distance between amino acid residues. Copied from (Quantock et al., 2015) and reprinted with permission from Elsevier Limited (see appendix IV.11).

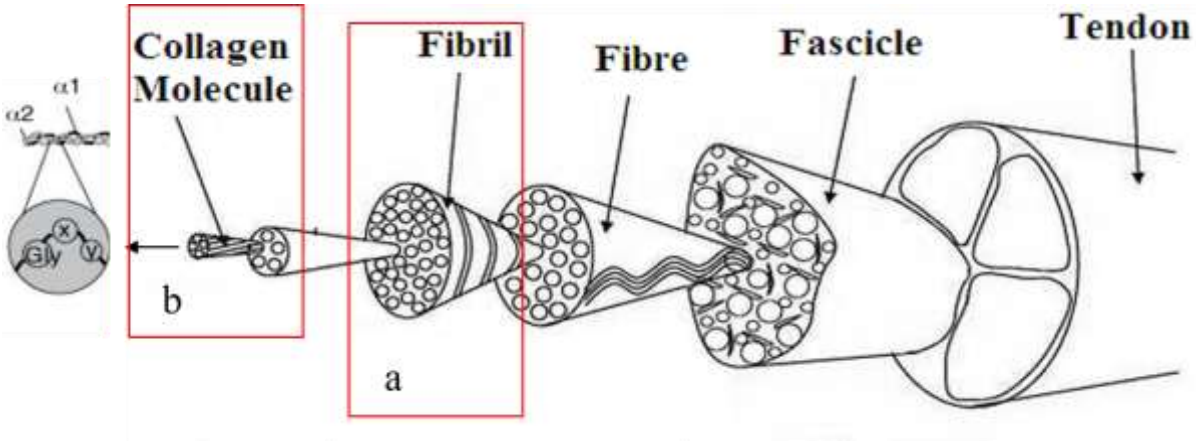

Figure 5.2. Schematic illustration of the hierarchical structure of collagen within a tendon. SAXS and WAXS allow the quantification of fibrillar collagen parameters (a) and molecular parameters (b), respectively. Note ONH collagen fibrils do not assemble into fascicles. Copied, adapted and reprinted from (Kannus, 2000) with permission from John Wiley and Sons Limited (see appendix IV.12).

In this chapter, SAXS and WAXS were performed, with the aim to investigate the nanostructure of collagen and elastin within the ONH's ppsclera and LC. To date, as far as this author is aware, no studies have previously characterised the nanostructure of the ONH using simultaneous SAXS and WAXS data acquisition. The hypothesis tested in this chapter was that ONH, ppsclera and LC, connective tissue nanostructure changes as a function of age. Since age is an important risk factor in glaucoma, any changes in ONH collagen and/or elastin nanostructure would likely contribute to changes in mechanical properties.

To achieve this, the objectives of this study were to:

1. identify ONH collagen and elastin using SAXS and WAXS and determine their distribution within the human ppsclera and LC.
2. quantify collagen parameters (fibril diameter, interfibrillar Bragg spacing, D periodicity) in the ppsclera and LC, and determine if they alter with age
3. quantify collagen molecular parameters (intermolecular Bragg spacing, distance between amino acids residues) in the ppscleara and LC, and determine if they alter with age

4. determine the effect of radial stretch on ONH collagen and/or elastin nanostructure

5.2 Materials and methods

5.2.1 Source of tissue

Fourteen human paired eye globes (aged 22 to 85 years) were received from the Filton Eye Bank (NHSBT, Filton, UK) in moist tissue chamber. Twelve were immersion fixed in 4% PFA as described in section 2.2.1, and stored at 4°C, and two were snap frozen and stored at -80 °C until needed.

Rat aorta (RTA) containing EF (Keech, 1960, O'Connell et al., 2008) and RTT, rich in collagen type I (Rowe, 1985) were harvested from Wistar rats as described in 3.2.1. Purified elastin preparations (i.e. digested preparations of bovine nuchal ligament and porcine ear) prepared as described in section 3.2.1. Additionally, two porcine ONHs were received from the local abattoir and processed as described in section 4.2.1.

5.2.2 Sample preparation

ONHs from globes were oriented and 250 μm longitudinal (LS) sections were cut as described in sections 2.2.2. 250 μm sections of RTA, bovine nuchal ligament and porcine ear (purified elastin tissue preparations) were also cut. The sections were then carefully wrapped in cling film, labelled and stored at -80° C. The RTA, bovine nuchal ligament and porcine ear (Helliwell et al., 2017, Morocutti et al., 1991, Turner et al., 2015) sections provided elastin positive controls, since very few studies on SAXS and WAXS of elastin exist (Ali et al., 2004, Gotte and Serafini-Fracassini, 1963, Serafini-Fracassini and Field, 1977). Hydrated RTT was dissected from fresh rat tail, collagen bundles removed, wrapped in cling film and stored at -20° C until experiment.

5.2.3 Data collection

Small angle (SAXS) and wide angle (WAXS) x ray scattering were simultaneously collected on beamline I22 (figure 5.3) at the Diamond Light Source (Didcot, Oxfordshire, UK). Data was collected with a PILATUS 2M and PILATUS 3-2M-L detectors for SAXS and WAXS, respectively.

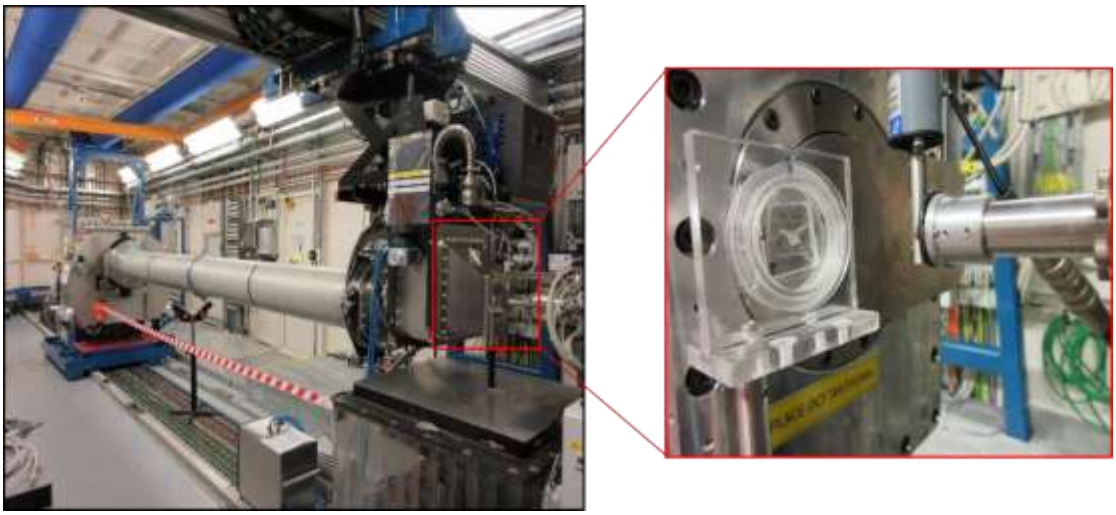

Figure 5.3. Experimental set up for simultaneous collection of SAXS and WAXS on station I22. The sample (red square) was positioned at 6.75 m from the detector (distance detector-sample) for SAXS and at 0.4 m for WAXS acquisition. The red box inset shows where the sample holder is placed in the beam path.

First, the alignment of the specimen was achieved by exposing x ray sensitive film within the sample holder to the beam path to locate incident beam position. Beam centre position was calculated by exposing silver behenate powder to x ray. This was used to calculate beam centre in both SAXS and WAXS data.

Data from human ONH sections was collected using a x ray beam of λ 0.1 nm (150 x 350 μm in size), in raster scans, at 500 μm intervals, using 10 or 5 seconds exposure times over areas up to 8 mm (horizontal) x 8 mm (vertical), as required to incorporate whole tissue sample. Sample-detector distance was 6.75 m or 0.4 m for SAXS and WAXS respectively. A lead beam-stop was positioned between the detector and sample to block the high intensity beam from hitting the detector. This was repeated for SAXS and WAXS data acquisition in RTT, RTA, bovine nuchal ligament and porcine ear skin, over a 2 mm (horizontal) x 2 mm (vertical) area.

SAXS and WAXS patterns were acquired through four beamtime experiments. For data collection, individual sections wrapped in cling film were placed into sealed Perspex (Lucite Group Ltd, Southampton, UK) chambers with Mylar (DuPont-Teijin, Middlesbrough, UK) windows (figure 5.4). Single data patterns of the empty chamber (Mylar only) were also acquired and used in data processing to remove non-sample background.

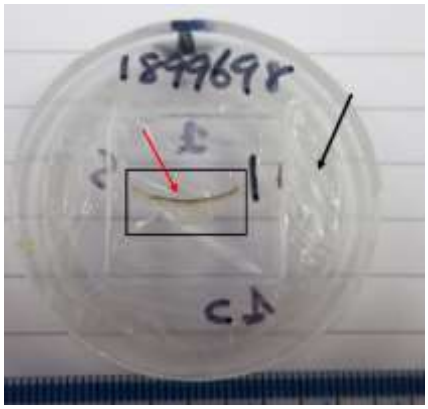

Figure 5.4. Custom made Perspex/Mylar sample holder. The tissue section (red arrow), wrapped in cling film, to prevent dehydration was mounted within a sample holder in between Mylar sheets (black arrow).

5.2.4 Small angle x ray scattering in human ONH

Each SAXS pattern (an individual scan point) was saved as a nexus (.nxs) file under its scan number. Each ONH dataset was opened with DAWN data analysis software (Basham et al., 2015, Filik et al., 2017) version 2.13. Montages of scatter patterns from a raster scan of an ONH were created using the DAWN "Stich" plugin, (see figure 5.5a). This enabled selection of scatter pattern within the LC (figure 5.5b), RoIns (figure 5.5e) or ppsclera (figure 5.5c) and postL ON (figure 5.5d). Collagen meridional reflections (figure 5.5c) and equatorial (figure 5.5c) were identified in the ppsclera, however, these were not observed in the LC Additionally, two circular reflections associated to myelin (figure 5.5d) and a faded arced reflection, likely elastin (figure 5.5e) were identified.

5.2.5 Quantification of fibrillar collagen parameters

Collagen fibril diameter, interfibrillar Bragg spacing and D period were quantified from SAXS data derived from fibril transform (FT), interference function (IF) (Oster & Riley, 1952, Meek & Quantock, 2001) and axial staggering of collagen, respectively, in both longitudinal (LS) and transverse (TS) ONH sections. Interference function and fibril transform arising from equatorial reflections, derived from the ordered lateral arrangement of collagen, contain information related to the interfibrillar Bragg spacing and and the fibril diameter, respectively. D period can be calculated from meridional

reflections; it is representative of the orders of 67 nm quarter stagger axial molecular spacing (Meek and Boote, 2009, Meek and Quantock, 2001).

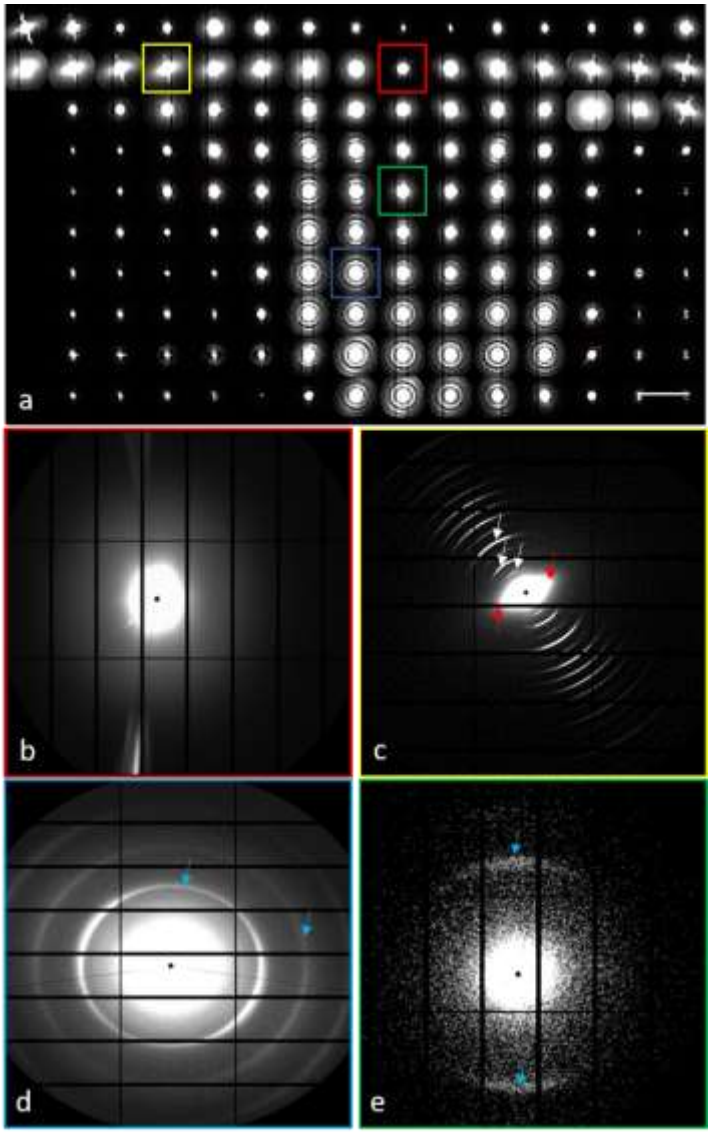

Figure 5.5. Panel of SAXS patterns identified in LS ONH sections at different levels. A montage (a) of SAXS patterns illustrating color-coded reflections from the LC (b), ppsclera (c), postL ON (d) and RoIns (e). After background removal equatorial (c, red arrow) and meridional (c, white arrows) were identified in the ppsclera. Note the absence of collagen derived reflections in the LC scatter pattern (b). Additionally, reflections associated to myelin (d, blue arrows) and elastin (e, blue arrows) were identified in the ON and RoIns respectively. Scale bar represents 500 μm.

5.2.5.1 Background subtraction and intensity plots

Raw nexus files were imported into DAWN data analysis software (Basham et al., 2015, Filik et al., 2017) and the "Subtract frame" plugin was used to batch subtract background scatter (within the empty sample holder) from all datasets .

Next, 1D X-ray intensity profiles of 2D scatter patterns were created along a line through the centre of a 2D scatter pattern as shown in figure 5.6. The "Radial profile" plugin (radial integration) was applied to create 1D plot.

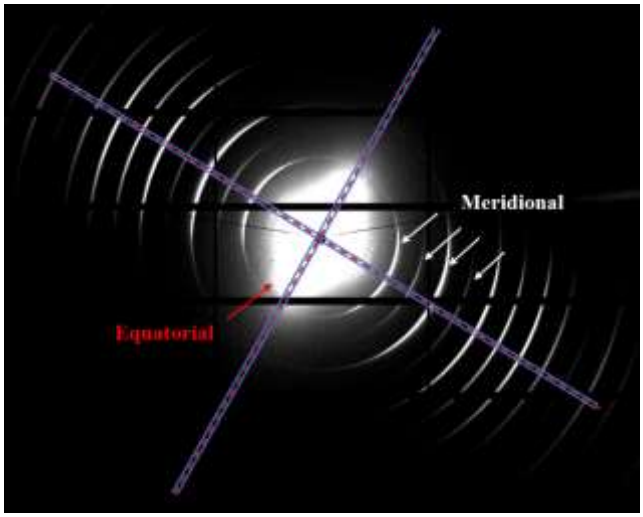

Figure 5.6. Typical SAXS pattern associated to fibrillar collagen. The intensity profiles were measured through a radial profile which incorporates both equatorial and meridional reflections. Radial lines were drawn on the SAXS patters through the centre of the patter and perpendicular to each other's.

5.2.5.2 Calibrant

Hydrated RTT (mainly type I collagen) was used as a calibrant for SAXS pattern positions (Grynpas, 1977) as it produces meridional Bragg reflections (figure 5.7a), in the orders of 67nm (Tomlin and Worthington, 1956, Folkhard et al., 1987, Fraser and MacRae, 1981), a result of the quarter stagger axial molecular spacing. 1D profile plots of RTT meridional diffraction patterns were generated in DAWN (figure 5.7b).

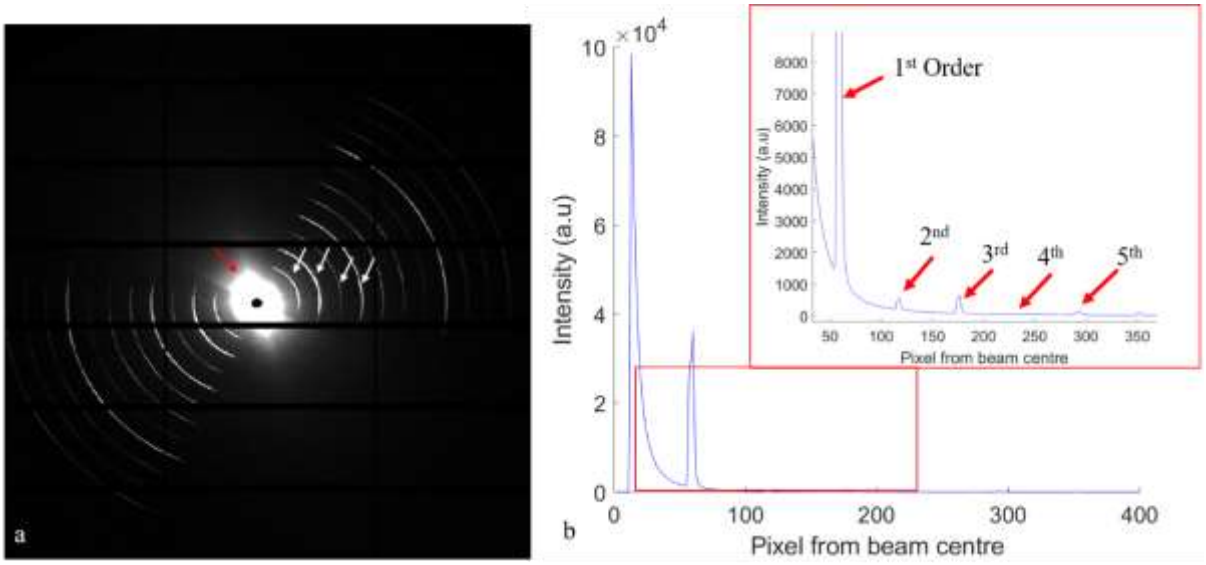

Figure 5.7. Typical SAXS pattern (a) and intensity 1D plot (b) of RTT. Note the orders of meridional reflections of RTT collagen (a, white arrows point to the 2nd, 3rd, 4th and 5th orders). Equatorial reflections were also identified (a, red arrow). Note that 1st order meridional reflection is obscured by the high intensity flare of the beam. 1D plot of intensity (b) shows peaks related to 1st, 2nd, 3rd, 4th and 5th orders of collagen.

5.2.5.3 Calibration of peaks position using rat tail tendon

The positions of intensity peaks of interest were converted from pixel number to distance in real space (nm) using:

$$\frac{1st\ order\ meridional\ position\ of\ calibrant\ (pixels) \times D\ spacing\ of\ calibrant\ (nm)}{position\ of\ data\ peak\ (pixels)}$$

The pixel number was inversely related to the distance in nm (i.e. the distance becomes smaller with progressing distance from beam centre). Intensity profiles were plotted against scattering vector, *Q*, which represents the structure (distance) in reciprocal space and it is expressed as:

$$Q = \frac{2\pi}{d}$$

Where:

d = the position of the data peak (nm)

Q = the length of the scattering vector (nm^{-1})

5.2.5.4 Calculation of collagen fibril parameters

Collagen fibril diameter, axial period and interfibrillar Bragg spacing, were quantified from SAXS data. Initially, to detect SAXS signal and to determine regional variation in collagen parameters, these were analysed and quantified in SAXS reflections (n=6) acquired from regions (superior, inferior, temporal and nasal) of each pair of LS tissue sections (n=8) from elderly ONHs (n=4). Meridional and equatorial (figure 5.8a) reflections of a SAXS profile from the ppsclera with radial intensity profile revealed a peak associated to interfibrillar Bragg spacing (figure 5.8b). However, the fibril diameter peak was obscured by the third order of meridional reflection (figure 5.8b). Next, fibrillar collagen parameters were quantified within the ageing ppsclera (from 22 to 85 years), and regionally, from 24 ONH tissue sections.

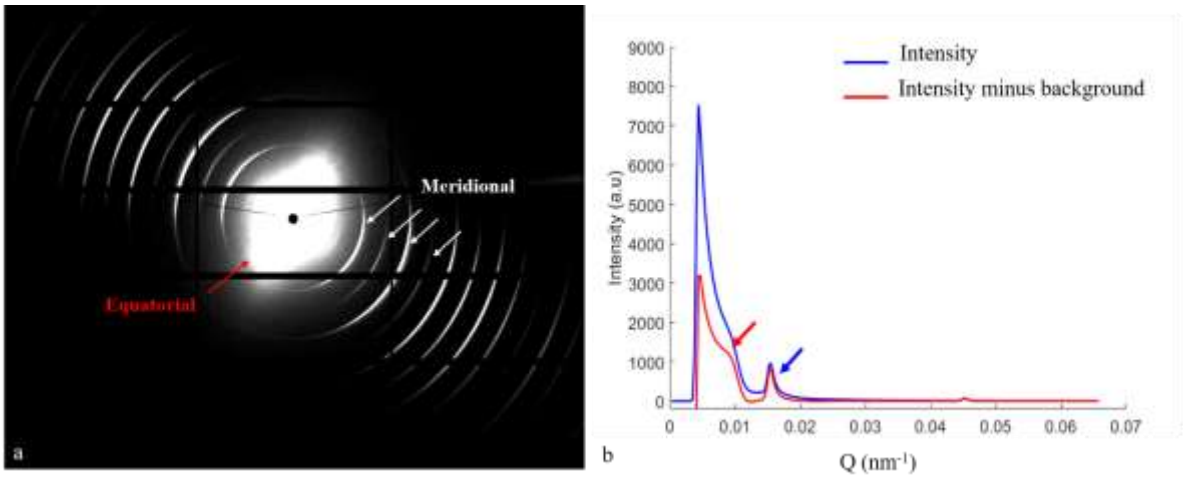

Figure 5.8. Typical SAXS pattern derived from fibrillar collagen in the human ppsclera. The scatter pattern (a) showed equatorial (red arrow) and meridional (white arrows) reflections. After radial profile was applied, a 1D plot was obtained as shown in b. Intensity profile of collagen is obtained before background subtraction (b, blue line). After background subtraction of scatter not associated to collagen, an intensity profile as shown in b, red line is obtained. After background subtraction, the interfibrillar Bragg spacing appeared more defined (b, red arrow). Note the first order meridional reflection (b, blue arrow).

5.2.5.4.1 D period

The positions of intensity peaks of meridional reflections to calculate D period were transformed from pixel number to distance in nm using the equation in 5.2.5.3.

5.2.5.4.2 Fibril transforms

The scattering of a single fibril is given by F2 and takes the form of the Bessel function of first kind where the position of the first subsidiary maximum (second peak) is related to the fibril diameter. Therefore, the position of the second peak of Bessel function was used to fit the Fibril Transform (FT), because this peak derives entirely from the FT with no contribution from the Interference Function (IF). As the fibril transform maximum is close to the third order of collagen meridional reflection (Meek and Quantock, 2001), the FT peak was fitted using an FT mathematical model, based on a first order Bessel function (Meek and Quantock, 2001) (figure 5.9). The fibril diameter (2r) can be calculated using equation:

$$2r = \frac{5.14}{(Q \times \pi)}$$

Where

2r = Fibril diameter (nm)

5.14 = numerical factor defined by the position of the first maximum of the Bessel function (Meek and Quantock, 2001, Oster and Riley, 1952, Worthington and Inouye, 1985)

Q = Reciprocal space position of the first subsidiary maximum (nm^{-1})

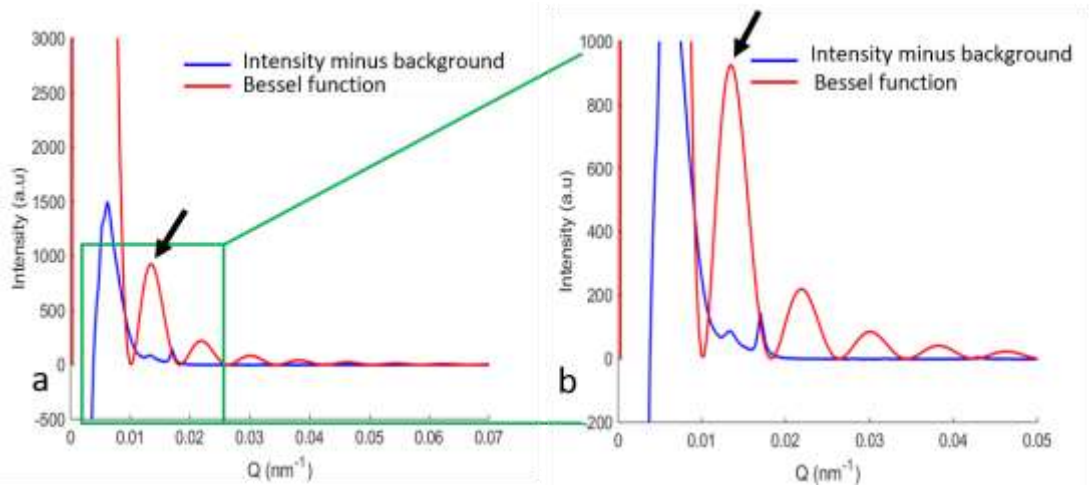

Figure 5.9. Bessel function fitting on FT peak from human ppsclera. The FT peak (a) (a closer view is shown in b) has the maximum near the third order of collagen meridional reflection. The second peak of Bessel function was used to fit the FT peak allowing a better visualisation and measure of the peak position. The black arrows in a,b point to the second peak of Bessel function used to fit the FT peak position of ppsclera.

Therefore, the position of the first subsidiary peak (second peak) of the Bessel function (figure 5.9a,b) was used to calculate the FT, without contribution from IF (Boote et al., 2003), by inserting the peak position into the equation above. All peak positions were measured with the DAWN "peak fitting" tool in Q (nm^{-1}), which determines the position of the highest point.

5.2.5.4.3 Interference function

To determine IF peak position, a baseline subtracted approach with a pseudo Voigt fitting was performed in DAWN. The "Baseline" plugin was applied to the ONH 1D intensity plots. Briefly, the peak was selected using the "Find peak" tool and a pseudo-Voigt profile (like a Gaussian curve) was fit to the IF. The peak position in Q was converted into nanometres (real space) by taking the reciprocal:

$$\text{IF (nm)} = \frac{1}{Q}$$

5.2.5.5 Myelin SAXS reflections in the human ONH

SAXS diffraction patterns attributed to myelin (Karthigasan and Kirschner, 1988, Kim et al., 2015) were identified within each LS postL ON section (figure 5.10a). Peaks position in pixel (figure 5.10b) of myelin reflection were converted into real space using hydrated RTT as the calibrant as described in section 5.2.5.3.

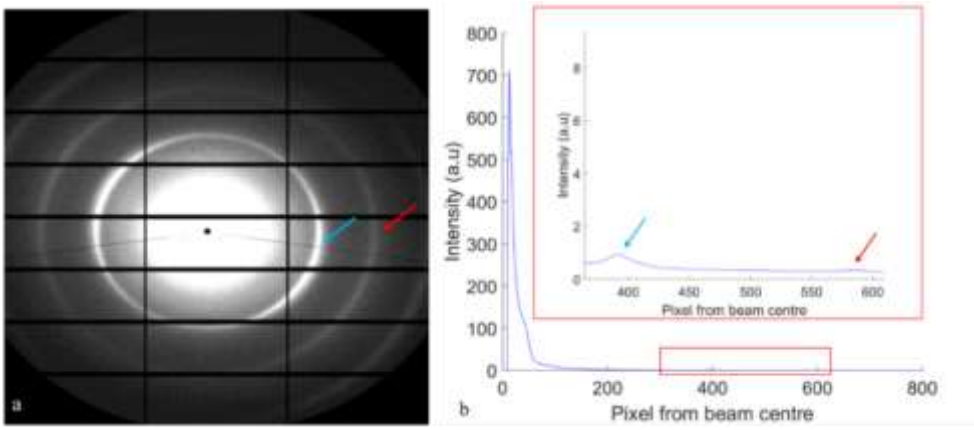

Figure 5.10. Typical SAXS pattern found in the human postL ON. In the scatter pattern (a) the inner (blue arrow) and outer (red arrow) ring distance were measured and 1D plot (b) created. Peak position in pixel of inner (b, blue arrow) and outer (b, red arrow) were converted into real space (nm) using the 1st order peak position of calibrant (RTT).

5.2.6 Wide angle x ray scattering in human ONH

Each WAXS pattern at an individual scan point was saved as nexus (.nxs) file under the scan number. An ONH raster scan dataset was imported into DAWN and montages were created as described in section 5.2.4. A representative montage of the ONH with scatter patterns originating from different locations is shown in figure 5.11. A montage of ONH patterns (figure 5.11a) shows ppsclera scatter patterns before (figure 5.11b) and after background removal (figure 5.11c), and elastin WAXS reflections (diffuse ring) (Ali et al., 2004, Serafini-Fracassini and Field, 1977) from the CRA (figure 5.11d) and the RoIns (figure 5.11e). Collagen meridional (figure 5.11c) and equatorial (figure 5.11c) reflections were identified in the ppsclera.

5.2.7 Quantification of collagen molecular parameters

Intermolecular Bragg spacing and distance between amino acid residues were quantified from WAXS data derived from equatorial and meridional reflections, respectively. WAXS meridional and equatorial reflections arise from the spacing between consecutive molecule amino acids and the lateral spacing between adjacent collagen molecules within fibrils (Meek et al., 1991).

5.2.7.1 Background subtraction and intensity plots

Raw nexus files were imported into DAWN, background subtracted and 1D profile created as described in section 5.2.5.1.

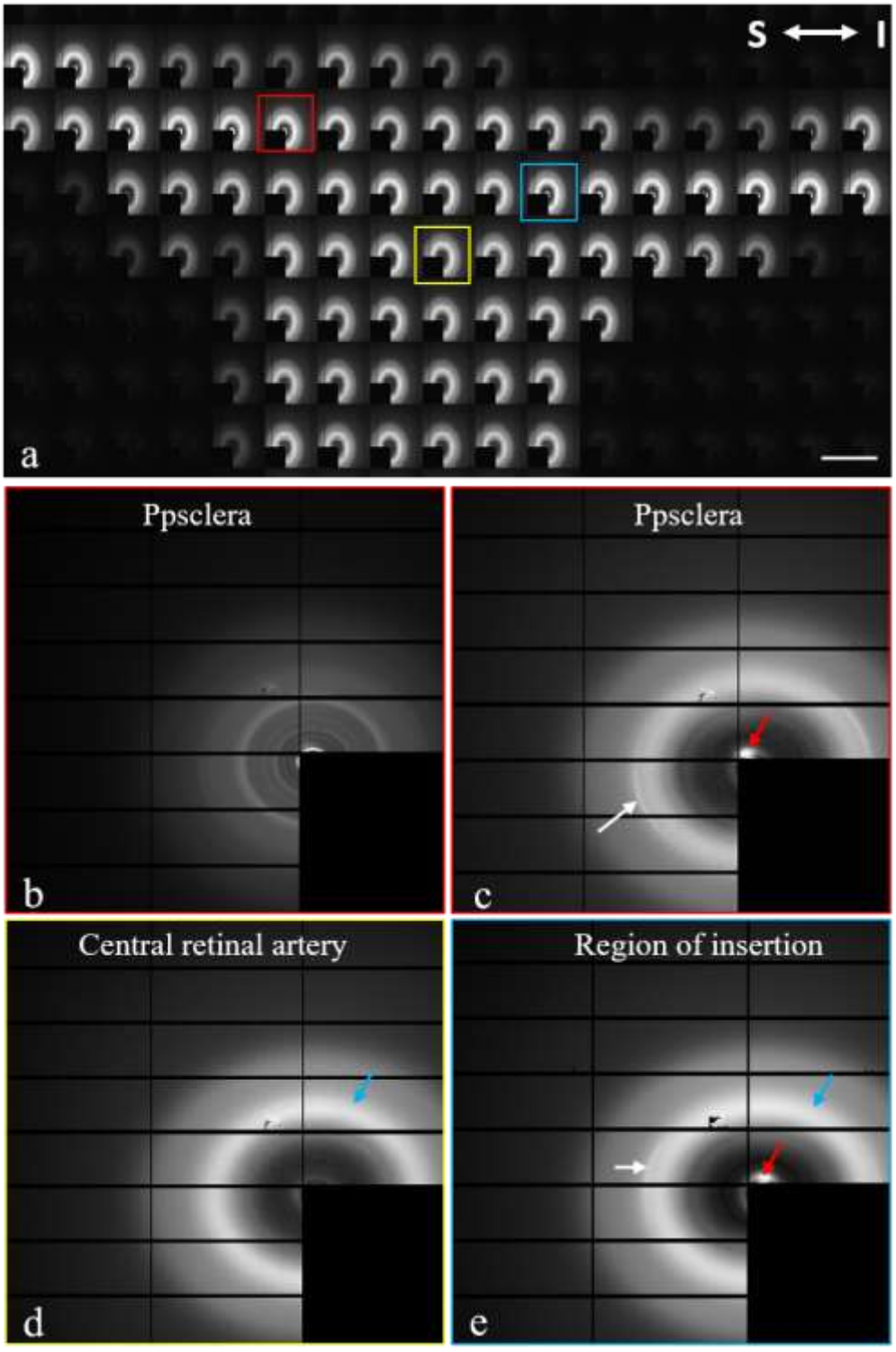

Figure 5.11. WAXS patterns identified in LS ONH. A montage (a) of WAXS patterns illustrating color-coded locations of reflections from the ppsclera before (b) and after (c) background removal showing equatorial (c, red arrow) and meridional (c, white arrows) reflections. Additionally, reflections associated to elastin within the ONH CRA (d, blue arrows) and RoIns (e, blue arrows) were identified. Scale bar represents 500 μm.

5.2.7.2 Calibrant

To calibrate the WAXS scatter pattern positions produced from ONH tissue sections, silicon powder (previously characterised distances for orders of reflections; first order at 0.314 nm; ~330 pixel distance from beam centre) (Jesche et al., 2016) was subjected to WAXS as described in section 5.2.3 (figure 5.12a). Silicon powder produced a well-defined order of rings (figure 5.12a), from which a 1D intensity profile was created in DAWN and the first peak position was determined using the "Find peak" tool (figure 5.12b).

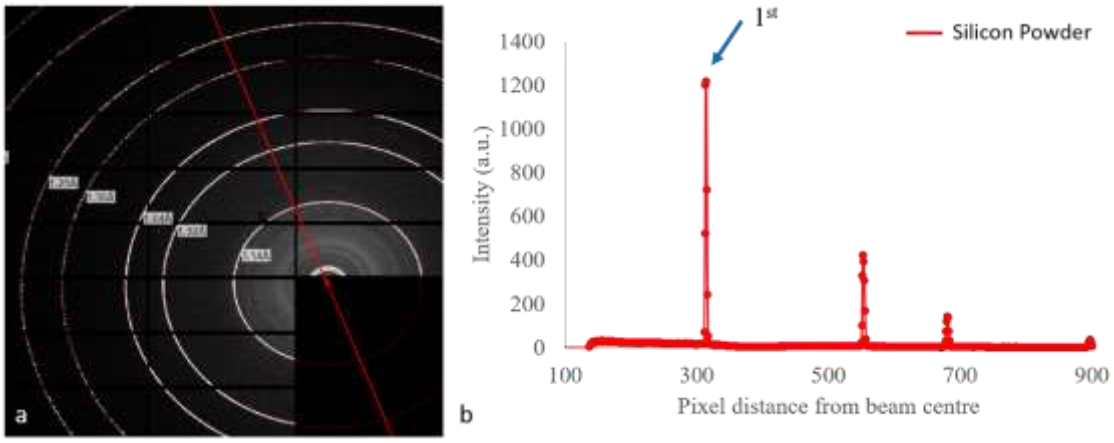

Figure 5.12. Silicon powder WAXS pattern (a) used as a calibrant for WAXS collagen molecular parameters calibration. 1D plot (b) showing the first order of ring at 0.314nm (b, blue arrow).

5.2.7.3 Calculation of collagen molecular parameters

Intermolecular Bragg spacing and distance between amino acid residues were quantified from WAXS reflections (n=6 per region per ONH) to determine regional (superior, inferior, temporal and nasal) variation within LS section as described in 5.2.5.4. Molecular parameters were analysed within the ageing ppsclera as in 5.2.5.4.

5.2.7.3.1 Intermolecular Bragg spacing and distance between amino acid residues

Peak positions (in pixels) of silicon powder and ONH collagen were imported in the following formula to calculate the intermolecular Bragg spacing (IMS) and distance between amino acid residues:

$$IMS = \frac{\lambda}{\sin\left(\tan^{-1}\left[\frac{\mathrm{Rscl}}{\mathrm{Rcal}}\tan\left(2\sin^{-1}(\lambda/2\mathrm{d})\right)\right]\right)}$$

Where

IMS = Intermolecular Bragg spacing

λ = 0.1 nm is the wavelength of the x ray beam

Rscl = pixel position of the scleral collagen

Rca = pixel position of the calibrant (silicon)

5.2.7.4 Elastin WAXS diffraction patterns

Elastin-derived WAXS diffraction patterns (figure 5.13a) were also characterised from each LS ONH. Peak position in pixels (figure 5.13b) of the outer edge of the reflection was imported into the equation described in 5.2.7.3.1, using silicon powder as the calibrant (see section 5.2.7.2).

.

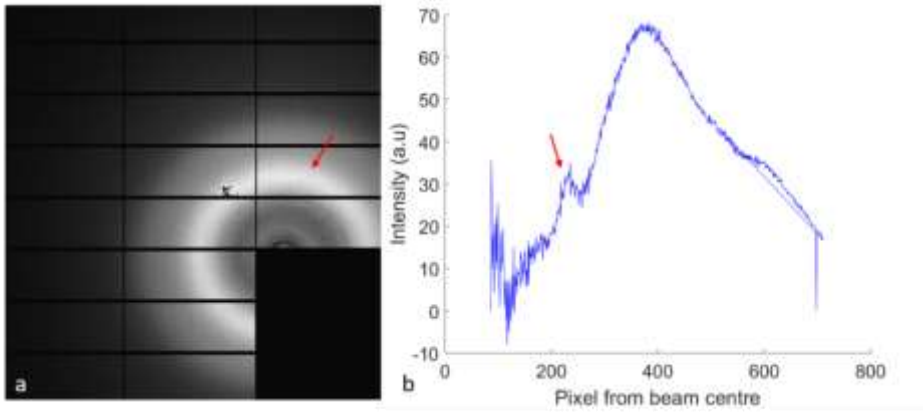

Figure 5.13. Typical elastin WAXS pattern within human ppsclera. Scatter patterns (a) were found at all ages in the ppsclera where the ring (a, red arrow) distance was measured and 1D plot (b) created. Peak position of elastin ring (b, red arrow) was imported into equation showed in section 5.2.7.3.1 to convert pixel number into real space (nm).

5.2.8 SAXS and WAXS data in PTA stained human ONH

Since fibrillar collagen-derived SAXS scatter patterns were not visible in the LC, in an attempt to enhance fibrillar collagen scatter signals, ONH sections from four eye globes were immersed in 2% phosphotungstic acid (PTA; used in electron microscopy for connective tissue enhancement) (Descamps et al., 2014, Disney et al., 2017, Metscher,

2009). In brief, four human ONHs, aged 46, 47, 62 and 84 years, were cut transversely in 100μm sections, immersed in 2% PTA (Sigma-Aldrich, UK; weight/volume in distilled water) for 20 minutes, then rinsed thrice in 5-minute washes in PBS. Sections were wrapped in cling film and subjected to SAXS-WAXS on i22 at Diamond synchrotron, as described above in 5.2.3.
Additionally, the same sections were subjected to second harmonic generation (SHG) microscopy (described in section 2.2.3) for the allocation of SAXS diffraction patterns in the LC and ppsclera.

Each SAXS and WAXS pattern from PTA-stained ONHs were saved as .nxs file and montages created as described in section 5.2.4. SAXS and WAXS analysis was also performed in PTA-stained ONH section as described above in 5.2.5 and 5.2.6, respectively. Regional analysis was performed as detailed below.

In order to quantify SAXS and WAXS collagenous parameters within LC regions, montages (figure 5.14a) were rescaled to match the size of SHG images. Both images were imported into MATLAB separately and SHG image was made semi-transparent (figure 5.14b). A numbered grid was created into Excel, relating to the horizontal or vertical raster scan of the SAXS and WAXS montage, saved as .png image and imported into MATLAB. This grid was made semi-transparent and overlapped to the already imported SHG and SAXS and WAXS montage. The grid position was adjusted so that position number 1 was at the top left corner and each SAXS and WAXS diffraction pattern corresponded to a number (figure 5.14c). Finally, a grid containing twelve sectors was created using a custom-made macro in Image J, named *ONH_seg* (figure 5.14d) as described in section 2.2.6.2. The SAXS and WAXS frames numbers that fell into the superior, inferior, nasal and temporal regions (n=6 patterns per region) as well as inner/outer ON canal were analysed.

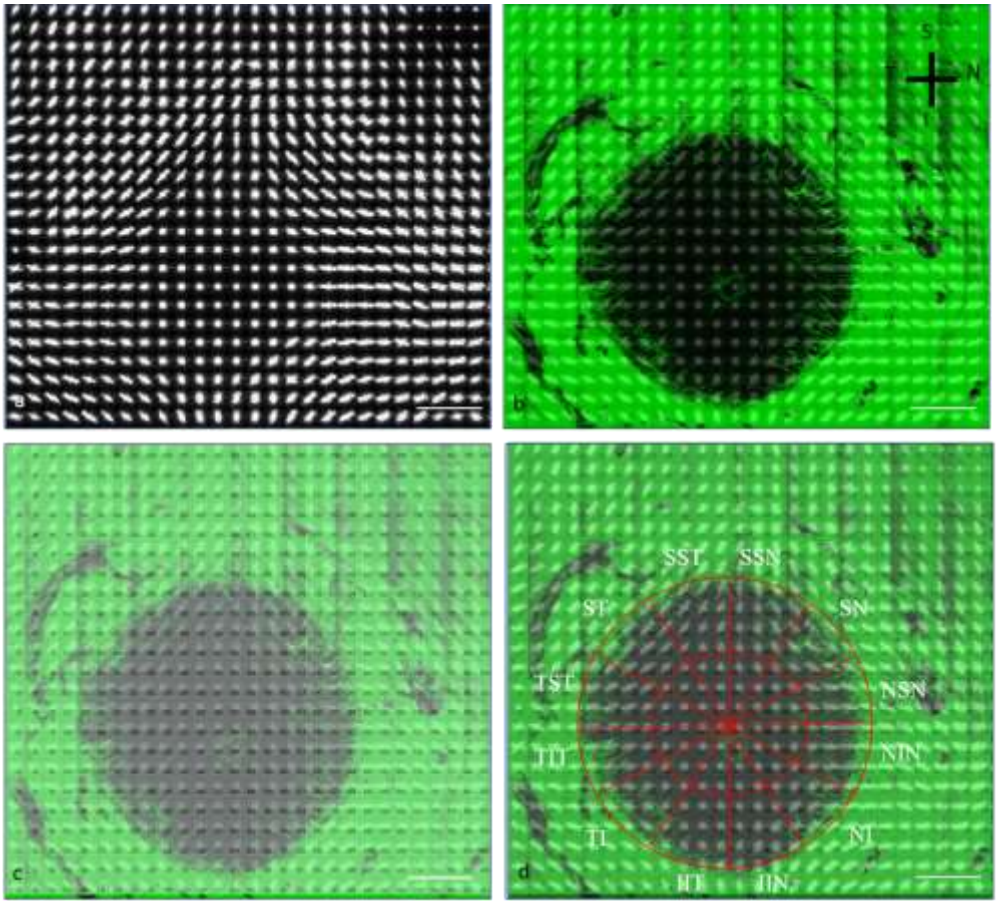

Figure 5.14. SAXS and WAXS data analysis of LC sections from PTA-stained ONHs. Montage of SAXS diffraction patterns (a) was overlapped with the corresponding SHG image (b), scan exposure numbers (c) and ROI grid (d) showing LC regions (i.e. superior, inferior, nasal and temporal) and inner/outer sectors of the ON canal. Data between sectors were excluded from analysis to avoid overlapping. Scale bar represents 200 μm.

5.2.9 Effects of radial stretch on collagen fibril and molecular parameters

Two porcine and two human ONHs (aged 60yr and 67yr) were subjected to SAXS and WAXS (low sample number due to beamtime constraints), as described in section 5.2.3. To simulate the scleral strain effect on the LC, proposed to occur in glaucomatous ONHs, porcine and human ONHs were inserted into a stretcher device and subjected to radial strain (figure 5.15)

To do this, the sclera surrounding the ONH (following dissection) was cut at 4 different points to produce a flat half-globe to fit within the stretcher (figure 5.15a). The ON was cut as close as possible to the scleral coat to remove postL ON. A gel-based super glue was applied to a BIONIKO manual lens stretcher (Bioniko Instruments, Arizona, USA)

in the un-stretched position for scleral attachment to the stretcher metal pins (figure 5.15b). Once glued properly, the sclera between pins was cut to enable (as much as possible) uniform radial stretch around the ONH. The ONH was moistened with PBS drops. Before mounting the stretcher onto the sample holder, preconditioning was performed prior to scanning in an attempt to restore tissue microstructure to normal state. The latter included three separate cycles of 10 minutes stretch, and 5 minutes relaxation. The tissue was placed in the relaxed position, wrapped in cling film to prevent dehydration and mounted onto sample holder and raster scanned as described in section 5.2.3. Without dismounting the device, the tissue was stretched, left to acclimatise for 10 minutes and rescanned.

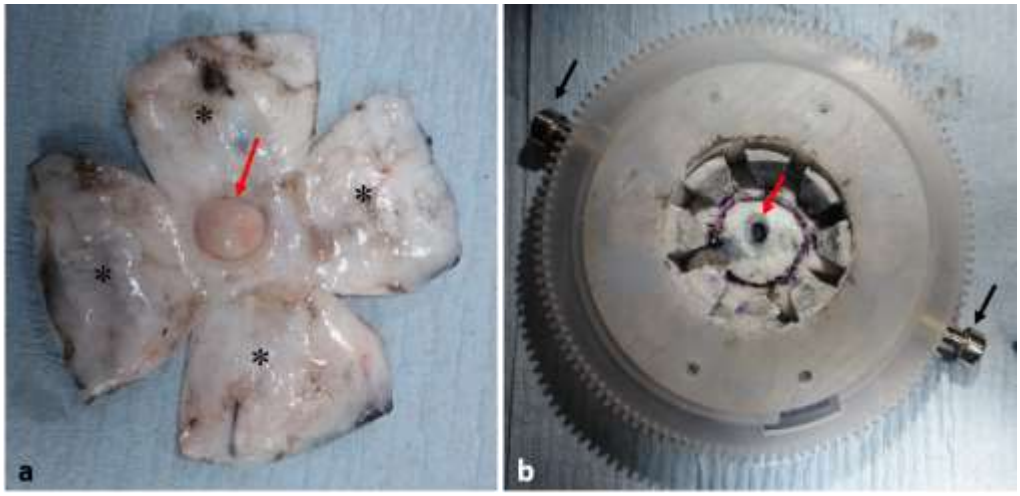

Figure 5.15. Porcine half globe mounted onto the stretcher device. Porcine globes were cleaned of the muscles and tendons and the sclera was cut at 4 points (a, asterisks) to flatten the half-globe for mounting in the device. The BIONIKO stretcher device (b) (Bioniko Instruments, Arizona, USA) presented eight metal pins onto which the half globe was glued. Red arrow in b shows the back portion of the ONH. On opposite sides, two screws (b, black arrows) are rotated clockwise to switch from relaxed to stretched mode.

The extent of the deformation of the lamina cribrosa was calculated as described in Albon et al., (2000b) as the change in length/original length. The radial strain was calculated separately in the horizontal (superior-inferior) and vertical (nasal-temporal) axis. The distance (length) between two opposite scleral points was measured in millimetres before and after the stretch was applied and values calculated as following:

$$Strain = \frac{Lx - L0}{L0}$$

Where
Lx = length after stretch
L0 = original length

Ten SAXS and WAXS patterns were analysed for fibrillar collagen, molecular parameter and elastin within each ONH region and quantified as described in sections 5.2.5 and 5.2.6, respectively. Full width at half maximum (FWHM) of the elastin peak was automatically calculated in DAWN using the "Fitting peak" function to analyse changes in elastin organisation as a function of radial stretch.

5.2.10 Fibrillar collagen orientation: polar plots

Polar orientation plots showing the angular distribution of fibrillar collagen (e.g. polar patch plots) were calculated from SAXS meridional scatter patterns. (Bell et al., 2018) (figure 5.16). Polar orientation plots, showing the predominant orientation of collagen within each SAXS patterns (Meek and Boote, 2009), were created using a custom-made MATLAB script previously developed for WAXS data, and adapted by Dr. James Bell (see appendix II.2 "Polar_plot_SAXS_ONH") (Abass et al., 2017). The azimuthal distribution of radially integrated collagen intensity (figure 5.16a,b) was generated to create the plot (figure 5.16c-e). Singular polar plots were then arranged into a grid according to the actual geometric position in the optic nerve head, giving a polar vector maps for each optic nerve head section. Points lacking collagen determined a gap into the map. Each assessed point in the ppsclera could thusly be addressed by a polar vector plot, in which the length of a vector toward any direction is proportional to the relative number of fibres preferentially aligned in that direction (Bell et al., 2018).

5.2.11 Statistical analysis

All statistical tests were performed with SPSS v.23. Normality of data was tested using Shapiro Wilk at a significance of $p>0.05$. Statistical analysis from SAXS and WAXS in the regional and PTA stained, and radial stretch ONH data was normally distributed so comparison between regions and inner and outer LC, and between LC and ppsclera, was performed with One-way ANOVA and independent T-test.

For SAXS and WAXS data in age range of ppsclera Spearman's rank and Pearson's correlation, were used respectively. SAXS myelin and WAXS elastin Data analysis was performed Pearson's correlation as a function of age.

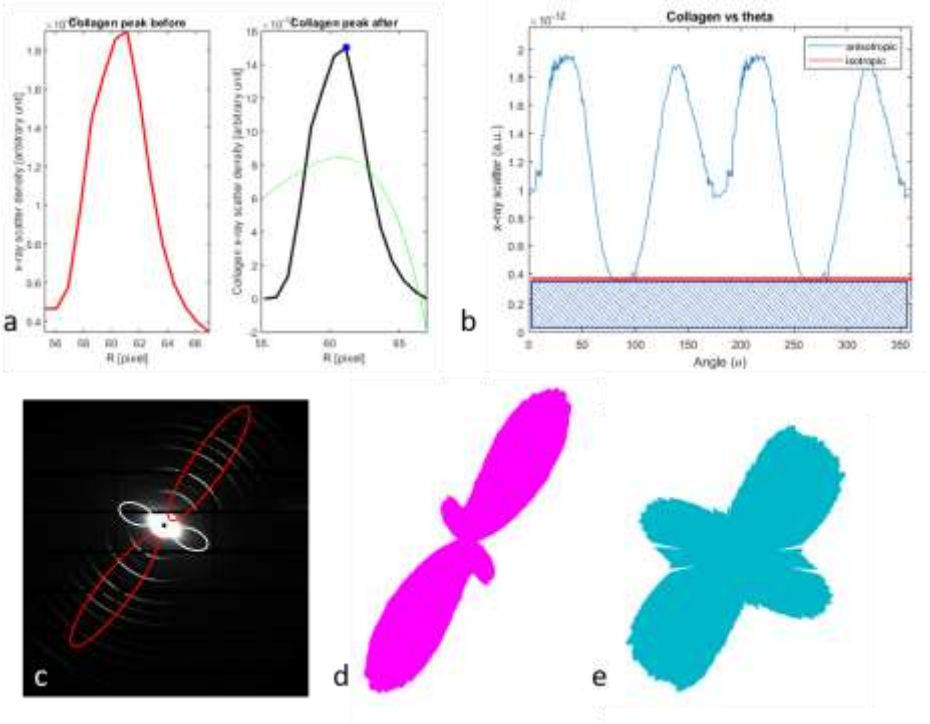

Figure 5.16. Collagen orientation polar plot. The aligned collagen scatter is represented as a polar vector plot. The meridional peak (a) is fitted and integrated as a function of angle (b). The total scatter can be divided into scatter from the preferentially aligned (anisotropic) collagen (b, clear area) and scatter from isotropically oriented collagen (b, shaded area). Each pattern (c) was analysed to produce contour polar plot (d,e).

5.3 Results

5.3.1 Detection of SAXS patterns in human ONH

In the first part of this study to determine if SAXS could be used to detect collagen and elastin, analysis was performed on four donors paired ONHs (aged 78-85 years) within eight LS ONH sections. Representative schematic diagram of the raster scan (figure 5.17a) used to create the montage of SAXS data acquired from a nasal-temporal oriented ONH section (figure 5.17b), with colour-coded positions of selected SAXS patterns (figure 5.17c-f) are shown in figure 5.17.

Although collagen reflections were identified in the ppsclera (figure 5.17c) in all sections, none were detected in the LC (figure 5.17d); here signals were a diffuse scatter around the beam centre. Faded and arced reflections were identified at the level of the CRA and within the RoIns (figure 5.17f), likely attributed to elastin. Circular reflections typical of myelin (Falzon et al., 2007) were observed in the postL ON (figure 5.17e). The LC-postL ON boundary was clearly visible due to the strong patterns obtained from myelin in the latter. Collagen reflections (meridional and equatorial) of ppsclera were similar to those of RTT collagen (figure 5.18d). Surprisingly, SAXS reflections were not detected within the bovine nuchal ligament (figure 5.18a), porcine skin (figure 5.18b) and RTA (figure 5.18c).

5.3.2 Detection of WAXS patterns in human ONH

In the first part of this study to determine if WAXS could be used to detect collagen and elastin, analysis was performed on donor paired ONHs (aged 78-85 years) as described in 5.3.1. Representative montages of superior-inferior axes before (figure 5.19a) and after background removal (figure 5.19b) showing colour-coded position of WAXS patterns are presented in figure 5.19. Collagen WAXS reflections were detected in the ppsclera (figure 5.19c) of all LS sections, however, these reflections were not clearly visible until background (i.e. attributed to Kapton ring and sample holder) removal. RTT scatter patterns, arising from collagen showed clear WAXS meridional and equatorial reflections (figure 5.19d).

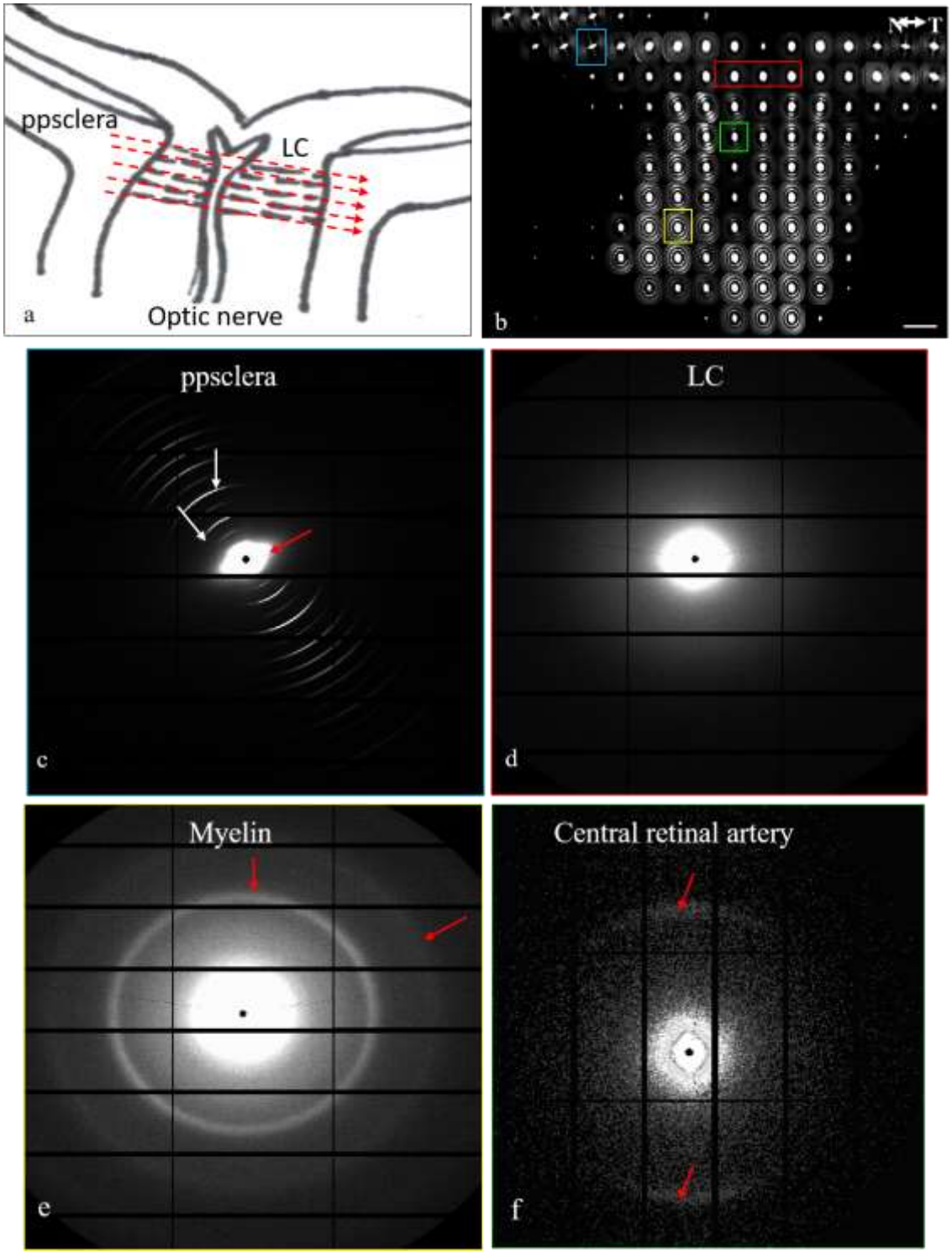

Figure 5.17. Panel of SAXS patterns identified in the longitudinal section of a 85 year old donor at different levels. A schematic diagram of a raster scan applied to ONH sections (a) and montage of a nasal-temporal ONH (b) with selected SAXS patterns illustrating reflections from the ppsclera (c), LC (d), myelin (d) and elastin (e). Meridional (c, white arrows) and equatorial (c, red arrow) reflections were visible in the ppsclera. Faded and circular rings (e, red arrows) associated to myelin were identified in the postL ON. Diffuse ring (f, red arrows) associated to elastin were identified in the CRA. Scale bars represent 500 µm.

5.3.2.1 Positive controls for elastin

Within the CRA (figure 5.19e), a diffuse circular ring was identified at 0.44nm. This diffuse ring was also identified within the ppsclera at 0.45nm (figure 5.19c). the bovine nuchal ligament (figure 5.19f), porcine skin (figure 5.19h) and RTA (figure 5.19g), providing support for this reflection being associated with elastin.

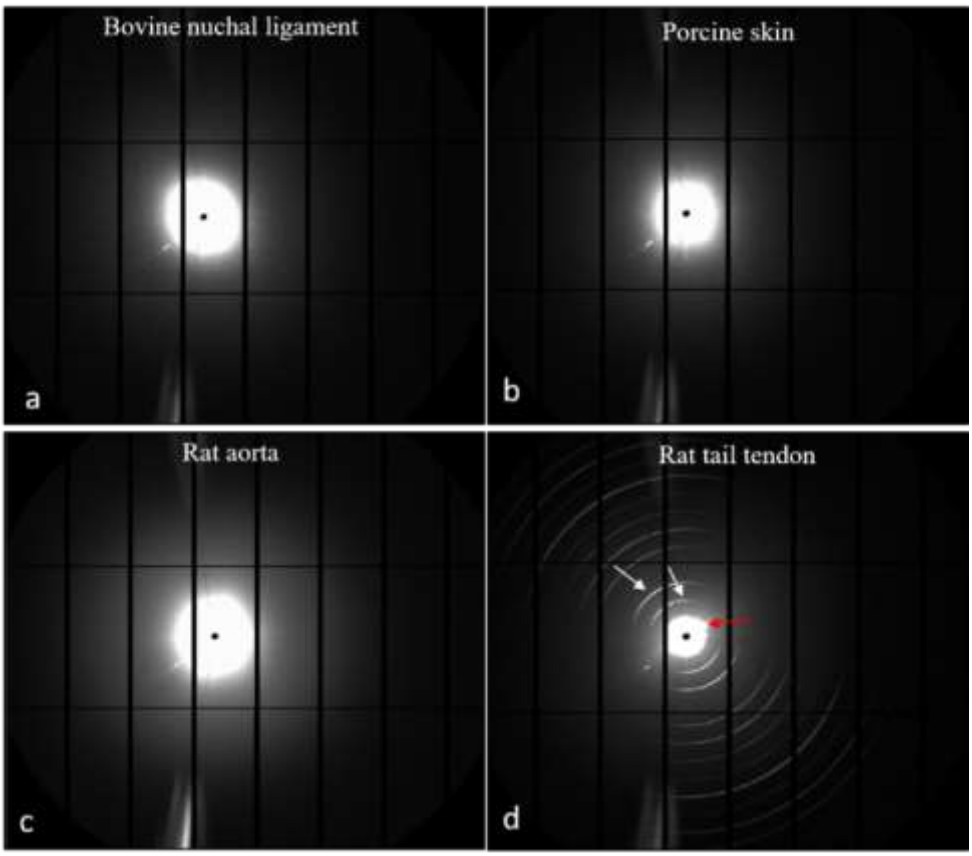

Figure 5.18. Panel of SAXS patterns identified in controls. Bovine nuchal ligament (a), porcine skin (b), RTA (c) did not show any collagen SAXS reflection whereas RTT scatter pattern (d) showed clear meridional (white arrow) and equatorial (red arrow) reflections.

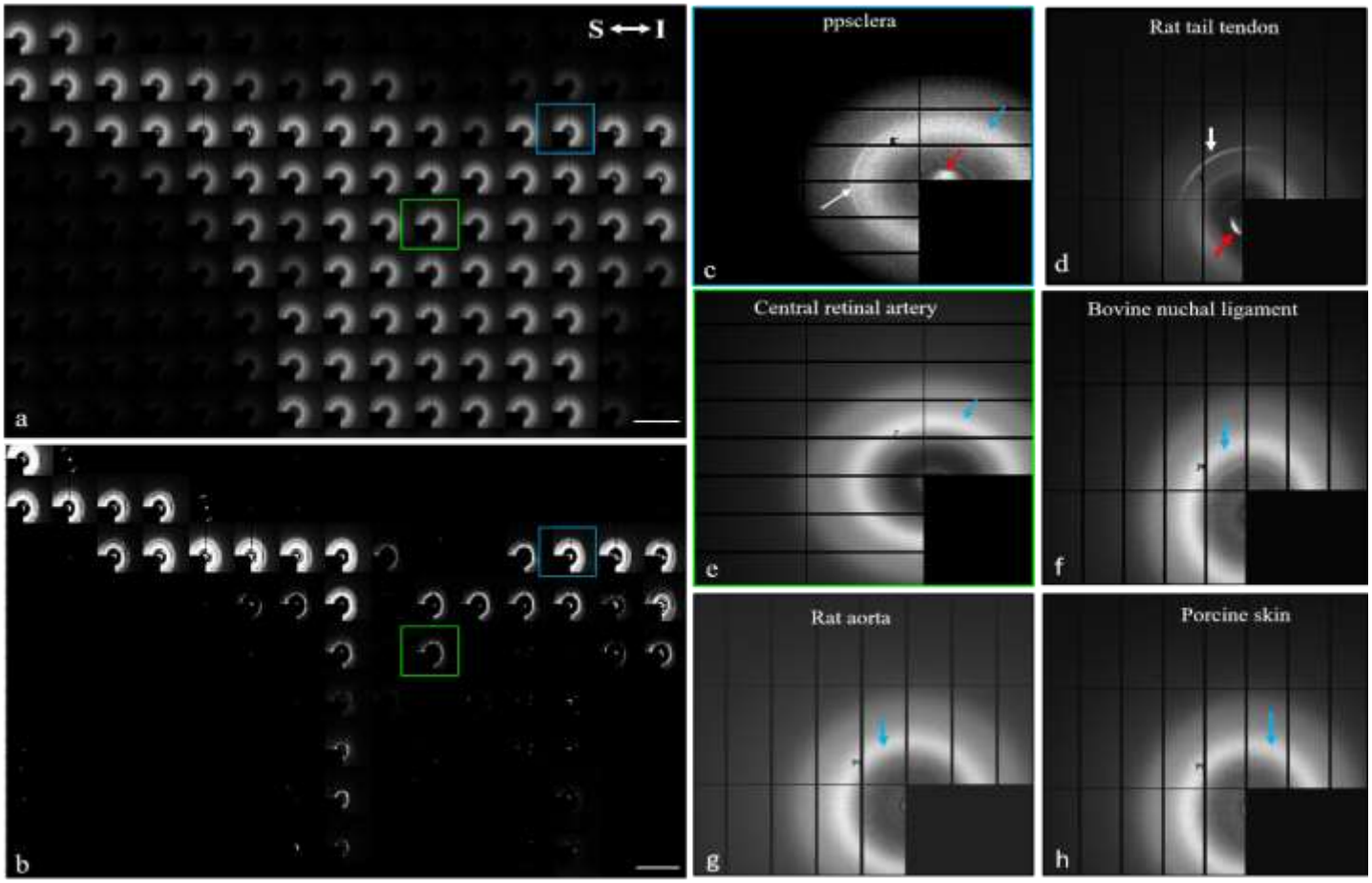

Figure 5.19. Panel of WAXS patterns identified in LS sections of an 85-year-old donor at different levels. Montage in the superior-inferior axes before (a) and after (b) background removal illustrating reflections from the ppsclera (c) and CRA(e). Meridional (c,d white arrows) and equatorial (c,d red arrow) reflections were visible in the ppsclera and RTT. Diffuse rings (f-h, blue arrows) associated to elastin were identified in the bovine nuchal ligament (f), RTA (g) and porcine skin (h). A similar diffuse ring associated to elastin was identified in the CRA (e, blue arrow) and ppsclera (c, blue arrow). Scale bars represent 500 μm.

5.3.3 Collagen fibril and molecular parameters within the ageing ppsclera

5.3.3.1 Fibril parameters in the ppsclera

Median ± interquartile range (IQR) of fibril parameters in the ppsclsra are summarised in Table 5.1. SAXS diffraction patterns in the ppsclera were identified in all aged ONHs, from 22yr to 85yr. Collagen fibril diameter significantly increased from 98.98 nm ± 0.9 at 22 years old to 113.01 nm ± 1.5 at the age of 85 (rs=0.636, p=0.026) (figure 5.20a). The D period showed no significant change as function of age (rs= -0.460, p=0.190) (figure 5.20d). Interfibrillar Bragg spacing showed no significant change as function of age and ranged from 136.28 nm ± 7.48 to 125.10 nm ± 15.62 (rs= -0.333, p=0.618) (figure 5.20b). However, as fibril diameter changed as a function of age, it would affect the latter. Therefore, the subtraction of twice the radius allowed the recalculation of the interfibrillar spacing, which significantly decreased from 37.63 nm ± 7.22 at the age of 22 years to 12.6 nm ± 4.54 at the age of 85 years (rs=-0.783, p=0.003) (figure 5.20c).

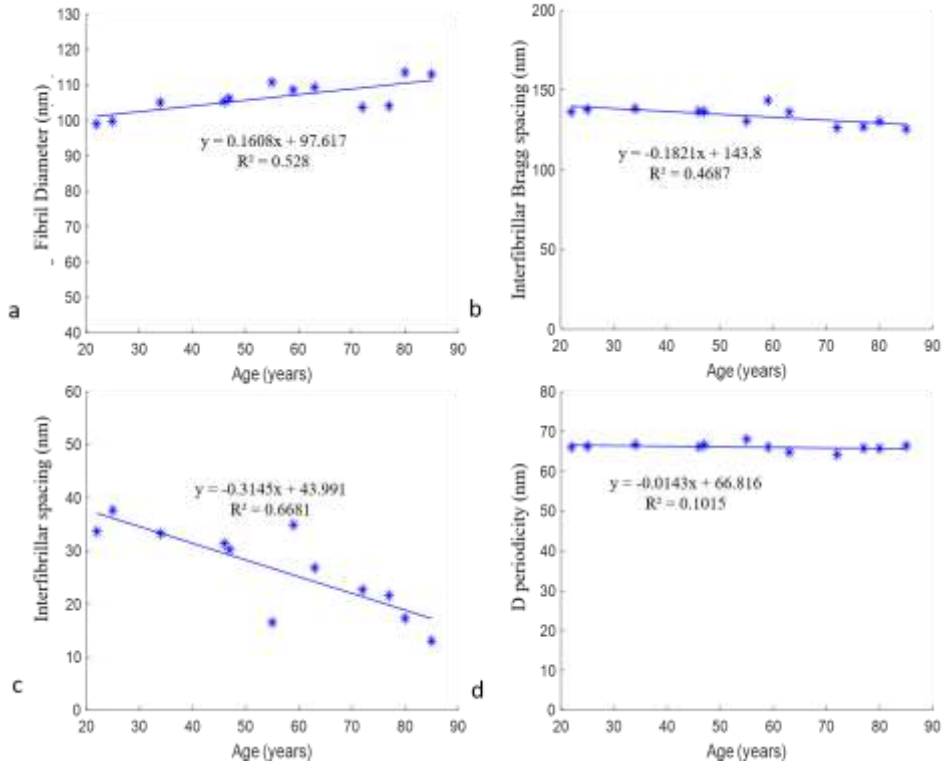

Figure 5.20. Fibrillar collagen parameters in the ageing ppsclera. Fibril diameter (a) significantly increased (p=0.026) whereas the interfibrillar spacing (c) significantly decreased (p=0.003) as a function of age. No differences were found in the interfibrillar Bragg spacing (b) and D periodicity (d).

5.3.3.2 Molecular parameter in the ppsclera

Molecular parameters in the ppsclera are summarised in Table 5.1. Collagen intermolecular Bragg spacing significantly increased from 1.44 nm ± 0.01 at the age of 34 years to 1.53 nm ± 0.03 at the age of 85 years (p=0.022, r=0.826) (figure 5.21a). Distance between amino acid residues did not change as a function of age (p=0.326, r=0.081) (figure 5.21b).

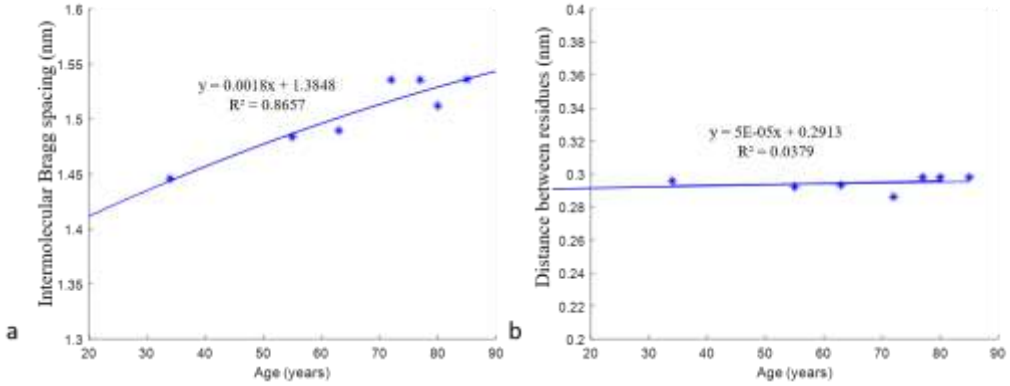

Figure 5.21.Collagen molecular parameters in the ageing ppsclera. Intermolecular Bragg spacing (a) significantly increased (p=0.022) as a function of age. No differences were found in the distance between amino acid residues (b).

Age (years)	Fibril Diameter (Median ± IQR)	Interfibrilla Bragg spacing (Median ± IQR)	Interfibrillar Spacing (Median ± IQR)	D period (Median ± IQR)	Intermolecular Bragg spacing (Mean ± sd)	Distance between amino acid residues (Mean ± sd)
22	98.98 ± 0.90	136.28 ± 7.48	37.63 ± 7.22	66.01 ± 0.12	N/A	N/A
25	99.75 ± 1.64	137.85 ± 14.83	38.61± 13.18	66.22 ± 0.19	N/A	N/A
34	105.04 ± 1.77	122.03 ± 4.66	16.33 ±4.32	66.67 ± 0.32	1.44 ± 0.01	0.29 ± 0.02
46	105.32 ± 2.77	120.36 ± 3.93	15.03 ± 9.91	66.15 ± 0.22	N/A	N/A
47	106.19 ± 0.67	121.56 ± 7.43	15.70 ± 5.04	66.57 ± 0.29	N/A	N/A
55	110.77 ± 5.63	130.48 ± 3.69	19.50 ±3.27	67.98 ± 0.55	1.48 ± 0.02	0.29 ± 0.01
59	99.55 ± 1.14	134.55 ± 10.17	35.87 ± 10.01	67 ± 0.25	N/A	N/A
63	104.33 ± 0.88	125.71 ± 2.83	21.48 ± 3.28	64.65 ± 0.16	1.48 ± 0.04	0.29 ± 0.01
72	103.71 ± 2.22	134.41 ± 5.59	30.05 ± 5.27	64.55 ± 1.12	1.53 ± 0.01	0.28 ± 0.01
77	104.05 ± 3.17	125.31 ± 7.71	21.53 ± 4.95	64.25 ± 0.98	1.53 ± 0.02	0.29 ± 0.02
80	113.58 ± 1.15	130.25 ± 5.81	16.11 ± 7.55	65.67 ± 1.19	1.51 ± 0.01	0.29 ± 0.01
85	113.01 ± 1.50	125.10 ± 15.62	12.67 ±4.54	66.34 ± 1.02	1.53 ± 0.03	0.29 ± 0.01

Table 5.1. Fibrillar collagen (Median ± IQR) parameters and mean ± sd collagen molecular parameters in the ageing ppsclera.

5.3.3.3 Elastin WAXS reflections within the human ONH

Elastin associated diffuse and circular rings were identified within the CRA and ppsclera following background removal. The distance of the reflection from beam centre was between 0.441 nm ± 0.002 and 0.444 nm ± 0.005 (Table 5.2) and did not change as a function of age (p=0.062, r=0.608).

Age (years)	Elastin ring distance (nm) ± sd
22	0.443 ± 0.008
25	0.448 ± 0.004
34	0.442 ± 0.005
55	0.442 ± 0.005
59	0.443 ± 0.008
63	0.443 ± 0.002
72	0.441 ± 0.002
77	0.442 ± 0.000
80	0.441 ± 0.008
85	0.441 ± 0.002

Table 5.2. Elastin ring distance (mean ± sd) from WAXS diffraction patterns. No significant changes were observed as a function of age.

5.3.3.4 Myelin patterns in the human ONH

As mentioned previously in 5.3.1 two diffuse rings, inner (R_I) and outer (R_O), were identified in the postL ON. These reflections appeared wide and diffuse and located at 8-8.3 nm for R_I and 5.5 nm for R_O from beam centre (Table 5.3). Since these reflections were not present in the LC and ppsclera, it is likely they arise from myelin. R_I and R_O were measured as a function of age. The distance from beam centre of R_I significantly increased from 8.01 nm ± 0.034 at the age of 22yr to 8.32 nm ± 0.030 at the age of 85yr (r=0.764, p=0.004) (figure 5.22). R_O significantly increased from 5.41 nm ± 0.100 at the age of 22yr to 5.59 nm ± 0.040 at the age of 85yr (r=0.745, p=0.005) (figure 5.22).

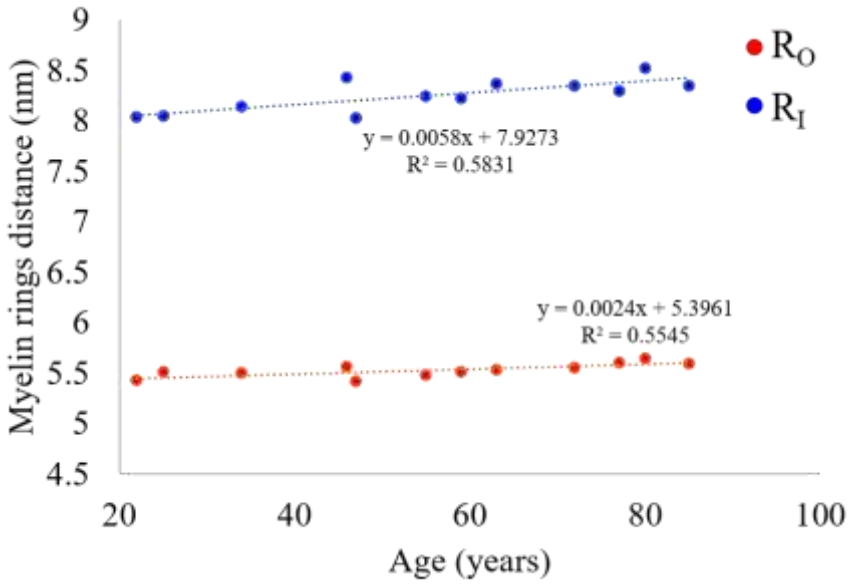

Figure 5.22. Myelin associated rings in the ageing ppsclera. Both R_I (p=0.004) and R_O (p=0.005) ring distance from beam centre significantly increased as a function of age.

Age (years)	Inner Ring (R_I) (nm) ± sd	Outer Ring (R_O) (nm) ± sd
22	8.01 ± 0.034	5.41 ± 0.100
25	8.02 ± 0.047	5.55 ± 0.120
34	8.12 ± 0.120	5.52 ± 0.130
46	8.41 ± 0.105	5.52 ± 0.075
47	8.05 ± 0.039	5.42 ± 0.040
55	8.21 ± 0.220	5.41 ± 0.060
59	8.22 ± 0.036	5.53 ± 0.039
63	8.33 ± 0.135	5.56 ± 0.040
72	8.33 ± 0.076	5.56 ± 0.050
77	8.21 ± 0.059	5.61 ± 0.060
80	8.55 ± 0.101	5.60 ± 0.070
85	8.32 ± 0.032	5.59 ± 0.040

Table 5.3. Myelin rings distance (mean ± sd) in the ageing ppsclera. These reflections appeared wide and diffuse and located at 8-8.3nm and 5.5nm from beam centre.

5.3.4 Collagen fibril, molecular and elastin reflections in PTA-stained human ONH

Following PTA staining, which enhanced LC collagen, SAXS and WAXS reflections were detected within the LC and ppsclera. Representative montages showing colour coded SAXS and WAXS positions of patterns are shown in figure 5.23a and figure 5.23b, respectively. Collagen meridional and equatorial reflections were detected, enabling fibril and molecular collagen parameters quantification in the LC (figure 5.23b,e) and ppsclera (figure 5.23c,f). Myelin SAXS reflections were not observed. Elastin WAXS reflections were detected in the ppsclera (figure 5.23f) but not in the LC.

5.3.4.1 Quantification of collagen parameters from SAXS PTA-stained ONHs

Fibrillar collagen parameters of the LC and its regions are summarised in Table 5.4. Fibril diameter in the four LCs had a mean of 78.23 nm ± 1.40, ranging from 76.42 nm ± 4.35 to 79.55 nm ± 1.04 (Table 5.5) (figure 5.24a). Interfibrillar Bragg spacing had a mean of 94.65 ± 1.16 and ranged from 93.21 nm ± 4.05 to 96.87 nm ± 4.12 (Table 5.4) (figure 5.24b). D periodicity did not vary, with a mean of 65.96 nm ± 0.71 and ranged from 64.07 nm ± 0.65 to 66.59 nm ± 0.82 (Table 5.5) (figure 5.24c).

Fibrillar collagen diameter in the PTA-stained LC was significant lower at the age of 46 ($p=0.007$) and 47 ($p=0.046$) compared to older ages of 62 and 84 years old (figure 5.24a). Interfibrillar Bragg spacing was significantly lower at the age of 62 years ($p=0.006$) compared to younger ages (figure 5.24b). Collagen parameters were also investigated between inner and outer LC (Table 5.5). However, no differences were found in the fibril diameter ($p=0.276$), interfibrillar Bragg spacing ($p=0.817$) or D periodicity ($p=0.969$). No regional or inter-donor differences in LC fibril parameters were observed.

Fibrillar collagen parameters of the ppsclera from PTA-stained ONH and regions are summarised in Table 5.4. Ppsclera fibril diameter of PTA-stained ONHs had a mean of 106.77 ± 4.55 and ranged from 105.04 nm ± 2.58 to 107.31 nm ± 4.66 (figure 5.24a). Interfibrillar Bragg spacing in the ppsclera of PTA-stained ONHs had a mean of 127.71 ± 2.75 and ranged from 110.39 nm ± 5.15 to 132.97 nm ± 4.25 (figure 5.24b), D periodicity did not vary, had a mean of 65.87 ± 0.56 and ranged from 64.07 nm ± 0.65 to 66.59 nm ± 0.82 (figure 5.24c). Fibrillar collagen diameter in the PTA-stained ppsclera

was significant lower at the age of 46 (p=0.034) and 47 (p=0.003) compared to elderly (figure 5.24a). Interfibrillar Bragg spacing was significantly lower at the age of 84 years (p=0.023) compared to younger ages (figure 5.24b). The ppsclera interfibrillar Bragg spacing (p=0.001) and diameter (p=0.001) were significantly greater than those of the LC (figure 5.24a,b). D period did not show any changes between LC and ppsclera (figure 5.24c) (p=0.251). No differences were observed in the pspclera fibril parameters between unstained and PTA-stained ONHs [fibril diameter (p=0.980), Interfibrillar Bragg spacing (p=0.907) or D period (p=0.056)].

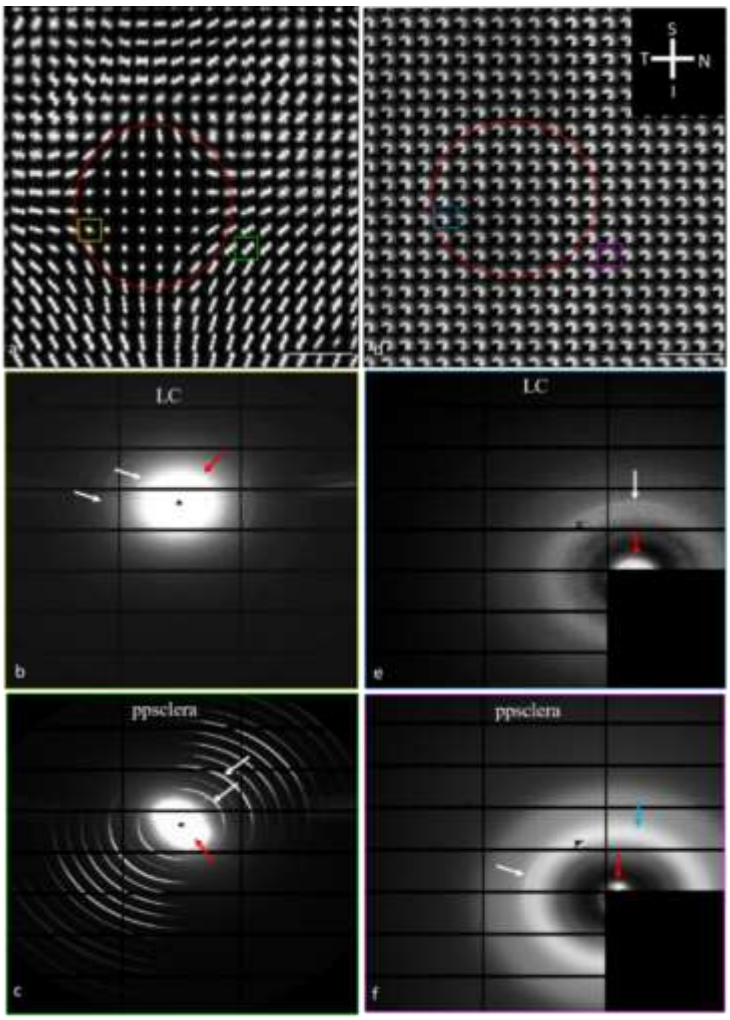

Figure 5.23. Panel of SAXS and WAXS diffraction patterns identified in TS PTA-stained ONH sections from a 62-year-old donor. A montage of SAXS (a) and WAXS (d) pattern illustrating colour-coded positions of reflections from the LC and ppsclera. SAXS (b) and WAXS (e) reflection from the LC and SAXS (c) and WAXS (f) reflection form the ppsclera. Collagen meridional (b,c,e,f, white arrows) and equatorial (b,c,e,f, red arrows) where indetinfied in both LC and ppsclera. A diffuse ring associated to elastin was identified in the WAXS ppsclera (f, blue arrow). Scale bars represent 500 μm.

Age (years)	Interfibrillar Bragg Spacing (nm) ± sd (LC / ppsclera)	D periodicity (nm) ± sd (LC / ppsclera)	Fibril Diameter (nm) ± sd (LC / ppsclera)
46	94.77 ± 3.25 / 110.39 ± 5.15	65.5 ± 0.20 / 66.32 ± 0.25	76.42 ± 4.35 / 105.47 ± 2.23
47	94.59 ± 4.12 / 132.39 ± 4.26	65.86 ± 0.95 / 65.19 ± 0.92	77.85 ± 2.44 / 105.04 ± 2.58
62	93.21 ± 4.05 / 126.56 ± 6.25	65.5 ± 0.59 / 65.75 ± 0.12	79.83 ± 1.42 / 103.12 ± 3.25
84	96.34 ± 3.02 / 132.97 ± 4.25	67 ± 0.25 / 65.26 ± 1.21	79.48 ± 2.70 / 106.28 ± 2.32
Superior	94.29 ± 5.22 / 132.97 ± 4.25	65.81 ± 0.15 / 65.32 ± 0.26	78.78 ± 1.49 /106.52 ± 3.15
Inferior	96.87 ± 4.12 / 119.14 ± 6.25	64.71 ± 0.16 / 65.75 ± 0.45	79.55 ± 1.04 / 106.87 ± 4.05
Nasal	93.97 ± 3.25 / 124.10 ± 3.25	65.81 ± 0.65 / 65.67 ± 0.15	78.98 ± 1.93 / 107.31 ± 4.66
Temporal	93.56 ± 3.02 / 122.88 ± 3.12	65.81 ± 0.33 / 66.07 ± 0.22	79.32 ± 2.04 / 106.28 ±4.06

Table 5.4. Mean ± sd of fibrillar collagen parameters in the LC and ppsclera of PTA-stained ONHs

Age (years)	Interfibrillar Bragg Spacing (nm) ± sd (Inner / Outer)	D periodicity (nm) ± sd (Inner / Outer)	Fibril Diameter (nm) ± sd (Inner / Outer)
46	95.39 ± 2.32 / 95.70 ± 1.36	65.86 ± 0.25 / 66.50 ± 0.55	79.45 ± 2.02 / 79.94 ± 3.25
47	96.55 ± 3.21 /96.89 ± 2.12	65.83 ± 0.36 / 65.98 ± 0.20	80.03 ± 2.98 / 80.52 ± 3.12
62	95.75 ± 3.15 / 95.73 ± 2.65	65.78 ± 0.84 / 65.14 ± 0.12	79.18 ± 3.01 / 79.68 ± 4.01
84	95.25 ± 4.15 / 95.54 ± 4.25	66.04 ± 0.78 / 65.95 ± 0.21	80.66 ± 3.52 / 81.16 ± 2.05

Table 5.5. Mean ± sd of fibrillar collagen parameters in the inner and outer LC of PTA-stained ONHs.

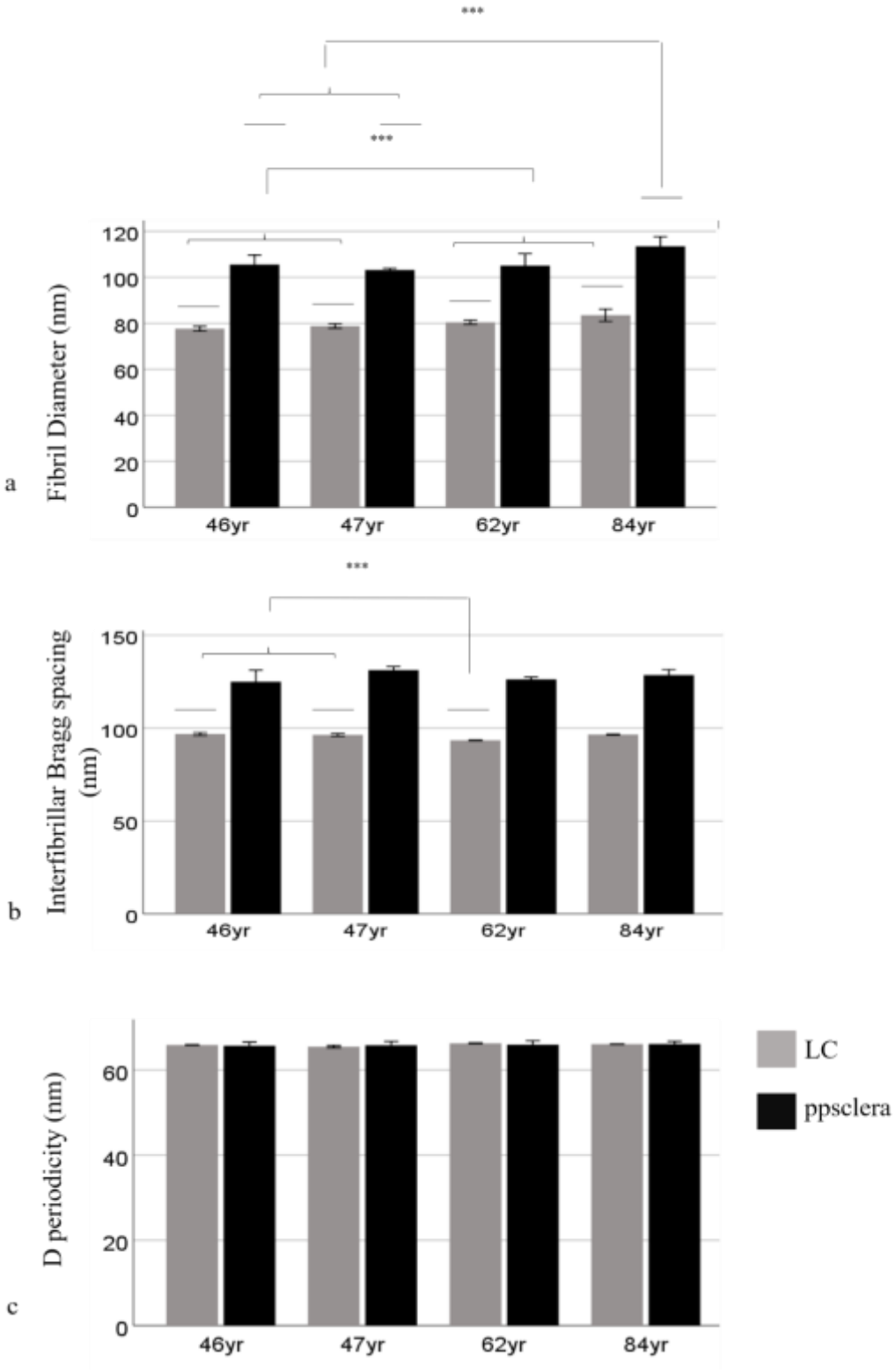

Figure 5.24. Fibrillar collagen (mean ± sd) parameters from PTA-stained ONH SAXS diffraction patterns within the LC and ppsclera. Fibrillar collagen diameter in the LC was significant lower at the age of 46 (p=0.007) and 47 (p=0.046) compared to elderly. Interfibrillar Bragg spacing was significantly lower at the age of 62 years (p=0.006) compared to younger ages. Fibrillar collagen diameter in the ppsclera was significant lower at the age of 46 (p=0.034) and 47 (p=0.003) compared to elderly. Interfibrillar Bragg spacing was significantly lower at the age of 84 years (p=0.023) compared to younger ages. Fibril diameter (p=0.001) and interfibrillar Bragg spacing (p=0.001) were greater in the ppsclera compared to LC.

5.3.4.2 Quantification of collagen parameters from WAXS PTA-stained ONHs

Intermolecular Bragg spacing in the PTA-stained LC had a mean of 1.00 nm ± 0.06 and ranged from 0.935 nm ± 0.02 to 1.077 nm ± 0.12 (Table 5.6) (figure 5.25a). The distance between amino acid residues had a mean of 0.291 nm ± 0.01 and ranged from 0.296 nm ± 0.06 to 0.29 nm ± 0.11 (Table 5.6) (figure 5.25b). Intermolecular Bragg spacing in the PTA-stained LC was significantly lower at the ages of 46 (p=0.002) and 47 years (p=0.008) compared to elderly (figure 5.25a). Molecular parameters were also investigated between inner and outer region of the LC, but no significant differences were found in intermolecular Bragg spacing and (p=0.943) and distance between residues (p=0.468) (Table 5.7). No regional or inter-donor differences in LC fibril parameters were observed.

Ppsclera intermolecular Bragg spacing had a mean of 1.01 nm ± 0.08 and ranged from 0.935 nm ± 0.01 to 1.11 nm ± 0.12 (figure 5.25a) (Table 5.7). The distance between amino acid residues had a mean of 0.296 ± 0.01 and ranged from 0.294 nm ± 0.06 to 0.296 nm ± 0.11 (figure 5.25b) (Table 5.7). Intermolecular Bragg spacing in the PTA-stained ppsclera was significantly lower at the ages of 46 (p=0.002) and 47 years (p=0.001) compared to elderly (figure 5.25a).

Additionally, ppsclera intermolecular Bragg spacing was greater than that observed in the LC at the age of 84 years old (p=0.001) (figure 5.25a). Intermolecular Bragg spacing was lower in PTA-stained ONHs compared to that within LS non-stained ONHs (p=0.030).

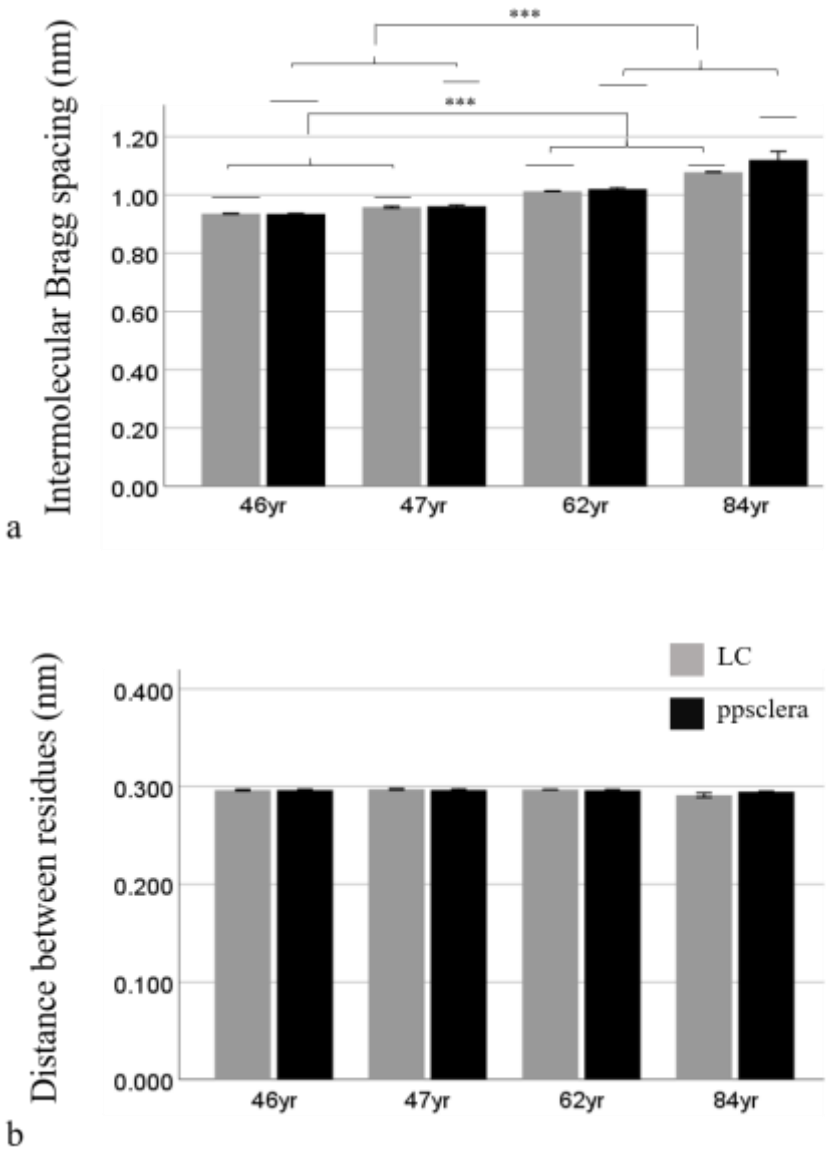

Figure 5.25. Collagen molecular parameters (mean ± sd) from PTA-stained ONH WAXS diffraction patterns within the LC and ppsclera. Intermolecular Bragg spacing in the PTA-stained LC was significantly lower at the ages of 46 (p=0.002) and 47 years (p=0.008) compared to elderly 62 and 85 years old. Intermolecular Bragg spacing in the PTA-stained ppsclera was significantly lower at the ages of 46 (p=0.002) and 47 years (p=0.001) compared to elderly. Intermolecular Bragg spacing (p=0.001) was greater in the ppsclera compared to LC at the age of 84 years old.

Age (years)	Intermolecular Bragg spacing (nm) ± sd (LC / ppsclera)	Distance between residues (nm) ± sd (LC / ppsclera)
46	0.935 ± 0.02 /0.934 ± 0.12	0.296 ± 0.01 /0.296 ± 0.02
47	0.957 ± 0.05 / 0.916 ± 0.22	0.297 ± 0.02 / 0.296 ± 0.03
62	1.012 ± 0.09 / 1.091 ± 0.15	0.296 ± 0.01 /0.296 ± 0.01
84	1.077 ± 0.12 / 1.112 ± 0.21	0.291 ± 0.06 /0.294 ± 0.04
Superior	0.998 ± 0.15 / 0.982 ± 0.32	0.297 ± 0.11 / 0.297 ± 0.04
Inferior	0.994 ± 0.02 / 0.946 ± 0.12	0.295 ± 0.01 / 0.296 ± 0.01
Nasal	0.995 ± 0.12 / 1.011 ± 0.15	0.294 ± 0.12 / 0.294 ± 0.01
Temporal	0.995 ± 0.16 / 1.031 ± 0.14	0.294 ± 0.05 /0.295 ± 0.03

Table 5.6. Collagen molecular parameters (mean ± sd) in the LC and ppsclera of PTA-stained ONHs

Age (years)	Intermolecular Bragg spacing (nm) ± sd (Inner / Outer)	Distance between residues (nm) ± sd (Inner / Outer)
46	0.949 ± 0.01 /0.935 ± 0.02	0.297 ± 0.04 / 0.295 ± 0.02
47	0.952 ± 0.02 / 0.956 ± 0.01	0.297 ± 0.02 / 0.297 ± 0.02
62	1.014 ± 0.01 /1.012 ± 0.01	0.293 ± 0.01 /0.290 ± 0.01
84	1.085 ± 0.01 / 1.083 ± 0.6	0.288 ± 0.02 / 0.300 ± 0.02

Table 5.7. Collagen molecular parameters (mean ± sd) in the inner and outer LC of PTA-stained ONHs.

5.3.4.3 Quantification of elastin distance from WAXS PTA-stained ONHs

Elastin reflections of the LC are summarised in Table 5.8. Elastin ring had a mean of 0.428 nm ± 0.004 and ranged from 0.425 nm ± 0.005 to 0.431 ± 0.002 (Table 5.8). No regional or inter-donor differences in LC fibril parameters were observed.

Age (years)	Elastin ring distance (nm) in the ppsclera ± sd
46	0.428 ± 0.004
47	0.429 ± 0.003
62	0.430 ± 0.002
84	0.425 ± 0.005
Superior	0.431 ± 0.002
Inferior	0.429 ± 0.003
Nasal	0.428 ± 0.003
Temporal	0.425 ± 0.005

Table 5.8. Elastin ring distance (mean ± sd) within the LC of PTA-stained ONHs.

5.3.5 Effect of radial stretch on ONH collagen and elastin

Stress is a measure of the load applied to a tissue, whereas strain is a measure of the local deformation of a material induced by stress. Stress-strain are normally represented by stress-strain curves. These are unique for each material and are found by recording the amount of deformation (strain) at distinct intervals of loads (stress) (Blum 2016, Downs et al., 2008).

5.3.5.1 SAXS and WAXS reflection detected in the ppsclera

The known orientation of the ONH within the stretcher device was determined after globes were cleaned as described in 2.2.2. ONHs were mounted onto the stretcher device with the superior ONH towards the top of the device and the temporal ONH to the left of the device. Marks were drawn onto the device to keep record of the position of the superior and temporal; with known inferior and nasal regions. The stretcher device was mounted into the beam path with the superior facing the roof and the temporal facing the wall of the experimental hutch. The ONHs were stretched without dismounting the device from the beam path, therefore, the orientation did not change. The vertical direction was defined as the distance between the superior and inferior metal pins, with the horizontal direction defined as the distance between nasal and temporal metal pins.

Quantifiable SAXS and WAXS patterns were detected before and after radial stretch was applied to two human and two porcine ONH. SAXS and WAXS diffraction patterns showed similar patterns in both human (figure 5.26) and porcine (figure 5.27) ONHs before (figure 5.26a,c and figure 5.27a,c) and after the stretch was applied (figure 5.26b,d and figure 5.27b,d). No visible SAXS and WAXS reflections in the LC were detected.

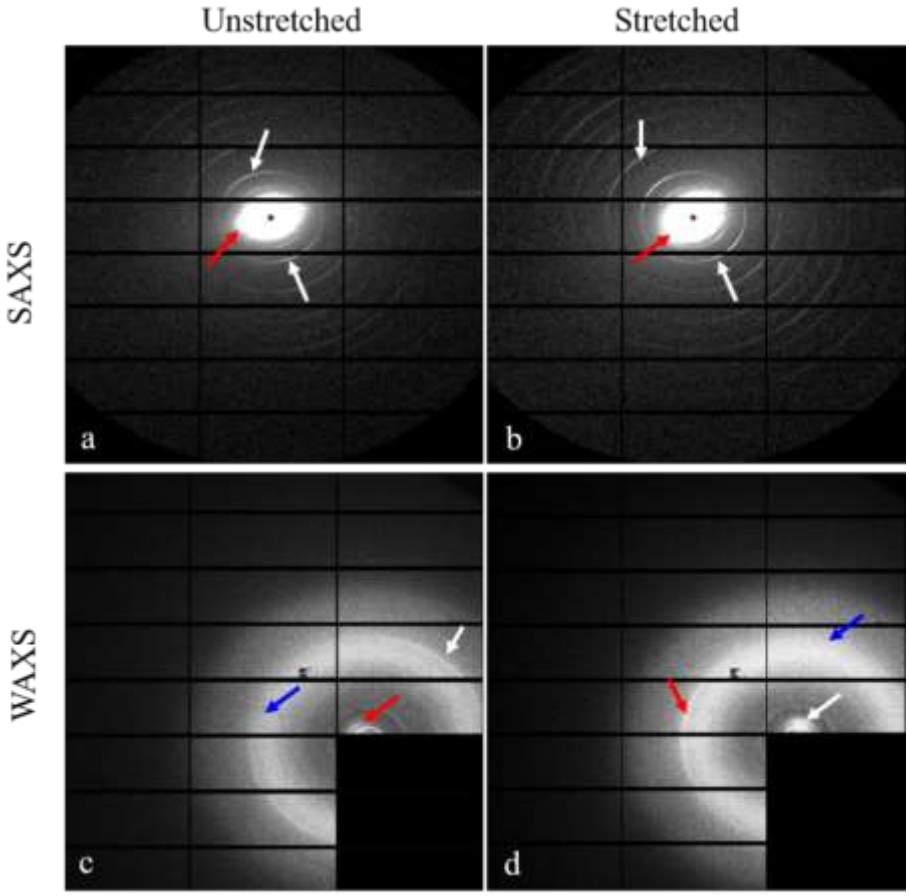

Figure 5.26. SAXS and WAXS patterns in the human ppsclera before and after radial stretch. Fibrillar collagen meridional (a-d, white arrows) and equatorial (a-d, red arrows) were identified before (a,c) and after (b,d) radial stretch. Collagen (c,d, white and red arrows) and elastin (e,f, blue arrows) WAXS patterns were visible only after background removal (i.e. removal of Kapton ring).

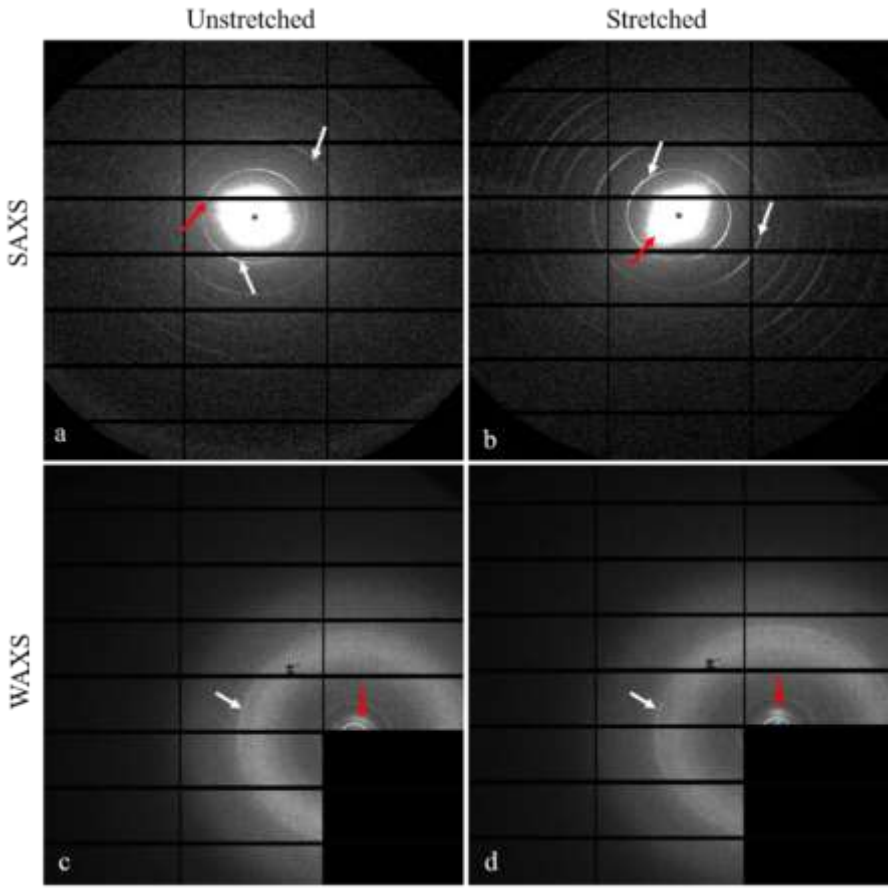

Figure 5.27. SAXS and WAXS patterns in the porcine ppsclera before and after radial stretch. Fibrillar collagen meridional (a-d, white arrows) and equatorial (a-d, red arrows) were identified before (a,c) and after (b,d) radial stretch. Collagen (c,d, white and red arrows) WAXS patterns were visible only after background removal (i.e. removal of Kapton ring).

Collagen meridional and equatorial reflections were clearly visible in both human and porcine ONHs from SAXS (figure 5.26a,b and figure 5.27a,b) and WAXS (figure 5.26c,d and figure 5.27c,d). Additionally, within WAXS patterns, a diffuse ring attributed to elastin was identified in human before (figure 5.26c) and after stretch (figure 5.26d) but not in porcine ONHs.

Calculation of LC strain in the X (nasal-temporal axis) and Y (superior-inferior axis) direction across the ONHs was performed as described in Albon et al., (2000). The LC strain was calculated in both directions and showed differences between human and porcine ONHs (figure 5.28). Different values between human and porcine ONHs might indicate that the two species present different anisotropy, likely due to the difference in structure between porcine and human ONH, and the response to stress is different.

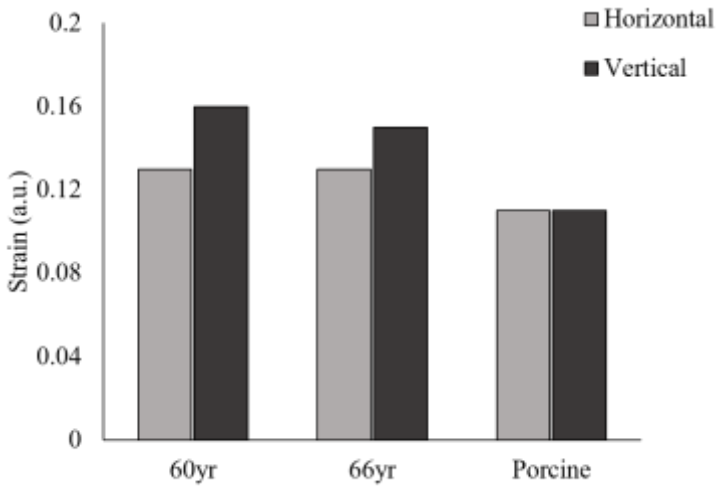

Figure 5.28. LC strains across human and porcine ONHs. The human ONHs (60- and 62-year olds) showed differences in the strain measured vertically and horizontally across the LC the porcine ONH strains did not differ.

Polar plots of the arrangement of fibrillar collagen in human and porcine ONH before and after stretch is shown in figure 5.28. Collagen fibrils in the ppsclera are circularly oriented around the optic canal in both human (figure 5.28e,f) and porcine (figure 5.28g,h) ONHs. Results suggested that after radial stretch changes in collagen orientation are observed in human (figure 5.28f) ONHs. The gap in the centre of each polar plot is due to the lack of collagen-derived SAXS reflections within the LC/optic canal (figure 5.28a-d).

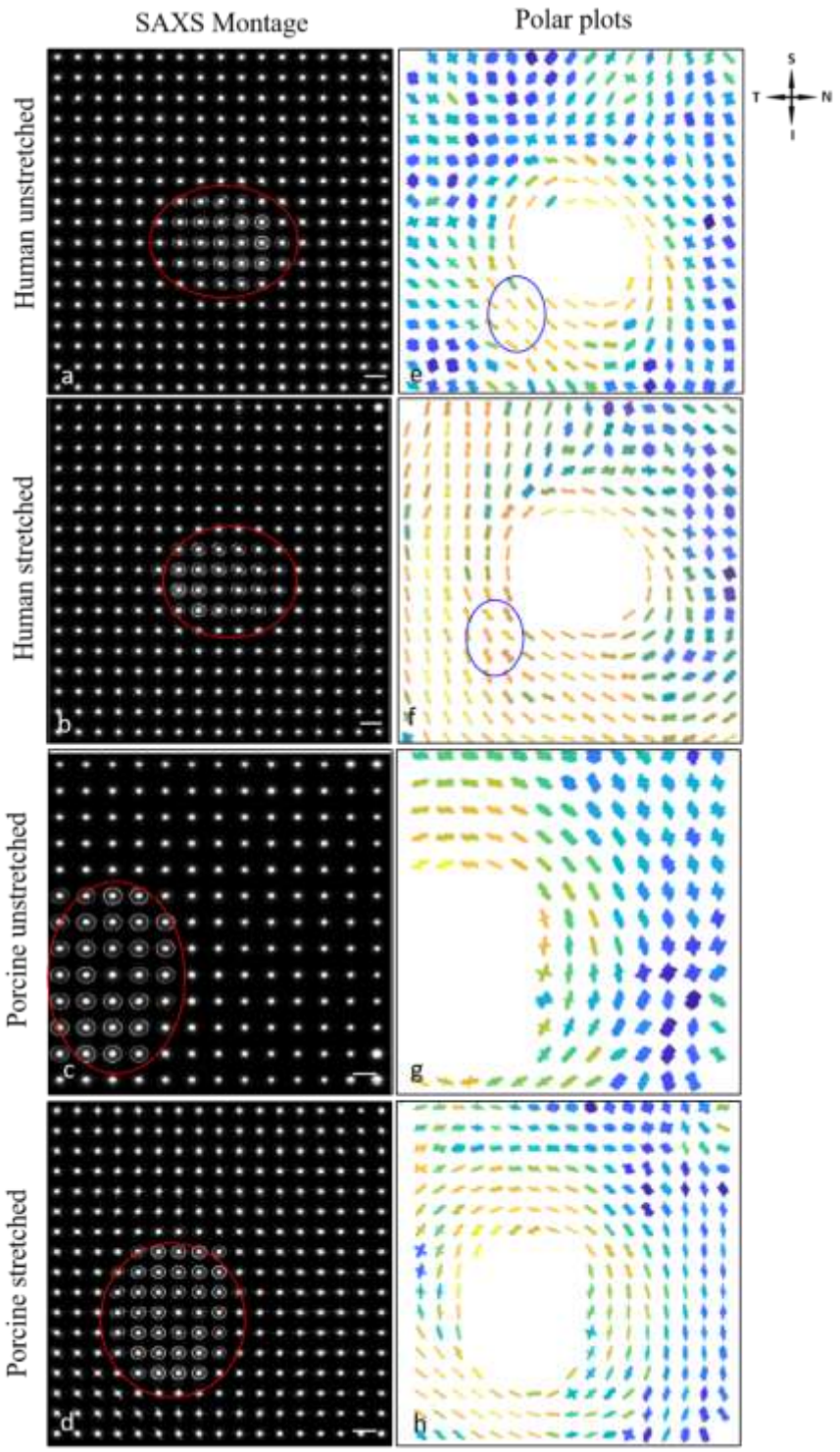

Figure 5.29. Representative polar plots of collagen fibril orientation. SAXS montages of human unstretched (a) and stretched (b) and porcine unstretched (c) and stretched (d) are shown. The correspondent polar plot montage of human unstretched (e) and stretched (f); porcine unstretched (g) and stretched (h) are shown. The red ellipses in a-d indicate the optic canal where fibrillar collagen SAXS patterns were not identified and therefore no polar plots were calculated. A circular ring of collagen is observed around the optic canal (e-h). Polar plots in the human ONH showed a different collagen orientation after stretch (f, blue ellipse). No peculiar changes in polar plot orientation were observed in the porcine ONH, before and after stretch (g,h, respectively). Scale bars represent 500μm.

5.3.5.2 Fibrillar collagen parameters

Fibrillar collagen parameters were measured within the ppsclera of both human and porcine ONHs. No significant changes were observed, before and after radial stretch, in fibril diameter (p=0.486) (figure 5.29a), interfibrillar Bragg spacing (p=0.686) (figure 5.29b) and interfibrillar spacing (p=0.343) (figure 5.29c) in both human and porcine ONHs. However, the D period was significantly greater after the stretch in the human 60 years old (p=0.029) and the 66 years old ONHs (p=0.029) (figure 5.29d), but not in the porcine ONH (p=0.325) compared to before stretch.

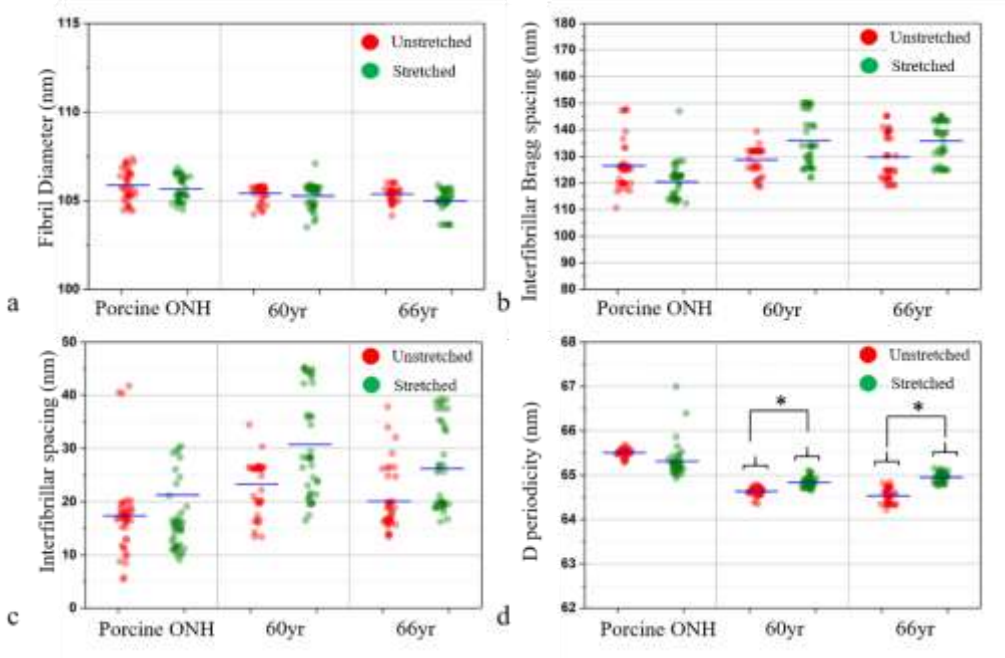

Figure 5.30. Fibrillar collagen parameters in the human and porcine ppsclera before and after the radial stretch. D period was significantly greater (d) after stretch in both human ONHs (p=0.029) but not in the porcine. Fibril diameter (a), interfibrillar Bragg spacing (b) and interfibrillar spacing (c) did not show any significant changes after radial stretch.

5.3.5.3 Collagen molecular parameters

Collagen molecular parameters were measured within the ppsclera of both human and porcine ONHs. Distance between amino acid residues was significantly greater in the 60 years (p=0.046) (figure 5.30b) and 66 years (p=0.044) (figure 5.30c) when subjected to radial strain. No differences in this parameter were found in the porcine ONH (p=0.139)

(figure 5.30a). The intermolecular Bragg spacing did not alter following application of radial stretch in 60 years old (p=0.575) (figure 5.30b) or 66 years old human ONH (p=0.256) and (figure 5.30c) porcine ONH (p=0.181) (figure 5.30a).

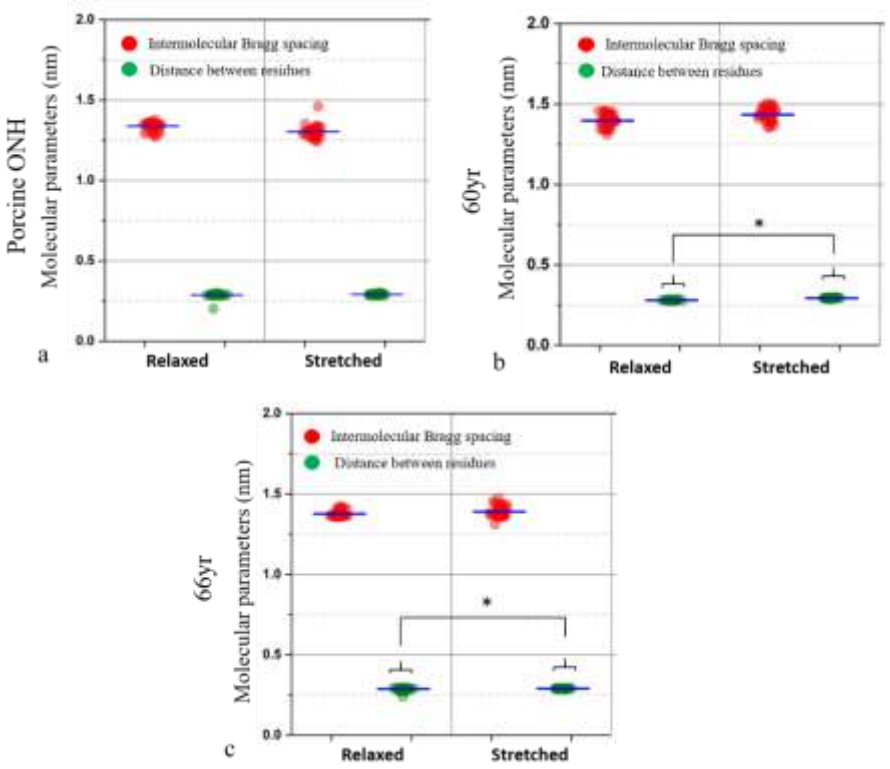

Figure 5.31. Collagen molecular parameters (i.e. intermolecular Bragg spacing and distance between residues) in human and porcine ppsclera before and after radial stretch. The distance between residues was significantly greater in the stretched 60yr (p=0.046) (b) and 66yr (p=0.044) (c), although no differences were found in the porcine (p=0.139) (a). The intermolecular Bragg spacing did not show any difference in the 60yr (p=0.575) (b), 66yr (p=0.256) (c) and porcine (a) (p=0.181) ONHs.

5.3.5.4 Elastin

Mean ± sd elastin ring distance from beam centre and FWHM are summarised in table 5.9.

The diffuse elastin ring was identified in both relaxed and stretched human ONH ppsclera, however, it was not observed in the porcine ONH. Elastin ring distance was measured before and after radial stretch in both human ONHs (Table 5.9) and did not show any significant difference in distance from beam stop following stretch in the 60 years old (p=0.753) and 63 years old (p=0.615) (figure 5.31a).

Additionally, to assess the degree of order of elastin the calculated FWHM of the elastin peak showed no significant changes following stretch in the human 60yr old (p=0.879) and 66yr old (p=0.822) (figure 5.31b) ONHs.

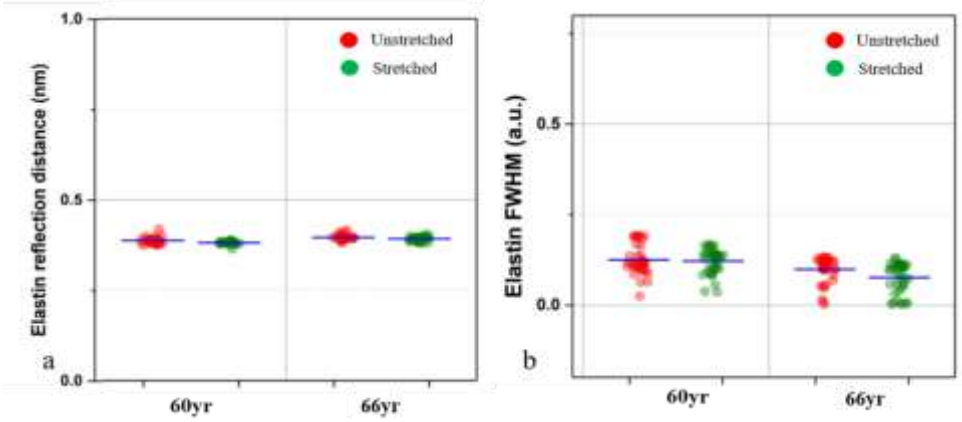

Figure 5.32. Elastin associated WAXS parameters as a function of radial stretch. Elastin ring distance (a) did not show any significant difference in the 60yr (p=0.753) and 66yr (p=0.953) human ppsclera. No significant changes were observed in the elastin FWHM (b) in the 60yr (p=0.879) and 66yr (p=0.822) human ppsclera.

Specimen	Elastin ring (nm) ± sd Before / after stretch	FWHM (a.u.) ± sd Before / after stretch
Human 60yr ONH	0.39 ± 0.007 / 0.39 ± 0.005	0.09 ± 0.037 / 0.08 ± 0.041
Human 66yr ONH	0.38 ± 0.006 / 0.38 ± 0.020	0.11 ± 0.003 / 0.11 ± 0.05

Table 5.9. Elastin rings (mean ± sd) in the human ppsclera before and after radial stretch.

5.4 Discussion

This chapter aimed to investigate the nanostructure of collagen and elastin in the aged ONH and ppsclera using small angle and wide-angle x ray diffraction. SAXS and WAXS diffraction patterns were clearly visible in the LS section at the level of the ppsclera, however, no measurable diffraction patterns were identified in the LC within LS ONHs sections at any age. This result was surprising as the major components of the LC are collagen and elastin (Albon et al., 1995, Albon et al., 2000a, Hernandez et al., 1986, Hernandez et al., 1987), however, expected and consistent with a previous study (Jones, 2014) which did not identify any SAXS diffraction patterns at the level of the LC. The lack of diffraction within the LC may reflect its low connective tissue density and the porosity of the structure in comparison to the dense surrounding sclera.

Although no SAXS and WAXS diffraction patterns became visible at the level of the LC within LS sections, the PTA-staining enhanced the fibrillar collagen signal, allowing SAXS and WAXS patterns from the LC to become visible. PTA is a common negative stain for biological tissues used in transmission electron microscopy. It is an anionic heavy metal, tungsten, which is likely to be a good candidate in electron microscopy to localise basic group. PTA selectively binds to the basic group (lysine and arginine residues) of proteins (e.g. collagen) (Jones, 1993, Höög et al., 2010). No differences were found in the aged LC and ppsclera within PTA-ONH stained sections, however, fibrillar collagen parameters in the LC were significantly lower compared to the ppsclera. This is consistent with a study on monkey and human healthy LC in which fibrillar diameter was lower in the LC than the ppsclera (Quigley et al., 1991). The PTA-staining successfully enhanced fibrillar collagen signal to detect SAXS patterns in the LC and it holds potential for the future quantification of LC collagen parameters.

Some interesting diffraction patterns were also identified within the controls. Surprisingly, no SAXS diffraction patterns were visible within the bovine nuchal ligament, porcine ear and RTA, although nuchal ligament and ear had been digested to remove none elastin and the RTA is mainly composed by elastic lamella and collagen fibres (Keech, 1960, O'Connell et al., 2008).

Clearly defined SAXS fibrillar collagen meridional and equatorial diffraction were identified in the RTT. This was expected as RTT is mainly composed by collagen type I

with no contribution of elastin (Tomlin and Worthington, 1956, Folkhard et al., 1987, Fraser and MacRae, 1981). SAXS diffraction patterns were also seen at the CRA which showed a diffuse and arced ring, likely associated to elastin as well as meridional and equatorial reflections. This result was expected as it is known the CRA contains elastic lamina in the wall and fibrillar collagen at the level of the tunica adventitia (Hayreh, 1963).

Interestingly, WAXS diffraction patterns from bovine nuchal ligament, porcine ear and RTA showed a diffuse and circular ring not associated to fibrillar collagen. Since nuchal ligament and porcine ear were previously digested to remove all except for elastin, it is likely that this diffraction pattern is associated to elastin. A similar pattern was also visible in the RTA and central retinal artery, since, as mentioned above, both tissues contain elastic lamellae/lamina in the tunica media (Hayreh, 1963). The same diffuse ring was not identified in RTT, implying that elastin is negligible within the RTT, consistent with the fact the RTT is mainly composed by collagen type I (Tomlin and Worthington, 1956, Folkhard et al., 1987, Fraser and MacRae, 1981).

5.4.1 SAXS within the ageing ONH

Although, no SAXS and WAXS diffraction patterns were available from the LC within LS sections, interestingly diffraction patterns from the ppsclera allowed the quantification of fibrillar collagen parameters as a function of age. Collagen fibril diameter and interfibrillar spacing significantly increased and decreased, respectively, as a function of age.

One of the major load-bearing components of the LC is fibrillar collagen. The distribution of collagen fibril diameter within a tissue, determines how effective collagen fibrils are in providing strength against a force (Hukins and Aspden, 1985, Parry, 1988). Fibril diameter has been shown to increase with age within other tissues. In rabbit patellar tendon (Sklenka et al., 2006), flexor tendon of horse (Parry et al., 1978a), RTT (Parry et al., 1978b) and human cornea (Daxer et al., 1998) fibril diameter increased as a function of age. It has been proposed in the cornea, that increase in fibril diameter might contribute to age-related changes in biomechanical properties, such an increased stiffness, which in turn might alter the mechanical function of the cornea (Daxer et al., 1998). The increased in stiffness might also be accompanied by the glycation-induced cross-linking of collagen

molecules shown in the cornea (Malik et al., 1992) as well as the incorporation of collagen molecules into the fibril during age (Daxer et al., 1998) which thus lead to an increase in the diameter.

Collagen fibril diameter in the human ppsclera fell within the previously published wide range of fibril diameters. Indeed, transmission electron microscopy (TEM) performed on human sclera showed a wide range of fibril diameter (from 25 to 230nm) randomly arranged when compared to those in the cornea (Komai and Ushiki, 1991). Although changes in ONH collagen as a function of age has been demonstrated before (Hernandez et al., 1987, Hernandez et al., 1989, Hernandez et al., 1991, Morrison et al., 1989, Albon et al., 1995, Albon et al., 2000a, Albon et al., 2000b) and scleral collagen fibril diameter has been characterised before (Komai and Ushiki, 1991) no studies have reported changes in ONH fibril diameter as a function of age.

Ppsclera D periodicity of 65-66 nm was found at all ages, indicating that the axial stagger of collagen fibrils is not affected by age. D periodicity is shorter than that observed in RTT collagen type I (~67nm) but it is closer to that observed in skin (Brodsky et al., 1980). The shorted D periodicity presented in this chapter might be caused by the presence of other collagen types other than collagen type I as well as by collagen molecular tilt along the fibril axis (Hulmes et al., 1981). The greater fibril tilt in this part of the sclera might explain a shorter D periodicity as it has been shown for the cornea where the short D period was due to a fibril tilt of 15 degrees (Yamamoto et al., 2000).

Interfibrillar Bragg spacing did not show any difference as a function of age, however, it was lower in the elderly ppclera compared to younger. Conversely, interfibrillar spacing significantly decreased in age. Malik et al., (1992) showed a decrease in interfibrillar spacing in the ageing human corneas, also confirmed by Kanai and Kaufmann from an electron microscopy study (Kanai and Kaufman, 1973). It has been suggested previously that proteoglycans play a key role in maintaining and regulating the spacing between collagen fibrils (Borcherding et al., 1975), therefore the decrease in interfibrillar Bragg spacing observed in the cornea might be related to the age related decrease in the ratio of proteoglycans to collagen (Scott et al., 1981).

A smaller interfibrillar spacing along with a greater fibril diameter, may imply that the fibrils are closer to each other, leading to a more closely packed tissue which result in

higher collagen fibril volume fraction. This may have an impact on the biomechanics of the elderly ppsclera, suggesting that fibrils are bigger, there is less space between fibrils therefore the connective tissue of the elderly ppsclera appear less flexible.
Interestingly, interfibrillar Bragg spacing and diameter measured in this study were found to be higher than those previously found with EM (Quigley et al., 1991).

In the cornea, almost every stage of EM processing produces a significant change in structural parameters. Glutaraldehyde fixation significantly increased the intermolecular spacings, while resin infiltration and resin polymerization each resulted in shrinkage of all the spacings. Fullwood and Meek (1993) suggested that post-fixation in osmium tetroxide caused the loss of the intermolecular pattern and increased the shrinkage in interfibrillar Bragg spacing and D periodicity.

Differences in measured fibril diameter are often caused by tissue hydration. X ray scattering measurements are estimated, being made at physiological conditions and hence hydration, whereas measurements made with electron microscopy are made after significant tissue preparation that involves drying the tissue below the critical point of hydration, when water is lost from the interfibrillar spacing (Fratzl and Daxer, 1993, Fullwood and Meek, 1993, Fullwood et al., 1992, Hayes et al., 2017).

It has been shown that different resins produce shrinkage of the tissue leading to an average decrease of fibril dimeter of 13.6% (Fullwood and Meek, 1993). These results suggest that interfibrillar Bragg spacing and diameter are lower when measured within EM images to those observed with SAXS, and likey explain the greater fibril diameters and interfibrillar Bragg spacing presented in the current chapter.

5.4.2 Myelin SAXS reflections

Interesting SAXS diffraction patterns at approximately 8 nm and 5.5 nm were found in LS sections at the level of the ON canal. These diffraction patterns were not produced by fibrillar collagen and were likely associated to myelin as myelin sheaths are known to surround axons in the postL ON, but not in the human preL or LC. The myelin membranes originate from and are a part of the Schwann cells in the peripheral nervous system (PNS) and oligodendrocytes in the central nervous system (CNS) (Raine, 1984). X-ray diffraction studies of myelin provided information of the repeating unit that showed three

peaks which corresponded to i) protein plus lipid polar groups and ii) two channels which corresponded to lipid hydrocarbon chains. Myelin structure is periodic and well ordered, with a period which is equal to the sum of twice the lipid membrane and the cytoplasmic thickness (Harker, 1972).

Data from mammalian optic nerve showed a repeat distance of 8nm, which included two protein layers (about 1.5nm each) and one layer of lipid (about 5nm). The main repeating unit of two unit membranes is twice this representation, or 16nm (Hirano and Dembitzer, 1967) (figure 5.33).

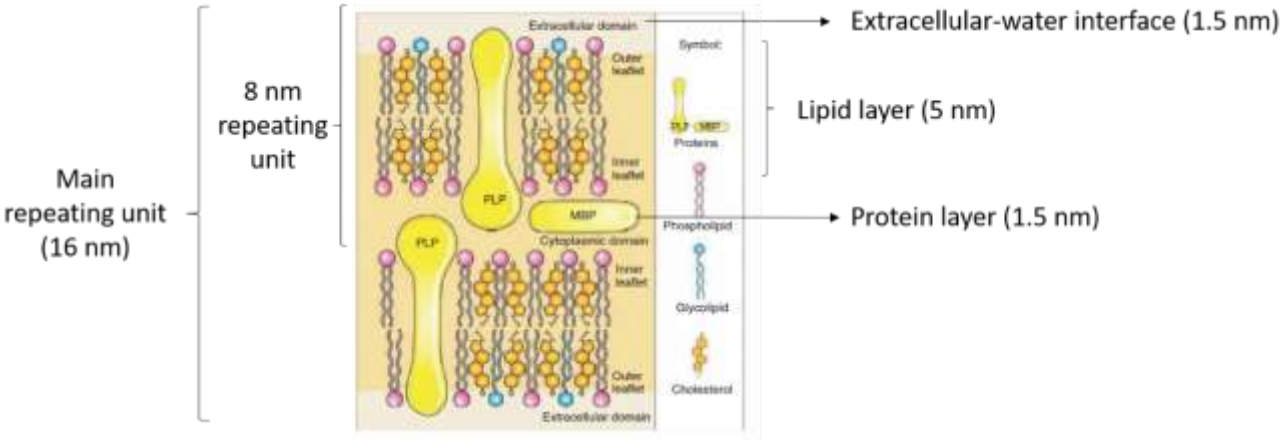

Figure 5.33. Schematic representation of myelin repeating unit. Myelin forms a bilayer of protein and lipid around axons of the central nervous system. The extracellular water interface measures 1.5 nm and contains the myelin protein zero (P0). Beneath, the phospholipid layer of 5 nm contains peripheral myelin protein (PMP). Beneath this layer, the protein layer of 1.5 nm thick, contains the myelin protein two (P2) and the myelin basic protein (MBP). The repeating unit measures in this thesis include the lipid layer and the repeating unit of 8 nm (protein-lipid-protein). The main repeating unit of myelin is shown to be 16 nm. Adapted from (Papini and Konig, 2015) with permission of Taylor & Francis (Appendix IV.13).

Depending on the species and whether the sample comes from the CNS or PNS, the period ranges approximately between 15-20nm (King and Thomas, 1984, Blaurock, 1981). Schmitt (1935), proposed an 18 nm periodic structure of the mammalian nerve, and suggested that the sheaths are composed by a periodic array of protein-bounded lipid layers (Schmitt et al., 1935). An electron microscopy study proposed that the periodic

structure of the sheaths arises from the spiral wrapping of the Schwann cells around axons (Ben Geren, 1954, Schmitt et al., 1941).

The 8nm reflection identified in this study it is likely to be the repeating distance previously found in the mammalian optic nerve (Hirano and Dembitzer, 1967). The additional ring found at 5 nm is likely produced by the lipid layer (Hirano and Dembitzer, 1967). The ring distance associated with the lipid and the protein-lipid-protein layers was significantly greater in the elderly ON compared to younger. This might suggest that myelin layers become thicker in age due to accumulation of lipid and/or protein in the sheaths. It has been proposed from a previous WAXS study on human brain that the ring associated to lipid layer becomes less intense in old brain implying that lipid myelin becomes less ordered with age (Chia et al., 1983). Degenerative changes also occur with age in the myelin sheaths, such as the formation of myelin balloons (Peters, 2002), which are enclosed by lamellae of myelin. Additionally, a study on monkey nerves illustrated that the ageing myelin exhibits an accumulation of vesicles in between the repeating unit (Sandell and Peters, 2001). These age-related changes and accumulation of substances, such as 2',3'-Cyclic nucleotide 3'-phosphodiesterase (CNP) protein (Yin et al., 1997) might imply a thickening of the layers which lead to a change in the SAXS diffraction patterns.

Chia et al, (1983) proposed a change in lipid behaviour and myelin as a function of age, following WAXS. The authors found a broad reflection in infant myelin and they proposed a disordered state of myelin sheaths when still in development. This reflection became and remained sharp until age of 30-50. Above the age of 50, it became less sharp and started to fade, proposing that at this age myelin lipid was less ordered (Chia et al., 1983). In addition, it has been proposed that the optic tract showed a change in myelin periodicity as a function of age, ranging from 16nm (9-months old) to 15.9 (41 years old) (Chandross et al., 1978).

5.4.3 WAXS within the ageing ONH

WAXS diffraction patterns from the ageing ppsclera showed a significant increase in intermolecular Bragg spacing as a function of age, from 1.44 nm ± 0.01 in the 34-year-old ppsclera to 1.53 nm ± 0.03 in the 85-year-old ppsclera. This increase might be explained by the deposition of new inter-molecular cross-links. Two major processes involve collagen cross-links: enzyme-mediated cross-links which involves lysyl oxidase

(LOX) and glucose-based reaction, also known as non-enzymatic glycation. LOX-mediated cross-linking involves oxidative deamination of terminal lysines by lysyl oxidase forming lysyl aldehyde. The latter can form covalent inter-molecular cross-links to form the subsequent fibril. Non-enzymatic cross-linking involves a reaction between glucose and lysine which undergo the Amadori mechanism and oxidative modifications. This results in the formation of advance glycation end (AGE) products which can form inter-molecular cross-links (Bailey, 2001).

Intermolecular cross-links are a key in the extracellular maturation of collagen, in fact, they provide the fibrils with mechanical strength essential for biological properties of collagen over a life time (Zimmermann et al., 1973). In 1992, Malik et al., showed an increase in intermolecular Bragg spacing in the ageing human cornea and sclera and they suggested that these changes might be due to an increase in non-enzymatic cross-linking between collagen molecules that occur with age (Malik et al., 1992). It is known that non-enzymatic collagen cross-linking increases with age (Albon et al., 1995) and it has also been shown that *in vitro* glycation leads to the expansion of the packing of collagen molecules within RTT (Tanaka et al., 1988). Malik and Meek (1994) showed that glycation of human corneas and sclera increased with age and it occurs with an increase in collagen cross-links and intermolecular Bragg spacing, suggesting that age-related cross-links are mostly intermolecular (Malik and Meek, 1994). This might suggest that new cross-links are deposited between tropocollagen molecules in the elderly ppsclera, altering the mechanical behaviour of the ONH tissues. Additionally, Daxer et a., (1998) suggested that the increase in intermolecular Bragg spacing observed in the human cornea was due to the deposition on collagen molecules within fibrils with age, pushing the molecules further apart (Daxer et al., 1998). The increase in ppsclera intermolecular Bragg spacing is therefore likely associated with an accumulation in intermolecular cross-links as a function of age. This may also explain the increase in fibril diameter, suggesting that molecules are further apart. If this is the case, a similar process could occur in the LC and it would be consistent with the age-related increase in AGE-products known to occur in the ageing LC (Albon et al., 1995).

5.4.4 Elastin WAXS reflections

EFs within the LC and ppsclera has been investigated with several techniques, including electron microscopy (Quigley et al., 1991), immunohistochemistry with antibodies

against elastin (Hernandez et al., 1987, Hernandez et al., 1989, Albon et al., 2000a) and histological staining (Oyama et al., 2006), however little is known about its nanostructure. X ray diffraction studies by Gotte and Fracassini (1963) showed a limited order in elastin (Gotte and Serafini-Fracassini, 1963) which was later confirmed by Seraffini-Fracassini (Serafini-Fracassini and Field, 1977) and Ali et al (Ali et al., 2004), with two broad diffraction rings observed at 0.45 nm and 0.93 nm. The spacing measured in the current study appeared constant at all ages and it is in accordance to that observed previously, which identified the 0.45 nm ring as the lateral spacing of β-sheets and 0.93 nm as the hydrophobic interactions between sheets (Ali et al., 2004). An interesting WAXS diffraction pattern became visible at the ppsclera and CRA from WAXS patterns following removal of Kapton ring. Similar diffraction patterns were also found in purified elastin preparations of bovine nuchal ligament and porcine ear skin. Evidence suggests elastin diffraction is minimal and its nanostructure has been difficult to characterise due to the amorphous nature of the protein. Serfani-Fracassini et al. (1977) isolated and dried elastin from bovine nuchal ligament and subjected the preparation to SAXS. This result reported diffraction patterns of 4.5-5 nm after extension of an elastin strip of 65% (Serafini-Fracassini and Field, 1977).

Therefore, it is likely that the diffraction presented in the current chapter is associated to elastin; it remained constant at 0.44 nm with no significant changes observed. The current study, however, only showed the ring at 0.44 nm. The absence of the 0.93 nm diffraction patterns could be due to different samples and preparation. From the structural point of view, there is a lack of literature regarding the presence or absence of an ordered structure of elastin. Therefore, further investigations are needed to better understand the ordered structure of elastin, if any, and how the WAXS diffraction patterns arises from the lateral spacing of β-sheets.

5.4.5 SAXS and WAXS within human and porcine ppsclera

SAXS and WAXS patterns from ppsclera collagen and elastin were identifiable in human and porcine ONHs in both the unstretched and stretched states. Preliminary results from quantification of SAXS and WAXS data revealed no significant differences in collagen fibril diameters, interfibrillar Bragg and interfibrillar spacing. However, collagen D period ($p=0.029$) and distance between amino acid residues ($p=0.044$) were significantly greater in stretched human ppsclera, but not in porcine ONH. Several studies have focused

on the hierarchical nature of collagenous tissue (Parry et al., 1978a, Kastelic et al., 1980, Kastelic et al., 1978) attempting to relate tissue's structure with the function (Kastelic et al., 1980, Viidik, 1972). Most of the studies focussed on the tissue at the fibril bundle level and have correlated uncrimping and stretching with the nonlinear response of the tissue (Belkoff and Haut, 1991, Comninou and Yannas, 1976, Lanir, 1979, Lanir, 1983, Liao and Belkoff, 1999, Stouffer et al., 1985). However, little has been investigated on the nanostructure. The increase in D period and distance between amino acid residues in the stretched ppsclera without a change in interfibrillar spacing suggest that the force applied by the radial stretch unwind collagen at fibril and molecular level. Collagen unwinding, or uncoiling, might refer to the denaturation of the triple helix which leads to its disruption. An uncoiled tropocollagen has significant effects on the mechanical properties of the whole tissue (Veres and Lee, 2012, Wang et al., 2002, Uzel and Buehler, 2009).

It has been proposed by computational modelling that the type of amino acids that define the tropocollagen molecule change its stiffness. For instance, axial strain applied on a single fibril uncoiled the molecule, leading to a modification of amino acids motifs; which was shown to change the stiffness of tropocollagen molecules (Uzel and Buehler, 2009). This finding is also supported by a scanning electron microscopy study which showed that when loaded, collagen fibrils undergo a failure mechanism which involved molecular denaturation (Veres and Lee, 2012). Taken together, these findings suggest that after loading, collagen molecules can uncoil, leading to a change in mechanical properties of the fibril. This in turn, would have effects on the response of the ONH to different levels of IOP-induced stress.

5.5 Limitations

This study presented few limitations. Firstly, the lack of human ONHs sections at young ages below 22yr, did not allow a complete investigation into the age-related changes of the nanostructure of collagen. Even though a good age-range was analysed, the study would benefit from investigation of nanostructure at very young ages. Secondly, due to date differences in experimental data collections, WAXS pattern acquisition was not available for the 22, 25, 46, 47 and 59-year-old ppsclera., as the WAXS set up at Diamond Light Source had not been optimised at this time. Even though this limited the WAXS analysis in those ages, the setup was optimised in Diamond Light Source to allow better

acquisition of diffraction patterns which allowed the investigation as a function of age. Thirdly, the preliminary study on the nanomechanics following radial stretching was limited by the number of samples due to beam time allocation. However, the results presented needed further investigation to confirm or dismiss the changes in D periodicity and the absence of changes in interfibrillar Bragg spacing, interfibrillar spacing and fibril diameter. Further investigations are also needed to improve the reliability of the data in calculating the strain in both X and Y direction. Discrepancy could be however explained by the Poisson ratio. Poisson's ratio is the ratio of lateral strain to longitudinal strain in a material. Large Poisson's ratio suggests that the lateral strain is more (for the same given longitudinal strain) compared to another material whose Poisson's ratio is small. However, discrepancy in the X and Y direction could be also due to the less connective tissue content in the superior-inferior axis versus nasal-temporal. In glaucoma, the neuroretinal rim appears to thin in the superior-inferior axis, leading to a potentially elongated LC in this direction (Bourne 2012), which could explain a difference in strain between the X and Y.

The longitudinal direction is defined as the direction of pull, whereas the lateral direction describes the perpendicular direction with respect to the direction of pull. The Poison's ratio of the strain in the X and Y direction could explain the differences in the calculated strain in X and Y for both human and porcine ONHs. Finally, even though PTA successfully stained the LC, only 4 ages were investigated which limited the age-range analysis of LC collagen parameters, more will be investigated in the future, now that techniques have been developed for this purpose.

5.6 Conclusion

The response of the LC and the ppsclera to stress is essential in maintaining a suitable environment to protect axons that pass through the ONH. The results from nanostructure and microstructural data analysis will aid in understanding why the LC and ppsclera structure is critical to its biomechanical performance, and how ageing alters its predisposition to glaucoma. Collagen fibrils provide support against an applied force depending on the fibril diameter and the organisation within the tissue (Parry, 1988, Hukins and Aspden, 1985). Ppsclera fibrillar collagen diameter increased as a function of age, leading to a more compact and less compliant tissue. Additionally, the axial arrangement of tropocollagen molecules increases, suggesting that as a consequence of

radial stretch, the collagen molecules unwind, altering the mechanical behavior of the fibrils. These connective tissue changes, at least in part contribute to the decreased resilience of the ageing human lamina cribrosa

5.7 Future work

The potential of the PTA to enhance the fibrillar collagen signal will allow an investigation of load-bearing components in the LC as a function of age and glaucoma. Hence, more data on the LC from ONH PTA-stained sections is required to fully understand the effects of age on the nanostructure of the LC. Observation of elastin in our WAXS data will enable the development of future experiments to characterise elastin and collagen nanostructural changes, together with microstructural ONH features, as a function of load, to determine which connective tissue components play a role in ONH biomechanics at different stages of the stress-strain curve.

Preliminary data from the effect of induced strain in this beam-time has permitted an insight into how collagen fibrils behave in the ppsclera. However, a stiffer and more rigid ppsclera may limit scleral canal expansion (Sigal and Ethier, 2009); hence further studies are required to ascertain the role of the ppsclera-LC interaction with the ONH in glaucoma. Future investigations are therefore required to i) analyse collagen and elastin in the human LC as a function of age and glaucoma (LC diffraction patterns following PTA labelling) and ii) fully explore collagen and elastin nanostructure as a function of ONH radial stretch (to mimic ONH biomechanics in glaucoma) in different aged ONHs.

Chapter 6 – Simultaneous Raman-Brillouin microscopy to map structure and micro-mechanics in the porcine optic nerve head

6.1 Introduction

Light scattering phenomena are divided into elastic and inelastic processes. When the light is scattered by matter, most of the scattering is elastic scattering (Rayleigh scattering) with no change in energy; i.e. the scattered light has the same energy as the incident light, therefore the same wavelength. A small portion of scattering is inelastic where the scattered light has different energy to the incident light.

6.1.1 Brillouin scattering

Brillouin light scattering is an inelastic process arising from the interaction of light with spontaneous thermodynamic fluctuations that are present in the tissue, known as acoustic vibrations, or phonons (figure 6.1) (Mattana et al., 2018).

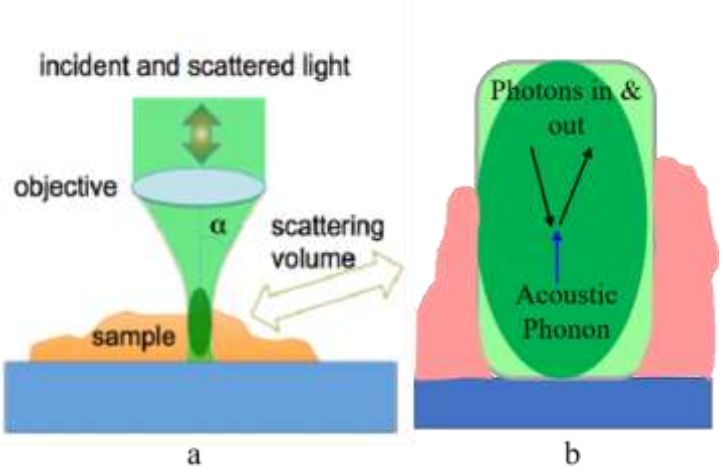

Figure 6.1.Schematic representation of Brillouin scattering. a) An incoming photon is radiated onto the sample at angle α. b) Closer view of the interaction between the incoming light and the acoustic phonon with the scattering volume, giving rise to the Brillouin scattering. Adapted from Mattana et al., (2018) and reprinted with permission. Copyright @ 2017, World Scientific Publishing Co. Pte. Ltd (see appendix IV.14)

Brillouin microscopy is a non-invasive technique used to map the micromechanical properties of tissue (Scarcelli and Yun, 2007a, Scarcelli et al., 2015) and for

characterisation of viscoelastic properties of biological materials. A visible laser light (photon) (λ = 500 nm – 600 nm) is radiated onto the sample. The photon interacts with the material lattice, releasing an acoustic wave (phonon) and therefore losing an amount of energy corresponding to the energy of the phonon. The change in energy corresponds to a change in the frequency of the scattered light, usually measured in the order of GHz (Mattana et al., 2017b).

The frequency of the scattered photon is measured by a spectrophotometer and the energy of the phonon is calculated as the difference between the energy of the incident and the energy of the scattered photons.

The process described, where the frequency of the scattered beam is slightly lower than that of the emitted beam, is known as Stokes process. An anti-Stokes process is, on the contrary, when the scattered photon has absorbed the phonon energy and its frequency results slightly higher than that of the emitted beam.

The frequency shift, known as Brillouin frequency shift ($\acute{\omega}_b$) (Wu et al., 2017) can be described as:

$$\acute{\omega}_b = \frac{2n}{\lambda}\sqrt{\frac{M}{\rho}}\sin\frac{\theta}{2}$$

where

ρ = density of the material

n = refractive index of the material

λ = wavelength (nm) of the incident laser

θ = angle between incident and scattered wave vectors

M = modulus describing the stress necessary to determine a change in volume within the material, by compression or expansion.

It can be noticed that the frequency shift is proportional to the square root of the modulus, therefore Brillouin graphs can be interpreted as “stiffness maps”, which could be used to determine variation in longitudinal modulus (Scarcelli et al., 2015, Antonacci et al., 2015, Zhang et al., 2017). From Brillouin experiments, three independent parameters can be extracted: i) the frequency shift, related to the elasticity of the material, ii) the linewidth (peak width) related to the viscosity of the material and iii) Brillouin intensity, related to the intensity of the Brillouin peak.

Brillouin microscopy has gained attention in the last decade as a promising optical technique to detect micromechanical changes in cardiovascular disease (Antonacci et al., 2015), ophthalmology (Scarcelli and Yun, 2012, Scarcelli et al., 2012, Scarcelli et al., 2013, Scarcelli et al., 2011, Scarcelli et al., 2014, Lepert et al., 2016, Reiß et al., 2011) and cell mechanics (Scarcelli et al., 2015, Antonacci and Braakman, 2016, Zhang et al., 2017, Meng et al., 2015).

6.1.2 Raman scattering

Raman spectroscopy is a technique used to provide information on molecular vibration and crystal structure. Raman scattering can be classified into two types, Stokes and anti-Stokes. The first involves absorption of energy by the molecules hence Stokes Raman scattered light has less energy than the incident light. On the other hand, anti-Stokes Raman scattering involves energy transfer to the scattered photon hence the anti-Stokes Raman scattered light has more energy than the incident light (figure 6.2).

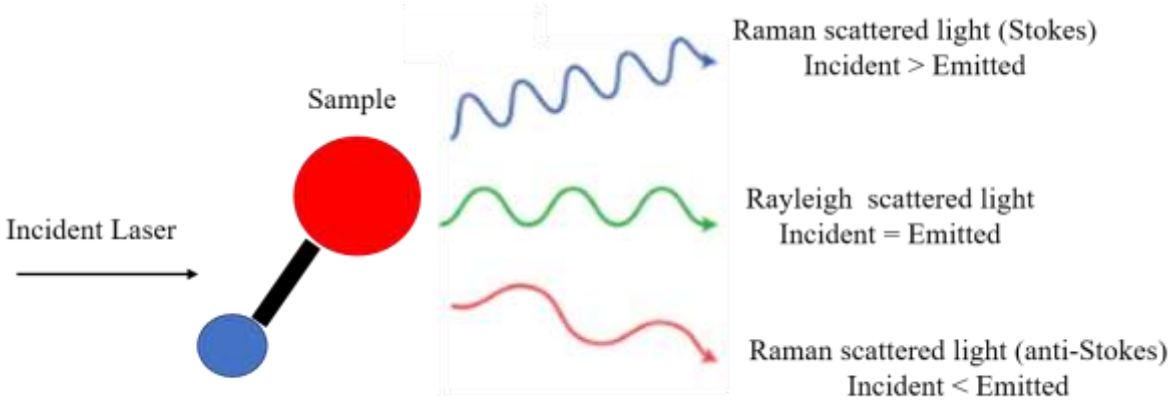

Figure 6.2. Raman and Rayleigh scattering. Anti-Stokes Raman scattering involves energy transfer to the scattered photon hence the anti-Stokes Raman scattered light has more energy than that of the incident laser. Stokes involves absorption of energy by the molecules hence Stokes Raman scattered light has less energy than that of the incident laser. Rayleigh scattering occurs when there is no energy exchange between molecules and hence the incident and scattered photons have the same energy.

The peak associated to Raman spectrum is derived from the vibration of molecular bonds. Peak position shows the specific vibrational mode of each molecular group included in the material. The same vibrational modes for each group will show a shift in peak position due to the surrounding environment, hence it is said the Raman spectrum shows the "molecular fingerprint" of the sample of interest. Important to note is that the shape of the Raman spectrum changes within different areas of a heterogeneous tissue. Considering

the frequency peak position of a given molecule within the material, the intensity of the Raman peak is proportional to the concentration of the molecule multiplied by its optical activity. Therefore, Raman spectroscopy can probe the changes in the concentration of the same molecule within the same material at different points and the differences in concentration between different materials (Mattana et al 2018).

Covalent chemical bonds have different molecular motion which includes rotation and vibration. Different types of vibration include symmetric, and asymmetric stretching, scissoring, rocking, wagging and twisting (figure 6.3).

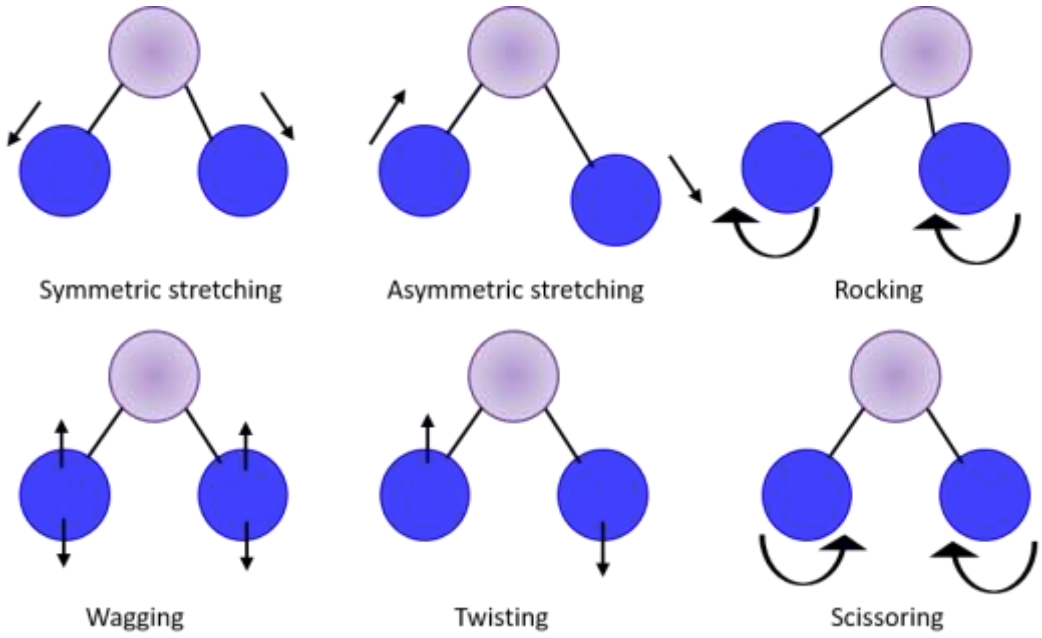

Figure 6.3. Schematic representation of various types of molecular vibration detected by Raman spectroscopy.

The thermal energy present in the surrounding environment makes the bonds vibrate and the light can interact with this molecular vibration. Raman spectroscopy uses scattered light from molecular vibrations to characterise the chemical composition of a sample, where the laser interacts with the molecular vibration resulting in the energy to be shifted up or down (i.e. Raman shift). This shift provides information about the vibrational modes in the systems and can be used to identify the types of bonds in the compound. Each type of bond (e.g C-H, C-C) has unique vibrational modes which leads to specific interaction with light and therefore produces a different Raman shift. The Raman spectrum is usually expressed as the intensity of scattered light versus wavenumber (cm^{-1}) (the reciprocal of wavelength) and Raman shift can be calculated using:

$$Raman\ shift\ (nm) = \lambda\ \text{excitation} - \lambda\ \text{emission}$$

Collagen and elastic fibres are altered in the ageing LC (Albon et al., 1995, Albon et al., 2000a, Hernandez et al., 1989) and the mechanical compliance of the LC decreases in age (Albon et al., 2000b) and glaucoma (Zeimer and Ogura, 1989). Therefore, understanding the mechanisms of biomechanical change is important. Coupled Raman/Brillouin micro-spectroscopy enables chemical composition of samples to be allocated to specific mechanical properties and has been applied to *ex vivo* epithelial tissue in the oesophagus (Palombo et al., 2016, Palombo et al., 2014).

The hypothesis of this study was that the dual approach of using simultaneous Brillouin and Raman microscopy would enable quantitative data of ONH micromechanics to be correlated with the ONH connective tissue composition.

The mechanical behaviour of a tissue depends on the organisation of the macromolecules and their interaction (Hukins et al., 1996), which includes hydrogen and carbon bonds within proteins. Therefore, understanding the micromechanical behaviour of collagen and elastic fibres within the ONH helps in understanding the response of the ONH to elevated IOP.

Thus, this chapter, provides preliminary data on the capability of Brillouin-Raman microscopy in determining differences within the porcine preL and LC. The combination of Brillouin-Raman was used to correlate elasticity and viscosity to specific molecular bonds. To achieve this, the objectives of this chapter were to:

- characterise typical Brillouin and Raman spectra generated from the LC
- determine if LC material properties (as determined by Brillouin elasticity and viscosity parameters) could be assigned to particular regions/components (as determined by Raman spectra) within the LC

6.2 Materials and methods

6.2.1 Source of tissue

Twelve fresh porcine globes were received from the local abattoir (W.T. Maddock, Wales, UK) and were cleaned as described in 4.2.1.

6.2.2 Sample preparation

All ONHs were mounted onto a sledge microtome (Microm HM 440E, Thermo Fisher, UK) and frozen at -35°C and serial 100µm transverse ONHs sections were cut, as described previously (2.2.2). Sections were mounted in PBS on 20 mm diameter calcium fluoride (CaF) slides (Crystran Ltd, Dorset, UK) under circular 20 mm diameter coverslips (0.17 mm thickness, Fisher Scientific, UK), then sealed with nail vanish (figure 6.4).

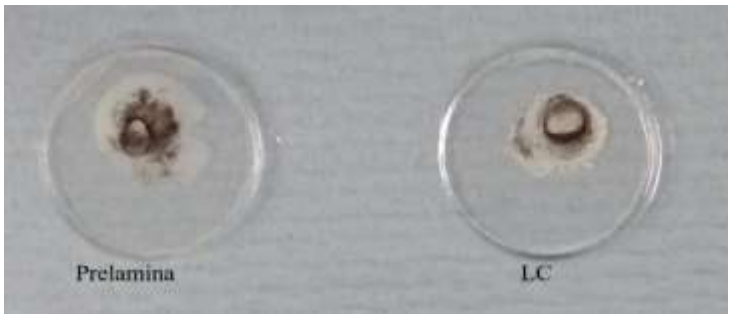

Figure 6.4. 100 µm thick porcine ONH sections mounted onto circular 20 mm diameter CaF slides and covered with 0.17 mm thick glass coverslip. PreL and LC are shown. Scale bar represents 20mm.

6.2.3 Brillouin/Raman set up

Brillouin and Raman spectroscopy were simultaneously carried out at the Department of Geology and Physics, University of Perugia, (Perugia, Italy). The experimental set up (figures 6.5 and 6.6) was coupled with custom-written LabSpec 5 software for Raman data acquisition and custom-written Group of High-resolution Optical Spectroscopy and related Techniques (JRS GHOST - University of Perugia, Perugia, Italy) software version 7 (Fioretto and Scarponi, 2009) for Brillouin data acquisition and analysis.

A single mode diode-pumped-solid state Excelsior laser (Spectra-Physics, Santa Clara, CA, USA) at wavelength 532 nm was passed through a temperature-controlled etalon filter to reduce laser intensity. The laser was focused onto the sample via a confocal microscope (JRS Scientific Instruments, Mettmenstetten, Switzerland). A tunable ultrasteep short-pass filter (TEF, Semrock SP01-561RU), with edge close to 532nm, transmitted the anti-Stokes inelastic scattered light into a Fabry-Perot interferometer for

Brillouin spectra collection and reflected the Stokes inelastic scattered light towards the Raman spectrometer.

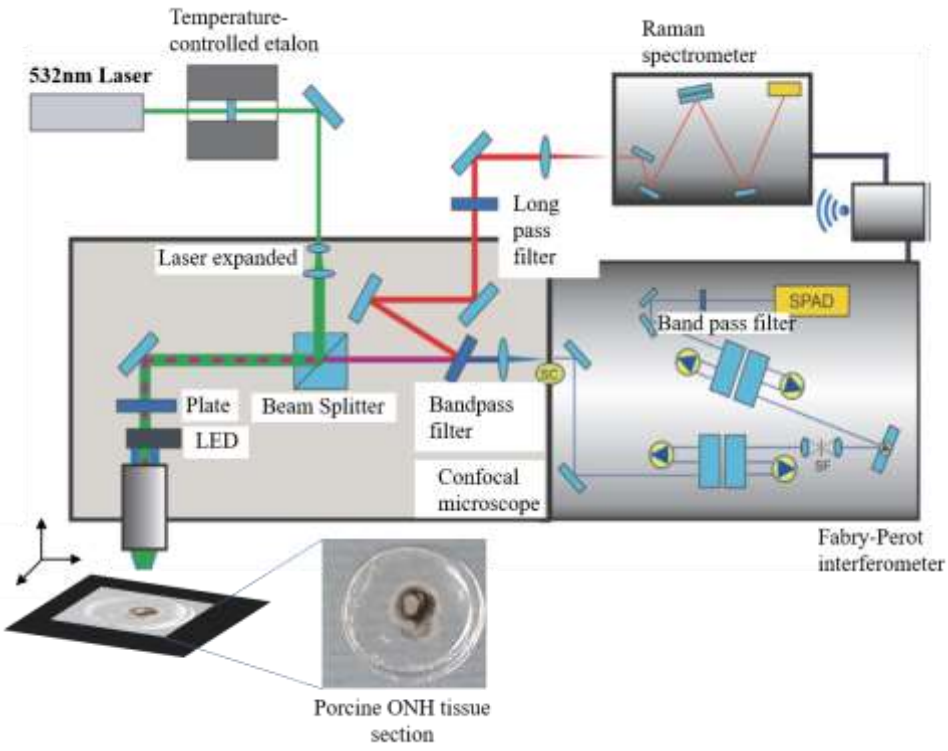

Figure 6.5. Schematic set up of the simultaneous Brillouin-Raman spectroscopy. A single mode diode-pumped-solid state Excelsior laser (Spectra-Physics, Santa Clara, CA, USA) at wavelength 532 nm was passed through a temperature-controlled etalon filter to reduce laser intensity. Then, the laser was focused onto the sample by the same objective lens used to collect backscattered light. A tunable ultrasteep short-pass filter (TEF, Semrock SP01-561RU), with edge close to 532nm, transmitted the anti-Stokes inelastic scattered light into a Fabry-Perot interferometer for Brillouin spectra collection and reflected the Stokes inelastic scattered light towards the Raman spectrometer. Adapted from Mattana et al., (2018) and reprinted with permission of Light: Science & Application under a Creative Commons Attribution 4.0 International License (https://creativecommons.org/licenses/by/4.0/).

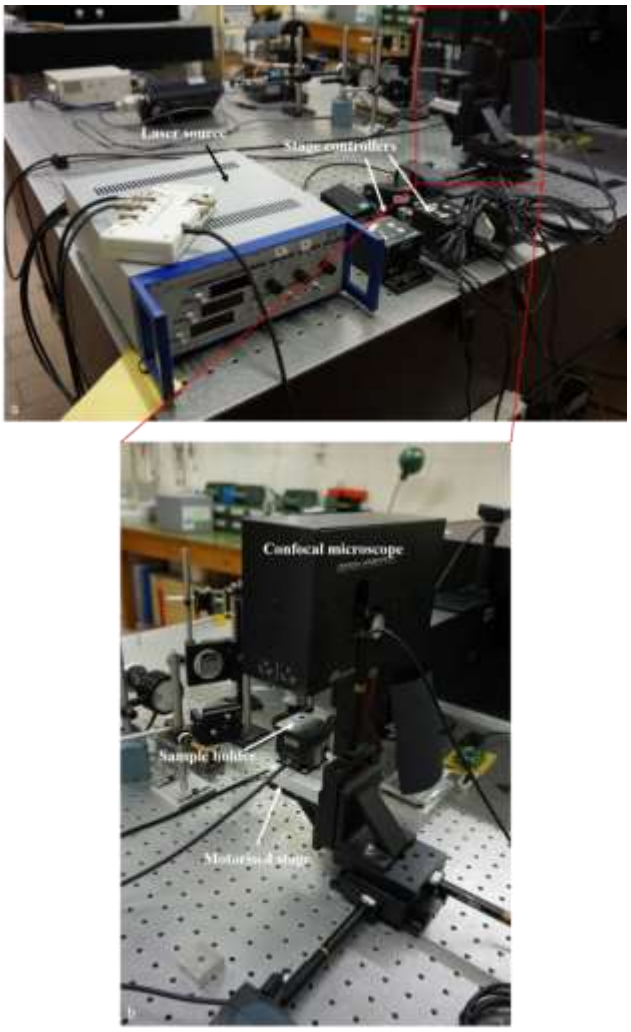

Figure 6.6. Brillouin/Raman set up. A single mode diode-pumped-solid state Excelsior laser at wavelength 532 nm is the laser source (a) and focused onto the sample by a confocal microscope (b). Manual stage controllers (a) allowed the movement in the xyz direction of the motorised stage (b) onto which the sample holder (b) was mounted.

The microscope was coupled with a light emitting diode (LED) at 470 nm to illuminate the sample surface to distinguish the ROI. A 20x Apochromat objective lens with a working distance of 20 mm and numerical aperture of 0.42 was used to collect Raman/Brillouin spectra. The same objective was used to focus the beam onto the sample, as well as collect backscattered light. A short pass filter then transmitted the anti-Stokes inelastic scattered light into a Fabry-Perot interferometer (to create an interference pattern) (HC-TFP -Table Stable Ltd., Mettmenstetten, Switzerland) for Brillouin spectra collection and reflected the Stokes inelastic scattered light towards the Raman spectrometer (iHR320 Triax, Horiba UK Limited, Northampton, UK). The Fabry-Perot

spectrophotometer included a short bandpass filter and a long pass filter to reject residual elastic scattering of the Raman line. For measurements, samples were mounted onto a piezoelectric stage (PI 611-3S Nanocube) with resolution of 1 nm and a motion range of 100 µm in the X and Y axes.

6.2.4 Data collection

Brillouin and Raman spectra were simultaneously collected from six LC sections and three preL sections. One ROI from each preL and LC section was selected and, thus, a total of nine regions of interest were analysed from preL (n=3) and LC (n=6). Each ONH tissue section was mounted onto the stage and the blue LED shone onto the surface. Each area of interest within preL and LC was manually aligned and the area to be raster-scanned was selected by moving the motorised stage in the XYZ until the preferred region was illuminated. The Z position was optimised by checking the intensity of the Raman spectrum which showed sharp peaks generated from the tissue and a small peak derived from the CaF slide (at ~300 cm^{-1}) (Gee et al., 1966, Russell, 1965).

A raster scan, using a motorised stage, was performed to acquire data from areas between 45x45 μm^2 (10 x 10 points, 5 µm step) and 100x100 μm^2 (20 x 20 points, 5 µm step) within preL and LC (Table 6.1). Raman and Brillouin spectra were simultaneously acquired at each point (90 seconds acquisition time per point) within the ONH regions over 2.5 or 10 hours.

Points	Steps (µm)	Area covered (μm^2)
10x10	5	45x45
12x12	5	55x55
13x13	5	60x60
20x20	5	100x100

Table 6.1. Scan parameters for simultaneous acquisition of Brillouin and Raman spectra; number of scan points (XY) at 5µm steps, collected over areas between 45x45μm^2 and 100x100 μm^2.

6.2.5 Raman and Brillouin spectroscopy analysis

The method presented in this chapter has been recently validated using wool fibres (Fioretto et al., 2019) and represents a reliable way to extract the intensity and the average frequency shift of Brillouin peaks and of the Raman bands based on the calculation of spectral moments. Figure 6.7 shows a flow diagram on the method used to analyse Raman and Brillouin spectra. All software used in Raman and Brillouin data analysis were developed by GHOST (Palombo et al., 2014) and are launched in the command prompt.

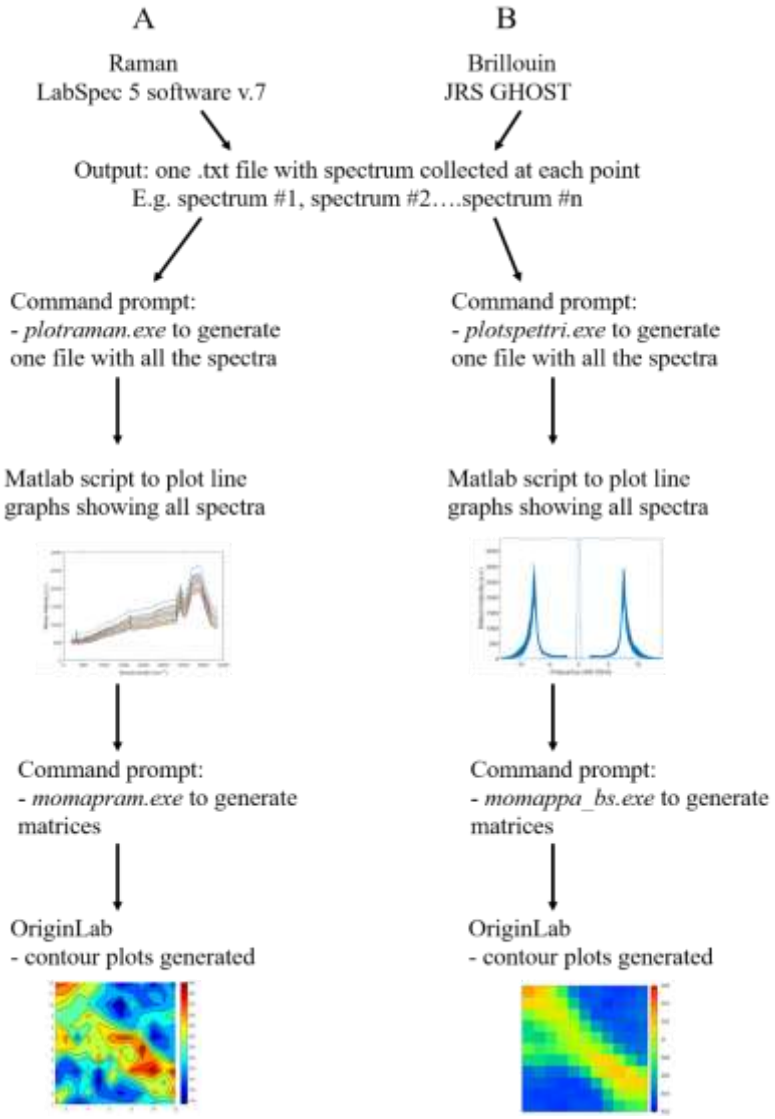

Figure 6.7. Flow diagram of Raman and Brillouin data collection and analysis using LabSpec 5 (A) and GHOST (B) respectively. *Plotraman.exe* and *plotspettri.exe* were used firstly to generate a .txt file with all the Raman and Brillouin spectra, respectively, for each scan. Subsequently, *momapram.exe* and *momappa_bs.exe* generated matrices of the spectra which were imported into OriginLab to create colour-coded plots.

6.2.5.1 Raman spectrum collection and analysis

Raman spectra at each point within the preL and LC were collected using LabSpec 5 software, which gave an output spectrum for each scanned point (between 100-400 spectra per scan) as a .txt file. These were imported into a GHOST software and the function called "*Plotraman.exe*" generated a single .txt file with all the spectra of a scan. The .txt file was imported into MATLAB and plotted using custom made script (see appendix II.3 "Raman_Intensity_profile_v1") to enable the visualisation of peaks associated to different vibrational modes and compounds.

6.2.5.2 Raman spectroscopy from porcine ONHs

Each Raman dataset derived from preL and LC contained between 100 (10 x 10 points area) and 400 (20 x 20 points area) spectra and were plotted as intensity (y-axis) against wavenumber (x-axis) (number of waves per cm, cm^{-1}). Each peak in the Raman spectrum corresponded to a specific molecular bond vibration, including individual bonds such as carbon-carbon (CC, C=C), nitrogen-oxygen (NO), carbon-hydrogen (CH) and nitrogen-hydrogen (NH).

Two features were analysed from Raman spectra corresponding to i) 0^{th} spectral moment, representing the intensity of the peak, related to a molecular vibration and ii) 1^{st} spectral moment, representing the "barycentre", i.e. the average of wavenumber weighed by their intensity.

In the case of a single peak, the 1^{st} moment provided its frequency position, while in case of a multi-peak spectral feature (even not well spectrally resolved or overlaid), it gives the average of peak positions. In this case, the high (low) frequency shift of the 1^{st} moment is proportional to the relative intensity of the high (low) frequency vibration, giving an estimate of the relative fraction of the corresponding molecules (Fioretto et al., 2019).

From the Raman spectra, markers of different chemical species were obtained by analysing frequency regions between 500 and 3000 cm^{-1} where the characteristic bands of the CH2 and CH3, Amide I, Amide III and collagen stretching vibrations were located (figure 6.8).

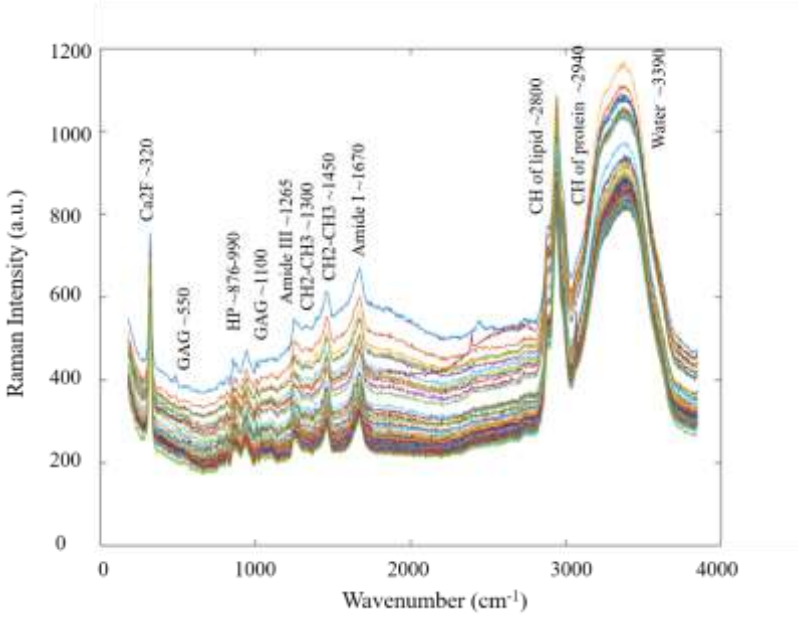

Figure 6.8. Raman set of graphs made by 90 spectra acquired from porcine LC at 10 x 9 points scan, covering an area of 45 x 40 μm^2. Each peak represents a unique chemical fingerprint of vibration mode of a chemical bond. Raman peaks found in the literature corresponding to CaF slide, glycosaminoglycans (GAG), collagen (HP), Amide I and III and CH bonds are shown. The band at the highest frequency is associated with water (~3390 cm^{-1}).

6.2.5.3 Raman colour-coded maps analysis

Hyperspectral analysis of the Raman datasets produced contour colour-coded maps of preL and LC. Colour-coded maps were produced for the intensity (0^{th} momentum) of each selected peak in the Raman spectrum by a GHOST software. Maps of frequency shift (1^{st} momentum) were also produced for the double well defined peak observed at high frequency shift (~2800-2900 cm^{-1}).

The function "*Momapram.exe*", generated two .txt files containing matrices with dimensions nX and nY (where n is the number of X rows and Y columns), corresponding to the intensity and the frequency of the spectra within the selected peak. Matrices were imported into OriginLab and plotted as colour-coded map using the "Contour plot" function (see, for example, figure 6.9). Maps were generated for each Raman peak associated to a particular molecular bond.

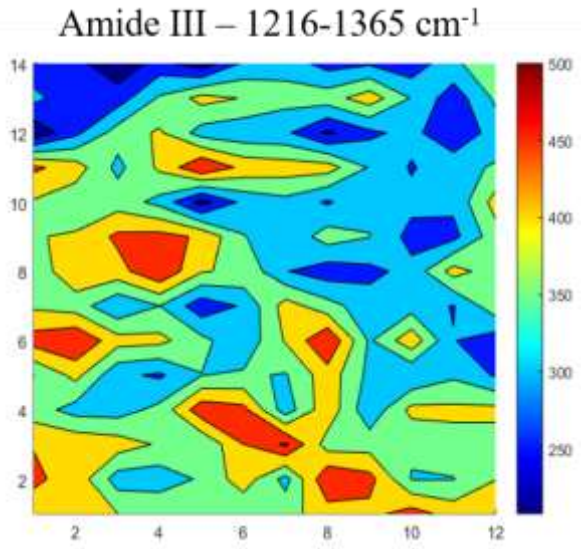

Figure 6.9. Contour colour-coded plot of Amide III peak within the LC Raman spectrum over an area of 55μm^2. Amide III peak centred at 1248 cm^{-1} showed a shift at higher frequency in the red-yellow areas.

6.2.6 Brillouin spectroscopy from porcine ONHs

A typical Brillouin spectrum obtained from the LC, acquired with GHOST v7, is shown in figure 6.10, Stokes and anti-Stokes peaks are illustrated. In hydrated specimens, such as those used in the current study, the Brillouin spectrum is highly affected by the presence of water, which appeared as a sharp peak at 7.5 GHz (figure 6.10). The contribution of the specimen in hydrated samples appeared as a small shoulder shifted at higher frequency (figure 6.10).

6.2.6.1 Brillouin spectrum collection and analysis: Damped Harmonic Oscillator (DHO) fitting

GHOST v7 automatically output a spectrum for each data point (between 100-400 spectra per scan, depending on the number of points) as a .dat file. These were imported into GHOST software and the function called "*Plotspettri.exe*" generated a single .txt file with all the spectra of a scan. The .txt file was imported into MATLAB and plotted using custom written script (see appendix II.4 "Brillouin_Intensity_profile_v1") to enable the visualisation of Brillouin peaks for each scan.

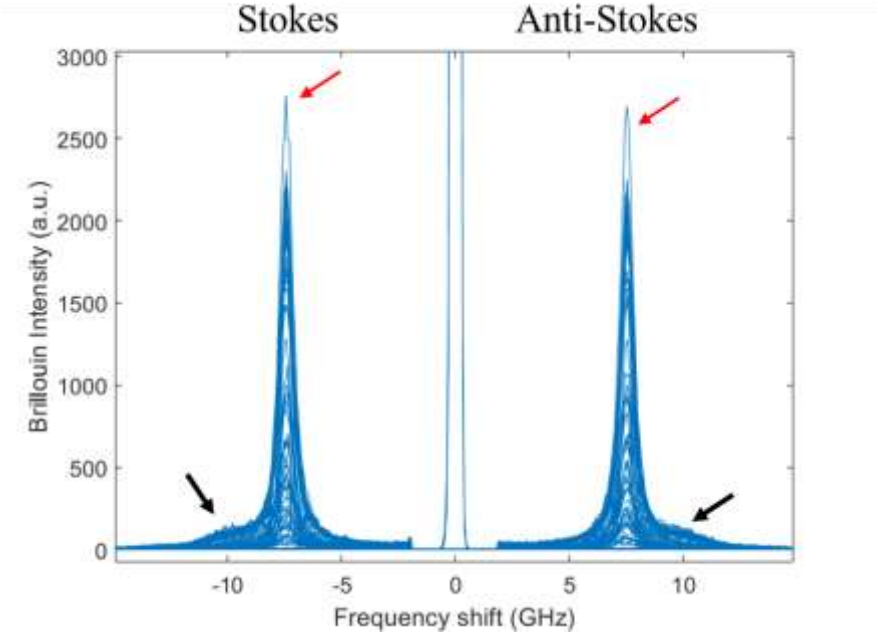

Figure 6.10. Brillouin spectra from porcine LC section. Brillouin graphs of 100 spectra, showing the sharp peak at 7.5 GHz associated with water (red arrows) and a little shoulder at higher frequency representing the contribution of the specimen to the Brillouin peak (black arrows).

Since the experiment involved using hydrated samples to best mimic physiological conditions, the decomposition (discrimination of two or more contributing peaks) of the Stokes peaks was performed to remove the water contribution, enabling the analysis of the sample only. To this aim, the intensity profile was fitted by two Damped Harmonic Oscillator (DHO) functions, using GHOST software as previously described (Palombo et al., 2014). Brillouin data analysis and the double DHO fitting was performed by a researcher (Martina Alunni Cardinali) at University of Perugia, Italy, based on the previously described methodology (Fioretto et al., 2019).

Briefly, fixed parameters of the DHO attributed to water, namely frequency shift (7.53 GHz) (Scarcelli and Yun, 2007b, Koski and Yarger, 2005), and linewidth (0.799 GHz) were imported into the GHOST script, together with the frequency range to be fitted, selected from the graph generated from "*Plotspettri.exe*" function. Since the linewidth of water peaks differs amongst materials, its value was left free in a first fitting run and fixed to the average of the obtained values (i.e. 0.799 GHz) in the second run. Table 6.3 summarises an example of parameters imported for peak separation.

Parameters	
Min Freq Stokes	4 GHz
Max Freq Stokes	12 GHz
Min Freq Anti-Stokes	-4 GHz
Max Freq Anti-Stokes	-12 GHz
Frequency (water)	7.57 GHz
Linewidth (water)	0.799 GHz

Table 6.2. Brillouin parameters imported for peaks separation. Stokes, anti-Stokes, frequency and linewidth of water were imported into the custom-made GHOST script to automatically decompose Brillouin water peak from the Brillouin contribution of the sample.

6.2.6.2 Brillouin colour-coded maps

Data extracted from the double-DHO fitting was output as .txt files and imported into a GHOST software. The function, named "*Momappa_bs.exe*" generated three .txt files organised as matrices of intensity, frequency shift and linewidth with dimension nX and nY (with n as the number of X rows and Y columns). The frequency shift measured in GHz, was related to the elasticity of the material, linewidth in GHz was related to the viscosity of the material and the Brillouin intensity to the intensity of the Brillouin peak. Matrices were imported into OriginLab and plotted as a colour-coded map using the "Contour plot" function. Maps were used to compare elasticity, viscosity and intensity of the spectra between ONH regions (preL and LC).

6.2.7 Distribution of prelamina and LC spectra

Matrices of frequency shift and linewidth generated from the function "*Momappa_bs.exe*" as described in 6.2.6.2 were opened with Microsoft Excel and values organised in ascending orders. Data was then subdivided into eight bins and plotted as histograms of spectra distribution for preL and LC.

6.2.8 Statistical analysis

Statistical tests were performed in SPSS version 25. Kolmogorov–Smirnov test was performed to compare the frequency shift and linewidth distribution between preL and LC and between LC plates and pores.

6.3 Results

The spectra peak wavenumber, and those of Raman spectra produced from the preL and the LC, together with their attributed molecular vibration/structure are shown in Table 6.4.

	ONH section	Peak (cm^{-1})	Identification	Reference
PreL	1	~ 2892 ~ 2947	CH vibration in lipid and protein	(Czamara et al., 2015)
	2 and 3	As above	As above	As above
LC	1	~ 555	GAG chondroitin 6 and 4 sulphate	(Bansil et al., 1978, Ellis et al., 2009)
		~ 865	CC stretch of proline ring (collagen)	(Ikoma et al., 2003, Nguyen et al., 2012, Sato and Martinho, 2018, Zhang et al., 2011)
		~ 940	CC stretching of aromatic ring of proline and collagen	(Ikoma et al., 2003, Nguyen et al., 2012, Sato and Martinho, 2018, Zhang et al., 2011)
		~ 1110	GAG, if sharp associated to chondroitin 6 sulphate, if broad associated to chondroitin 4 sulphate	(Bansil et al., 1978, Ellis et al., 2009)
		~ 1235	Amide III, CN stretch and NH deformation amide III.	(Malini et al., 2006, Notingher et al., 2004, Tuma, 2005)
		~ 1469	CH2/CH3 deformation of lipids & collagen.	(Cheng et al., 2005, Frank et al., 1995, Stone et al., 2002, Stone et al., 2004)
		~ 1685	Amide I, CH3 symmetrical stretching; NH2 symmetrical and asymmetrical stretching.	(Cheng et al., 2005, Frank et al., 1995, Shetty et al., 2006, Stone et al., 2002, Stone et al., 2004, Tuma, 2005)
		~ 2873 ~ 2934	CH vibration in lipid and protein	(Czamara et al., 2015)
	2-5	As above	As above	As above
	6	As above	As above	As above
		~ 815	COC stretching of glucosyl-galactosyl hydroxy-lysinonor-leucine cross-link	(Borel, 1991, Ikoma et al., 2003)
		~ 1139	CC stretching, CH3 deformation of fatty acids	(Czamara et al., 2015, Krafft et al., 2005)

Table 6.3. Molecular bonds and vibrational modes of Raman spectra from porcine preL and LC.

6.3.1 Brillouin and Raman spectroscopy from the prelamina

Representative Raman spectra within a preL are shown in figure 6.11. Raman spectra from porcine preL showed one well defined peak identified at higher frequency, composed of two small shoulder at 2892 and 2947 cm^{-1} (see Table 6.4, figure. 6.11a-c, red boxes). Different undefined peaks were also identified at lower frequency, however, intensity and shape appeared negligible, therefore no investigation of those was performed. Additionally, the three preL spectra presented a broad peak at 3350 cm^{-1} which was attributed to water (Leikin et al., 1997).

Representative Raman color-coded maps from preL are shown in figure 6.12. Intensity (figure 6.12a) and frequency shift (figure 6.12a) maps over a 100x100 μm^2 area (20 x 20 points) are shown. Spectral assignment, based on previous studies determined this peak to be attributed to CH2-CH3 stretch and CH vibrations in lipids and proteins (Czamara et al., 2015).

Raman intensity (figure 6.12a) and weighted average intensity peak position (figure 6.12b) showed regions of higher intensity. In the latter, the higher frequency shifts observed corresponded to areas of higher intensity, suggesting that these regions were rich in protein (Caponi et al., 2013, Mattana et al., 2017a, Mattana et al., 2018). The lower intensity and frequency regions also corresponded and were indicative of lipid-rich regions (Caponi et al., 2013, Mattana et al., 2017a, Mattana et al., 2018).

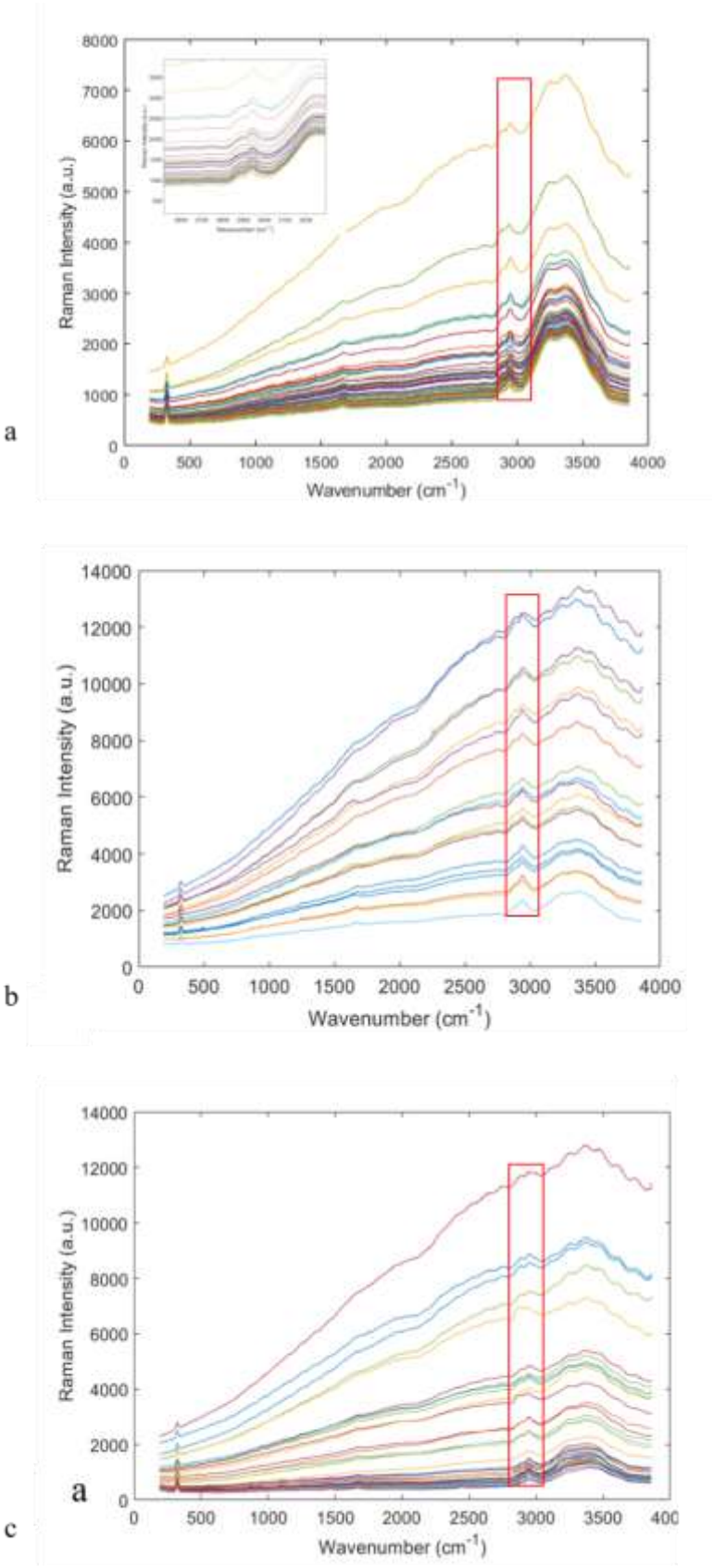

Figure 6.11. Raman spectra from three (a-c) porcine prelamina sections. Representative Raman graph of 90 spectra showed wide water-associated peaks at ~2900 cm^{-1} (red box in a-c).

Brillouin spectra of preL are shown in figure 6.13. An intense central peak at 0 GHz due to the elastic scattering can be seen in figure 6.13a,c,d, with a Stokes/anti-Stokes peaks due to water inelastic scattering at 7.5 GHz. A very small shoulder, almost negligible was seen in the Brillouin spectra (figure 6.12b), however, not well defined, suggesting the water predominated on the sample contribution to the Brillouin spectra.

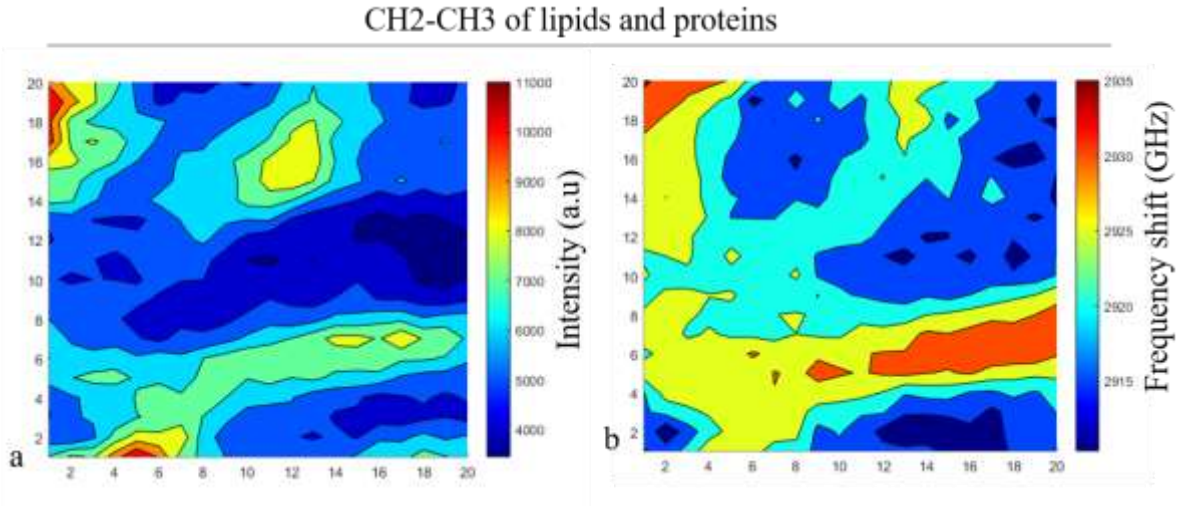

Figure 6.12. Representative colour-coded maps of the CH2-CH3 peak showed the distribution of protein and lipid within the prelamina. 0^{th} moment (a) and 1^{st} moment (b) showed shifts at higher frequency (orange-red areas) within similar regions. In the latter, the higher frequency shifts observed corresponded to areas of higher intensity, suggesting that these regions were rich in protein (Caponi et al., 2013, Mattana et al., 2017, Mattana et al., 2018). The lower intensity and frequency regions also corresponded and were indicative of lipid-rich regions (Caponi et al., 2013, Mattana et al., 2017, Mattana et al., 2018).

Representative Brillouin color-coded stiffness maps from preL over a 100x100 μm^2 area (20 x 20 points) are shown in figure 6.14. The higher the intensity (figure 6.14a) the lower is the frequency shift (figure 6.14b) and vice versa, suggesting that regions of higher intensity correspond to regions of low elasticity. Frequency shift ranged from 8.2 – 8.36 GHz and no regions at highest frequency (8.42 GHz) were observed. Linewidth (figure 6.14c) ranged from 1.1 – 1.9 GHz. Although small, Brillouin maps showed the heterogenous nature of the sample due to the contribution of both water and sample. The greater contribution of water to the Brillouin spectra suggests that the sample was very diluted into a solution of mostly water.

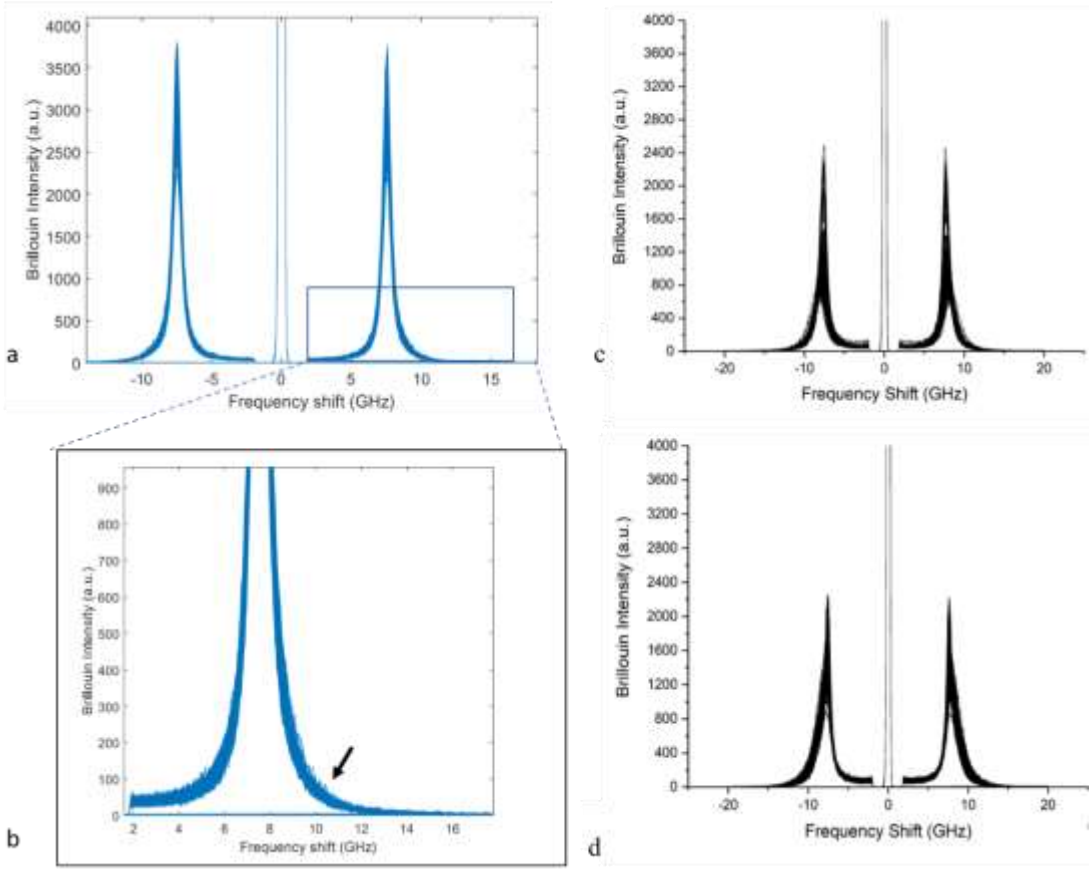

Figure 6.13. Brillouin spectra from three prelamina tissue sections. Raw data (a,c,d) showed a central peak at 0 GHz due to the elastic scattering and also both Stokes and anti-Stokes are shown. Magnification (b) of the Brillouin peak in a, showed a small, almost negligible shoulder at higher frequency (b, black arrow).

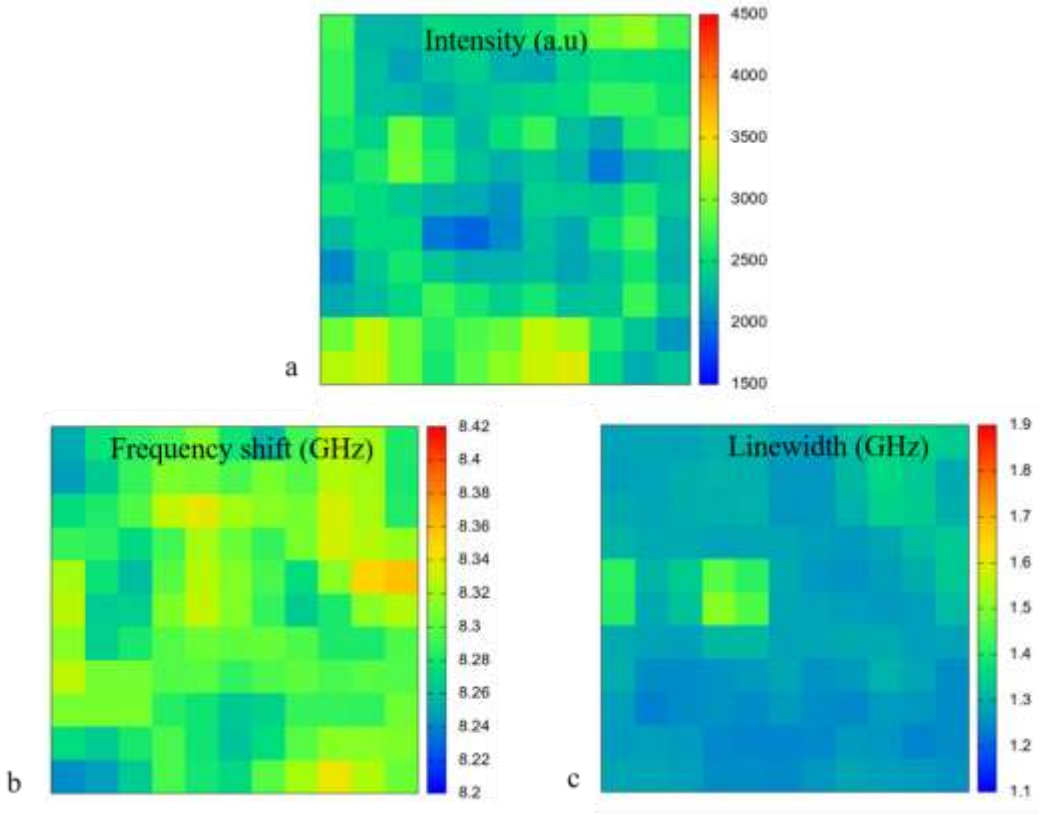

Figure 6.14. Brillouin stiffness maps from the porcine preL. The higher the intensity (a) the lower is the frequency shift (b) and vice versa. Linewidth (c) appeared homogenous throughout the map.

6.1.1 Brillouin and Raman spectroscopy from the LC

Representative Raman spectra within six LC are shown in figure 6.15. Several peaks were identified different and attributed to several molecular vibration. Raman spectra from the LC appeared more complex than that of the preL, indicating several constituents (figure 6.15a-e). The six LC sections presented similar spectra, in which peaks were attributed to different molecule vibrations, identified in Table 6.4. Single peaks were observed at 555 cm^{-1} (figure 6.16b), 865 cm^{-1} and 924 cm^{-1} (figure 6.16c), 1252 cm^{-1} (figure 6.16c), 1466 cm^{-1} (figure 6.16d) and 1671 cm^{-1} (figure 6.16d). Two broad peaks at 2873 cm^{-1} and 2934 cm^{-1} (figure 6.16e), attributed to CH2-CH3, which appeared more pronounced than those in the preL. Additionally, the peak corresponding to water bonds at ~3370 cm^{-1} (figure 6.16e) appeared more distinct than that observed in the preL.

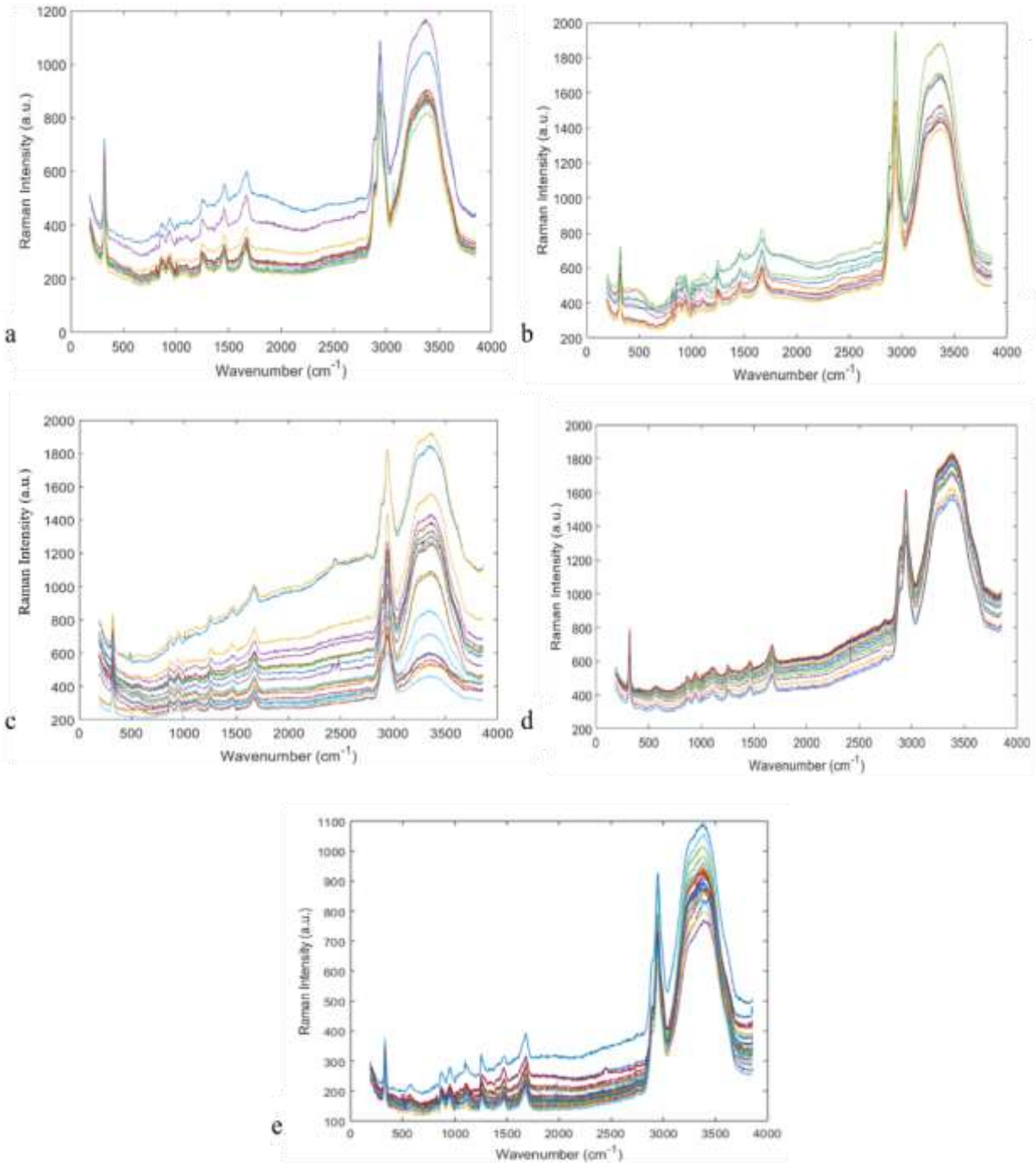

Figure 6.15. Raman spectra of five porcine LC sections. Representative Raman graphs of 50 spectra from the porcine are shown (a-e). Raman spectra appeared well defined and several peaks were identified. Broad peaks were observed at 555 cm^{-1}, 865 cm^{-1} and 924 cm^{-1}, 1252 cm^{-1}, 1466 cm^{-1}, 1671 cm^{-1}, 2873 cm^{-1} and 2934 cm^{-1}. Peat at ~3370 cm^{-1} was also identified.

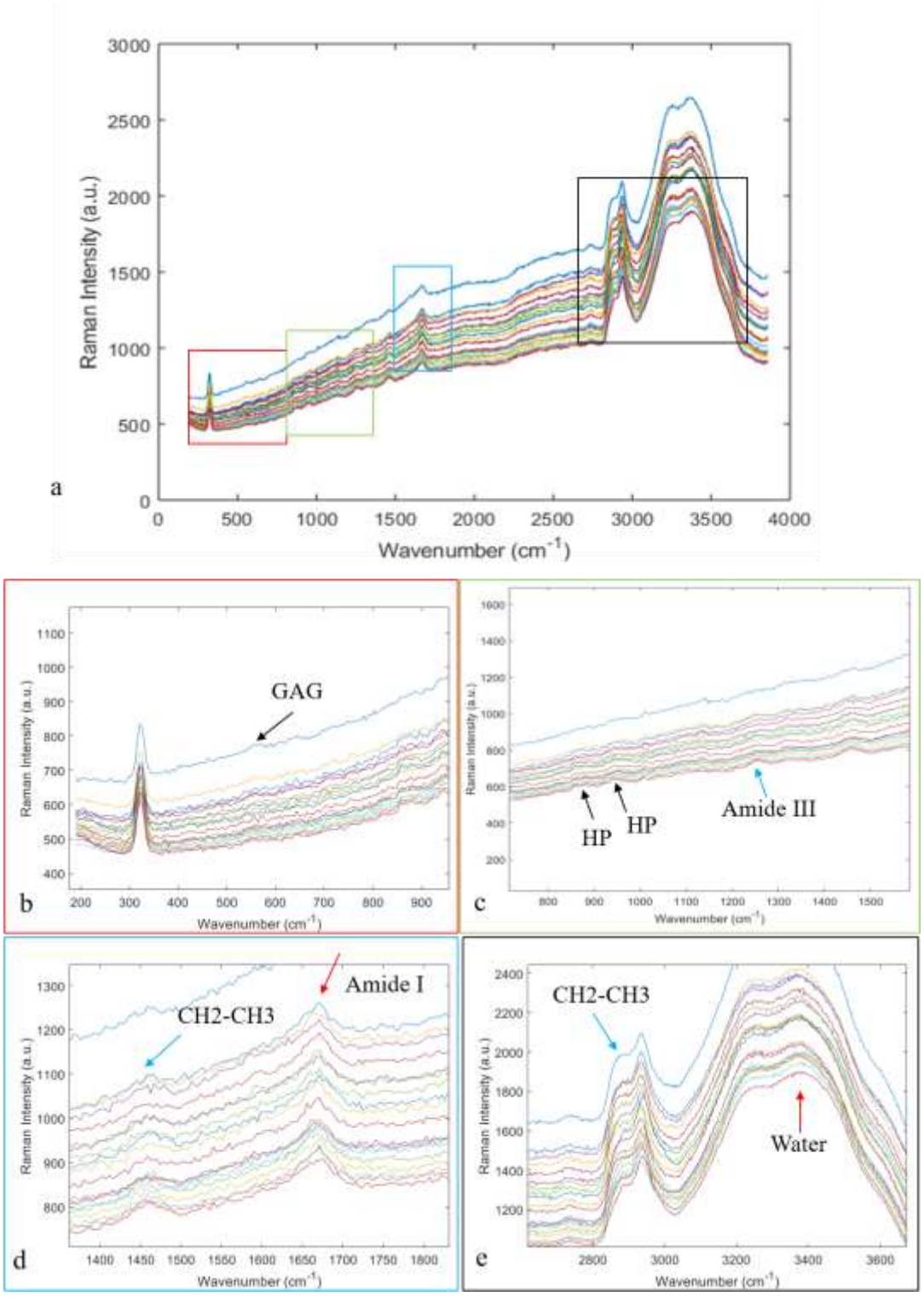

Figure 6.16. Representative graph of 70 Raman spectra over a 55x55 μm^2 area of porcine LC. Raman spectrum (a) appeared more defined of that observed in the preL and peaks attributed to different molecule vibrations were observed. Broad peaks were observed at 555 cm^{-1} (b, black arrow), 865 cm^{-1} and 924 cm^{-1} (c, black arrows), 1252 cm^{-1} (c, blue arrow), 1466 cm^{-1} (d, blue arrow), 1671 cm^{-1} (d, red arrow), 2873 cm^{-1} and 2934 cm^{-1} (e, blue arrow). Peat at ~3370 cm^{-1} (e, red arrow) was also identified.

Representative Raman colour-coded maps over a 55x55 μm^2 area (12 x 12 points) within the LC are shown in figure 6.17. Spectral assignment of peaks is shown in Table 6.4. In brief, a proline-rich composition (i.e. hydroxyproline) (HP) due to the CC stretching and CH bending modes, was determined by peaks at 865 cm^{-1} and 924 cm^{-1}, (figure 6.17a) which likely correspond to fibrillar collagen within the LC plates. The peak at 555 cm^{-1} (due to CC aromatic ring stretching) (figure 6.17b) indicated that glycosaminoglycans (GAG) within the LC included chondroitin (C) 6 and C 4 sulphate. Peaks 1252 cm^{-1} (figure 6.17c) and 1671 cm^{-1} (figure 6.17e) were assigned to Amide III and Amide I of protein, due to the CN symmetrical stretch and NH2 asymmetrical stretch, respectively. The spectral assignment of peak at 1466 cm^{-1} (figure 6.17d) due to CH2/CH3 deformation of protein (Hanlon et al., 2000), could be attributed to collagen type I. GAG (figure 6.17b) and CH2/CH3 of protein and lipids (figure 6.17f) map did not show similar features, however, the averaged intensity map of CH2/CH3 (figure 6.17g) showed a clear correlation with the other maps was observed.

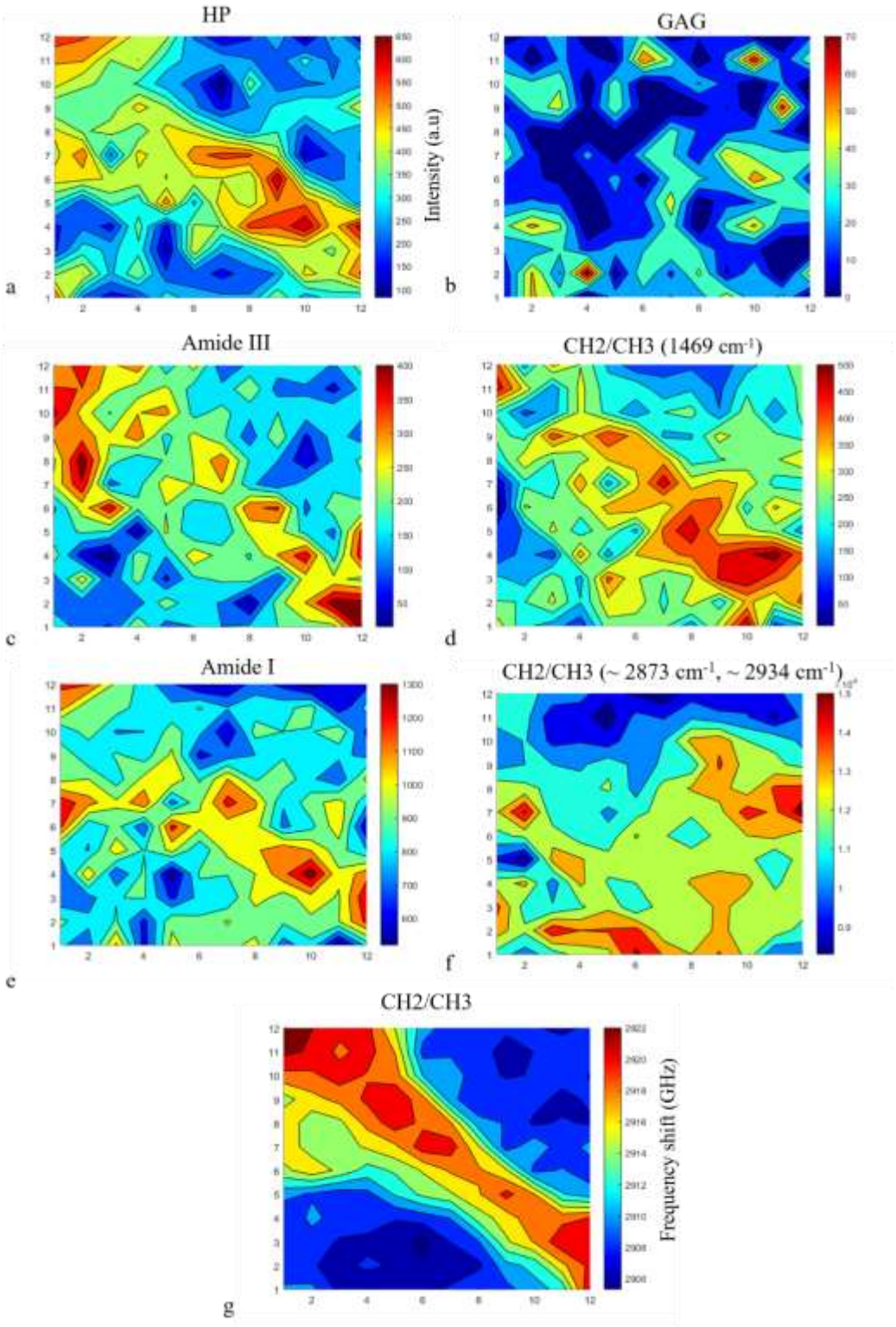

Figure 6.17. Raman colour-coded maps of the different molecular vibrations within porcine LC. Raman maps of HP (a), Amide III (c), CH2/CH3 of protein (d) and Amide I (e) correlated well showing shift at higher frequency within similar area. GAG (b) and CH2/CH3 (f) map did not show similar features, however, the averaged frequency shift map of CH2/CH3 (g) showed a clear correlation with the other maps. The legend represents intensity (a.u.) in all maps except for g) where it represents frequency shift (GHz).

Brillouin spectra over a 55x55 μm^2 area (12 x 12 points) within a porcine LC are shown in figure 6.18. The peak at 7.5 GHz, due to the inelastic scattering of water, appeared less sharp and wider at the base than that observed in the preL. A small shoulder was observed on both Stokes/Anti-Stokes sides of the Brillouin graph (figure 6.18a-e), suggesting the sample contributes to the Brillouin spectra. This shoulder was not observed in the preL, consistent with the more heterogenous composition of the LC compared to the preL.

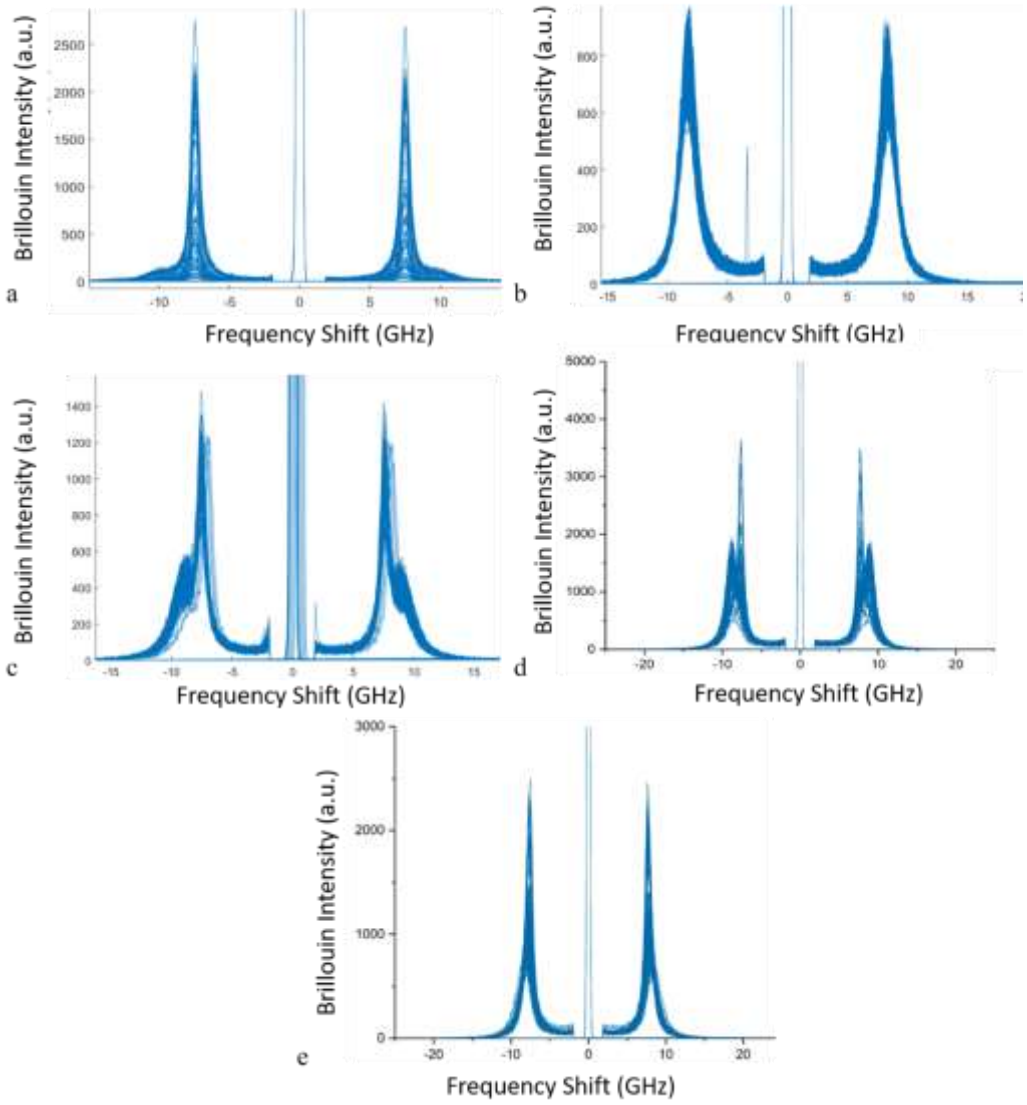

Figure 6.18. Brillouin spectra of five porcine LC sections. Representative Brillouin graphs of 50 spectra from the porcine are shown (a-e). A sharp Stokes and anti-Stokes peak, representing that of water bonds vibration is visible in all spectra. A small shoulder, indicating the contribution of the sample, appeared in all spectra.

Brillouin maps of frequency shift (figure 6.19b) and linewidth (figure 6.19c) showed regions with consistent high values that corresponded to Raman-generated regions containing HP, CH2/CH3, Amide I and Amide III. In these regions, Brillouin frequency shifts and linewidths appeared inversely correlate to Brillouin intensity values (figure 6.19a). Frequency shift had a higher range of 8.2 – 9.6 GHz, compared to that of the preL (8.2 – 8.42 GHz). Similarly, linewidth, ranged from 1.2 – 2.6 GHz, which is higher than the linewidth range of the preL (1.1 – 1.9 GHz).

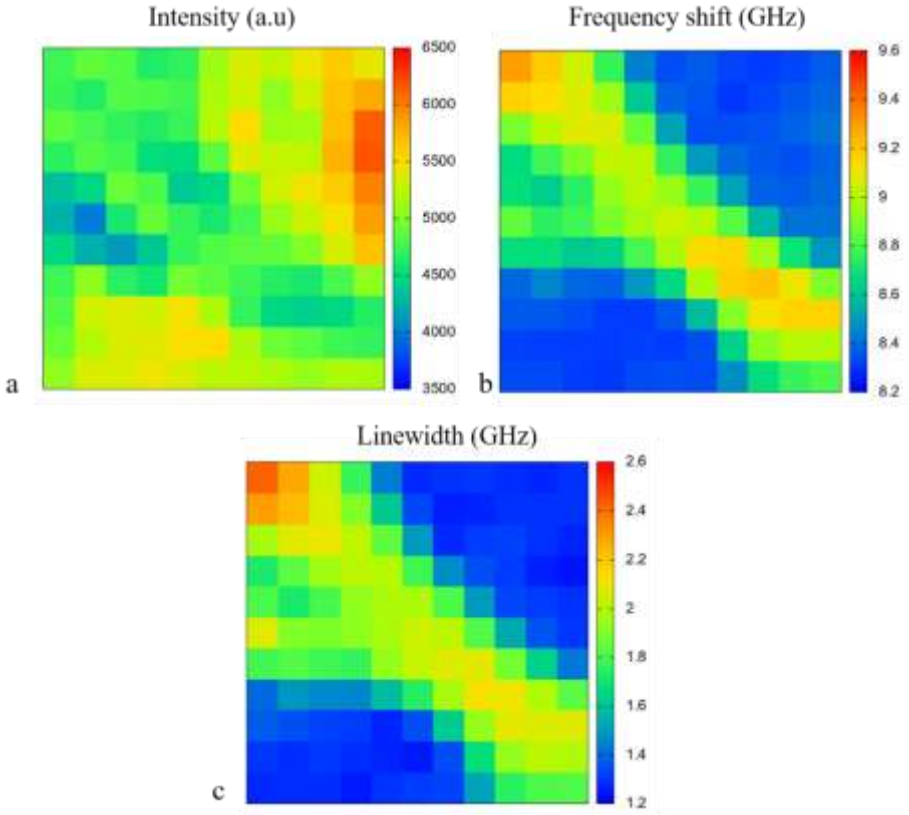

Figure 6.19. Brillouin colour-coded maps in the porcine LC. Frequency shift (b) and linewidth (c) correlated well, showing higher elasticity and viscosity, respectively, within similar areas. Brillouin frequency shifts and linewidths appeared inversely correlate to Brillouin intensity (a) values.

6.3.2 Distribution of prelamina and LC spectra

Raw Brillouin spectra from preL and LC are shown in figure 6.20.

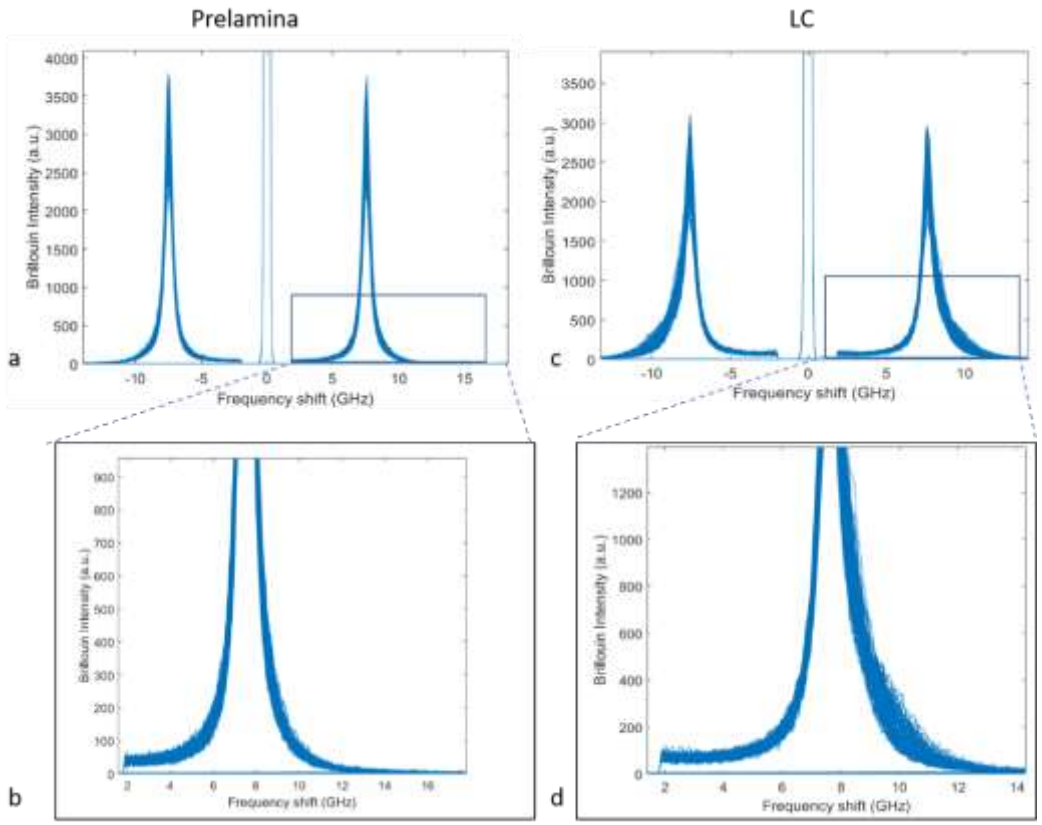

Figure 6.20. Prelamina and LC spectra used to output matrices of frequency shift and linewidth using the function "*Momappa_bs.exe*" in the command prompt. Prelamina (a) and LC (c) showed different shifts and linewidth. A magnification of the anti-Stokes peak is shown for the prelamina (b) and the LC (d).

PreL spectra are characterised by a low-frequency mode, which covers values from 3 to 9 GHz (figure 6.21a). Distribution from the LC showed more spectra at higher frequency from 8 to 9.4 GHz (figure 6.21b), and no spectra below 8 GHz were observed, compared to those of preL. GHz. Linewidth of preL is characterised by spectra between 0 and 3 GHz (figure 6.21c), whereas those of the LC between 1.2 and 2.4 GHz and no spectra were observed at 1 GHz or above 2.5 GHz (figure 6.21d). Spectra from both frequency shift ($p=0.001$) and linewidth ($p=0.031$) in the LC were significantly different from the preL and did not show a normal distribution. Spectra distribution from LC pores and plates showed significant differences in both frequency shift ($p=0.001$) and linewidth ($p=0.000$).

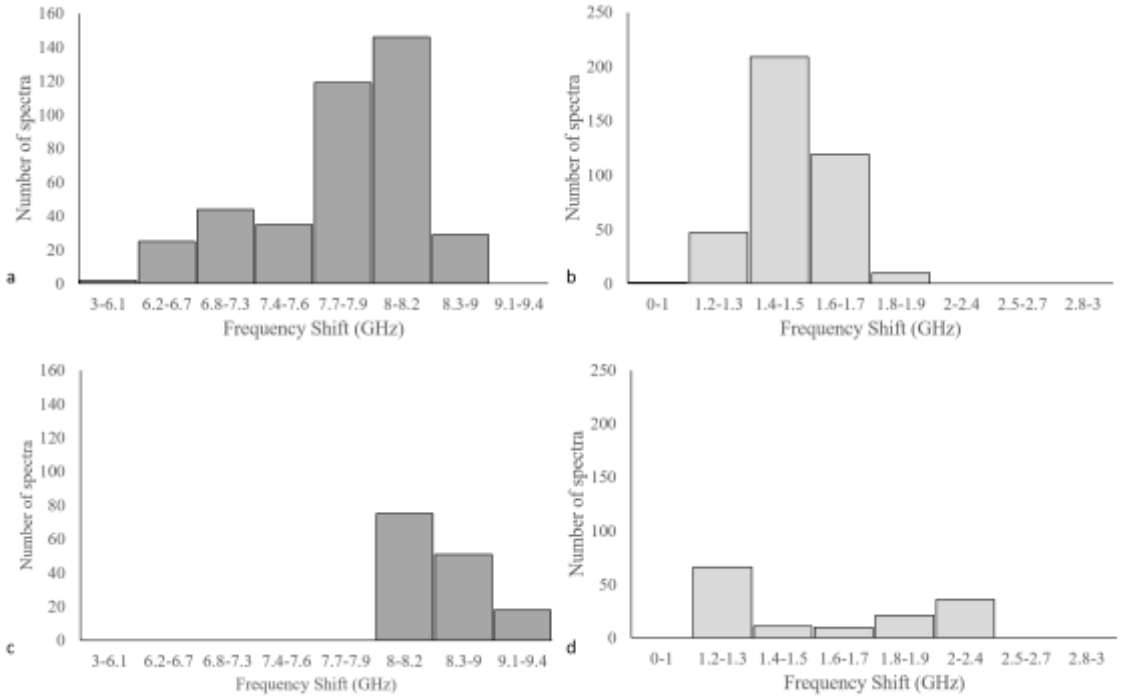

Figure 6.21. Distribution of Brillouin spectra of frequency shift and linewidth in the preL and LC. Spectra of frequency shift in the LC (b) showed higher GHz values that those observed in the preL (a). Linewidth of LC showed spectra from 1.2 to 2.4 GHz (d), compared to those of preL from 1 to 3 GHz (c). Both frequency shift (p=0.001) and linewidth (p=0.031) distribution were significant different between preL and LC.

6.4 Discussion

Spontaneous Brillouin scattering, first reported by Leon Brillouin in 1922 (Brillouin, 1922) arises when light is scattered by thermal density fluctuations propagating inside the media. Since 1922, Brillouin microscopy has been widely used to characterise the biomechanical properties of cells (Antonacci and Braakman, 2016), fibroatheroma cup stiffness (Antonacci et al., 2015) and *ex vivo* corneal biomechanics (Scarcelli et al., 2012, Scarcelli et al., 2013).

Proteins are large and complex molecules containing many amino acids which result in complex Raman spectra. However, investigation into protein structure using Raman spectroscopy, which started decades ago, is leading to the discovery of several specific Raman bands. Raman spectra are qualitative and quantitative; therefore, information can be obtained from peak position and peak intensity, which vary based on the concentration and the nature of the bond.

The combination of Brillouin and Raman spectroscopy has been introduced to characterise mechanical and chemical properties of materials (Mattana et al., 2018, Palombo et al., 2014). In this chapter preliminary results relating to ONH micromechanics are presented. These demonstrated the feasibility of a combined Raman/Brillouin spectroscopy to simultaneously map the micromechanical, structural and chemical properties of the ONH.

Raman spectra presented differences between preL and LC. In the preL, the spectra of three ONH sections appeared similar, and only one peak at 2940 cm^{-1} was identified. This peak has been previously attributed to the CH2-CH3 stretching and vibration of lipid and proteins (Czamara et al., 2015). This peak is composed of an overlapping of multiple contributions from the CH2 stretching vibration primarily arising from lipids at ~ 2850 cm^{-1}, and the CH3 stretching vibration primarily arising from proteins at ~ 2935 cm^{-1}. The absence of specific collagen and/or amide peaks correlates with the known composition of the preL, which is mainly neuronal tissue, cells and RGC axons (Anderson, 1969).

Brillouin maps of elasticity and viscosity from the preL appeared to show no specific region of higher frequency or linewidth, respectively. In the preL, glial fibrillar acidic protein (GFAP) positive astrocytes form glial columns between the axons fascicles and they extend thin processes into the axons forming supporting scaffold (Elkington et al., 1990, Oyama et al., 2006). The only collagen found in the prelamina is associated to blood vessels (Elkington et al., 1990). This implies that the preL is mostly neuronal tissue, with glial astrocytes supporting the axons.

Raman maps of preL showed a characteristic shape which might resemble an astrocyte process or a small vessel. PreL map of 100 μm^2 showed a ~13 μm width region where the Raman intensity was higher, and the weighted average intensity showed CH2-CH3 of both protein and lipid. It might be anticipated that the region observed corresponded to a small vessel, as the glial tissue projections in the preL, are delimited by capillaries.

However, in the preL, sometimes bundles of axons are separated by large astrocytes processes, which contain many intermediate filaments (Elkington et al., 1990). Hence, it might be also possible that the region observed in the preL map corresponded to an astrocytes process.

A previous study showed that in guinea pig, both neurons and glial cells are very soft tissue and glial cells are even softer that the neurons (Lu et al., 2006). These results might explain the brillouin maps observed in the preL, where no regions of higher elasticity and viscosity were observed.

In the LC, peaks at 555 cm^{-1} and 1110 cm^{-1} were also found. The first GAG spectrum was published more than 50 years ago (Orr, 1954). Raman spectra for hyaluronan (HA) (Alkrad et al., 2003, Bansil et al., 1978), chondroitin-4-suplhate (C4S), chondroitin-6-sulphate (C6S) (Alkrad et al., 2003), heparin (Atha et al., 1996), and a small dermatan sulphate proteoglycan (Renugopalakrishnan et al., 1989) were reported some time ago and more recently by Ellis et al (Ellis et al., 2009). The extracellular matrix of the LC also comprises GAG, specifically chondroitin-6-sulphate (Morrison et al., 1994) and chondroitin-4-sulphate (Caparas et al., 1991, Morrison et al., 1994). Heparan sulphate has also been reported along the margins of the LC plates (Sawaguchi et al., 1992, Sawaguchi et al., 1993), extending into the region of insertion. It is likely that peaks observed at 555 cm^{-1} and 1110 cm^{-1} were derived from chondroitin-4 and 6 sulphate contribution to the spectrum.

Several peaks identified in the LC sections, at 865-940 cm^{-1}, Amide I at 1252 cm^{-1}, Amide III at 1671 cm^{-1} and CH2-CH3 deformation of protein at 1466 cm^{-1} have been attributed to collagen type I.

Peaks between 865-940 cm^{-1} have been associated with different vibrational modes of collagen. Peaks at 865 cm^{-1} have been related to the hydroxypyridinoline (HP) ring (Ikoma et al., 2003, Nguyen et al., 2012, Sato and Martinho, 2018, Zhang et al., 2011) and at 940 cm^{-1} have been identified as vibrational modes of the proline ring (Ikoma et al., 2003, Nguyen et al., 2012, Sato and Martinho, 2018, Zhang et al., 2011). Finally, peaks at 938 cm^{-1} corresponded to the CC stretching vibration of the collagen backbone formed by the Glycine–X–Y sequences (Zhang et al., 2011). An additional peak at lower frequency was identified in one LC section only occurring at 815 cm^{-1} and it has been assigned to the COC stretching, associated with the glucosyl-galactosyl hydroxylysinonorleucine cross-link between the tropocollagens (Borel, 1991, Ikoma et al., 2003). Glycosylated hydroxylysinonorleucine cross-links have been shown before to be involved in rat collagen fibre formation and its concentration significantly increased with the age of the animal (Boucek et al., 1979). More recently, Naffa et al. (2019) isolated hydroxylysinonorleucine cross-links in collagen type I from bovine skin (Naffa

et al., 2019). Since fibrillar collagen is present in the LC (Albon et al., 1995, Hernandez et al., 1986, Hernandez et al., 1987); it is likely that these peaks are arising from the different vibrational modes of collagen within the cribriform plates.

Peaks at 1252 cm^{-1}, 1466 cm^{-1} and 1671 cm^{-1} , identified in the LC, have been attributed, by previous studies, to Amide I (Cheng et al., 2005, Frank et al., 1995, Shetty et al., 2006, Stone et al., 2002, Stone et al., 2004, Tuma, 2005), CH2-CH3 stretching (Cheng et al., 2005, Frank et al., 1995, Shetty et al., 2006, Stone et al., 2002, Stone et al., 2004) and Amide III (Malini et al., 2006, Notingher et al., 2004, Tuma, 2005), respectively. NH2 stretching of Amide I is likely to be attributed to collagen type I (de Campos Vidal and Mello, 2011), known to be part of the LC connective tissue (Albon et al., 1995, Albon et al., 2000a, Goldbaum et al., 1989, Hernandez et al., 1986, Hernandez et al., 1987, Morrison et al., 1989b, Rehnberg et al., 1987). Similarly, the CH bend of Amide III is likely attribute to collagen I as previously shown (Gasior-Glogowska et al., 2010).
The spectral assignment of peak at 1466 cm^{-1}, due to CH2-CH3 deformation of protein (Hanlon et al., 2000), could be attributed to collagen type I. This band has been previously attributed to collagen or phospholipid scissoring (Huang et al., 2003, Katainen et al., 2007); the former is likely here, as it followed the HP distribution observed in the Raman maps.

Peaks observed at higher frequencies 2950 cm^{-1} and 3350 cm^{-1} can attributed to CH2-CH3 stretching of amino acids and different lipids (Czamara et al., 2015) and water hydrogen-bond (Leikin et al., 1997), respectively. The peak at 2950 cm^{-1} appeared sharper than that observed in the preL, suggesting that the preL contained more lipid than the LC.
Previous studies have probed the typical Raman spectrum for elastin and desmosine/isodesmosine (Frushour and Koenig, 1975, Haston et al., 2003). Elastin Raman spectrum is complex and there are significant variations for peak position of different vibrational modes in the literature. However, peak at 529 cm^{-1} has been attributed to the cross-link desmosine (Frushour and Koenig, 1975). Raman spectra from LC sections were complex and did not contain any peak at 529 cm^{-1}, suggesting that elastin was absent in the porcine LC. TPEF imaging shown in chapter 4, confirmed this.

Brillouin maps of the LC showed a region-dependence variation in elasticity and viscosity. According to the area shaped in the maps, it is likely that the region scanned is part of a cribriform plates surrounded by a softer area. Brillouin maps showed shift at

higher frequency in both elasticity and viscosity within similar regions, correlating well with Raman maps. These suggested that all molecular components had an impact on the elasticity and viscosity of the tissue.

It is thus possible to associate areas of higher frequency shift (8.8-9.6 GHz, see figure 6.16b) and linewidth (1.8-2.6 GHz, see figure 6.16c) to a cribriform plate surrounded by areas of low elasticity (8.2-8.4 GHz) and viscosity (1.2-1.4 GHz), likely attributed to a neuronal pore. These maps suggest that the higher elasticity and viscosity are represented within the same region.

The results presented in the Brillouin maps is consistent with previous studies suggesting that the LC is capable of resisting tensile, compressive and shear (Grytz et al., 2014, Sigal et al., 2011) stresses. Therefore, it is likely that the region observed in both Raman and Brillouin maps correspond to a cribriform plate surrounded by a pore.

The LC and its insertion into the sclera is supported by tightly packed collagen and elastin containing fibres (Hernandez et al., 1987, Hernandez et al., 1986), which presumably dominated the Brillouin measurements reported in this study. However, the presence of water bonds, due to the hydrated condition in which the samples were scanned, had a significant effect on the Brillouin peak frequency. In this study, the investigation of the Brillouin maps was achieved after peak deconvolution which allowed a full description of elasticity and viscosity within a porcine LC. A similar approach has been proposed before (Mattana et al., 2018), in which the authors successfully separated the Brillouin peak of cells from the surrounding buffer.

Analysis of the raw data showed that the Brillouin peak of ONH samples was located at higher frequency with respect to the water. This feature was also found by Mattana et al (2018). This was a key result, suggesting that asymmetrical peaks highlight the contribution of the material to the Brillouin data. The innovative analysis method enabledthis study to report for the first time the accurate modification of the position and shape of the Brillouin peak applied to the porcine ONH. In turn, the latter enabled the comparison of micromechanics between preL and LC. Brillouin maps correlated with Raman maps, suggesting that the molecular composition of the LC contributed to viscosity and elasticity of the tissue.

Brillouin/Raman spectroscopy does not involve contact with chemical agents and specimens itself, therefore, it is ideal and suitable for human *in vivo* application, as it has been demonstrated before on *in vivo* lens (Scarcelli et al., 2011) and cornea (Scarcelli et al., 2012). Thus, Brillouin and/or Raman has potential as an important tool for early diagnosis of disease (Day et al., 2009, Day and Stone, 2013).

6.5 Conclusion

This chapter demonstrated a proof of concept of the capabilities of the simultaneous Raman-Brillouin micro spectroscopy approach for application on *ex vivo* samples of the optic nerve head. This approach offers frequency variation of the order of GHz and provides access to vibrational properties of the connective tissue as well as its molecular modes. Collagen and elastin are the major load bearing components of the ONH and the mechanical properties of the LC and therefore the ONH, are due to a balance between elastin, responsible of elastic properties of the tissue and collagen, which provides tensile strength. The mechanical behaviour of the LC appeared to change with age (Albon et al., 2000b) and glaucoma (Zeimer and Ogura, 1989) due to changes in the connective tissue which make the lamina cribrosa less flexible and stiffer. This concept provided the starting point of this investigation, which is the first study to offer information on the simultaneous micromechanics and chemical/structural properties of the preL and LC from *ex vivo* samples.

6.6 Limitation

This study presented limitations. Firstly, the confocal microscope coupled to the system set up requires further optimisation for future investigation, to enable better image mapping of the ROI to the scan. This is a preliminary study on porcine ONH which allowed proof of concept to enable further investigation into the micromechanics of the human optic nerve head, therefore future work will require additional time to increase the number of samples, enabling a full investigation into differences between preL and LC and regionally (ppsclera and RoIns).

6.7 Future work

Future work will include the application of the current set up to human ONH. Brillouin frequency shifts will be mapped across ONH tissue and microregions will be probed at a

higher resolution to determine the ability of this technique to detect micromechanical changes regionally and within young, elderly and glaucomatous ONHs to test the hypothesis that collagenous structure changes influence fibril stiffness and tissue mechanics. Simultaneous Raman acquisition will enable chemical composition comparison in scanned areas.

Chapter 7 - General discussion

Age is an important risk factor in glaucoma (Anderson, 1989) and both collagen and elastin have been shown to increase as a function of age (Albon et al., 1995, Albon et al., 2000a, Hernandez et al., 1989). Elevated IOP [(above 21 mmHg (NICE 2017)] is considered one of the most important risk factors for the development of primary open angle glaucoma (POAG) (Alward et al., 1998). IOP acts as a source of stress, resulting in a possible chain of cellular events which culminate in RGC axonal damage. Although the IOP-related stress and strain play an important role in the pathophysiologic process of glaucoma, it is likely the interaction between connective tissue damage, axonal damage and ageing that determine the susceptibility of an ONH to glaucomatous optic neuropathy (Burgoyne et al., 2005).

The purpose of this thesis was to further characterise the nanostructure and microstructure of the human ONH in ageing and glaucoma, to aid in understanding how age-related changes in ONH connective tissue influence LC susceptibility to development of glaucomatous optic neuropathy.

7.1 Anatomical features in ageing and glaucomatous ONHs

Anatomical changes of the ageing ONH are summarised in figure 7.1, left panel. Important factors that are likely to contribute to the mechanical response of the ONH to IOP, and therefore influence ONH susceptibility to glaucoma, are the thickness of LC, plates and ppsclera. Results presented in this thesis did not show any correlation between age and LC/LC plates and ppsclera thickness. Previous studies have investigated the morphometry of the LC and found that the LC thickness is not associated with age (Jonas and Holbach, 2005, Ren et al., 2010, Ren et al., 2009), which support the result presented in this thesis.

It has been previously demonstrated that there is an increase in connective tissue content in age (Albon et al., 1995, Albon et al., 2000a, Hernandez et al., 1989), where collagen and elastin accumulates throughout life, leading to stiffer and less compliant LC (Albon et al., 2000b). As mentioned above, the increase in LC thickness is not associated with age (Jonas and Holbach, 2005, Ren et al., 2010, Ren et al., 2009), which might imply that the increase in connective tissue content, does not affect the LC thickness.

The increase in connective tissue content is however consistent with the proportion of the LC that is occupied by pores decreasing with age, causing a subsequent change in the ratio of pore : inter pore tissue (Ogden et al. 1988). In more susceptible eyes, the increased in connective tissue content, might lead to a decreased pore area and therefore to a stiffer and less resilient LC. This might result in a greater response of the ONH to changes of the IOP, leading to a permanent deformation of the LC (Albon et al., 2000b) which can result in axonal loss. As the LC is known to become stiffer with age (Albon et al., 2000b), it might be that changes in IOP would cause more damage within the ppsclera, pulling the LC taut but not affecting the LC thickness. Therefore, it might be the extra strain experienced by the LC to result in RGC axonal damage.

Anatomical changes of the glaucomatous ONH are summarised in figure 7.1, right panel. LC volume was significantly larger in moderate and advanced glaucoma when compared to controls. LC thickness was significantly lower in glaucoma following XMT but not within SHG datasets. Thinning of the LC in glaucoma is consistent with previous studies which showed a thinner LC in both *in vivo* (Lee et al., 2012, Park et al., 2012) and *ex vivo* (Jonas et al., 2009, Jonas et al., 2012, Ren et al., 2009). The difference in thickness measurements between XMT and SHG datasets, could be due to tissue processing techniques used in histological studies, causing tissue shrinkage and/or warping. XMT does not require tissue sectioning and the 3D reconstruction is performed without optical slices alignment. The latter might have caused inaccuracy within SHG optical stacks during tissue section alignment. Additionally, the limited number of moderate (n=2) and advanced (n=2) glaucomatous ONHs used in chapter 2 for SHG reconstruction could have influenced the statistical confidence.

3D measures, presented in this thesis are, however, proof of principle that the LC thickness could be measured within 3D image volume. Therefore, future work will require more samples at different stage of disease to further investigate into changes in LC thickness in glaucoma.

Thinning of the LC in glaucomatous ONH might be due to the continuous stress and strain the LC is subjected to, caused by elevated IOP. The IOP produces an expansion of the scleral shell which generates tensile forces on the scleral wall. As a result, the scleral canal opening expands, which stretches the LC and therefore causing it to thin.

In this thesis, the LC volume was shown to be significantly greater in moderate and advanced glaucoma compared to controls, which is consistent with the LC thickening and remodeling as described in monkey models (Yang et al., 2011). This has not been shown in human glaucoma, however, as shown in monkey experimental glaucoma, one of the physiological responses in glaucoma is the expansion of the scleral canal (Bellezza et al., 2003), which might suggest an increase in LC volume along with an increase in connective tissue volume (Reynaud et al., 2016, Roberts et al., 2009).

However, if the LC thins in glaucoma, it is likely that even though the sclera canal expands, the LC volume decreases. The latter is not consistent with the findings presented in this thesis, which might suggest that discrepancy between techniques occur.

In vivo studies are generally cross sectional in nature and therefore do not address the glaucoma related changes in the ONH or LC over time, but instead focus on the morphological features in glaucoma eyes versus controls. LC volumes presented in the current thesis were achieved following SHG imaging which arises from fibrillar collagen and do not consider EFs and proteoglycans within the LC. This might have been a limitation and might explain different volumes calculation.

It is clear from these findings that the LC morphology and structure changes markedly in glaucoma, beginning with early stage of disease. Additionally, IOP-related responses strongly depend on the eye-specific ONH and LC morphology (Roberts et al., 2010), scleral stiffness (Coudrillier et al., 2016), level of cerebrospinal fluid pressure (Feola et al., 2017) and it is extremely complex, varying amongst individuals. Further studies as needed to fully understand the best biomechanical markers for LC structural and morphological changes and to better elucidate the relationship between LC thickness and expansion of the scleral canal opening.

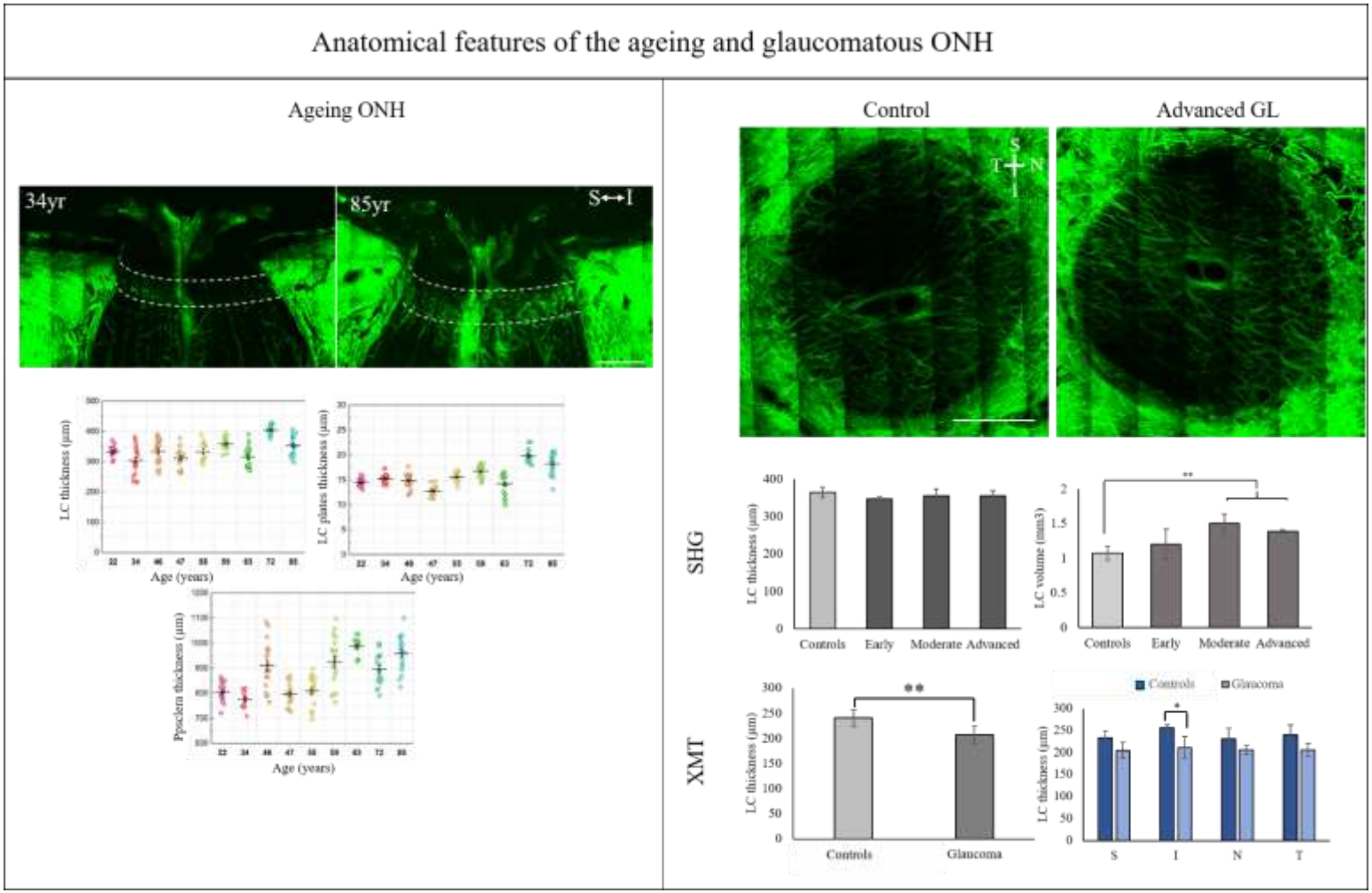

Figure 7.1. Anatomical features of the ageing and glaucomatous ONH. LC/LC plates and ppsclera thickness did not show any correlation as a function of age. LC thickness appeared significantly lower in glaucoma compared to controls when measured within XMT images, but not within 3D reconstructed SHG images. LC volume appeared significantly greater in moderate and advanced glaucoma compared to controls.

7.1.1 Pore parameters in the glaucomatous ONH

Pore parameters analysis within glaucomatous ONHs are summarised in figure 7.3. Pore circularity and pore count were significantly lower in advanced and all stages of glaucoma, respectively. Several investigations have focused on LC and pore shape *in vivo* (Akagi et al., 2012, Fontana et al., 1998, Ivers et al., 2015, Miller and Quigley, 1988, Nadler et al., 2014, Omodaka et al., 2018, Shoji et al., 2017, Sredar et al., 2013, Tezel et al., 2004, Wang et al., 2013, Zwillinger et al., 2016) and *ex vivo* (Reynaud et al., 2016, Voorhees et al., 2017, Winkler et al., 2010) and changes related to glaucomatous neuropathy have been the interest of several studies (Omodaka et al., 2018, Shoji et al., 2017, Tezel et al., 2004, Wang et al., 2016, Wang et al., 2013, Zwillinger et al., 2016).

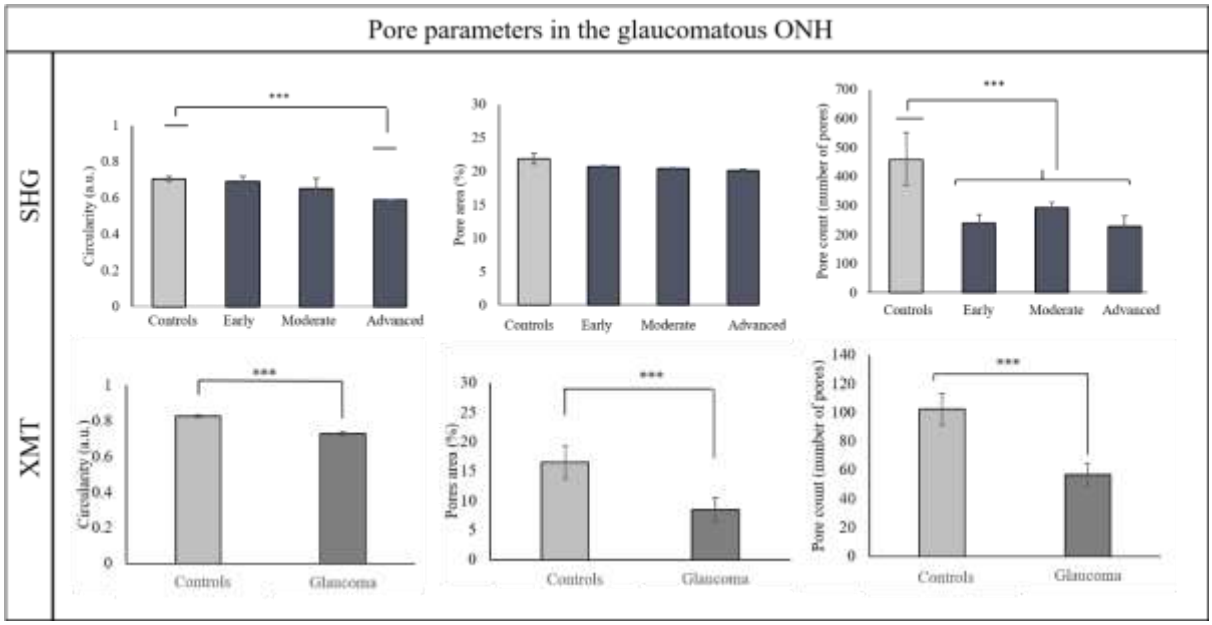

Figure 7.2. Pore parameters within glaucomatous ONHs. Investigation in pore parameters showed similar results with both SHG and XMT. Pore circularity, count and area were significantly lower in glaucoma compared to controls.

These researchers concluded that differences in pore shape in glaucomatous eyes have been associated with increasing severity of the disease. The largest pores of a healthy ONH are arranged as an hour glass with the greatest in the superior and inferior poles (Quigley and Addicks, 1981, Radius and Gonzales, 1981), which are associated with

areas conducting fibres of the arcuate bundles (Hoyt, 1962, Quigley and Addicks, 1981). If axons passing through larger pores are at greater risk of being damaged because of elevated IOP and if pores elongate as a function of glaucoma progression, it is likely that axonal resistance to damage decreases as glaucomatous neurography worsen (Miller and Quigley, 1988).

As shown in this thesis, pores appeared elongated in the nasal-temporal direction in glaucoma compared to controls, suggesting that the LC stretches in one direction. This might be caused by either the IOP pulling the LC taut at the ppsclera or lack of axons maintaining the pore shape. If the LC and the pores assume an elongated shape, it is possible that this results in the RGC axons damage as subjected to more compression within a neuronal pore that no longer present a circular shape.

In glaucoma, eyes with minimal visual field loss present a predominance of small round pores on the anterior surface of the LC, however, with the increasing damage the proportion of elongated pores increase (Miller and Quigley, 1988, Susanna 1983). It is known that the superior and inferior regions of the LC contains larger pores and less connective tissue than temporal and nasal (Quigley and Addicks 1981; Miller and Quigley 1988), and the inferior and infero-nasal have lower collagen density compared to other regions (Quigley et al. 1991b). If axons passing through large pores are more susceptible to damage and elongated pores increase with the increase in glaucomatous damage and IOP, it can be concluded that the LC is more vulnerable within these regions.

Miller and Quigley (1988) suggested that axonal resistance to damage decrease as glaucoma progresses, and that RGC axons become less resistant to elevated IOP either as a consequence of the decrease in connective tissue density at ONH, or because of changes in other parameters, such as reduced nutrition from compromised blood vessels. This in turn might lead to axons damage and eventually axons death.

The LC beams thicken in glaucoma and become predominantly horizontally orientated (Roberts et al., 2009). It is thought that this organization might influence the orientation of pores, therefore analysing pores orientation and shape could be a good indicator of glaucoma disease. Recent *in vivo* studies, have shown reliability of producing repeatable results of the LC pores (Akagi et al., 2012, Ivers et al., 2011, Nadler et al., 2013, Wang

et al., 2013). From these studies, OCT has been shown to be a reliable way to assess the ONH and the LC.

The result presented in the current thesis following SHG and XMT imaging allowed to improve the knowledge of the pores parameters. Understanding regional differences and difference between healthy and glaucomatous ONHs would help to improve the knowledge of the ONH's biomechanics. This would in turn enable the future development of *in vivo* analysis techniques, for instance using OCT for early diagnosis of glaucoma.

Even though results presented from both techniques correlated well, there are a few limitations that could be taken into consideration. As mentioned in chapter 2, SHG arises from fibrillar collagen and therefore represent the LC as for collagen only. SHG does not consider EFs, therefore pore parameters might not be as accurate as analysed following XMT. To improve SHG analysis, few amendments could be required for the accuracy of the method. For instance, selecting a presumed pore range would also improve the reliability of the results as this will ensure that only specific pores are included in the analysis.

Pore analyses presented in this thesis, however, gave accurate results, which are comparable to previous studies. This shows that both nonlinear microscopy and XMT are beneficial methods for the analysis of pore parameters and would help to create a standardised method for pore analysis for future *in vivo* studies.

7.2 Fibrillar collagen within the ageing and glaucomatous ONH

Investigations of fibrillar collagen in the ageing and glaucomatous ONH are summarised in figure 7.4. Age-related analysis of the microstructure of fibrillar collagen showed changes in both the LC and ppsclera. Collagen crimp represents the relaxed state of collagen when fibres are not under mechanical stress (Weiss and Gardiner, 2001). This wavy-like appearance was clearly identified in the young ONH in LC, RoIns and ppsclera, whereas in the elderly ONHs, collagen crimp was negligible and values low. The relaxed (crimped) state of fibrillar collagen in the young ONH tissue and the negligible appearance of crimping in the elderly may contribute to the age-related decrease in LC reversibility/compliance and increased stiffness (Albon et al., 2000b).

Collagen crimp period (distance between two consecutive peaks) significantly increased in the ageing ppsclera, but not in the LC and RoIns.

Microstructural analysis of glaucomatous ONH presented in chapter 2 showed an increase in collagen crimp period in the LC and RoIns, but not the in ppsclera in moderate and advanced glaucoma compared to healthy controls. As mentioned above, an increase in collagen crimp period implies an increase in straight collagen fibrils, therefore less wavy-like appearance. This result might suggest that in the LC and RoIns, collagen fibrils lose their wavy-appearance and become elongated/straight only at late stage of disease. This result might correlate with the fact that at late stage of disease, the chronic exposure of the LC and RoIns to IOP, leads to the incapability of collagen fibrils to resist strain and therefore become straight.

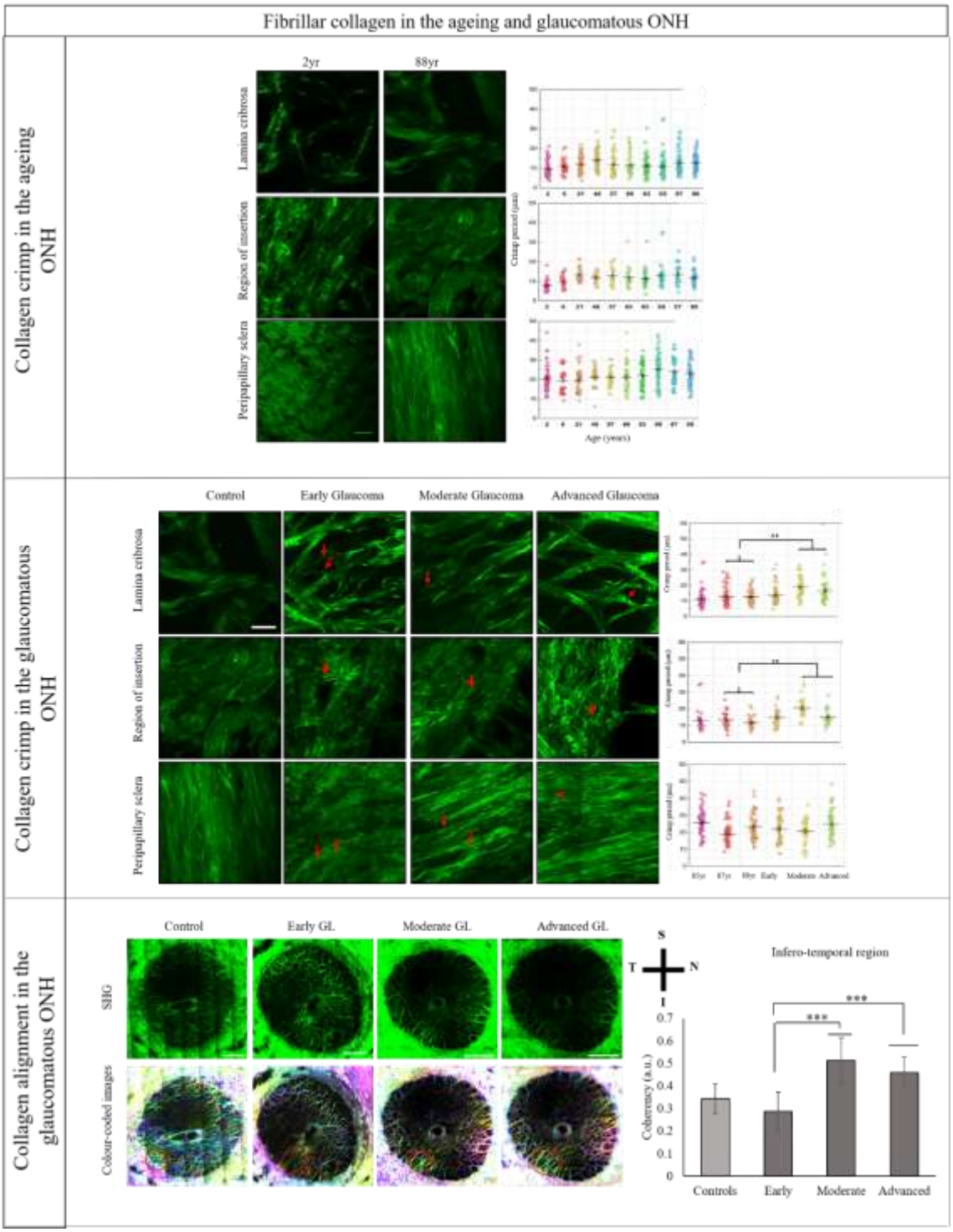

Figure 7.3. Fibrillar collagen investigations within the ageing and glaucomatous ONHs. Fibrillar collagen crimp period significantly increased in the ageing ppsclera but not in the LC and RoIns. In glaucoma, collagen crimp was visible at all stages and crimp period significantly increased within the LC and RoIns but not in ppsclera in moderate and advanced glaucoma compared to controls. Coherency, as a measure of collagen alignment, was significantly lower within the infero-temporal in early glaucoma compared to moderate and advanced glaucoma. Additionally, regions of highly aligned collagen were found in glaucoma within the infero-temporal region.

However, in the glaucomatous ONH, collagen waviness was observed at all stages of disease, which does not correlate with the increase in crimp period. This discrepancy could be explained by the extensive remodelling of the extracellular matrix (ECM) observed in glaucoma and explained below.

The ONH ECM is very much disturbed in glaucoma, resulting in extensive remodelling (Hernandez, 2000, Kirwan et al., 2004, Quigley et al., 1981, Quigley and Broman, 2006, Quigley et al., 1983). Additionally, the detachment of collagen and EFs from the surrounding ECM (Quigley et al., 1991a) has been observed. This implies there is a loss or partial degradation of the straight collagen fibres and suggests they are no longer under tension, which normally keeps them in the stretched state such that the collagen fibres appear wavy-like in glaucoma.

As described in 2.4.2, the alteration of collagen structure and composition, as shown in tendon uncrimping (Connizzo et al., 2013, Dourte et al., 2012), could lead to altered mechanical behaviour and function. The absence of collagen crimp in the elderly ONH, causes a stiffer LC, which under elevated IOP, might be subjected to remodelling, which in turn alters the ECM as previously described (Hernandez et al., 1990, Hernandez and Pena, 1997, Hernandez et al., 1994, Hernandez and Ye, 1993, Quigley et al., 1994, Quigley et al., 1991a, Quigley et al., 1991b), leading to the reestablishment of the wavy-like appearance of the collagen fibrils observed in this thesis.

An already uncrimped, and therefore stiff, elderly ppsclera might be more susceptible to damage. As a result, the chronic exposure of the elderly ppsclera to IOP, might transfer the stress and strain towards the RoIns and LC, which collagen fibrils, in turn, become straighter at late stage of disease.

Coherency, as a measure of collagen alignment, was significantly greater in moderate and advanced compared to early glaucoma. Orientation and alignment of connective tissue strongly depends on the amount and nature of stress it experience (Culav et al., 1999). In fact, connective tissues become stiffer as they are extended due to uncrimp, and collagen fibres become more aligned in the direction of the stretch. Therefore, regions of higher collagen alignment might present greater stiffness due to the uncrimping.

This concept might explain the events that occur in glaucoma as a function of IOP. As the IOP-related stress increases, the strain applied onto the LC, leads to a more oriented collagen fibrils in the direction of the stress. The higher collagen alignment observed in the infero-temporal region in this thesis and previously (Jones at al., 2015) might suggest that this region becomes more aligned due to either a direct strain applied onto this region, pulling the fibrils which become straight, or possible damage to other regions that result in changes of infero-temporal alignment. This might suggest that the infero-temporal region is potentially more susceptible to stress, which might explain the predominance of focal defects (Kiumehr et al., 2012) and disc haemorrhages (Siegner and Netland, 1996) in this region.

In early glaucoma, collagen fibrils were less aligned that moderate and advanced stage of disease. This is consistent with a previous SALS study, which found that glaucomatous LC with a mean deviation of -1.54 dB had a less aligned collagen than a glaucomatous LC with mean deviation of -12.48 dB (Jones et al., 2015). The low collagen fibrils alignment in the early glaucoma might be due to the ECM remodelling that occurs only at later stages. This could explain the similar alignment of collagen fibrils in early glaucoma and controls; as the disease progresses, the IOP acts as a chronic force onto the LC, leading to a change in collagen alignment.

As mentioned above, the superior and inferior regions of the LC contain less connective tissue and larger pores (Quigley and Addicks 1981; Radius and Gonzales 1981) compared to nasal and temporal. This is consistent with the backward moving of the LC as a function of glaucoma progression, which is more pronounced in the superior and inferior regions (Quigley et al. 1983). Winkler et al. (2010) suggested that collagen density in the infero-temporal region was lower compared to other regions, consistent with the glaucomatous loss of neuroretinal rim being greater in this region (Garway-Heath et al., 1997, Jonas et al., 1993). Therefore, the higher collagen alignment presented in this thesis could be linked to greater level of glaucomatous damage reported in the infero-temporal region.

To date, however, there seems to be no consensus on the effects of glaucoma on fibrillar collagen alignment of human sclera. However, it remains to be determined if these regions identified in the infero-temporal of highly aligned collagen, which seems to increase as the disease progresses, are a consequence of the altered mechanism within other regions.

For instance, the adaption of collagen alignment within the infero-temporal region of the LC might be a response to the softening of the infero-temporal region of the ppsclera, as previously shown (Fazio et al., 2014). This preferred alignment of the infero-temporal region might assist the LC to resist forces that occur in the direction of the fibre alignment, limiting the scleral canal expansion. In turn, this might contribute to the regional susceptibility of RGC axons to damage (Quigley and Addicks, 1981).

7.3 Elastic fibre within the ageing and glaucomatous ONH

Investigations of EF content in the ageing and glaucomatous ONH are summarised in figure 7.5. As mentioned in 2.1, TPEF is a nonlinear imaging technique used to detect endogenous fluorophores within tissues, such as NAD(P)H (Zipfel et al., 2003), retinol (Zipfel et al., 2003) and EFs (Jiang et al., 2011, Zhuo et al., 2007). The segmentation of the EFs within the human ONH has not been possible previously due to the great amount of endogenous fluorescence detected through TPEF imaging. In chapter 3, an innovative method based on spectral imaging, a combination of imaging and spectroscopy, has been developed to separate the EF TPEF signal from other sources of endogenous fluorescence.

Spectral imaging is an analytical technique that allowed the unmixing (isolating) of the EF fluorescence from these other endogenous fluorophores and consequently quantification of EF content. EF content significantly increased in the ageing LC, RoIns and ppsclera up to nearly 50%. This result is consistent with previous studies that showed an increase in elastin content in the ageing ONH (Albon et al., 2000a, Hernandez et al., 1989). In this thesis, no EFs were observed in the LC at young ages, consistent with electron microscopy (Quigley et al., 1991a, Hernandez, 1992, Oyama et al., 2006) and immunolabelling studies of human elastin (Hernandez, 1992, Morrison et al., 1989, Albon et al., 2000a) which showed no labelling in foetal and young LC (less than 18 years old) (Hernandez, 1992, Morrison et al., 1989).

Although the elderly LC contained more elastin, it has been shown that the LC become stiffer with age (Albon et al., 2000b), and there is no indication of EF degradation (Hernandez, 1992). Non-enzymatic glycation, a process by which glucose can directly condense with free amino acid group on lysine residue, is one the main ageing process of long-lived protein, such as collagen and elastin.

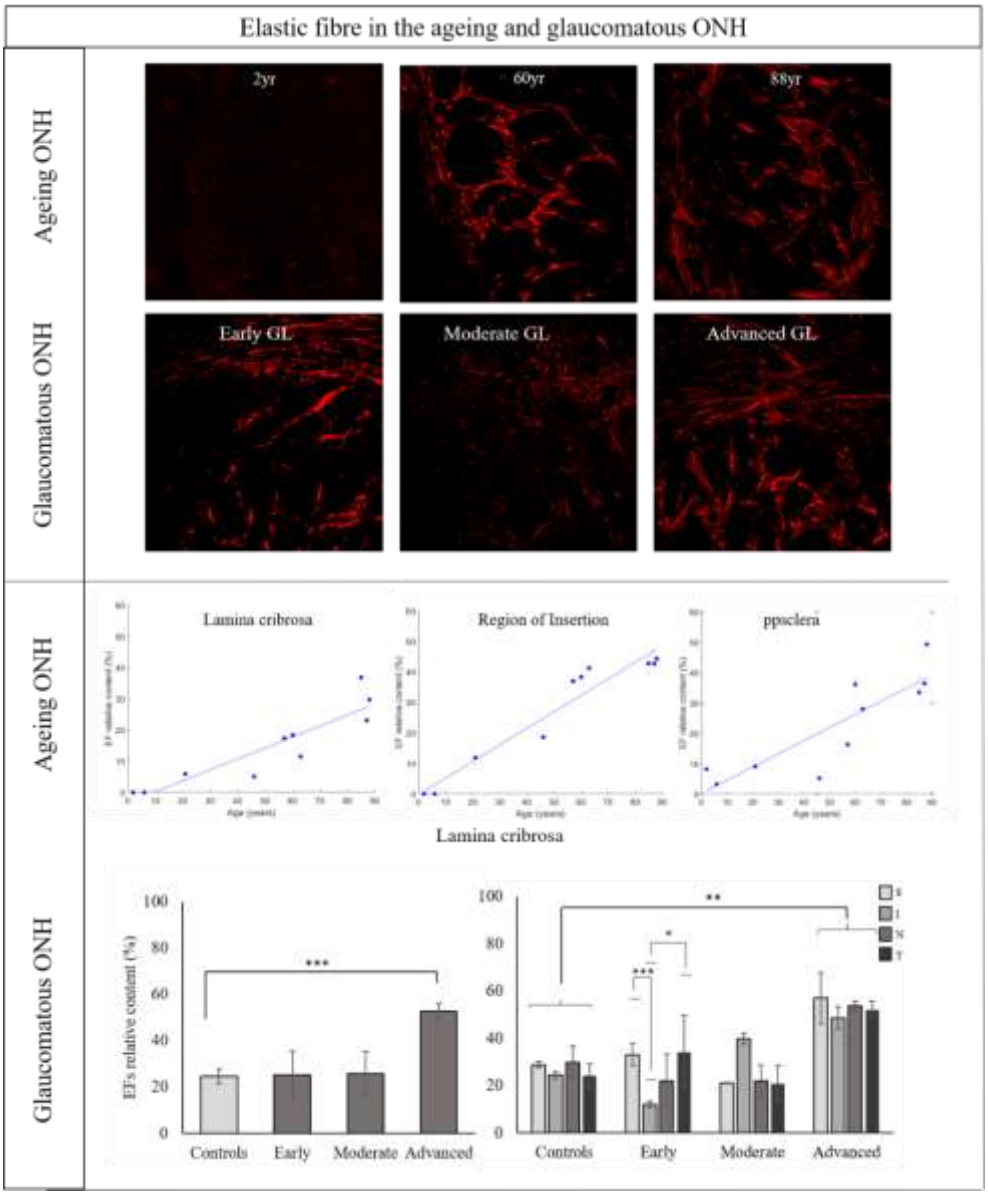

Figure 7.4. Elastic fibre in the ageing and glaucomatous ONH. EF content significantly increased in LC, RoIns and ppsclera as a function of age. In glaucoma, EF appeared more disorganised compared to controls and the content significantly increased in advanced glaucoma. Regional analysis showed all regions of advanced glaucoma with greater EF content and it was also greater in the nasal and superior region compared to inferior within early glaucoma.

Non-enzymatic glycation cross-links have been shown to be an ageing related process that affects the mechanical properties of collagen and elastin (Bailey, 2001). Elastin glycation has been shown before in the rat (Bruel and Oxlund, 1996) and human aortic elastin (Baydanoff et al., 1994, Baydanoff et al., 1996, Konova et al., 2004) and it has been proposed to have effects on the compliance of elastin (Winlove et al., 1996).

Therefore, it is likely that the age-related glycation of elastin contributes towards the LC stiffening that occurs with age, which could result in a decreased capability of the EF to support the LC from glaucomatous damage.

EF content was significantly increased in the LC in advanced glaucoma compared to controls, but not in the RoIns and ppsclera. Regional analyses showed that the content was significantly higher in all regions in advanced glaucoma compared to controls. Changes in EFs have been previously reported in glaucoma (Hernandez et al., 1990, Hernandez, 1992, Quigley et al., 1991a). Quigley et al., (1994) showed a curled appearance of the EFs, which was more pronounced with the progression of the disease (Quigley et al., 1994). EFs in glaucoma appeared to be elastotic (Hernandez, 1992, Hernandez et al., 1990, Netland et al., 1995, Pena et al., 1998) which is defined as the aberrant proliferation and degeneration of EFs.

The accumulation of EFs in advanced glaucoma could be a result of earlier upregulation as shown previously as an increase in elastin (Hernandez et al., 1994) and tropoelastin mRNA expression (Pena et al., 1996). These investigations might explain the increases in EF content shown in the current thesis, however, only at late stage of disease. This result correlates well with the findings of an increased crimp period in the LC and RoIns only at late stage of glaucoma, suggesting that the connective tissue of the LC and RoIns might experience damage only at late stage. This also correlates well with the increase in fibrillar collagen alignment observed in moderate and advanced glaucoma, which imply that the LC at late stage of disease is subjected to greater damage to the ECM.

As mentioned above, advanced glycation end products have been shown to increase with age (Albon et al., 1995) and glaucoma (Tezel et al., 2007) and may be involved in the stiffening of the ONH (Albon et al., 2000b, Zeimer and Ogura, 1989). Therefore, it can be speculated that the increase in non-enzymatic glycation of collagen leads to stiffening of the connective tissue, and so contributes to the decreased compliance of the ONH, despite the increased EF content. This might result in a more susceptible elderly eye to damage due to chronic exposure to IOP.

7.4 Fibrillar collagen and elastin nanostructure within the ageing ONH

Nanostructure investigation of fibrillar collagen and elastin within the ageing ONH are summarised in figure 7.6. Fibrillar collagen diameter and interfibrillar spacing in the ageing ppsclera significantly increased and decreased, respectively. This result might imply that fibrils are closer to each other, leading to a more closely packed tissue due to a higher collagen fibril volume fraction, which might increase the mechanical strength leading to a stiffer ppsclera. The increased fibril diameter correlates well with the increased intermolecular Bragg spacing presented in this thesis, consistent with previous work on cornea (Malik and Meek, 1994). The increased space between molecules is likely due to increased intermolecular cross-links which are a key in collagen extracellular maturation, in fact, they provide the fibrils with mechanical strength essential for biological properties of collagen over a life time (Zimmermann et al., 1973). This suggests that molecules are further apart, which would also explain the greater fibril diameter. If this is the case, it would be consistent with the age-related increase in the AGE-product, pentosidine, shown to occur in the ageing ONH (Albon et al., 1995).

PTA-stained ONH sections significantly enhanced collagen signal allowing, for the first time, the acquisition of SAXS and WAXS diffraction patterns in the LC. However, the limited number of samples did not allow a characterisation as a function of age. This requires further experiments, but it holds potential for the future quantification of LC collagen parameters.

Despite the alteration of EF as a function of age, its nanostructure seemed unaltered in the ageing ONH. WAXS analysis of elastin showed a diffraction pattern derived from the lateral spacing of the β-sheets of elastin (Narayanan and Dias, 2013) but no changes in the ring distance from beam centre were observed with age. This result suggests that at nanoscale level, elastin is not affected by age, however, little is known about elastin nanostructure.

The presence of a diffraction ring associated to elastin might introduce the concept that elastin could show a potentially ordered structure within the amorphous core, which may not be affected by age. Since the elastin ring appeared more diffuse and wider compared to those observed for collagen, and little is known about the ordered structure of elastin, it is worth further investigations.

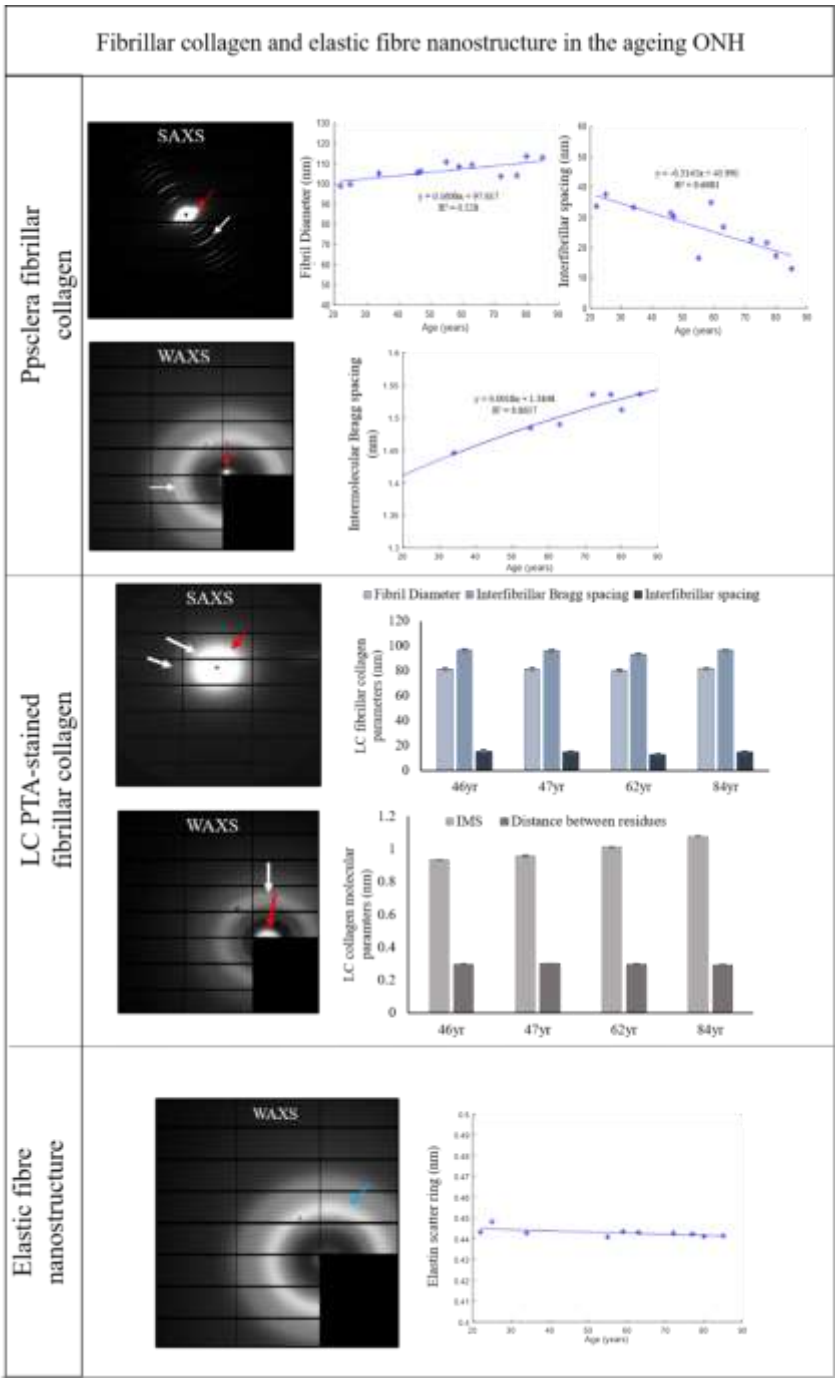

Figure 7.5. Nanostructure investigation of fibrillar collagen and elastin within the ageing ONH. Fibril diameter and intermolecular Bragg spacing significantly increased in the ageing ppsclera whereas the interfibrillar spacing decreased significantly. PTA enhanced collagen signal within the LC and it holds potential for future investigation into the nanostructure of fibrillar collagen in the LC. The distance of the diffuse ring associated to elastin did not show differences as a function of age.

7.5 Biomechanics of the ONH

Micro and nanomechanics of fibrillar collagen within the porcine ONH are summarised in figure 7.7. SAXS and WAXS investigation on human ONHs provided evidence of an altered nanostructure of collagen after radial stretch was applied. Results showed an increase in collagen D periodicity and in the molecular distance between amino acid residues in the stretched ppsclera, without changes in the interfibrillar Bragg spacing and/or fibril diameter. These results suggest that the force applied by the radial stretch cause collagen to unwind at molecular level and collagen fibrils to elongate as the D period becomes greater. If damage occurs, an uncoiled tropocollagen has significant effects on the mechanical properties of the whole tissue (Veres and Lee, 2012, Wang et al., 2002, Uzel and Buehler, 2009).

The elongation of collagen fibrils due to the increase in D period and crimp period might imply a straighten of the fibrils which in turn lead to a stiffer tissue. These results suggest that collagen fibrils alter at both micro and nanostructure and it is likely that all together these would contribute to the susceptibility of the elderly eye to develop glaucomatous damage.

As part of the biomechanical investigation, this thesis also probed a preliminary investigation into the porcine ONHs micromechanics using Brillouin microscopy. The preliminary results showed differences in elasticity and viscosity between preL and LC. Both maps of elasticity and viscosity appeared more heterogenous in the LC than those observed in the preL. Even though some studies have shown the potential of Brillouin microscopy to assess *ex vivo* corneal (Scarcelli et al., 2012, Scarcelli et al., 2013) and lens (Reiß et al., 2012) micromechanics and *in vivo* biomechanics of the eye (Scarcelli and Yun, 2012, Scarcelli et al., 2011, Besner et al., 2016) to date no studies have attempted to investigate the micromechanics of the optic nerve head with Brillouin microscopy. The result presented in chapter 6 demonstrates a proof of concept of the capabilities of Brillouin micro-spectroscopy approach for application on *ex vivo* samples of the optic nerve head, showing differences in elasticity and viscosity between preL and LC.

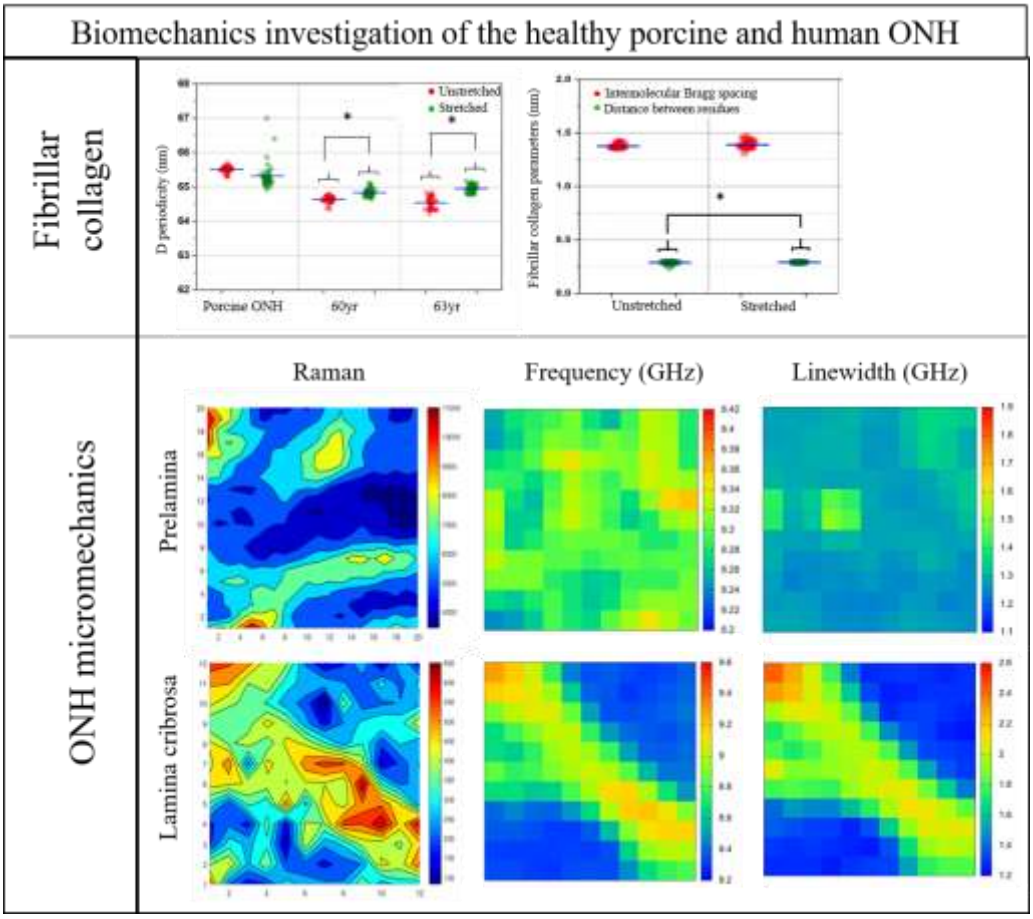

Figure 7.6. Biomechanical investigation of the human and porcine ONH. Collagen D period and distance between amino acid residues was greater in the human ONH after radial stretch was applied. Micromechanics investigation using Brillouin microscopy showed changes in elasticity and viscosity within the preL and LC.

7.6 Conclusion

The overall aim of this thesis was to provide further evidence on how the macro, micro and nanostructure of the ONH changes in relation to age and glaucoma, likely affecting the biomechanical environment and thus influencing the susceptibility of the elderly eye to develop glaucoma. Changes in the connective tissue of the ageing ONH included the loss of the wavy-like appearance of collagen crimp in the elderly ONH, an increase in collagen crimp period in the ppsclera along with an increase in fibril diameter. These results all suggest that the ppsclera becomes stiffer with age. A stiffer ppsclera might protect the LC from insult and prevent the sclera canal expansion and hence protecting the RGC axons from damage.

This thesis also provided evidence of an altered connective tissue as a function of glaucoma progression, including an increased in collagen crimp in the LC and RoIns and changes in elastin content in the LC. These results all together suggest that, as a function of glaucoma progression, the damage is transferred from the ppsclera, which can no longer withstand pressure, to the LC through the region of insertion. Results presented in this thesis, aided in a better understanding of the micro and nanoarchitecture of the ONH in age and glaucoma, which is important as it is known that age-related alteration in the connective tissue of the LC and ppsclera are likely to influence ONH biomechanics and therefore the response to IOP, thus understanding if the changes are results of elevated IOP or are the primary original factor causing glaucoma.

7.7 Limitation

This thesis presented few limitations, which are fully discussed separately in each result chapter. Briefly, the small number of glaucomatous ONHs for connective tissue analysis limited the statistical confidence. Similarly, the lack of ONHs below the age of 22 years limited the age-related investigation of collagen and EF as well as anatomical features of the LC (i.e. thickness). Future work will require additional specimen to further investigate into the connective tissue changes in ageing and disease and to confirm results presented in this thesis. Another important limitation is the lack of contrast within ONH stacks acquired with XMT, which limited the pores and connective tissue analysis within 3D images. However, representative optical slices were used as proof of concept to support XMT as a reliable technique to investigate into ONH features.

7.8 Future work

- The goal of this research will be to determine structural parameters within the ONH that predispose the eye to develop the disease. For instance, regions of high collagen alignment in the infero-temporal LC sector previously found (Jones et al., 2015) and confirmed in this thesis using Orientation J analysis, might be a suitable marker for glaucomatous development. These parameters will be investigated using *in vivo* techniques such as optical coherence tomography in order to identify regions within the ONH as an early indicator of ONH at risk of developing glaucoma.

- Future work will include the increase in sample size in all studies presented in this thesis. More donors at young ages below 20s are needed to have an optimal age range. This will enable to further characterise age-related changes and increase statistical confidence.
- More glaucomatous ONH are needed to better understand the connective tissue changes that occur in glaucoma as a representation of a true population. This will enable a 3D reconstruction and analysis of the connective tissue network to better understand how it macroscopically changes as a function of glaucoma progression.
- Even though within SAXS and WAXS experiment PTA-stained ONH enabled the collection of diffraction patterns from the LC, more samples are needed to investigate into the age-related changes in collagen and elastin in the LC. PTA has been shown to increase collagen signal before and in the current thesis therefore more samples at different ages are needed to further characterise the nanostructure changes in the LC.
- Future work is also required to enable the segmentation of EF within the whole ONH. Spectral imaging method developed in the current thesis will be applied to a whole ONH to 3D reconstruct the EF network and enable the quantification of EF in the ageing ONH. Immunohistochemistry and electron microscopy will be also performed to confirm the location of the EF within the LC and RoIns and to investigate into the fine structure of EF to confirm the observation within the 3D images, respectively.
- The suitability of XMT as a cutting-free technique has been explored in this thesis and it has been proposed as a suitable tool to investigate into the macro and microarchitecture of the ONH, avoiding cutting samples and time-consuming computational analysis to align tissue sections for 3D reconstruction. Future work will include an increased in sample size to investigate into pore changes as a function of glaucoma progression and an optimised method to increase the contrast of phase-images to segment pores and connective tissue. A long-term goal of this research will involve the development of an optimised BROPA staining procedure to count and track axons within neuronal pores. The result presented in the current thesis showed the potential of BROPA to stain axons, however, the magnification was not suitable enough due to sample movement to

discriminate axons. Therefore, further studies are needed to optimise the method which will enable axons count as a function of disease progression.

- Future work will also involve the development of mathematical models similar to that presented by Grytz and Meschke (2009) to predict stiffness of collagen fibril within ppsclera, RoIns and LC (Grytz and Meschke, 2009). This model will consider collagen fibril diameter measured with SAXS (see chapter 5) and collagen crimp parameters (see chapter 2) to investigate and determine potential differences in stiffness between a soft tissue as the LC and a hard tissue as the ppsclera. This in turn will confirm the role of the ppscleta to support and prevent expansion of the sclera canal to prevent the damage to be transferred to the LC.

Appendix

Appendix I: Laboratory stock solutions

I.1 4% Paraformaldehyde (PFA)

To make 100ml of 8% stock solution:

1. Dissolve 8g of paraformaldehyde (Fisher Scientific, UK) into 50ml of double PBS
2. Warming to approximately 60ºC whilst stirring on a magnetic hot plate stirrer
3. When paraformaldehyde has dissolved, add drops of sodium hydroxide (NaOH) (Fisher, UK) until solution clears.
4. Add 50 ml of double PBS
5. Allow to cool and store in aliquots in the freezer.

I.2 Phosphate Buffered Saline (PBS)

10X PBS stock:

To make 1000 ml of 10X stock solution:

1) To 800 ml of double distilled water, add:
    i. 80 g sodium chloride (NaCl; Sigma, UK)
    ii. 2 g potassium chloride (KCl; Sigma, UK)
    iii. 4.4 g sodium phosphate dibasic (Na2HPO4; Sigma, UK)
    iv. 2.5 g potassium phosphate (KH2PO4; Sigma, UK)
2) pH solution to 7.4, and top up to 1000 ml with double distilled water

I.3 Phosphotungstic acid (PTA)

To prepare 2% PTA in distilled water

- Weight 2 g of PTA powder in 100 ml of distilled water

To prepare 2% PTA in 70% ethanol

- Weight 2 g of PTA powder in 100 ml of ethanol at 70%

I.4 Lugol's iodine

To prepare 10% Lugol's iodine solution in distilled water

- Dilute 10 ml of Lugol's into 100 ml of distilled water

I.5 Tannic acid (TA)

To prepare 2% of Tannic acid in distilled water

- Weight 2 g of TA powder in 100 ml of distilled water

I.6 Osmium Tetroxide

Stock solution: 2% osmium at 80 mM
To prepare 100 ml of solution at 40 mM:

- Dilute the stock solution 1:2

Molecular weight of osmium tetroxide = 254.2g/mol

I.7 Potassium Hexaferrocyanate

To prepare 300 ml of 35 mM of potassium hexaferrocyanate solution

- Weight 4.43 g of powder in 300 ml of distilled water

Molecular weight = 422.41g/mol

I.8 Sodium Cacodylate Buffer

To prepare 100ml of 0.2M (or 200mM) of buffer (to be prepared under fume cupboard)

- Dissolve 4.28g of cacodylate powder in 50ml distilled water
- Dissolve 0.044g of calcium chloride in distilled water
- Correct pH with HCl to 7.4
- Make up to 100ml of distilled water (add the remaining water up to 100ml)

To prepare 100ml of 100mM of buffer

- Dilute the 200mM in distilled water 1:2 (100ml of 200mM buffer + 100ml of distilled water)

I.9 Formamide 99.5%

Stock solution at 99.5%
To prepare 200 ml of 2.5 M solution

- Dilute 22.6 ml of stock solution into distilled water up to 200 ml

Molecular weight of formamide = 45.04g/mol

I.10 Pyrogallol

To prepare 300 ml of pyrogallol at 320 mM, pH 4.1

- Weight 12.10 g of pyrogallol (Sigma, UK) into 300ml of distilled water

Molecular weight of pyrogallol = 126.11g/

Appendix II: MATLAB codes

II.1 EF_Intensity_Profile_v1

```
close all
clear all
clc

%% file with calibration data
calfile = '..\LSM_CalData.txt';

%% file with intensity
filename = 'Em_spectra.xlsx';

%% excel sheet name
sheetname = 'code';

%% excitation wavelenght
waveexcitation = [740,760,780,800];
markers = ['s';'o';'d';'v'];
colors = ['b';'r';'m';'g'];


%% Load files
CALDATA = load(calfile);
[NUM,TXT,RAW] = xlsread(filename,sheetname);



wavelength = NUM(2:end,1);
%% columns with intensity values
INTENSITY = NUM(2:end,3:6);

%% check wavelengths
if length(waveexcitation) ~= size(INTENSITY,2)
   disp('wavelengths-error')
   return
end


hf = figure;
ha = axes;
hold on
grid on

%% Loop
for ww = 1:length(waveexcitation)
   lambda = waveexcitation(ww);
```

```
    II = find(CALDATA(:,1)== lambda);
    calcoeff =(CALDATA(II,2)/100)^2;
    INTCORR(:,ww) = INTENSITY(:,ww)/calcoeff;
end

%% normalisation to the maximum
INTNORM = INTCORR/max(max(INTCORR));

for ww = 1:length(waveexcitation)
plot(wavelength,INTNORM(:,ww),'Linewidth',2,'Marker',markers(ww,:),'Color',colors(
ww,:))
end
set(ha,'XLim',[min(wavelength)
max(wavelength)],'XTick',[min(wavelength):20:max(wavelength)],'YLim',[0 1])

legend(num2str(waveexcitation.'))

xlabel('Emission Wavelength (nm)')
ylabel('Normalized Pixel Value')
```

II.2 Polar_plots_SAXS_ONH

```
close all; clear all;
path_name = {'F:\Techniques\SAXS\polar_plots'};                    % Files are all
in folder
%scan_file_name = {'B33119B_tare.xlsx'};       % Enter scan file name in ''
% Sample_name = {'LC_'};            % Enter image file base name in ''

extension1 = {'LC_'};
extension2 = {'ONH_'};
extension3 = {'0_pc_strainM22509A_postprecondition_1_'};
extension4 = {'1.4_pc_strainM22509A_1_'};
extension5 = {'2.8_pc_strainM22509A_1_'};

file_ext = {'.tif'};                        % Enter file name ext
leading_zeros = 1;                          % Enter '1' for leading zeroes in file names
output_filename = {'G:\Diamond Aug2017\M22543B\all_outputs.mat'};          %
Enter output file name


% Autmoatically generates scan file
automate_scan_file = 1;          % Enter 1 to automate scan file generation
    % This is based on Diamond Light Source, top-down followed by left-right
    % Otherwise, manually generate scan file

x_spacing = 200;                % X-grid spacing in mm
y_spacing = 200;                % Y-grid spacing in mm
```

```
all_hits = 1;                % Enter 1 to set all spaces to 'hits'


% Data parameters from visit
same_visit_params = 1;          % Enter 1 if the visit parameters are the same for each
image
                          % Otherwise, will use scan file tab 4 'I'
P = 300;                    % WAXS power in mA
A = 15000;                       % Area of the WAXS beam in um^2
t = 3;                    % WAXS beam exposure in seconds
K = 1/(P*A*t);                % Scaling factor between WAXS visits


% Limits to remove outliers
scatter_upper = 1e2;            % Upper limit of scatter noise
scatter_lower = 1e-180;              % Lower limit of scatter noise


xc = 652;% +1050;%1.2371e+03;
yc = 703;% +1050;%1.2441e+03;

% Limits of radial intergration for collagen peak
R_lower = 5;               % Log(R) lower limit for collagen peak, if not automatically
found (Fig 2)
R_upper = 6.1;                % Log(R) upper limit for collagen peak, if not automatically
found (Fig 2)


automate_limits = 0;             % Enter 1 to automate limits, 2 is manual, otherwise is set
to R_lower and R_upper


% Low-pass filter frequency (normalized to 1)
w2 = 0.05;                  % Cut-off-frequency for anisotropic collagen vs theta (Fig 4)


% Polar plot scaling factor, suggested 45% of spacing
plot_scale = 135;             % Polar plot scaling (Fig 5)

plot_figures = 0;               % 1 = yes, anything else is no
polar_plot_figures = 1;


% Variable to pause code after processing 1 image
pause_on = 0 ;                % 1 is on, anything is off


%% Original calculation - verify meaning
D0 = 3.04 ;                 % Calcite peak in angstroms (3.05 = bright one, second in
from middle)
```

```
Calcite_R = 679.29;              % R value in angstroms after fitting the 3.05 peak using
centering.m
n = 1;                    % Order of mode (keep as 1)
lumda = 0.9795;                  % Wavelength in angstroms of X-ray beam
Calcite_THETA = asind(n*lumda/(2*D0));


%% Processing
% Calculate rows and columns
D = dir([char(path_name),char(strcat(extension1,'*'))]);%,file_ext))]);
N_r1 = length(D);%(not([D.isdir])));              % Number of files for first stretch
D = dir([char(path_name),char(strcat(extension2,'*'))]);%,file_ext))]);
N_r2 = length(D);%(not([D.isdir])));              % Number of files for second stretch
D = dir([char(path_name),char(strcat(extension3,'*'))]);%,file_ext))]);
N_r3 = length(D);%(not([D.isdir])));              % Number of files for third stretch
D = dir([char(path_name),char(strcat(extension4,'*'))]);%,file_ext))]);
N_r4 = length(D);%(not([D.isdir])));              % Number of files for fourth stretch
D = dir([char(path_name),char(strcat(extension5,'*'))]);%,file_ext))]);
N_r5 = length(D);%(not([D.isdir])));              % Number of files for fifth stretch
clear D

a = [N_r1 N_r2 N_r3 N_r4 N_r5 0];
N_c = find(a==0, 1, 'first')-1;
N_r = max(a,[],2);

% Modify Ks if you will be scanning multiple samples
for Ks = 1%1:length(scan_file_name)


   % Tabs of the scan file, make sure that the tabs correspond to the
   % index following the file name

   if automate_scan_file ~= 1
      NN        = xlsread(scan_file_name{Ks},1);    % File number
      XXg       = xlsread(scan_file_name{Ks},2);    % X coordinate
      YYg       = xlsread(scan_file_name{Ks},3);    % Y coordinate
   else
      NN = zeros(N_r,N_c); k = 1;
      for kc = 1:N_c
         for kr = 1:N_r; NN(kr,kc) = k; k = k+1; end
      end; clear k;

      XXg = zeros(N_r,N_c); k = 0;
      for kc = 1:N_c
         for kr = 1:N_r; XXg(kr,kc) = k;end
         k = k+x_spacing;
      end; clear k;

      YYg = zeros(N_r,N_c); k = (N_r-1)*y_spacing;
      for kc = 1:N_c
         for kr = 1:N_r; YYg(kr,kc) = k;
```

```
        k = k-y_spacing;end
      k = (N_r-1)*y_spacing;
      end; clear k;
   end

   if same_visit_params ~= 1;
      intensity = xlsread(scan_file_name{Ks},4);    % Intensity
      clear K; K = 1./intensity;
   end

   if all_hits == 1
      NI = ones(size(NN,1),size(NN,2));
   else
      NI  = xlsread(scan_file_name{Ks},5);
      % 0 = do not process, 1 = process, 2 = select range for scatter density vs R plot
%       NI = load('NI_matrix.mat');
%       NI = NI.I;
   end

   % Creating empty matrices for index purposes
   Anisotropy                  = zeros(size(NN));
   total_collagen_per_point       = zeros(size(NN,1),size(NN,2));
   aligned_collagen_per_point     = zeros(size(NN,1),size(NN,2));
   ccomp                       = zeros(size(NN,1)*size(NN,2),721);
   Width                       = zeros(size(NN,1),size(NN,2));
   theta_Pmax_all              = zeros(size(NN,1),size(NN,2));
   intermolecular_spacing         = zeros(size(NN,1),size(NN,2));
   peak_subtration_scatter        = zeros(size(NN,1),size(NN,2));
   peak_subtraction_R             = zeros(size(NN,1),size(NN,2));
   Q_limits_lower              = zeros(size(NN,1),size(NN,2));
   Q_limits_upper              = zeros(size(NN,1),size(NN,2));
   Q_limits_lower_horiz           = zeros(size(NN,1),size(NN,2));
   Q_limits_upper_horiz           = zeros(size(NN,1),size(NN,2));
   Q_limits_lower_vert            = zeros(size(NN,1),size(NN,2));
   Q_limits_upper_vert            = zeros(size(NN,1),size(NN,2));
   peakangle = zeros(N_r,N_c);
   spreadvstot = zeros(N_r,N_c);
   spreadvsorthog = zeros(N_r,N_c);

   for counter = 1:sum(a) % sum(a) is total number of image files
      if counter <= N_r1
         Kc = 1;
         Kr = counter;
         Dtemp = dir([char(path_name),char(strcat(extension1,'*'))]);
         Image_file_base_name = Dtemp(counter).name;
      elseif counter <= N_r1+N_r2
         Kc = 2;
         Kr = counter - N_r1;
         Dtemp = dir([char(path_name),char(strcat(extension2,'*'))]);
         Image_file_base_name = Dtemp(counter-N_r1).name;
      elseif counter <= N_r1+N_r2+N_r3
```

```
            Kc = 3;
            Kr = counter - N_r1 - N_r2;
            Dtemp = dir([char(path_name),char(strcat(extension3,'*'))]);
            Image_file_base_name = Dtemp(counter-N_r1-N_r2).name;
        elseif counter <= N_r1+N_r2+N_r3+N_r4
            Kc = 4;
            Kr = counter - N_r1 - N_r2 - N_r3;
            Dtemp = dir([char(path_name),char(strcat(extension4,'*'))]);
            Image_file_base_name = Dtemp(counter-N_r1-N_r2-N_r3).name;
        elseif counter <= N_r1+N_r2+N_r3+N_r4+N_r5
            Kc = 5;
            Kr = counter - N_r1 - N_r2 - N_r3 - N_r4;
            Dtemp = dir([char(path_name),char(strcat(extension5,'*'))]);
            Image_file_base_name = Dtemp(counter-N_r1-N_r2-N_r3-N_r4).name;
        end

       if isnan(NN(Kr,Kc))~=1
        % File counter
        disp(strcat(['Reading file number ' num2str(counter) ' of ' num2str(sum(a))]))

        % NI of 0 means do not process, 1 means process, 2 means select range for scatter
density vs R plot
        if NI(Kr,Kc) == 1 || NI(Kr,Kc) == 2;

            % Reading in the files
           %temppwd = pwd;
           %cd([char(path_name),char(Image_file_base_name)])
           cd 'G:\James Matlab\Laura\data\'
           oi = dir;
           Z = imread(oi(2+counter).name);
            Z = double(Z)*K;
            Z(Z>scatter_upper) = NaN;
            Z(Z<scatter_lower) = NaN;

            % Centering the image
            [M,N] = size(Z);
            [X,Y] = meshgrid(0:1:N-1, 0:1:M-1);
            Y = flipud(Y);
            X = X-xc;
            Y = Y-yc;
Xcheck=X;
Ycheck=Y;
Zcheck=Z;
            cropsize = 600;
            X = X(round(size(X,1)/2)-
cropsize:round(size(X,1)/2)+cropsize,round(size(X,2)/2)-
cropsize:round(size(X,2)/2)+cropsize);
            Y = Y(round(size(Y,1)/2)-
cropsize:round(size(Y,1)/2)+cropsize,round(size(Y,2)/2)-
cropsize:round(size(Y,2)/2)+cropsize);
```

```
Z = Z(round(size(Z,1)/2)-
cropsize:round(size(Z,1)/2)+cropsize,round(size(Z,2)/2)-
cropsize:round(size(Z,2)/2)+cropsize);


R0 = sqrt(X.^2+Y.^2);
RI = meshgrid(linspace(0,max(X(:)),2*360+1),linspace(0,max(X(:)),2*360+1));
th = meshgrid(0:0.5:360,0:0.5:360);
th = th'.*pi./180;
[XI,YI] = pol2cart(th,RI);
%digits(5);
%Z(isnan(Z)) = 0;
%ZI = interp2(X,Y,Z,XI,YI);

XR = reshape(X,(2*cropsize+1)^2,1);
YR = reshape(Y,(2*cropsize+1)^2,1);
ZR = reshape(Z,(2*cropsize+1)^2,1);
FSI = scatteredInterpolant(XR,YR,ZR);
ZI = zeros(721,721);
for j = 1:721
   for i = 1:721
      ZI(i,j) = FSI({[XI(i+(j-1)*721)],[YI(i+(j-1)*721)]});
   end
end



% Filling in the gaps in the data from sensors - reflection
ZI_1 = ZI(1:360,:);
ZI_2 = ZI(361:720,:);
II1 = isnan(ZI_1);
II2 = isnan(ZI_2);

ZI_1(II1)=ZI_2(II1);
ZI_2(II2)=ZI_1(II2);
ZI_3 = ZI_1(1,:);
ZII = [ZI_1;ZI_2;ZI_3];


% Interpolating remaining gaps or NaNs
for k = 1:360*2+1
   DATA = ZII(k,:);
   T = reshape(1:length(DATA),size(DATA));
   inan = isnan(DATA);
   if nansum(DATA) ~= 0
   DATA(inan) = interp1(T(~inan),DATA(~inan),T(inan));
   ZII(k,:) = DATA;
   end
end

for k = 1:360*2+1
```

```
    DATA = ZII(:,k);
    T = reshape(1:length(DATA),size(DATA));
    inan = isnan(DATA);
    if nansum(DATA) ~= 0
    DATA(inan) = interp1(T(~inan),DATA(~inan),T(inan));
    ZII(:,k) = DATA;
    end
end

% Plotting the reflected image with gaps filled in
if plot_figures == 1
    figure(1)
    surf(XI,YI,ZII,'EdgeColor','none')
    grid off; view(2)
    xlabel('x [pixel]'); ylabel('y [pixel]')
    zlabel('x-ray scatter [arbitrary unit]')
    title('Scatter image'); colorbar; colormap jet
    xlim([1.1*min(min(XI)) 1.1*max(max(XI))]);
    ylim([1.1*min(min(YI)) 1.1*max(max(YI))]);
    caxis([0.000015 0.00004])
    hold on
end

Z  = ZII;
ZI = ZII;



R = linspace(0,max(X(:)),2*360+1);
S = nansum(ZI);
Svert = nansum(ZI([91:270 451:630],:));
Shoriz = nansum(ZI([1:90 271:450 631:720],:));
scatter_theta = atand((R/Calcite_R)*tand(Calcite_THETA));

Q = 4*pi*sind(scatter_theta)/lumda;

total_S = S;

%       if plot_figures == 1
    figure(2)
    plot(log(Q),log(S),'LineWidth',2,'color','k'); hold on
    plot(log(Q),log(Shoriz),'LineWidth',2,'color','b'); hold on
    plot(log(Q),log(Svert),'LineWidth',2,'color','r'); hold on
    legend('S_{total}','S_{horiz}','S_{vert}');
    xlabel('log(Q)')
    ylabel('log x-ray scatter density [arbitrary unit]')
    title('Circumferentially integrated scatter')
    xlim([-2.5 1]);ylim([-5 0]);
    ffs = strcat(path_name,'precon',num2str(counter),'.fig');
%       saveas(2,ffs{1})
linepoint1 = 17;
```

```
            for linepoint2 = 29:49
%                 [PF1,~] = polyfit(log(Q([linepoint1 linepoint2])),log(S([linepoint1
linepoint2])),1);
%                 f1(:,linepoint1,linepoint2) = polyval(PF1,log(Q));
                BG=linspace(log(S(linepoint1)),log(S(linepoint2)),linepoint2-
linepoint1+1);
BGhoriz=linspace(log(Shoriz(linepoint1)),log(Shoriz(linepoint2)),linepoint2-
linepoint1+1);

                BGvert=linspace(log(Svert(linepoint1)),log(Svert(linepoint2)),linepoint2-
linepoint1+1);

%                 peakarea(linepoint1,linepoint2) = sum(log(S(linepoint1:linepoint2))'-
f1(linepoint1:linepoint2,linepoint1,linepoint2));
                peakarea(linepoint1,linepoint2) = sum(log(S(linepoint1:linepoint2))-BG);
%                 peakareahoriz(linepoint1,linepoint2) =
sum(log(Shoriz(linepoint1:linepoint2))'-
fhoriz1(linepoint1:linepoint2,linepoint1,linepoint2));
                peakareahoriz(linepoint1,linepoint2) =
sum(log(Shoriz(linepoint1:linepoint2))-BGhoriz);
%                 peakareavert(linepoint1,linepoint2) =
sum(log(Svert(linepoint1:linepoint2))'-
fvert1(linepoint1:linepoint2,linepoint1,linepoint2));
                peakareavert(linepoint1,linepoint2) =
sum(log(Svert(linepoint1:linepoint2))-BGvert);
            end


        [Xfind1,Xfind2] = find(peakarea==max(max((peakarea))));
        [Xfindhoriz1,Xfindhoriz2] = find(peakareahoriz==max(max((peakareahoriz))));
        [Xfindvert1,Xfindvert2] = find(peakareavert==max(max((peakareavert))));
%         if plot_figures==1
        BG=linspace(log(S(Xfind1)),log(S(Xfind2)),Xfind2-Xfind1+1);

BGhoriz=linspace(log(Shoriz(Xfindhoriz1)),log(Shoriz(Xfindhoriz2)),Xfindhoriz2-
Xfindhoriz1+1);
        BGvert=linspace(log(Svert(Xfindvert1)),log(Svert(Xfindvert2)),Xfindvert2-
Xfindvert1+1);

        figure(2);plot(log(Q([Xfind1 Xfind2])),BG([1 end]),'bo')
        figure(2);plot(log(Q([Xfind1 Xfind2])),BG([1 end]),'g')

        figure(2);plot(log(Q([Xfindhoriz1 Xfindhoriz2])),BGhoriz([1 end]),'bo')
        figure(2);plot(log(Q([Xfindhoriz1 Xfindhoriz2])),BGhoriz([1 end]),'g')

        figure(2);plot(log(Q([Xfindvert1 Xfindvert2])),BGvert([1 end]),'bo')
        figure(2);plot(log(Q([Xfindvert1 Xfindvert2])),BGvert([1 end]),'g')

%         export_fig(strcat('image_',num2str(counter)))
        hold off
        clear peakarea peakareahoriz peakareavert
```

```
%        end

        I1 = Xfind1;%find(log(R)<=x1); I1=I1(end);
        I2 = Xfind2;%find(log(R)>=x2); I2=I2(1);

        Q_limits_lower(Kr,Kc) = R(I1);
        Q_limits_upper(Kr,Kc) = R(I2);
        Q_limits_lower_horiz(Kr,Kc) = R(I1);
        Q_limits_upper_horiz(Kr,Kc) = R(I2);
        Q_limits_lower_vert(Kr,Kc) = R(I1);
        Q_limits_upper_vert(Kr,Kc) = R(I2);
        % limits
        xx1 = R(I1).*cosd(0:360);
        yy1 = R(I1).*sind(0:360);
        xx2 = R(I2).*cosd(0:360);
        yy2 = R(I2).*sind(0:360);

        % Plots circles on original scatter map
        if plot_figures == 1
           figure(1)
           hold on
           plot3(xx1,yy1,10000*ones(1,length(xx1)),'k')
           plot3(xx2,yy2,10000*ones(1,length(xx2)),'k')
           hold off
        end

        % Creates 2 plots: linear scale of total scattering vs R and
        % total scattering vs R
        if plot_figures == 1
           figure(3); subplot(121)
           % plot(R,S,'k','LineWidth',2,'color','r')
           plot(R(I1:I2),S(I1:I2),'r','LineWidth',2); hold on
           plot(R',exp(f1(:,Xfind1,Xfind2)),'g','LineWidth',2)
           ylim([min(S(I1:I2)) max(S(I1:I2))]); xlim([min(R(I1:I2)) max(R(I1:I2))])
           xlabel('R [pixel]'); ylabel('x-ray scatter density [arbitrary unit]')
           title('Collagen peak before')
           hold off
        end

        R12 = R(I1:I2);
        S12 = S(I1:I2);
        Net_Colagen = S12'-exp(BG'); % total_net_collagen_scatter
        Net_Colagen(Net_Colagen<0) = 0;
        Net_Colagenh = Shoriz(Xfindhoriz1:Xfindhoriz2)'-exp(BGhoriz');
        Net_Colagenh(Net_Colagenh<0) = 0;
        Net_Colagenv = Svert(Xfindvert1:Xfindvert2)'-exp(BGvert');
        Net_Colagenv(Net_Colagenv<0) = 0;

        %II1 = (Net_Colagen==max(Net_Colagen));
        [num,II1] = max(Net_Colagen);
        II1 = II1(1);
```

```
        if length(R12(II1)) > 1
            R(I1) = R(I2)-1;
        end

        peak_subtration_scatter(Kr,Kc) = Net_Colagen(II1);
        peak_subtraction_R(Kr,Kc) = R12(II1);

        RHR = linspace(R(I1),R(I2),10000);
        Gfit = fit(R(I1:I2)',Net_Colagen,'gauss2','StartPoint',[-5.363e-05 117.9 25.6
0.001995 103.4 23.85],'TolX',1e-12,'TolFun',1e-12);
        Gfitcurve = feval(Gfit,RHR);
        Gpeak = RHR((Gfitcurve==max(Gfitcurve)));

        RHRhoriz = linspace(R(Xfindhoriz1),R(Xfindhoriz2),10000);
        Ghfit = fit(R(Xfindhoriz1:Xfindhoriz2)',Net_Colagenh,'gauss2','StartPoint',[-
5.363e-05 117.9 25.6 0.001995 103.4 23.85],'TolX',1e-12,'TolFun',1e-12);
        Ghfitcurve = feval(Ghfit,RHRhoriz);
        Ghpeak = RHR((Ghfitcurve==max(Ghfitcurve)));

        RHRvert = linspace(R(Xfindvert1),R(Xfindvert2),10000);
        Gvfit = fit(R(Xfindvert1:Xfindvert2)',Net_Colagenv,'gauss2','StartPoint',[-
5.363e-05 117.9 25.6 0.001995 103.4 23.85],'TolX',1e-12,'TolFun',1e-12);
        Gvfitcurve = feval(Gvfit,RHRhoriz);
        Gvpeak = RHR((Gvfitcurve==max(Gvfitcurve)));

        if plot_figures == 1
            figure(3); subplot(122)
            plot(R(I1:I2),Net_Colagen,'k','LineWidth',2); hold on
            plot(R(Xfindhoriz1:Xfindhoriz2),Net_Colagenh,'b','LineWidth',2);
            plot(R(Xfindvert1:Xfindvert2),Net_Colagenv,'r','LineWidth',2);
            plot(R12(II1),Net_Colagen(II1),'b+','LineWidth',4);
            plot(RHR,Gfitcurve,'g');
            plot(RHRhoriz,Ghfitcurve,'g');
            plot(RHRvert,Gvfitcurve,'g');
            xlabel('R [pixel]'); ylabel('Collagen x-ray scatter density [arbitrary unit]')
            title('Collagen peak after')
            hold off
            %saveas(3,strcat(Image_file_base_name{1},num2str(counter),'_fig3'),'fig');
        end


        IIp = find(R == R12(II1));
        Ipeak = IIp;

        Calcite_THETA = asind(n*lumda/(2*D0));
        THETA_Col = atand((Gpeak/Calcite_R)*tand(Calcite_THETA));
        D1 = D0*sind(Calcite_THETA)/sind(THETA_Col);
        intermolecular_spacing(Kr,Kc) = D1;
        if counter<=N_r1
            intermolecular_spacing(Kr,Kc) = D1*735.4185/335.4185;
        end
```

```
        THETA_Col = atand((Ghpeak/Calcite_R)*tand(Calcite_THETA));
        D1 = D0*sind(Calcite_THETA)/sind(THETA_Col);
        intermolecular_spacing_horiz(Kr,Kc) = D1;
        if counter<=N_r1
           intermolecular_spacing_horiz(Kr,Kc) = D1*735.4185/335.4185;
        end

        THETA_Col = atand((Gvpeak/Calcite_R)*tand(Calcite_THETA));
        D1 = D0*sind(Calcite_THETA)/sind(THETA_Col);
        intermolecular_spacing_vert(Kr,Kc) = D1;
        if counter<=N_r1
           intermolecular_spacing_vert(Kr,Kc) = D1*735.4185/335.4185;
        end



        %% End

    % Filtering data
        ZI(RI<R(I1))=NaN;
        ZI(RI>R(I2))=NaN;
        Col_per_sigment = zeros(1,2*360+1);

        % Determining collagen per segment of theta
        for k = 1:2*360+1
           ZZ = ZI(k,:);
           [P,~] = polyfit(log(R([I1 I2])),log(ZZ([I1 I2])),1);
           Bf = polyval(P,log(R(I1:I2)));
           Col_sigment = ZZ(I1:I2)-exp(Bf);
           Col_sigment(Col_sigment<0) = 0;
           Col_per_sigment(k) = nansum(Col_sigment);
        end

 %% Averages over the center
        collagen = 0.5*(Col_per_sigment(1:361) + Col_per_sigment(361:721));
        total_collagen = [collagen collagen(2:end)];

1));
collagen_f = total_collagen; % No filtering


        %% Calculates collagen types

        % Isotropic collagen
        isotropic_collagen = min(collagen_f);
        p_data = collagen_f-isotropic_collagen;

        % Total collagen
        total_collagen_per_point(Kr,Kc) = sum(collagen_f);
```

```
        % Aligned collagen
        aligned_collagen_per_point(Kr,Kc) = sum(p_data);


        %% Highlights value above 50% of max
        Ia = find(p_data>0.5*max(p_data));
        Ip = ones(1,length(p_data));
        Width(Kr,Kc) = 0.5*0.5*length(Ia

        %% Plots anisotropic collagen vs theta


        theta = 0:0.5:360;
        collagen_f2 = zeros(size(collagen_f,1),size(collagen_f,2));
        collagen_f2(:,1:541) = collagen_f(:,181:721);
        collagen_f2(:,542:721) = collagen_f(:,1:180);
        collagen_f = collagen_f2;
        % 90 degree shift

oi = [collagen_f collagen_f collagen_f]; % Three repeats of curve, in case peak is within
first or last 15 degrees

        if plot_figures == 1
            figure(4)
            plot(theta,collagen_f); hold on
            plot([min(theta) max(theta)],[isotropic_collagen isotropic_collagen],'r'); hold
off
            title('Collagen vs theta');
            xlabel('Angle (\o)'); ylabel('x-ray scatter (a.u.)');
            legend('anisotropic','isotropic')
            xlim([min(theta) max(theta)])
            if max(collagen_f) > 0; ylim([0 1.1*max(collagen_f)]); end
        end

                % Anisotropy calculations
            peakangle(Kr,Kc) = find(collagen_f == max(collagen_f),1,'first');
            spread15 = sum(oi((peakangle(Kr,Kc)+706):(peakangle(Kr,Kc)+736))) +
sum(oi((peakangle(Kr,Kc)+346):(peakangle(Kr,Kc)+376)));
            spreadorthog15 = sum(oi((peakangle(Kr,Kc)+526):(peakangle(Kr,Kc)+556)))
+ sum(oi((peakangle(Kr,Kc)+166):(peakangle(Kr,Kc)+196)));
            spreadvstot15(Kr,Kc) = spread15/sum(collagen_f);
            spreadvsorthog15(Kr,Kc) = spread15/spreadorthog15;

            spread5 = sum(oi((peakangle(Kr,Kc)+716):(peakangle(Kr,Kc)+726))) +
sum(oi((peakangle(Kr,Kc)+356):(peakangle(Kr,Kc)+366)));
            spreadorthog5 = sum(oi((peakangle(Kr,Kc)+536):(peakangle(Kr,Kc)+546)))
+ sum(oi((peakangle(Kr,Kc)+176):(peakangle(Kr,Kc)+186)));
            spreadvstot5(Kr,Kc) = spread5/sum(collagen_f);
            spreadvsorthog5(Kr,Kc) = spread5/spreadorthog5;

                % Creating segmented figures
```

```
            for i = 1:12
            pmean(i) = mean(oi((346+(i-1)*60):(375+(i-
1)*60)))/total_collagen_per_point(Kr,Kc);
            end

        % Checkpoint to check quality of filter
%           return

        ccomp(counter,:) = collagen_f;
        p_data = collagen_f-isotropic_collagen;
        theta_Pmax = theta(p_data==max(p_data(1:721)));
        theta_Pmax_all(Kr,Kc) = theta_Pmax(1);
        Anisotropy(Kr,Kc) = sum(p_data)/sum(collagen_f);


        %% Creates and plots polar vectors

        collagen_f = 0.5*(collagen_f(1:361) + collagen_f(361:721));
        total_collagen_f = [collagen_f collagen_f(2:end)];
        %p_data = total_collagen_f-isotropic_collagen;
        p_data = total_collagen_f;
        %P_colore = p_data;
        P_colore = 1-(isotropic_collagen./total_collagen_f);
        p_data = plot_scale*p_data./max(p_data);

        if polar_plot_figures == 1
            figH = figure(5);
            Xp = p_data.*cosd(0:0.5:360)+XXg(Kr,Kc);
            Yp = p_data.*sind(0:0.5:360)+YYg(Kr,Kc);
            patch(Xp,Yp,max(P_colore),'edgecolor','none')


             % PATCH METHOD
%              for i = 1:12
%                  Xp=pmean(i)*cosd(-7.5:352.5)*3e4+XXg(Kr,Kc);
%                  Yp=pmean(i)*sind(-7.5:352.5)*3e4+YYg(Kr,Kc);
%                  patch([XXg(Kr,Kc) Xp(30*i-29:30*i-15)],[YYg(Kr,Kc) Yp(30*i-
29:30*i-15)],pmean(i),'edgecolor','none')
%              end

            xlabel('Strain'); ylabel('y (\mum)')
            axis equal
            set(gcf,'Color','w')
            title('Polar maps of collagen orientation at varying strain')
        end


        %% Check quality of figures 1-5

%           return
```

```
        % Pausing to view Figures 1-5
        if pause_on == 1 && plot_figures == 1
           pause
        end


     end
    end
  end

%    return
end
figure(5)
axis([-70 650 5300 7500]);
ax = gca;
set(ax,'XTick',[0:x_spacing:(N_c-1)*x_spacing])
set(ax,'XTickLabel',{'tare','1.4%','2.8%','5%','8%','100%','OVER 9000%!!'})
cb=colorbar;%set(cb,'yticklabel',num2str(str2num(get(cb,'yticklabel')),'%0.1f'))
ylabel(cb,'Relative amount of collagen (a.u.)')


time = clock;

n = 1;
```

II.3 Raman_Intensity_Profile_v1

```
clear all
clc
close all

filename = 'totspettri_Abis.txt';
A = load(filename);

intensity = A(:,2);
freq_shift = A(:,1);


plot(freq_shift,intensity)
xlabel('Wavenumber (cm^{-1})')
ylabel('Raman Intensity (a.u.)')
```

II.4 Brillouin_Intensity_Profile_v1

```
clear all
clc
close all
```

```
filename = 'totspettri_Abis.txt';
A = load(filename);

intensity = A(:,2);
freq_shift = A(:,1);


plot(freq_shift,intensity)
xlabel('Frequency shift (GHz)')
ylabel('Brillouin Intensity (a.u.)')
```

Appendix III: X ray microtomography Savu commands

III.1 Tomo centre

```
->tomo-centre -h


        Welcome to the DLS compute cluster

        For MPI jobs, please use 'module load openmpi'.

        If using a different OpenMPI installation,
        or manually specifying path to OpenMPI, option
        '-mca orte_forward_job_control 1'
        must be added to mpirun to ensure cluster functionality.

        Please report any issues to linux.manager@diamond.ac.uk

Loading 64-bit Oracle instantclient, version 11.2
Loading 64-bit python, version 2.7.2
Loading 64-bit numpy, version 1.6.1
Usage: selection_recon.py [options] data output_directory

Options:
  -h, --help            show this help message and exit
  -m MACHINES, --machines=MACHINES
                        Number of machines to deploy to
  -s SLICE, --slice=SLICE
                        Slice selected for processing
  -t TEMPLATE, --template=TEMPLATE
                        Template XML file
  -w WSAMP, --width_sample=WSAMP
                        Set the subsampling of the sinograms width
  -l LSAMP, --length_sample=LSAMP
                        Set the subsampling of the sinograms length
  -c CSTART, --cstart=CSTART
                        Starting value for the centre of rotation
  --ctot=CTOT           Total number of different values for the centre of
                        rotation
  --cstep=CSTEP         The step between two consecutive values for the centre
                        of rotation
  -r RUN_SLICES, --run_slices_loc=RUN_SLICES
                        set the run_slices.sh location
  -n, --new_cluster     use the new cluster
  --dark_file=DARK_FILE
                        Path to the file containing dark images
  --dark_path=DARK_PATH
                        path in the dark file to the data
  --flat_file=FLAT_FILE
                        Path to the file containing flat images
  --flat_path=FLAT_PATH
                        path in the dark file to the data
  --recon_range=RECON_RANGE
                        range for the reconstruction to be done over
  --d0f1                If option included (True), use 0's for dark- and 1's
                        for flat-field images
  --scan_id             If option included (True), incorporate the ID of the
                        input Nexus scan file into output filenames
->
```

III.2 Tomo recon

```
~>tomo-recon -h


         Welcome to the DLS compute cluster

         For MPI jobs, please use 'module load openmpi'.

         If using a different OpenMPI installation,
         or manually specifying path to OpenMPI, option
         '-mca orte_forward_job_control 1'
         must be added to mpirun to ensure cluster functionality.

         Please report any issues to linux.manager@diamond.ac.uk

Loading 64-bit Oracle instantclient, version 11.2
Loading 64-bit python, version 2.7.2
Loading 64-bit numpy, version 1.6.1
Starting Full Recon
Usage: full_recon.py [options] data output_directory

Options:
  -h, --help            show this help message and exit
  -m MACHINES, --machines=MACHINES
                        Number of machines to deploy to
  -b SLICE_BEGIN, --slice_begin=SLICE_BEGIN
                        Start Slice number
  -e SLICE_END, --slice_end=SLICE_END
                        End Slice Number
  -t TEMPLATE, --template=TEMPLATE
                        Template XML file
  -w WSAMP, --width_sample=WSAMP
                        Set the subsampling of the sinograms width
  -l LSAMP, --length_sample=LSAMP
                        Set the subsampling of the sinograms length
  -c CENTRE, --centre=CENTRE
                        Set the centre of rotation
  -r RUN_SLICES, --run_slices_loc=RUN_SLICES
                        set the run_slices.sh location
  -n, --new_cluster     use the new cluster
  -p, --preview         Run a preview reconstruction
  -a, --angles          Use angular information to reconstruct, do not use
                        with a ROI
  -o, --old_cluster     Use the old cluster
  --dark_file=DARK_FILE
                        Path to the file containing dark images
  --dark_path=DARK_PATH
                        path in the dark file to the data
  --flat_file=FLAT_FILE
                        Path to the file containing flat images
  --flat_path=FLAT_PATH
                        path in the dark file to the data
  --recon_range=RECON_RANGE
                        range for the reconstruction to be done over
  --d0f1                If option included (True), use 0's for dark- and 1's
                        for flat-field images
  --scan_id             If option included (True), incorporate the ID of the
                        input Nexus scan file into output filenames
~>
```

III.3 NxtomoLoader

```
>>> disp -avv

--------------------------------------------------------------------------------
 1) NxtomoLoader
  A class for loading standard tomography data in Nexus format.
    1)              preview : []
    A slice list of required frames.
    2)       image_key_path : entry1/tomo_entry/instrument/detector/image_key
    Path to the image key entry inside the nxs file.
    3)                 name : tomo
    The name assigned to the dataset.
    4)            3d_to_4d : False
    Set to true if this reshape is required.
    5)                 flat : [None, None, 1]
    Optional Path to the flat field data file, nxs path and scale value.
    6)            data_path : entry1/tomo_entry/data/data
    Path to the data inside the file.
    7)                 dark : [None, None, 1]
    Optional path to the dark field data file, nxs path and scale value.
    8)               angles : None
    A python statement to be evaluated or a file.
    9)         ignore_flats : None
    List of batch numbers of flats (start at 1) to ignore.
--------------------------------------------------------------------------------

>>>
```

III.4 Distortion correction

```
>>> disp -avv
--------------------------------------------------------------------------------
 1) DistortionCorrection
  A plugin to apply a distortion correction.
    1)           crop_edges : 0
    When applied to previewed/cropped data, the result may contain zeros around the
    edges, which can be removed by cropping the edges by a specified number of
    pixels.
    2)          in_datasets : []
    Create a list of the dataset(s) to process.
    3)       centre_from_top : 995.24
    The centre of distortion in pixels from the top of the image.
    4)          out_datasets : []
    Create a list of the dataset(s) to create.
    5)      polynomial_coeffs : (1.00015076, 1.9289e-06, -2.4325e-08, 1.00439e-11, -
3.99352e-15)
```

Parameters of the radial distortion function.
6) centre_from_left : 1283.25
The centre of distortion in pixels from the left of the image.

>>>

III.5 Dark-Flat-Field-Correction

Savu Configurator command: add DarkFlatFieldCorrection

>>> disp -avv

---
3) DarkFlatFieldCorrection
A Plugin to apply a simple dark and flatfield correction to raw timeseries data.
1) in_datasets : []
Create a list of the dataset(s) to process.
2) upper_bound : None
Set all values above the upper bound to this value.
3) out_datasets : []
Create a list of the dataset(s) to create.
4) lower_bound : None
Set all values below the lower_bound to this value.
5) pattern : PROJECTION
Data processing pattern is 'PROJECTION' or 'SINOGRAM'.
6) warn_proportion : 0.05
Output a warning if this proportion of values, or greater, are below and/or above the lower/upper bounds, e.g enter 0.05 for 5%.

III.6 Ring Artefact Filter

>>> disp -avv

---
1) CcpiRingArtefactFilter
A plugin to perform ring artefact removal
1) num_series : 1
High aspect ration compensation (for plate-like objects only) .
2) param_r : 0.005
The correction strength - decrease (typically in order of magnitude steps) to increase ring supression, or increase to reduce ring supression.
3) in_datasets : []
Create a list of the dataset(s) to process.
4) out_datasets : []

Create a list of the dataset(s) to create.
5) param_n : 0
Unknown description (for plate-like objects only).

III.7 AstraReconGpu

>>> disp -avv

---
8) AstraReconGpu
Wrapper around the Astra toolbox for gpu reconstruction.
1) init_vol : None
Dataset to use as volume initialiser (doesn't currently work with preview).
2) preview : []
A slice list of required frames.
3) log : True
Take the log of the data before reconstruction (True or False).
4) algorithm : FBP_CUDA
Reconstruction type (FBP_CUDA|SIRT_CUDA| SART_CUDA (not currently working)|CGLS_CUDA|FP_CUDA|BP_CUDA| SIRT3D_CUDA|CGLS3D_CUDA).
5) n_iterations : 1
Number of Iterations - only valid for iterative algorithms.
6) res_norm : False
Output the residual norm at each iteration (Error in the solution - iterative solvers only).
7) centre_of_rotation : 0.0
Centre of rotation to use for the reconstruction.
8) FBP_filter : ram-lak
The FBP reconstruction filter type (none|ram-lak| shepp-logan|cosine|hamming|hann|tukey|lanczos|triangular|gaussian| barlett-hann|blackman|nuttall|blackman-harris|blackman-nuttall| flat-top|kaiser|parzen).
9) in_datasets : []
Create a list of the dataset(s) to process.
10) ratio : 0.95
Ratio of the masks diameter in pixels to the smallest edge size along given axis.
11) out_datasets : []
Create a list of the dataset(s) to create.
12) centre_pad : False
Pad the sinogram to centre it in order to fill the reconstructed volume ROI for asthetic purposes. NB: Only available for selected algorithms and will be ignored otherwise. WARNING: This will significantly increase the size of the data and the time to compute the reconstruction).
13) outer_pad : False
Pad the sinogram width to fill the reconstructed volume for asthetic purposes. Choose from True (defaults to sqrt(2)), False or float <= 2.1. NB: Only available for selected algorithms and will be ignored otherwise. WARNING: This will increase the size of the data and the time to compute the reconstruction).
14) log_func : np.nan_to_num(-np.log(sino))

Override the default log function.
15) force_zero : [None, None]
Set any values in the reconstructed image outside of this range to zero.

III.8 Tiff saver

>>> disp 1 -avv

---
5) TiffSaver
A class to save data to a tiff output file
1) in_datasets : []
The name of the dataset to save.
2) pattern : optimum
Optimise data storage to this access pattern: 'optimum' will automate this process by choosing the output pattern from the previous plugin, if it exists, else the first pattern.

III.9 Paganin filter

>>> disp -avv

---
1) PaganinFilter
A plugin to apply the Paganin filter
1) Ratio : 250.0
ratio of delta/beta.
2) in_datasets : []
Create a list of the dataset(s) to process.
3) Distance : 1.0
Distance from sample to detection - Unit is metre.
4) Padtopbottom : 10
Pad to the top and bottom of projection.
5) out_datasets : []
Create a list of the dataset(s) to create.
6) Padmethod : edge
Numpy pad method.
7) Energy : 53.0
Given X-ray energy in keV.
8) increment : 1.0
Increment all values by this amount before taking the log.
9) Resolution : 1.28
Pixel size - Unit is micron.
10) Padleftright : 10
Pad to the left and right of projection.

Appendix IV: Copyright Licence Agreement

IV.1 Copyright Licence Agreement for figure 1.1

SPRINGER NATURE LICENSE TERMS AND CONDITIONS

Mar 04, 2019

This Agreement between Miss. L Paletto ("You") and Springer Nature ("Springer Nature") consists of your license details and the terms and conditions provided by Springer Nature and Copyright Clearance Center.

License Number	4541900895823
License date	Mar 04, 2019
Licensed Content Publisher	Springer Nature
Licensed Content Publication	Eye
Licensed Content Title	The structure of the lamina cribrosa of the human eye: An immunocytochemical and electron microscopical study
Licensed Content Author	A R Elkington, C B E Inman, P V Steart, R O Weller
Licensed Content Date	Jan 1, 1990
Licensed Content Volume	4
Licensed Content Issue	1
Type of Use	Thesis/Dissertation
Requestor type	academic/university or research institute
Format	print and electronic
Portion	figures/tables/illustrations
Number of figures/tables/illustrations	1
Will you be translating?	no
Circulation/distribution	<501
Author of this Springer Nature content	no
Title	Connective tissue micro- and nanostructure as an indicator for optic nerves at risk of glaucomatous optic neuropathy
Institution name	Cardiff University
Expected presentation date	May 2019
Portions	Figure 8
Requestor Location	Miss. L Paletto Maindy Road Cardiff, CF24 4HQ United Kingdom Attn: Miss. Laura Paletto
Billing Type	Invoice
Billing Address	Miss. Laura Paletto Maindy Road Cardiff, United Kingdom CF24 4HQ Attn: Miss. Laura Paletto
Total	0.00 GBP
Terms and Conditions	

IV.2 Copyright Licence Agreement for figure 1.2

Dear Laura Paletto,
thank you for your email. As to your request, I am pleased to inform you that permission is granted hereby to use **Figure 1** from the article
Thale A, Tillmann B, Rochels R: SEM Studies of the Collagen Architecture of the Human Lamina cribrosa: Normal and Pathological Findings. Ophthalmologica 1996;210:142-147. doi: 10.1159/00031069
in the **printed and electronic version of your doctoral dissertation,** provided that proper credit will be given to the original source and that S. Karger AG, Basel will be mentioned.
Please note that this is a non-exclusive permission, hence any further use, edition, translation or distribution, either in print or electronically, requires written permission again as this permission is valid for the above mentioned purpose only.
This permission applies only to copyrighted content that S. Karger AG owns, and not to copyrighted content from other sources. If any material in our work appears with credit to another source, you must also obtain permission from the original source cited in our work. All content reproduced from copyrighted material owned by S. Karger AG remains the sole and exclusive property of S. Karger AG. The right to grant permission to a third party is reserved solely by S. Karger AG.
Thank you for your understanding and cooperation.
Hopefully, I have been of assistance to you with the above.
Best regards,
Samuel Lei
Manager ePartners, Rights & Permissions
s.lei@karger.com
KARGER
S.KARGER AG, Medical and Scientific Publishers, Allschwilerstrasse 10, 4009 Basel Switzerland
T+41 61 306 11 11, f +41 61 306 1234, www.karger.com

IV.3 Copyright Licence Agreement for figure 1.3

ELSEVIER LICENSE
TERMS AND CONDITIONS

Feb 28, 2019

This Agreement between Miss. L Paletto ("You") and Elsevier ("Elsevier") consists of your license details and the terms and conditions provided by Elsevier and Copyright Clearance Center.

License Number	4537720317019
License date	Feb 28, 2019
Licensed Content Publisher	Elsevier
Licensed Content Publication	Journal of Voice
Licensed Content Title	Insights Into the Role of Collagen in Vocal Fold Health and Disease
Licensed Content Author	Sharon S. Tang,Vidisha Mohad,Madhu Gowda,Susan L. Thibeault
Licensed Content Date	Sep 1, 2017
Licensed Content Volume	31
Licensed Content Issue	5
Licensed Content Pages	8
Start Page	520
End Page	527
Type of Use	reuse in a thesis/dissertation
Portion	figures/tables/illustrations
Number of figures/tables/illustrations	1
Format	both print and electronic
Are you the author of this Elsevier article?	No
Will you be translating?	No
Original figure numbers	Figure 1
Title of your thesis/dissertation	Connective tissue micro- and nanostructure as an indicator for optic nerves at risk of glaucomatous optic neuropathy
Expected completion date	May 2019
Estimated size (number of pages)	280
Requestor Location	Miss. L Paletto Maindy Road Cardiff, CF24 4HQ United Kingdom Attn: Miss. Laura Paletto
Publisher Tax ID	GB 494 6272 12
Total	0.00 USD
Terms and Conditions	

INTRODUCTION

1. The publisher for this copyrighted material is Elsevier. By clicking "accept" in connection with completing this licensing transaction, you agree that the following terms and conditions apply to this transaction (along with the Billing and Payment terms and conditions

IV.4 Copyright Licence Agreement for figure 1.4

ELSEVIER LICENSE
TERMS AND CONDITIONS

Feb 28, 2019

This Agreement between Miss. L Paletto ("You") and Elsevier ("Elsevier") consists of your license details and the terms and conditions provided by Elsevier and Copyright Clearance Center.

License Number	4537720621237
License date	Feb 28, 2019
Licensed Content Publisher	Elsevier
Licensed Content Publication	Structure
Licensed Content Title	The In Situ Supermolecular Structure of Type I Collagen
Licensed Content Author	Joseph P.R.O Orgel,Andrew Miller,Thomas C Irving,Robert F Fischetti,Andrew P Hammersley,Tim J Wess
Licensed Content Date	Nov 1, 2001
Licensed Content Volume	9
Licensed Content Issue	11
Licensed Content Pages	9
Start Page	1061
End Page	1069
Type of Use	reuse in a thesis/dissertation
Intended publisher of new work	other
Portion	figures/tables/illustrations
Number of figures/tables/illustrations	1
Format	both print and electronic
Are you the author of this Elsevier article?	No
Will you be translating?	No
Original figure numbers	Figure 1
Title of your thesis/dissertation	Connective tissue micro- and nanostructure as an indicator for optic nerves at risk of glaucomatous optic neuropathy
Expected completion date	May 2019
Estimated size (number of pages)	280
Requestor Location	Miss. L Paletto Maindy Road Cardiff, CF24 4HQ United Kingdom Attn: Miss. Laura Paletto
Publisher Tax ID	GB 494 6272 12
Total	0.00 USD
Terms and Conditions	

INTRODUCTION

IV.5 Copyright Licence Agreement for figure 1.6

Hi Laura,

Thank you for the additional information. Permission is granted without charge.

The acknowledgement should state "reproduced/adapted with permission" and give the source journal name - the acknowledgement should either provide full citation details or refer to the relevant citation in the article reference list - the full citation details should include authors, journal, year, volume, issue and page citation.

Where appearing online or in other electronic media, a link should be provided to the original article (e.g. via DOI).

Journal of Cell Science: http://www.biologists.com/journal-of-cell-science

We wish you the best of luck with your thesis.

Kind regards

Richard

Richard Grove
Commercial Manager
The Company of Biologists Ltd
Bidder Building, Station Road, Histon, Cambridge, CB24 9LF, UK
T: +44 (0) 1223 632 850 | richard.grove@biologists.com | www.biologists.com

IV.6 Copyright Licence Agreement for figure 1.7

ELSEVIER LICENSE
TERMS AND CONDITIONS

Feb 27, 2019

This Agreement between Miss. L Paletto ("You") and Elsevier ("Elsevier") consists of your license details and the terms and conditions provided by Elsevier and Copyright Clearance Center.

License Number	4536980694129
License date	Feb 27, 2019
Licensed Content Publisher	Elsevier
Licensed Content Publication	The Lancet
Licensed Content Title	Glaucoma
Licensed Content Author	Harry A Quigley
Licensed Content Date	16–22 April 2011
Licensed Content Volume	377
Licensed Content Issue	9774
Licensed Content Pages	11
Start Page	1367
End Page	1377
Type of Use	reuse in a thesis/dissertation
Portion	figures/tables/illustrations
Number of figures/tables/illustrations	1
Format	both print and electronic
Are you the author of this Elsevier article?	No
Will you be translating?	No
Original figure numbers	Figure 1
Title of your thesis/dissertation	Connective tissue micro- and nanostructure as an indicator for optic nerves at risk of glaucomatous optic neuropathy
Expected completion date	May 2019
Estimated size (number of pages)	280
Requestor Location	Miss. Laura Paletto Maindy Road Cardiff, (State) CF24 4HQ United Kingdom Attn: Miss. Laura Paletto
Publisher Tax ID	GB 494 6272 12
Total	0.00 USD
Terms and Conditions	

INTRODUCTION

1. The publisher for this copyrighted material is Elsevier. By clicking "accept" in connection with completing this licensing transaction, you agree that the following terms and conditions apply to this transaction (along with the Billing and Payment terms and conditions

IV.7 Copyright Licence Agreement for figure 1.8

ELSEVIER LICENSE
TERMS AND CONDITIONS

Feb 27, 2019

This Agreement between Miss. L Paletto ("You") and Elsevier ("Elsevier") consists of your license details and the terms and conditions provided by Elsevier and Copyright Clearance Center.

License Number	4537000188674
License date	Feb 27, 2019
Licensed Content Publisher	Elsevier
Licensed Content Publication	Current Opinion in Pharmacology
Licensed Content Title	Altering the way the optic nerve head responds to intraocular pressure—a potential approach to glaucoma therapy
Licensed Content Author	Nicholas G Strouthidis,Michael JA Girard
Licensed Content Date	Feb 1, 2013
Licensed Content Volume	13
Licensed Content Issue	1
Licensed Content Pages	7
Start Page	83
End Page	89
Type of Use	reuse in a thesis/dissertation
Intended publisher of new work	other
Portion	figures/tables/illustrations
Number of figures/tables/illustrations	1
Format	both print and electronic
Are you the author of this Elsevier article?	No
Will you be translating?	No
Original figure numbers	Figure 1
Title of your thesis/dissertation	Connective tissue micro- and nanostructure as an indicator for optic nerves at risk of glaucomatous optic neuropathy
Expected completion date	May 2019
Estimated size (number of pages)	280
Requestor Location	Miss. Laura Paletto Maindy Road Cardiff, (State) CF24 4HQ United Kingdom Attn: Miss. Laura Paletto
Publisher Tax ID	GB 494 6272 12
Total	0.00 USD
Terms and Conditions	

INTRODUCTION

IV.8 Copyright Licence Agreement for figure 1.9

ELSEVIER LICENSE
TERMS AND CONDITIONS

Feb 27, 2019

This Agreement between Miss. L Paletto ("You") and Elsevier ("Elsevier") consists of your license details and the terms and conditions provided by Elsevier and Copyright Clearance Center.

License Number	4537010919340
License date	Feb 27, 2019
Licensed Content Publisher	Elsevier
Licensed Content Publication	Experimental Eye Research
Licensed Content Title	Optic nerve head biomechanics in aging and disease
Licensed Content Author	J. Crawford Downs
Licensed Content Date	Apr 1, 2015
Licensed Content Volume	133
Licensed Content Issue	n/a
Licensed Content Pages	11
Start Page	19
End Page	29
Type of Use	reuse in a thesis/dissertation
Intended publisher of new work	other
Portion	figures/tables/illustrations
Number of figures/tables/illustrations	1
Format	both print and electronic
Are you the author of this Elsevier article?	No
Will you be translating?	No
Original figure numbers	Figure 6
Title of your thesis/dissertation	Connective tissue micro- and nanostructure as an indicator for optic nerves at risk of glaucomatous optic neuropathy
Expected completion date	May 2019
Estimated size (number of pages)	280
Requestor Location	Miss. L Paletto Maindy Road Cardiff, CF24 4HQ United Kingdom Attn: Miss. Laura Paletto
Publisher Tax ID	GB 494 6272 12
Total	0.00 GBP
Terms and Conditions	

INTRODUCTION

IV.9 Copyright Licence Agreement for figure 1.10

SPRINGER NATURE

Title:	Pressure balance and imbalance in the optic nerve chamber: The Beijing Intracranial and Intraocular Pressure (iCOP) Study
Author:	Ruowu Hou, Zheng Zhang, Diya Yang et al
Publication:	Science China Life Sciences
Publisher:	Springer Nature
Date:	Jan 1, 2016

IV.10 Copyright Licence Agreement for figure 2.1

ELSEVIER LICENSE
TERMS AND CONDITIONS

May 22, 2019

This Agreement between Miss. L Paletto ("You") and Elsevier ("Elsevier") consists of your license details and the terms and conditions provided by Elsevier and Copyright Clearance Center.

License Number	4594120196599
License date	May 22, 2019
Licensed Content Publisher	Elsevier
Licensed Content Publication	Journal of Hepatology
Licensed Content Title	Fibrillar collagen scoring by second harmonic microscopy: A new tool in the assessment of liver fibrosis
Licensed Content Author	Luc Gailhouste,Yann Le Grand,Christophe Odin,Dominique Guyader,Bruno Turlin,Frédéric Ezan,Yoann Désille,Thomas Guilbert,Anne Bessard,Christophe Frémin,Nathalie Theret,Georges Baffet
Licensed Content Date	Mar 1, 2010
Licensed Content Volume	52
Licensed Content Issue	3
Licensed Content Pages	9
Start Page	398
End Page	406
Type of Use	reuse in a thesis/dissertation
Portion	figures/tables/illustrations
Number of figures/tables/illustrations	1
Format	both print and electronic
Are you the author of this Elsevier article?	No
Will you be translating?	No
Original figure numbers	Figure 1A
Title of your thesis/dissertation	Connective tissue micro- and nanostructure as an indicator for optic nerves at risk of glaucomatous optic neuropathy
Publisher of new work	Cardiff University
Expected completion date	May 2019
Estimated size (number of pages)	280
Requestor Location	Miss. L Paletto Maindy Road Cardiff, CF24 4HQ United Kingdom Attn: Miss. Laura Paletto
Publisher Tax ID	GB 494 6272 12
Total	0.00 GBP
Terms and Conditions	

IV.11 Copyright Licence Agreement for figure 5.1

ELSEVIER LICENSE
TERMS AND CONDITIONS

Apr 08, 2019

This Agreement between Miss. L Paletto ("You") and Elsevier ("Elsevier") consists of your license details and the terms and conditions provided by Elsevier and Copyright Clearance Center.

License Number	4564231084680
License date	Apr 08, 2019
Licensed Content Publisher	Elsevier
Licensed Content Publication	Experimental Eye Research
Licensed Content Title	From nano to macro: Studying the hierarchical structure of the corneal extracellular matrix
Licensed Content Author	Andrew J. Quantock,Moritz Winkler,Geraint J. Parfitt,Robert D. Young,Donald J. Brown,Craig Boote,James V. Jester
Licensed Content Date	Apr 1, 2015
Licensed Content Volume	133
Licensed Content Issue	n/a
Licensed Content Pages	19
Start Page	81
End Page	99
Type of Use	reuse in a thesis/dissertation
Portion	figures/tables/illustrations
Number of figures/tables/illustrations	1
Format	both print and electronic
Are you the author of this Elsevier article?	No
Will you be translating?	No
Original figure numbers	Figure 1
Title of your thesis/dissertation	Connective tissue micro- and nanostructure as an indicator for optic nerves at risk of glaucomatous optic neuropathy
Publisher of new work	Cardiff University
Expected completion date	May 2019
Estimated size (number of pages)	280
Requestor Location	Miss. L Paletto Maindy Road Cardiff, CF24 4HQ United Kingdom Attn: Miss. Laura Paletto
Publisher Tax ID	GB 494 6272 12
Total	0.00 EUR
Terms and Conditions	

INTRODUCTION

IV.12 Copyright Licence Agreement for figure 5.2

JOHN WILEY AND SONS LICENSE TERMS AND CONDITIONS

Mar 22, 2019

This Agreement between Miss. L Paletto ("You") and John Wiley and Sons ("John Wiley and Sons") consists of your license details and the terms and conditions provided by John Wiley and Sons and Copyright Clearance Center.

License Number	4554191230000
License date	Mar 22, 2019
Licensed Content Publisher	John Wiley and Sons
Licensed Content Publication	Scandinavian Journal of Medicine & Science In Sports
Licensed Content Title	Structure of the tendon connective tissue
Licensed Content Author	P. Kannus
Licensed Content Date	Jul 7, 2008
Licensed Content Volume	10
Licensed Content Issue	6
Licensed Content Pages	9
Type of use	Dissertation/Thesis
Requestor type	University/Academic
Format	Print and electronic
Portion	Figure/table
Number of figures/tables	1
Original Wiley figure/table number(s)	Figure 1
Will you be translating?	No
Title of your thesis / dissertation	Connective tissue micro- and nanostructure as an indicator for optic nerves at risk of glaucomatous optic neuropathy
Expected completion date	May 2019
Expected size (number of pages)	280
Requestor Location	Miss. L Paletto Maindy Road Cardiff, CF24 4HQ United Kingdom Attn: Miss. Laura Paletto
Publisher Tax ID	EU826007151
Total	0.00 GBP
Terms and Conditions	

TERMS AND CONDITIONS

This copyrighted material is owned by or exclusively licensed to John Wiley & Sons, Inc. or one of its group companies (each a"Wiley Company") or handled on behalf of a society with which a Wiley Company has exclusive publishing rights in relation to a particular work (collectively "WILEY"). By clicking "accept" in connection with completing this licensing transaction, you agree that the following terms and conditions apply to this transaction (along with the billing and payment terms and conditions established by the Copyright Clearance Center Inc., ("CCC's Billing and Payment terms and conditions"), at the time that

IV.13 Copyright Licence Agreement for figure 5.33

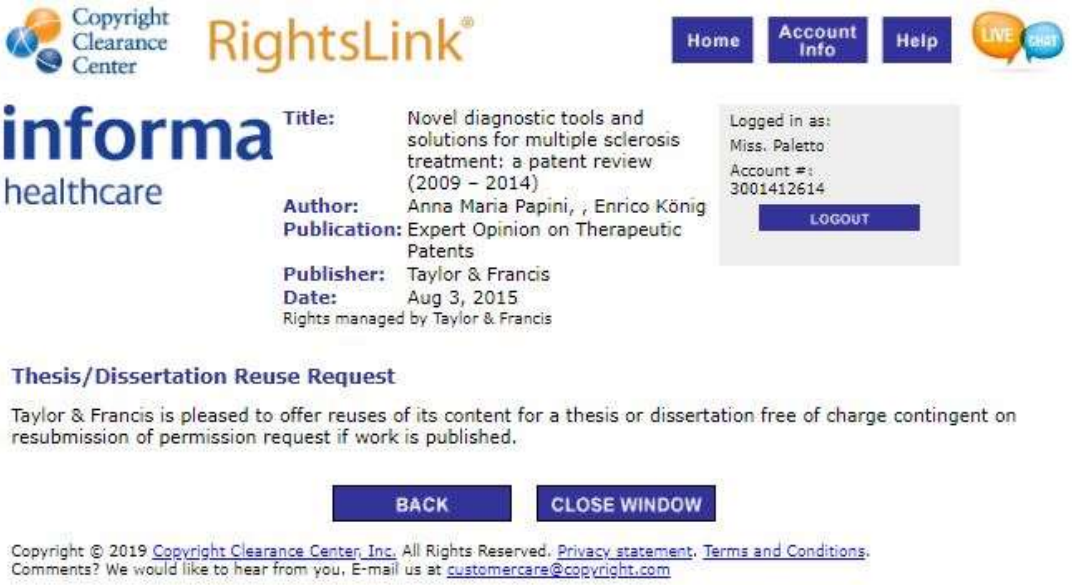

IV.14 Copyright Licence Agreement for figure 6.1

Dear Laura Paletto,
We will be pleased to grant you the permission of reproducing Fig 2 from the below journal article in your thesis, provided that full credit been given to the original source in the following format:
Viscoelasticity of amyloid plaques in transgenic mouse brain studied by Brillouin microspectroscopy and correlative Raman analysis.
Sara Mattana, Silvia Caponi, Francesco Tamagnini, Daniele Fioretto, and Francesca Palombo
Published online 2017 Apr 21. doi: 10.1142/S1793545817420019
Title of the Work, Author (s) and/or Editor(s) Name (s), Title of the Journal, Vol and Issue No., Copyright @ year and name of the publisher
Kind regards,
Tu Ning

References

Abass, A., Bell, J. S., Spang, M. T., Hayes, S., Meek, K. M. & Boote, C. 2017. Saxs4coll: An Integrated Software Tool For Analysing Fibrous Collagen-Based Tissues. Journal Of Applied Crystallography, 50, 1235-1240.

Afzelius, B. A. 1992. Section Staining For Electron Microscopy Using Tannic Acid As A Mordant: A Simple Method For Visualization Of Glycogen And Collagen. Microscopy Research And Technique, 21, 65-72.

Agapova, O. A., Kaufman, P. L., Lucarelli, M. J., B'ann, T. G. & Hernandez, M. 2003. Differential Expression Of Matrix Metalloproteinases In Monkey Eyes With Experimental Glaucoma Or Optic Nerve Transection. Brain Research, 967, 132-143.

Akagi, T., Hangai, M., Takayama, K., Nonaka, A., Ooto, S. & Yoshimura, N. 2012. In Vivo Imaging Of Lamina Cribrosa Pores By Adaptive Optics Scanning Laser Ophthalmoscopy. Investigative Ophthalmology & Visual Science, 53, 4111-4119.

Albon, J., Karwatowski, W. S., Avery, N., Easty, D. L. & Duance, V. C. 1995. Changes In The Collagenous Matrix Of The Aging Human Lamina Cribrosa. Br J Ophthalmol, 79, 368-75.

Albon, J., Purslow, P. P., Karwatowski, W. S. & Easty, D. L. 2000b. Age Related Compliance Of The Lamina Cribrosa In Human Eyes. British Journal Of Ophthalmology, 84, 318-323.

Aldred, M. A., Baumber, L., Hill, A., Schwalbe, E. C., Goh, K., Karwatowski, W. & Trembath, R. C. 2004. Low Prevalence Of Myoc Mutations In Uk Primary Open-Angle Glaucoma Patients Limits The Utility Of Genetic Testing. Hum Genet, 115, 428-31.

Ali, L., Green, E., Ellis, R., Bradley, D., Grossmann, J. & Winlove, C. 2004. Study Of The Molecular And Supramolecular Organisation Of Elastic Tissue By X-Ray Diffraction. Radiation Physics And Chemistry, 71, 951-952.

Alkrad, J. A., Mrestani, Y., Stroehl, D., Wartewig, S. & Neubert, R. 2003. Characterization Of Enzymatically Digested Hyaluronic Acid Using Nmr, Raman, Ir, And Uv-Vis Spectroscopies. J Pharm Biomed Anal, 31, 545-50.

Allingham, R. R., De Kater, A. W., Ethier, C. R., Anderson, P. J., Hertzmark, E. & Epstein, D. L. 1992. The Relationship Between Pore Density And Outflow Facility In Human Eyes. Invest Ophthalmol Vis Sci, 33, 1661-9.

Alvarado, J., Murphy, C. & Juster, R. 1984. Trabecular Meshwork Cellularity In Primary Open-Angle Glaucoma And Nonglaucomatous Normals. Ophthalmology, 91, 564-79.

Alward, W. L., Fingert, J. H., Coote, M. A., Johnson, A. T., Lerner, S. F., Junqua, D., Durcan, F. J., Mccartney, P. J., Mackey, D. A., Sheffield, V. C. & Stone, E. M. 1998. Clinical Features Associated With Mutations In The Chromosome 1 Open-Angle Glaucoma Gene (Glc1a). N Engl J Med, 338, 1022-7.

Amano, S., Kaji, Y., Oshika, T., Oka, T., Machinami, R., Nagai, R. & Horiuchi, S. 2001. Advanced Glycation End Products In Human Optic Nerve Head. The British Journal Of Ophthalmology, 85, 52-55.

Anderson, D. R. & Hendrickson, A. 1974. Effect Of Intraocular Pressure On Rapid Axoplasmic Transport In Monkey Optic Nerve. Invest Ophthalmol, 13, 771-83.

Anderson, D. R. 1969. Ultrastructure Of Human And Monkey Lamina Cribrosa And Optic Nerve Head. Arch Ophthalmol, 82, 800-14.

Anderson, D. R. 1973. Fine Structure And Function Of Ocular Tissues. The Optic Nerve. Int Ophthalmol Clin, 13, 229-42.

Anderson, D. R. 1989. Glaucoma: The Damage Caused By Pressure. Xlvi Edward Jackson Memorial Lecture. Am J Ophthalmol, 108, 485-95.

Antonacci, G. & Braakman, S. 2016. Biomechanics Of Subcellular Structures By Non-Invasive Brillouin Microscopy. Scientific Reports, 6, 37217.

Antonacci, G., Pedrigi, R. M., Kondiboyina, A., Mehta, V. V., De Silva, R., Paterson, C., Krams, R. & Török, P. 2015. Quantification Of Plaque Stiffness By Brillouin Microscopy In Experimental Thin Cap Fibroatheroma. Journal Of The Royal Society Interface, 12.

Armaly, M. F. & Sayegh, R. E. 1969. The Cup/Disc Ratio: The Findings Of Tonometry And Tonography In The Normal Eye. Archives Of Ophthalmology, 82, 191-196.

Atha, D. H., Gaigalas, A. K. & Reipa, V. 1996. Structural Analysis Of Heparin By Raman Spectroscopy. J Pharm Sci, 85, 52-6.

Atwood, R. C., Bodey, A. J., Price, S. W., Basham, M. & Drakopoulos, M. 2015. A High-Throughput System For High-Quality Tomographic Reconstruction Of Large Datasets At Diamond Light Source. Philos Trans A Math Phys Eng Sci, 373.

Aubin, J. E. 1979. Autofluorescence Of Viable Cultured Mammalian Cells. J Histochem Cytochem, 27, 36-43.

Bailey, A. J. 2001. Molecular Mechanisms Of Ageing In Connective Tissues. Mech Ageing Dev, 122, 735-55.

Baldock, C., Oberhauser, A. F., Ma, L., Lammie, D., Siegler, V., Mithieux, S. M., Tu, Y., Chow, J. Y. H., Suleman, F., Malfois, M., Rogers, S., Guo, L., Irving, T. C., Wess, T. J. & Weiss, A. S. 2011. Shape Of Tropoelastin, The Highly Extensible Protein That Controls Human Tissue Elasticity. Proceedings Of The National Academy Of Sciences, 108, 4322-4327.

Balu, M., Zachary, C. B., Harris, R. M., Krasieva, T. B., Konig, K., Tromberg, B. J. & Kelly, K. M. 2015. In Vivo Multiphoton Microscopy Of Basal Cell Carcinoma. Jama Dermatol, 151, 1068-74.

Bansil, R., Yannas, I. V. & Stanley, H. E. 1978. Raman Spectroscopy: A Structural Probe Of Glycosaminoglycans. Biochim Biophys Acta, 541, 535-42.

Basham, M., Filik, J., Wharmby, M. T., Chang, P. C. Y., El Kassaby, B., Gerring, M., Aishima, J., Levik, K., Pulford, B. C. A., Sikharulidze, I., Sneddon, D., Webber, M., Dhesi, S. S., Maccherozzi, F., Svensson, O., Brockhauser, S., Náray, G. & Ashton, A. W. 2015. Data Analysis Workbench (Dawn). Journal Of Synchrotron Radiation, 22, 853-858.

Baydanoff, S., Konova, E. & Ivanova, N. 1996. Determination Of Anti-Age Antibodies In Human Serum. Glycoconj J, 13, 335-9.

Baydanoff, S., Konova, E., Dosheva, I. & Dorovski, P. 1994. Non-Enzymatic Glycation Of Elastin. Glycosylation & Disease, 1, 53-58.

Belkoff, S. M. & Haut, R. C. 1991. A Structural Model Used To Evaluate The Changing Microstructure Of Maturing Rat Skin. J Biomech, 24, 711-20.

Bell, J. S., Hayes, S., Whitford, C., Sanchez-Weatherby, J., Shebanova, O., Vergari, C., Winlove, C. P., Terrill, N., Sorensen, T., Elsheikh, A. & Meek, K. M. 2018. The Hierarchical Response Of Human Corneal Collagen To Load. Acta Biomaterialia, 65, 216-225.

Bellezza, A. J., Hart, R. T. & Burgoyne, C. F. 2000. The Optic Nerve Head As A Biomechanical Structure: Initial Finite Element Modeling. Investigative Ophthalmology & Visual Science, 41, 2991-3000.

Bellezza, A. J., Rintalan, C. J., Thompson, H. W., Downs, J. C., Hart, R. T. & Burgoyne, C. F. 2003a. Anterior Scleral Canal Geometry In Pressurised (Iop 10) And Non-Pressurised (Iop 0) Normal Monkey Eyes. British Journal Of Ophthalmology, 87, 1284-1290.

Bellezza, A. J., Rintalan, C. J., Thompson, H. W., Downs, J. C., Hart, R. T. & Burgoyne, C. F. 2003b. Deformation Of The Lamina Cribrosa And Anterior Scleral Canal Wall In Early Experimental Glaucoma. Investigative Ophthalmology & Visual Science, 44, 623-637.

Bellezza, A. J., Rintalan, C. J., Thompson, H. W., Downs, J. C., Hart, R. T. & Burgoyne, C. F. 2003. Anterior Scleral Canal Geometry In Pressurised (Iop 10) And Non-Pressurised (Iop 0) Normal Monkey Eyes. British Journal Of Ophthalmology, 87, 1284-1290.

Ben Geren, B. 1954. The Formation From The Schwann Cell Surface Of Myelin In The Peripheral Nerves Of Chick Embryos. Exp Cell Res, 7, 558-62.

Benson, R., Meyer, R., Zaruba, M. & Mckhann, G. 1979. Cellular Autofluorescence--Is It Due To Flavins? Journal Of Histochemistry & Cytochemistry, 27, 44-48.

Beotra, M. R., Wang, X., Tun, T. A., Zhang, L., Baskaran, M., Aung, T., Strouthidis, N. G. & Girard, M. J. A. 2018. In Vivo Three-Dimensional Lamina Cribrosa Strains In Healthy, Ocular Hypertensive, And Glaucoma Eyes Following Acute Intraocular Pressure Elevation. Invest Ophthalmol Vis Sci, 59, 260-272.

Berdahl, J. P., Allingham, R. R. & Johnson, D. H. 2008. Cerebrospinal Fluid Pressure Is Decreased In Primary Open-Angle Glaucoma. Ophthalmology, 115, 763-8.

Besner, S., Scarcelli, G., Pineda, R. & Yun, S. H. 2016. In Vivo Brillouin Analysis Of The Aging Crystalline Lens. Invest Ophthalmol Vis Sci, 57, 5093-5100.

Bigi, A., Ripamonti, A., Roveri, N., Jeronimidis, G. & Purslow, P. 1981. Collagen Orientation By X-Ray Pole Figures And Mechanical Properties Of Media Carotid Wall.

Birk, D. E. 2001. Type V Collagen: Heterotypic Type I/V Collagen Interactions In The Regulation Of Fibril Assembly. Micron, 32, 223-37.

Blaurock, A. E. 1981. The Spaces Between Membrane Bilayers Within Pns Myelin As Characterized By X-Ray Diffraction. Brain Research, 210, 383-387.

Blomfield, J. & Farrar, J. F. 1969. The Fluorescent Properties Of Maturing Arterial Elastin. Cardiovasc Res, 3, 161-70.

Blum A. 2915. Stress, strain, signaling, and adaptation-not just a matter of definition. 2016 Feb;67(3):562-5. doi: 10.1093/jxb/erv497. J Exp Bot.Epub

Boote, C., Dennis, S., Newton, R. H., Puri, H. & Meek, K. M. 2003. Collagen Fibrils Appear More Closely Packed In The Prepupillary Cornea: Optical And Biomechanical Implications. Investigative Ophthalmology & Visual Science, 44, 2941-2948.

Boote, C., Dooley, E. P., Gardner, S. J., Kamma-Lorger, C. S., Hayes, S., Nielsen, K., Hjortdal, J., Sorensen, T., Terrill, N. J. & Meek, K. M. 2013. Quantification Of Collagen Ultrastructure After Penetrating Keratoplasty - Implications For Corneal Biomechanics. Plos One, 8, E68166.

Borcherding, M. S., Blacik, L. J., Sittig, R. A., Bizzell, J. W., Breen, M. & Weinstein, H. G. 1975. Proteoglycans And Collagen Fibre Organization In Human Corneoscleral Tissue. Exp Eye Res, 21, 59-70.

Borel, J. P. 1991. [Uterine Collagens. General Review]. Rev Fr Gynecol Obstet, 86, 715-22.

Boucek, R. J., Noble, N. L. & Gunja-Smith, Z. 1979. A Possible Role For Dehydrodihydroxylysinonorleucine In Collagen Fibre And Bundle Formation. The Biochemical Journal, 177, 853-860.

Boulton, M. & Marshall, J. 1985. Repigmentation Of Human Retinal Pigment Epithelial Cells In Vitro. Exp Eye Res, 41, 209-18.

Bourne RR. 2012. The optic nerve head in glaucoma. Community Eye Health 25(79-80): 55–57.

Bramley, T., Peeples, P., Walt, J. G., Juhasz, M. & Hansen, J. E. 2008. Impact Of Vision Loss On Costs And Outcomes In Medicare Beneficiaries With Glaucoma. Arch Ophthalmol, 126, 849-56.

Braverman, I. M. & Fonferko, E. 1982. Studies In Cutaneous Aging: I. The Elastic Fiber Network. J Invest Dermatol, 78, 434-43.

Braverman, I. M. 1989. Elastic Fiber And Microvascular Abnormalities In Aging Skin. Clin Geriatr Med, 5, 69-90.

Brillouin, L. 1922. Diffusion De La Lumière Et Des Rayons X Par Un Corps Transparent Homogène. Ann. Phys., 9, 88-122.

Brodsky, B., Eikenberry, E. F. & Cassidy, K. 1980. An Unusual Collagen Periodicity In Skin. Biochim Biophys Acta, 621, 162-6.

Broman, A. T., Quigley, H. A., West, S. K., Katz, J., Munoz, B., Bandeen-Roche, K., Tielsch, J. M., Friedman, D. S., Crowston, J., Taylor, H. R., Varma, R., Leske, M. C., Bengtsson, B., Heijl, A., He, M. & Foster, P. J. 2008. Estimating The Rate Of Progressive Visual Field Damage In Those With Open-Angle Glaucoma, From Cross-Sectional Data. Invest Ophthalmol Vis Sci, 49, 66-76.

Brown Jr, R. M., Millard, A. C. & Campagnola, P. J. 2003. Macromolecular Structure Of Cellulose Studied By Second-Harmonic Generation Imaging Microscopy. Optics Letters, 28, 2207-2209.

Brown, D. J., Morishige, N., Neekhra, A., Minckler, D. S. & Jester, J. V. 2007. Application Of Second Harmonic Imaging Microscopy To Assess Structural Changes In Optic Nerve Head Structure Ex Vivo. Journal Of Biomedical Optics, 12, 024029-024029-5.

Bruel, A. & Oxlund, H. 1996. Changes In Biomechanical Properties, Composition Of Collagen And Elastin, And Advanced Glycation Endproducts Of The Rat Aorta In Relation To Age. Atherosclerosis, 127, 155-65.

Burgoyne, C. F. 2011. A Biomechanical Paradigm For Axonal Insult Within The Optic Nerve Head In Aging And Glaucoma. Exp Eye Res, 93, 120-32.

Burgoyne, C. F., Crawford Downs, J., Bellezza, A. J., Francis Suh, J. K. & Hart, R. T. 2005a. The Optic Nerve Head As A Biomechanical Structure: A New Paradigm For Understanding The Role Of Iop-Related Stress And Strain In The Pathophysiology Of Glaucomatous Optic Nerve Head Damage. Progress In Retinal And Eye Research, 24, 39-73.

Burgoyne, C. F., Downs, J. C., Bellezza, A. J., Suh, J. K. & Hart, R. T. 2005b. The Optic Nerve Head As A Biomechanical Structure: A New Paradigm For Understanding The Role Of Iop-Related Stress And Strain In The Pathophysiology Of Glaucomatous Optic Nerve Head Damage. Prog Retin Eye Res, 24, 39-73.

Burgoyne, C. F., Quigley, H. A., Thompson, H. W., Vitale, S. & Varma, R. 1995. Early Changes In Optic Disc Compliance And Surface Position In Experimental Glaucoma. Ophthalmology, 102, 1800-9.

Campbell, I. C., Coudrillier, B., Mensah, J., Abel, R. L. & Ethier, C. R. 2015. Automated Segmentation Of The Lamina Cribrosa Using Frangi's Filter: A Novel Approach For Rapid Identification Of Tissue Volume Fraction And Beam
Orientation In A Trabeculated Structure In The Eye. J R Soc Interface, 12, 20141009.

Caparas, V. L., Cintron, C. & Hernandez-Neufeld, M. R. 1991. Immunohistochemistry Of Proteoglycans In Human Lamina Cribrosa. Am J Ophthalmol, 112, 489-95.

Caponi, S., Liguori, L., Giugliarelli, A., Mattarelli, M., Morresi, A., Sassi, P., Urbanelli, L. & Musio, C. 2013. Raman Micro-Spectroscopy: A Powerful Tool For The Monitoring Of Dynamic Supramolecular Changes In Living Cells. Biophysical Chemistry, 182, 58-63.

Caprioli, J., Sears, M. & Miller, J. M. 1987. Patterns Of Early Visual Field Loss In Open-Angle Glaucoma. Am J Ophthalmol, 103, 512-7.

Cattell, M. A., Hasleton, P. S. & Anderson, J. C. 1993. Increased Elastin Content And Decreased Elastin Concentration May Be Predisposing Factors In Dissecting Aneurysms Of Human Thoracic Aorta. Cardiovascular Research, 27, 176-181.

Chandross, R. J., Bear, R. S. & Montgomery, R. L. 1978. An X-Ray Diffraction Comparison Of Myelins From The Human Nervous System. Journal Of Comparative Neurology, 177, 1-9.

Chen, G., Chen, J., Zhuo, S., Xiong, S., Zeng, H., Jiang, X., Chen, R. & Xie, S. 2009. Nonlinear Spectral Imaging Of Human Hypertrophic Scar Based On Two-Photon Excited Fluorescence And Second-Harmonic Generation. Br J Dermatol, 161, 48-55.

Chen, V. L., Fleischmajer, R., Schwartz, E., Palaia, M. & Timpl, R. 1986. Immunochemistry Of Elastotic Material In Sun-Damaged Skin. J Invest Dermatol, 87, 334-7.

Cheng, W. T., Liu, M. T., Liu, H. N. & Lin, S. Y. 2005. Micro-Raman Spectroscopy Used To Identify And Grade Human Skin Pilomatrixoma. Microsc Res Tech, 68, 75-9.

Chia, L., Thompson, J. & Moscarello, M. 1983. Changes In Lipid Phase Behaviour In Human Myelin During Maturation And Aging. Febs Letters, 157, 155-158.
Cintron, C., Schneider, H. & Kublin, C. 1973. Corneal Scar Formation. Exp Eye Res, 17, 251-9.

Clayson, K., Pan, X., Pavlatos, E., Short, R., Morris, H., Hart, R. T. & Liu, J. 2017. Corneoscleral Stiffening Increases Iop Spike Magnitudes During Rapid Microvolumetric Change In The Eye. Experimental Eye Research, 165, 29-34.

Coleman, A. L. & Miglior, S. 2008. Risk Factors For Glaucoma Onset And Progression. Surv Ophthalmol, 53 Suppl1, S3-10.

Comninou, M. & Yannas, I. V. 1976. Dependence Of Stress-Strain Nonlinearity Of Connective Tissues On The Geometry Of Collagen Fibres. Journal Of Biomechanics, 9, 427-433.

Connizzo, B. K., Sarver, J. J., Birk, D. E., Soslowsky, L. J. & Iozzo, R. V. 2013a. Effect Of Age And Proteoglycan Deficiency On Collagen Fiber Re-Alignment And Mechanical Properties In Mouse Supraspinatus Tendon. J Biomech Eng, 135, 021019.

Connizzo, B. K., Yannascoli, S. M. & Soslowsky, L. J. 2013b. Structure-Function Relationships Of Postnatal Tendon Development: A Parallel To Healing. Matrix Biol, 32, 106-16.

Coudrillier, B., Campbell, I. C., Read, A. T., Geraldes, D. M., Vo, N. T., Feola, A., Mulvihill, J., Albon, J., Abel, R. L. & Ethier, C. R. 2016. Effects Of Peripapillary Scleral Stiffening On The Deformation Of The Lamina Cribrosa. Investigative Ophthalmology & Visual Science, 57, 2666-2677.

Coudrillier, B., Geraldes, D. M., Vo, N. T., Atwood, R., Reinhard, C., Campbell, I. C., Raji, Y., Albon, J., Abel, R. L. & Ethier, C. R. 2016. Phase-Contrast Micro-Computed Tomography Measurements Of The Intraocular Pressure-Induced Deformation Of The Porcine Lamina Cribrosa. Ieee Trans Med Imaging, 35, 988-99.

Coudrillier, B., Pijanka, J., Jefferys, J., Sorensen, T., Quigley, H. A., Boote, C. & Nguyen, T. D. 2015. Collagen Structure And Mechanical Properties Of The Human Sclera: Analysis For The Effects Of Age. J Biomech Eng, 137, 041006.

Coudrillier, B., Tian, J., Alexander, S., Myers, K. M., Quigley, H. A. & Nguyen, T. D. 2012. Biomechanics Of The Human Posterior Sclera: Age- And Glaucoma-Related Changes Measured Using Inflation Testing. Invest Ophthalmol Vis Sci, 53, 1714-28.

Cox, P. G. & Jeffery, N. 2011. Reviewing The Morphology Of The Jaw-Closing Musculature In Squirrels, Rats, And Guinea Pigs With Contrast-Enhanced Microct. Anat Rec (Hoboken), 294, 915-28.

Cubeddu, R., Taroni, P., Hu, D. N., Sakai, N., Nakanishi, K. & Roberts, J. E. 1999. Photophysical Studies Of A2-E, Putative Precursor Of Lipofuscin, In Human Retinal Pigment Epithelial Cells. Photochem Photobiol, 70, 172-5.

Culav, E. M., Clark, C. H. & Merrilees, M. J. 1999. Connective Tissues: Matrix Composition And Its Relevance To Physical Therapy. Phys Ther, 79, 308-19.

Czamara, K., Majzner, K., Pacia, M. Z., Kochan, K., Kaczor, A. & Baranska, M. 2015. Raman Spectroscopy Of Lipids: A Review. Journal Of Raman Spectroscopy, 46, 4-20.
Damiano, V. V., Tsang, A., Christner, P., Rosenbloom, J. & Weinbaum, G. 1979. Immunologic Localization Of Elastin By Electron Microscopy. The American Journal Of Pathology, 96, 439-456.

Danford, F. L., Yan, D., Dreier, R. A., Cahir, T. M., Girkin, C. A. & Vande Geest, J. P. 2013. Differences In The Region- And Depth-Dependent Microstructural Organization In Normal Versus Glaucomatous Human Posterior Sclerae. Invest Ophthalmol Vis Sci, 54, 7922-32.

Davis, E. C. 1993a. Endothelial Cell Connecting Filaments Anchor Endothelial Cells To The Subjacent Elastic Lamina In The Developing Aortic Intima Of The Mouse. Cell Tissue Res, 272, 211-9.

Davis, E. C. 1993b. Smooth Muscle Cell To Elastic Lamina Connections In Developing Mouse Aorta. Role In Aortic Medial Organization. Lab Invest, 68, 89-99.

Dawson, D. G., Edelhauser, H. F. & Grossniklaus, H. E. 2005. Long-Term Histopathologic Findings In Human Corneal Wounds After Refractive Surgical Procedures. Am J Ophthalmol, 139, 168-78.

Day, J. C. & Stone, N. 2013. A Subcutaneous Raman Needle Probe. Appl Spectrosc, 67, 349-54.
Day, J., Bennett, R., Smith, B., Kendall, C., Hutchings, J., Meaden, G., Born, C., Yu, S. & Stone, N. 2009. A Miniature Confocal Raman Probe For Endoscopic Use. Physics In Medicine & Biology, 54, 7077.

De Campos Vidal, B. & Mello, M. L. S. 2011. Collagen Type I Amide I Band Infrared Spectroscopy. Micron, 42, 283-289.

De Castro Jp, F., Mullins, R., Manea, A. M., Hernandez, J., Wallen, T. & Kuehn, M. H. 2013. Lipofuscin In Human Glaucomatous Optic Nerves. Exp Eye Res, 111.

Degenhardt, K., Wright, A. C., Horng, D., Padmanabhan, A. & Epstein, J. A. 2010. Rapid 3d Phenotyping Of Cardiovascular Development In Mouse Embryos By Micro-Ct With Iodine Staining. Circ Cardiovasc Imaging, 3, 314-22.

Delori, F. C., Goger, D. G. & Dorey, C. K. 2001. Age-Related Accumulation And Spatial Distribution Of Lipofuscin In Rpe Of Normal Subjects. Invest Ophthalmol Vis Sci, 42, 1855-66.

Descamps, E., Sochacka, A., De Kegel, B., Van Loo, D., Van Hoorebeke, L. & Adriaens, D. 2014. Soft Tissue Discrimination With Contrast Agents Using Micro-Ct Scanning. Belgian Journal Of Zoology, 144.

Deyl, Z., Macek, K., Adam, M. & Vancikova, O. 1980. Studies On The Chemical Nature Of Elastin Fluorescence. Biochim Biophys Acta, 625, 248-54.

Diamant, J., Keller, A., Baer, E., Litt, M. & Arridge, R. G. 1972. Collagen; Ultrastructure And Its Relation To Mechanical Properties As A Function Of Ageing. Proc R Soc Lond B Biol Sci, 180, 293-315.

Dimitrow, E., Ziemer, M., Koehler, M. J., Norgauer, J., Konig, K., Elsner, P. & Kaatz, M. 2009. Sensitivity And Specificity Of Multiphoton Laser Tomography For In Vivo And Ex Vivo Diagnosis Of Malignant Melanoma. J Invest Dermatol, 129, 1752-8.

Disney, C. M., Madi, K., Bodey, A. J., Lee, P. D., Hoyland, J. A. & Sherratt, M. J. 2017. Visualising The 3d Microstructure Of Stained And Native Intervertebral Discs Using X-Ray Microtomography. Scientific Reports, 7, 16279.

Dolman, C. L., Mccormick, A. Q. & Drance, S. M. 1980. Aging Of The Optic Nerve. Archives Of Ophthalmology, 98, 2053-2058.

Dourte, L. M., Pathmanathan, L., Jawad, A. F., Iozzo, R. V., Mienaltowski, M. J., Birk, D. E. & Soslowsky, L. J. 2012. Influence Of Decorin On The Mechanical, Compositional, And Structural Properties Of The Mouse Patellar Tendon. J Biomech Eng, 134, 031005.

Dourte, L. M., Pathmanathan, L., Jawad, A. F., Iozzo, R. V., Mienaltowski, M. J., Birk, D. E. & Soslowsky, L. J. 2012. Influence Of Decorin On The Mechanical, Compositional, And Structural Properties Of The Mouse Patellar Tendon. J Biomech Eng, 134, 031005.

Downs, J. C. & Girkin, C. A. 2017. Lamina Cribrosa In Glaucoma. Current Opinion In Ophthalmology, 28, 113-119.

Downs, J. C. 2015. Optic Nerve Head Biomechanics In Aging And Disease. Exp Eye Res, 133, 19-29.

Downs, J. C., Roberts, M. D. & Burgoyne, C. F. 2008. Mechanical Environment Of The Optic Nerve Head In Glaucoma. Optom Vis Sci, 85, 425-35.

Downs, J. C., Yang, H., Girkin, C., Sakata, L., Bellezza, A., Thompson, H. & Burgoyne, C. F. 2007. Three-Dimensional Histomorphometry Of The Normal And Early Glaucomatous Monkey Optic Nerve Head: Neural Canal And Subarachnoid Space Architecture. Invest Ophthalmol Vis Sci, 48, 3195-208.

Duenwald, S. E., Vanderby, R., Jr. & Lakes, R. S. 2010. Stress Relaxation And Recovery In Tendon And Ligament: Experiment And Modeling. Biorheology, 47, 1-14.

Eilaghi, A., Flanagan, J. G., Simmons, C. A. & Ethier, C. R. 2010. Effects Of Scleral Stiffness Properties On Optic Nerve Head Biomechanics. Ann Biomed Eng, 38, 1586-92.

El-Domyati, M., Attia, S., Saleh, F., Brown, D., Birk, D. E., Gasparro, F., Ahmad, H. & Uitto, J. 2002. Intrinsic Aging Vs. Photoaging: A Comparative Histopathological, Immunohistochemical, And Ultrastructural Study Of Skin. Exp Dermatol, 11, 398-405.

Elkington, A. R., Inman, C. B. E., Steart, P. V. & Weller, R. O. 1990. The Structure Of The Lamina Cribrosa Of The Human Eye: An Immunocytochemical And Electron Microscopical Study. Eye, 4, 42-57.

Elliott, J. & Dover, S. 1982. X-Ray Microtomography. Journal Of Microscopy, 126, 211-213.

Ellis, R., Green, E. & Winlove, C. P. 2009. Structural Analysis Of Glycosaminoglycans And Proteoglycans By Means Of Raman Microspectrometry. Connect Tissue Res, 50, 29-36.

Escoffier, C., De Rigal, J., Rochefort, A., Vasselet, R., Leveque, J. L. & Agache, P. G. 1989. Age-Related Mechanical Properties Of Human Skin: An In Vivo Study. J Invest Dermatol, 93, 353-7.

Ethier, C. R., Johnson, M. & Ruberti, J. 2004. Ocular Biomechanics And Biotransport. Annu Rev Biomed Eng, 6, 249-73.

Fallas, J. A., Gauba, V. & Hartgerink, J. D. 2009. Solution Structure Of An Abc Collagen Heterotrimer Reveals A Single-Register Helix Stabilized By Electrostatic Interactions. J Biol Chem, 284, 26851-9.

Falzon, G., Pearson, S., Murison, R., Hall, C., Siu, K., Round, A., Schultke, E., Kaye, A. H. & Lewis, R. 2007. Myelin Structure Is A Key Difference In The X-Ray Scattering Signature Between Meningioma, Schwannoma And Glioblastoma Multiforme. Phys Med Biol, 52, 6543-53.

Fata, B., Zhang, W., Amini, R. & Sacks, M. S. 2014. Insights Into Regional Adaptations In The Growing Pulmonary Artery Using A Meso-Scale Structural Model: Effects Of Ascending Aorta Impingement. J Biomech Eng, 136, 021009.

Fautsch, M. P. & Johnson, D. H. 2001. Characterization Of Myocilin-Myocilin Interactions. Invest Ophthalmol Vis Sci, 42, 2324-31.

Fazio, M. A., Grytz, R., Morris, J. S., Bruno, L., Gardiner, S. K., Girkin, C. A. & Downs, J. C. 2014. Age-Related Changes In Human Peripapillary Scleral Strain. Biomech Model Mechanobiol, 13, 551-63.

Fazio, M. A., Johnstone, J. K., Smith, B., Wang, L. & Girkin, C. A. 2016. Displacement Of The Lamina Cribrosa In Response To Acute Intraocular Pressure Elevation In Normal Individuals Of African And European Descentracial Differences In Onh Mechanical Compliance. Investigative Ophthalmology & Visual Science, 57, 3331-3339.

Fechtner, R. D. & Weinreb, R. N. 1994. Mechanisms Of Optic Nerve Damage In Primary Open Angle Glaucoma. Surv Ophthalmol, 39, 23-42.

Feldman, T. B., Yakovleva, M. A., Dontsov, A. E. & Ostrovsky, M. A. 2010. Fluorescence Emission And Excitation Spectra Of Fluorophores Of Lipofuscin Granules Isolated From Retinal Pigment Epithelium Of Human Cadaver Eyes. Russian Chemical Bulletin, 59, 276-283.

Feola, A. J., Coudrillier, B., Mulvihill, J., Geraldes, D. M., Vo, N. T., Albon, J., Abel, R. L., Samuels, B. C. & Ethier, C. R. 2017. Deformation Of The Lamina Cribrosa And Optic Nerve Due To Changes In Cerebrospinal Fluid Pressure. Invest Ophthalmol Vis Sci, 58, 2070-2078.

Filik, J., Ashton, A. W., Chang, P. C. Y., Chater, P. A., Day, S. J., Drakopoulos, M., Gerring, M. W., Hart, M. L., Magdysyuk, O. V., Michalik, S., Smith, A., Tang, C. C., Terrill, N. J., Wharmby, M. T. & Wilhelm, H. 2017. Processing Two-Dimensional X-Ray Diffraction And Small-Angle Scattering Data In Dawn 2. J Appl Crystallogr, 50, 959-966.

Fioretto, D. & Scarponi, F. 2009. Dynamics Of A Glassy Polymer Studied By Brillouin Light Scattering. Materials Science And Engineering: A, 521-522, 243-246.

Fioretto, D., Caponi, S. & Palombo, F. 2019. Brillouin-Raman Mapping Of Natural Fibers With Spectral Moment Analysis. Biomed Opt Express, 10, 1469-1474.

Fleischmajer, R., Macdonald, E. D., Perlish, J. S., Burgeson, R. E. & Fisher, L. W. 1990. Dermal Collagen Fibrils Are Hybrids Of Type I And Type Iii Collagen Molecules. J Struct Biol, 105, 162-9.

Folkhard, W., Mosler, E., Geercken, W., Knörzer, E., Nemetschek-Gansler, H., Nemetschek, T. & Koch, M. 1987. Quantitative Analysis Of The Molecular Sliding Mechanisms In Native Tendon Collagen—Time-Resolved Dynamic Studies Using Synchrotron Radiation. International Journal Of Biological Macromolecules, 9, 169-175.

Fonck, E., Feigl, G. G., Fasel, J., Sage, D., Unser, M., Rüfenacht, D. A. & Stergiopulos, N. 2009. Effect Of Aging On Elastin Functionality In Human Cerebral Arteries. Stroke, 40, 2552-2556.

Foster, P. J., Buhrmann, R., Quigley, H. A. & Johnson, G. J. 2002. The Definition And Classification Of Glaucoma In Prevalence Surveys. The British Journal Of Ophthalmology, 86, 238-242.

Franchi, M., Quaranta, M., Macciocca, M., Leonardi, L., Ottani, V., Bianchini, P., Diaspro, A. & Ruggeri, A. 2010. Collagen Fibre Arrangement And Functional Crimping Pattern Of The Medial Collateral Ligament In The Rat Knee. Knee Surg Sports Traumatol Arthrosc, 18, 1671-8.

Frank, C. J., Mccreery, R. L. & Redd, D. C. B. 1995. Raman Spectroscopy Of Normal And Diseased Human Breast Tissues. Analytical Chemistry, 67, 777-783.

Fraser, R. & Macrae, T. 1981. Unit Cell And Molecular Connectivity In Tendon Collagen. International Journal Of Biological Macromolecules, 3, 193-200.

Fratzl, P. & Daxer, A. 1993. Structural Transformation Of Collagen Fibrils In Corneal Stroma During Drying. An X-Ray Scattering Study. Biophysical Journal, 64, 1210-1214.

Freed, A. D. & Doehring, T. C. 2005. Elastic Model For Crimped Collagen Fibrils. J Biomech Eng, 127, 587-93.

Freund, I., Deutsch, M. & Sprecher, A. 1986. Connective Tissue Polarity. Optical Second-Harmonic Microscopy, Crossed-Beam Summation, And Small-Angle Scattering In Rat-Tail Tendon. Biophysical Journal, 50, 693.

Frushour, B. G. & Koenig, J. L. 1975. Raman Scattering Of Collagen, Gelatin, And Elastin. Biopolymers, 14, 379-91.

Fukuchi, T., Sawaguchi, S., Hara, H., Shirakashi, M. & Iwata, K. 1992. Extracellular Matrix Changes Of The Optic Nerve Lamina Cribrosa In Monkey Eyes With Experimentally Chronic Glaucoma. Graefes Arch Clin Exp Ophthalmol, 230, 421-7.

Fullwood, N. J. & Meek, K. M. 1993. A Synchroton X-Ray Study Of The Changes Occurring In The Corneal Stroma During Processing For Electron Microscopy. J Microsc, 169, 53-60.

Fullwood, N. J., Tuft, S. J., Malik, N. S., Meek, K. M., Ridgway, A. E. & Harrison, R. J. 1992. Synchrotron X-Ray Diffraction Studies Of Keratoconus Corneal Stroma. Invest Ophthalmol Vis Sci, 33, 1734-41.

Furlanetto, R. L., Park, S. C., Damle, U. J., Sieminski, S. F., Kung, Y., Siegal, N., Liebmann, J. M. & Ritch, R. 2013. Posterior Displacement Of The Lamina Cribrosa In Glaucoma: In Vivo Interindividual And Intereye Comparisons. Invest Ophthalmol Vis Sci, 54, 4836-42.

Gaasterland, D., Tanishima, T. & Kuwabara, T. 1978. Axoplasmic Flow During Chronic Experimental Glaucoma. 1. Light And Electron Microscopic Studies Of The Monkey Optic Nervehead During Development Of Glaucomatous Cupping. Invest Ophthalmol Vis Sci, 17, 838-46.

Gabella, G. 1987. The Cross-Ply Arrangement Of Collagen Fibres In The Submucosa Of The Mammalian Small Intestine. Cell And Tissue Research, 248, 491-497.

Gailhouste, L., Le Grand, Y., Odin, C., Guyader, D., Turlin, B., Ezan, F., Desille, Y., Guilbert, T., Bessard, A., Fremin, C., Theret, N. & Baffet, G. 2010. Fibrillar Collagen Scoring By Second Harmonic Microscopy: A New Tool In The Assessment Of Liver Fibrosis. J Hepatol, 52, 398-406.

Gao, D., Ning, N., Hao, G. & Niu, X. 2012. Pioglitazone Attenuates Vascular Fibrosis In Spontaneously Hypertensive Rats. Ppar Research, 2012, 856426-856426.

Garway-Heath, D. F. & Hitchings, R. A. 1998. Quantitative Evaluation Of The Optic Nerve Head In Early Glaucoma. Br J Ophthalmol, 82, 352-61.

Garway-Heath, D. F., Wollstein, G. & Hitchings, R. A. 1997. Aging Changes Of The Optic Nerve Head In Relation To Open Angle Glaucoma. Br J Ophthalmol, 81, 840-5.

Gasior-Glogowska, M., Komorowska, M., Hanuza, J., Ptak, M. & Kobielarz, M. 2010. Structural Alteration Of Collagen Fibres--Spectroscopic And Mechanical Studies. Acta Bioeng Biomech, 12, 55-62.

Gee, A. R., O'shea, D. C. & Cummins, H. Z. 1966. Raman Scattering And Fluorescence In Calcium Fluoride. Solid State Communications, 4, 43-46.

Gignac, P. M. & Kley, N. J. 2014. Iodine-Enhanced Micro-Ct Imaging: Methodological Refinements For The Study Of The Soft-Tissue Anatomy Of Post-Embryonic Vertebrates. J Exp Zool B Mol Dev Evol, 322, 166-76.

Girard, M. J., Downs, J. C., Burgoyne, C. F. & Suh, J. K. 2009. Peripapillary And Posterior Scleral Mechanics--Part I: Development Of An Anisotropic Hyperelastic Constitutive Model. J Biomech Eng, 131, 051011.

Gkogkolou, P. & Böhm, M. 2012. Advanced Glycation End Products: Key Players In Skin Aging? Dermato-Endocrinology, 4, 259-270.

Gobeil, S., Rodrigue, M. A., Moisan, S., Nguyen, T. D., Polansky, J. R., Morissette, J. & Raymond, V. 2004. Intracellular Sequestration Of Hetero-Oligomers Formed By Wild-Type And Glaucoma-Causing Myocilin Mutants. Invest Ophthalmol Vis Sci, 45, 3560-7.

Goetz, C. G. 2007. Textbook Of Clinical Neurology, Elsevier Health Sciences.

Goldbaum, M. H., Jeng, S. Y., Logemann, R. & Weinreb, R. N. 1989. The Extracellular Matrix Of The Human Optic Nerve. Arch Ophthalmol, 107, 1225-31.

Gonzalez, A. D., Gallant, M. A., Burr, D. B. & Wallace, J. M. 2014. Multiscale Analysis Of Morphology And Mechanics In Tail Tendon From The Zdsd Rat Model Of Type 2 Diabetes. Journal Of Biomechanics, 47, 681-686.

Gotte, L. & Serafini-Fracassini, A. 1963. Electron Microscope Observations On The Structure Of Elastin. J Atheroscler Res, 3, 247-51.

Goulam Houssen, Y., Gusachenko, I., Schanne-Klein, M.-C. & Allain, J.-M. 2012. Imaging Rat-Tail Collagen Organization Using Shg Microscopy Upon Mechanical Strain.

Grant, W. M. 1955. Facility Of Flow Through The Trabecular Meshwork. Ama Arch Ophthalmol, 54, 245-8.

Grant, W. P., Sullivan, R., Sonenshine, D. E., Adam, M., Slusser, J. H., Carson, K. A. & Vinik, A. I. 1997. Electron Microscopic Investigation Of The Effects Of Diabetes Mellitus On The Achilles Tendon. J Foot Ankle Surg, 36, 272-8; Discussion 330.

Greenlee, T. K., Jr., Ross, R. & Hartman, J. L. 1966. The Fine Structure Of Elastic Fibers. J Cell Biol, 30, 59-71.

Greenwald, S. E. 2007. Ageing Of The Conduit Arteries. J Pathol, 211, 157-72.

Grieshaber, M. C., Orgul, S., Schoetzau, A. & Flammer, J. 2007. Relationship Between Retinal Glial Cell Activation In Glaucoma And Vascular Dysregulation. J Glaucoma, 16, 215-9.

Grytz, R. & Meschke, G. 2009. Constitutive Modeling Of Crimped Collagen Fibrils In Soft Tissues. Journal Of The Mechanical Behavior Of Biomedical Materials, 2, 522-533.

Grytz, R., Fazio, M. A., Libertiaux, V., Bruno, L., Gardiner, S., Girkin, C. A. & Downs, J. C. 2014. Age- And Race-Related Differences In Human Scleral Material Properties. Invest Ophthalmol Vis Sci, 55, 8163-72.

Grytz, R., Meschke, G. & Jonas, J. B. 2011. The Collagen Fibril Architecture In The Lamina Cribrosa And Peripapillary Sclera Predicted By A Computational Remodeling Approach. Biomechanics And Modeling In Mechanobiology, 10, 371-382.

Halloran, B. G., Davis, V. A., Mcmanus, B. M., Lynch, T. G. & Baxter, B. T. 1995. Localization Of Aortic Disease Is Associated With Intrinsic Differences In Aortic Structure. J Surg Res, 59, 17-22.

Hanlon, E. B., Manoharan, R., Koo, T. W., Shafer, K. E., Motz, J. T., Fitzmaurice, M., Kramer, J. R., Itzkan, I., Dasari, R. R. & Feld, M. S. 2000. Prospects For In Vivo Raman Spectroscopy. Phys Med Biol, 45, R1-59.

Hansen, K. A., Weiss, J. A. & Barton, J. K. 2002. Recruitment Of Tendon Crimp With Applied Tensile Strain. J Biomech Eng, 124, 72-7.

Harker, D. 1972. Myelin Membrane Structure As Revealed By X-Ray Diffraction. Biophys J, 12, 1285-95.

Haston, J. L., Engelsen, S. B., Roessle, M., Clarkson, J., Blanch, E. W., Baldock, C., Kielty, C. M. & Wess, T. J. 2003. Raman Microscopy And X-Ray Diffraction, A Combined Study Of Fibrillin-Rich Microfibrillar Elasticity. Journal Of Biological Chemistry, 278, 41189-41197.

Hayat, M. A. 1981. Principles And Techniques Of Electron Microscopy. Biological Applications, Edward Arnold.

Hayes, S., Kamma-Lorger, C. S., Boote, C., Young, R. D., Quantock, A. J., Rost, A., Khatib, Y., Harris, J., Yagi, N., Terrill, N. & Meek, K. M. 2013. The Effect Of Riboflavin/Uva Collagen Cross-Linking Therapy On The Structure And Hydrodynamic Behaviour Of The Ungulate And Rabbit Corneal Stroma. Plos One, 8, E52860.

Hayes, S., White, T., Boote, C., Kamma-Lorger, C. S., Bell, J., Sorenson, T., Terrill, N., Shebanova, O. & Meek, K. M. 2017. The Structural Response Of The Cornea To Changes In Stromal Hydration. J R Soc Interface, 14.

Hayes, S., Young, R., Boote, C., Hawksworth, N., Huang, Y. & Meek, K. M. 2010. A Structural Investigation Of Corneal Graft Failure In Suspected Recurrent Keratoconus. Eye (Lond), 24, 728-34.

Hayreh, S. S. 1963. Arteries Of The Orbit In The Human Being. Br J Surg, 50, 938-53.
Hedin, U., Roy, J., Tran, P. K., Lundmark, K. & Rahman, A. 1999. Control Of Smooth Muscle Cell Proliferation--The Role Of The Basement Membrane. Thromb Haemost, 82 Suppl 1, 23-6.

Heijl, A., Leske, M. C., Bengtsson, B., Hyman, L., Bengtsson, B. & Hussein, M. 2002. Reduction Of Intraocular Pressure And Glaucoma Progression: Results From The Early Manifest Glaucoma Trial. Arch Ophthalmol, 120, 1268-79.

Helliwell, J. A., Thomas, D. S., Papathanasiou, V., Homer-Vanniasinkam, S., Desai, A., Jennings, L. M., Rooney, P., Kearney, J. N. & Ingham, E. 2017. Development And Characterisation Of A Low-Concentration Sodium Dodecyl Sulphate Decellularised Porcine Dermis. Journal Of Tissue Engineering, 8, 2041731417724011-2041731417724011.

Hernandez, M. R. & Pena, J. D. 1997. The Optic Nerve Head In Glaucomatous Optic Neuropathy. Arch Ophthalmol, 115, 389-95.

Hernandez, M. R. & Ye, H. 1993. Glaucoma: Changes In Extracellular Matrix In The Optic Nerve Head. Ann Med, 25, 309-15.

Hernandez, M. R. 1992. Ultrastructural Immunocytochemical Analysis Of Elastin In The Human Lamina Cribrosa. Changes In Elastic Fibers In Primary Open-Angle Glaucoma. Invest Ophthalmol Vis Sci, 33, 2891-903.

Hernandez, M. R. 2000. The Optic Nerve Head In Glaucoma: Role Of Astrocytes In Tissue Remodeling. Prog Retin Eye Res, 19, 297-321.

Hernandez, M. R., Andrzejewska, W. M. & Neufeld, A. H. 1990. Changes In The Extracellular Matrix Of The Human Optic Nerve Head In Primary Open-Angle Glaucoma. American Journal Of Ophthalmology, 109, 180-188.

Hernandez, M. R., Igoe, F. & Neufeld, A. H. 1986. Extracellular Matrix Of The Human Optic Nerve Head. American Journal Of Ophthalmology, 102, 139-148.

Hernandez, M. R., Igoe, F. & Neufeld, A. H. 1988. Cell Culture Of The Human Lamina Cribrosa. Invest Ophthalmol Vis Sci, 29, 78-89.

Hernandez, M. R., Luo, X. X., Andrzejewska, W. & Neufeld, A. H. 1989. Age-Related Changes In The Extracellular Matrix Of The Human Optic Nerve Head. Am J Ophthalmol, 107, 476-84.

Hernandez, M. R., Luo, X. X., Igoe, F. & Neufeld, A. H. 1987. Extracellular Matrix Of The Human Lamina Cribrosa. Am J Ophthalmol, 104, 567-76.

Hernandez, M. R., Wang, N., Hanley, N. M. & Neufeld, A. H. 1991. Localization Of Collagen Types I And Iv Mrnas In Human Optic Nerve Head By In Situ Hybridization. Invest Ophthalmol Vis Sci, 32, 2169-77.

Hernandez, M. R., Yang, J. & Ye, H. 1994. Activation Of Elastin Mrna Expression In Human Optic Nerve Heads With Primary Open-Angle Glaucoma. Journal Of Glaucoma, 3, 214-225.
Glaucoma, 3, 214-225.

Hernandez, M. R., Ye, H. & Roy, S. 1994b. Collagen Type Iv Gene Expression In Human Optic Nerve Heads With Primary Open Angle Glaucoma. Exp Eye Res, 59, 41-51.

Hewitt, A. W., Mackey, D. A. & Craig, J. E. 2008. Myocilin Allele-Specific Glaucoma Phenotype Database. Hum Mutat, 29, 207-11.

Hill, M. R., Duan, X., Gibson, G. A., Watkins, S. & Robertson, A. M. 2012. A Theoretical And Non-Destructive Experimental Approach For Direct Inclusion Of Measured Collagen Orientation And Recruitment Into Mechanical Models Of The Artery Wall. J Biomech, 45, 762-71.

Hirano, A. & Dembitzer, H. M. 1967. A Structural Analysis Of The Myelin Sheath In The Central Nervous System. J Cell Biol, 34, 555-67.

Hitchings, R. & Spaeth, G. 1976. The Optic Disc In Glaucoma. I: Classification. British Journal Of Ophthalmology, 60, 778-785.

Hoeve, C. & Flory, P. 1974. The Elastic Properties Of Elastin. Biopolymers, 13, 677-686.

Hogan, M. J., Alvarado, J. A. & Weddell, J. E. 1971. Histology Of The Human Eye: An Atlas And Textbook [By] Michael J. Hogan, Jorge A. Alvarado [And] Joan Esperson Weddell, Saunders.

Holzapfel, G. A., Sommer, G., Auer, M., Regitnig, P. & Ogden, R. W. 2007. Layer-Specific 3d Residual Deformations Of Human Aortas With Non-Atherosclerotic Intimal Thickening. Ann Biomed Eng, 35, 530-45.

Höög, J. L., Gluenz, E., Vaughan, S. & Gull, K. 2010. Chapter 8 - Ultrastructural Investigation Methods For Trypanosoma Brucei. In: Müller-Reichert, T. (Ed.) Methods In Cell Biology. Academic Press.

Hou, R., Zhang, Z., Yang, D., Wang, H., Chen, W., Li, Z., Sang, J., Liu, S., Cao, Y., Xie, X., Ren, R., Zhang, Y., Sabel, B. A. & Wang, N. 2016. Pressure Balance And Imbalance In The Optic Nerve Chamber: The Beijing Intracranial And Intraocular Pressure (Icop) Study. Sci China Life Sci, 59, 495-503.

Howell, G. R., Libby, R. T., Jakobs, T. C., Smith, R. S., Phalan, F. C., Barter, J. W., Barbay, J. M., Marchant, J. K., Mahesh, N., Porciatti, V., Whitmore, A. V., Masland, R. H. & John, S. W. 2007. Axons Of Retinal Ganglion Cells Are Insulted In The Optic Nerve Early In Dba/2j Glaucoma. J Cell Biol, 179, 1523-37.

Hoyt, W. F. 1962. Anatomic Considerations Of Arcuate Scotomas Associated With Lesions Of The Optic Nerve And Chiasm. A Nauta Axon Degeneration Study In The Monkey. Bull Johns Hopkins Hosp, 111, 57-71.

Hua, Y., Tong, J., Ghate, D., Kedar, S. & Gu, L. 2017. Intracranial Pressure Influences The Behavior Of The Optic Nerve Head. J Biomech Eng, 139.

Huang, Z., Mcwilliams, A., Lui, H., Mclean, D. I., Lam, S. & Zeng, H. 2003. Near-Infrared Raman Spectroscopy For Optical Diagnosis Of Lung Cancer. Int J Cancer, 107, 1047-52.

Hudson, B. G., Reeders, S. T. & Tryggvason, K. 1993. Type Iv Collagen: Structure, Gene Organization, And Role In Human Diseases. Molecular Basis Of Goodpasture And Alport Syndromes And Diffuse Leiomyomatosis. J Biol Chem, 268, 26033-6.

Hukins, D. W. L. & Aspden, R. M. 1985. Composition And Properties Of Connective Tissues. Trends In Biochemical Sciences, 10, 260-264.

Hukins, D. W. L., Weston, S. A., Humphries, M. J. & Freemont, A. J. 1996. Chapter 8 Extracellular Matrix. In: Bittar, E. E. & Bittar, N. (Eds.) Principles Of Medical Biology. Elsevier.

Hulmes, D. J., Jesior, J. C., Miller, A., Berthet-Colominas, C. & Wolff, C. 1981. Electron Microscopy Shows Periodic Structure In Collagen Fibril Cross Sections. Proceedings Of The National Academy Of Sciences Of The United States Of America, 78, 3567-3571.

Hunter, G. C., Smyth, S. H., Aguirre, M. L., Baxter, B. T., Bull, D. A., King, D. D., Wang, Y. P., Hall, K. A. & Putnam, C. W. 1996. Incidence And Histologic Characteristics Of Blebs In Patients With Abdominal Aortic Aneurysms. J Vasc Surg, 24, 93-101.

Hur, C. & Yachimski, P. S. 2019. 26 - Screening For Esophageal Squamous Cell Carcinoma. In: Chandrasekhara, V., Elmunzer, B. J., Khashab, M. A. & Muthusamy, V. R. (Eds.) Clinical Gastrointestinal Endoscopy (Third Edition). Philadelphia: Content Repository Only!

Ikoma, T., Kobayashi, H., Tanaka, J., Walsh, D. & Mann, S. 2003. Physical Properties Of Type I Collagen Extracted From Fish Scales Of Pagrus Major And Oreochromis Niloticas. Int J Biol Macromol, 32, 199-204.

Ivers, K. M., Li, C., Patel, N., Sredar, N., Luo, X., Queener, H., Harwerth, R. S. & Porter, J. 2011. Reproducibility Of Measuring Lamina Cribrosa Pore Geometry In Human And Nonhuman Primates With In Vivo Adaptive Optics Imaging. Invest Ophthalmol Vis Sci, 52, 5473-80.

Jacob, M. P. 2006. [Extracellular Matrix And Vascular Ageing]. Med Sci (Paris), 22, 273-8.

Jacobson, N., Andrews, M., Shepard, A. R., Nishimura, D., Searby, C., Fingert, J. H., Hageman, G., Mullins, R., Davidson, B. L., Kwon, Y. H., Alward, W. L., Stone, E. M., Clark, A. F. & Sheffield, V. C. 2001. Non-Secretion Of Mutant Proteins Of The Glaucoma Gene Myocilin In Cultured Trabecular Meshwork Cells And In Aqueous Humor. Hum Mol Genet, 10, 117-25.

Jakobiec, F. A., Rashid, A. & Yoon, M. 2015. Massive And Diffuse Elastosis Of The Temporal Artery. Graefes Arch Clin Exp Ophthalmol, 253, 493-5.

Jan, N.-J., Brazile, B. L., Hu, D., Grube, G., Wallace, J., Gogola, A. & Sigal, I. A. 2018. Crimp Around The Globe; Patterns Of Collagen Crimp Across The Corneoscleral Shell. Experimental Eye Research, 172, 159-170.

Jeffery, N. S., Stephenson, R. S., Gallagher, J. A., Jarvis, J. C. & Cox, P. G. 2011. Micro-Computed Tomography With Iodine Staining Resolves The Arrangement Of Muscle Fibres. J Biomech, 44, 189-92.

Jesche, A., Fix, M., Kreyssig, A., Meier, W. R. & Canfield, P. C. 2016. X-Ray Diffraction On Large Single Crystals Using A Powder Diffractometer. Philosophical Magazine, 96, 2115-2124.

Jiang, X., Zhong, J., Liu, Y., Yu, H., Zhuo, S. & Chen, J. 2011. Two-Photon Fluorescence And Second-Harmonic Generation Imaging Of Collagen In Human Tissue Based On Multiphoton Microscopy. Scanning, 33, 53-56.

Joe, M. K., Sohn, S., Hur, W., Moon, Y., Choi, Y. R. & Kee, C. 2003. Accumulation Of Mutant Myocilins In Er Leads To Er Stress And Potential Cytotoxicity In Human Trabecular Meshwork Cells. Biochem Biophys Res Commun, 312, 592-600.

John, R. & Thomas, J. 1972. Chemical Compositions Of Elastins Isolated From Aortas And Pulmonary Tissues Of Humans Of Different Ages. Biochemical Journal, 127, 261-269.

Johnson, B., Miao, M. & Sadun, A. 1987. Age-Related Decline Of Human Optic Nerve Axon Populations. Age, 10, 5-9.

Johnson, E. C., Jia, L., Cepurna, W. O., Doser, T. A. & Morrison, J. C. 2007. Global Changes In Optic Nerve Head Gene Expression After Exposure To Elevated Intraocular Pressure In A Rat Glaucoma Model. Invest Ophthalmol Vis Sci, 48, 3161-77.

Johnson, M., Chan, D., Read, A. T., Christensen, C., Sit, A. & Ethier, C. R. 2002. The Pore Density In The Inner Wall Endothelium Of Schlemm's Canal Of Glaucomatous Eyes. Invest Ophthalmol Vis Sci, 43, 2950-5.

Jonas, J. B. & Holbach, L. 2005. Central Corneal Thickness And Thickness Of The Lamina Cribrosa In Human Eyes. Invest Ophthalmol Vis Sci, 46, 1275-9.

Jonas, J. B., Berenshtein, E. & Holbach, L. 2003. Anatomic Relationship Between Lamina Cribrosa, Intraocular Space, And Cerebrospinal Fluid Space. Invest Ophthalmol Vis Sci, 44, 5189-95.

Jonas, J. B., Fernandez, M. C. & Sturmer, J. 1993. Pattern Of Glaucomatous Neuroretinal Rim Loss. Ophthalmology, 100, 63-8.

Jonas, J. B., Hayreh, S. S. & Tao, Y. 2009. Central Corneal Thickness And Thickness Of The Lamina Cribrosa And Peripapillary Sclera In Monkeys. Arch Ophthalmol, 127, 1395-6.

Jonas, J. B., Jonas, R. A., Jonas, S. B. & Panda-Jonas, S. 2012. Lamina Cribrosa Thickness Correlated With Peripapillary Sclera Thickness. Acta Ophthalmol, 90, E248-50.

Jonas, J., Mardin, C. Y., Schlotzer-Schrehardt, U. & Naumann, G. 1991. Morphometry Of The Human Lamina Cribrosa Surface. Invest Ophthalmol Vis Sci, 32, 401-405.

Jones, D. G. 1993. Chapter 6 - Electron Microscopic Exploration Of Synaptic Organization. In: Parvez, S. H., Naoi, M., Nagatsu, T. & Parvez, S. (Eds.) Techniques In The Behavioral And Neural Sciences. Elsevier.

Jones, H. 2014. Connective Tissue In The Human Optic Nerve Head.

Jones, H. J., Girard, M. J., White, N., Fautsch, M. P., Morgan, J. E., Ethier, C. R. & Albon, J. 2015. Quantitative Analysis Of Three-Dimensional Fibrillar Collagen Microstructure Within The Normal, Aged And Glaucomatous Human Optic Nerve Head. Journal Of The Royal Society Interface, 12.

Jung, K. I., Jung, Y., Park, K. T. & Park, C. K. 2014. Factors Affecting Plastic Lamina Cribrosa Displacement In Glaucoma Patientsfactors Affecting Lc Depth In Glaucoma. Investigative Ophthalmology & Visual Science, 55, 7709-7715.

Kadler, K. E., Hill, A. & Canty-Laird, E. G. 2008. Collagen Fibrillogenesis: Fibronectin, Integrins, And Minor Collagens As Organizers And Nucleators. Current Opinion In Cell Biology, 20, 495-501.

Kadler, K. E., Holmes, D. F., Trotter, J. A. & Chapman, J. A. 1996. Collagen Fibril Formation. Biochemical Journal, 316, 1-11.

Kageyama, M., Takagi, M., Parmley, R. T., Toda, M., Hirayama, H. & Toda, Y. 1985. Ultrastructural Visualization Of Elastic Fibres With A Tannate--Metal Salt Method. Histochem J, 17, 93-103.

Kajikawa, K., Yamaguchi, T., Katsuda, S. & Miwa, A. 1975. An Improved Electron Stain For Elastic Fibers Using Tannic Acid. J Electron Microsc (Tokyo), 24, 287-9.

Kalaria, R. N. & Pax, A. B. 1995. Increased Collagen Content Of Cerebral Microvessels In Alzheimer's Disease. Brain Research, 705, 349-352.

Kamma-Lorger, C. S., Boote, C., Hayes, S., Moger, J., Burghammer, M., Knupp, C., Quantock, A. J., Sorensen, T., Di Cola, E., White, N., Young, R. D. & Meek, K. M. 2010. Collagen And Mature Elastic Fibre Organisation As A Function Of Depth In The Human Cornea And Limbus. J Struct Biol, 169, 424-30.

Kanai, A. & Kaufman, H. E. 1973. Electron Microscopic Studies Of Corneal Stroma: Aging Changes Of Collagen Fibers. Ann Ophthalmol, 5, 285-7 Passim.
Kannus, P. 2000. Structure Of The Tendon Connective Tissue. Scand J Med Sci Sports, 10, 312-20.

Kannus, P. 2000. Structure Of The Tendon Connective Tissue. Scand J Med Sci Sports, 10, 312-20.

Karali, A., Russell, P., Stefani, F. H. & Tamm, E. R. 2000. Localization Of Myocilin/Trabecular Meshwork--Inducible Glucocorticoid Response Protein In The Human Eye. Invest Ophthalmol Vis Sci, 41, 729-40.

Karthigasan, J. & Kirschner, D. A. 1988. Membrane Interactions Are Altered In Myelin Isolated From Central And Peripheral Nervous System Tissues. J Neurochem, 51, 228-36.

Kastelic, J., Galeski, A. & Baer, E. 1978. The Multicomposite Structure Of Tendon. Connect Tissue Res, 6, 11-23.

Kastelic, J., Palley, I. & Baer, E. 1980. A Structural Mechanical Model For Tendon Crimping. J Biomech, 13, 887-93.

Katainen, E., Elomaa, M., Laakkonen, U. M., Sippola, E., Niemela, P., Suhonen, J. & Jarvinen, K. 2007. Quantification Of The Amphetamine Content In Seized Street Samples By Raman Spectroscopy. J Forensic Sci, 52, 88-92.

Keech, M. 1960. Electron Microscope Study Of The Normal Rat Aorta. The Journal Of Biophysical And Biochemical Cytology, 7, 533-537.

Keene, D. R., Engvall, E. & Glanville, R. W. 1988. Ultrastructure Of Type Vi Collagen In Human Skin And Cartilage Suggests An Anchoring Function For This Filamentous Network. J Cell Biol, 107, 1995-2006.

Kelleher, C. M., Mclean, S. E. & Mecham, R. P. 2004. Vascular Extracellular Matrix And Aortic Development. Curr Top Dev Biol, 62, 153-88.

Kielty, C. M. 2006. Elastic Fibres In Health And Disease. Expert Rev Mol Med, 8, 1-23.

Kielty, C. M., Sherratt, M. J. & Shuttleworth, C. A. 2002. Elastic Fibres. J Cell Sci, 115, 2817-28.

Kielty, C. M., Stephan, S., Sherratt, M. J., Williamson, M. & Shuttleworth, C. A. 2007. Applying Elastic Fibre Biology In Vascular Tissue Engineering. Philosophical Transactions Of The Royal Society Of London. Series B, Biological Sciences, 362, 1293-1312.

Kiernan, J. 2001. Histological And Histochemical Methods. Theory And Practice. Arnold Editor.

Kim, B., Na, H., Byun, S. H., Shin, T., Ryu, T. & Jung, J. 2015. Structural Analysis Of A Ligatured Rat Sciatic Nerve In The Ex Vivo State Using Synchrotron Small-Angle X-Ray Scattering (Saxs). Anesthesia And Pain Medicine, 10, 245-251.

Kimball, E. C., Nguyen, C., Steinhart, M. R., Nguyen, T. D., Pease, M. E., Oglesby, E. N., Oveson, B. C. & Quigley, H. A. 2014. Experimental Scleral Cross-Linking Increases Glaucoma Damage In A Mouse Model. Experimental Eye Research, 128, 129-140.

King, R. H. & Thomas, P. K. 1984. The Occurrence And Significance Of Myelin With Unusually Large Periodicity. Acta Neuropathol, 63, 319-29.

Kirkpatrick, N. D., Brewer, M. A. & Utzinger, U. 2007. Endogenous Optical Biomarkers Of Ovarian Cancer Evaluated With Multiphoton Microscopy. Cancer Epidemiol Biomarkers Prev, 16, 2048-57.

Kirsch, R. E. & Anderson, D. R. 1973. Clinical Recognition Of Glaucomatous Cupping. American Journal Of Ophthalmology, 75, 442-454.

Kirwan, R. P., Crean, J. K., Fenerty, C. H., Clark, A. F. & O'brien, C. J. 2004. Effect Of Cyclical Mechanical Stretch And Exogenous Transforming Growth Factor-[Beta] 1 On Matrix Metalloproteinase-2 Activity In Lamina Cribrosa Cells From The Human Optic Nerve Head. J Glaucoma, 13.

Kirwan, R. P., Crean, J. K., Fenerty, C. H., Clark, A. F. & O'brien, C. J. 2004. Effect Of Cyclical Mechanical Stretch And Exogenous Transforming Growth Factor-[Beta] 1 On Matrix Metalloproteinase-2 Activity In Lamina Cribrosa Cells From The Human Optic Nerve Head. J Glaucoma, 13.

Kiumehr, S., Park, S. C., Syril, D., Teng, C. C., Tello, C., Liebmann, J. M. & Ritch, R. 2012. In Vivo Evaluation Of Focal Lamina Cribrosa Defects In Glaucoma. Arch Ophthalmol, 130, 552-9.

Klein, B. E., Klein, R., Sponsel, W. E., Franke, T., Cantor, L. B., Martone, J. & Menage, M. J. 1992. Prevalence Of Glaucoma. The Beaver Dam Eye Study. Ophthalmology, 99, 1499-504.

Knox Cartwright, N. E., Tyrer, J. R. & Marshall, J. 2011. Age-Related Differences In The Elasticity Of The Human Cornea. Invest Ophthalmol Vis Sci, 52, 4324-9.

Ko, M. L., Hu, D. N., Ritch, R. & Sharma, S. C. 2000. The Combined Effect Of Brain-Derived Neurotrophic Factor And A Free Radical Scavenger In Experimental Glaucoma. Invest Ophthalmol Vis Sci, 41, 2967-71.

Koehler, M. J., König, K., Elsner, P., Bückle, R. & Kaatz, M. 2006. In Vivo Assessment Of Human Skin Aging By Multiphoton Laser Scanning Tomography. Optics Letters, 31, 2879-2881.

Koehler, M. J., Preller, A., Elsner, P., Konig, K., Hipler, U. C. & Kaatz, M. 2012. Non-Invasive Evaluation Of Dermal Elastosis By In Vivo Multiphoton Tomography With Autofluorescence Lifetime Measurements. Exp Dermatol, 21, 48-51.

Komai, Y. & Ushiki, T. 1991. The Three-Dimensional Organization Of Collagen Fibrils In The Human Cornea And Sclera. Investigative Ophthalmology & Visual Science, 32, 2244-2258.

Konig, K., Schenke-Layland, K., Riemann, I. & Stock, U. A. 2005. Multiphoton Autofluorescence Imaging Of Intratissue Elastic Fibers. Biomaterials, 26, 495-500.

Konova, E., Baydanoff, S., Atanasova, M. & Velkova, A. 2004. Age-Related Changes In The Glycation Of Human Aortic Elastin. Exp Gerontol, 39, 249-54.

Koski, K. & Yarger, J. 2005. Brillouin Imaging. Applied Physics Letters, 87, 061903.

Kotecha, A., Izadi, S. & Jeffery, G. 2006. Age-Related Changes In The Thickness Of The Human Lamina Cribrosa. The British Journal Of Ophthalmology, 90, 1531-1534.

Koudouna, E., Mikula, E., Brown, D. J., Young, R. D., Quantock, A. J. & Jester, J. V. 2018a. Cell Regulation Of Collagen Fibril Macrostructure During Corneal Morphogenesis. Acta Biomaterialia, 79, 96-112.

Koudouna, E., Winkler, M., Mikula, E., Juhasz, T., Brown, D. J. & Jester, J. V. 2018b. Evolution Of The Vertebrate Corneal Stroma. Progress In Retinal And Eye Research, 64, 65-76.

Krauhs, J. M. 1983. Microfibrils In The Aorta. Connect Tissue Res, 11, 153-67.

Kreutzberg, G. W. 1996. Microglia: A Sensor For Pathological Events In The Cns. Trends Neurosci, 19, 312-8.

Labella, F. S. & Lindsay, W. G. 1963. The Structure Of Human Aortic Elastin As Influenced By Age. J Gerontol, 18, 111-8.

Labella, F. S., Vivian, S. & Thornhill, D. P. 1966. Amino Acid Composition Of Human Aortic Elastin As Influenced By Age1. Journal Of Gerontology, 21, 550-555.

Lacomb, R., Nadiarnykh, O. & Campagnola, P. J. 2008. Quantitative Second Harmonic Generation Imaging Of The Diseased State Osteogenesis Imperfecta: Experiment And Simulation. Biophysical Journal, 94, 4504-4514.

Lanir, Y. 1979. A Structural Theory For The Homogeneous Biaxial Stress-Strain Relationships In Flat Collagenous Tissues. J Biomech, 12, 423-36.

Lanir, Y. 1983. Constitutive Equations For Fibrous Connective Tissues. J Biomech, 16, 1-12.

Lansing, A. I. Aging Of Elastic Tissue And The Systemic Effects Of Elastase. Ciba Foundation Colloquia On Ageing, 1955. 88-108.

Lansing, A., Roberts, E., Ramasarma, G., Rosenthal, T. B. & Alex, M. 1951. Changes With Age In Amino Acid Composition Of Arterial Elastin.∗. Proceedings Of The Society For Experimental Biology And Medicine, 76, 714-717.

Learoyd, B. M. & Taylor, M. G. 1966. Alterations With Age In The Viscoelastic Properties Of Human Arterial Walls. Circulation Research, 18, 278-292.

Lee, E. J., Kim, T. W., Weinreb, R. N., Suh, M. H., Kang, M., Park, K. H., Kim, S. H. & Kim, D. M. 2012. Three-Dimensional Evaluation Of The Lamina Cribrosa Using Spectral-Domain Optical Coherence Tomography In Glaucoma. Invest Ophthalmol Vis Sci, 53, 198-204.

Lee, W., Rahman, H., Kersh, M. E. & Toussaint, K. C. Crimp Analysis Of Connective Tissue Using Quantitative Second-Harmonic Generation Microscopy. Frontiers In Optics 2017, 2017/09/18 2017a Washington, D.C.: Optical Society Of America, Fw5d.5.

Lee, W., Rahman, H., Kersh, M. E. & Toussaint, K. C., Jr. 2017b. Application Of Quantitative Second-Harmonic Generation Microscopy To Posterior Cruciate Ligament For Crimp Analysis Studies. J Biomed Opt, 22, 46009.

Legerlotz, K., Dorn, J., Richter, J., Rausch, M. & Leupin, O. 2014. Age-Dependent Regulation Of Tendon Crimp Structure, Cell Length And Gap Width With Strain. Acta Biomater, 10, 4447-55.

Leikin, S., Parsegian, V. A., Yang, W.-H. & Walrafen, G. E. 1997. Raman Spectral Evidence For Hydration Forces Between Collagen Triple Helices. Proceedings Of The National Academy Of Sciences, 94, 11312-11317.

Lentsch, G., Balu, M., Williams, J., Lee, S., Harris, R. M., Konig, K., Ganesan, A., Tromberg, B. J., Nair, N., Santhanam, U. & Misra, M. 2019. In Vivo Multiphoton Microscopy Of Melasma. Pigment Cell Melanoma Res, 32, 403-411.

Lepert, G., Gouveia, R. M., Connon, C. J. & Paterson, C. 2016. Assessing Corneal Biomechanics With Brillouin Spectro-Microscopy. Faraday Discussions, 187, 415-428.

Liao, H. & Belkoff, S. M. 1999. A Failure Model For Ligaments. J Biomech, 32, 183-8.
Lin, S.-J., Jee, S.-H., Kuo, C.-J., Wu, R., Jr., Lin, W.-C., Chen, J.-S., Liao, Y.-H., Hsu, C.-J., Tsai, T.-F., Chen, Y.-F. & Dong, C.-Y. 2006. Discrimination Of Basal Cell Carcinoma From Normal Dermal Stroma By Quantitative Multiphoton Imaging. Optics Letters, 31, 2756-2758

Liu, B., Mcnally, S., Kilpatrick, J. I., Jarvis, S. P. & O'brien, C. J. 2018. Aging And Ocular Tissue Stiffness In Glaucoma. Surv Ophthalmol, 63, 56-74.

Liu, Y. & Vollrath, D. 2004. Reversal Of Mutant Myocilin Non-Secretion And Cell Killing: Implications For Glaucoma. Hum Mol Genet, 13, 1193-204.

Lo, W., Teng, S.-W., Tan, H.-Y., Kim, K. H., Chen, H.-C., Lee, H.-S., Chen, Y.-F., So, P. T. C. & Dong, C.-Y. 2006. Intact Corneal Stroma Visualization Of Gfp Mouse Revealed By Multiphoton Imaging. Microscopy Research And Technique, 69, 973-975.

Lu, Y.-B., Franze, K., Seifert, G., Steinhäuser, C., Kirchhoff, F., Wolburg, H., Guck, J., Janmey, P., Wei, E.-Q., Käs, J. & Reichenbach, A. 2006. Viscoelastic Properties Of Individual Glial Cells And Neurons In The Cns. Proceedings Of The National Academy Of Sciences, 103, 17759-17764.

Lutjen-Drecoll, E., May, C. A., Polansky, J. R., Johnson, D. H., Bloemendal, H. & Nguyen, T. D. 1998. Localization Of The Stress Proteins Alpha B-Crystallin And Trabecular Meshwork Inducible Glucocorticoid Response Protein In Normal And Glaucomatous Trabecular Meshwork. Invest Ophthalmol Vis Sci, 39, 517-25.

Lutz, V., Sattler, M., Gallinat, S., Wenck, H., Poertner, R. & Fischer, F. 2012. Impact Of Collagen Crosslinking On The Second Harmonic Generation Signal And The Fluorescence Lifetime Of Collagen Autofluorescence. Skin Research And Technology, 18, 168-179.

Malatesta, M. 2016. Histological And Histochemical Methods - Theory And Practice. European Journal Of Histochemistry : Ejh, 60, 2639.

Malik, N. S. & Meek, K. M. 1994. The Inhibition Of Sugar-Induced Structural Alterations In Collagen By Aspirin And Other Compounds. Biochem Biophys Res Commun, 199, 683-6.

Malik, N. S., Moss, S. J., Ahmed, N., Furth, A. J., Wall, R. S. & Meek, K. M. 1992. Ageing Of The Human Corneal Stroma: Structural And Biochemical Changes. Biochim Biophys Acta, 1138, 222-8.

Malini, R., Venkatakrishna, K., Kurien, J., Pai, K. M., Rao, L., Kartha, V. B. & Krishna, C. M. 2006. Discrimination Of Normal, Inflammatory, Premalignant, And Malignant Oral Tissue: A Raman Spectroscopy Study. Biopolymers, 81, 179-93.

Masters, B. R., So, P. T. & Gratton, E. 1997. Multiphoton Excitation Fluorescence Microscopy And Spectroscopy Of In Vivo Human Skin. Biophysical Journal, 72, 2405-2412.

Masters, B. R., So, P. T. & Gratton, E. 1998a. Multiphoton Excitation Microscopy Of In Vivo Human Skin. Functional And Morphological Optical Biopsy Based On Three-Dimensional Imaging, Lifetime Measurements And Fluorescence Spectroscopy. Ann N Y Acad Sci, 838, 58-67.
Masters, B. R., So, P. T. C. & Gratton, E. 1998b. Optical Biopsy Of In Vivo Human Skin: Multi-Photon Excitation Microscopy. Lasers In Medical Science, 13, 196-203.

Mattana, S., Alunni Cardinali, M., Caponi, S., Casagrande Pierantoni, D., Corte, L., Roscini, L., Cardinali, G. & Fioretto, D. 2017a. High-Contrast Brillouin And Raman Micro-Spectroscopy For Simultaneous Mechanical And Chemical Investigation Of Microbial Biofilms. Biophysical Chemistry, 229, 123-129.

Mattana, S., Caponi, S., Tamagnini, F., Fioretto, D. & Palombo, F. 2017b. Viscoelasticity Of Amyloid Plaques In Transgenic Mouse Brain Studied By Brillouin Microspectroscopy And Correlative Raman Analysis. Journal Of Innovative Optical Health Sciences, 10, 1742001.

Mattana, S., Mattarelli, M., Urbanelli, L., Sagini, K., Emiliani, C., Serra, M. D., Fioretto, D. & Caponi, S. 2018. Non-Contact Mechanical And Chemical Analysis Of Single Living Cells By Microspectroscopic Techniques. Light: Science &Amp; Applications, 7, 17139.

Mcelnea, E. M., Hughes, E., Mcgoldrick, A., Mccann, A., Quill, B., Docherty, N., Irnaten, M., Farrell, M., Clark, A. F., O'brien, C. J. & Wallace, D. M. 2014. Lipofuscin Accumulation And Autophagy In Glaucomatous Human Lamina Cribrosa Cells. Bmc Ophthalmology, 14, 153.

Medeiros, F. A., Weinreb, R. N., Sample, P. A., Gomi, C. F., Bowd, C., Crowston, J. G. & Zangwill, L. M. 2005. Validation Of A Predictive Model To Estimate The Risk Of Conversion From Ocular Hypertension To Glaucoma. Arch Ophthalmol, 123, 1351-60.

Meek, K. M. & Boote, C. 2009. The Use Of X-Ray Scattering Techniques To Quantify The Orientation And Distribution Of Collagen In The Corneal Stroma. Progress In Retinal And Eye Research, 28, 369-392.

Meek, K. M. & Leonard, D. W. 1993. Ultrastructure Of The Corneal Stroma: A Comparative Study. Biophysical Journal, 64, 273-280.

Meek, K. M. & Quantock, A. J. 2001. The Use Of X-Ray Scattering Techniques To Determine Corneal Ultrastructure. Progress In Retinal And Eye Research, 20, 95-137.

Meek, K. M. 2009. Corneal Collagen-Its Role In Maintaining Corneal Shape And Transparency. Biophys Rev, 1, 83-93.

Meek, K. M., Blamires, T., Elliott, G. F., Gyi, T. J. & Nave, C. 1987. The Organisation Of Collagen Fibrils In The Human Corneal Stroma: A Synchrotron X-Ray Diffraction Study. Current Eye Research, 6, 841-846.

Meek, K. M., Fullwood, N. J., Cooke, P. H., Elliott, G. F., Maurice, D. M., Quantock, A. J., Wall, R. S. & Worthington, C. R. 1991. Synchrotron X-Ray Diffraction Studies Of The Cornea, With Implications For Stromal Hydration. Biophysical Journal, 60, 467-474.

Meijering, E., Jacob, M., Sarria, J. C. F., Steiner, P., Hirling, H. & Unser, M. 2004. Design And Validation Of A Tool For Neurite Tracing And Analysis In Fluorescence Microscopy Images. Cytometry Part A, 58a, 167-176.

Melles, G. R. J. & Binder, P. S. 1990. A Comparison Of Wound Healing In Sutured And Unsutured Corneal Wounds. Archives Of Ophthalmology, 108, 1460-1469.
Meng, Z., Petrov, G. I. & Yakovlev, V. V. 2015. Flow Cytometry Using Brillouin Imaging And Sensing Via Time-Resolved Optical (Bistro) Measurements. Analyst, 140, 7160-7164.

Metscher, B. D. 2009. Microct For Comparative Morphology: Simple Staining Methods Allow High-Contrast 3d Imaging Of Diverse Non-Mineralized Animal Tissues. Bmc Physiol, 9, 11.

Metscher, B. D. 2009b. Microct For Developmental Biology: A Versatile Tool For High-Contrast 3d Imaging At Histological Resolutions. Dev Dyn, 238, 632-40.
Mikula, S. & Denk, W. 2015. High-Resolution Whole-Brain Staining For Electron Microscopic Circuit Reconstruction. Nature Methods, 12, 541.

Millard, A., Jin, L., Wuskell, J., Boudreau, D., Lewis, A. & Loew, L. 2005. Wavelength-And Time-Dependence Of Potentiometric Non-Linear Optical Signals From Styryl Dyes. The Journal Of Membrane Biology, 208, 103-111.

Millen, J. W. & Woollam, D. H. 1961. On The Nature Of The Pia Mater. Brain, 84, 514-20.

Miller, A. & Wray, J. S. 1971. Molecular Packing In Collagen. Nature, 230, 437-439.
Miller, K. M. & Quigley, H. A. 1988. The Clinical Appearance Of The Lamina Cribrosa As A Function Of The Extent Of Glaucomatous Optic Nerve Damage. Ophthalmology, 95, 135-138.

Minckler, D. S., Bunt, A. H. & Johanson, G. W. 1977. Orthograde And Retrograde Axoplasmic Transport During Acute Ocular Hypertension In The Monkey. Invest Ophthalmol Vis Sci, 16, 426-41.

Mitchell, G. F. 2008. Effects Of Central Arterial Aging On The Structure And Function Of The Peripheral Vasculature: Implications For End-Organ Damage. J Appl Physiol (1985), 105, 1652-60.

Mitchell, R. E. 1967. Chronic Solar Dermatosis: A Light And Electron Microscopic Study Of The Dermis*. Journal Of Investigative Dermatology, 48, 203-220.
Mithieux, S. M. & Weiss, A. S. 2005. Elastin. Adv Protein Chem, 70, 437-61.

Modesti, A., Kalebic, T., Scarpa, S., Togo, S., Grotendorst, G., Liotta, L. A. & Triche, T. J. 1984. Type V Collagen In Human Amnion Is A 12 Nm Fibrillar Component Of The Pericellular Interstitium. Eur J Cell Biol, 35, 246-55.

Moeller, H. D., Bosch, U. & Decker, B. 1995. Collagen Fibril Diameter Distribution In Patellar Tendon Autografts After Posterior Cruciate Ligament Reconstruction In Sheep: Changes Over Time. Journal Of Anatomy, 187 (Pt 1), 161-167.

Mohler, W., Millard, A. C. & Campagnola, P. J. 2003. Second Harmonic Generation Imaging Of Endogenous Structural Proteins. Methods, 29, 97-109.

Molnár-Perl, I. 2005. Quantitation Of Amino Acids And Amines By Chromatography: Methods And Protocols, Elsevier.

Monnier, V. M. 1990. Nonenzymatic Glycosylation, The Maillard Reaction And The Aging Process. J Gerontol, 45, B105-11.

Montes, G. S., Bezerra, M. S. & Junqueira, L. C. 1984. Collagen Distribution In Tissues. Ultrastructure Of The Connective Tissue Matrix. Springer.

Morgan, W. H., Chauhan, B. C., Yu, D. Y., Cringle, S. J., Alder, V. A. & House, P. H. 2002. Optic Disc Movement With Variations In Intraocular And Cerebrospinal Fluid Pressure. Invest Ophthalmol Vis Sci, 43, 3236-42.

Morgan, W. H., Yu, D. Y. & Balaratnasingam, C. 2008. The Role Of Cerebrospinal Fluid Pressure In Glaucoma Pathophysiology: The Dark Side Of The Optic Disc. J Glaucoma, 17, 408-13.

Morissette, J., Cote, G., Anctil, J. L., Plante, M., Amyot, M., Heon, E., Trope, G. E., Weissenbach, J. & Raymond, V. 1995. A Common Gene For Juvenile And Adult-Onset Primary Open-Angle Glaucomas Confined On Chromosome 1q. Am J Hum Genet, 56, 1431-42.

Morocutti, M., Raspanti, M., Ottani, V., Govoni, P. & Ruggeri, A. 1991. Ultrastructure Of The Bovine Nuchal Ligament. J Anat, 178, 145-54.

Morrison, J. C., Dorman-Pease, M. E., Dunkelberger, G. R. & Quigley, H. A. 1990. Optic Nerve Head Extracellular Matrix In Primary Optic Atrophy And Experimental Glaucoma. Arch Ophthalmol, 108, 1020-4.

Morrison, J. C., Jerdan, J. A., Dorman, M. E. & Quigley, H. A. 1989a. Structural Proteins Of The Neonatal And Adult Lamina Cribrosa. Arch Ophthalmol, 107, 1220-4.

Morrison, J. C., Jerdan, J. A., L'hernault, N. L. & Quigley, H. A. 1988. The Extracellular Matrix Composition Of The Monkey Optic Nerve Head. Invest Ophthalmol Vis Sci, 29, 1141-50.

Morrison, J. C., L'hernault, N. L., Jerdan, J. A. & Quigley, H. A. 1989b. Ultrastructural Location Of Extracellular Matrix Components In The Optic Nerve Head. Arch Ophthalmol, 107, 123-9.

Morrison, J. C., Rask, P., Johnson, E. C. & Deppmeier, L. 1994. Chondroitin Sulfate Proteoglycan Distribution In The Primate Optic Nerve Head. Investigative Ophthalmology & Visual Science, 35, 838-845.

Murakami, T. 1973. A Metal Impregnation Method Of Biological Specimens For Scanning Electron Microscopy. Arch Histol Jpn, 35, 323-6.

Muto, J., Kuroda, K., Wachi, H., Hirose, S. & Tajima, S. 2007. Accumulation Of Elafin In Actinic Elastosis Of Sun-Damaged Skin: Elafin Binds To Elastin And Prevents Elastolytic Degradation. J Invest Dermatol, 127, 1358-66.

Na, R., Stender, I. M., Henriksen, M. & Wulf, H. C. 2001. Autofluorescence Of Human Skin Is Age-Related After Correction For Skin Pigmentation And Redness. J Invest Dermatol, 116, 536-40.

Nadler, Z., Wang, B., Wollstein, G., Nevins, J. E., Ishikawa, H., Kagemann, L., Sigal, I. A., Ferguson, R. D., Hammer, D. X., Grulkowski, I., Liu, J. J., Kraus, M. F., Lu, C. D., Hornegger, J., Fujimoto, J. G. & Schuman, J. S. 2013. Automated Lamina Cribrosa Microstructural Segmentation In Optical Coherence Tomography Scans Of Healthy And Glaucomatous Eyes. Biomed Opt Express, 4, 2596-608.

Naffa, R., Edwards, P. J. B. & Norris, G. 2019. Isolation And Characterization Of Collagen Type I Crosslink From Skin: High-Resolution Nmr Reveals Diastereomers Of Hydroxylysinonorleucine Crosslink. Amino Acids, 51, 705-715.

Narayanan, C. & Dias, C. L. 2013. Hydrophobic Interactions And Hydrogen Bonds In B-Sheet Formation. The Journal Of Chemical Physics, 139, 09b640_1.

Nejjar, I., Pieraggi, M.-T., Thiers, J. C. & Bouissou, H. 1990. Age-Related Changes In The Elastic Tissue Of The Human Thoracic Aorta. Atherosclerosis, 80, 199-208.

Netland, P. A., Ye, H., Streeten, B. W. & Hernandez, M. R. 1995. Elastosis Of The Lamina Cribrosa In Pseudoexfoliation Syndrome With Glaucoma. Ophthalmology, 102, 878-86.

Neufeld, A. H. 1999a. Microglia In The Optic Nerve Head And The Region Of Parapapillary Chorioretinal Atrophy In Glaucoma. Arch Ophthalmol, 117, 1050-6.

Neufeld, A. H. 1999b. Nitric Oxide: A Potential Mediator Of Retinal Ganglion Cell Damage In Glaucoma. Survey Of Ophthalmology, 43, Supplement 1, S129-S135.

Neufeld, A. H., Hernandez, M. R. & Gonzalez, M. 1997. Nitric Oxide Synthase In The Human Glaucomatous Optic Nerve Head. Arch Ophthalmol, 115, 497-503.

Nguyen, T. D., Chen, P., Huang, W. D., Chen, H., Johnson, D. & Polansky, J. R. 1998. Gene Structure And Properties Of Tigr, An Olfactomedin-Related Glycoprotein Cloned From Glucocorticoid-Induced Trabecular Meshwork Cells. J Biol Chem, 273, 6341-50.

Nguyen, T., Gobinet, C., Feru, J., Pasco, S. B., Manfait, M. & Piot, O. 2012. Characterization Of Type I And Iv Collagens By Raman Microspectroscopy: Identification Of Spectral Markers Of The Dermo-Epidermal Junction. Journal Of Spectroscopy, 27, 421-427.

Nierenberger, M., Remond, Y., Ahzi, S. & Choquet, P. 2015. Assessing The Three-Dimensional Collagen Network In Soft Tissues Using Contrast Agents And High Resolution Micro-Ct: Application To Porcine Iliac Veins. C R Biol, 338, 425-33.

Norman, R. E., Flanagan, J. G., Rausch, S. M., Sigal, I. A., Tertinegg, I., Eilaghi, A., Portnoy, S., Sled, J. G. & Ethier, C. R. 2010. Dimensions Of The Human Sclera: Thickness Measurement And Regional Changes With Axial Length. Exp Eye Res, 90, 277-84.

Norman, R. E., Flanagan, J. G., Sigal, I. A., Rausch, S. M., Tertinegg, I. & Ethier, C. R. 2011. Finite Element Modeling Of The Human Sclera: Influence On Optic Nerve Head Biomechanics And Connections With Glaucoma. Exp Eye Res, 93, 4-12.

Notingher, I., Green, C., Dyer, C., Perkins, E., Hopkins, N., Lindsay, C. & Hench, L. L. 2004. Discrimination Between Ricin And Sulphur Mustard Toxicity In Vitro Using Raman Spectroscopy. J R Soc Interface, 1, 79-90.

O'connell, M. K., Murthy, S., Phan, S., Xu, C., Buchanan, J., Spilker, R., Dalman, R. L., Zarins, C. K., Denk, W. & Taylor, C. A. 2008. The Three-Dimensional Micro-And Nanostructure Of The Aortic Medial Lamellar Unit Measured Using 3d Confocal And Electron Microscopy Imaging. Matrix Biology, 27, 171-181.

Ogden, T. E., Duggan, J., Danley, K., Wilcox, M. & Minckler, D. S. 1988. Morphometry Of Nerve Fiber Bundle Pores In The Optic Nerve Head Of The Human. Experimental Eye Research, 46, 559-568.

Orgel, J. P., Miller, A., Irving, T. C., Fischetti, R. F., Hammersley, A. P. & Wess, T. J. 2001. The In Situ Supermolecular Structure Of Type I Collagen. Structure, 9, 1061-9.
O'rourke, M. F. & Hashimoto, J. 2007. Mechanical Factors In Arterial Aging: A Clinical Perspective. J Am Coll Cardiol, 50, 1-13.

Orr, S. F. 1954. Infra-Red Spectroscopic Studies Of Some Polysaccharides. Biochim Biophys Acta, 14, 173-81.

Oster, G. & Riley, D. P. 1952. Scattering From Isotropic Colloidal And Macro-Molecular Systems. Acta Crystallographica, 5, 1-6.

Oyama, T., Abe, H. & Ushiki, T. 2006. The Connective Tissue And Glial Framework In The Optic Nerve Head Of The Normal Human Eye: Light And Scanning Electron Microscopic Studies. Arch Histol Cytol, 69, 341-56.

Palay, S. L., Mcgee-Russell, S., Gordon, S. & Grillo, M. A. 1962. Fixation Of Neural Tissues For Electron Microscopy By Perfusion With Solutions Of Osmium Tetroxide. The Journal Of Cell Biology, 12, 385-410.

Palombo, F., Madami, M., Fioretto, D., Nallala, J., Barr, H., David, A. & Stone, N. 2016. Chemico-Mechanical Imaging Of Barrett's Oesophagus. J Biophotonics, 9, 694-700.

Palombo, F., Madami, M., Stone, N. & Fioretto, D. 2014. Mechanical Mapping With Chemical Specificity By Confocal Brillouin And Raman Microscopy. Analyst, 139, 729-733.

Papini, A. M. & Konig, E. 2015. Novel Diagnostic Tools And Solutions For Multiple Sclerosis Treatment: A Patent Review (2009 - 2014). Expert Opin Ther Pat, 25, 873-84.

Park, H. Y., Jeon, S. H. & Park, C. K. 2012. Enhanced Depth Imaging Detects Lamina Cribrosa Thickness Differences In Normal Tension Glaucoma And Primary Open-Angle Glaucoma. Ophthalmology, 119, 10-20.

Park, H. Y., Jeon, S. H. & Park, C. K. 2012. Enhanced Depth Imaging Detects Lamina Cribrosa Thickness Differences In Normal Tension Glaucoma And Primary Open-Angle Glaucoma. Ophthalmology, 119, 10-20.

Park, S. C., Furlanetto, R., Netto, C., Liu, Y., Kung, Y., Fernando-Sieminski, S., Liebmann, J. & Ritch, R. 2013. Posterior Lamina Cribrosa Displacement At Different Stages Of Glaucoma. Investigative Ophthalmology & Visual Science, 54, 5917-5917.

Parry, D. A. 1988. The Molecular And Fibrillar Structure Of Collagen And Its Relationship To The Mechanical Properties Of Connective Tissue. Biophys Chem, 29, 195-209.

Parry, D. A. D., Craig, A. S., Barnes, G. R. G. & Phillips David, C. 1978b. Tendon And Ligament From The Horse: An Ultrastructural Study Of Collagen Fibrils And Elastic Fibres As A Function Of Age. Proceedings Of The Royal Society Of London. Series B. Biological Sciences, 203, 293-303.
Parry, D. A., Barnes, G. R. & Craig, A. S. 1978a. A Comparison Of The Size Distribution Of Collagen Fibrils In Connective Tissues As A Function Of Age And A Possible Relation Between Fibril Size Distribution And Mechanical Properties. Proc R Soc Lond B Biol Sci, 203, 305-21.

Partridge, S. M. & Keeley, F. W. 1974. Age Related And Atherosclerotic Changes In Aortic Elastin. In: Wagner, W. D. & Clarkson, T. B. (Eds.) Arterial Mesenchyme And Arteriosclerosis. Boston, Ma: Springer Us.

Pasquali-Ronchetti, I. & Baccarani-Contri, M. 1997. Elastic Fiber During Development And Aging. Microsc Res Tech, 38, 428-35.

Paulus, M. J., Gleason, S. S., Kennel, S. J., Hunsicker, P. R. & Johnson, D. K. 2000. High Resolution X-Ray Computed Tomography: An Emerging Tool For Small Animal Cancer Research. Neoplasia, 2, 62-70.

Pena, J. D., Netland, P. A., Vidal, I., Dorr, D. A., Rasky, A. & Hernandez, M. R. 1998. Elastosis Of The Lamina Cribrosa In Glaucomatous Optic Neuropathy. Exp Eye Res, 67, 517-24.

Pena, J. D., Roy, S. & Hernandez, M. R. 1996. Tropoelastin Gene Expression In Optic Nerve Heads Of Normal And Glaucomatous Subjects. Matrix Biol, 15, 323-30.

Peters, A. 2002. The Effects Of Normal Aging On Myelin And Nerve Fibers: A Review. J Neurocytol, 31, 581-93.

Petruska, J. A. & Hodge, A. J. 1964. A Subunit Model For The Tropocollagen Macromolecule. Proceedings Of The National Academy Of Sciences, 51, 871-876.

Pijanka, J. K., Abass, A., Sorensen, T., Elsheikh, A. & Boote, C. 2013. A Wide-Angle X-Ray Fibre Diffraction Method For Quantifying Collagen Orientation Across Large Tissue Areas: Application To The Human Eyeball Coat. Journal Of Applied Crystallography, 46, 1481-1489.

Pijanka, J. K., Coudrillier, B., Ziegler, K., Sorensen, T., Meek, K. M., Nguyen, T. D., Quigley, H. A. & Boote, C. 2012. Quantitative Mapping Of Collagen Fiber Orientation In Non-Glaucoma And Glaucoma Posterior Human Sclerae. Invest Ophthalmol Vis Sci, 53, 5258-70.

Pijanka, J. K., Markov, P. P., Midgett, D., Paterson, N. G., White, N., Blain, E. J., Nguyen, T. D., Quigley, H. A. & Boote, C. 2019. Quantification Of Collagen Fiber Structure Using Second Harmonic Generation Imaging And Two-Dimensional Discrete Fourier Transform Analysis: Application To The Human Optic Nerve Head. J Biophotonics, 12, E201800376.

Porta, E. A. 2002. Pigments In Aging: An Overview. Ann N Y Acad Sci, 959, 57-65.

Porter, K. & Kallman, F. 1953. The Properties And Effects Of Osmium Tetroxide As A Tissue Fixative With Special Reference To Its Use For Electron Microscopy. Experimental Cell Research, 4, 127-141.

Purslow, P. P. 1989. Strain-Induced Reorientation Of An Intramuscular Connective Tissue Network: Implications For Passive Muscle Elasticity. J Biomech, 22, 21-31.

Purushothaman, K. R., Purushothaman, M., Turnbull, I. C., Adams, D. H., Anyanwu, A., Krishnan, P., Kini, A., Sharma, S. K., O'connor, W. N. & Moreno, P. R. 2017. Association Of Altered Collagen Content And Lysyl Oxidase Expression In Degenerative Mitral Valve Disease. Cardiovasc Pathol, 29, 11-18.

Puspoki, Z., Storath, M., Sage, D. & Unser, M. 2016. Transforms And Operators For Directional Bioimage Analysis: A Survey. Adv Anat Embryol Cell Biol, 219, 69-93.

Quantock, A. J. & Meek, K. M. 1988. Axial Electron Density Of Human Scleral Collagen. Location Of Proteoglycans By X-Ray Diffraction. Biophys J, 54, 159-64.

Quantock, A. J., Winkler, M., Parfitt, G. J., Young, R. D., Brown, D. J., Boote, C. & Jester, J. V. 2015. From Nano To Macro: Studying The Hierarchical Structure Of The Corneal Extracellular Matrix. Experimental Eye Research, 133, 81-99.

Quigley, E. N., Quigley, H. A., Pease, M. E. & Kerrigan, L. A. 1996. Quantitative Studies Of Elastin In The Optic Nerve Heads Of Persons With Primary Open-Angle Glaucoma. Ophthalmology, 103, 1680-1685.

Quigley, H. & Anderson, D. R. 1976. The Dynamics And Location Of Axonal Transport Blockade By Acute Intraocular Pressure Elevation In Primate Optic Nerve. Invest Ophthalmol, 15, 606-16.

Quigley, H. & Broman, A. 2006. The Number Of People With Glaucoma Worldwide In 2010 And 2020. Br J Ophthalmol, 90.

Quigley, H. A. & Addicks, E. M. 1981. Regional Differences In The Structure Of The Lamina Cribrosa And Their Relation To Glaucomatous Optic Nerve Damage. Arch Ophthalmol, 99, 137-43.

Quigley, H. A. & Broman, A. T. 2006. The Number Of People With Glaucoma Worldwide In 2010 And 2020. Br J Ophthalmol, 90, 262-7.

Quigley, H. A. & Green, W. R. 1979. The Histology Of Human Glaucoma Cupping And Optic Nerve Damage: Clinicopathologic Correlation In 21 Eyes. Ophthalmology, 86, 1803-30.

Quigley, H. A. 2011. Glaucoma. Lancet, 377, 1367-77.
Quigley, H. A., Addicks, E. M. & Green, W. R. 1982. Optic Nerve Damage In Human Glaucoma: Iii. Quantitative Correlation Of Nerve Fiber Loss And Visual Field Defect In Glaucoma, Ischemic Neuropathy, Papilledema, And Toxic Neuropathy. Archives Of Ophthalmology, 100, 135-146.

Quigley, H. A., Addicks, E. M., Green, W. R. & Maumenee, A. E. 1981. Optic Nerve Damage In Human Glaucoma. Ii. The Site Of Injury And Susceptibility To Damage. Arch Ophthalmol, 99, 635-49.

Quigley, H. A., Brown, A. & Dorman-Pease, M. E. 1991a. Alterations In Elastin Of The Optic Nerve Head In Human And Experimental Glaucoma. Br J Ophthalmol, 75, 552-7.

Quigley, H. A., Brown, A. E., Morrison, J. D. & Drance, S. M. 1990. The Size And Shape Of The Optic Disc In Normal Human Eyes. Arch Ophthalmol, 108, 51-7.

Quigley, H. A., Dorman-Pease, M. E. & Brown, A. E. 1991. Quantitative Study Of Collagen And Elastin Of The Optic Nerve Head And Sclera In Human And Experimental Monkey Glaucoma. Curr Eye Res, 10, 877-88.

Quigley, H. A., Hohman, R. M., Addicks, E. M., Massof, R. W. & Green, W. R. 1983. Morphologic Changes In The Lamina Cribrosa Correlated With Neural Loss In Open-Angle Glaucoma. Am J Ophthalmol, 95, 673-91.
Open-Angle Glaucoma. Am J Ophthalmol, 95, 673-91.

Quigley, H., Pease, M. E. & Thibault, D. 1994. Change In The Appearance Of Elastin In The Lamina Cribrosa Of Glaucomatous Optic Nerve Heads. Graefe's Archive For Clinical And Experimental Ophthalmology, 232, 257-261.

Radius, R. L. & Gonzales, M. 1981. Anatomy Of The Lamina Cribrosa In Human Eyes. Arch Ophthalmol, 99, 2159-62.

Raine, C. S. 1984. Morphology Of Myelin And Myelination. In: Morell, P. (Ed.) Myelin. Boston, Ma: Springer Us.

Rajpal, G. & Arvan, P. 2013. Chapter 236 - Disulfide Bond Formation. In: Kastin, A. J. (Ed.) Handbook Of Biologically Active Peptides (Second Edition). Boston: Academic Press.

Ramachandran, G. N. & Kartha, G. 1954. Structure Of Collagen. Nature, 174, 269-270.
Rao, P. V., Allingham, R. R. & Epstein, D. L. 2000. Tigr/Myocilin In Human Aqueous Humor. Exp Eye Res, 71, 637-41.

Rau, C., Bodey, A., Storm, M., Cipiccia, S., Marathe, S., Zdora, M.-C., Zanette, I., Wagner, U., Batey, D. & Shi, X. 2017. Micro- And Nano-Tomography At The Diamond Beamline I13l Imaging And Coherence, Spie.

Rau, C., Wagner, U., Pešić, Z. & De Fanis, A. 2011. Coherent Imaging At The Diamond Beamline I13. Physica Status Solidi (A), 208, 2522-2525.

Rawe, I. M., Meek, K. M., Leonard, D. W., Takahashi, T. & Cintron, C. 1994. Structure Of Corneal Scar Tissue: An X-Ray Diffraction Study. Biophys J, 67, 1743-8.

Regini, J. W., Grossmann, J. G., Burgio, M. R., Malik, N. S., Koretz, J. F., Hodson, S. A. & Elliott, G. F. 2004. Structural Changes In Alpha-Crystallin And Whole Eye Lens During Heating, Observed By Low-Angle X-Ray Diffraction. J Mol Biol, 336, 1185-94.

Rehnberg, M., Ammitzböll, T. & Tengroth, B. 1987. Collagen Distribution In The Lamina Cribrosa And The Trabecular Meshwork Of The Human Eye. British Journal Of Ophthalmology, 71, 886-892.

Reiß, S., Burau, G., Stachs, O., Guthoff, R. & Stolz, H. 2011. Spatially Resolved Brillouin Spectroscopy To Determine The Rheological Properties Of The Eye Lens. Biomedical Optics Express, 2, 2144-2159.

Reiß, S., Sperlich, K., Hovakimyan, M., Martius, P., Guthoff, R. F., Stolz, H. & Stachs, O. 2012. Ex Vivo Measurement Of Postmortem Tissue Changes In The Crystalline Lens By Brillouin Spectroscopy And Confocal Reflectance Microscopy. Ieee Transactions On Biomedical Engineering, 59, 2348-2354.

Ren, R., Jonas, J. B., Tian, G., Zhen, Y., Ma, K., Li, S., Wang, H., Li, B., Zhang, X. & Wang, N. 2010. Cerebrospinal Fluid Pressure In Glaucoma: A Prospective Study. Ophthalmology, 117, 259-66.

Ren, R., Li, B., Gao, F., Li, L., Xu, X., Wang, N. & Jonas, J. B. 2010. Central Corneal Thickness, Lamina Cribrosa And Peripapillary Scleral Histomorphometry In Non-Glaucomatous Chinese Eyes. Graefes Arch Clin Exp Ophthalmol, 248, 1579-85.

Ren, R., Wang, N., Li, B., Li, L., Gao, F., Xu, X. & Jonas, J. B. 2009. Lamina Cribrosa And Peripapillary Sclera Histomorphometry In Normal And Advanced Glaucomatous Chinese Eyes With Various Axial Length. Invest Ophthalmol Vis Sci, 50, 2175-84.

Renugopalakrishnan, V., Zheng, S., Tu, A. T. & Damle, S. P. 1989. Secondary Structure Of Pig Skin Proteodermatan Sulfate: A Perspective From Raman Spectroscopic Studies In Aqueous Solution. Biopolymers, 28, 1935-8.

Reynaud, J., Lockwood, H., Gardiner, S. K., Williams, G., Yang, H. & Burgoyne, C. F. 2016. Lamina Cribrosa Microarchitecture In Monkey Early Experimental Glaucoma: Global Change. Investigative Ophthalmology & Visual Science, 57, 3451-3469.

Rezakhaniha, R., Agianniotis, A., Schrauwen, J. T. C., Griffa, A., Sage, D., Bouten, C., Van De Vosse, F., Unser, M. & Stergiopulos, N. 2012. Experimental Investigation Of Collagen Waviness And Orientation In The Arterial Adventitia Using Confocal Laser Scanning Microscopy. Biomechanics And Modeling In Mechanobiology, 11, 461-473.

Ricard-Blum, S. & Ruggiero, F. 2005. The Collagen Superfamily: From The Extracellular Matrix To The Cell Membrane. Pathol Biol (Paris), 53, 430-42.

Ricard-Blum, S. 2011. The Collagen Family. Cold Spring Harbor Perspectives In Biology, 3, A004978.

Roberts, M. D., Grau, V., Grimm, J., Reynaud, J., Bellezza, A. J., Burgoyne, C. F. & Downs, J. C. 2009. Remodeling Of The Connective Tissue Microarchitecture Of The Lamina Cribrosa In Early Experimental Glaucoma. Invest Ophthalmol Vis Sci, 50.

Roberts, M. D., Liang, Y., Sigal, I. A., Grimm, J., Reynaud, J., Bellezza, A., Burgoyne, C. F. & Downs, J. C. 2010. Correlation Between Local Stress And Strain And Lamina Cribrosa Connective Tissue Volume Fraction In Normal Monkey Eyes. Investigative Ophthalmology & Visual Science, 51, 295-307.

Robins, S. P. 2007. Biochemistry And Functional Significance Of Collagen Cross-Linking. Biochem Soc Trans, 35, 849-52.

Robinson, B. K., Cortes, E., Rice, A. J., Sarper, M. & Del Rio Hernandez, A. 2016. Quantitative Analysis Of 3d Extracellular Matrix Remodelling By Pancreatic Stellate Cells. Biol Open, 5, 875-82.

Rodnan, G. P., Lipinski, E. & Luksick, J. 1979. Skin Thickness And Collagen Content In Progressive Systemic Sclerosis And Localized Scleroderma. Arthritis Rheum, 22, 130-40.

Rogers, R., Dharsee, M., Ackloo, S. & Flanagan, J. G. 2012. Proteomics Analyses Of Activated Human Optic Nerve Head Lamina Cribrosa Cells Following Biomechanical Strainprotein Regulation Analysis After Activation Of Human Onh Lc Cells. Investigative Ophthalmology & Visual Science, 53, 3806-3816.

Roholl, P. J., Leene, W., Kapsenberg, M. L. & Vos, J. G. 1981. The Use Of Tannic Acid Fixation For The Electron Microscope Visualization Of Fluorochrome-Labelled Antibodies Attached To Cell Surface Antigens. J Immunol Methods, 42, 285-9.

Rosenbloom, J., Abrams, W. R. & Mecham, R. 1993. Extracellular Matrix 4: The Elastic Fiber. Faseb J, 7, 1208-18.

Ross, R. & Bornstein, P. 1969. The Elastic Fiber. I. The Separation And Partial Characterization Of Its Macromolecular Components. J Cell Biol, 40, 366-81.

Ross, R. & Bornstein, P. 1969. The Elastic Fiber. I. The Separation And Partial Characterization Of Its Macromolecular Components. J Cell Biol, 40, 366-81.

Roveri, N., Ripamonti, A., Pulga, C., Jeronimidis, G., Purslow, P. P., Volpin, D. & Gotte, L. 1980. Mechanical Behaviour Of Aortic Tissue As A Function Of Collagen Orientation. Die Makromolekulare Chemie, 181, 1999-2007.

Rowe, R. W. 1985. The Structure Of Rat Tail Tendon. Connect Tissue Res, 14, 9-20.

Russell, J. P. 1965. The Raman Spectrum Of Calcium Fluoride. Proceedings Of The Physical Society, 85, 194-199-2.

Russell, P., Tamm, E. R., Grehn, F. J., Picht, G. & Johnson, M. 2001. The Presence And Properties Of Myocilin In The Aqueous Humor. Invest Ophthalmol Vis Sci, 42, 983-6.

Sacca, S. C., Pascotto, A., Camicione, P., Capris, P. & Izzotti, A. 2005. Oxidative Dna Damage In The Human Trabecular Meshwork: Clinical Correlation In Patients With Primary Open-Angle Glaucoma. Arch Ophthalmol, 123, 458-63.

Sakai, H., Shen, X., Koga, T., Park, B. C., Noskina, Y., Tibudan, M. & Yue, B. Y. 2007. Mitochondrial Association Of Myocilin, Product Of A Glaucoma Gene, In Human Trabecular Meshwork Cells. J Cell Physiol, 213, 775-84.

Sandell, J. H. & Peters, A. 2001. Effects Of Age On Nerve Fibers In The Rhesus Monkey Optic Nerve. J Comp Neurol, 429, 541-53.

Sans, M. & Moragas, A. 1993. Mathematical Morphologic Analysis Of The Aortic Medial Structure. Biomechanical Implications. Anal Quant Cytol Histol, 15, 93-100.

Sato, E. & Martinho, H. 2018. First-Principles Calculations Of Raman Vibrational Modes In The Fingerprint Region For Connective Tissue. Biomedical Optics Express, 9, 1728-1734.

Sawaguchi, S., Yue, B. Y., Fukuchi, T., Iwata, K. & Kaiya, T. 1992. Sulfated Proteoglycans In The Human Lamina Cribrosa. Invest Ophthalmol Vis Sci, 33, 2388-98.

Sawaguchi, S., Yue, B. Y., Fukuchi, T., Iwata, K. & Kaiya, T. 1993. Age-Related Changes Of Sulfated Proteoglycans In The Human Lamina Cribrosa. Curr Eye Res, 12, 685-92.

Sayers, Z., Koch, M. H., Whitburn, S. B., Meek, K. M., Elliott, G. F. & Harmsen, A. 1982. Synchrotron X-Ray Diffraction Study Of Corneal Stroma. Journal Of Molecular Biology, 160, 593-607.

Scarcelli, G. & Yun, S. H. 2007a. Confocal Brillouin Microscopy For Three-Dimensional Mechanical Imaging. Nature Photonics, 2, 39.

Scarcelli, G. & Yun, S. H. 2012. In Vivo Brillouin Optical Microscopy Of The Human Eye. Optics Express, 20, 9197-9202.

Scarcelli, G. & Yun, S. H. Three-Dimensional Brillouin Confocal Microscopy. Conference On Lasers And Electro-Optics, 2007b. Optical Society Of America, Ctuv5.

Scarcelli, G., Besner, S., Pineda, R. & Yun, S. H. 2014. Biomechanical Characterization Of Keratoconus Corneas Ex Vivo With Brillouin Microscopy. Investigative Ophthalmology & Visual Science, 55, 4490-4495.

Scarcelli, G., Kim, P. & Yun, S. H. 2011. In Vivo Measurement Of Age-Related Stiffening In The Crystalline Lens By Brillouin Optical Microscopy. Biophysical Journal, 101, 1539-1545.

Scarcelli, G., Kling, S., Quijano, E., Pineda, R., Marcos, S. & Yun, S. H. 2013. Brillouin Microscopy Of Collagen Crosslinking: Noncontact Depth-Dependent Analysis Of Corneal Elastic Modulus. Investigative Ophthalmology & Visual Science, 54, 1418-1425.

Scarcelli, G., Pineda, R. & Yun, S. H. 2012. Brillouin Optical Microscopy For Corneal Biomechanics. Investigative Ophthalmology & Visual Science, 53, 185-190.

Scarcelli, G., Polacheck, W. J., Nia, H. T., Patel, K., Grodzinsky, A. J., Kamm, R. D. & Yun, S. H. 2015. Noncontact Three-Dimensional Mapping Of Intracellular Hydro-Mechanical Properties By Brillouin Microscopy. Nature Methods, 12, 1132-1134.

Schenke-Layland, K. 2008. Non-Invasive Multiphoton Imaging Of Extracellular Matrix Structures. Journal Of Biophotonics, 1, 451-462.

Schenke-Layland, K., Riemann, I., Opitz, F., Konig, K., Halbhuber, K. J. & Stock, U. A. 2004. Comparative Study Of Cellular And Extracellular Matrix Composition Of Native And Tissue Engineered Heart Valves. Matrix Biol, 23, 113-25.

Schmidt, A. M., Yan, S. D., Yan, S. F. & Stern, D. M. 2000. The Biology Of The Receptor For Advanced Glycation End Products And Its Ligands. Biochim Biophys Acta, 1498, 99-111.

Schmitt, F. O., Bear, R. S. & Clark, G. L. 1935. X-Ray Diffraction Studies On Nerve. Radiology, 25, 131-151.

Schmitt, F. O., Bear, R. S. & Palmer, K. J. 1941. X-Ray Diffraction Studies On The Structure Of The Nerve Myelin Sheath. Journal Of Cellular And Comparative Physiology, 18, 31-42.

Scott, J. E. 1980. Collagen--Proteoglycan Interactions. Localization Of Proteoglycans In Tendon By Electron Microscopy. Biochem J, 187, 887-91.

Scott, J. E., Orford, C. R. & Hughes, E. W. 1981. Proteoglycan-Collagen Arrangements In Developing Rat Tail Tendon. An Electron Microscopical And Biochemical Investigation. Biochemical Journal, 195, 573-581.

Selhorst, J. B. & Chen, Y. 2009. The Optic Nerve. Semin Neurol, 29, 29-35.
Serafini-Fracassini, A. & Field, J. M. 1977. X-Ray Analysis Of Enzymically Purified Elastin From Bovine Ligamentum Nuchae. Adv Exp Med Biol, 79, 679-83.

Shadwick, R. E. 1999. Mechanical Design In Arteries. J Exp Biol, 202, 3305-13.
Shah, R. R., Nerurkar, N. L., Wang, C. C. & Galloway, J. L. 2015. Tensile Properties Of Craniofacial Tendons In The Mature And Aged Zebrafish. J Orthop Res, 33, 867-73.

Shapiro, S. D., Endicott, S. K., Province, M. A., Pierce, J. A. & Campbell, E. J. 1991.
Marked Longevity Of Human Lung Parenchymal Elastic Fibers Deduced From Prevalence Of D-Aspartate And Nuclear Weapons-Related Radiocarbon. J Clin Invest, 87, 1828-34.

Shetty, G., Kendall, C., Shepherd, N., Stone, N. & Barr, H. 2006. Raman Spectroscopy: Elucidation Of Biochemical Changes In Carcinogenesis Of Oesophagus. British Journal Of Cancer, 94, 1460-1464.

Shirshin, E. A., Gurfinkel, Y. I., Priezzhev, A. V., Fadeev, V. V., Lademann, J. & Darvin, M. E. 2017. Two-Photon Autofluorescence Lifetime Imaging Of Human Skin Papillary Dermis In Vivo: Assessment Of Blood Capillaries And Structural Proteins Localization. Scientific Reports, 7, 1171.

Shoulders, M. D. & Raines, R. T. 2009. Collagen Structure And Stability. Annu Rev Biochem, 78, 929-58.

Siegner, S. W. & Netland, P. A. 1996. Optic Disc Hemorrhages And Progression Of Glaucoma. Ophthalmology, 103, 1014-24.

Sigal, I. A. & Ethier, C. R. 2009. Biomechanics Of The Optic Nerve Head. Experimental Eye Research, 88, 799-807.

Sigal, I. A. 2009. Interactions Between Geometry And Mechanical Properties On The Optic Nerve Head. Invest Ophthalmol Vis Sci, 50, 2785-95.

Sigal, I. A., Flanagan, J. G. & Ethier, C. R. 2005a. Factors Influencing Optic Nerve Head Biomechanics. Investigative Ophthalmology & Visual Science, 46, 4189-4199.

Sigal, I. A., Flanagan, J. G., Tertinegg, I. & Ethier, C. R. 2004. Finite Element Modeling Of Optic Nerve Head Biomechanics. Invest Ophthalmol Vis Sci, 45, 4378-87.

Sigal, I. A., Flanagan, J. G., Tertinegg, I. & Ethier, C. R. 2005b. Reconstruction Of Human Optic Nerve Heads For Finite Element Modeling. Technol Health Care, 13, 313-29.

Sigal, I. A., Flanagan, J. G., Tertinegg, I. & Ethier, C. R. 2009. Modeling Individual-Specific Human Optic Nerve Head Biomechanics. Part Ii: Influence Of Material Properties. Biomech Model Mechanobiol, 8, 99-109.

Sigal, I. A., Yang, H., Roberts, M. D., Burgoyne, C. F. & Downs, J. C. 2011a. Iop-Induced Lamina Cribrosa Displacement And Scleral Canal Expansion: An Analysis Of Factor Interactions Using Parameterized Eye-Specific Models. Invest Ophthalmol Vis Sci, 52, 1896-907.

Sigal, I. A., Yang, H., Roberts, M. D., Grimm, J. L., Burgoyne, C. F., Demirel, S. & Downs, J. C. 2011b. Iop-Induced Lamina Cribrosa Deformation And Scleral Canal Expansion: Independent Or Related? Invest Ophthalmol Vis Sci, 52, 9023-32.

Silver, D., Miller, J., Harrison, R. & Prockop, D. J. 1992. Helical Model Of Nucleation And Propagation To Account For The Growth Of Type I Collagen Fibrils From Symmetrical Pointed Tips: A Special Example Of Self-Assembly Of Rod-Like Monomers. Proc Natl Acad Sci U S A, 89, 9860-4.

Sklenka, A. M., Levy, M. S. & Boivin, G. P. 2006. Effect Of Age On Collagen Fibril Diameter In Rabbit Patellar Tendon Repair. Comp Med, 56, 8-11.

Smalls, L. K., Randall Wickett, R. & Visscher, M. O. 2006. Effect Of Dermal Thickness, Tissue Composition, And Body Site On Skin Biomechanical Properties. Skin Res Technol, 12, 43-9.

Söderhäll, C., Marenholz, I., Kerscher, T., Rüschendorf, F., Esparza-Gordillo, J., Worm, M., Gruber, C., Mayr, G., Albrecht, M., Rohde, K., Schulz, H., Wahn, U., Hubner, N. & Lee, Y.-A. 2007. Variants In A Novel Epidermal Collagen Gene (Col29a1) Are Associated With Atopic Dermatitis. Plos Biology, 5, E242.

Soskel, N. T., Wolt, T. B. & Sandberg, L. B. 1987. Isolation And Characterization Of Insoluble And Soluble Elastins. Methods Enzymol, 144, 196-214.

Spina, M. & Garbin, G. 1976. Age-Related Chemical Changes In Human Elastins From Non-Atherosclerotic Areas Of Thoracic Aorta. Atherosclerosis, 24, 267-79.

Spina, M., Garbisa, S., Hinnie, J., Hunter, J. C. & Serafini-Fracassini, A. 1983. Age-Related Changes In Composition And Mechanical Properties Of The Tunica Media Of The Upper Thoracic Human Aorta. Arteriosclerosis, 3, 64-76.

Stallmach, A., Schuppan, D., Riese, H. H., Matthes, H. & Riecken, E. O. 1992. Increased Collagen Type Iii Synthesis By Fibroblasts Isolated From Strictures Of Patients With Crohn's Disease. Gastroenterology, 102, 1920-1929.

Stoller, P., Celliers, P. M., Reiser, K. M. & Rubenchik, A. M. 2003. Quantitative Second-Harmonic Generation Microscopy In Collagen. Appl Opt, 42, 5209-19.

Stone, N., Kendall, C., Shepherd, N., Crow, P. & Barr, H. 2002. Near-Infrared Raman Spectroscopy For The Classification Of Epithelial Pre-Cancers And Cancers. Journal Of Raman Spectroscopy, 33, 564-573.

Stone, N., Kendall, C., Smith, J., Crow, P. & Barr, H. 2004. Raman Spectroscopy For Identification Of Epithelial Cancers. Faraday Discuss, 126, 141-57; Discussion 169-83.

Stouffer, D. C., Butler, D. L. & Hosny, D. 1985. The Relationship Between Crimp Pattern And Mechanical Response Of Human Patellar Tendon-Bone Units. J Biomech Eng, 107, 158-65.

Streeten, B. W. & Licari, P. A. 1983. The Zonules And The Elastic Microfibrillar System In The Ciliary Body. Invest Ophthalmol Vis Sci, 24, 667-81.

Strouthidis, N. G. & Girard, M. J. 2013. Altering The Way The Optic Nerve Head Responds To Intraocular Pressure-A Potential Approach To Glaucoma Therapy. Curr Opin Pharmacol, 13, 83-9.

Sulzer, D., Mosharov, E., Talloczy, Z., Zucca, F. A., Simon, J. D. & Zecca, L. 2008. Neuronal Pigmented Autophagic Vacuoles: Lipofuscin, Neuromelanin, And Ceroid As Macroautophagic Responses During Aging And Disease. J Neurochem, 106, 24-36.

Sun, W., Chang, S., Tai, D. C. S., Tan, N., Xiao, G., Tang, H. & Yu, H. 2008. Nonlinear Optical Microscopy: Use Of Second Harmonic Generation And Two-Photon Microscopy For Automated Quantitative Liver Fibrosis Studies, Spie.

Suwabe, H., Serizawa, A., Kajiwara, H., Ohkido, M. & Tsutsumi, Y. 1999. Degenerative Processes Of Elastic Fibers In Sun-Protected And Sun-Exposed Skin: Immunoelectron Microscopic Observation Of Elastin, Fibrillin-1, Amyloid P Component, Lysozyme And Alpha1-Antitrypsin. Pathol Int, 49, 391-402.

Svidnicki, P. V., Braghini, C. A., Costa, V. P., Schimiti, R. B., De Vasconcellos, J. P. C. & De Melo, M. B. 2018. Occurrence Of Myoc And Cyp1b1 Variants In Juvenile Open Angle Glaucoma Brazilian Patients. Ophthalmic Genet, 39, 717-724.
Takema, Y., Yorimoto, Y., Kawai, M. & Imokawa, G. 1994. Age-Related Changes In The Elastic Properties And Thickness Of Human Facial Skin. Br J Dermatol, 131, 641-8.

Tamm, E. R. 2002. Myocilin And Glaucoma: Facts And Ideas. Prog Retin Eye Res, 21, 395-428.

Tamura, Y., Konomi, H., Sawada, H., Takashima, S. & Nakajima, A. 1991. Tissue Distribution Of Type Viii Collagen In Human Adult And Fetal Eyes. Invest Ophthalmol Vis Sci, 32, 2636-44.

Tanaka, S., Avigad, G., Brodsky, B. & Eikenberry, E. F. 1988. Glycation Induces Expansion Of The Molecular Packing Of Collagen. J Mol Biol, 203, 495-505.

Tang, S. S., Mohad, V., Gowda, M. & Thibeault, S. L. 2017. Insights Into The Role Of Collagen In Vocal Fold Health And Disease. Journal Of Voice, 31, 520-527.

Tatham, A. J., Weinreb, R. N., Zangwill, L. M., Liebmann, J. M., Girkin, C. A. & Medeiros, F. A. 2013. The Relationship Between Cup-To-Disc Ratio And Estimated Number Of Retinal Ganglion Cellscdr And Retinal Ganglion Cell Number. Investigative Ophthalmology & Visual Science, 54, 3205-3214.

Tezel, G. 2006. Oxidative Stress In Glaucomatous Neurodegeneration: Mechanisms And Consequences. Prog Retin Eye Res, 25, 490-513.

Tezel, G., Luo, C. & Yang, X. 2007. Accelerated Aging In Glaucoma: Immunohistochemical Assessment Of Advanced Glycation End Products In The Human Retina And Optic Nerve Head. Invest Ophthalmol Vis Sci, 48, 1201-11.
Tezel, G., Trinkaus, K. & Wax, M. 2004. Alterations In The Morphology Of Lamina Cribrosa Pores In Glaucomatous Eyes. British Journal Of Ophthalmology, 88, 251-256.

Thale, A., Tillmann, B. & Rochels, R. 1996. Sem Studies Of The Collagen Architecture Of The Human Lamina Cribrosa: Normal And Pathological Findings. Ophthalmologica, 210, 142-7.

Thornalley, P. J. 1998. Cell Activation By Glycated Proteins. Age Receptors, Receptor Recognition Factors And Functional Classification Of Ages. Cell Mol Biol (Noisy-Le-Grand), 44, 1013-23.

Tielsch, J. M., Katz, J., Sommer, A., Quigley, H. A. & Javitt, J. C. 1994. Family History And Risk Of Primary Open Angle Glaucoma. The Baltimore Eye Survey. Arch Ophthalmol, 112, 69-73.

Timpl, R. 1989. Structure And Biological Activity Of Basement Membrane Proteins. Eur J Biochem, 180, 487-502.

Toda, T., Tsuda, N., Nishimori, I., Leszczynski, D. E. & Kummerow, F. A. 1980. Morphometrical Analysis Of The Aging Process In Human Arteries And Aorta. Acta Anat (Basel), 106, 35-44.

Tomlin, S. G. & Worthington, C. R. 1956. Low-Angle X-Ray Diffraction Patterns Of Collagen. Proceedings Of The Royal Society Of London A: Mathematical, Physical And Engineering Sciences, 235, 189-201.

Tovar-Vidales, T., Wordinger, R. J. & Clark, A. F. 2016. Identification And Localization Of Lamina Cribrosa Cells In The Human Optic Nerve Head. Experimental Eye Research, 147, 94-97.

Tsamis, A., Krawiec, J. T. & Vorp, D. A. 2013. Elastin And Collagen Fibre Microstructure Of The Human Aorta In Ageing And Disease: A Review. J R Soc Interface, 10, 20121004.

Tsamis, A., Rachev, A. & Stergiopulos, N. 2011. A Constituent-Based Model Of Age-Related Changes In Conduit Arteries. Am J Physiol Heart Circ Physiol, 301, H1286-301.

Tsamis, A., Stergiopulos, N. & Rachev, A. 2009. A Structure-Based Model Of Arterial Remodeling In Response To Sustained Hypertension. J Biomech Eng, 131, 101004.

Tsuji, T. & Hamada, T. 1981. Age-Related Changes In Human Dermal Elastic Fibres. Br J Dermatol, 105, 57-63.

Tsurui, H., Nishimura, H., Hattori, S., Hirose, S., Okumura, K. & Shirai, T. 2000. Seven-Color Fluorescence Imaging Of Tissue Samples Based On Fourier Spectroscopy And Singular Value Decomposition. J Histochem Cytochem, 48, 653-62.

Tuma, R. 2005. Raman Spectroscopy Of Proteins: From Peptides To Large Assemblies. Journal Of Raman Spectroscopy, 36, 307-319.

Turner, N. J., Pezzone, D. & Badylak, S. F. 2015. Regional Variations In The Histology Of Porcine Skin. Tissue Eng Part C Methods, 21, 373-84.

Tzaphlidou, M., Cummings, C. & Chapman, J. A. 1992. A Study Of Staining For Electron Microscopy Using Collagen As A Model System—Ix. The Effect Of Tannic Acid Fixation. Micron And Microscopica Acta, 23, 25-35.

Ushiki, T. & Murakumo, M. 1991. Scanning Electron Microscopic Studies Of Tissue Elastin Components Exposed By A Koh-Collagenase Or Simple Koh Digestion Method. Arch Histol Cytol, 54, 427-36.

Uzel, S. G. & Buehler, M. J. 2009. Nanomechanical Sequencing Of Collagen: Tropocollagen Features Heterogeneous Elastic Properties At The Nanoscale. Integr Biol (Camb), 1, 452-9.

Uzel, S. G. & Buehler, M. J. 2009. Nanomechanical Sequencing Of Collagen: Tropocollagen Features Heterogeneous Elastic Properties At The Nanoscale. Integr Biol (Camb), 1, 452-9.

Veres, S. P. & Lee, J. M. 2012. Designed To Fail: A Novel Mode Of Collagen Fibril Disruption And Its Relevance To Tissue Toughness. Biophys J, 102, 2876-84.

Viidik, A. 1972. Simultaneous Mechanical And Light Microscopic Studies Of Collagen Fibers. Z Anat Entwicklungsgesch, 136, 204-12.

Vlassenbroeck, J., Dierick, M., Masschaele, B., Cnudde, V., Van Hoorebeke, L. & Jacobs, P. 2007. Software Tools For Quantification Of X-Ray Microtomography At The Ugct. Nuclear Instruments And Methods In Physics Research Section A: Accelerators, Spectrometers, Detectors And Associated Equipment, 580, 442-445.

Vogel, H. G. 1980. Influence Of Maturation And Aging On Mechanical And Biochemical Properties Of Connective Tissue In Rats. Mech Ageing Dev, 14, 283-92.

Vogel, K. G., Paulsson, M. & Heinegard, D. 1984. Specific Inhibition Of Type I And Type Ii Collagen Fibrillogenesis By The Small Proteoglycan Of Tendon. Biochem J, 223, 587-97.

Von Der Mark, K. 1981. Localization Of Collagen Types In Tissues. Int Rev Connect Tissue Res, 9, 265-324.

Vrabec, F. 1976. Glaucomatous Cupping Of The Human Optic Disk. Albrecht Von Graefes Archiv Für Klinische Und Experimentelle Ophthalmologie, 198, 223-234.

Wagenseil, J. E. & Mecham, R. P. 2007. New Insights Into Elastic Fiber Assembly. Birth Defects Res C Embryo Today, 81, 229-40.

Wagenseil, J. E. & Mecham, R. P. 2009. Vascular Extracellular Matrix And Arterial Mechanics. Physiological Reviews, 89, 957-989.

Wang, B., Nevins, J. E., Nadler, Z., Wollstein, G., Ishikawa, H., Bilonick, R. A., Kagemann, L., Sigal, I. A., Grulkowski, I. & Liu, J. J. 2013. In Vivo Lamina Cribrosa Micro-Architecture In Healthy And Glaucomatous Eyes As Assessed By Optical Coherence Tomography. Investigative Ophthalmology & Visual Science, 54, 8270-8274.

Wang, X., Li, X., Bank, R. A. & Agrawal, C. M. 2002. Effects Of Collagen Unwinding And Cleavage On The Mechanical Integrity Of The Collagen Network In Bone. Calcif Tissue Int, 71, 186-92.

Watson, J. M., Marion, S. L., Rice, P. F., Utzinger, U., Brewer, M. A., Hoyer, P. B. & Barton, J. K. 2013. Two-Photon Excited Fluorescence Imaging Of Endogenous Contrast In A Mouse Model Of Ovarian Cancer. Lasers Surg Med, 45, 155-66.

Weinreb, R. N. & Khaw, P. T. 2004. Primary Open-Angle Glaucoma. Lancet, 363, 1711-20.

Weiss, J. A. & Gardiner, J. C. 2001. Computational Modeling Of Ligament Mechanics. Crit Rev Biomed Eng, 29, 303-71.

Wender, R., Brown, A. M., Fern, R., Swanson, R. A., Farrell, K. & Ransom, B. R. 2000. Astrocytic Glycogen Influences Axon Function And Survival During Glucose Deprivation In Central White Matter. J Neurosci, 20, 6804-10.

Werth, V. P., Shi, X., Kalathil, E. & Jaworsky, C. 1996. Elastic Fiber-Associated Proteins Of Skin In Development And Photoaging. Photochem Photobiol, 63, 308-13.

Westerhof, N., Stergiopulos, N. & Noble, M. I. M. 2018. Snapshots Of Hemodynamics : An Aid For Clinical Research And Graduate Education.
Wigglesworth, V. B. 1975. Lipid Staining For The Electron Microscope: A New Method. J Cell Sci, 19, 425-37.

Williams, R. M., Zipfel, W. R. & Webb, W. W. 2005. Interpreting Second-Harmonic Generation Images Of Collagen I Fibrils. Biophysical Journal, 88, 1377-1386.

Winkler, M., Jester, B., Nien-Shy, C., Massei, S., Minckler, D. S., Jester, J. V. & Brown, D. J. 2010. High Resolution Three-Dimensional Reconstruction Of The Collagenous Matrix Of The Human Optic Nerve Head. Brain Res Bull, 81, 339-48.

Winlove, C. P., Ellis, R. E., Green, E. M., Petrov, P. G. & Bradley, D. A. 2004. The Organization Of Lipids In Monolayers At The Air–Water Interface Using Glancing Angle X-Ray Diffraction (Gixd). Radiation Physics And Chemistry, 71, 959-960.

Winlove, C. P., Parker, K. H., Avery, N. C. & Bailey, A. J. 1996. Interactions Of Elastin And Aorta With Sugars In Vitro And Their Effects On Biochemical And Physical Properties. Diabetologia, 39, 1131-1139.

Wolfs, R. C., Klaver, C. C., Ramrattan, R. S., Van Duijn, C. M., Hofman, A. & De Jong, P. T. 1998. Genetic Risk Of Primary Open-Angle Glaucoma. Population-Based Familial Aggregation Study. Arch Ophthalmol, 116, 1640-5.

Wong, M., Siegrist, M., Gaschen, V., Park, Y., Graber, W. & Studer, D. 2002. Collagen Fibrillogenesis By Chondrocytes In Alginate. Tissue Eng, 8, 979-87.

Worthington, C. R. & Inouye, H. 1985. X-Ray Diffraction Study Of The Cornea. International Journal Of Biological Macromolecules, 7, 2-8.

Wu, P.-J., Kabakova, I., Ruberti, J., Sherwood, J. M., Dunlop, I. E., Paterson, C., Török, P. & Overby, D. R. 2017. Brillouin Microscopy, What Is It Really Measuring? Arxiv Preprint Arxiv:1711.03312.

Yamamoto, S., Hashizume, H., Hitomi, J., Shigeno, M., Sawaguchi, S., Abe, H. & Ushiki, T. 2000. The Subfibrillar Arrangement Of Corneal And Scleral Collagen Fibrils As Revealed By Scanning Electron And Atomic Force Microscopy. Archives Of Histology And Cytology, 63, 127-135.

Yan, D. B., Coloma, F. M., Metheetrairut, A., Trope, G. E., Heathcote, J. G. & Ethier, C. R. 1994. Deformation Of The Lamina Cribrosa By Elevated Intraocular Pressure. Br J Ophthalmol, 78, 643-8.

Yan, X., Tezel, G., Wax, M. B. & Edward, D. P. 2000. Matrix Metalloproteinases And Tumor Necrosis Factor Alpha In Glaucomatous Optic Nerve Head. Arch Ophthalmol, 118, 666-73.

Yanagishita, M. 1993. Function Of Proteoglycans In The Extracellular Matrix. Acta Pathol Jpn, 43, 283-93.

Yang, H., Downs, J. C., Girkin, C., Sakata, L., Bellezza, A., Thompson, H. & Burgoyne, C. F. 2007. 3-D Histomorphometry Of The Normal And Early Glaucomatous Monkey Optic Nerve Head: Lamina Cribrosa And Peripapillary Scleral Position And Thickness. Invest Ophthalmol Vis Sci, 48, 4597-607.

Yang, H., Downs, J. C., Sigal, I. A., Roberts, M. D., Thompson, H. & Burgoyne, C. F. 2009. Deformation Of The Normal Monkey Optic Nerve Head Connective Tissue After Acute Iop Elevation Within 3-D Histomorphometric Reconstructions. Invest Ophthalmol Vis Sci, 50, 5785-99.

Yang, H., Williams, G., Downs, J. C., Sigal, I. A., Roberts, M. D., Thompson, H. & Burgoyne, C. F. 2011. Posterior (Outward) Migration Of The Lamina Cribrosa And Early Cupping In Monkey Experimental Glaucoma. Investigative Ophthalmology & Visual Science, 52, 7109-7121.

Yin, X., Peterson, J., Gravel, M., Braun, P. E. & Trapp, B. D. 1997. Cnp Overexpression Induces Aberrant Oligodendrocyte Membranes And Inhibits Mbp Accumulation And Myelin Compaction. J Neurosci Res, 50, 238-47.

Young, R. D., Knupp, C., Koudouna, E., Ralphs, J. R., Ma, Y., Lwigale, P. Y., Jester, J. V. & Quantock, A. J. 2019. Cell-Independent Matrix Configuration In Early Corneal Development. Experimental Eye Research, 187, 107772.

Zeimer, R. C. & Ogura, Y. 1989. The Relation Between Glaucomatous Damage And Optic Nerve Head Mechanical Compliance. Arch Ophthalmol, 107, 1232-4.

Zhang, J., Nou, X. A., Kim, H. & Scarcelli, G. 2017. Brillouin Flow Cytometry For Label-Free Mechanical Phenotyping Of The Nucleus. Lab On A Chip, 17, 663-670.

Zhang, L., Albon, J., Jones, H., Gouget, C. L., Ethier, C. R., Goh, J. C. & Girard, M. J. 2015. Collagen Microstructural Factors Influencing Optic Nerve Head Biomechanics. Invest Ophthalmol Vis Sci, 56, 2031-42.

Zhang, Q., Andrew Chan, K. L., Zhang, G., Gillece, T., Senak, L., Moore, D. J., Mendelsohn, R. & Flach, C. R. 2011. Raman Microspectroscopic And Dynamic Vapor Sorption Characterization Of Hydration In Collagen And Dermal Tissue. Biopolymers, 95, 607-15.

Zhou, L., Li, Y. & Yue, B. Y. 1999. Oxidative Stress Affects Cytoskeletal Structure And Cell-Matrix Interactions In Cells From An Ocular Tissue: The Trabecular Meshwork. J Cell Physiol, 180, 182-9.

Zhuo, S. M., Chen, J. X., Luo, T. S., Chen, H. L. & Zhao, J. J. 2007. High-Contrast Multimodel Nonlinear Optical Imaging Of Collagen And Elastin. Journal Of Physics: Conference Series, 48, 1476-1481.

Zimmermann, B. K., Timpl, R. & Küuhn, K. 1973. Intermolecular Cross-Links Of Collagen: Participation Of The Carboxy-Terminal Nonhelical Region Of The A1-Chain. European Journal Of Biochemistry, 35, 216-221.

Zimmermann, T. 2005. Spectral Imaging And Linear Unmixing In Light Microscopy. Microscopy Techniques. Springer.

Zimmermann, T., Marrison, J., Hogg, K. & O'toole, P. 2014. Clearing Up The Signal: Spectral Imaging And Linear Unmixing In Fluorescence Microscopy. Methods Mol Biol, 1075, 129-48.

Zimmermann, T., Rietdorf, J. & Pepperkok, R. 2003. Spectral Imaging And Its Applications In Live Cell Microscopy. Febs Letters, 546, 87-92.

Zimmermann, T., Rietdorf, J., Girod, A., Georget, V. & Pepperkok, R. 2002. Spectral Imaging And Linear Un-Mixing Enables Improved Fret Efficiency With A Novel Gfp2–Yfp Fret Pair. Febs Letters, 531, 245-249.

Zipfel, W. R., Williams, R. M. & Webb, W. W. 2003. Nonlinear Magic: Multiphoton Microscopy In The Biosciences. Nature Biotechnology, 21, 1369-1377.

Zipfel, W. R., Williams, R. M., Christie, R., Nikitin, A. Y., Hyman, B. T. & Webb, W. W. 2003a. Live Tissue Intrinsic Emission Microscopy Using Multiphoton-Excited Native Fluorescence And Second Harmonic Generation. Proceedings Of The National Academy Of Sciences, 100, 7075-7080.

Zoumi, A., Lu, X., Kassab, G. S. & Tromberg, B. J. 2004. Imaging Coronary Artery Microstructure Using Second-Harmonic And Two-Photon Fluorescence Microscopy. Biophysical Journal, 87, 2778-2786.

Zulliger, M. A., Fridez, P., Hayashi, K. & Stergiopulos, N. 2004. A Strain Energy Function For Arteries Accounting For Wall Composition And Structure. J Biomech, 37, 989-1000.